Technical Reports for Deepwater Horizon Water Column Injury Assessment

WC_TR.14: Modeling Oil Fate and Exposure Concentrations in the Deepwater Plume and Rising Oil Resulting from the Deepwater Horizon Oil Spill

Authors: Deborah French McCay, Katherine Jayko, Zhengkai Li, Matthew Horn, Yong Kim, Tatsu Isaji, Deborah Crowley, Malcolm Spaulding, Lauren Decker, Cathleen Turner, Stefanie Zamorski, Jeremy Fontenault, Rachel Shmookler, and Jill Rowe

Revised: September 29, 2015
Project Number: 2011-144
RPS ASA 55 Village Square Drive, South Kingstown, RI 02879

Table of Contents

List of Appendices

List of Figures

List of Tables

1 Executive Summary

Approach

The scope of the Deepwater Horizon (DWH) oil spill was extensive, with areas potentially affected including the entire Northeastern Gulf of Mexico. Oil released from the broken riser both dispersed at depth and rose through nearly a mile of water column before reaching the surface. In addition, there were logistical constraints in obtaining sufficient field sample data to completely characterize the contamination in space and time over and after the 87 days of oil and gas release. For these reasons, a modeling effort was undertaken to analyze the blowout, deepwater oil plume, rising oil droplets and fate of the spilled oil during its journey through the water column to (just below) the surface. The SIMAP (Spill Impact Model Application Package) oil fate model (French McCay 2003, 2004; described herein) was used to evaluate concentrations of oil and components in the water column encompassing the deepwater plume and rising oil resulting from the spill.

The modeling analysis began with pipe-discharge, blowout and droplet size sub-models (Spaulding et al. 2015) to evaluate the release conditions and the height above the discharge where the oil and gas plume had entrained enough water to become neutrally-buoyant with the surrounding seawater. At this so-called trap height, oil droplets were released into the water and rose at varying rates towards the surface according to their individual buoyancy. The analysis by Spaulding et al. (2015) provided the initial release conditions, i.e., oil mass and droplet sizes released at the trap height, that were used as input to the SIMAP oil fate model calculations.

For the water column exposure analysis, the three-dimensional SIMAP oil fate model estimated oil droplet and dissolved hydrocarbon concentrations in waters between 1,400 m and 20 m (below the water surface). Oil droplets reaching 20 m would rapidly surface to form floating oil slicks. The Trustees' evaluation of the oil fate and concentrations resulting from surface oil was based on observational data and chemistry measurements in surface waters (Travers et al. 2015a, b). The processes affecting surfaced oil and determination of hydrocarbon concentrations in the water column above 20 m are not evaluated herein.

The oil fate model estimates the distribution and mass of oil in the water column and on the sediments through time. Processes simulated by the physical fates modeling include oil droplet transport and dispersion, dissolution of soluble components into the water column, partitioning of oil between water and suspended particulate matter (SPM), sedimentation of oil droplets, and degradation. The model results provide estimates of water volumes that were exposed to hydrocarbon concentrations above several thresholds. The output of the fate model includes the concentrations of hydrocarbon constituents in the water and fluxes of hydrocarbons to the sediment over time. Concentrations of particulate (oil droplet) and dissolved hydrocarbon concentrations are saved to files for later viewing and calculations, as well as providing input data for exposure, toxicity, and biological effects evaluations.

In addition to the initial conditions provided by the blowout model (i.e., the locations, oil masses, and droplet sizes of the oil droplets released at the trap height), the oil fate model may utilize current data as an input. The IAS ROMS hydrodynamic model simulation provided currents from April to September of 2010 (Chao et al. 2014). These currents were used to evaluate the transport of oil in the water column below 1,100 m from the initial release at the trap height. This simulation provides time- and spatially-varying oil droplet and dissolved hydrocarbon component concentrations, describing the fate of the oil within a region identified as the "deep plume."

For the purposes of evaluating exposure and toxicity to water column biota (i.e., fish and invertebrate plankton), a simpler static approach without currents was utilized. The approach for evaluating toxicity in the water column (Morris et al. 2015a, b; Forth et al. 2015a) used daily mean total polycyclic aromatic hydrocarbon (PAH) concentrations in a three-dimensional spatial grid extending from 1400 m to 20 m. The currents used in the oil fate model simulation described above moves the oil contamination at each time step of the simulation. Plankton would be moving with the water and oil plume throughout the day. Thus, averaging concentrations over time at a particular location (i.e., for one static grid cell) would not characterize the exposures to plankton because the oil and plankton would be flowing through that cell together and be highly variable over time. Thus, for exposure calculations, the oil fate model was run without currents (i.e., Static Cone, with the larger oil droplets rising vertically, and the smaller oil droplets and dissolved components only dispersing by diffusive processes) to enable averaging of concentrations in each spatial grid cell for each day of the simulation. These cells were representative of the moving parcels of water that were affected by the oil (i.e., as if the modeled cells were allowed to move with the water). The underlying assumption is that the dissolved PAHs, oil droplets remaining in the water column, and the plankton all moved together. Therefore, the gridded daily-average concentrations, based on the simulation without currents, characterize the exposure experienced by plankton for each day as they moved with the oil plume. The plume was held in place within each grid cell in the simulation for the purposes of estimating plankton exposure.

Report Objectives

The objectives of this report are to describe:

- Oil transport and physical, chemical, and biological processes important to the fate of released oil as it rose through the water column and was transported in the deep plume;
- Algorithms used to quantify processes occurring below 20 m in the water column that are part of RPS ASA's oil fate model SIMAP;
- Data requirements and compiled input data for oil fate modeling;
- Available data that may be used to evaluate the oil fate model results and exposure concentrations produced; and
- Application to and validation of the model for the DWH spill, with model results that may be used for exposure and injury evaluations.

Observational Data Related to the DWH Spill

During the DWH blowout release, a considerable amount of oil was dispersed as oil droplets into the water column. The smaller droplets remained in the water column for an extended period of time due to their slow rise velocities, while larger droplets rose to the surface on the time scale of hours. The data reviewed in this report support the conceptual model that large droplets rose quickly in the immediate vicinity of the leaking wellhead, intermediate sized droplets extended further afield in the mid water column as they weathered and continued to rise through the water column, and a number of small droplets remained suspended in the deep water column intrusion layer (deep plume), where they weathered by dissolution processes, were colonized by microbes and degraded, and in some cases combined with SPM to eventually settle to the sea floor as marine snow. Observational data were compiled and reviewed for use in validation the model results.

Changes in the chemical composition of the MC252 oil at depth also support the preceding description of the transport of dissolved compounds, dispersed oil, and larger droplets. Most water soluble compounds such as benzene, alkylated mono-aromatics, and soluble C5-C10 alkanes were enriched in the deep plume. Compounds with lower water solubility were present both in the deep water and in the upper water column as mixtures of dissolved and particulate oil droplets.

Considerable spatial heterogeneity was evident in the observed distribution of hydrocarbons at various depths. These resulted from variations in the oil release rate and subsea dispersant applications over time (changing droplet size distributions of the oil over time), slow (< 5-20 cm/sec) but spatially- and temporally-varying currents (both horizontally and vertically), dissolution, dispersion, and degradation of hydrocarbon constituents, as well as irregularly positioned sampling stations and different sampled depths. The multiple plumes that were observed moving in various directions presumably originated at different times, and indicated that complex and meandering current patterns were present in the area before sampling.

Maximum hydrocarbon and dispersant concentrations were observed in samples taken at the surface (<20 m) and at depths between roughly 1,000 and 1,400 m deep (Payne and Driskel 2015a; Horn et al. 2015b). The highest observed values were near the wellhead, and the concentrations typically decreased as distance from the wellhead increased. While some surface observations of hydrocarbons exceeded method detection limits beyond 150 km from the wellhead, the majority of concentrations greater than 1-10 µg/L were within approximately 50 km of the wellhead. The highest concentrations at depth were of the BTEX group (i.e., benzene, toluene, ethylbenzene and xylene) and soluble alkanes. Elevated dispersant concentrations were also identified between 1,000-1,300 m.

While most attention has been focused on hydrocarbon concentrations near surface waters and the region between 1,000-1,300 m, it is important to note that elevated concentrations in excess of the method detection limits were identified in patchy “clouds” of particulate and dissolved hydrocarbons throughout the water column. Sampling in the depth range between 100-1,000 m was much more sporadic. The highest concentrations at depth in this region were for the BTEX group and soluble alkanes. The spatial extent in these intermediate waters is slightly more proximal to the wellhead, with highest concentrations observed typically within 25 km of the wellhead.

There were consistently observed fluorescence anomalies, as relative high values or “peaks”, at depths between approximately 1,000-1,300 m. Peak fluorescence values at depth typically tapered to lower values in shallower waters. It was very common to observe significantly elevated fluorescence values up to 600 m and occasionally shallower. There were also consistent anomalous dissolved oxygen (DO) “sags” (i.e., relatively low values of dissolved oxygen in vertical profiles when compared to baseline profiles) at depths between approximately 700-1,300 m, indicative of microbial degradation of released hydrocarbons, and in many cases the fluorescence peaks and DO sags were co-located.

The large gaps between sampling locations in space and time contributed to the considerable uncertainty of any interpolation of the sample concentrations in this dynamic environment. Furthermore, the sampling efforts to depict hydrocarbon distributions within the water column may be complicated by the unavoidable heterogeneity within the water column and sampling complications. For these reasons, sampling gaps in space and time can be quite difficult to interpret conclusively. Furthermore, there is no evidence of either the presence or absence of oil from regions that were not sampled.

Model Results and Validation

In the model simulations, the highest total hydrocarbon concentrations were near the wellhead (as was observed in field chemistry samples), decreasing with distance from the spill site as oil droplets rose to the surface, diluted and decayed. Smaller droplets were transported farther from the wellhead by currents before rising out of the modeled domain. Complex patterns can arise as rising droplets are transported and sheared by the variable currents at different depths. This makes the oil droplet (and resulting dissolved) concentrations highly patchy in three-dimensional space and time.

In April 2010, the oil was released in relatively large droplets, which rapidly rose to the surface. Because of the transient nature of large droplets, subsurface hydrocarbon concentrations below 20 m were only above 1 µg/L within a few km of the wellhead. Between May and July 2010, progressively smaller droplet sizes, produced by flow through small holes in the riser at the kink and due to subsea dispersant applications, increased hydrocarbon concentrations in waters below 20 m. Based on field sample observations (summarized in Appendix E), elevated concentrations extended further from the wellhead to at least 70 km from the well during June and July 2010.

The modeled concentrations of BTEX remaining in the oil droplets were very low throughout the simulations. Comparison of the BTEX content between the oil droplets and dissolved concentrations in the water column indicates that the BTEX was mostly in the dissolved phase at all depths of the water column and in highest concentrations below 1,100 m in the deep plume. BTEX dissolved quickly in the deep plume and at shallower depths as the oil droplets rose through the water column. The semi-soluble components (i.e., C2-benzenes, C3-benzenes, naphthalenes, low molecular weight alkanes, isoalkanes, and cycloalkanes) had partially dissolved while the oil droplets were at depths below 1,100 m, but there was additional dissolution as droplets continued to rise to shallower depths. The sparingly soluble 3-ring PAHs were primarily in the droplet phase in the simulations. Dissolved concentrations of PAH components were only >1 µg/L below 800 m. These partitioning patterns are consistent with the weathering models and analyses of chemistry samples, where dissolved and particulate fractions were measured (Payne and Driskell 2015a, b, c).

The highest hydrocarbon concentrations below 20 m were consistently measured in water samples taken at a depth of approximately 1,000-1,300 m. Elevated concentrations at depth were observed in each of the investigated chemical groups ranging from BTEX through PAHs to the soluble alkanes. When considered together, the total soluble compounds, the total investigated compounds, and PAH groups all had highest observed concentrations between 1,000-1,300 m. Elevated concentrations were also measured at shallower depths, however they had lower concentrations than those found between 1,000-1,300 m. The highest measurements of total investigated compounds in the deep plume were >100-700 µg/L, with concentrations up to ~80 µg/L between 200-1,000 m. When considered individually, soluble alkanes typically had the highest concentrations between 1,000-1,300 m with values of >100-400 µg/L, while BTEX were typically >100-200 µg/L, and PAHs were typically <120 µg/L. Peaks in fluorescence data and sags in dissolved oxygen data were observed between 1,000-1,300 m in the same depth zone where the highest BTEX and PAH concentrations were measured. The model-simulated hydrocarbons have similar distributions and concentrations.

The modeled concentrations of each of the oil components were compared to measurement data from chemistry samples collected for the NRDA chemistry program. Due to the differences between the modeled and actual field conditions and the patchiness of observed chemistry, there is the potential for displacement between modeled and observed concentrations in both

space and time. Therefore, a direct overlay of the detectable chemistry measurements on the model would be insufficient for evaluating if the concentrations predicted by the model were realistic and reliable for injury quantification. To account for likely displacement, results are plotted as probability distributions within a spatial and time window, containing a population of chemistry samples. The chemistry samples and modeled results were ordered by concentration so that the distributions could be compared.

Model versus observational chemistry comparisons were made for five vertical intervals within a 25 km by 25 km box centered on the wellhead. As components have different properties and dissolution rates, their concentration distributions varied. Therefore, in order to be meaningful, comparisons needed to be made on a component-by-component basis.

The modeled concentrations of the various components were generally of the same order of magnitude as the measured concentrations. In many instances, the frequency distributions of the modeled concentrations compared well to the frequency distribution of the measured samples. In some cases, the model overestimated concentrations, whereas in others it underestimates the concentrations described by the samples. However, the differences between observed and modeled concentrations were not large and there was no obvious bias, overall. As the modeled TPAH50 concentrations were carried forward into the analysis of toxicity (Morris et al. 2015a, b; Travers et al. 2015b) and injuries (French McCay et al. 2015), the comparisons of the PAH components AR5 through AR8 were of the most interest. The frequency distributions of the modeled and measured concentrations were more similar for PAH components than for some of the other components. Additionally, the frequency distributions of the concentrations produced by the two model simulations (with and without currents) in the 1100-1400 m depth interval (and within the 25 km by 25 km box centered on the wellhead) were very similar. These findings support the use of the Static Cone simulation for exposure evaluations. The magnitudes of the peak concentrations for the modeled and measured samples compared well, giving confidence that the concentrations used for exposure and toxicity evaluations were reliable.

Model Results for Use in Exposure Analysis

No currents were utilized as inputs to the model simulation used to determine the plankton exposure. However, the model did simulate dispersive spreading via turbulent mixing processes. The footprint of the deep plume and rising oil droplets was in the shape of an inverted cone, and the simulations are referred to herein as the Static Cone. The vertex of the cone was at the trap height and the widest radius was at 20 m below the water surface (the upper depth limit of the simulation). Rising oil droplets with the largest diameter were found in the center of the cone, along the cone axis. Progressively smaller droplets were found moving out from the cone axis due to the slower rise rates of smaller droplets, which increased their residence time and dispersion in the water column. Typical of dispersion from a central source, concentrations of oil and all components were highest along the axis, decreasing in a Gaussian shape toward the edges.

The results of the Static Cone simulation had the following features and trends.

- The volume of water contaminated with daily average TPAH50 > 0.5 μg/L increased rapidly in April and early May, when the kink holes developed and much more oil was released in smaller droplet sizes. This increase continued throughout the oil release period until about July 24, 9 days after the release was stopped.
- The TPAH50 dissolved over time, primarily from slowly rising droplets 100s of microns in diameter. The dissolved TPAH50 remained in the water column, building up over time,

while the droplets rose through the depth zones towards the surface. The fraction of oil mass released in droplets <100 μm, which would remain in the deep plume, was 5% on average, limiting the concentrations of TPAH50 in the deep plume somewhat.

- The dissolved TPAH50 degraded over time such that by September 30, 2010 (the end of the simulation), most of the TPAH50 in the water column below 20 m had degraded.
- The volume contaminated with daily averaged total TPAH50 > 0.5 μg/L is highest between 800-1100 m. Lower volumes were contaminated in shallower layers. A smaller volume was contaminated above 0.5 μg/L TPAH50 (daily averaged total) in the 1100-1400 m depth range than the value in the 800-1100 m range. The decrease is the result of the trap height of the plume intrusion layer, which for most of the released oil was at ~1200 m. Therefore the interval of 1100-1400 m only contained oil in a 100 m layer (1100-1200 m).
- The change with depth of the volume of water exceeding a daily average total TPAH50 of 0.5 μg/L and 1.0 μg/L is relatively modest, whereas for a higher threshold daily average total TPAH50 of 79 μg/L, only the deep water layers below 800 m exceed the thresholds.

Table 1-1 lists the maximum volume of water where the daily average total TPAH50 concentration exceeded the indicated threshold in each the indicated depth zones, estimated for the entire simulation of the Static Cone. The volumes for total TPAH50 at these and other thresholds (formulated as dose-response curve toxicity models, Morris et al. 2015a, b) were used for exposure and mortality calculations (see French McCay et al. 2015 for a summary). Water volumes exceeding daily average TPAH50 thresholds (0.5 μg/L and 1.0 μg/L), as well as the maximum concentrations at any time step, were quite similar, although at higher thresholds more sensitivity to this input was found.

Table 1-1. Maximum volume of water where the daily average total TPAH50 concentration exceeded the indicated threshold, estimated for the entire simulation of the Static Cone in each of the depth zones.

Depth Range	Volume (m^3) >0.5 ug/L	Volume (m^3) >1 ug/L
20-200 m	3.44×10^9	1.96×10^9
200-500m	7.78×10^9	4.63×10^9
500-800m	1.06×10^{10}	6.92×10^9
800-1100 m	1.17×10^{10}	8.08×10^9
1100-1400 m	3.52×10^9	2.61×10^9
40-1400 m	3.60×10^{10}	2.34×10^{10}

2 Introduction and Approach

2.1 Introduction

Oil released from the Deepwater Horizon (DWH) oil spill both dispersed at depth and rose through nearly a mile of water column. The composition of the released gas-liquid mixture changed over time and space as the result of dilution, changes in pressure, dissolution, and the addition of dispersants. Oil droplets and dissolved components were transported large distances at various levels of the water column. Subsurface oil also picked up sediments and other particulate matter from the water column, a portion of which became neutrally or negatively buoyant, sinking to various depths. The oil dispersed at the wellhead (both via turbulence and by injection of dispersants) was transported by currents that varied in time and space. This yields a complex pathway of subsurface oil contamination that affected abyssal, bathypelagic, and mesopelagic waters of the Gulf of Mexico.

Consideration of the movements and fate of subsurface oil are important in the evaluation of pathway to and exposure of aquatic organisms in the water column to contaminants from the DWH spill. Soluble and semi-soluble hydrocarbons (primarily monoaromatic hydrocarbons (MAHs) and PAHs), but also including low molecular weight alkanes) dissolved from oil droplets into the water column over time. The rates of dissolution of hydrocarbons from rising and surface-entrained oil droplets are functions of the droplet sizes present (because it involves mass transfer across the surface area of the droplet); thus, the amount of hydrocarbon mass dissolved is a function of the oil mass and droplet size distribution. Dissolution rates are a function of soluble hydrocarbon content of the oil, oil-water interfacial tension (which is reduced by surfactant dispersants), and the energy in the system (the higher the energy the smaller the droplets). Large droplets (greater than a few hundred microns in diameter) would have surfaced rapidly (in hours), whereas smaller droplets would have remained in the water column for progressively longer times. Dissolution from small droplets is rapid and significantly enhanced by the application of dispersants (Payne and Driskell 2015c). Thus, exposure of water column biota to smaller droplets and dissolved components was much more wide spread than it was to the surfacing large droplets.

The objectives of this report are to describe:

- Oil transport and physical, chemical, and biological processes important to the fate of released oil as it rose through the water column and was transported in the deep plume (Sections 3.1 and 3.2.1);
- Algorithms used to quantify the processes affecting oil concentrations below 20 m that are part of RPS ASA's oil fate model SIMAP (Sections 3.2.2 and Appendix A);
- Data requirements and compiled input data for oil transport and fate modeling (Section 4);
- Available data that may be used to evaluate the pathways of oil, fate of oil components, and exposure concentrations in the water column (Section 5, Appendix E);
- Application to and validation of the model for the DWH spill (Section 6); and
- Model results that may be used for exposure and injury evaluations (Section 6.4).

2.2 Modeling Approach

A modeling analysis of the transport and fate of the spill in waters below 20m was undertaken, using the SIMAP oil fate model (French McCay 2003, 2004; described herein), to evaluate concentrations of oil and components (e.g., PAHs) in the water column. Pipe-discharge, blowout and droplet size models (Spaulding et al. 2015) were used to provide needed initial release conditions (i.e., oil mass and droplet sizes released at depth from the blowout) to the SIMAP oil fate model calculations.

Figure 2-1 is a schematic of the conceptual model of the blowout and rising oil droplet phases, whereby oil moved upward through the water column. The initial jet phase coming out of the broken riser is governed by the momentum of the oil and gas coming out of a well. In the buoyant plume phase, seawater is entrained into the oil and gas plume, which remains buoyant and rises until the fluid reaches the density of the surrounding water at the trap height. Oil droplets are released from the buoyant plume (oil-gas-water) at the trap height, and subsequently rise according to their individual buoyancy. The smaller droplets rise more slowly, such that they are progressively transported by currents farther from the rising large droplets, forming an inverted cone. Large droplets are found in the center of the cone and more dispersed smaller droplets are found farther out and up in the water column. Oil reaching the sea surface is initially opaque (typically black or brown) and very fluid. Once on the surface, volatile components can rapidly evaporate, after which the oil can form higher-viscosity water-in-oil emulsions, or mousse. Sheens can form from the spreading oil or from the mousse.

The core model is based on the SIMAP oil fate model (French McCay 2003, 2004); several other models provide needed input to the SIMAP oil fate model calculations. The blowout model (RPS ASA Technical Report: Spaulding et al. 2015) evaluates the jet and buoyant plume of the oil and gas release near to the wellhead and broken riser. This “near field” model follows the movements of the oil and gas as it comes out of holes in the riser pipe as a jet. The model characterizes the release as it entrains surrounding sea water and rises as a buoyant oil-gas-water plume until the plume reaches neutral buoyancy. At this point, the density of the oil-gas-water plume has increased enough to match the surrounding seawater. At the neutral-buoyancy depth (trap height), the oil droplets separate from the buoyant plume and are transported horizontally by currents and vertically by their individual buoyancies. At this stage the blowout model outputs the locations (i.e., trap height), oil masses, and droplet sizes of the released oil droplets. These are then used as inputs to the (far field) oil transport and fate model (SIMAP).

For the water column exposure analysis, the SIMAP oil fate model was used to estimate oil droplet and dissolved hydrocarbon concentrations from the trap height to 20 m below the water surface. Oil droplets reaching 20 m would rapidly surface to form floating oil slicks. The Trustee’s evaluation of the oil fate and concentrations resulting from surfaced oil was based on observational data and chemistry measurements in surface waters. Therefore, processes affecting surfaced oil and concentrations in the water column above 20 m are not evaluated herein.

The oil fate model estimates the distribution and mass of oil in the water column and on the sediments through time. Processes simulated by the physical fates modeling include oil droplet transport and dispersion, dissolution of soluble components into the water column, partitioning of oil between water and SPM, sedimentation of oil droplets, and degradation. In the model, the oil is treated as being comprised of 9 soluble (and volatile, including 8 aromatic and 1 aliphatic) and 9 insoluble (8 volatile and one non-volatile residual oil) saturated components, described in Section 3.1.

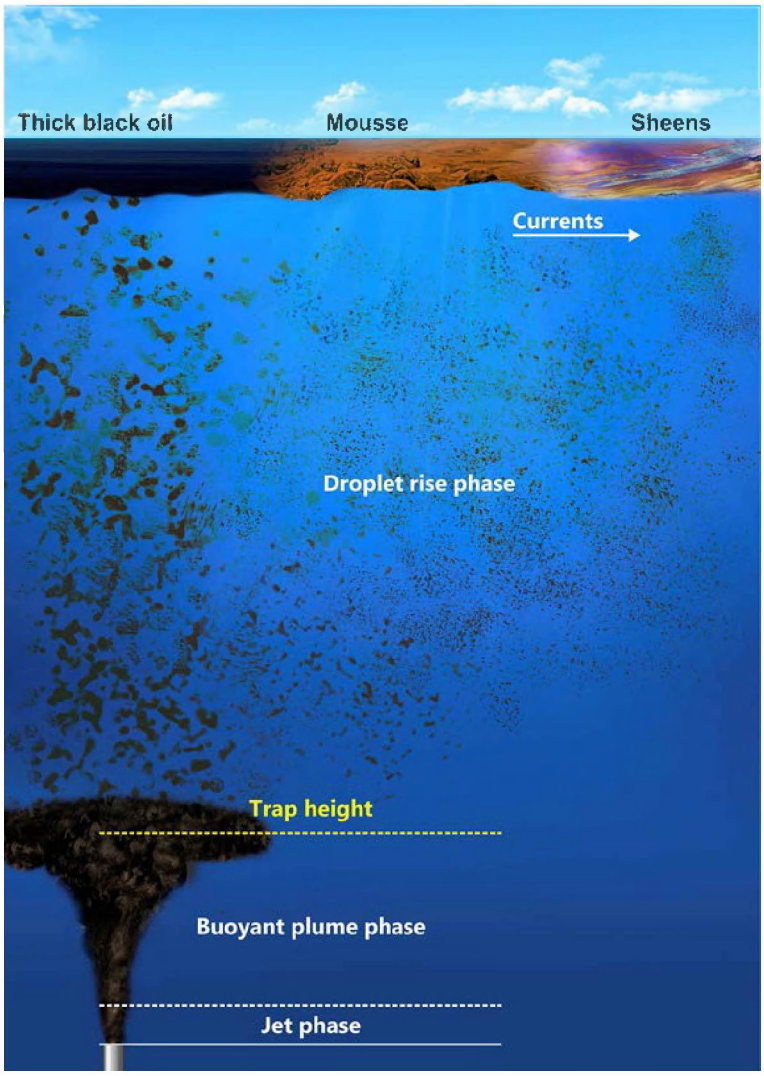

Figure 2-1. Conceptual model of the near-field blowout and rising oil droplet phases whereby oil moved upward through the water column.

For model input, bathymetry of the Gulf of Mexico was obtained from NOAA's National Geophysical Data Center (NGDC) and gridded at 600 m resolution. Water temperature and salinity vary spatially, with depth, and by month. Climatic monthly mean water temperature and salinity data sets were obtained from the National Oceanographic Data Center (NODC) Ocean Climate Laboratory's Monthly Climatology for the Gulf of Mexico and used to develop model inputs. Oil property specifications were based on measurements of the source oil by Stout (2015a, b). The total amount of oil released to the water column was 3.19 million barrels, based on the Phase II Court findings (USDC 2015). The oil was released into the (SIMAP) model from April 22 to July 15, 2010, using relative release volume fractions based on the analysis by the Flow Rate Technical Group (FRTG, McNutt et al. 2011). The effects of subsea dispersant applications are accounted for in the nearfield blowout modeling (Spaulding et al. 2015).

Degradation rates for each component and compartment are based on data obtained from literature reviews that included estimates for compounds and/or components of MC252 oil and crude oil generally.

The model results provide estimates of water volumes exposed above various thresholds. The output of the fate model includes the concentrations of hydrocarbon constituents in water and fluxes of hydrocarbons to sediment over time. Concentrations of particulate (oil droplet) and dissolved aromatic concentrations are saved to files for later viewing and calculations. Concentration files are also used for exposure and toxicity evaluations (Morris et al. 2015b; Travers et al. 2015b), the results of which were utilized in the injury quantification for plankton (French McCay et al. 2015).

In addition to the initial conditions provided by the blowout model (i.e., the locations, oil masses, and droplet sizes of the oil droplets released at the trap height), the oil fate model may utilize current data as input. Current data are available for the offshore continental slope area of the northern Gulf of Mexico from Acoustic Doppler Current Profilers (ADCPs) that were moored or attached to offshore platforms and are included in NOAA's online data sets. Other field data designed to measure currents are also available for 2010. However, these current data sets do not adequately characterize shelf waters or the parts of the Gulf of Mexico outside of areas with direct measurement data. Thus, several existing hydrodynamic models were evaluated for use in the modeling of transport. The IAS ROMS model simulation of currents from April to September of 2010 (Chao et al. 2014) was used to evaluate transport and fate of oil in the deepwater plume. This simulation provides time- and spatially-varying oil droplet and dissolved hydrocarbon component concentrations in waters below 1,100 m.

However, for the purposes of evaluating exposure and toxicity to water column biota (i.e., fish and invertebrate plankton), a simpler approach was utilized. The approach for evaluating toxicity (Morris et al. 2015a,b; Forth et al. 2015a) used daily mean hydrocarbon (PAH) concentrations in a three-dimensional spatial grid extending from 1,400 m to 20 m in the water column. Because the use of currents in the oil fate model moves the oil contamination each time step of the simulation, averaging over time at a particular location (i.e., for one static grid cell) would not characterize exposures to plankton moving with the oil plume throughout the day. Thus, the oil fate model was run without currents (referred to as the Static Cone simulation) to enable averaging of concentrations in each spatial grid cell for each day of the simulation, representative of the moving parcels of water affected by the oil. The assumption is that the dissolved hydrocarbons, oil droplets remaining in the water column, and the plankton all moved together. The gridded daily-average concentrations, based on the simulation without currents, characterize the exposure experienced by plankton each day as they moved with the oil plume. The plume was held in place in the simulation for the purposes of estimating plankton exposure.

2.3 SIMAP Model Background

The SIMAP (Spill Impact Model Analysis Package) oil trajectory and fate model developed by Applied Science Associates (now RPS ASA) originated from the oil fate submodel in the Natural Resource Damage Assessment Model for Coastal and Marine Environments (NRDAM/CME), which ASA developed in the early 1990s for the U.S. Department of the Interior for use in "type A" Natural Resource Damage Assessment (NRDA) regulations under the Comprehensive Environmental Response, Compensation and Liability Act of 1980 (CERCLA). The most recent version of the type A model, the NRDAM/CME (Version 2.4, April 1996) was published as part of the CERCLA type A NRDA Final Rule (Federal Register, May 7, 1996, Vol. 61, No. 89, p.

20559-20614). The technical documentation for the NRDAM/CME is in French et al. (1996). This technical development involved several in-depth peer reviews, as described in the Final Rule.

While the NRDAM/CME was developed for simplified natural resource damage assessments of small spills in the United States, SIMAP (French McCay 2002, 2003, 2004, 2009) is designed to evaluate fates and effects of both real and hypothetical spills in marine, estuarine and freshwater environments worldwide. Additions and modifications to SIMAP were made to increase model resolution, allow modification and site-specificity of input data, allow incorporation of temporally varying current data, evaluate subsurface releases and movements of subsurface oil, track multiple chemical components of the oil, enable stochastic modeling, and facilitate analysis of results.

Below is a description of the subsurface portion of the oil trajectory and fate model in SIMAP. Additional information may be found in French McCay (2003, 2004) and the NRDAM/CME Technical Report (Version 2.4, April 1996; French et al. 1996); and in Appendix A. The model has been validated with more than 20 case histories, including the *Exxon Valdez* and other large spills (French and Rines 1997, French McCay 2003, 2004, French McCay and Rowe 2004) as well as test spills designed to verify the model (French et al. 1997).

3 Description of Oil Transport and Fate Processes and Model

3.1 Oil Fate Model Design

The SIMAP three-dimensional oil fate model estimates distribution (as mass and concentrations) of whole oil and oil components on the water surface, on shorelines, in the water column, and in sediments. Oil fate processes included in SIMAP are oil spreading (gravitational and by shearing), evaporation, transport, randomized dispersion, water-in-oil emulsification, entrainment (natural and facilitated by dispersant), dissolution, volatilization of dissolved hydrocarbons from the surface water, adherence of oil droplets to SPM, adsorption of soluble and semi-soluble aromatics to SPM, sedimentation, and degradation. In this report, only the processes applicable to waters below 20 m are described.

Oil is a mixture of tens of thousands of hydrocarbons of varying physical and chemical characteristics. Thus, oil hydrocarbons have varying fates. In the model, oil is represented by component categories, and the fate of each component is tracked separately. The "pseudo-component" approach (Payne et al. 1984, 1987, French et al. 1996, Jones 1997, Lehr et al. 2010) is used, where chemicals in the oil mixture are grouped by physical-chemical properties, and the resulting component category behaves as if it were a single chemical with characteristics typical of the chemical group.

The oil fates model focuses on tracking the lower molecular weight soluble and semi-soluble hydrocarbons divided into chemical groups (components) based on volatility, solubility, and hydrophobicity (using the octanol-water partition coefficient (K_{ow}) of the chemicals). The water solubility of compounds having $\log(K_{ow})$ values greater than about 6 is very limited (Di Toro et al. 2000, French McCay 2002). In the model, the oil is treated as comprising aliphatic and aromatic components with $\log(K_{ow}) < 6$ (defined in Table 3-1; included compounds are listed in Table 3-2). All but the residual oil component (representing non-volatile and insoluble aromatics and aliphatics) dissolve at rates specific to the component. Solubility is strongly correlated with volatility, and the solubility of aromatics is higher than aliphatics of the same volatility (Appendix B). Of the aromatics, the MAHs are the most soluble, the 2-ring PAHs are less soluble, and the 3-ring PAHs slightly soluble (Mackay et al. 1992, 2006a,b). The solubility of the aliphatic hydrocarbons is much less than for the aromatics of similar molecular weight. Dissolved concentrations are calculated in the model for each of the soluble and semi-soluble components (named AR1 to AR9). Note that non-aromatic (aliphatic) compounds that are soluble (i.e., C1-C10 n-alkanes, isoalkanes and cycloalkanes) are included in the "AR9" component.

The initial (at the point of release to the water column) mass concentrations of the eight aromatic components (AR1 - AR8) and the soluble aliphatic component (AR9) are computed using measured source oil sample concentrations. The mass concentrations of the eight non-soluble aliphatic components (AL1 - AL8) were based on measured weight fractions of a boiling curve for fresh source oil, using the boiling point ranges listed in Table 3-2. For components AL1 and AL2, all of the measured compounds are soluble, and so their mass concentrations were included in component AR9. Thus, AL1 and AL2 represent unmeasured compounds in their respective boiling ranges (where solubility is unknown and not considered in the model). This approach avoids "double counting" aliphatics that would otherwise be included in AL1 and AL2 as well as AR9. Component AL9 is reserved for tracking dispersant component(s) or other

contaminants. Each of the components is tracked in both the whole oil (droplets and floating) and dissolved phases.

This number of components provides sufficient resolution and accuracy for the dissolution calculations, particularly given the time frame (minutes) over which these processes occur. The simplistic alternative of treating oil as a single compound with empirically-derived rates (e.g., Mackay et al. 1980, Stiver and Mackay 1984) does not provide sufficient accuracy for environmental effects analyses because soluble and semi-soluble hydrocarbons have specific properties that differ from the other volatile and insoluble compounds. The model has been validated for predicting dissolved concentrations from several spills, supporting the adequacy of the use of this number of components (French McCay 2002, 2003).

Table 3-1. The 19 pseudo-components modeled in the SIMAP oil fates model, including definition of 9 soluble/semi-soluble and volatile/semi-volatile components defined by log(Kow) range, volatile aliphatic hydrocarbons (HCs) by boiling point (BP) range in 9 distillation cuts, 8 insoluble and volatile/semi-volatile aliphatic components, 1 dispersant constituent component, and 1 residual oil component. (*Comprised of unmeasured non-soluble compounds in the BP range.)

AR or AL	All HCs	Soluble and semi-soluble HCs (AR Components)		Non-soluble aliphatic HCs (AL Components)	
Compo-nent #	Volatility	Compounds	Range of log(K_{ow})	Compounds	BP Range (°C)
1	Volatiles	MAHs (BTEX)	1.9-2.8	Volatile aliphatics *	< 150
2		C3-benzenes	2.8-3.6	Volatile aliphatics *	150-180
3	Intermediate Volatility	C4-benzenes	3.1-3.8	Semi-volatile aliphatics (C11)	180-200
4		Decalins	4.1-6.0	Semi-volatile aliphatics (C12)	200-230
5		C0-C2 Naphthalenes	2.3-4.3	Semi-volatile aliphatics (C13-C16)	230-280
6	Semi-Volatile	C3-C4 Naphthalenes	4.2-5.20	Low volatility aliphatics (C17-C18)	280 - 300
7		Fluorenes & C0-C1 3-ring PAHs	4.0-5.6	Low volatility aliphatics (C19-C20)	300-350
8		4-ring PAHs & C2-C3 3-ring PAHs	4.9-6.0	Low volatility aliphatics (C21-C23)	350-380
9	Highly Volatile and Soluble Aliphatics	Low MW Alkanes, Isoalkanes, Cycloalkanes	2.3-5.6	N.A. (Used for Dispersant Indicators)	<180
Residual	Residual (non-volatile)	High MW PAHs	>6.0	High molecular weight aliphatics (C24+)	>380

The soluble and semi-soluble hydrocarbons that dissolve from the whole oil are further are partitioned in the water column between the water phase and SPM according to equilibrium partitioning theory (French et al. 1996, French McCay 2004). The residual fractions in the model are composed of non-volatile and insoluble compounds that remain in the "whole oil" droplets.

Table 3-2. Code designations and included compounds for the 19 pseudo-components. [BP = boiling point].

Code	Group	Includes
AR1	BTEX	BTEX, styrene
AR2	C3-benzenes	C3-benzenes
AR3	C4-benzenes	C4-benzenes
AR4	Decalins	cis/trans decalin to C4-decalin
AR5	C0-C2 Naphthalenes	C0-C2 Naphthalenes, C0-C2 Benzothiophenes, biphenyl, acenaphthene, acenaphthylene
AR6	C3-C4 Naphthalenes	C3-C4 Naphthalenes, C3-C4 Benzothiophenes, dibenzofuran
AR7	Fluorenes & C0-C1 3-ring PAHs	C0-C3 Fluorenes, C0-C1 dibenzothiophenes, C0-C1 phenanthrenes
AR8	4-ring PAHs & C2-C3 3-ring PAHs	C0-C2 pyrenes & fluoranthenes, C2-C3 dibenzothiophenes, C2-C3 phenanthrenes, chrysene
AR9	Soluble alkanes	Low mol. wt. Alkanes, Isoalkanes, Cycloalkanes
AL1	Aliphatics: BP < 150	(unmeasured compounds)
AL2	Aliphatics: BP 150-180	(unmeasured compounds)
AL3	Aliphatics: BP 180-200	C11 Alkanes
AL4	Aliphatics: BP 200-230	C12 Alkanes
AL5	Aliphatics: BP 230-280	C13-C16 Alkanes
AL6	Aliphatics: BP 280-300	C17-C18 Alkanes
AL7	Aliphatics: BP 300-350	C19-C20 Alkanes
AL8	Aliphatics: BP 350-380	C21-C23 Alkanes
AL9	Dispersant indicator(s)	(dispersant indicator(s) on oil droplets)
Residual	Residual	Other non-volatile, non-soluble hydrocarbons

3.2 Oil Fate Model Processes In the Water Column Below 20m

3.2.1 Overview

The schematic in Figures 3-1 depicts oil fate processes simulated by the SIMAP model in the water column below 20 m. The oil separates into different phases or parts of the environment:

- Oil droplets suspended in the water column
- Oil adhering to SPM in the water
- Dissolved lower molecular weight components (MAHs, PAHs, and other soluble components) in the water column
- Oil on and in the sediments

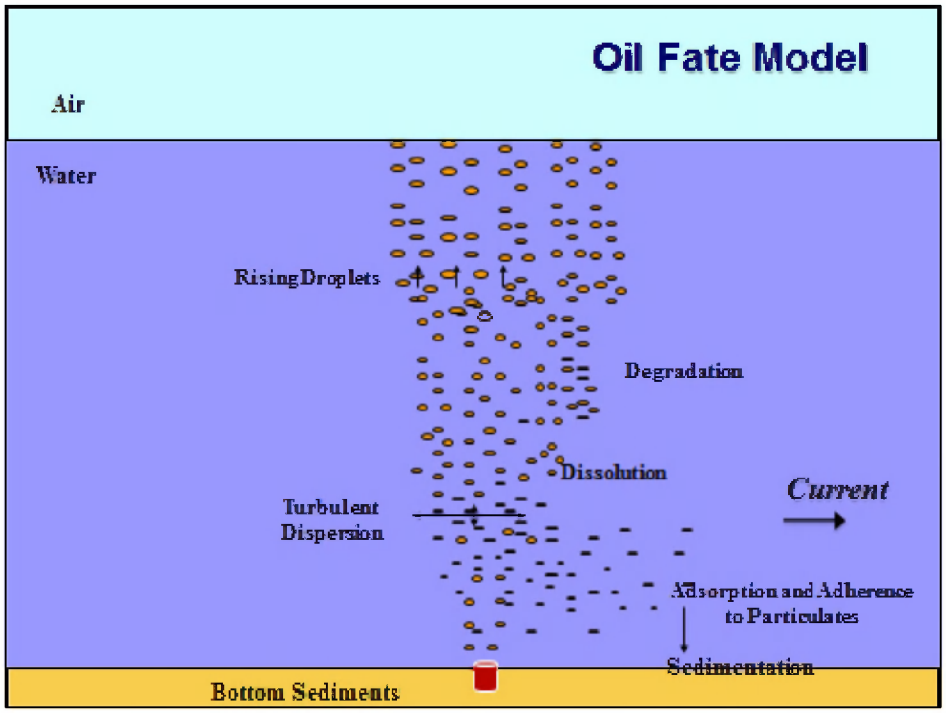

Figure 3-1. Oil fate processes for subsurface oil originating from the blowout plume.

Below are descriptions of the applicable processes:

- **Transport** is the process where oil droplets and dissolved constituents are carried by ambient currents. Subsurface oil droplets also rise due to their buoyancy or sink if combined with SPM such that the combined specific gravity of the oil-SPM is greater than that of the surrounding seawater.
- **Turbulent dispersion**: Typically there are also "sub-scale" currents (not characterized by the current data), better known as turbulence that move oil and mix it in three dimensions. The process by which turbulence mixes and spreads oil components in the water column is called turbulent dispersion.
- **Dilution** occurs when water of lower concentration is mixed into water with higher concentration by turbulence and currents.
- **Dissolution** is the process where water-soluble components diffuse out of the oil into the water. Dissolution rate increases the higher the surface area of the oil relative to its volume. As the surface area to volume ratio is higher for smaller than larger spherical droplets, the smaller the droplets the higher the dissolution rate. Higher turbulence and the application of dispersant creates smaller oil droplets. In deep water when oil droplets suspended or rising for some period of time, there is no chance for evaporation to compete with dissolution and the soluble components dissolve readily and exclusively. Smaller dispersant-treated droplets generated by subsurface dispersant treatment release PAH to the dissolved phase faster than non-treated oil (Payne and Driskell 2015c; Spaulding et al. 2015).
- **Adsorption** of dissolved components to SPM in the water occurs, with less adsorption occurring for higher solubility compounds. Higher-molecular-weight MAHs and PAHs with higher degrees of alkyl substitution preferentially adsorb to particulates when the

latter are present. The higher the concentration of SPM, the more adsorption. Also, the higher the molecular weight of the compound, the less soluble, and the more the compound adsorbs to particulate matter.

- **Adherence** is the process where oil droplets combine with SPM in the water. If the particles are suspended sediments, the combined oil/suspended sediment agglomerate is heavier than the oil itself or the water. If turbulence subsides sufficiently, the oil-sediment agglomerates will settle. Adherence may also occur to particulate organic matter. Those combined particles are of variable buoyancy, but much closer to neutrally buoyant than are the oil/suspended sediment agglomerates.
- **Sedimentation** (settling) is the process where oil-SPM agglomerates and SPM with adsorbed soluble and semi-soluble hydrocarbon components settle to the bottom sediments. Adherence and sedimentation may have been an important process in the deep water areas surrounding the MC252 release, as particulate organic matter and drilling muds were present at times in the water column in much higher-than-baseline concentrations. Generally, oil-sediment agglomerates transfer more soluble and semi-soluble hydrocarbons to the bottom than SPM with oil constituents that were adsorbed from the dissolved phase in the water column.
- **Resuspension** of settled oil-sediment particles and particles with adsorbed soluble and semi-soluble hydrocarbons may occur if current speeds and turbulence exceed threshold values where cohesive forces can be overcome.
- **Degradation** is the process where oil components are changed either chemically or biologically (biodegradation) to another compound. It includes breakdown to simpler organic carbon compounds by bacteria and other organisms, photo-oxidation by solar energy (near the water surface), and other chemical reactions.

When oil is released underwater, as it was in the case of the DWH spill, it forms droplets of varying sizes. The more turbulent are the conditions, the smaller the droplet sizes that are released. From Stoke's Law, larger droplets rise faster and surface whereas the smallest droplets remain in the water permanently.

While the droplets are under water, dissolution of the light and soluble components occurs. Dissolution rate is a function of the surface area available. Thus, most dissolution occurs from small as opposed to large droplets, since smaller droplets have a higher surface area to volume ratio. Chemical dispersants decrease the oil droplet size and so increase the dissolution rate of soluble components.

These processes that increase the rate of supply of dissolved constituents are balanced by dispersion and losses from the water column: (1) adsorption to SPM and sedimentation and (2) degradation (photo-oxidation or biologically mediated). Thus, the model-predicted concentrations are the resulting balance of all these processes based on our quantitative understanding of the individual processes.

3.2.2 Oil Fate Algorithms Applicable to Modeling Rising Oil and the Deep Plume

The algorithms used to model the processes applicable to the deep plume and rising oil up to 20 m below the surface are described in Appendix A and summarized below. Lagrangian elements (LEs, called "spillets") are used to simulate the movements of oil components in three dimensions over time. Oil droplets and dissolved components are tracked in separate spillets.

3.2.2.1 Oil Transport

Transport is the sum of advective velocities by currents input to the model, vertical movement according to buoyancy, and randomized turbulent diffusive velocities in three dimensions. The horizontal and vertical diffusion coefficients are model inputs. For each model time step, the new vector position of the spillet center is calculated from the old plus the vector sum of east-west, north-south, and vertical components of advective and diffusive velocities:

$$X_t = X_{t-1} + \Delta t\,(U_t + D_t + R_t)$$

where X_t is the vector position at time t, X_{t-1} is the vector position the previous time step, Δt is the time step, U_t is the sum of all the advective (current) velocity components in three dimensions at time t, D_t is the sum of the randomized diffusive advective velocities in three dimensions at time t, and R_t is the rise or sinking velocity of suspended whole oil droplets (with associated SPM and water) in the water column. The magnitudes of the components of D_t are scaled by horizontal and vertical diffusion coefficients (Okubo and Ozmidov 1970, Okubo 1971, equations are described in Appendix A). R_t is computed by Stoke's law, where velocity is related to the difference in density between the particle and the water, and to the particle diameter. Appendix A provides equations used for transport.

3.2.2.2 Dissolution

Dissolution is the process by which soluble hydrocarbons enter the water from subsurface oil droplets. The lower molecular weight hydrocarbons tend to be more soluble than those of higher molecular weight. Dissolution can be significant from subsurface droplets because of the lack of atmospheric exposure.

The modeling approach developed by Mackay and Leinonen (1977) is used in SIMAP for dissolution. The oil droplet is treated as a sphere, with a mass flux (Hines and Maddox 1985) related to solubility and temperature. It assumes a well-mixed layer with most of the resistance to mass transfer lying in an assumed stagnant region close to the oil. The dissolution algorithm was developed in French et al. (1996) and is described in Appendix A. The algorithm simulates the higher dissolution rates that occur from smaller droplets created by dispersant application and high turbulence. Payne and Driskell (2015c) found that dispersants injected at depth during spill response increased the abiotic dissolution of PAH compared to non-dispersant-treated oil.

3.2.2.3 Adsorption, Adherence and Sedimentation

Algorithms for adsorption and sedimentation are described in Appendix A. Aromatics dissolved in the water column are to some extent carried to the sediments by adsorption to SPM and subsequent settling. The ratio of adsorbed (C_a) to dissolved (C_{dis}) concentrations is computed from standard equilibrium partitioning theory as

$$C_a / C_{dis} = K_{oc}\, C_{ss}$$

K_{oc} is a dimensionless partition coefficient and C_{ss} is the concentration of SPM in the water column expressed as mass of particulate per volume of water. In typical coastal waters, the concentration of SPM is on the order of 10 mg/L (Kullenberg 1982); however, SPM is specified as model input. When SPM <10 mg/L, most of the soluble and semi-soluble hydrocarbons are in the dissolved form.

Sedimentation of oil droplets occurs when the specific gravity of oil increases over that of the surrounding water. Several processes may act on subsurface oil droplets to increase density: weathering (dissolution and degradation), adherence (adhesion or sorption) onto SPM, colonization of droplets by microbes and accumulation of extracellular polymeric substances, and incorporation of sediment into oil during interaction with suspended particulates and bottom sediments. Rates of sedimentation depend on the concentration of suspended particulates and the rates of particulate flux into and out of an area. In areas with high suspended particulate concentrations, rapid dispersal and removal of oil is found due to sorption and adhesion (Payne and McNabb 1984).

Kirstein et al. (1987) and Payne et al. (1987) used a reaction term to characterize the water column interactions of oil and SPM. The reaction term represents the collision of oil droplets and SPM, and both oiled and unoiled particulates are accounted for. The model formulation developed by Kirstein et al. (1987) is used to calculate the volume of oil adhered to particles. Table 3-3 provided the model parameters needed. In the case where the oil mass is larger than the adhered sediment (i.e., the sediment has been incorporated into the oil) the buoyancy of the oil droplet will control its settling or rise rate. The Stoke's law formulation is used to adjust vertical position of these particles. If the mass of adhered droplets is small relative to the mass of the sediment it has adhered to, the sediment settling velocity will control the fate of the combined particulate.

Table 3-3. Model parameters related to adherence of oil droplets to SPM, based on physical properties and empirical data from the literature.

Parameter	Description	Units	Values	Source of Information
Adhesion rate to SPM	Coefficient of equation from Kolpack et al. (1977)	$(m^3/hr) / (g/m^3)$	0.010080	Kolpack et al. (1977)
Adhesion salinity coefficient	Coefficient of equation from Kolpack et al. (1977)	1/ppt	0.023	Kolpack et al. (1977)

3.2.2.4 Degradation

Degradation may occur as the result of photolysis, which is a chemical process, energized by ultraviolet light from the sun, and by biological (microbial) breakdown, termed biodegradation. Below 20 m, degradation is primarily by microbial action. A first order decay algorithm is used, with a specified (total) degradation rate for each of the hydrocarbon components (or pseudo-components) in each compartment of the model. (See Appendix C.)

3.2.2.5 Estimation of Concentrations from Mass Distribution in Spillets

The dissolved and droplet hydrocarbon concentrations in the water column, by hydrocarbon component, are calculated from the mass in the spillets, as follows. Concentration is contoured on a three dimensional grid system. This grid is fixed in dimensions to provide concentration output of a consistent resolution throughout the model run.

Distribution of mass around the spillet center is described as Gaussian in three dimensions, with one standard deviation equal to twice the local diffusive distance ($2Dxt$ in the horizontal, $2Dzt$ in the vertical, where Dx is the horizontal and Dz is the vertical spreading diffusion coefficient, and t is particle age).

Concentrations depend highly on the resolution of the concentration grid used. Thus, a post-processor is used to calculate concentrations in user-defined resolutions, as well as in specific spatial and temporal windows.

3.3 Model Output

The physical fates model creates output files recording the distribution of oil components in three dimensional space and time. The quantities recorded for each time step of the model are:

- Mass of oil and the 19 components in each spillet, as well as weathering and related properties such as oil density, viscosity, water content, droplet diameter, SPM adhered to the oil, dissolved mass);
- Volumes in the water column at various concentrations of dissolved hydrocarbons;
- Volumes in the water column at various concentrations of total hydrocarbons in suspended droplets;
- Droplet size distribution and concentrations of oil and components in various droplet size ranges; and
- Total hydrocarbon and component mass in surface sediment.

4 Model Input Data

4.1 Geographical and Model Grid

For geographical reference, the model uses a rectilinear grid to designate the location of the shoreline, the water depth (bathymetry), and habitat type. The grid is generated from a digital shoreline or other geographical information using the ESRI Arc/Info compatible Spatial Analyst program. The cells are then coded for depth and habitat type.

Ecological habitat types are broadly categorized into two zones: intertidal (i.e., shoreline) and subtidal. For the modeling analysis described herein, subtidal habitats were not resolved by type; all grid cells were assigned as open water silt-mud bottom.

A map of the habitat grid is provided in Appendix D.1.1. Below is a summary of the grid resolution of the 600-m resolution grid used for modeling.

- Origin Longitude, Latitude (degrees): -95.0, 25.0
- Number of cells W-E, S-N: 2000, 1000
- Cell size (degrees) W-E, S-N: 0.006, 0.006
- Cell size (meters) W-E, S-N: 605.36 m x 667.94 m

A depth grid was created matching the extent and resolution of the habitat grid. Each subtidal (water) grid cell was assigned a depth (meters). Bathymetry for the Gulf of Mexico was obtained from NOAA's NGDC at the addresses identified in Appendix D.1.2.

4.2 Environmental Data

4.2.1 Water Temperature and Salinity

Water temperature and salinity vary spatially, with depth, and by month. Climatic monthly mean water temperature and salinity data obtained from the NODC Ocean Climate Laboratory's Monthly Climatology data set for the Gulf of Mexico (Boyer et al. 2005, 2009, Locarnini et al. 2010, Garcia et al. 2010a,b, Antonov et al. 2010) were used to develop model inputs. This NODC analysis uses all data for the region that had been collated in the World's Ocean Database to provide gridded monthly-mean climatological data. The most recent version of the NODC database contains data through 2013, gridded on a ¼ degree grid. The data source and figures displaying the information are in Appendix D.2.

The vertical temperature profiles measured by *Brooks McCall* and other cruises in summer of 2010 were consistent with the climatology (see Grennan et al. 2015 and Figure E.1-1 in Appendix E.1). Typical temperatures in the upper mixed layer were 20-31ºC, in the thermocline below the mixed layer 7-20ºC, and in deep water (>800 m) 4-7ºC. Additional description of the data is in Grennan et al. (2015). Vertical profiles from climatology are in Appendix D.

Water density was calculated from temperature and salinity using the algorithm of Bryden (1973). Figure D.2.20 in Appendix D shows a composite of all water density (as sigma-t) profiles based on consensus CTD (conductivity, temperature and depth) data that have been QA/QC'd as part of the NRDA program (Grennan et al. 2015; Figure E.1-2 in Appendix E summarizes

these data). The mixed layer depth varies in space and time, and in some cases the upper 50 m can be quite stratified. Below 200 m, there is only a small change in water density with depth.

4.2.2 Currents

Oceanographic and tidal currents are variable in space and time at a range of scales as short as a few hours to seasonally. River discharge may vary by an order of magnitude or more over the course of the year, which in turn affects water velocity in coastal waters and in the area of the Mississippi River discharge into the offshore region. Several current data sets were available and evaluated for use as input to SIMAP for modelling subsurface transport.

4.2.2.1 Observational Data

Acoustic Doppler Current Profiler (ADCP) sensors were moored in place along the continental slope of the Northeastern Gulf of Mexico (Figure 4-1). These instruments measured currents during 2010 before and during the spill period. The National Data Buoy Center (NDBC) supports the IOOS® Sensor Observation Service (SOS) that provides real time access to current observations, as well as archived data. Archived data can be obtained from http://www.ndbc.noaa.gov/station_page.php?station=42885 (42885 being the ADCP station number; other stations are also available). Data from all NDBC stations selected for analyses were downloaded from www.ndbc.noaa.gov in March 2011.

In addition, ADCPs were deployed near the MC252 wellhead site, including a pair sampling the upper water column and waters deeper than 1000 m set out by a DWH NRDA cooperative work plan (Mulcahy 2010).

The ADCP station closest to the DWH well is number '42916', which was installed on the *Development Driller 3* that operated one of relief wells within 1 km of the DWH wellhead. During the period from April-July 2010, the temporally averaged current velocity at that station was 2.2 cm/sec (0.04 knot) to the northeast and 3.9 cm/sec (0.08 knot) to the southwest in 64 and 1,087 m below the water surface, respectively.

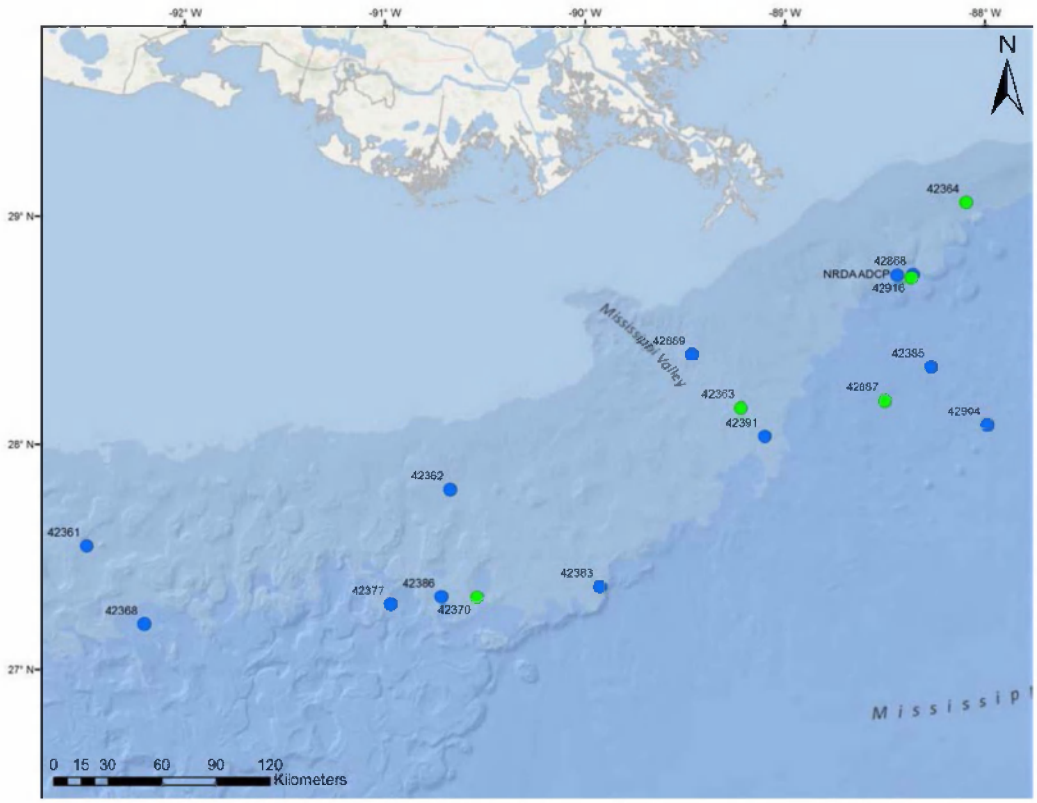

Figure 4-1. Locations of 18 ADCP moorings where sufficient data were available for 2010. Stations depicted in green extend deeper (typically >800m) into the water column than the blue stations.

4.2.2.2 Hydrodynamic Models

Several hydrodynamic model simulations of currents in the deep waters of the north-eastern Gulf of Mexico were available and evaluated for use in model simulations. Available model products are briefly described below. In this analysis, the IAS ROMs simulation was used for simulations of the DWH deepwater plume.

IAS ROMS (Principal Investigator: Yi Chao, UCLA))

IAS ROMS is a Regional Ocean Modeling System (ROMS) application (built off the South Atlantic Bight and Gulf of Mexico (SABGOM) model, Hyun and He 2010), that consists of a single domain covering the entire Gulf of Mexico and much of the western Atlantic Ocean (between the equator and 40°N). The model has a grid resolution of ~6 km in the horizontal, with 30 levels in the vertical (Chao et al. 2014). The lateral boundary conditions for the model domain are provided by real-time global 1/12° Hybrid Coordinate Ocean Model (HYCOM) currents (Chassignet et al. 2009). Outputs were generated by the Naval Research Laboratory (NRL) at Stennis Space Center and distributed by Florida State University. Every 12 hours, IAS ROMS assimilates observational data (e.g., temperature, salinity, sea surface height, and ADCP data) using its 3-dimensional variational (3DVAR) data assimilation algorithm (Li et al. 2008a,b; Chao et al. 2009). The solution is a combination of the observational data and the model first-guess field, which is the 12-hour IAS ROMS forecast (without data assimilation) initialized from the previous nowcast. An IAS ROMS simulation for 2010, that included a 2-km nested grid

within the larger IAS ROMS domain, was provided by Chao et al. (2014) in April 2014. This simulation was forced with North American Mesoscale (NAM) winds.

NGOM (NOAA/NOS/OCS; Principal Investigator: Richard Patchin)

The NOS Gulf of Mexico Nowcast/Forecast Model (NGOM) is the NOAA/NOS Coast Survey Development Laboratory (CSDD) Gulf of Mexico implementation of the Princeton Ocean Model (POM, developed by Dynalysis of Princeton). During the Response, NGOM was run for 2010 as a nowcast in real time, forced with winds and river discharges. NOAA's surface winds (12 km resolution) and atmospheric forecasts from the NAM model were used. Synoptic river flow discharges are specified from 36 rivers at 29 discharge model locations along the U. S. coastline, based on USGS and USACE gages. The resolution of NGOM is 2-3 km in the northwestern Gulf, 5-6km in the northeastern and central basin, with 37 levels in the vertical. Predictions were provided every 3 hours.

NRL GLOBAL HYbrid Coordinate Ocean Model (HYCOM) (Navy)

The NRL provides its GLOBAL HYbrid Coordinate Ocean Model (HYCOM) simulations on its government website, and many transport modelers download and utilize these data products. The model is forced with NOGAP winds. Model resolution is 1/25° (~3.5 km) in the horizontal, with 20 vertical layers. Data for the Gulf of Mexico during 2010 were downloaded and formatted in netCDF files.

4.2.3 Suspended Particulate Matter

Suspended particulate matter (SPM) includes minerals, referred to as total suspended sediments (TSS) and organic particulate matter. Oil can adhere to SPM and be transported in the water column in accordance to the density, shape, and size of the combined oil-sediment particulates. Typically, sedimentation of oil and PAHs, via mineral-SPM interactions, becomes significant above suspended sediment concentrations of about 100 mg/L (Payne et al. 1987, French et al. 1996, French McCay et al. 2004, 2005). MC252 oil from the spill was identified on the sediments in the offshore area surrounding and down-stream of the well site (Montagna et al. 2013; Valentine et al. 2014). Thus, there is evidence that there was a flux of spilled oil to the sediments. Because mineral SPM concentrations are typically very low in the offshore Gulf of Mexico near the wellhead (D'Sa et al. 2007, D'Sa and Ko 2008, Salisbury et al. 2004), the transport flux to the seafloor was more likely due to oil adherence to organic matter, rather than mineral sediments.

Water quality data were evaluated to estimate baseline total suspended sediment (mineral) concentrations for use in model inputs. In the north-eastern Gulf of Mexico, suspended sediment concentrations are generally very low in offshore waters and the outer shelf areas affected by the DWH spill. Based on a review of the surface SPM distribution in the Northern Gulf of Mexico, the mean total suspended sediment concentration in the offshore Northern Gulf of Mexico is 3 mg/L (D'Sa et al. 2007, D'Sa and Ko 2008, Salisbury et al. 2004).

In the near shore area, especially off the Louisiana coast, suspended sediment concentrations are generally much higher, as they are influenced by the Mississippi-Atchafalaya River system. The Mississippi river discharges suspended sediments into the Gulf of Mexico through the Bird's Foot Delta, and through the Atchafalaya River Delta (Meade 1995). The Bird's Foot Delta is a deeper water shelf, when compared to the broad and shallow western shelf of the Atchafalaya River Delta. Away from river discharge plumes, and in the absence of frontal systems and tropical storms, concentrations of suspended solids on the shelf are in the range of a few mg/L

(Anderson et al. 1979; Danek and Tomlinson 1980; Brooks et al. 1981). This is consistent with the 3 mg/L average noted above.

For the SIMAP modelling, a mean total suspended sediment concentration of 3 mg/L was used in the Northern Gulf of Mexico for SPM in offshore waters with depths >20 m. TSS concentration were assumed uniform through the entire water column. Nearshore TSS concentrations in waters <20 m deep were not needed or used in the model simulations.

Estimates of organic matter concentrations in the area and time of the spill were not identified. Therefore, adherence of oil to varying amounts of organic matter was not included in the modelling to date. This may result in an underestimated flux of oil to the sediments.

4.2.4 Horizontal and Vertical Dispersion

For subsurface oil droplet and dissolved spillets, two scales of dispersion are modelled: advective and spreading. Spillets undergo a random walk, along with the transport by currents, as described in Section 3.2.2.1. The horizontal and vertical dispersion coefficients used for the random-walk portion of the advection of subsurface spillet centers are also used for spreading dispersion within subsurface spillets, as described in Section 3.2.2.5.

When currents (i.e., IAS ROMS) are input to the model, dispersion coefficients used in all locations are as follows.

- Horizontal dispersion coefficients used when current data are input to the model (such that they characterize small-scale motion)
  - 2 m^2/sec in the upper 40 m of the water column (above the pycnocline); and
  - 0.1 m^2/sec in the water column below 40 m.
- Vertical dispersion coefficients (characterizing small-scale motion)
  - 10 cm^2/sec in the upper 40 m of the water column; and
  - 0.1 cm^2/sec in the water column below 40 m.

These dispersion values are reasonable for offshore waters based on empirical data (Okubo and Ozmidov 1970, Okubo 1971, Csanady 1973, Socolofsky and Jirka 2005) and modeling experience based on dye studies (French et al. 1997, French McCay et al. 2007).

In the no-current case, the assumption is that currents are multidirectional at random such that currents effectively disperse the rising oil analogous to diffusion. The horizontal dispersion coefficients for the no-current case were scaled to disperse the contaminants (oil) at rates indicated by the variance of the ADCP-measured currents at the wellhead; i.e., the horizontal dispersion coefficients were estimated from the dispersive distance, defined as 2 standard deviations of a Gaussian-shaped spread of mass around the release location (Appendix A.2.1.1.), using the standard deviations of ADCP data at the 2 stations next to the wellhead (Figure 4-1): #42916 (4.7 cm/sec) and #42868 (5.2 cm/sec). The horizontal dispersion coefficient scaled from a standard deviation of 5 cm/sec and using a 30-min time step was 2.25 m^2/sec. The vertical dispersion coefficients used for the no-current case were the same as described above for the with-current case.

4.3 Oil Properties

The spilled MC252 oil is characterized by a number of physical-chemical properties (Table 4-1). Table 4-2 provides a summary of the oil properties used in the modelling. The sources and derivation of these data inputs are described in Appendix B.

Table 4-1. Model inputs for physical-chemical properties of oil.

Property	Description	Units	Common Range of Values
Pour point	Temperature above which oil is fluid (liquid)	°C	-20 to 20
Density	Density, specific gravity or API at specific temperature(s))	g/cm^3 or API	0.7 – 1.1 g/cm^3
Viscosity	Viscosity of the oil (at specific temperature(s))	Centipoise (cP)	100 – 3000
Interfacial tension	Oil-water interfacial tension	mN/m	10 – 30
Total volatile and semi-volatile fraction	Fraction of oil with boiling points <380°C, which will volatilize (aromatics + aliphatics)	fraction	0 – 0.99
Volatile and semi-volatile aromatic fraction	Monoaromatics (BTEX) and 2-3 ring aromatics (PAHs)	fraction	0 – 0.10

Table 4-2. Oil Parameters for MC252 Oil (based on Stout 2015b; sample ID GU2988-A0521-09805).

Physical Parameters	MC252 Oil
Oil Type	Light Crude Oil
Surface tension (mNm) at 20°C	3.43
Interfacial tension (mNm) at 20°C	19.63
Pour Point (°C)	-28
Density at 30°C (g/cm^3)	0.8372
Density at 15°C (g/cm^3)	0.8483
Density at 5°C (g/cm^3)	0.8560
Dynamic Viscosity (cP) @ 30°C	4.503
Dynamic Viscosity (cP) @ 15°C	7.145
Dynamic Viscosity (cP) @ 5°C	10.93
Resin Content (weight %)	10.1
Asphaltene Content (weight %)	0.27

The oil's contents of volatile and semi-volatile aliphatics and aromatics need to be defined and input to the model. Table 3-1 defines the groupings of volatile and semi-volatile aliphatics and aromatics into components of the MC252 oil. The 1- to 4-ring aromatics, as well as cyclic hydrocarbons and alkanes that are soluble or semi-soluble are listed in Appendix B with their assigned component. Tables 4-3 and 4-4 summarize the fractional composition of MC252 oil by

component group, based on measurements by Stout (2015a). The sum of AR and AL components totals approximately 61% of the whole oil. The remaining 39% is treated as an insoluble and non-volatile "residual" fraction.

Table 4-3. Fractional composition of whole MC252 source oil by component group: soluble and semi-soluble components where measured concentrations in the oil were summed.

Code	Hydrocarbon Component	Fraction in Oil (g g^{-1} oil)
AR1	BTEX	0.019124
AR2	C3-benzenes	0.007836
AR3	C4-benzenes	0.004674
AR4	Decalins	0.003786
AR5	C0-C2 Naphthalenes	0.005634
AR6	C3-C4 Naphthalenes	0.002434
AR7	Fluorenes & C0-C1 3-ring PAHs	0.002339
AR8	4-ring PAHs & C2-C3 3-ring PAHs	0.001667
AR9	Soluble alkanes	0.133190

Table 4-4. Fractional composition of whole MC252 source oil by component group: insoluble components where concentrations in the oil were based on boiling curve cuts.

Code	Hydrocarbon Component	Fraction in Oil (g g^{-1} oil)
AL1	Aliphatics: BP < 150	0.006923
AL2	Aliphatics: BP 150-180	0.060913
AL3	Aliphatics: BP 180-200 (C11)	0.034279
AL4	Aliphatics: BP 200-230 (C12)	0.053814
AL5	Aliphatics: BP 230-280 (C13-C16)	0.095099
AL6	Aliphatics: BP 280-300 (C17-C18)	0.036292
AL7	Aliphatics: BP 300-350 (C19-C20)	0.092923
AL8	Aliphatics: BP 350-380 (C21-C23)	0.049473
Σ AR#s + Σ AL#s	Total volatiles and semi-volatiles	0.610400

4.4 Oil Hydrocarbon Degradation Rates

Degradation rates in the water column below 20 m for each component are summarized in Table 4-5. These rates are based on data obtained from literature reviews that included estimates for compounds and/or components of MC252 oil and crude oil generally. The rates for residual oil are consistent with studies by Zahed et al. (2011) and Atlas and Bragg (2009). See Appendix C for details regarding the literature review and derivation of the values in Table 4-5.

Table 4-5. Degradation rates (k_d, instantaneous, daily) and corresponding half-lives ($0.693/k_d$) for components of oil in the water column used as model input.

AR or AL	Instantaneous Rate (day^{-1})	Half-Life (days)
Component Group	**In Water**	**In Water**
AR1	0.23	3.0
AR2	0.29	2.4
AR3	0.28	2.5
AR4	0.06	11.6
AR5	0.28	2.5
AR6	0.18	3.9
AR7	0.15	4.6
AR8	0.10	6.9
AR9	0.17	4.1
AL1	0.24	2.9
AL2	0.12	5.8
AL3	0.06	11.6
AL4	0.06	11.6
AL5	0.06	11.6
AL6	0.05	13.9
AL7	0.04	17.3
AL8	0.04	17.3
Residual	0.02	34.7

4.5 Response Activities

Response activities such as booming, mechanical removal from the water surface and shoreline, *in situ* burning and surface applications of dispersants were not applicable to the simulation of the rising oil to 20 m below the surface, and so are not included in the modeling. Figure 4-2 summarizes the dispersant application volumes at the water surface and subsea at the oil release points over the time period of the spill in 2010 (based on data in Lehr et al. 2010). Note the increase in the dispersant volume applied subsurface over time. The subsea dispersant applications are accounted for in the nearfield blowout modeling (see Spaulding et al. 2015), and so in the inputs to the SIMAP far-field model.

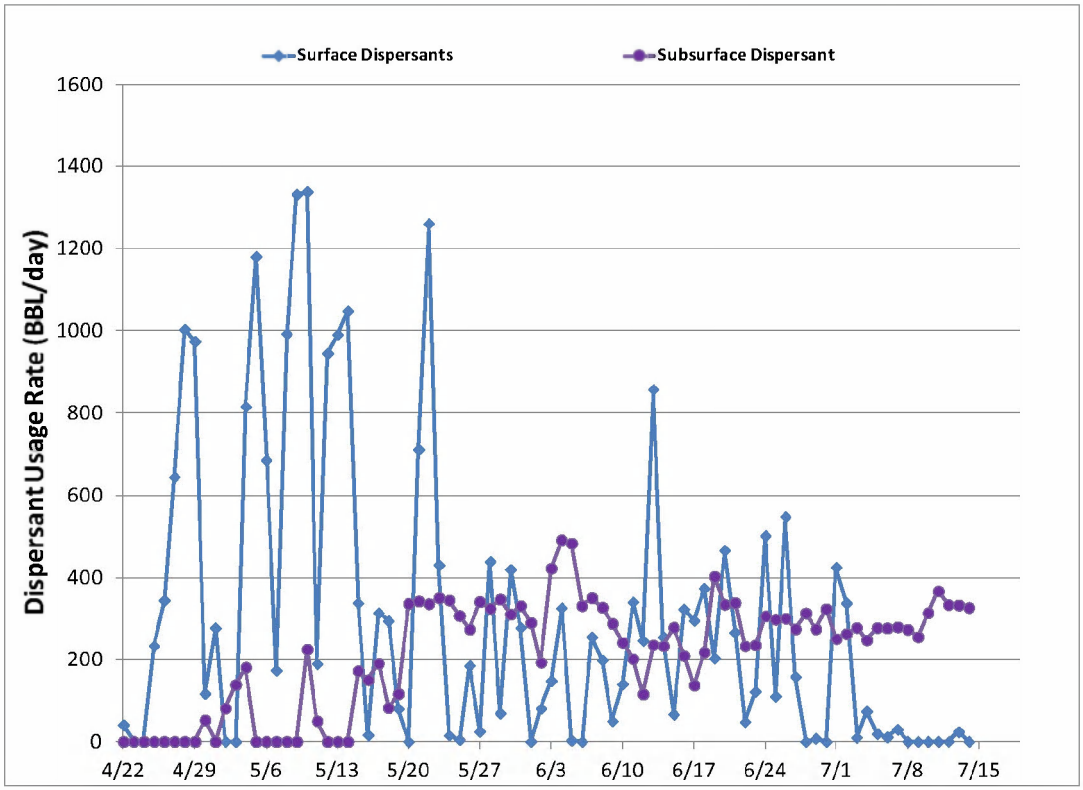

Figure 4-2. Summary of dispersant application rates from April 22 to July 15, 2010, as reported by Lehr et al. (2010).

4.6 Scenario Specifications

4.6.1 Time Line of Events

The release of oil and gas to the water column varied in amount released per day, location, and the amount treated with dispersant throughout the spill event. Early in the spill event, oil and gas was only released from the end of the broken riser. After approximately six days, it was discovered that oil and gas were flowing from two different locations, the end of the broken riser and from holes in the riser, where a kink formed when the rig sunk and the riser collapsed. This division of flow between the riser and kink varied over time, with the kink release increasing with time due to the evolution of more kink holes. As the number of holes increased, the larger cross-sectional area of the exit openings allowed more flow through. The kink flow occurred for 34 days, after which time the riser was cut just above the BOP (i.e., on June 3rd). This meant from that point on, all oil and gas was released from the cut riser at the wellhead. Throughout the spill event, there were various levels of collection and dispersant treatment. While the amount of time pre-cut versus post-cut was the same (42 days each), the resulting mass of oil released to the water column during pre-cut and post-cut was 60% and 40%, respectively, based on the analysis by the FRTG (McNutt et al. 2011).

Table 4-6 summarizes the timeline of events, consistent with the Phase II Court findings (USDC 2015). See Spaulding et al. (2015) for a detailed discussion of the time line and sources of the

information. Oil collection at the release points, i.e., the Riser Insertion Tube (RITT) and the Top Hat, was assumed to not have entered the environment, and is not tracked in the modeling of oil fate. These events are important to what was modeled and have been considered in the evaluation of the model results.

Table 4-6. DWH spill event timeline condensed into broad date intervals indicating release configurations and operations.

Start Date (mm/dd/yyyy) (HH:MM)	End Date (mm/dd/yyyy) (HH:MM)	Days	Description	Operational: Collection	Operational: Subsea Dispersant
4/22/2010 10:30	4/28/2010 15:33	6	Leak from end of broken riser only	-	-
4/28/2010 15:33	5/26/2010	28	Release from end of broken riser & Kink	RITT collection small volumes, typically <5,000 bbl/day	highly variable use and volume, low effectiveness
5/26/2010	5/29/2010	3	Release from broken riser & kink, Top Kill	-	-
5/29/2010	6/3/2010 9:05	5	Release from broken riser and kink. Cutting operations	-	consistent use, variable volumes, low effectiveness
6/3/2010 9:05	6/4/2010	1	Riser flow only, post riser cut	-	-
6/4/2010	6/6/2010	2	Riser flow only, post cut, with Top Hat #4	consistent use, volume ramped up to ~11,000 bbl/day	consistent use, variable large volumes, low effectiveness
6/6/2010	6/13/2010	7	Riser flow only, post cut, with Top Hat #4	consistent use, at ~15,000 bbl oil/day	highly variable volumes, low effectiveness
6/13/2010	7/10/2010 12:35	27	Riser Flow only, post cut, with Top Hat #4	steady, increases to ~22,000 bbl/day	consistent use & volumes, moderate effectiveness
7/10/2010 12:35	7/14/10 17:00	4	Riser Flow only, post cut, Top Hat Removed, operations to set up capping stack	~8,000 to ~16,000 bbl/day	dispersant volume high, moderate effectiveness
7/14/10 17:00	7/15/2010 14:27	1	Riser Flow only, post cut, capping stack	-	-

4.6.2 Oil Volume Released to the Water Column

The spill volume, as implemented by Spaulding et al. (2015) as part of the nearfield modeling used to develop inputs to SIMAP, was based on the Phase II Court findings (USDC 2015) of 4.0 million bbls (oil barrels of 42 gallons/barrel) released from the reservoir and 3.19 million bbls of oil discharged to the Gulf of Mexico. The portion of this volume discharged each day (April 22–July 15 of 2010) was assumed proportional to the daily release volumes estimated by the Flow Rate Technical Group (McNutt et al. 2011), as summarized in the Oil Budget Calculator (OBC) report, and included consideration of oil recovered at the release site and therefore not released to the environment (Lehr et al. 2010, referred to here after as OBC). Figure 4-3 depicts the oil release rate to the environment as estimated by the OBC (used in previous modeling), along with the modeled released rate based on the Phase II Court findings (USDC 2015, which is 22%

less than the OBC release rate) used herein. After the riser was cut, the "Top Hat" was installed and a portion of the oil released from the well was recovered. The amount recovered was measured by BP and Response on a daily basis. The amount released to the environment was estimated by taking the difference between the amounts released and recovered. Note that, in general, the amount of oil released to the water column decreased over time (Figure 4-3).

Oil was released in one of two different configurations; the first configuration had varying percentages of the total release from two primary locations:

(1) Before June 3, at the end of the riser (Figure 4-4), and from up to six small holes in the vicinity of a kink that developed in the riser pipe immediately above the Blowout Preventer (BOP), and

(2) After June 3, flow only from the cut riser pipe immediately above the BOP.

Figure 4-5 depicts estimates of the amount of oil released from the riser and kink for the time period when both release locations were active, as well as the release from the riser only after June 3. The discrete stepping of the kink release is a result of the increase in the number of holes at the kink. These estimates were based on application of the pipeline model described in Spaulding et al. (2015).

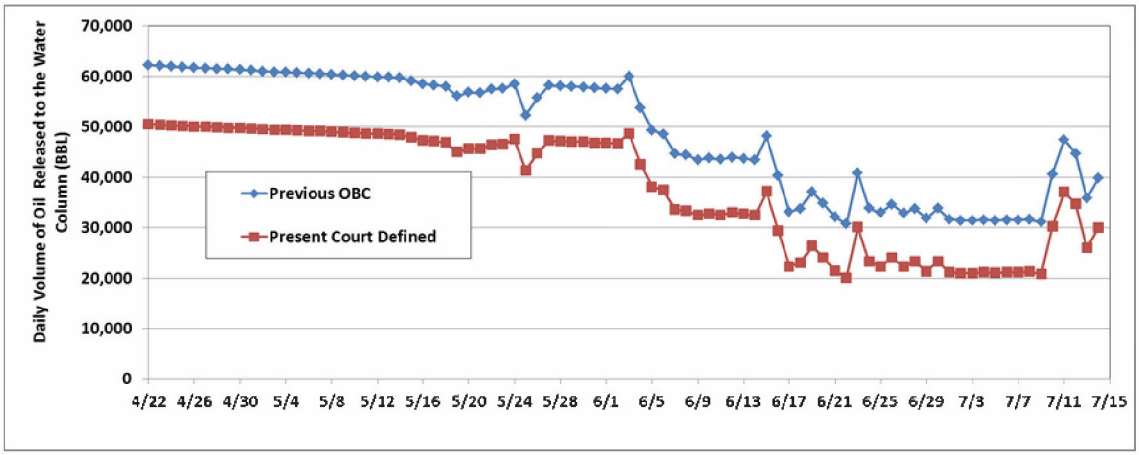

Figure 4-3. Time history of the estimated total oil release rate to the environment based on the Oil Budget Calculator (OBC) (Lehr et al. 2010) and in the present modeling analysis using the Phase II Court findings (USDC 2015) volume. All rates in barrels per day.

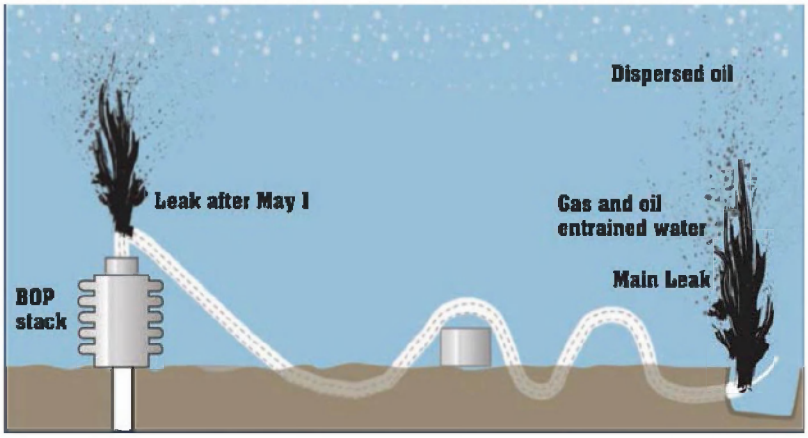

Figure 4-4. Schematic of releases of oil and gas from the end of the riser pipe and from small holes at a kink in the riser pipe above the BOP (Lehr et al. 2010).

The riser release started on April 22, with the kink release beginning on April 28. An in depth review of the available ROV video imagery indicated that the number of holes at the kink increased with time from two (2) beginning on April 28, 2010 to six (6) just before the riser was cut. Both releases were present through June 3, at which point the riser pipe was cut above the BOP, thereby eliminating the kink releases. Each of the releases had distinct droplet size distributions (developed by Spaulding et al. 2015; summarized below), which influenced concentration distributions resulting from the SIMAP modeling.

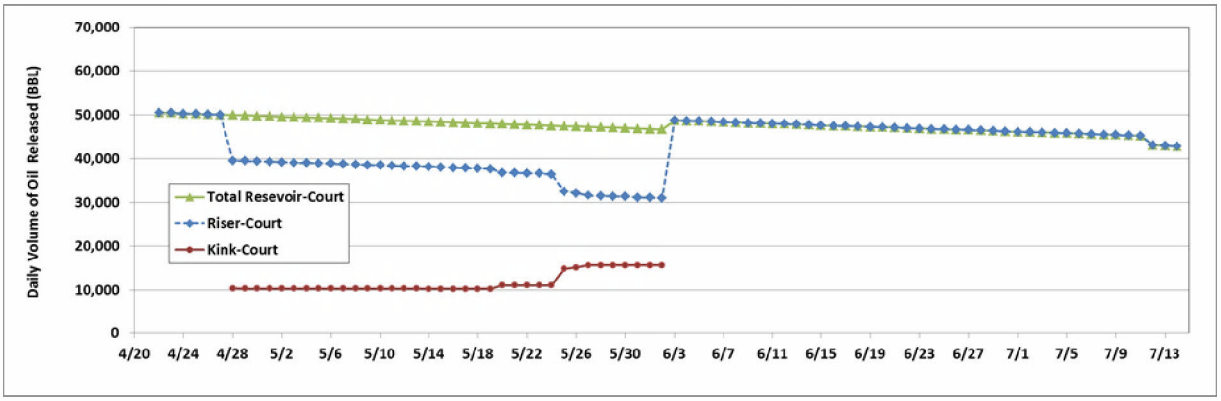

Figure 4-5. Estimated amount of oil released from the riser and kink for the time period when both release locations were active, and the release from the riser after June 3.

4.6.3 Nearfield Modeling of the Blowout and Buoyant Plume

The main objective of the blowout modeling (Spaulding et al. 2015) was to determine the blowout plume characteristics, namely the trap height of the oil above the release points. At this depth, the buoyancy of the plume became negligible due to entrainment of seawater and the amount of mass released via out-gassing and individual droplets. These parameters are then used to initialize the (far field) oil fate model (SIMAP). In order to capture the various release

conditions (i.e., different amounts, release locations and configurations), the different release 'types' were modeled individually within OILMAP DEEP. The three release types were riser not dispersed (RND), riser dispersed (RD), and kink (K).

Figure 4-6 shows the time series of trap heights for plumes from the riser and kink holes, estimated by Spaulding et al. (2015) using the blowout model with the OBC and the Court release volumes. Table 4-7 summarizes the locations of these release points, as well as trap heights relative to the water depths given in the table. The release from the kink was trapped at about 1280-1300m, whereas the (larger flow rate) release from the end of the riser trapped between 1160m and 1245m. The lower volume release rate in the court specified volume leads to a reduction in the trap height of about 40 m (12% of the OBC estimate). This is within the uncertainty of the analysis of field CDOM data used to estimate the trap height in the field (Grennan et al. 2015) and the uncertainty of the blowout modeling approach (Spaulding et al. 2015).

The plume trap height (and 'z' positioning within the water column) input to SIMAP was not updated from prior modeling analyses using the OBC results due to the insignificant difference between the OBC and Court volume estimates. Random lateral positioning of the droplets within a specified radius at the trap height was implemented for initializing the oil droplets within the water column. Droplets were positioned within a 130 m radius from the kink and 180 m radius from the riser; these radii were based on estimates of the dimensions of the end of the near field intrusion (see Spaulding et al. 2015).

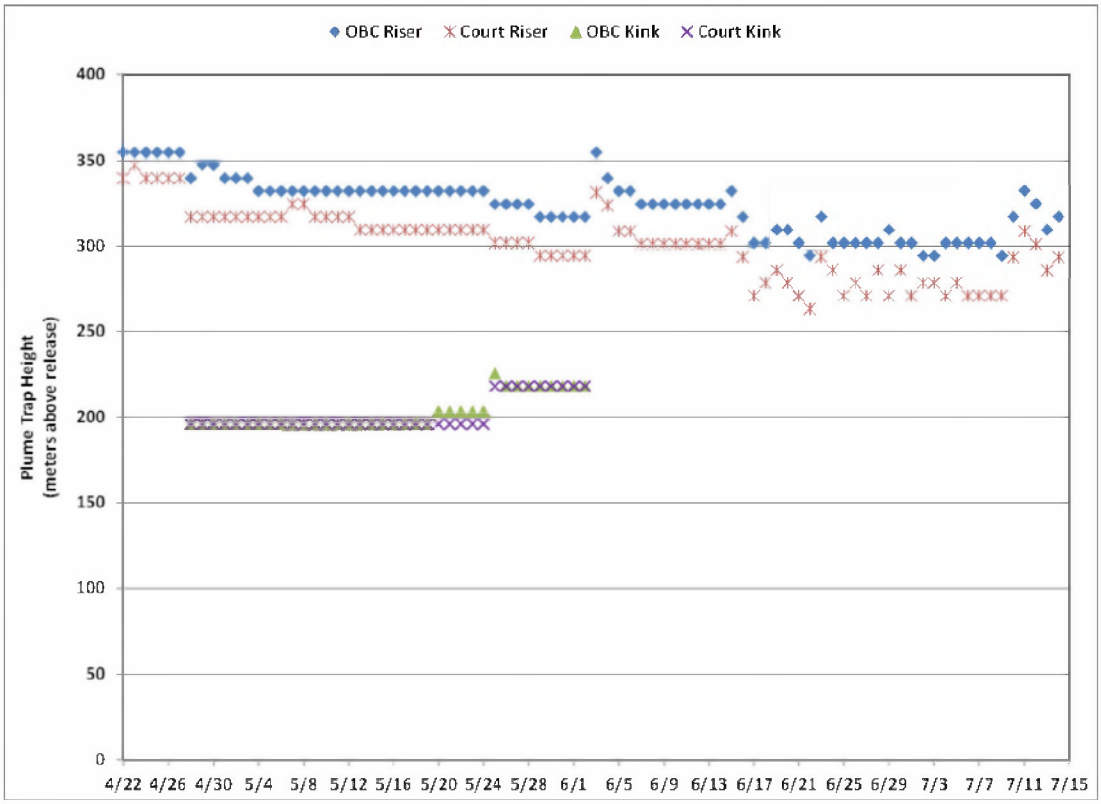

Figure 4-6. Time series of trap heights for plumes from the riser and kink holes estimated by the blowout model for the OBC and Court release rates.

Table 4-7. Coordinates of release locations used in the spill simulations. The trap height range for releases from the broken riser is for April 22 – June 3, and for the cut riser it is for June 4 – July 15.

Location	Latitude (N)	Longitude (W)	Water Column Depth (m)	Trap Height (m)
Well	28.73814	88.3659453	1,523	(N/A)
Kink - Above BOP	28.73814	88.3659453	1,503	1,280-1,300
End of Broken Riser	28.74002	88.3668618	1,509	1,160-1,210
Cut Riser	28.73814	88.3659453	1,505	1,175-1,245

In addition, estimates were made by Spaulding et al. (2015) of the fraction of the riser release effectively treated by dispersant, which was then used to estimate the daily volume treated, since the release rate to the water column from the riser was not constant. This volume was then used along with the volume of dispersant applied on the same day to calculate the dispersant to oil ratio (DOR). The DOR is used to adjust the oil-water interfacial tension for the fraction treated; this is of significance to calculating the droplet sizes within the fraction treated, as a lowered oil-water interfacial tension with dispersant application allows for the formation of smaller droplets. There were different DORs and fractions of riser release treated on each day. The DOR increased as fraction treated decreased and vice versa. Therefore, varying dispersant treatment effectiveness changed the resulting estimate of fraction of oil mass in smaller (dispersed) droplet sizes and the estimated size of these dispersed droplets.

An estimate of flow from each release type was made by Spaulding et al. (2015) based on total flow released from the reservoir, the amount collected, amount released from the kink flow, and the estimated dispersant treatment effectiveness. The riser and kink releases were then simulated in the blowout plume model to estimate the resulting trap height from these locations. Then, Spaulding et al. (2015) simulated each release type (RND, RD & K) with the droplet size model (varying mainly exit velocity per release type and oil-water interfacial tension) to estimate the resulting droplets size distributions from each source. These two sets of results were combined to generate the far field model input of the mass of oil released in different droplet sizes, initialized at different locations (end of broken riser, kink, cut riser), and at different heights in the water column (trap height).

Beginning on April 22, 2010 at 10:30AM (local time), oil was released from the end of the riser. Because the initial release was through a large pipe orifice, the oil droplets sizes were large (>800 µm; see Spaulding et al. 2015).

On April 28, 2010, the riser pipe just above the BlowOut Preventer (BOP) began to leak at a point where the pipe had been severely kinked during the collapse. Between April 28 and June 3, 2010, the number of holes in the kink area increased from the initial two up to six holes. As the release continued, the holes in the kinked riser increased in size and number. Together, they released a large amount of oil and gas that might otherwise have travelled the length of the riser to the severed end of the pipe several hundred meters away. The oil and gas released through the kink holes was under considerable pressure and was forced through fairly small holes, creating high velocity oil and gas jets. The exiting oil/gas mixture was therefore driven by far greater energy than if it had exited from the much larger riser pipe outlet. The increased energy has the effect of shifting the droplet size distribution to smaller sizes, increasing the amount of oil becoming trapped in the lower water column. This changes the oil mass balance,

reducing the mass surfacing and increasing the amount remaining at depth. The *pipeline release model* was employed by Spaulding et al. (2015) to determine the flow spilt between the kink holes and the riser outlet. Using the total flow estimates made by the FRTG (McNutt et al. 2011), the predicted amount of oil released from the kink was on the order of 18% of the total on the first day, increasing to 28% immediately before the riser was cut. (See Spaulding et al. 2015, for further details.)

The analysis of the releases from the riser (pre- or post-cut on June 3) indicates that if all of the oil was effectively treated with dispersant, then the droplet size would range from 20 to 500 µm; if all the oil was untreated the range would be from 1,000 to 10,000 µm. More than 99% of the dispersant treated oil droplets would have diameters, d, ≤ 500 µm, whereas more than 99% of non-treated oil droplets would have d ≥ 1,000 µm. Because the droplets with d ≥ 1,000 µm would surface after a few hours from ~1,500 m, the droplet size distribution remaining in the water column would be dominated by dispersant-treated oil (Spaulding et al. 2015).

Table 4-8 summarizes the predicted droplet size distributions for the different kink and riser release scenarios examined by Spaulding et al. (2015), using the OBC release rate. The median diameters of the riser flows are significantly larger than those predicted from the kink release, due to the much higher release velocity from the kink. These large droplets are expected to ascend in the immediate vicinity of the riser release location due to their large size and buoyancy. For example, a droplet of fresh oil 2,000 µm in diameter rises at a terminal velocity of ~7 cm/s, and travels from a buoyant plume trap depth of 1,100 m to the surface in ~5 hours. In comparison, a droplet of 500 µm, rises at ~1.7 cm/s and takes ~20 hours to reach the surface; a droplet of 200 µm, rises at ~0.4 cm/s and takes ~96 hours to reach the surface; and a droplet of 100 µm, rises at ~0.1 cm/s and takes ~370 hours to reach the surface.

Table 4-8. Predictions of the volume median diameter of droplet size distribution for release scenarios occurring over the time period of the spill. (LMRP = Lower Marine Riser Package)

Scenario	Release description	Release opening diameter (cm)	Volume median diameter (VD_{50}, µm)
A	Kink release, Stage I	2.0	328
B	Kink release, Stage II	2.2	356
C	Kink release, Stage III	2.6	361
D	Riser release, end of pipe, prior to kink onset	50	2257
E	Riser release, end of pipe, split with kink release at stage II	50	2972
F	Riser release, LMRP, post-cut, without dispersant	25	2744

The analysis by Spaulding et al. (2015) indicates that during the pre-riser cut time period (prior to June 3), oil dispersion (formation of smaller droplets) was a result of mechanical processes (e.g., high exit velocities) at the kink holes and, to a more limited extent, dispersant application of low effectiveness at the end of the riser. During the post-cut period, oil dispersion appeared to be primarily due to more effective dispersant treatment above the BOP.

Table 4-9 summarizes the predicted cumulative droplet size distribution using the OBC and the Court release volumes. The cumulative fraction vs droplet size analysis shows that the droplet size distributions are very similar for both the Court and OBC volumes. The differences are mainly in the sizes of the large size droplets for untreated oil, droplets being a bit larger using the lower Court volume. (See Spaulding et al. 2015 for further detail). The droplet size predictions using the Court release volume were used as input to the SIMAP model.

Table 4-9. Predicted cumulative droplet size distribution (fraction in each size range, diameter in microns) over the entire spill using the OBC and Court release volumes.

Microns	OBC Volume	Court Volume
<100	0.04	0.05
<200	0.14	0.14
<300	0.20	0.20
<400	0.24	0.23
<500	0.26	0.26
<1,000	0.39	0.29
<2,000	0.69	0.47
<5,000	0.96	0.90
<10,000	1.00	1.00

The time history of mass distribution in the varying droplet size bins (for the Court release volume) is presented in Figure 4-7. Figures 4-8 and 4-9 show the average droplet size distribution and its cumulative distribution over all days of the release. Figures 4-10 to 4-16 show cumulative droplet size distributions for the daily release on selected dates.

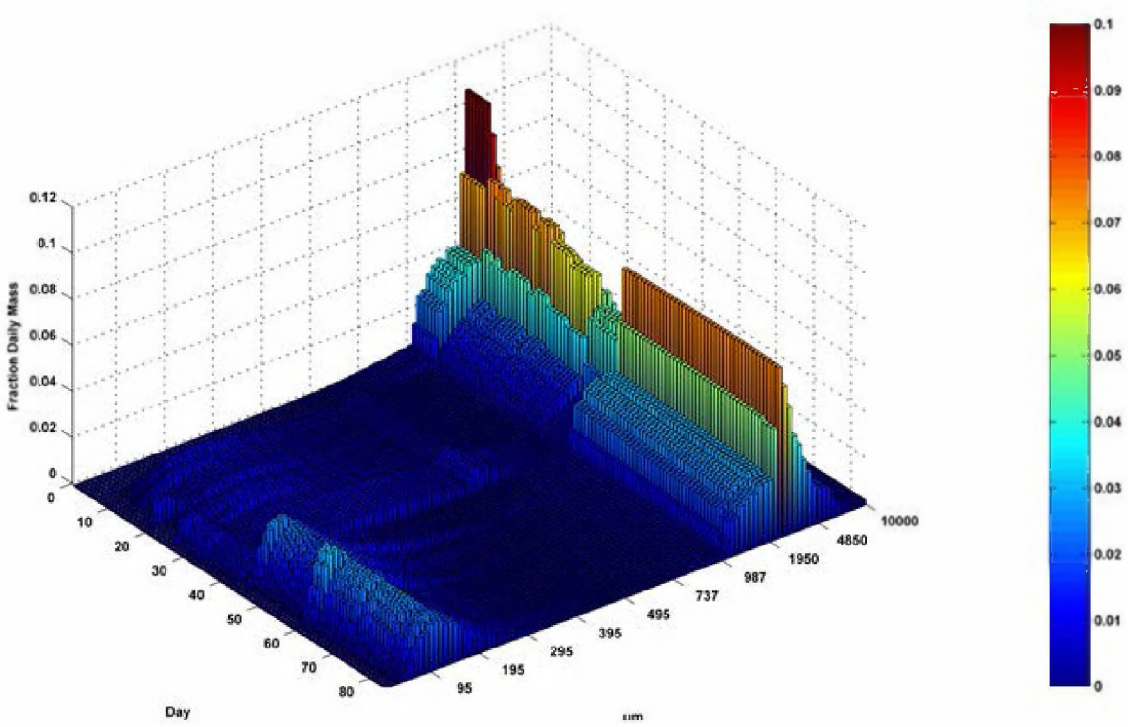

Figure 4-7. Daily fractional distribution of mass in various sizes bins (microns) throughout the release.

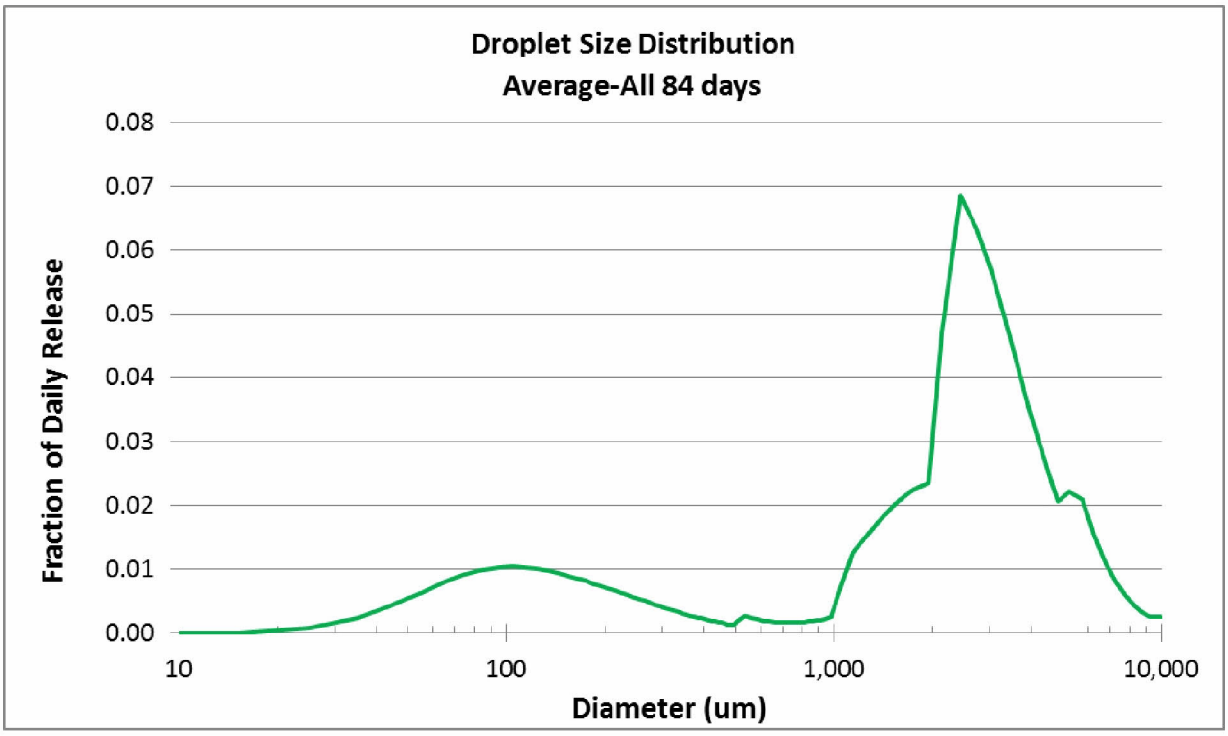

Figure 4-8. Average droplet size distribution over all days of the release.

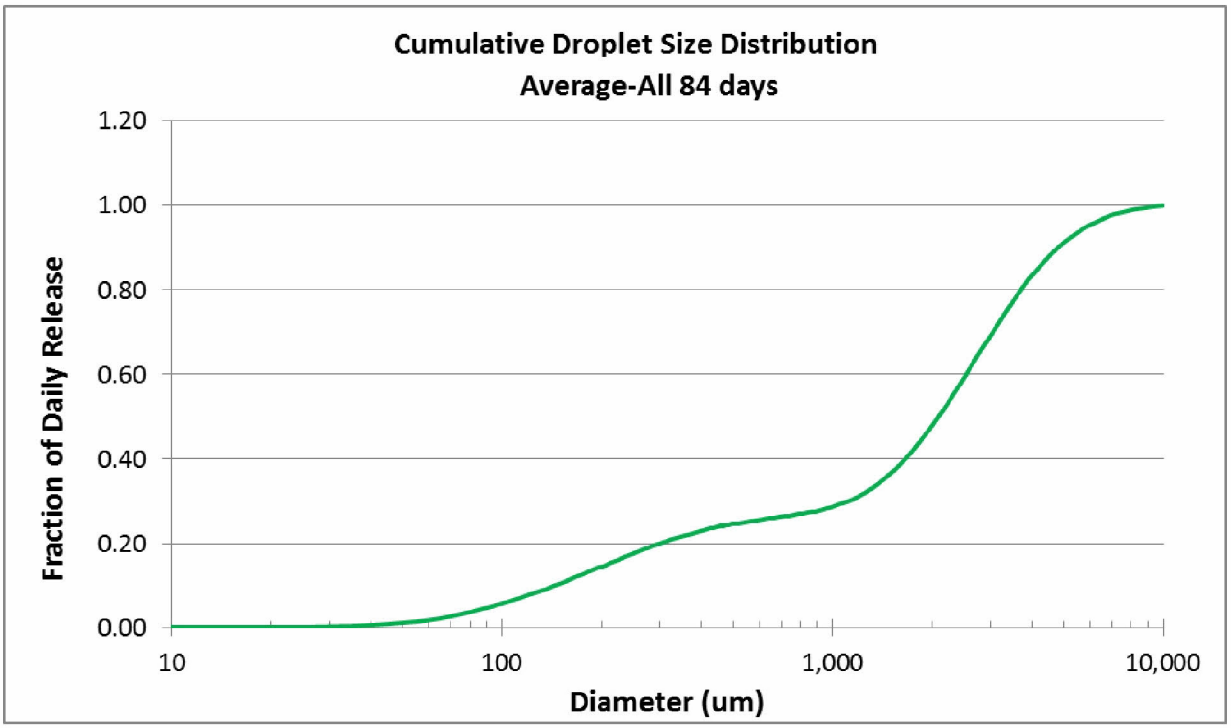

Figure 4-9. Cumulative droplet size distribution, averaged over all days of the release.

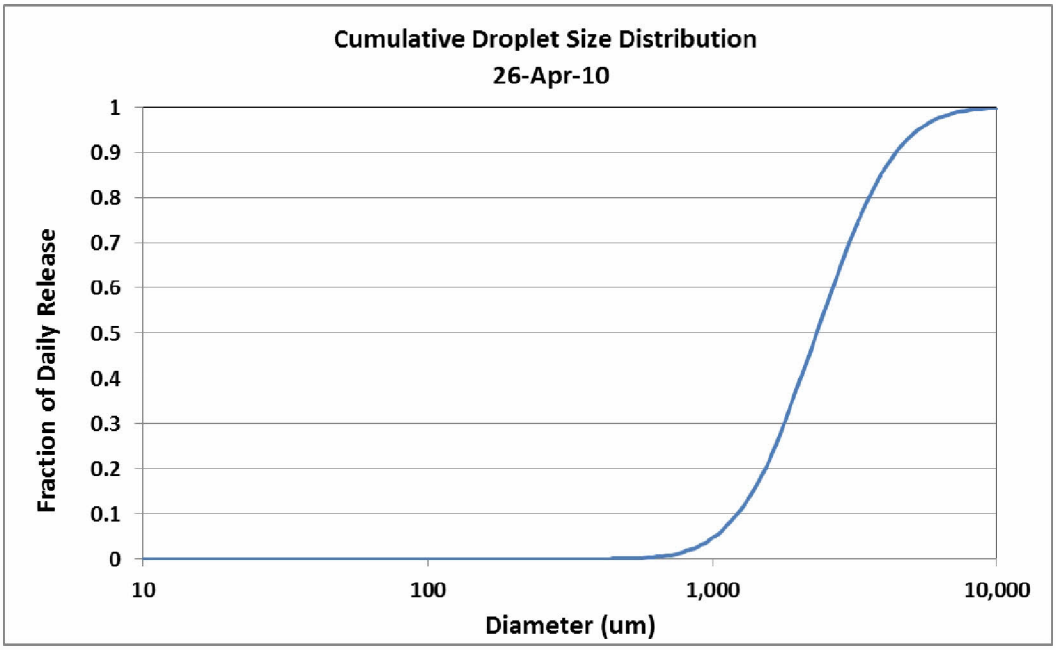

Figure 4-10. Cumulative droplet size distribution typical of April 22 – 28 when there were no kink holes and no subsea dispersant applied.

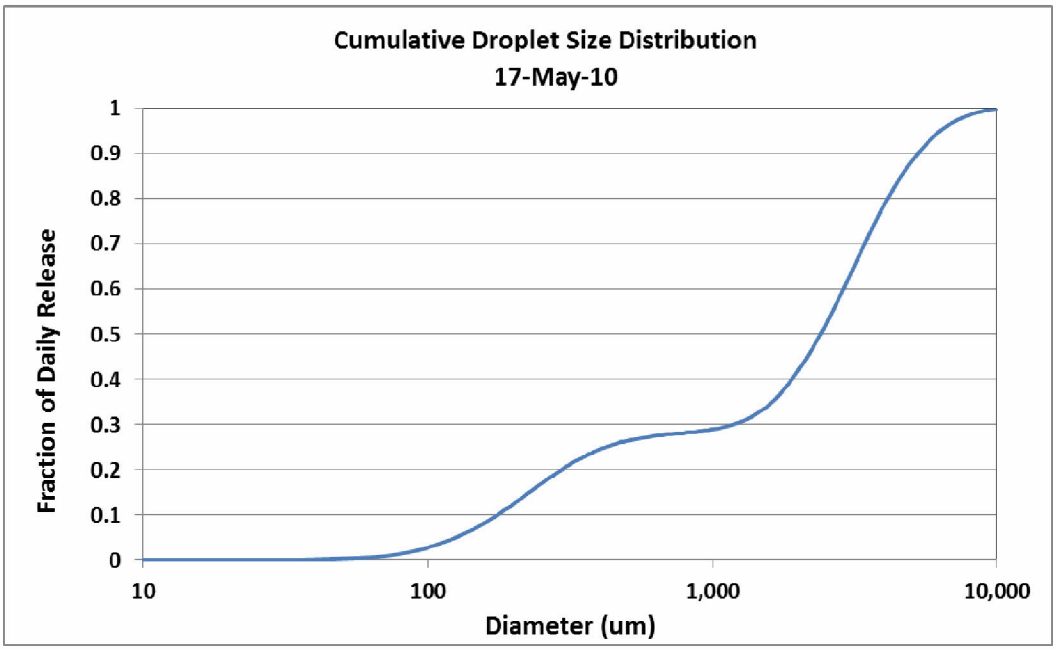

Figure 4-11. Cumulative droplet size distribution typical of April 29 – May 20 when there were two kink holes and subsea dispersant was applied using the wand (which treated only part of the release).

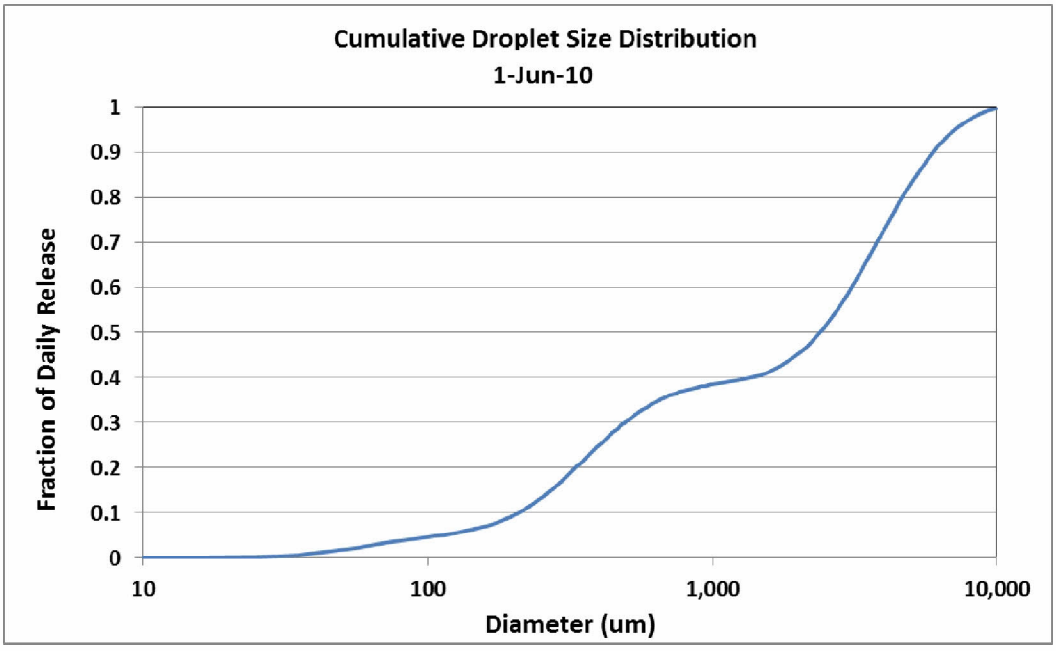

Figure 4-12. Cumulative droplet size distribution typical of May 21 – June 3 when there were 4-6 kink holes and subsea dispersant was applied using the wand (which treated only part of the release).

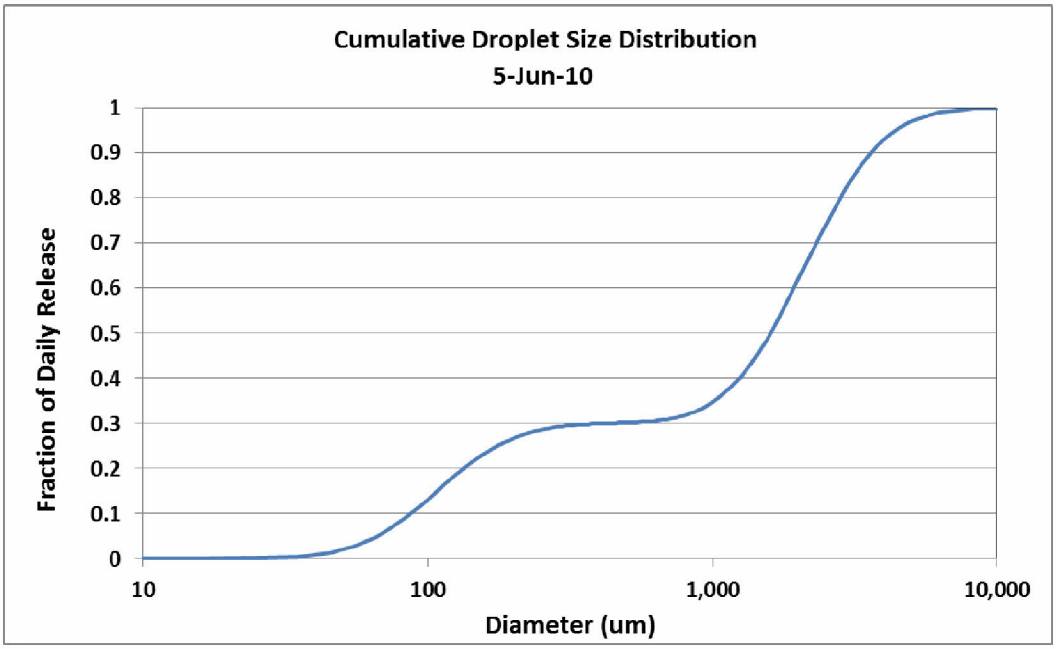

Figure 4-13. Cumulative droplet size distribution on June 5 after the riser was cut and subsea dispersant was applied using the trident or similar highly effective techniques. The maximum amount of dispersant for any given date was applied at the riser on June 5.

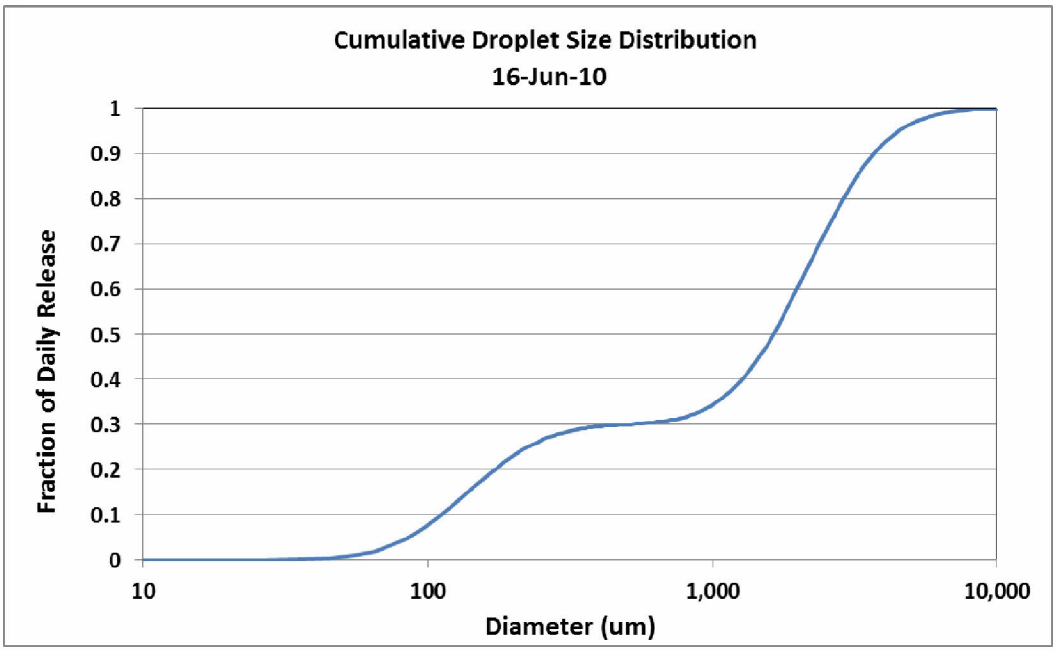

Figure 4-14. Cumulative droplet size distribution typical of June 7 – June 19 after the riser was cut and subsea dispersant was applied using the trident or similar highly effective techniques. Subsea dispersant volumes applied were about 150-250 bbl/day.

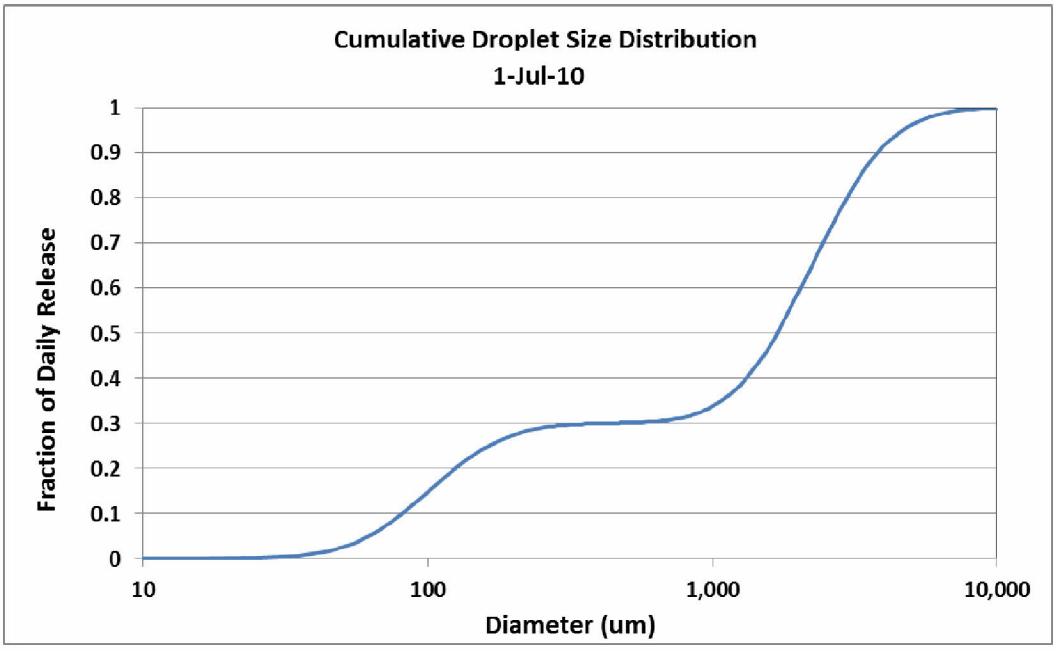

Figure 4-15. Cumulative droplet size distribution typical of June 20 – July 10 after the riser was cut and subsea dispersant was applied using the trident or similar highly effective techniques. Subsea dispersant volumes applied were about 250-300 bbl/day.

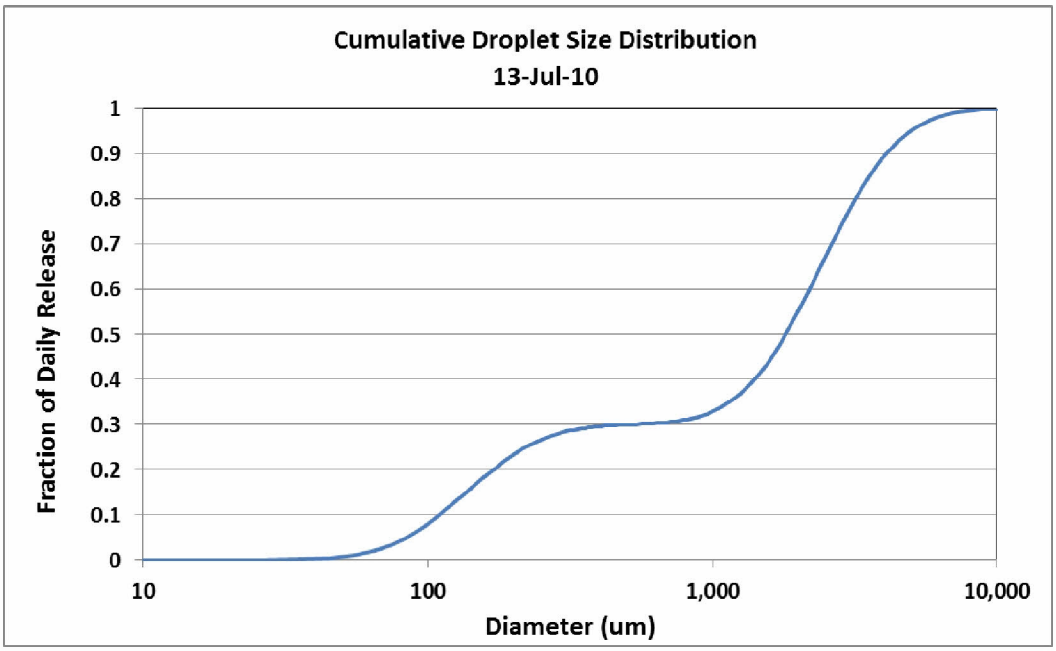

Figure 4-16. Cumulative droplet size distribution typical of July 11 – July 15 when subsea dispersant was applied using highly effective techniques, but oil volume flow increased after the Top Hat was removed and the capping stack was being set in place. Subsea dispersant volume applied was about 350 bbl/day.

The results of these analyses serve as inputs to the SIMAP oil fate model to specify the initial oil mass and the droplet size distributions for the released mass. The daily release volumes were divided into 48 half-hour increments and incremental masses were tabulated with locations and identified droplet sizes (based on the results summarized in Figures 4-7 to 4-16) to create input files for the far field (SIMAP) model runs.

4.7 Model Parameters

The start of the oil release is simulated as April 22, 2010 at 10:30AM CDT (local time). The release duration is 2015 hours (84 days), i.e., until July 15, 2010 at 14:30 CDT.

Below is a summary of model input parameters defining the model resolution:

- Number of spillets (Lagrangian elements):
  - Surface or subsurface oil: 100,000
  - Dissolved aromatics: 1,600,000
- Simulation Time Step: 0.5 hr
- Length of the Simulation: 161 days (until September 30, 2010)

In order to obtain sufficient resolution of modeled concentrations, and allow for the ranges of the vertical distributions of biota exposed, concentration mapping was performed using a 500m resolution horizontal grid at 20-m depth intervals throughout the water column (20-1400 m). The number of spillets, the time step, and the concentration gridding resolution are all model inputs and are adjusted in accordance with the resolution desired.

5 Observational Data Related to the DWH Spill

5.1 Subsurface Oil Concentrations and Sensor Responses

5.1.1 Literature Studies on DWH Oil Contamination in Deep Water

Appendix E provides a review of DWH observational data from offshore waters reported in published literature that were used for model validation, including water column chemistry and oil particle size information. When considered alongside the NRDA QA/QC'd data summarized below, in Appendix E and in more detail in the reports by Horn et al. (2015a,b) and Payne and Driskell (2015a,b,c), a more complete understanding of the DWH spill becomes apparent, illustrating the transport, fate, and behavior of the oil and gas that was released into the environment.

After the oil and gas was released from the blowout near the seafloor, the jets and subsequently buoyant plumes of oil and gas mixture quickly rose through the water column, entraining ambient seawater until the plume reached neutral buoyancy due to the balance of densities from the increasing density of the plumes and the decreasing density of ambient seawater (i.e., at the trap height). During this fast rising stage, little oil and gas would escape from the rising plume as the deep water currents were too weak to compete with the upward movement. Once the trap height of the initially ascending plume was reached, transport of oil and gas and dispersant became more complex, potentially resulting in different pathways (Spaulding et al. 2015).

After being released from the trapped plume, a considerable amount of oil was dispersed as oil droplets into the water column. The smaller droplets remained in the water column for an extended period of time due to their slow rise velocities, while larger droplets rose to the surface on the time scale of hours. The data and studies reviewed herein support the conceptual model that large droplets rose quickly in the immediate vicinity of the leaking wellhead, forming surface oil slicks in a relatively confined area near the wellhead (as described in Ryerson et al. 2012); intermediate sized droplets extended further afield in the mid water column as they continued to rise through the water column; and a number of small droplets remained suspended in the deep water column intrusion layer.

Hydrocarbons were repeatedly detected in the deep water intrusion layer plume. Camilli et al. (2010) confirmed a large plume at ~1,000- to 1,200-m depth and in some areas >2km wide at ~ 4 km from the leak source during 23-27 June 2010. Their Sentry's methane m/z signal at 35km from the source was only 53% less than that at 5.8km, suggesting that plume extended considerably beyond the 35km survey bound at that time. GC analysis focused on mono-aromatic hydrocarbons confirmed the presence of BTEX (50 µg/L) within the plume at 16 km downrange from the wellhead, suggesting a mechanism existed for direct hydrocarbon transfer to the deep plume.

The larger droplets continued rising to the upper layer and the surface, in a volume described as a rising cone (e.g., Ryerson et al. 2011; 2012; Spier et al. 2013), due to the buoyancy of larger droplets relative to the ambient seawater. However, due to current shear and varying rise rates for different diameter droplets, "plumes" of rising oil droplets would have followed different trajectories on their way toward the surface.

In addition, while rising in the cone, the intermediate-sized droplets lost some of their relative buoyancy due to weathering (dissolution and degradation of the lighter hydrocarbons, fully-weathered oil having a density of ~980 kg/m^3; Stout 2015a), as well as potentially combining with SPM in the water column. Meanwhile, the ambient current higher in the upper water column is increasingly stronger than in deep water (Hyun and He 2010), possibly causing separation of these intermediate sized droplets such that they left the cone and formed "multiple plumes" of slowly rising droplets in the upper layers mimicking the deep water plume.

Fluorescence anomalies (peaks) and water column hydrocarbon chemistry data (Spier et al. 2013, Camilli et al. 2010, Valentine et al. 2010, as well as NRDA data; Appendix E) show relatively high concentrations of hydrocarbons at various depths above the trap height of ~1,100-1,200 m (i.e., the deep plume that is much more strongly evident in the data). This phenomenon is in agreement with the theoretical prediction of a multiphase flow plume model (Socolofsky et al. 2011), although the mechanism proposed by these authors differs from the model of rising independent droplets, and the possibility that some of the oil droplets alone or in combination with SPM became neutrally buoyant. If multiphase flow plumes occurred, one would expect similar fresh-oil chemistry signatures at the multiple depths, as opposed to more weathered oil signatures higher in the water column. With oil droplets rising through currents that are highly variable in direction vertically and over time, those shallower peaks may reflect different oil released at different times. We have not identified a vertical profile of samples containing similar fresh-oil chemistry signatures at the deep plume trap height and shallower depths; however, very few sample profiles were taken within 1-2km of the release point. Samples taken from stations with vertical profiles having peaks at multiple depths show complex and differing chemistry (Payne and Driskell 2015a,b,c; Horn et al. 2015b).

Camilli et al. (2010) identified a more diffuse "plume" existing between 50- and 500-m depth in addition to the deep water plume, based on their mass spectrometric and fluorescence data. Brown et al. (2011) and Boehm et al. (2012) have described chemistry results from the response program. Spier et al. (2013) compared hydrocarbons in two broad regions, indicating that Region 1 (i.e., the deep water intrusion layer plume plus the confined rising cone) had the highest concentrations of hydrocarbons, whereas Region 2 (i.e., the rest of the water column of 45 km radius surrounding the wellhead) also contained substantial concentrations of hydrocarbons, mainly at shallower depths of 25 m, 265 m, and 865 m. After Top Hat #4 became operational (i.e., after June 3, post riser cut), both the sample concentrations and the percentage of detectable results decreased for the 865 and 1,175 m plumes. In addition, there was a significant increase in the frequency of detections and sample concentrations with high dispersant indicator concentrations typically associated with less water-soluble compounds, including di- and poly-cyclic aromatics/alkylated aromatics and alkanes >C8, which is consistent with wider dispersion of reduced oil droplet sizes with application of dispersants (Chan et al. 2014).

Changes in chemical composition with depth also support the preceding description of the transport of dissolved compounds, dispersed oil, and larger droplets. Most water soluble compounds such as benzene, alkylated mono-aromatics, and soluble C5-C10 alkanes were enriched in the deep plume. Less water soluble compounds were present both in the deep water plumes and in the upper water column: C13-C22 PAHs and C11-C22 alkanes were found at 1,175m and 865m, as well as even deeper water and near the surface; C23-C40 alkanes were found at 1175m and 265m, in surface waters, and also at lower concentrations in the 865m plume (see Horn et al. 2015b, for details). These vertical changes in measured chemical composition indicate that dissolved hydrocarbons and (likely the smallest) droplets were trapped in the intrusion layer plume.

Water column gas and dispersant chemistry data are also reviewed in Appendix E. For instance, Kujawinski et al. (2011) reported that the dispersant constituent dioctyl sodium sulfosuccinate (DOSS) was in general sequestered in deep water hydrocarbon plumes at 1,000-1,200 m water depth; although, in Cast 07 of their study, DOSS occurred at higher concentrations at shallower depths (850 - 900m), where it did NOT correlate with peaks in fluorescence or methane concentration. However, DOSS is an ingredient of cleaning products used during the sampling; thus, some observations of DOSS may actually be the result of contamination from cleaning the sampling gear. On the other hand, DOSS was frequently observed in deep water samples concurrent with fluorescence peaks, suggesting dispersant was associated with trapped oil droplets.

Valentine et al. (2010) focused on gas distribution and fate in the water column. They found that propane, ethane, and methane were most abundant at depths greater than 799 m and formed plume structures with dissolved concentrations as high as 8 µM, 16 µM, and 180 µM for the three gases, respectively. Concentrations were orders of magnitude lower at shallower depths. The persistent plume at 1,000- to 1,200-m depth was located to the southwest of the spill site, consistent with other reports (Camilli et al. 2010; Hazen et al. 2010). Separate plumes were also identified by Valentine et al. (2010) at similar depths to the north and to the east. A distinctive shallower plume was observed at 800- to 1000-m depth located to the east. Spier et al. (2013) calculated frequencies in each of 8 cardinal directions of detectable hydrocarbon concentrations in samples taken at various depths and within 45km of the wellhead, finding the highest frequency of detectable results to the southwest, but also detections in the other directions. These findings, as well as other data sets compiled by the NRDA program, suggest that multiple plumes moved in varying and sometimes opposite directions, presumably originated at different times and indicative of complex current patterns in the area before sampling.

Dissolved oxygen profiles are shown and discussed in Grennan et al. (2015). Propane and ethane were identified by Valentine et al. (2010) as the primary drivers of microbial respiration, accounting for up to 70% of the observed oxygen depletion in fresh plumes. The sum of these values, ~1.5×10^{12} g of O_2, provides an estimate of the maximum integrated deep-water O_2 anomaly expected from this event, with ~15% of the oxygen loss occurring in fresh plumes from respiration of propane and ethane, and ~two-thirds of the ultimate microbial productivity in deep plumes would arise from metabolism of natural gases. The remaining oxygen loss would have been due to oil hydrocarbon degradation.

Davis and Loomis (2014) made measurements of the oil droplet size distribution using a Holocam during the *M/V Jack Fitz* (JF) 3 cruise. The average volume median droplet diameter from the JF3 cruises was 128 µm, with values ranging from 86 to 176 µm. Thus, the Holocam data provides evidence of small (volume mean diameter <300um) chemically dispersed oil droplets in deepwater and intermediate waters. Further discussions of the Holocam and other particle size data are in Appendix E.3 and in Li et al. (2015).

Model simulations employing the well-known Stoke's Law (where rise rate increases with droplet diameter) provide additional evidence for the separation of small droplets (in the intrusion layer) from intermediate and large droplets (slowly or rapidly rising to the surface, respectively). For example, sensitivity analyses by North et al.'s (2011; 2015) showed that droplets with diameters of 10 - 50 µm would form distinct subsurface plumes that would be transported horizontally and remain in the subsurface for >1 month. Droplets with diameters ≥90 µm would rise more rapidly to the surface.

5.1.2 Summary of NRDA Chemistry and Sensor Data

During the DWH blowout and resulting spill, a variety of environmental data were collected by NRDA samplers aboard numerous ships. Discrete surface and water column samples were collected, sub-sampled, and analyzed from various vessels using NRDA protocols. While similar sampling protocols were followed, each vessel had slightly different objectives and sampling equipment. Alongside collected chemical and forensic data, concurrent and continuous measurements of dissolved oxygen and UV fluorescence were recorded.

A detailed description of the chemistry data used for validating the model may be found in Horn et al. (2015a,b). A detailed description of forensic findings may be found in forensics reports by Payne and Driskell (2015a,b). Physical findings are described in Grennan et al. (2015). Summary figures and discussion are in Appendix E of this report.

Considerable spatial heterogeneity was evident in the distribution of hydrocarbons at various depths and as a function of distance from the wellhead. These resulted from variations in the oil release rate and subsea dispersant applications over time (changing droplet size distributions of the oil over time, see Section 4.8), spatially- and temporally-varying currents (both horizontally and vertically), dissolution, dispersion, and degradation of hydrocarbon constituents, as well as irregularly positioned sampling stations and different sampled depths. The multiple plumes observed moving in opposing directions presumably originated at different times, and indicated the complex current patterns in the area before sampling.

The spatial and temporal patterns of chemical sampling events may have partly driven the observed trends discussed below and in Appendix E, and does not lend itself decisively to determining the complete distribution of hydrocarbons throughout the Gulf of Mexico. The large gaps between sampling locations in space and time render much uncertainty for any interpolation of the results in this dynamic environment. Furthermore, the sampling efforts to depict hydrocarbon distributions throughout the water column may be complicated by the unavoidable heterogeneity within the water column. For these reasons, sampling gaps in space and time can be quite difficult to interpret conclusively as evidence of either the presence or absence of oil in regions not sampled. Sparse sampling requires systematic compiling and synthesis of all available field data, in combination with modeling analyses, in order to expand the scope of our understanding of spill impact.

Hydrocarbon concentrations, fluorescence, and dissolved oxygen varied at several scales ranging from factors to orders-of-magnitude in both space and time. Based on the analysis of the water column chemical and physical data, as well as the consideration of major events during response, four distinct periods of time are identifiable during the spill period in 2010. These are described as separate Observable Chemistry Regimes (OCR):

- OCR 1: pre-top-kill (Apr-20 to May-26)
- OCR 2: top-kill, riser-cutting, and initial top-hat (May-26 to June-6)
- OCR 3: post-cut and collection (June-6 to July-15)
- OCR 4: post-cap (after July-15) phase

Sampling of the active release of oil and gas during the three phases (OCR 1-3) was focused around the wellhead (<20 km), while more extensive and broad-scale sampling into the far-field (focused to the south and southwest) did not commence until after the well shut-in was completed (OCR 4). (See Figures E.2-3 to E.2-7 in Appendix E.) In-water concentrations

remained elevated during the blowout and the released hydrocarbons began to dissipate just after the well was contained and eventually capped.

In April and May, oil was released from the broken riser (at 1509 m deep) and from holes that developed at the kink in the riser pipe (at 1,503 m deep). The fluorescence and DO anomalies, chemical concentrations, and blowout models (Socolofsky et al. 2011; Spaulding et al. 2015) indicate that a considerable portion of the released oil rose from the depth of release to several hundred meters above the release depth as part of the buoyant plume. Several times during May 26-28, the spill responders attempted to fill the riser pipe with heavy drilling mud and bridging material, but the procedures did not stop the release and the mud and "junk" were forced out of the riser. Relatively high hydrocarbon concentrations and fluorescence anomalies were observed during this period. During June 1-3, while the riser pipe was being cut, oil flowed freely from the riser, and this is evident in the data as elevated fluorescence peaks and hydrocarbon concentrations between 1,000 and 1,300m compared to periods prior to and after this event. In OCR 3, oil was released from the blowout preventer (BOP) at a depth of 1,506 m deep from the opening of the Top Hat oil recovery installation or the gap between the Top Hat and the BOP. During OCR 4, after the release was stopped on July 15, in water hydrocarbon concentrations decreased with increasing time and space.

As may be seen in summary figures in Appendix E, the maximum hydrocarbon and dispersant concentrations occurred at the surface (<40 m) and at depths between roughly 1,100 and 1,300 m deep (Figure E.2-8 and Figure E.2-10). The subsurface maximum in hydrocarbon and dispersant concentrations was the result of the high-energy discharge of oil from the kink and riser. Small droplets of oil were produced under high-pressure flows, made even smaller with the application of dispersant (Spaulding et al. 2015). With slow rise rates, these small droplets were trapped below 1,100 m, where both whole oil and dissolved phase hydrocarbons were found alongside dispersants. Elevated dispersant concentrations were identified between 1,000-1,300m near the wellhead and between 1,100-1,200 m to out beyond 150 km.

Forensically identified MC252 oil was commonly observed radially within roughly 50 km of the wellhead (Figure E.2-8 and Figure E.2-10). See Payne and Driskell (2015a) for a full description of forensically identified MC252 oil in subsurface water samples, including as particulate- and dissolved-phase hydrocarbons.

Elevated hydrocarbon concentrations at depth were observed in each of the investigated groupings ranging from BTEX (AR1) through to the soluble alkanes (AR9). The highest concentrations at depth were of the BTEX group and soluble alkanes (Figure E.2-8). When considered together, the total soluble compounds, the total investigated compounds, and PAH50 groups all had highest observed concentrations between 1,000-1,300 m. The highest measurements of total investigated compounds in the deep plume were >100-700 µg/L, with concentrations up to ~80 µg/L between 200-1,000 m. When considered individually, soluble alkanes (AR9) typically had the highest concentrations between 1,000-1,300 m with values of >100-400 µg/L, while BTEX (AR1) were typically >100-200 µg/L, and PAH50 were typically <120 µg/L.

While most attention has been focused on hydrocarbon concentrations near surface waters and the region between 1,000-1,300 m, it is important to note that elevated concentrations in excess of the method detection limits were identified throughout the water column beyond 150 km (Figure E.2-9). Sampling in the depth range between 100-1,000 m was much more sporadic. The highest concentrations at depth in this region were for the BTEX group and soluble alkanes (Figure E.2-11). The spatial extent in these intermediate waters is slightly more proximal to the wellhead, with highest concentrations observed typically within 25 km of the wellhead.

There were consistently observed fluorescence anomalies, as relative high values or "peaks", at depths between approximately 1,000-1,300 m. Figures E.1-3 to E.1-6 in Appendix E summarize the observed fluorescence anomalies. Maximum anomalies occurred between roughly 1,100-1,200 m. The highest values were observed near the wellhead; the anomalies decreased as distance from the wellhead increased. Anomalies of high fluorescence values at depths of 1,000 - 1,300 m were typically associated with elevated hydrocarbon concentrations in the water column, when water samples were collected concurrently with fluorescence measurements. These fluorescence peaks were observed mainly to the southwest of the wellhead. Although maximum fluorescence peaks were identified within a narrow range at depth, significantly elevated fluorescence values were noted throughout large portions of profiles. Peak fluorescence values at depth typically tapered to lower values in shallower waters. It was very common to observe significantly elevated fluorescence values up to 600 m and occasionally shallower.

There were consistent anomalous dissolved oxygen "sags" (i.e., relatively low values of dissolved oxygen in vertical profiles when compared to baseline profiles) at depths between approximately 700-1300 m. Figures E.1-7 and E.1-8 in Appendix E summarize the dissolved oxygen anomalies. The maximum anomalies occurred between ~1,100 and 1,200 m deep. As distance from the wellhead increased, dissolved oxygen anomalies first increased and then decreased. As sags decreased in magnitude, they frequently became slightly broader, covering larger depth ranges. These observations are indicative of microbial degradation (i.e. hydrocarbon consumption) at depth followed by mixing with surrounding waters.

The various chemical and physical observations depicted relatively consistent anomalies between 1,000-1,400 m that were generally observed as enhanced chemical concentrations, increased fluorescence, and decreased dissolved oxygen. A consistent pattern of observed anomalies at depth supports the assessment of trapping of the buoyant oil and gas plume between 1,000-1,400 m. This subsurface region of hydrocarbon contamination contained trapped oil, dissolved hydrocarbons (primarily BTEX and soluble alkanes), and dispersants, which were slowly dispersed and consumed at depth. Results from chemical and physical measurements suggest that in general, after about July 1 hydrocarbons in this "deep plume" predominantly moved to the southwest. The southwestward movement of the deep water contamination continued throughout the fall of 2010. Deep ocean currents in the region are dominated by cyclonic flows along the isobaths, which near the spill site are generally to the southwest (Schmitz et al. 2005); therefore, the chemistry and sensor indicators are consistent with understanding of the circulation in the area.

When investigated alone, each sensor and measurement provides some evidence of contamination from MC252 oil. It is highly likely that hydrocarbons extended into regions that were not sampled or summarized in the data presented here. Furthermore, there were numerous compounds in MC252 oil that were not quantified through the spill (McKenna et al. 2013).

5.2 Oil Settled to Offshore Sediments

MC252 oil from the spill was identified on the sediments in the offshore area surrounding and down-stream of the well site (Joye et al. 2011; Montagna et al. 2013; Valentine et al. 2014). Valentine et al. (2014) estimated 4-31% of the released oil was sequestered in the deep sea. They noted that the pattern of contamination indicates deep-ocean intrusion layers as the source, consistent with deposition of a "bathtub ring" formed from an oil-rich layer of water impinging laterally upon the continental slope (at a depth of ~900–1,300 m) and a higher-flux

"fallout plume" where oil-SPM aggregates sank to underlying sediment (at a depth of ~1,300–1,700 m). Stout et al. (2015) estimated the extent of Macondo oil from the Deepwater Horizon oil spill in benthic sediments using a combination of chemical fingerprinting and a geostatistical interpolation method of kriging for 2,397 sediments from 875 cores collected in 2010-2011 and 2014. Their conservative estimate was that the settled oil surrounding the wellhead is about 6.9 – 7.7% of the released oil mass.

Thus, there is evidence that there was a flux of spilled oil to the sediments. Because mineral SPM concentrations are typically very low in the offshore Gulf of Mexico near the wellhead, the transport flux to the seafloor was more likely due to oil adherence to organic matter, rather than mineral sediments. Indeed Passow et al. (2012) and Passow (2014) measured considerable sedimentation of organic marine snow in the offshore area near the wellhead in 2010-2011.

The carbon-flux in oil-contaminated surface water near the spill site was greatly affected by activities of microbes associated with macroscopic oil aggregates (Ziervogel et al. 2012). Roller bottles incubated with oil-amended water for 21 days showed rapid formation of oil aggregates that were similar in size and appearance compared to oil aggregates observed in surface waters near the spill site. Formation of oil aggregates following the Ixtoc oil spill in shallow (and relatively turbid) waters of the Gulf of Mexico has been reported previously (Patton et al. 1981), causing a major fraction of spilled oil to settle the seabed (Jernelov and Linden 1981; Lehr et al. 2010). In the DWH oil spill, visual observations of sinking oil/mucus strings out to 9 km (Payne and Driskell 2015d) and chemical analysis of sediments in the vicinity of the wellhead (discussed above) also indicated oil-SPM sedimentation. Sinking of oil aggregates near the well head was observed throughout the water column in the second half of May 2010 (observations by Dierckst al. 2010, cited by Ziervogel et al. 2012). Sinking oil aggregates likely transferred oil and organic carbon from the surface (Ziervogel et al. 2012) and the deep water plume (Ziervogel and Arnosti 2014) onto the sea floor. However, sufficient quantitative data with which to model organic SPM-oil flux to sediments was not available for this study.

6 Results

6.1 Simulations Modeled

Two simulations were performed:

- Static Cone: For the purposes of estimating concentrations of PAHs as daily means in the exposure volume affected by rising oil and the deep plume, the oil fate model was run without currents. This simplification allowed daily averaging of concentrations in a stationary grid and so generated a better representation of plankton exposures than possible if horizontal transport and displacements were included. The analysis assumes that the dissolved hydrocarbons and oil droplets remaining in the water column and the plankton all moved together; such that the gridded daily-average concentrations based on the simulation without currents characterizes the exposure experienced by plankton each day as they moved with the oil plume. Daily average exposure concentrations of total (dissolved plus particulate) PAHs (using 50 analytes, "TPAH50", Forth et al. 2015b) were calculated for each horizontal grid cell and by 20-m depth layer of the water column.
- Deep plume: SIMAP was run for the entire release utilizing IAS ROMs currents as inputs. The modeled concentrations of oil components in the depth range of 1,100-1,400 m were analyzed to describe the transport and fate of the oil in the deep plume.

The model inputs for these simulations were the same, as described in Section 4, except for (1) inclusion or not of the currents as input and (2) the advective and spreading dispersion coefficients in the horizontal directions. The horizontal dispersion coefficients are described in section 4.2.4.

6.2 Results of the Static Cone Simulation

Because the Static Cone simulation does not include currents as input, but does simulate dispersive spreading from the central axis of the rising oil via turbulent mixing processes, the footprint of the rising oil droplets is in the shape of an inverted cone; hence the terminology. The vertex of the cone is at the trap height and the widest radius is at 20 m below the water surface (the upper depth limit of the simulation). Rising oil droplets with the largest diameter are found in the center of the cone along the cone axis. Progressively smaller droplets are found moving out from the axis, as the slower rise rates of smaller droplets increases their residence time in the water column, therefore increasing their dispersion. Concentrations of contaminants are highest along the cone axis, decreasing toward the edges in a Gaussian shape that is typical of dispersion from a central source. The concentrations of droplets and dissolved constituents are also higher closer to the source at the bottom (i.e., at and just above ~1,200 or ~1,300 m). Because of these patterns, the cross-section of the *concentration* field looks more like a cylinder, or even has a bell shape with highest concentrations at the center just above the base of the bell near 1,100 - 1,220 m (and around 1,300 m near the kink holes present in May), and much less like an inverted cone. Because the smaller oil droplets spread out considerably at the top of the cone, the concentration profiles show much lower concentrations higher in the water column and farther from the axis of the inverted cone.

Snapshots of the concentration distributions produced by the Static Cone simulation typical of each month (April 26, May 17, Jun 16, and July 15) are provided in Appendix F. Figures F.2-1 to F.2-40 in Appendix F.2 depict the Gaussian shape of the concentrations as they spread

horizontally. Each figure depicts a top-down view providing the vertical maximum concentration in the water column in horizontal space, with an associated west-east cross-section through the center of the inverted cone (bell). There are 10 figures for each of the 4 dates, one for each of the 9 soluble components and the total of all components. Each figure is a pair showing concentrations in the particulate (i.e., droplet) and dissolved phases.

The cone diameter is relatively small during April (Figures F.2-1 to F.2-10 in Appendix F.2) when subsea dispersants were not applied, the kink holes had not yet formed, and most droplets were > 1mm in diameter (Figure 4-10), rising to the surface within hours. The diameter of the cone (measured at the point where the vertical maximum total hydrocarbon concentrations are greater than 1 μg/L, a conservatively low concentration) is about 3 km on April 26. From May through mid-July (Figures F.2-11 to F.2-40 in Appendix F.2), the cone diameter grows to 12 km by May 17, 16 km by June 16, and 20 km by July 15. After the well is shut in, this diameter shrinks as concentrations disperse and components degrade. Total hydrocarbon concentrations are <100 μg/L in all locations on August 20 and on September 30 they are <10 μg/L, for the most part. In the simulation, dissolved soluble and semi-soluble hydrocarbon concentrations decrease to <1 μg/L in all locations by August 20.

Figures such as F.2-11 (for May 17) in Appendix F show that most of the oil surfaced within a 2-km radius of the wellhead in the Static Cone simulation, consistent with observations by Ryerson et al. (2012). Payne and Driskell (2015d) reported fresh oil surfacing between 1.5 and 4 km from the wellhead, slightly further out but in the real situation with currents. This is consistent with our no-current near-surface 2-km radius.

Note that the total hydrocarbon concentrations in droplets that are predicted by the model are based on the total mass of the release (i.e., the mass equivalent of 3.19 million bbl), much of which cannot be chemically measured in water samples. Thus, the modeled total hydrocarbon concentration is not comparable to a total petroleum hydrocarbon measurement. For this reason, model-predicted concentrations of the soluble and semi-soluble hydrocarbons, i.e., of the AR components, are compared to field sample measurements of those same chemical components. Note that the aliphatic AL components are defined by boiling point ranges, and so those components contain much more mass then is measurable using GC/MS or other existing techniques to measure aliphatic hydrocarbons in the water.

The concentrations for each of the modeled chemical components are depicted in the figures in Appendix F.2. The soluble and semi-soluble hydrocarbon concentrations are in low concentrations in a narrow cylinder stretching toward the surface in April, when the release was mostly of large droplets (Spaulding et al. 2015; see Section 4.6.3). During May when the kink holes appeared and subsea dispersant began to be applied, the concentrations are much higher and over a wider diameter. The higher concentrations continue in June when more effective subsea dispersant applications were used (Spaulding et al. 2015). The highest dissolved concentrations are of BTEX and soluble alkanes, whereas most of the 3-ring PAHs are still in the particulate phase.

In Figure F.2-12 of Appendix F, concentrations of BTEX (AR1) produced by the Static Cone simulation on May 17 show two vertical maxima at the two depths of release: the deeper (~1,300 m) from the kink holes in the riser and the shallower ~1,200 m from the end of the broken riser. BTEX dissolution rates are obviously rapid based on the concentration distribution; in agreement with publish accounts of field observations, such as those by Reddy et al. (2011), and the NRDA chemistry data (Appendix E, Figures E.2-8 to E.2-11). Outside of the core at the release location (where field samples were not taken), the maximum BTEX concentrations in the rising oil were predicted by the model to be 25-100 μg/L (Figures F.2-12 and F.2-22,

Appendix F), in agreement with observations by Reddy et al. (2012) during June 19-28, 2010, which had a plume layer concentration as high as 78 µg/L. This is also consistent with the NRDA cruise data (Horn et al. 2015a,b), in which, the pre-cut (i.e., prior to Jun 3) plume layer median BTEX concentration value was 92 µg/L (range 4.5 – 228 µg/L) and the post-cut plume layer median value 60 µg/L, (range 4.9 – 176 µg/L).

After the riser was cut June 3, new oil was released at about 1,200m. However, some concentrations persisted at ~1,200 – 1,300 m because the oil released in that depth range in May was in very small droplets that had very slow rise rates. The small droplets (<100µm) remained in the deep plume layer of ~1,100 – 1,300 m. In the field, the deep plume was advected predominantly to the southwest.

For the evaluation of toxicity to water column biota (Morris et al. 2015b), the components of concern are total PAHs. Most of the released mass of the fifty PAHs (TPAH50) included in analyses used in the Trustee's NRDA toxicity program (Forth et al. 2015b), is encompassed by AR5 to AR8 in the SIMAP modeling. The remaining PAHs in TPAH50 have log(K_{ow}) values >6.0, and so are included in the residual (non-soluble and non-volatile) component for the modeling. The fraction of the residual represented by these PAHs with log(K_{ow}) >6.0 is 0.000385 (0.0385%). The TPAH50 concentrations in the dissolved and particulate (droplet) phases were calculated from the SIMAP model output and the total of these (i.e., dissolved + particulate = total TPAH50) was used for the toxicity evaluations and injury quantification (French McCay et al. 2015).

The maxima of the daily average TPAH50 concentrations estimated by the model in any 500 m x 500 m x 20 m cell (i.e., 20 m "vertical slices") of the concentration grid characterizing the rising oil in 20-1,100 m, as well as in the deep plume (1,100-1,400 m), are plotted in Figures 6-1 and 6-2. Figure 6-1 provides the total TPAH50 concentrations in the water, as the sum of dissolved and particulate (droplet) phases. Figure 6-2 provides the maxima for dissolved TPAH50. The deep plume maxima are at the center axis of the cone at ~1,100-1,200 m. (See the Figures in Appendix F.2, where TPAH50 = AR5 + AR6 + AR7 + AR8 in both dissolved and particulate phases, plus 0.0385% of the residual in droplets). The maximum at ~1,100-1,200 m reaches 872 µg/L total TPAH50 (dissolved and particulate) on one date (June 7) and in one cell. However, generally on other dates the total TPAH50 maxima (for the central cell at ground zero) are between 300-600 µg/L. The corresponding maximum (at ~1,100-1,200 m) for dissolved concentrations is 186 µg/L dissolved TPAH50 for one cell on June 7, and generally 80-140 µg/L dissolved TPAH50 from May to July. Note that all droplet sizes were included in the total TPAH50, but given the rapid rise rate of droplets >1mm in diameter, the droplet sizes included in the total concentrations of TPAH50 generally ranged from 10s to a few 100s of microns in diameter.

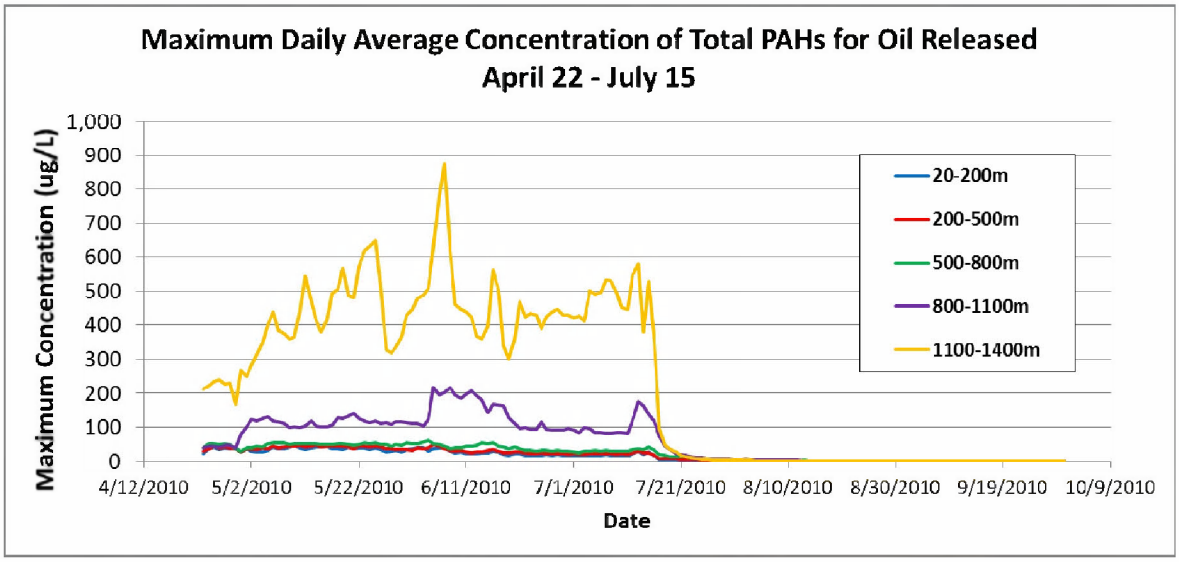

Figure 6-1. Maxima of the daily average TPAH50 concentrations, as sum of dissolved and droplet concentrations, estimated by the Static Cone simulation in each of the indicated depth zones.

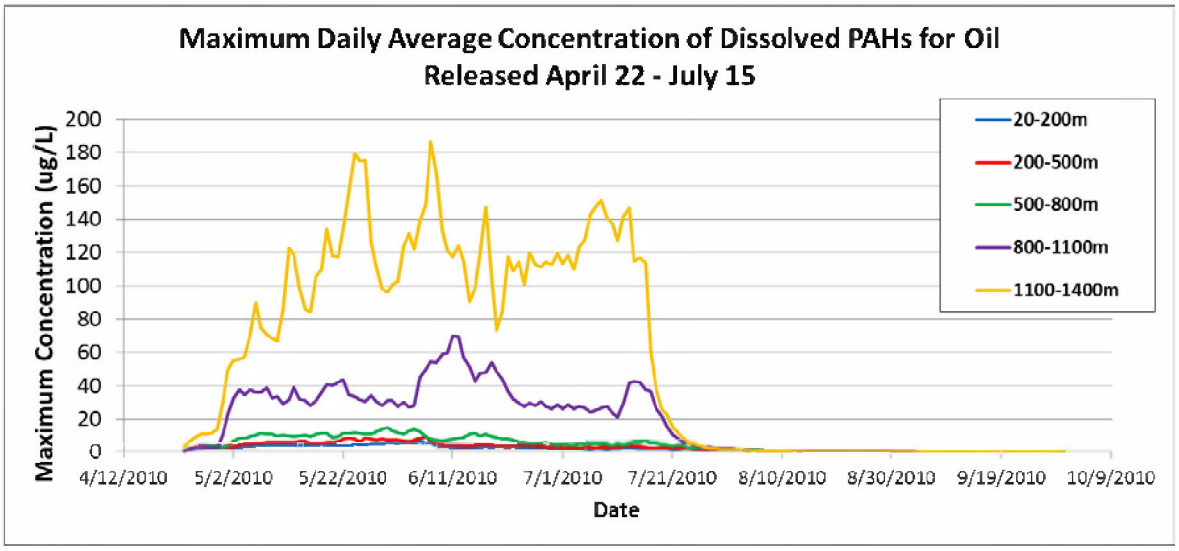

Figure 6-2. Maxima of the daily average TPAH50 concentrations in the dissolved phase, estimated by the Static Cone simulation in each of the indicated depth zones.

Higher in the water column (shallower) and away from the cone axis, concentrations are much lower than these maxima. Careful consideration should be used when comparing the model results to measurements from samples. Samples were not collected at the maxima at the center axis of the inverted cone, and therefore much lower concentrations would be anticipated further from the center axis. The highest PAH concentrations below 20 m (up to ~5 µg/L) were consistently measured in water samples taken at depths between approximately 1,000-1,300 m, but elevated PAHs were also measured at shallower depths in lower concentrations (Figures

E.2-8 to E.2-11 in Appendix E.2; "PAH50" in these figures corresponds to TPAH50). Further comparisons to observations are made in Section 6.4.

The highest measurements of total investigated hydrocarbons (including BTEX, other MAHs, PAHs, and soluble alkanes) in the deep plume were >100-700 µg/L, and concentrations up to ~80 µg/L were measured at other depths between 200-1,000 m. Fluorescence peaks and dissolved oxygen sags in the depth zone where the highest BTEX and PAH concentrations were measured, were observed between 1,000-1,300 m (compare Figures E.1-3, E.1-5, E.1-6, and E.1-8 in Appendix E.1 with Figures E.2-8 to E.2-11 in Appendix E.2). The model-simulated concentrations (Appendix F.2) depict similar distributions and concentrations.

The modeled concentrations of BTEX remaining in the oil droplets above 1,100 m (Appendix F.2, Figure F.2-22) were very low throughout the simulation. Comparisons between the BTEX content of the oil droplets and the dissolved concentrations indicate that the BTEX was rapidly dissolved below 1,100 m in the deep plume. Dissolution continued at shallower depths as oil droplets rose through the water column (cross sections within Appendix F.2 Figures). Semi-soluble components (i.e., C2-benzenes, C3-benzenes, naphthalenes, low molecular weight alkanes, isoalkanes, cycloalkanes) partially dissolved while the oil droplets were at depths below 1,100 m (Appendix F.2 figures). Additionally, substantial dissolution of semi-soluble compounds occurred at shallower depths, as droplets continued to rise. In the simulation, the sparingly soluble 3-ring PAHs were primarily in the droplet phase. Dissolved concentrations of components AR6, AR7 and AR8 (PAHs) were only >1 µg/L below 800 m (see Figures in Appendix F.2 as compared to Appendix E, Figures E.2-8 to E.2-11). These partitioning patterns are generally consistent with the weathering models and analyses of chemistry samples, where dissolved and particulate fractions were measured (Payne and Driskell 2015a,b,c)

6.3 Results of the Simulation Using Currents from IAS ROMS

In the model simulation using currents from IAS ROMS, total hydrocarbons within oil droplets at concentrations >1 µg/L were highly variable in space and over time, as the currents shifted. Figures F.3-1 to F.3-14 in Appendix F provide snapshots of the vertical maximum concentrations in the deep plume (1,100-1,300 m) at several dates within the simulation. Each figure depicts two top-down views mapping the vertical maximum in droplet and dissolved total hydrocarbon concentrations in the modeled depth range between 1,100-1,400 m. The concentration at any point in space or time changes rapidly, as the water and oil move during the continuing release. Therefore, it is difficult to portray the results in static figures. To portray the movement of the oil, the "age" of the spillets (time since each particle was released) was plotted. Snapshots of the trajectory, integrating spillets over the water column and color-coded by the age of spillets, are provided in Figures F.3-15 to F.3-27 within Appendix F.3.

The simulation using currents from IAS ROMS depicts the extent to which currents may transport and shear the rising oil. The shape of the cone is not depicted in the 1,100 – 1,400 m simulation, as there is substantial displacement; later in the simulation spillets move in different directions. ADCP data in ~30-60 m vertical bins in the water column showed slow (<10 cm/sec) currents in adjacent depths differing by as much as 120° in the May-June 2010 timeframe. Transport at shallower layers (not shown) may also shear the oil plume in multiple directions. Some of the described shear is evident in the figures (Appendix F.3) that depict the age of the spillets as they move throughout the simulation.

In the simulation, dissolved concentrations move horizontally, as droplets rise out of the 1,100 – 1,400 m layer. Of the droplets, smaller droplets were transported farther from the wellhead before rising out of the layer. This makes the oil droplet (and resulting dissolved) concentrations

highly patchy in three-dimensional space. Successful sampling of such patches would be rare occurrences using a regularly-spaced sampling design. For this reason, NRDA sampling was focused on locations where fluorescence and dissolved oxygen sensors indicated the potential presence of in-water hydrocarbon concentrations (Payne and Driskell 2015d). This targeted sampling approach was used on NRDA *Jack Fitz* 1, 2, 3 cruises of May and June 2010, but did not began in earnest on the response vessels until late July and August of 2010 (Figure E.2-2 in Appendix E).

Using the chemistry sample results (see Appendix E), observations of particulate oil (Li et al. 2015 and Payne and Driskell 2015d), and modeling analyses (Spaulding et al. 2015), it was concluded that much of the oil was released in relatively large droplets, which rose rapidly to the surface near the wellhead. In April 2010, the oil was released primarily as >1 mm diameter droplets. Therefore, subsurface hydrocarbon concentrations below 1,100 m were only above 1 μg/L within a radius of approximately 2 km of the wellhead. In May 2010, the progressively smaller oil droplet sizes released (Spaulding et al. 2015) resulted in increasing concentrations of oil in the deepwater plume. After May 2010, observed concentrations from field sampling extended further from the wellhead, to a distance of at least 40 km on May 15 and 70 km on May 31 (see Appendix E.2, Figure E.2-8). While the IAS ROMS currents were weak between April 22-24, they transported the deep oil plume (1,100-1,300m) with concentrations > 1 μg/L in the simulation to ~70 km to the southwest by May 3 (Figure F.3-3) and to ~150km to the southwest by May 17 (Figure F.3-6). However, on May 31 (Figure F.3-8), the deep plume was within 50 km of the wellhead in the simulation. In June and July 2010, eddies are evident in the simulation as IAS ROMS transported the deep plume oil in multiple directions. Figures F.3-9 to F.3-14 in Appendix F.3 depict this variable transport. Transport to the southwest, particularly from July through the fall, was observed in fluorescence and dissolved oxygen indicators and chemistry samples collected in June to September 2010 (Payne and Driskell 2015a and Appendix E.1). Southwest transport was also observed in the deep plume of the IAS ROMS simulation for 1,100-1,400m (see Appendix F.3). Note that the concentration maps in Figures F.3-1 to F.3-14 only depict concentrations > 1 μg/L.

6.4 Comparison of the Modeled Concentrations to Field Measurements

The modeled concentrations of oil components were compared to measurement data reported in the literature, as available, and from chemistry samples collected for the NRDA chemistry program (described in Horn et al. 2015a). Comparisons to literature reports are discussed in Section 7. Results of comparisons of the model results to the NRDA chemistry data are presented in this section and discussed further in Section 7.

The modeled concentrations of each of the oil components were compared to measurement data of each component from chemistry samples collected for the NRDA chemistry program (see Horn et al. 2015a for a description of the sample data sets and QA/QC procedures, as well as Horn et al. 2015b for presentation of the chemical measurement results). Due to the differences between the modeled and actual field conditions and the patchiness of observed chemistry, there is the potential for displacement between modeled and observed concentrations in both space and time. Therefore, a direct overlay of the detectable chemistry measurements on the model would be insufficient for evaluating if the concentrations produced by the model are reasonable. To account for this displacement, results are plotted as probability distributions within a spatial and time window, containing a population of chemistry samples.

The chemistry samples and modeled results were ordered by concentration so that the distributions may be compared.

Most of the chemistry samples were analyzed as whole water samples, which includes both the in-droplet and dissolved concentrations. The chemistry sampling was targeted at fluorescence peaks and dissolved oxygen sags, which indicated the presence of oil and preferentially targeted regions with higher chemical values (Payne and Driskell 2015d). If a randomized sampling plan were used both horizontally and vertically, then many more samples would likely be present with non-detectable hydrocarbons. Therefore, only the modeled concentrations with hydrocarbon concentrations greater than zero were compared to the chemistry results.

The comparisons were made for five vertical intervals within a 25 km by 25 km box centered on the wellhead. Table 6-1 summarizes the nine time domains (based on the OCRs, described in Section 5.1.2) considered for the statistical analysis. However, only the OCR1, OCR2 and OCR3 time intervals had sufficient samples (>5 samples in each depth interval and the domain considered) for meaningful comparisons. The single latitude, longitude, and depth domain is:

Longitude: 88.628° to 88.130° W

Latitude: 28.51° to 28.96° N

Depth range: 40-1400 m (divided into 5 depth intervals: 40-200 m, 200-500 m, 500-800 m, 800-1100 m, 1100-1400 m)

Table 6-1. Time domains considered for the comparison of modeled to observed component concentrations.

Time Period	Date Range	
	Starting Date	Ending Date
OCR1	4/22/2010	5/26/2010
OCR2	5/26/2010	6/6/2010
OCR3	6/6/2010	7/15/2010
OCR4	7/15/2010	9/30/2010

Figures in Appendix G graphically depict the comparisons of modeled to observed chemistry values. A single figure is provided within this section of the report as an example (Figure 6-3). The depth range listed in the figure legend specifies the investigated region as a layer of the ocean. Only chemistry samples and SIMAP prediction data within this depth interval and the geographic bounds are presented for the specified time period.

Histograms are used to compare the frequency distribution of the modeled concentrations within each grid cell to the frequency distribution of the measured samples. This is presented in a cumulative percentile format (left panel) and a histogram of percentage in each concentration bin indicated on the x-axis of the upper-right panel. The maximum modeled chemistry concentration is provided at the top of the left panel figure. Selected percentiles of modeled concentration are plotted as horizontal lines (minty green) for representative values between 50-100%. For example, if the observed chemistry data, plotted as points in the left panel, are above the frequency distribution for the SIMAP model, then it indicates that the observed chemistry values as a whole are higher than the modeled values. If one follows a horizontal percentile line (e.g. 75th percentile model concentration) to the left, the intersection with the blue chemistry

data indicates that this concentration corresponds with the 50th percentile value for observed chemistry (Figure 6-3).

In the top right panel of Figure 6-3, a histogram of binned chemistry concentrations (μg/L) for observed samples (blue) and gridded model results (green) are plotted as the percentage of the total number of samples/grid cells. Results have been binned into concentration ranges. The first bar on the left represents all concentrations between 0.1 and 0.5 μg/L. Note the range increases non-linearly to the right and that the sum of all percentages may not add up to 100%. A large number of observed samples and modeled grid cells may fall below 0.1 μg/L and are not presented here. In this example, the model results (green) match the observed chemistry (blue) in the concentration interval 0.1 to 0.5 μg/L. For the 0.5-1.0 μg/L bin, the observed chemistry is above the model results, indicating that the observed chemistry is higher than the modeled values in this concentration bin.

The two spatial maps in Figure 6-3 depict the 95th percentile (left) and maximum (right) modeled concentrations in the vertical direction (over the specified depth range) for each of the horizontal grid cells (500 m x 500 m) of the 25 km by 25 km box, evaluated over the specified time interval (OCR). Overlaid on the model predictions are dots representing the concentrations of measured chemistry samples. Open symbols depict chemical concentrations that were greater than zero, but below the analytical method detection limit (MDL). In other words, open symbols represent the qualitative presence of analytes that make up the component grouping, as the concentration was not high enough to report a quantified value. The modeled concentration in each horizontal grid cell considers all of the 20-m vertical layers over each time step. Each grid cell (in 3D) and at each time step is considered an individual sample for the model at the location in the map. Note that the variation in the spatial distribution of the chemistry sample measurements is typically much higher than that shown by the model results in the maps, particularly when the model result is presented as a maximum (or 95th percentile) over time. However, in the probability distributions (upper left and right panels), where model-predicted concentrations for all grid cells and time steps in the overall depth range are treated as the set of predictions, the variance of the modeled results is completely characterized.

In the example in Figure 6-3, 62% of the model predictions are <10^{-3} μg/L for the AR7 PAH group (fluorenes & C0-C1 3-ring PAHs), whereas approximately 14% of chemistry sample measurements in the same domain (within 12.5 km of the wellhead between 1100-1400 m) and time interval (June 6 – July 15) are below that concentration. The highest 20% of the modeled concentrations agree well with the highest 20% of chemistry measurements of the AR7 PAH group. That 20% is in the range of concentrations (>0.1 μg/L) plotted in the upper right panel histogram. The threshold TPAH50 concentration of concern for toxicity to water column biota is 0.5 μg/L (Morris et al. 2015a). Note that AR7 represents only a portion of TPAH50, which includes AR5-8. Thus, the most important comparisons to be made between the model-predicted and measured concentrations for evaluation of exposures and toxicity to water column biota are those in the upper right panel for PAH groups AR5, AR6, AR7 and AR8.

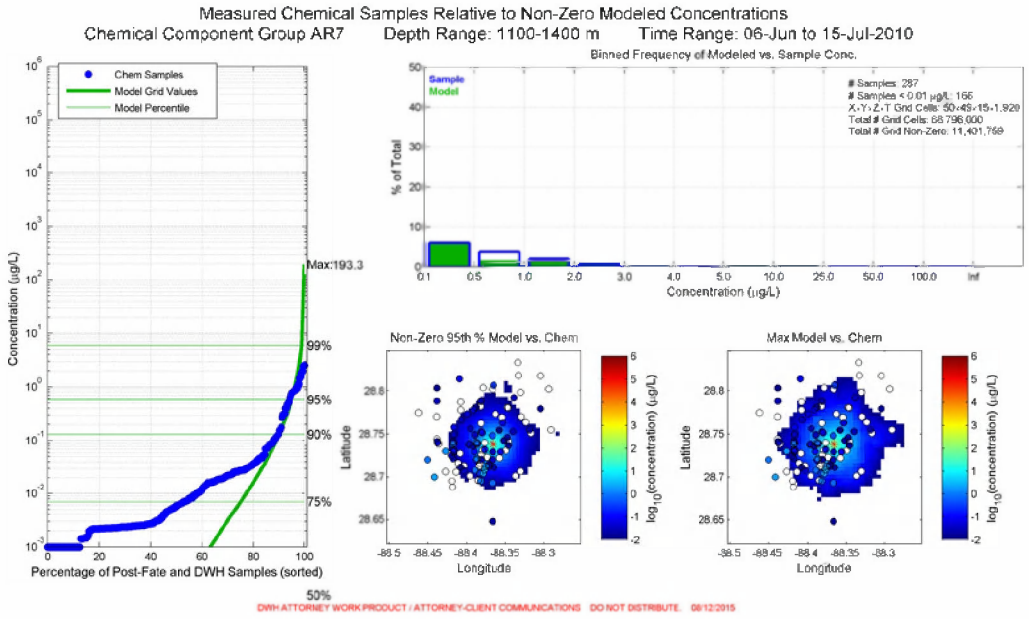

Figure 6-3. Probabilistic comparison of modeled AR7 (fluorenes & C0-C1 3-ring PAHs) concentrations for the Static Cone simulation to those measured in chemistry samples in the depth range 1100-1400 m for time domain OR3 (June 6 – July 15).

Figures in Appendix G depict comparisons of results to data for April-July 2010 (OCR1 through OCR3), for both the no-current (Appendix G.2) and the IAS ROMS currents (Appendix G.3) simulations of the spill. For the IAS ROMS simulation, comparisons are only made for the deep plume depth interval between 1,100-1,400 m.

The maximum BTEX concentrations predicted by the model were generally ~25-100 µg/L, with the exception of a core cell with concentration >100 µg/L. Comparisons of the model predictions to observational data are summarized in Figures G.2-1, G.2-7, G.2-31, G.2-37, G.2-61, G.2-67 of Appendix G. The typical pattern of the comparisons is that there were occasional (a few percent of) observations above 100 µg/L and many observations less than the MDL, whereas the model results smoothly transition between these values. Thus, the non-zero concentration model results agree with the >MDL BTEX concentrations, but do not show as many (500 m x 500 m x 20 m) cells with concentrations >100 µg/L as there are samples with concentrations >100 µg/L. It is clear from this comparison that statistical analyses of these relationships would be complex and dependent on the resolution of the model concentration grid cells; they are not attempted herein.

Components AR5 and AR6 include the C0-C4 naphthalenes and C0-C4 benzothiophenes; see Figures G.2-2, G.2-3, G.2-8, G.2-9, G.2-32, G.2-33, G.2-38, G.2-39, G.2-62, G.2-63, G.2-68 G.2-69 of Appendix G for the 800-1,100 m and 1,100-1,400 m comparisons. These comprise the semi-soluble PAHs, whereas AR7 and AR8 are slightly soluble. The typical pattern for the comparison of modeled AR5 and AR6 to observed is that the highest concentrations are of similar magnitude (~1-3 µg/L), but the frequency distributions of the observations show somewhat higher concentrations than the model's frequency distribution of concentrations (i.e., there are more samples with concentrations > 1 µg/L than there are grid cells with concentrations of that magnitude.

Components AR7 and AR8, which include the 3-ring PAHs, are compared in Figures G.2-4, G.2-5, G.2-10, G.2-11, G.2-34, G.2-35, G.2-40, G.2-41, G.2-64, G.2-65, G.2-70 G.2-71 of Appendix G (for 800-1,100 m and 1,100-1,400 m). The comparisons at 1,100-1,400 m show a similar pattern as the naphthalenes (AR5 and AR6), whereas for the 800 – 1,000 m depth range the model and observed frequency distributions of concentrations overlay well. For all chemical components, the closest results to the observed are in this depth range.

For the AR9 component, the modeled concentrations and the frequency distributions of concentrations compare favorably with the observations. The AR9 component contributes the most to the total soluble and semi-soluble hydrocarbon concentrations, so the comparisons of modeled to observed are similar for total soluble and semi-soluble hydrocarbon concentrations as well.

Thus in summary, the modeled concentrations of the various components are generally of the same order of magnitude as the measured concentrations. In order to be meaningful, comparisons need to be made on a component basis, as the components have different properties and behaviors (e.g. dissolution rates) that would cause their concentration distributions to vary. In many instances, the frequency distributions between the modeled concentrations and the measured samples compared well. However, in some cases the model overestimated concentrations observed in the samples, whereas in others it underestimated the concentrations. The differences between observed and modeled concentrations were not large and there was no obvious bias, overall.

As the modeled TPAH50 concentrations were carried forward to the analysis of toxicity (Morris et al. 2015a, b), the comparisons of the PAH components AR5 through AR8 were of the most interest. The frequency distributions of the modeled and measured concentrations were more similar for PAH components than for some of the other components. Additionally, the frequency distributions between the two modeled simulations (i.e., for 1,100-1,400 m) were very similar. These findings support the use of the Static Cone simulation for exposure evaluations. The magnitudes of the peak concentrations between the modeled and measured samples compared well, providing further confidence that the concentrations used for exposure and toxicity evaluations were reliable.

Uncertainties in these comparisons may result from the modeled transport or rate processes, field measurements of hydrocarbon chemistry (e.g., GC/MS has constrained TPAH50 values only reflecting the target analytes amenable to analytical methods that can be measured, see details in Payne and Driskell 2015b), or the input data used for modeling. In addition, the large gaps between sampling locations in both space and time contributed a considerable amount of uncertainty, which precludes any interpolation of the sample concentrations in this dynamic environment. Furthermore, the sampling efforts to depict hydrocarbon distributions within the water column may be complicated by the unavoidable heterogeneity in the water column and sampling complications. For these reasons, sampling gaps in space and time can make conclusive interpretation of field observations quite difficult when attempting to assess the contaminant conditions on a larger scale. Furthermore, there is no evidence of either the presence or absence of oil in regions that were not sampled.

6.5 Volumes of Water Contaminated above Thresholds

Using the results of the Static Cone simulation, the volume of water contaminated with modeled TPAH50 concentrations exceeding 0.5 μg/L, a threshold above which effects on water column biota may occur (Morris et al. 2015a), was calculated for daily averaged dissolved TPAH50 and total TPAH50 concentrations (Figures 6-4 and 6-5, respectively). The volume of water

exceeding 0.5 μg/L dissolved TPAH50 is about half of that exceeding 0.5 μg/L for total TPAH50. Figure 6-6 depicts the volume of water contaminated above 1 μg/L total TPAH50, indicating the sensitivity of this calculation to a change in the threshold. Adjusting the threshold by a factor two results in change of the volume affected by about 1/3, when comparing 0.5 μg/L to 1 μg/L total TPAH50. Table 6-2 lists the maximum volume of water where the daily average total TPAH50 concentration exceeded the indicated threshold in each the identified depth zones and estimated for the entire simulation of the Static Cone. The volumes for total TPAH50 at these and other thresholds (formulated as dose-response curve toxicity models, Morris et al. 2015a, b) were used for exposure and mortality calculations (see French McCay et al. 2015).

Figures 6-7 to 6-12 depict vertical profiles of the volume of water exceeding 0.5 μg/L and 1 μg/L in each of the 20-m layers, as estimated by the Static Cone simulation. Figure 6-13 plots the time series of volumes of water exceeding 0.5 μg/L for several 20-m layers, at ~ 200 m intervals throughout the water column.

The results of Figure 6-1 through 6-13 have the following features and trends.

- The volume of water contaminated with TPAH50 > 0.5 μg/L increased rapidly in April and early May, when the kink holes developed and much more oil was released in smaller droplet sizes. This increase continued throughout the oil release period until about July 24, 9 days after the release was stopped.
- The TPAH50 dissolved over time, primarily from slowly rising droplets 100s of microns in diameter. The dissolved TPAH50 remained in the water column, building up over time, while the droplets rose through the depth zones towards the surface. The fraction of oil mass released in droplets <100 μm, which would remain in the deep plume, was 5% on average, limiting the concentrations of TPAH50 in the deep plume somewhat.
- The dissolved TPAH50 degraded over time such that by September 30, 2010, most of the TPAH50 in the water column below 20 m had degraded.
- The volume of seawater contaminated with total TPAH50 > 0.5 μg/L is highest between 800-1,100 m. Lower volumes were contaminated in shallower layers. A smaller volume was contaminated above 0.5 μg/L in the 1,100-1,400-m depth range than in the 800-1,100-m range. The decrease is the result of the trap height, which for most of the released oil was at ~1,200 m. Therefore the interval of 1,100-1,400 m only contained oil in a 100 m layer (1,100-1,200 m).
- Figure 6-7 to 6-12 show the trap height and trend of volume of water exceeding 0.5 μg/L and 1.0 μg/L with depth in the water column. For these thresholds, the trend of volume of water exceeding 0.5 μg/L and 1.0 μg/L with depth in the water column is relatively modest, whereas for a higher threshold of 79 μg/L, only the deep water layers below 800 m exceed the thresholds. The model results in Figures F.2-1 to F.2-40 of Appendix F show the concentrations highest at 800-1,200 m.

Table 6-2. Maximum volume of water where the daily average total TPAH50 concentration exceeded the indicated threshold, estimated for the entire simulation of the Static Cone in each the indicated depth zones.

Depth Range (m)	Volume (m^3) >0.5 ug/L	Volume (m^3) >1 ug/L
20-200	3.44×10^9	1.96×10^9
200-500	7.78×10^9	4.63×10^9
500-800	1.06×10^{10}	6.92×10^9
800-1100	1.17×10^{10}	8.08×10^9
1100-1400	3.52×10^9	2.61×10^9
40-1400	3.60×10^{10}	2.34×10^{10}

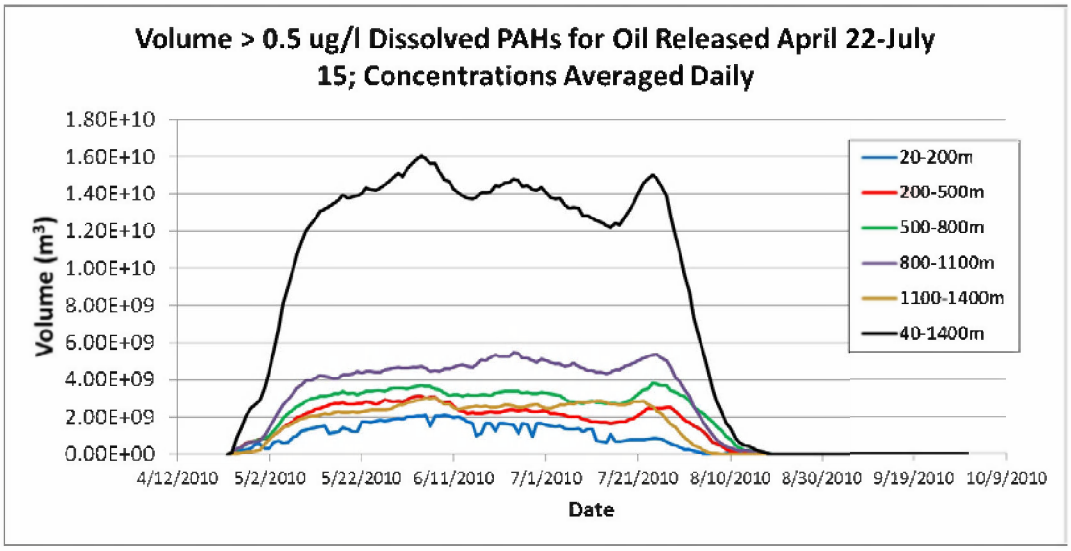

Figure 6-4. Volume of water where the daily average dissolved TPAH50 concentration exceeded 0.5 μg/L, estimated by the Static Cone simulation in each the indicated depth zones.

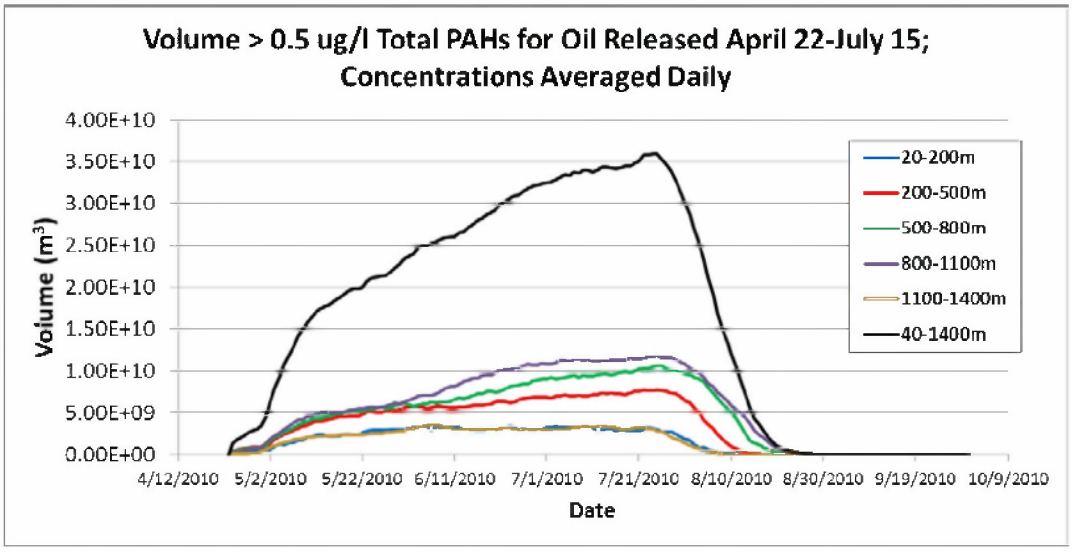

Figure 6-5. Volume of water where the daily average total TPAH50 concentration exceeded 0.5 μg/L, estimated by the Static Cone simulation in each the indicated depth zones.

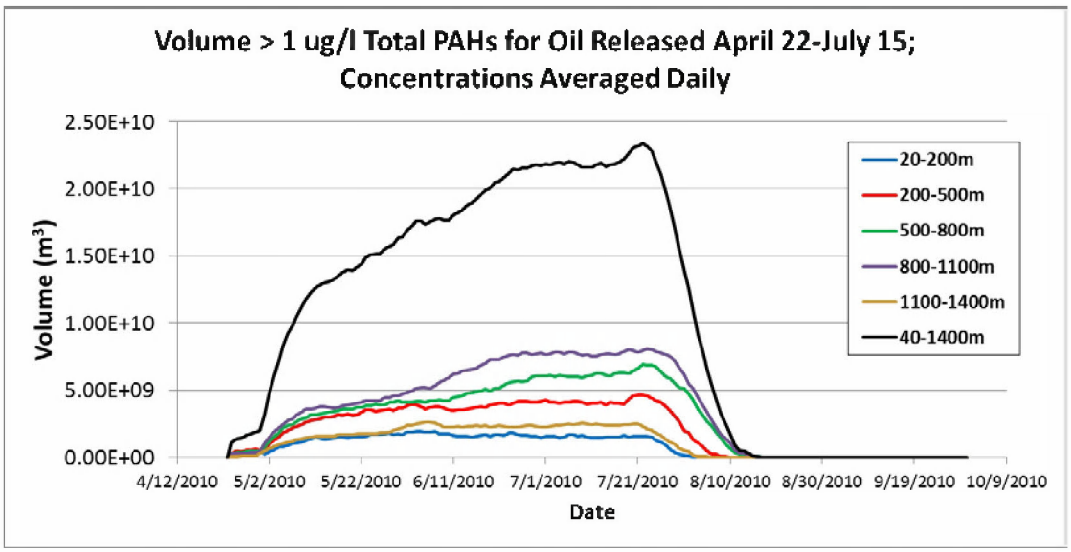

Figure 6-6. Volume of water where the daily average total TPAH50 concentration exceeded 1 μg/L, estimated by the Static Cone simulation in each the indicated depth zones.

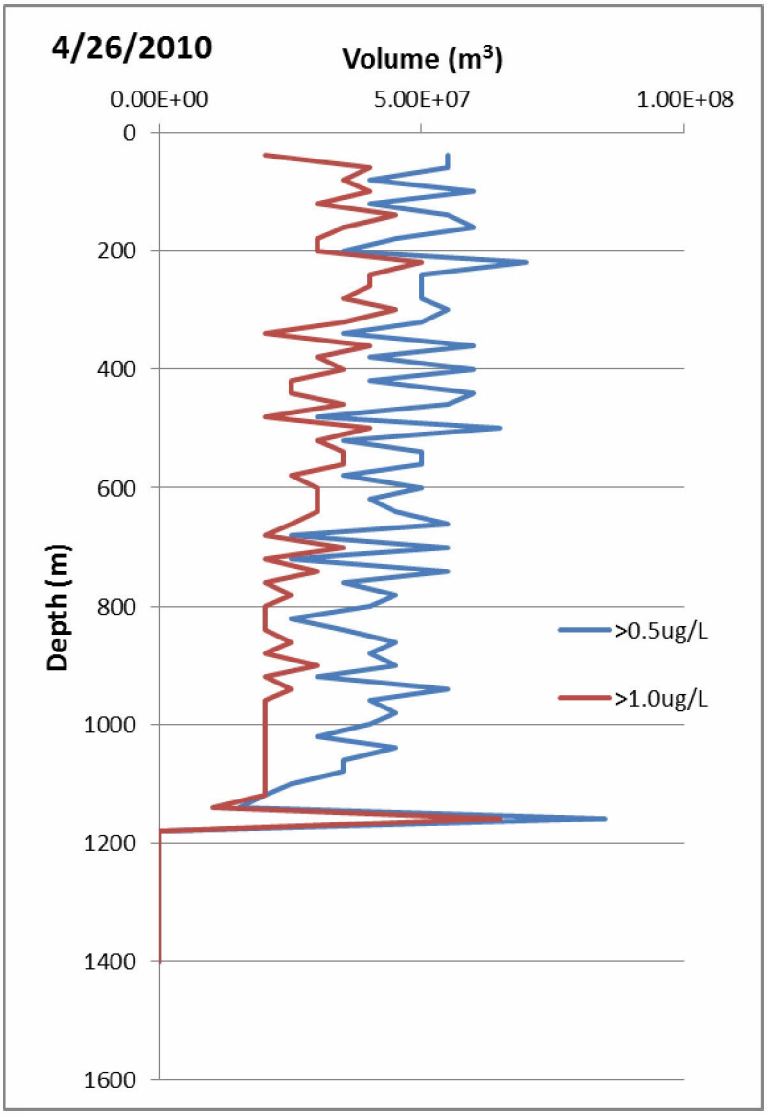

Figure 6-7. Volume of water in each 20-m high layer of the water column where the daily average total TPAH50 concentration exceeded 0.5 μg/L and 1 μg/L, estimated by the Static Cone simulation: Vertical profiles for April 26 when oil was released entirely from the end of the broken riser at ~1200 m.

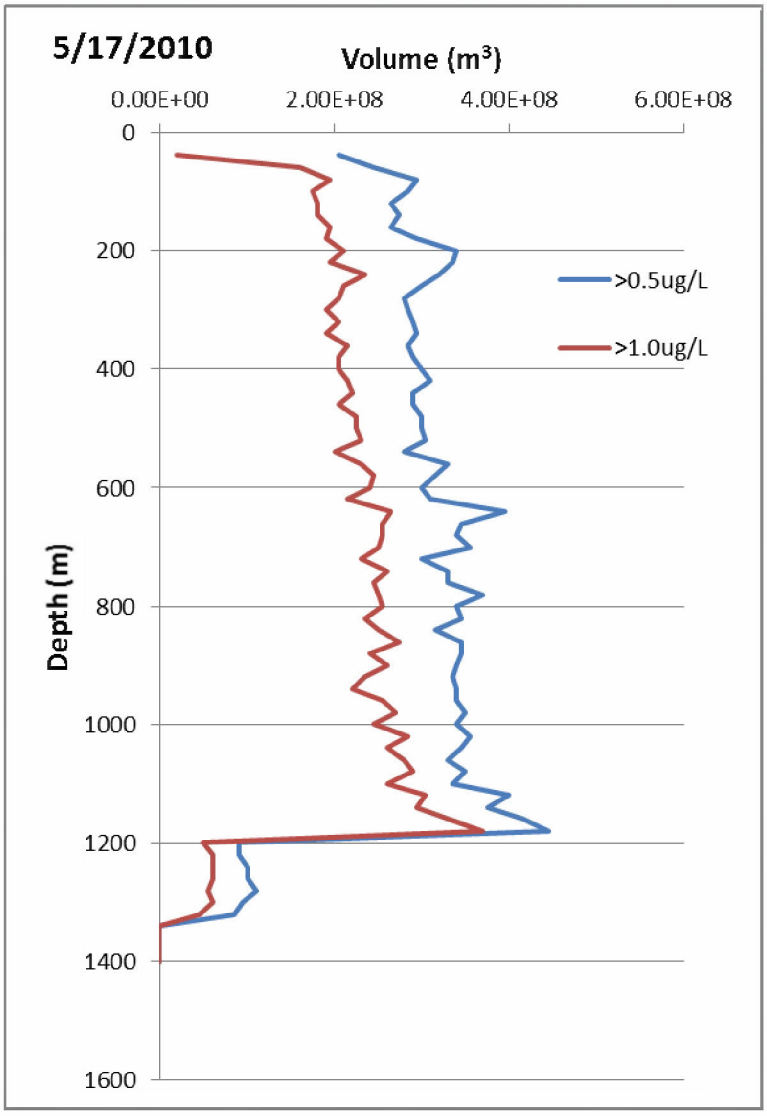

Figure 6-8. Volume of water in each 20-m high layer of the water column where the daily average total TPAH50 concentration exceeded 0.5 μg/L and 1 μg/L, estimated by the Static Cone simulation: Vertical profiles for May 17 when oil was released from kink holes at ~1300 m and the broken riser at ~1200 m.

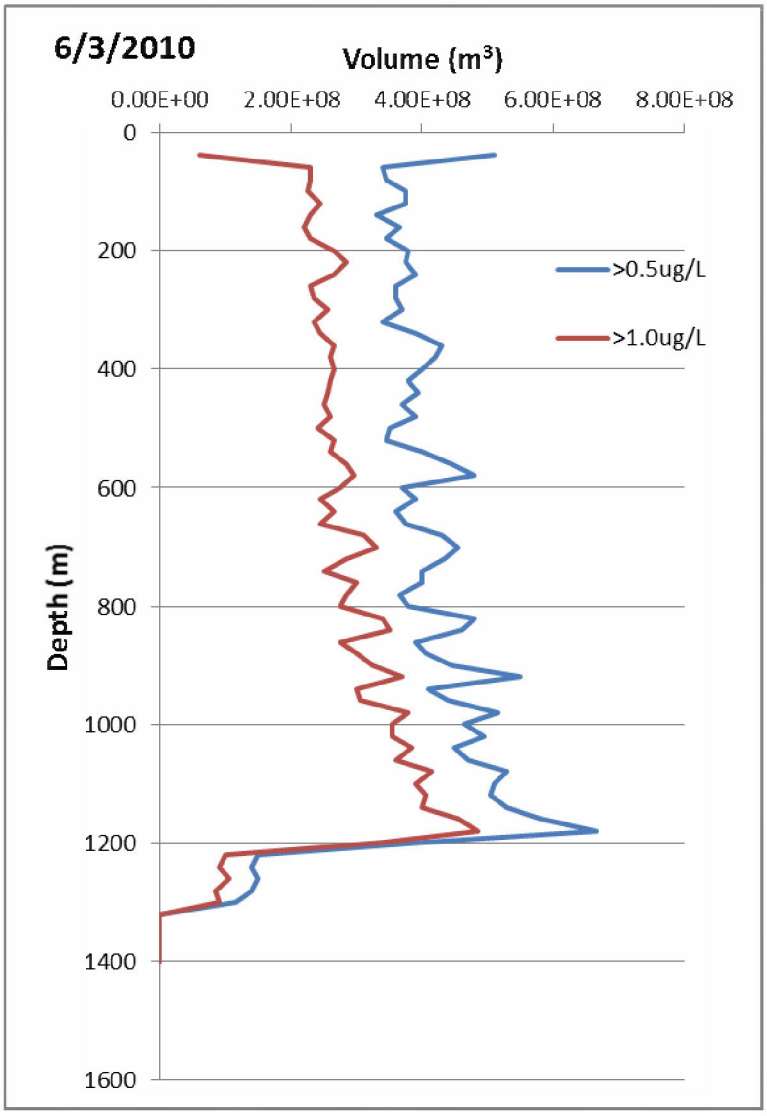

Figure 6-9. Volume of water in each 20-m high layer of the water column where the daily average total TPAH50 concentration exceeded 0.5 μg/L and 1 μg/L, estimated by the Static Cone simulation: Vertical profiles for June 3. The deep plume resulting from releases from the kink hole is evident at 1240-1300 m.

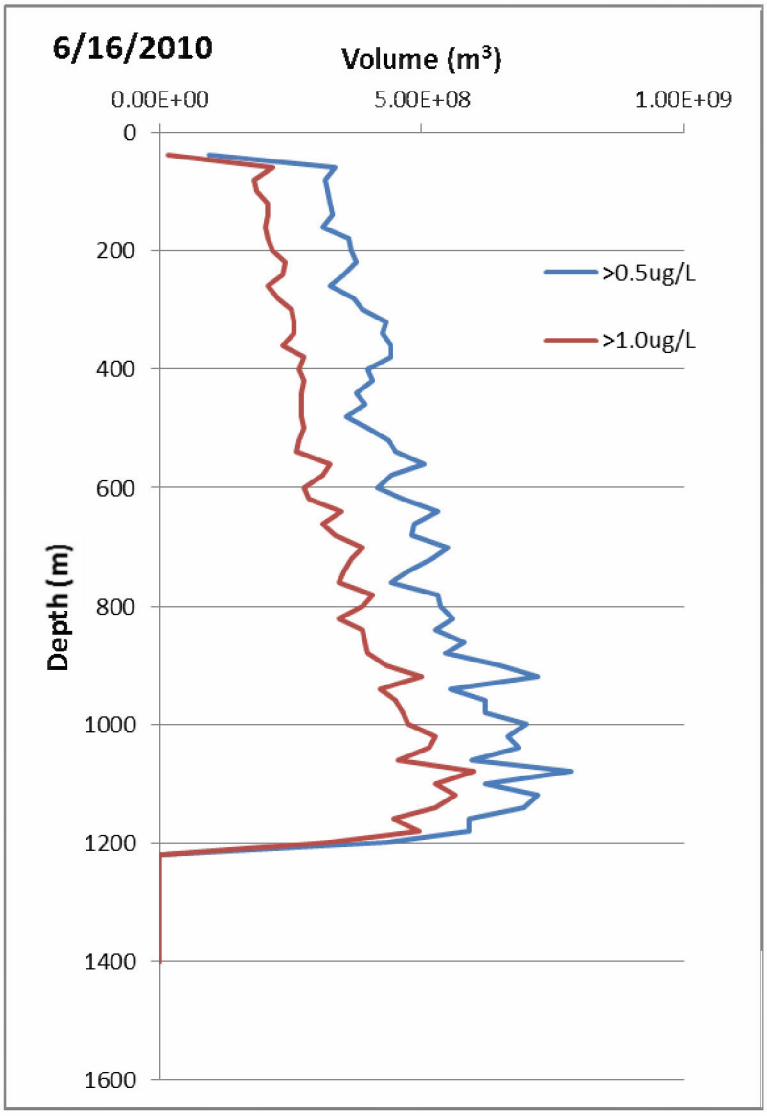

Figure 6-10. Volume of water in each 20-m high layer of the water column where the daily average total TPAH50 concentration exceeded 0.5 μg/L and 1 μg/L, estimated by the Static Cone simulation: Vertical profiles for June 16 when oil was released entirely from the Tophat on the cut riser and the release initiated at ~1200 m.

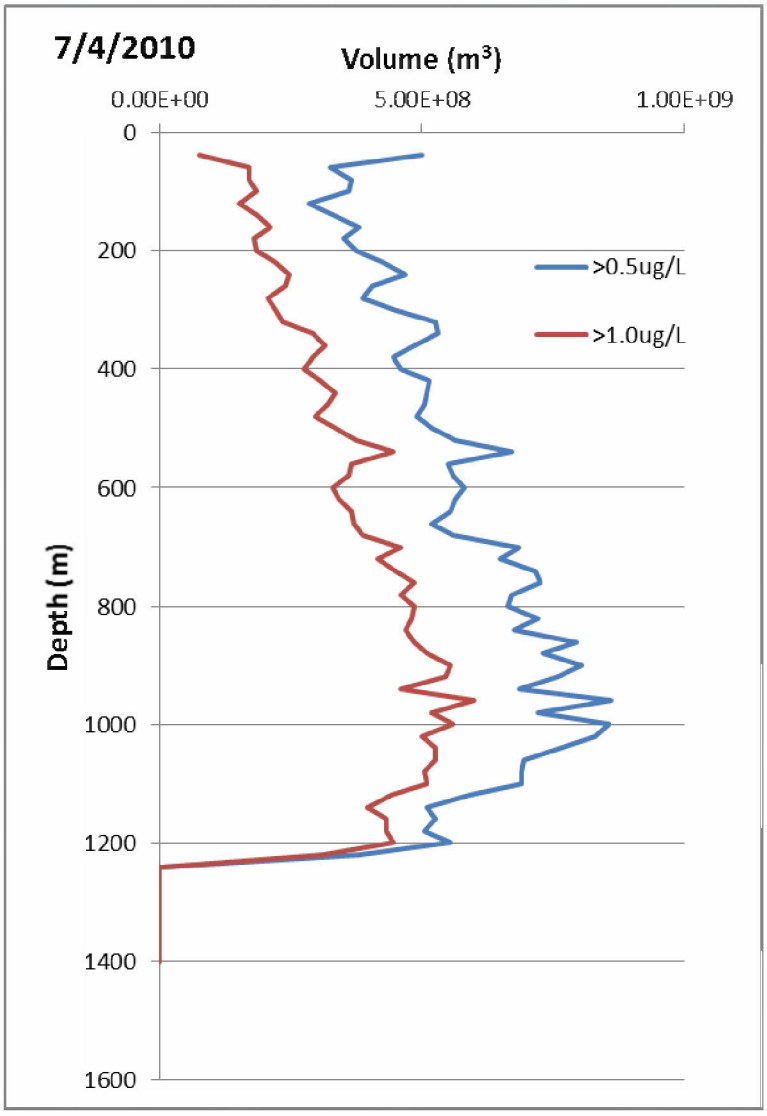

Figure 6-11. Volume of water in each 20-m high layer of the water column where the daily average total TPAH50 concentration exceeded 0.5 μg/L and 1 μg/L, estimated by the Static Cone simulation: Vertical profiles for July 4 when oil was released entirely from the Tophat on the cut riser and the release initiated at ~1240 m.

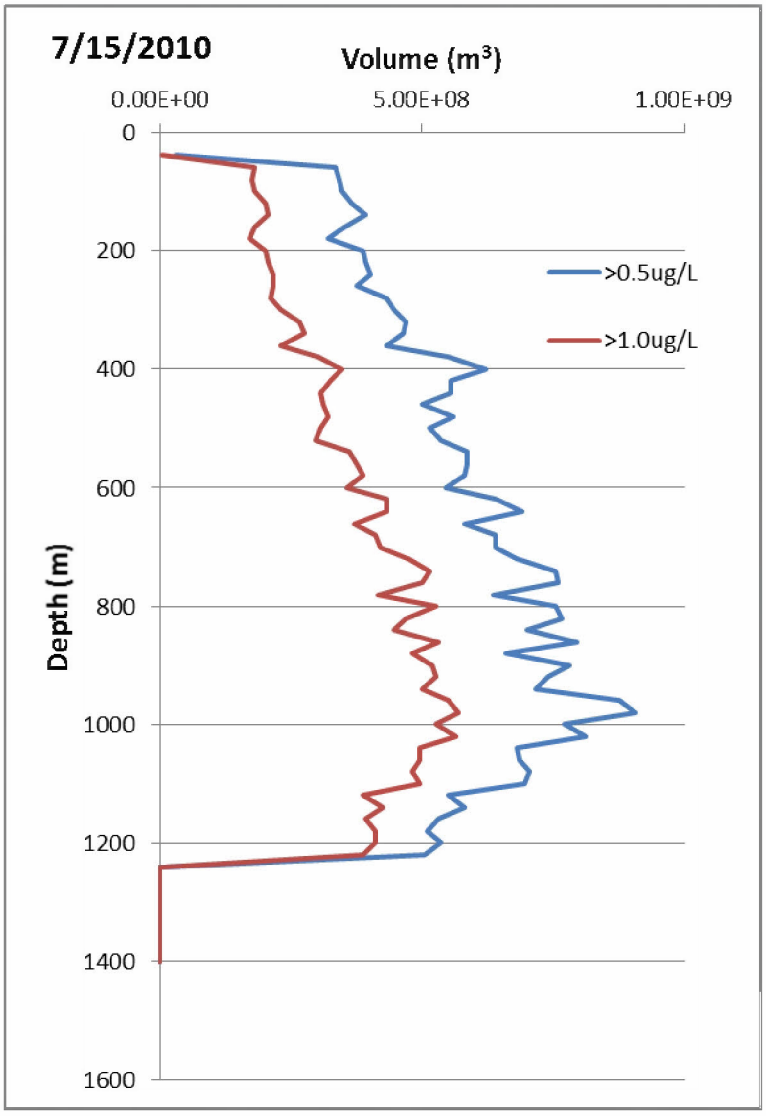

Figure 6-12. Volume of water in each 20-m high layer of the water column where the daily average total TPAH50 concentration exceeded 0.5 μg/L and 1 μg/L, estimated by the Static Cone simulation: Vertical profiles for July 15, the day the release to the water column was stopped.

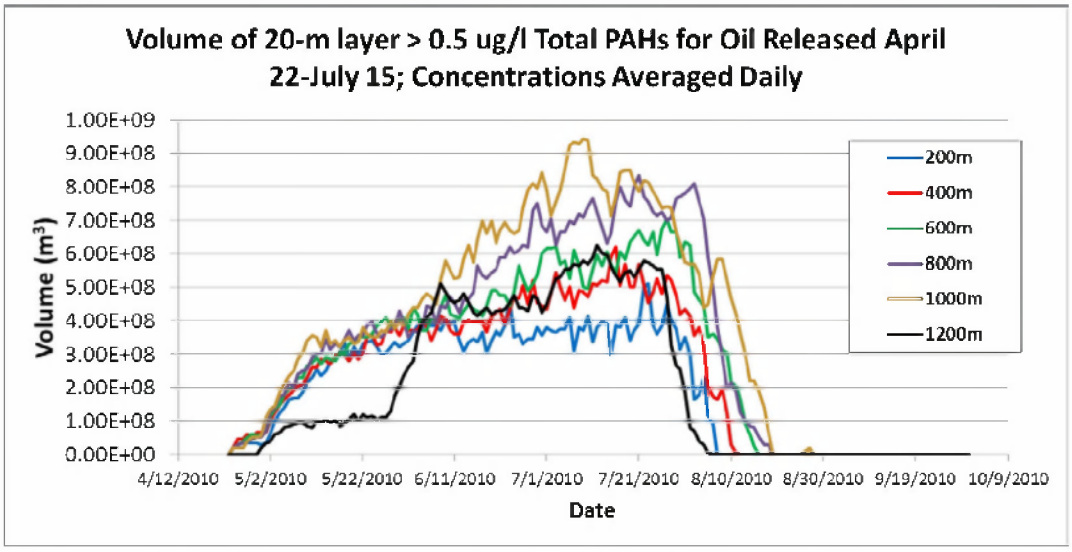

Figure 6-13. Volume of water in each of several 20-m high layers of the water column where the daily average total TPAH50 concentration exceeded 0.5 μg/L, estimated by the Static Cone simulation.

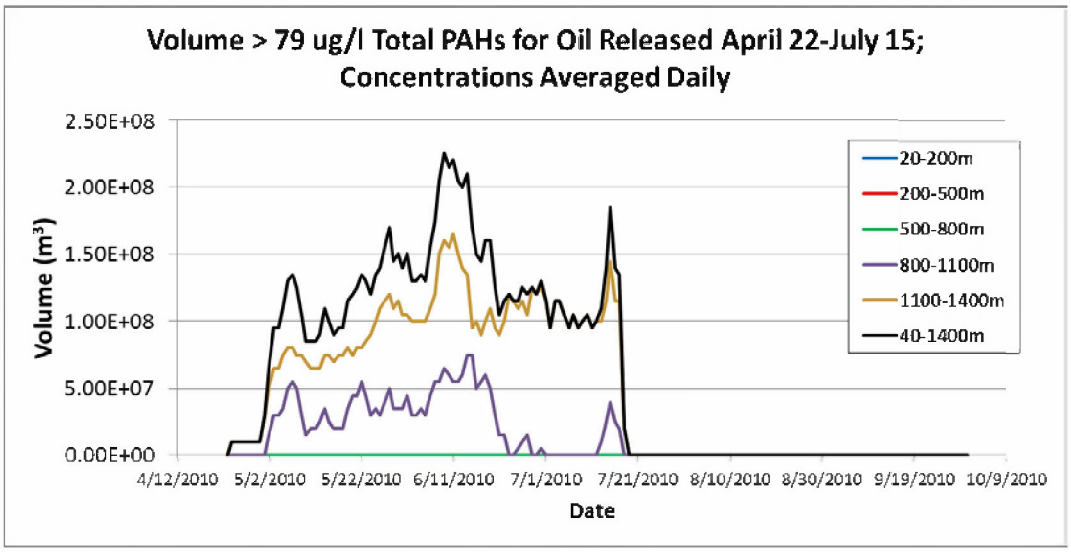

Figure 6-14. Volume of water where the daily average total TPAH50 concentration exceeded 79 μg/L, estimated by the Static Cone simulation in each of the indicated depth zones.

6.6 Mass Balance and Comparison of Simulations

The two model simulations were compared in order to evaluate whether the simulation without currents provided results in line with those predicted by a simulation using currents as input. The mass balances of the two simulations are compared in Figures 6-15 and 6-16, as summarized in Table 6-3.

Both the Static Cone and IAS ROMS simulations (Figures 6-15 and 6-16, respectively) provide modeled mass balance of oil over time, as the percent of total mass spilled to date. The output is broken into four categories: oil that was in the water column, that surfaced (through the upper boundary of the model domain), that had settled to the sediments, or that degraded in the water column. Table 6-3 summarizes the overall mass balance on September 30, 2010. In both simulations, the percentage of the released oil that surfaced was 87%, and that settled to the sediment was <0.1%. The results indicated that the modeled mass balance of subsurface oil (below 20 m) was essentially unaffected by the inclusion of current transport.

Stout et al. (2015) estimated ~7% of the released oil settled near the wellhead by 2011 with most settling before late August 2010. The NRDA model simulation ended September 30, 2010. Estimates of organic SPM concentrations needed to model oil flux in marine snow are unavailable prior to September 30, 2010; therefore flux is not included in the modeling. To the extent that oil settling in marine snow occurred prior to September 30, 2010, the model underestimates the flux to the sediments.

The 13% degraded in the water column (by September 30, 2010), represents the total percentage that remained in the water in the model simulation, either as the released components or as degradation products and microbial biomass. This falls within the predicted range of 4-31% of the released oil that was reportedly sequestered in the deep sea (Valentine et al. 2014). Daling et al. (2014) estimated dissolution loss into the water during the ascent from 1,500 m water depth to the surface was ~15% of the oil, comprised of: saturates < C7 (10 wt % of the stabilized source oil), BTEX (3 wt % of the source oil), C-3-Benzenes (1.5 wt % of the source oil). The 15% estimate accounts for all of the water soluble hydrocarbons in the released oil, so the implicit assumption is dissolution of the soluble hydrocarbons was complete for all droplet sizes before the oil surfaced. Additionally, Daling et al. (2014) estimated about 18% of the total PAH's representing 1.1 wt % of the total oil, corresponding to about 0.2 wt % of the source oil, was dissolved into the water before the oil surfaced. In the SIMAP model results, about 40-50% of the degraded mass (13% of the oil) derived from dissolved soluble (AR1, AR2, AR3, AR5, and AR9; Table 4-3) and semi-soluble (AR4, AR6, AR7, and AR8; Table 4-3) hydrocarbons. On average over the entire spill, 6% of the total oil hydrocarbons released into the environment dissolved before oil droplets reached 20 m on the way to the water surface (18% of the oil being soluble and semi-soluble hydrocarbons; Appendix B, Table B-8 and B-9). The remainder (12% of the oil) rose through 20 m to the surface water, and either dissolved in the upper 20 m or volatilized. All soluble and semi-soluble hydrocarbons in droplets remaining below 20 m dissolved and eventually degraded in the model simulation, whereas soluble components did not completely dissolve from the large droplets that rise to the surface in a few

hours. One would expect this to be the case, as surfaced fresh oil did contain measurable BTEX and soluble alkanes (Stout 2015c), which volatilized rapidly. Ryerson et al. (2012) measured these volatiles in the atmosphere above the rising oil and fresh oil slicks.

Ryerson et al. (2012), using chemical analysis of hydrocarbon data, estimated that, on June 10, 2015, 19-20% of the total oil hydrocarbon mass released to the environment was trapped in the deep plume, 8-9% was in the surface slicks, 17.4-18.4% was evaporated; leaving ~54% unaccounted for in their analysis. The missing fraction of oil would presumably be biodegraded, suspended in the water column other than in the intrusion layer deep plume, and/or sunken to the seabed (see Appendix E, Section E.2.1.1 for further detail). The Ryerson et al. (2012) mass balance analysis has a number of sources of uncertainty, including that it depends on an estimate of the total integrated DO anomaly by Kessler et al. (2011) and Hazen et al.'s (2010) estimated ratios of alkanes to toluene in the plume phase versus in the leaking fluid phase being a surrogate of the ratio of droplet to dissolved phase hydrocarbons – on the premise of the co-location of the dissolved versus droplet phases. To the extent that droplets rose out of the deep plume preferentially leaving dissolved-phased hydrocarbons at depth (a process known to have occurred), the Ryerson et al. (2012) estimate of 19-20% being in the deep plume is an overestimate. The SIMAP model estimates for June 10 are about 5% in the water column, 8% degraded, and 87% surfaced (which would be either as slicks, evaporated or ashore), i.e., that more oil rose to the surface than derived from Ryerson et al.'s analysis.

Figure 6-17 depicts the mass of oil (in metric tons, MT, where 1 MT = 1,000 kg) remaining in the water and sediments throughout the Static Cone simulation. Figure 6-18 depicts the mass settling to the sediments using an expanded vertical axis scale. Oil mass that surfaced would have subsequently evaporated, transported ashore, entrained back into the water column, and degraded. The model results and mass balance support the following description of the fate of oil droplets. Initially, all of the oil was subsurface, but after 3 hours (on April 22) larger droplets began to surface. In April, most of the oil was released as large droplets that surfaced rapidly. During May, holes developed at the kink in the riser and some of the oil was released through relatively small holes, thereby causing highly turbulent releases, resulting in a droplet size distribution that had a large percentage of small droplets (~30% of the oil mass was <1mm in diameter on average over the spill; Table 4.9). These small droplets remained dispersed in the deep water. Oil flow from the riser continued to mainly include large droplets (>1mm in diameter) that surfaced rapidly. Beginning on May 20, the daily subsea application volumes of dispersant increased substantially, resulting in an increased fraction of oil remaining dispersed in the water column. On June 3, 2010 the riser was cut, and the percentage of oil in the water column increased rapidly. The subsea application rates of dispersant were also substantially higher in June and July (Figure 4-2), increasing the percentage of the released oil that remained in the water column. The oil release rate to the environment decreased throughout June and early July due to subsea recovery which began on Jun 5 (Figure 4-3).

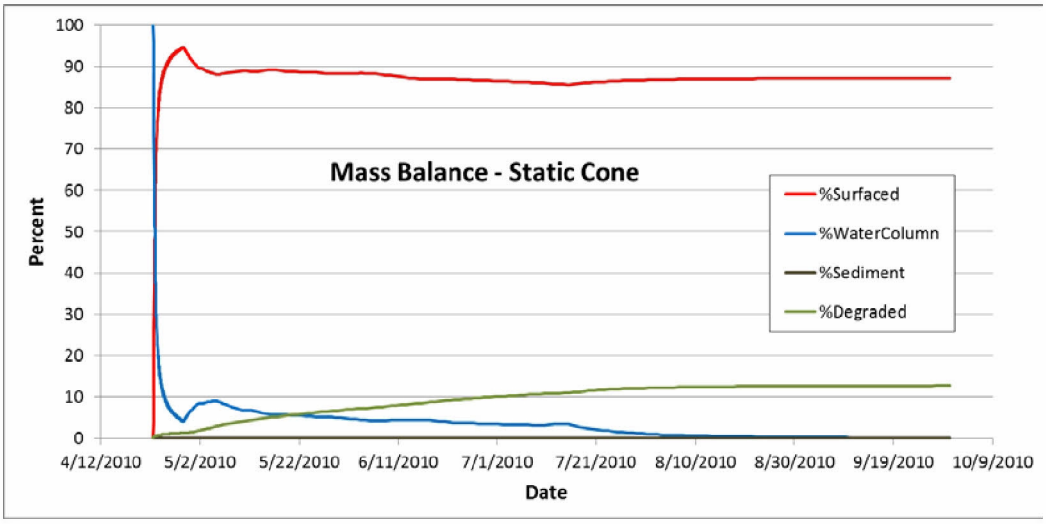

Figure 6-15. Static Cone simulation: Modeled mass balance of oil over time as percentages of oil released to date.

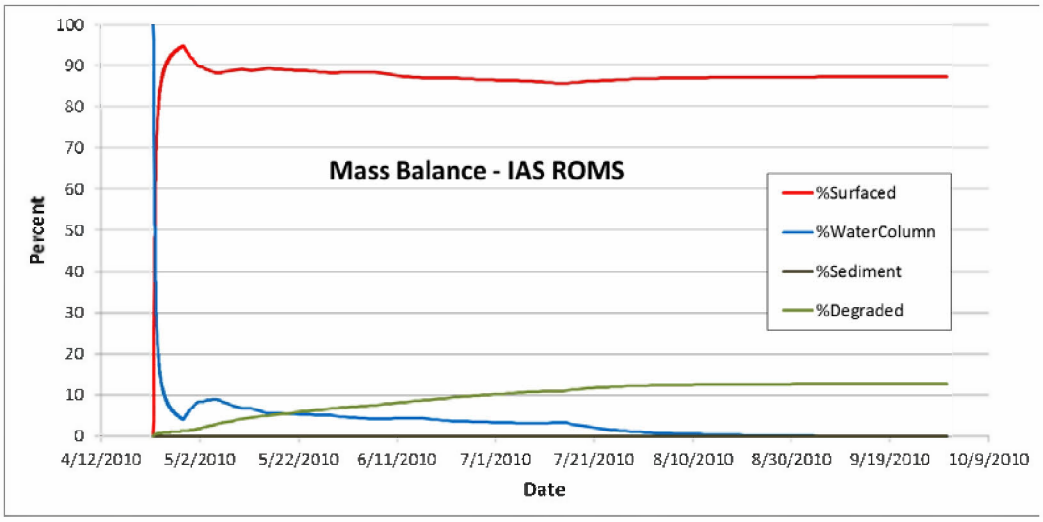

Figure 6-16. IAS ROMS simulation: Modeled mass balance of oil over time as percentages of oil released to date.

Table 6-3. Mass balance from SIMAP model runs on September 30, 2010. Note that about 40-50% of the degraded mass was of dissolved soluble and semi-soluble hydrocarbons.

Fate	Static Cone simulation	IAS ROMS simulation
Surfaced	87.3	87.2
Water column	0.057	0.025
Degraded in water column	12.7	12.7
Sediments	0.0015	0.0319

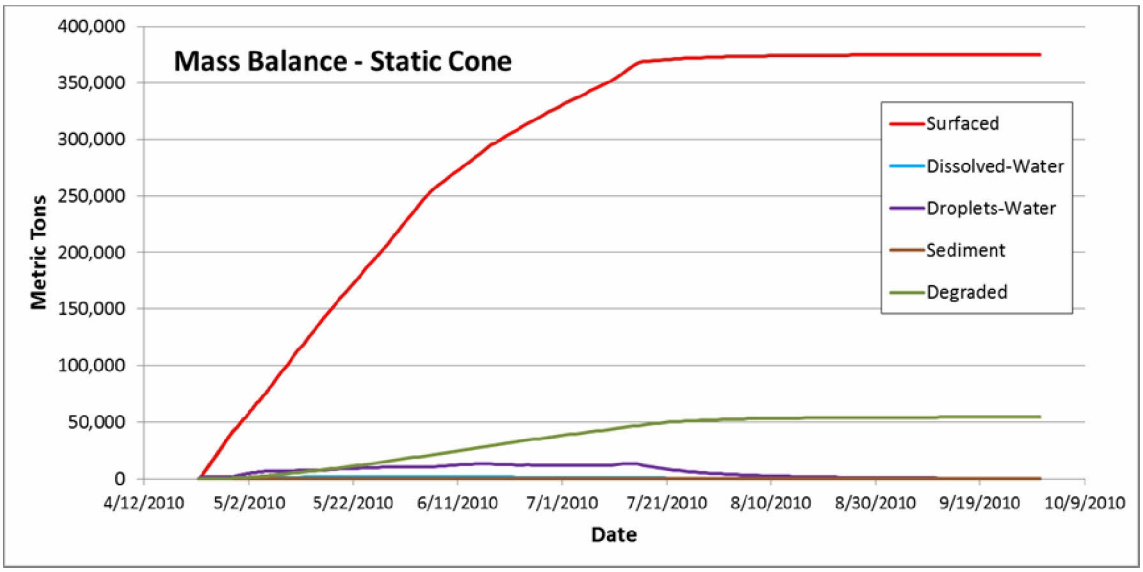

Figure 6-17. Static Cone simulation: Modeled mass of oil over time as metric tons surfaced, remaining in the water, in/on sediments or degraded in the water column.

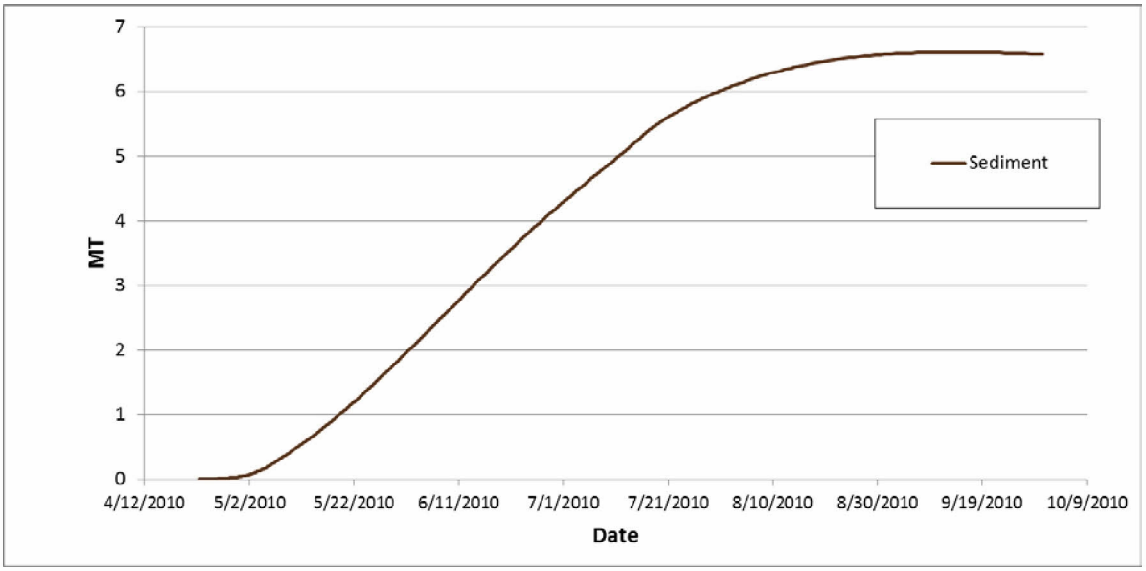

Figure 6-18. Static Cone simulation: Mass of oil settling to deep sea sediments (as metric tons).

Figures 6-19 through Figure 6-22 depict the mass of each of the components of the oil (Table 3-1) in the water column below 20 m in droplets and dissolved. The soluble alkanes, isoalkanes, and cycloalkanes made up 13% of the fresh oil, making up the largest percentage of the oil

droplets. The soluble components rapidly dissolved from the droplets (BTEX being the most soluble), appeared in the dissolved phase (Figure 6-21 to Figure 6-22), and then degraded. The insoluble aliphatic components (Figure 6-20) remain in the oil droplets in proportion to their concentrations in the source oil. Figure 6-23 and Figure 6-24 depict the cumulative mass of the oil (by component) in the water column below 20 m that had degraded over time.

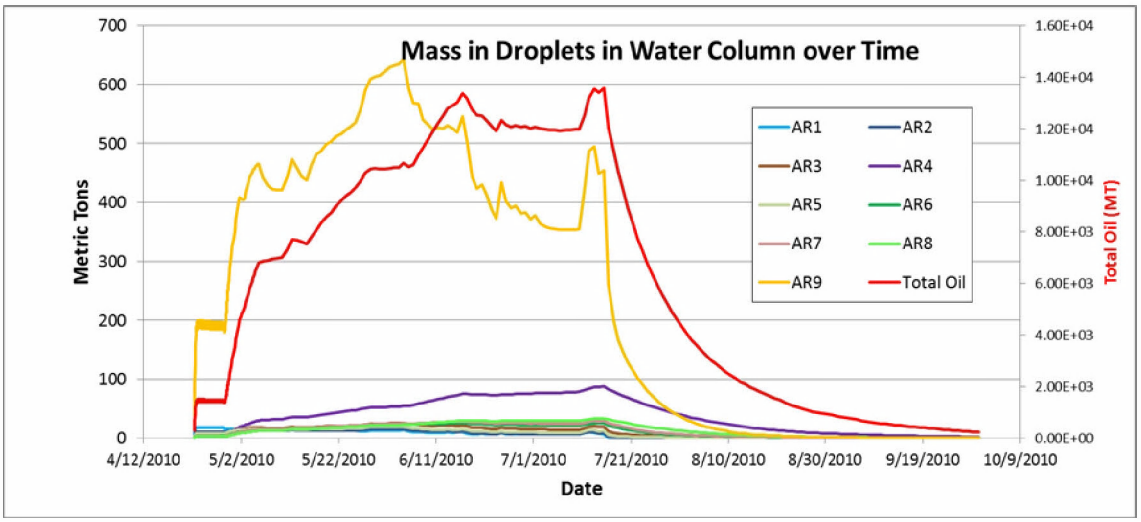

Figure 6-19. Static Cone simulation: Modeled mass of soluble and semi-soluble oil components within oil droplets in the water column over time. Key: AR1 – BTEX, AR2 – C3-benzenes, AR3 – C4-benzenes, AR4 – decalins, AR5 – C0-C2 Naphthalenes, AR6 – C3-C4 Naphthalenes, AR7 – Fluorenes & C0-C1 3-ring PAHs, AR8 – 4-ring PAHs & C2-C3 3-ring PAHs, AR9 – soluble alkanes/isoalkanes/cycloalkanes.

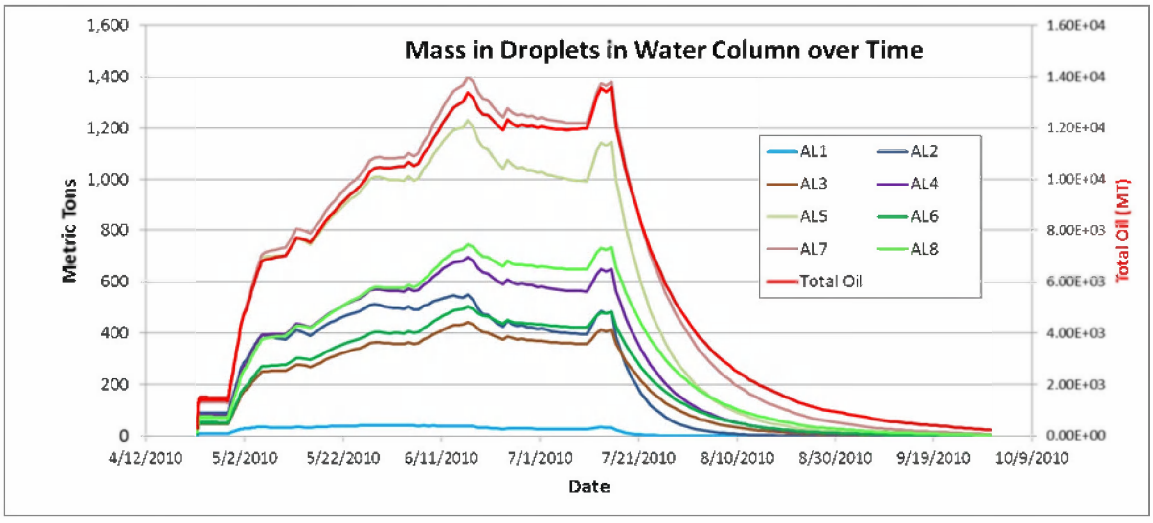

Figure 6-20. Static Cone simulation: Modeled mass of volatile (and insoluble) oil components within oil droplets in the water column over time. The volatile aliphatic hydrocarbon components are defined by boiling range. (See Table 3-1 for ranges.)

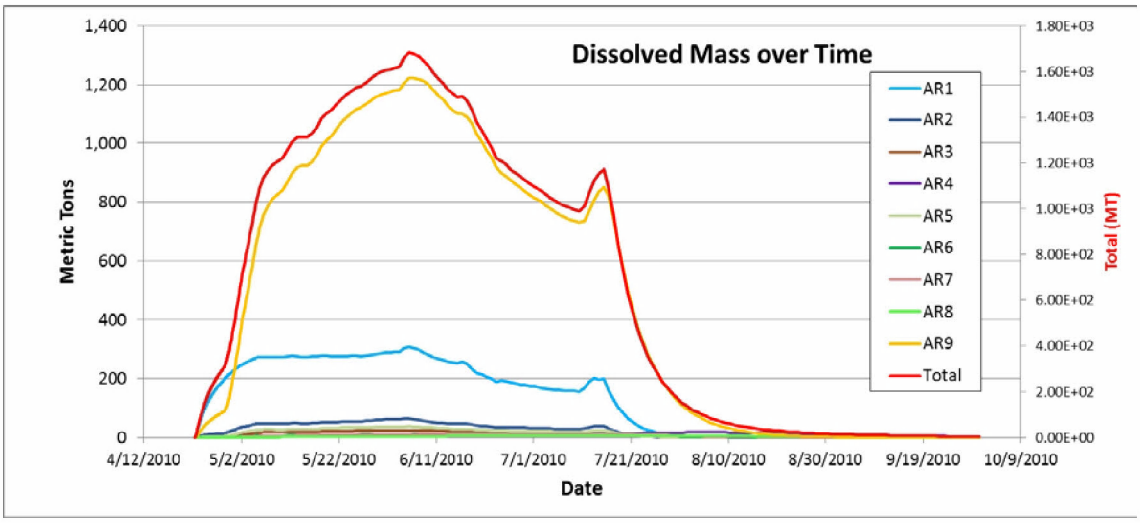

Figure 6-21. Static Cone simulation: Modeled mass of soluble and semi-soluble oil components dissolved in the water column over time. Key: AR1 – BTEX, AR2 – C3-benzenes, AR3 – C4-benzenes, AR4 – decalins, AR5 – C0-C2 Naphthalenes, AR6 – C3-C4 Naphthalenes, AR7 – Fluorenes & C0-C1 3-ring PAHs, AR8 – 4-ring PAHs & C2-C3 3-ring PAHs, AR9 – soluble alkanes/isoalkanes//cycloalkanes.

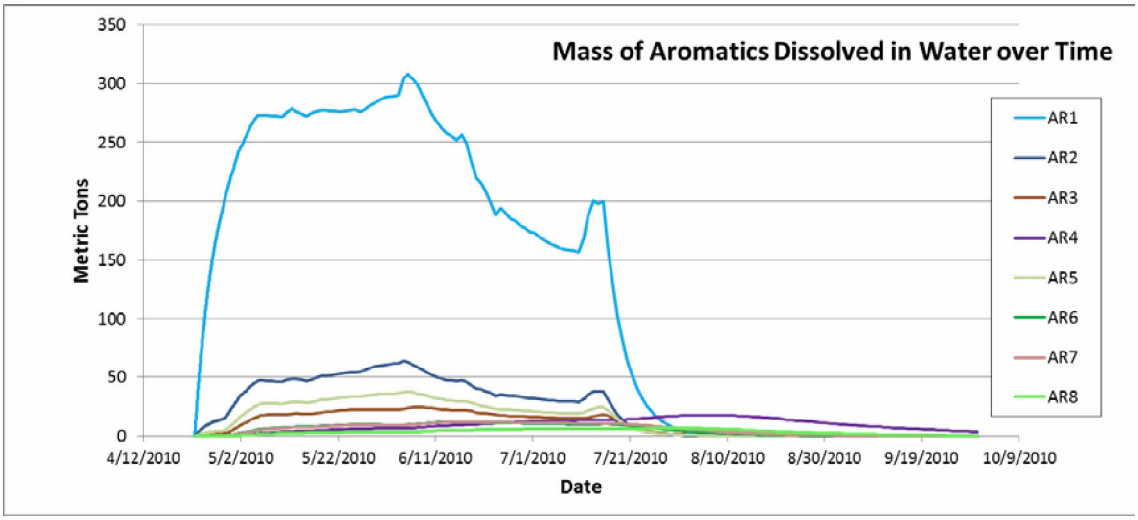

Figure 6-22. Static Cone simulation: Modeled mass of soluble and semi-soluble aromatic components dissolved in the water column over time. Key: AR1 – BTEX, AR2 – C3-benzenes, AR3 – C4-benzenes, AR4 – decalins, AR5 – C0-C2 Naphthalenes, AR6 – C3-C4 Naphthalenes, AR7 – Fluorenes & C0-C1 3-ring PAHs, AR8 – 4-ring PAHs & C2-C3 3-ring PAHs.

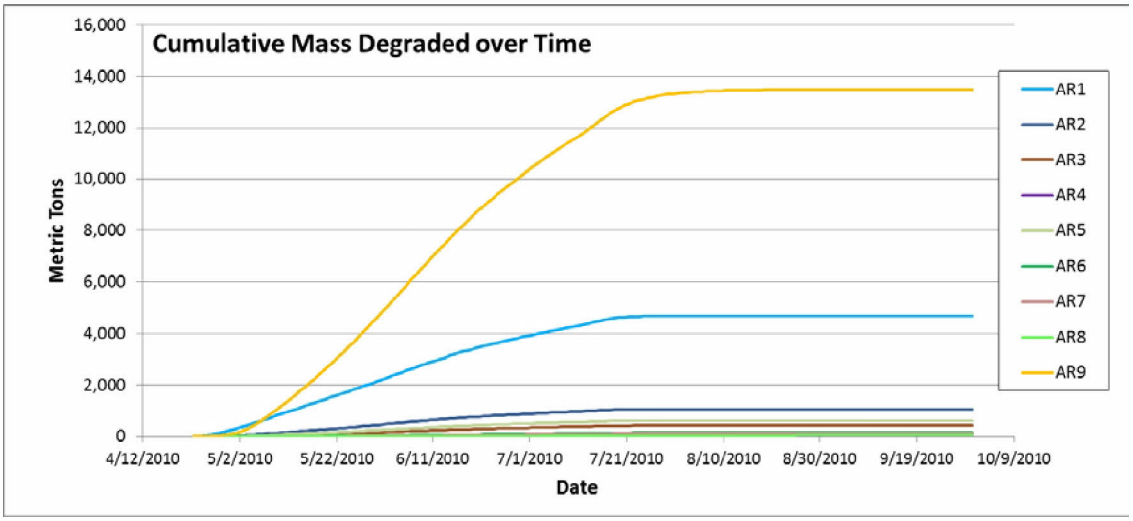

Figure 6-23. Static Cone simulation: Modeled mass of soluble and semi-soluble aromatic components degraded in the water column over time. Key: AR1 – BTEX, AR2 – C3-benzenes, AR3 – C4-benzenes, AR4 – decalins, AR5 – C0-C2 Naphthalenes, AR6 – C3-C4 Naphthalenes, AR7 – Fluorenes & C0-C1 3-ring PAHs, AR8 – 4-ring PAHs & C2-C3 3-ring PAHs, AR9 – soluble alkanes/isoalkanes/cycloalkanes.

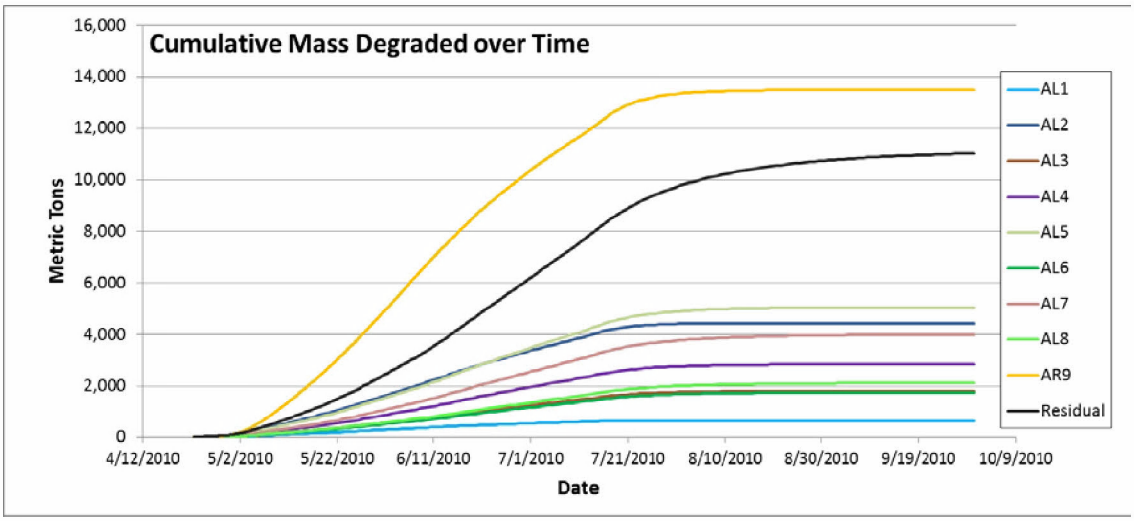

Figure 6-24. Static Cone simulation: Modeled mass of volatile (and insoluble) oil components within oil droplets degraded in the water column over time. The volatile aliphatic hydrocarbon components are defined by boiling range. (See Table 3-1 for ranges.)

The model estimates of the mass of oil hydrocarbons settling to subtidal sediments, and their distribution, was compared to the field samples and observational data (mass balance being discussed above). The deposition of total hydrocarbons to the sediments, as predicted by the model simulations, is mapped in Figures 6-25 and 6-26. The sedimentation pattern for the simulation using IAS ROMS is stretched to the SW and NE, aligned with current transport

(Figure 6-26). For the Static Cone simulation, the sedimentation remained within the basin around the MC252 wellhead (Figure 6-25). MC252 oil from the spill was identified on the sediments in the offshore area surrounding and down-stream of the well site, primarily within the basin area around the well, but also extending somewhat SW and NE (Joye et al. 2011; Montagna et al. 2013; Valentine et al. 2014; Stout 2015d). Thus, the sedimentation pattern in the Static Cone simulation might appear to be more comparable than the IAS ROMS simulation. However, sampling was very sparse outside of the basin area, such that the IAS ROMS pattern of sedimentation could potentially be supported with more sampling data, as suggested by Montagna et al. (2013) and Valentine et al. (2014).

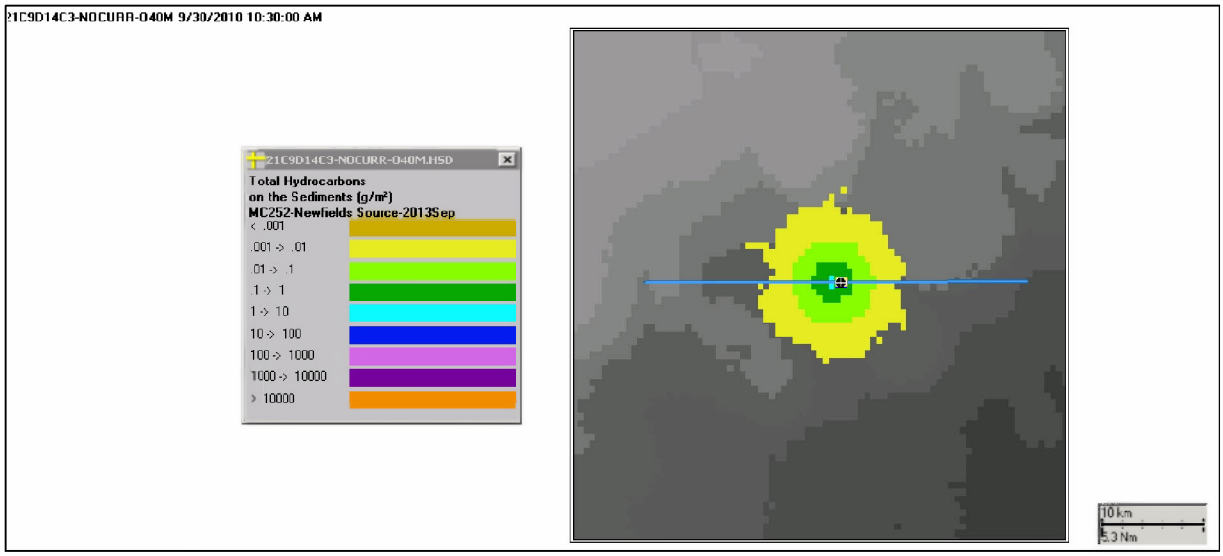

Figure 6-25. Static Cone simulation: Modeled mass distribution of total hydrocarbons settled to the sediments by September 30, 2010.

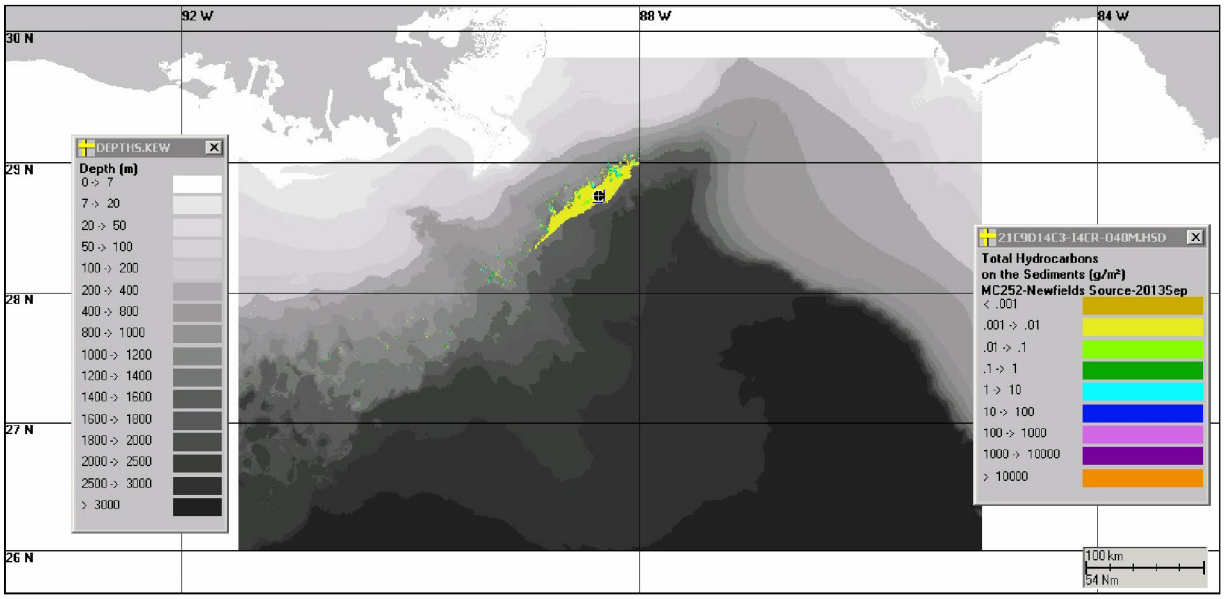

Figure 6-26. IAS ROMS simulation: Modeled mass distribution of total hydrocarbons settled to the sediments by September 30, 2010.

To evaluate the model's sensitivity to the inclusion of currents or lack-there-of and because the concentrations of TPAH50 predicted by the Static Cone simulation were used for toxicity evaluation (Morris et al. 2015b), the volumes affected above 1 μg/L TPAH50 for the simulation using no currents were compared to those with the simulation that used currents in the 1,100- to 1,400-m depth interval. The volume of water contaminated above 1 μg/L TPAH50 at each time step in the simulation using IAS ROMS is plotted in Figure 6-27. In comparing these results to those for the Static Cone (Figure 6-28), the total water volume contaminated (1,100-1,400 m) is within a factor three. In the IAS ROMS simulation, the maximum volume affected over time was 7.86×10^9 m^3, compared to 2.65×10^9 m^3 for the Static Cone (Table 6-4). However, the trends and peaks in the time series vary between the two simulations, indicating the influence of current transport and shear; the currents spread the plume over a larger volume. Thus, the evaluation of exposure and toxicity to plankton used for the injury quantification is not highly sensitive to the currents, or lack thereof, used as an input to the simulation.

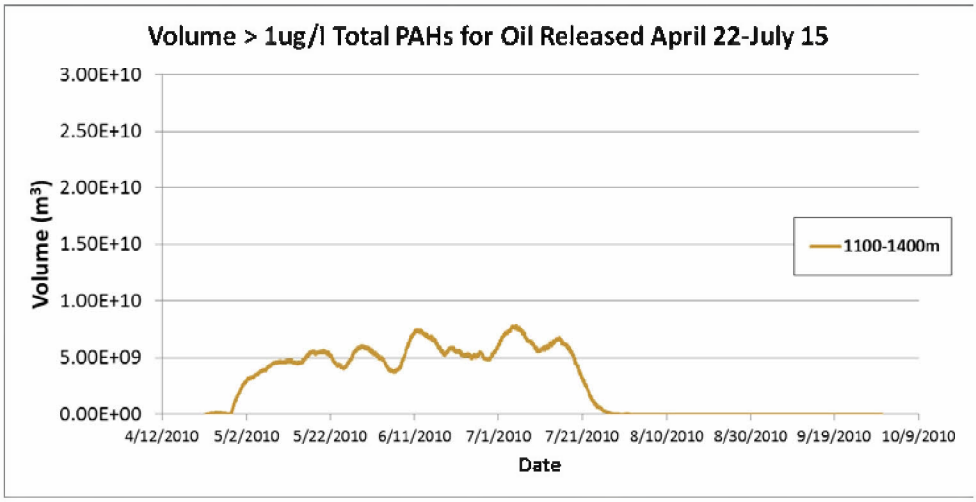

Figure 6-27. Volume of water in 1,100 – 1,400 m where the total TPAH50 concentration exceeded 1 μg/L, calculated each time step of the simulation using IAS ROMS.

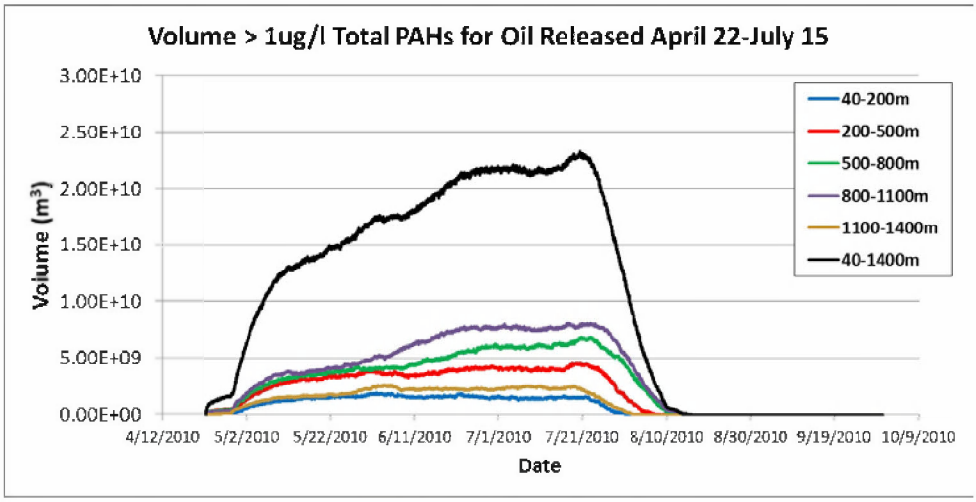

Figure 6-28. Volume of water where the total TPAH50 concentration exceeded 1 μg/L, calculated each time step of the Static Cone simulation in each the indicated depth zones.

Table 6-4. Maximum volume of water where the total TPAH50 concentration exceeded 1 μg/L and maximum concentration at any time step, in the 1,100 – 1,400-m depth layer, for the two simulations.

	Static Cone Simulation		IAS ROMS Simulation	
Depth Range (m)	Maximum Volume (m^3)	Maximum Concentration (μg/L)	Maximum Volume (m^3)	Maximum Concentration (μg/L)
1100-1400 m	2.65E+09	981	7.86E+09	677

7 Discussion and Conclusions

Model Validation

The modeled concentrations agreed well with field observations, based on comparisons with the NRDA chemistry results, data from multiple sensors that indicated the presence of oil, and reported information (e.g., water column hydrocarbon concentrations and microbial activities) in the literature (as reviewed in Appendix E).

Large droplets released at the wellhead in April 2010 rose rapidly to the surface. Later, after holes formed at the kink in the riser and after dispersant application began, smaller oil droplets were released. Smaller droplets were found further away from the wellhead as currents transported them horizontally and they rose through the water column. Small oil droplets in the water column resulted in large volumes of contaminated water due to dissolution of the soluble fraction of the hydrocarbons and the long residence time of the droplets.

Modeled droplet size distributions in the water column were skewed to the smallest size droplets near the trap height and towards progressively larger droplets further up in the water column, owing to higher buoyancies of larger droplets. This is consistent with field evidence related to droplet sizes reviewed in Section E.3 of Appendix E. LISST-100X and Holocam analyses indicated large numbers of small particles consistent with oil droplets in the depth range 1,100 – 1,300 m. Holocam analysis showed oil droplets with diameters of one to several hundred microns were present above the trap height. ROV video and camera images showed particulates, including oil droplets, throughout the water column, with large oil droplets (>1 mm) tending to be more prevalent in the upper part of the water column.

Vertical distributions of dissolved and total TPAH50 (Figures 6-7 to 6-12) indicated the highest concentrations in the deep plume layer and up to about 800 m, with substantial concentrations throughout the water column. These model results compare favorably to fluorescence signals and DO sags indicating presence of oil hydrocarbons at these depths (JAG 2010, Grennan et al. 2015, Horn et al. 2015b, Payne and Driskell 2015 a,b) and literature reports of hydrocarbon distributions in the water column (Diercks et al. 2010, Hazen et al. 2010, Camilli et al. 2010, Ryerson et al. 2011, 2012, Reddy et al. 2012, Spier et al. 2013). Diercks et al. (2010) observed total PAH concentrations up to 189 µg/L in sampling on May 9-16, 2010 in discrete depth layers between 1,000 and 1,400 m southwest of the wellhead site and extending at least as far as 13 km. From sampling performed May 25 – June 2, Hazen et al. (2010) detected a deep-sea oil plume from 1,099 m – 1,219 m at distances up to 10 km from the wellhead. In their samples, volatile aromatic hydrocarbon concentrations were significantly higher in the plume (mean, 139 µg/L) than in the non-plume samples. Boehm et al. (2012) reported highest concentrations of total PAH in field chemistry samples as 10–100 µg/L. Dissolved concentrations of BTEX and soluble alkanes were highest below 800 m, consistent with findings reported in the literature (e.g., Camilli et al. 2010, Reddy et al. 2011, and Ryerson et al. 2012, Payne and Driskell 2015 a, b) in that the deep water plume layer was primarily comprised of dissolved hydrocarbons, particularly BTEX.

The model successfully simulated the partitioning of PAHs between deep water and the surface. PAHs partially dissolved from droplets as they rose through the water column. Chemical measurements of floating oil and surface waters indicate that some of the PAHs remained in the larger oil droplets when they reached the surface; floating oil and surface water samples were observed to be enriched with 3- and 4-ring PAHs (Diercks et al. 2010, Spier et al. 2013; Stout 2015c, Payne and Driskell 2015a, b). Diercks et al. (2010) noted that the PAHs in the deep plume were enriched in naphthalenes, as compared to surface samples where 3- ring PAHs were relatively enriched, a pattern consistent with water partitioning of more water soluble PAH compounds during transport to the surface. This pattern was predicted by the modeling.

Use of the Static Cone Simulation Results for Plankton Exposure and Toxicity Evaluations

The favorable comparisons of the SIMAP model-predicted and the field-observed distributions of hydrocarbon components of varying physical chemical properties for the duration of the release period indicates the model provides a realistic simulation of the fate processes and exposure concentrations resulting from the Deepwater Horizon spill. The comparisons of volume affected above PAH concentration thresholds and mass balance of released hydrocarbons between the Static Cone and IAS ROMS simulations indicate that the mass balance of subsurface oil and PAH concentrations (below 1,100 m) were essentially unaffected by the transport.

Uncertainty and Best Estimate

While there is uncertainty in the model estimates of pathway and hydrocarbon concentrations, the Static Cone model simulation provides reliable estimates of exposure concentrations for water column biota. In order to quantitatively characterize the hydrocarbon contamination in the water column by field sampling alone, water samples would need to have been taken in a comprehensive sampling design. This sampling would have had to cover all the potentially-contaminated areas, as well as unaffected areas. In addition, the frequency of sampling would have had to occur at frequent time intervals over the entire release period (87 days) and a period after the well was shut in. Because hydrocarbon contamination from any spill is patchy in distribution, large numbers of stations and samples would be needed to map concentrations reliably. Such extensive sampling of all affected areas was not feasible, given the rapidity at which the contamination may be reduced by dilution and degradation.

Thus, the practical and realistic approach undertaken to define the scope of water column contamination and exposure was to combine the available field sampling data with a modeling approach that evaluated oil component fate. The concentrations of hydrocarbons were estimated using the spill volume, knowledge of the physical and chemical properties of the oil, and understanding of current transport in the environment. The mass balance must be maintained in the model, such that all of the oil is accounted for and alternatively, concentrations are constrained to not exceed the total amount of hydrocarbons spilled.

In summary, the strengths of this modeling analysis are that the model:

- Completes the mass balance and provides an analysis of pathways and exposure;
- Differentiates background from spilled contamination;
- Provides an objective measure that falls out of what is known and scientific understanding; and

- Fills the gaps of the field sampling of water column distribution of dissolved and total hydrocarbon component distributions, making possible the estimation of TPAH50 exposure concentrations in all locations and times of interest.

By using a probability distribution approach of the hydrocarbon carbon components in the water column, rather than point-to-point comparison of the predicted results with the measurements, a robust comparison of the model prediction and field observation data was made possible to account for the inevitable uncertainty.

8 References

Adams, E. E., S. A. Socolofsky and M. Boufadel. 2013. Comment on "Evolution of the Macondo Well Blowout: Simulating the Effects of the Circulation and Synthetic Dispersants on the Subsea Oil Transport". Environmental Science & Technology 47(20):11905-11905.

Anderson, J. B., Schwarzer, R. R., Clark, H. C., Wheeler, R. B., Hokanson, C. L., Anderson, J. E., and Okafor, J., 1979. pp. 2.3.2/2.4.2-1 to 2.3.2/2.4.2-118. in: Jackson, W. B. (ed.), Environmental Assessment of an Active Oil Field in the Northwestern Gulf of Mexico, 1977-1978. Volume III: Chemical and Physical Investigations. US National Oceanic and Atmospheric Administration (NOAA), National Marine Fisheries Service, Southeast Fisheries Center, 709p. [Available from: NTIS, Springfield, Virginia, Accession No. PB80107899.]

Antonov, J. I., D. Seidov, T. P. Boyer, R. A. Locarnini, A. V. Mishonov, H. E. Garcia, O. K. Baranova, M. M. Zweng, and D. R. Johnson. 2010: World Ocean Atlas 2009, Volume 2: Salinity. S. Levitus, Ed. NOAA Atlas NESDIS 69, U.S. Government Printing Office, Washington, D.C., 184 pp.

Atlas, R. and J. Bragg. 2009. Bioremediation of marine oil spills: when and when not – the Exxon Valdez experience. Microbial Biotechnology 2(2):213-221.

Boyer, T., S. Levitus, H. Garcia, R. A. Locarnini, C. Stephens, J. Antonov. 2005. Objective analyses of annual, seasonal, and monthly temperature and salinity for the world ocean on a 0.25 degree grid. Int. J. Clim., 25, 931-945.

Boyer, T. P., J. I. Antonov , O. K. Baranova, H. E. Garcia, D. R. Johnson, R. A. Locarnini, A. V. Mishonov, T. D. OBrien, D. Seidov, I. V. Smolyar, M. M. Zweng. 2009: World Ocean Database 2009. S. Levitus, Ed., NOAA Atlas NESDIS 66, U.S. Gov. Printing Office, Wash., D.C., 216 pp.

Brooks, J.M., Wiesenburg, D.A., and C.R. Schwab, 1981. Surfical Sediments and Suspended Particulate Matter. Environmental Effects of Offshore Oil Production. Marine Science Volume 14, 1981, pp 69-115.

Boehm, P.D., Murray, K.J., Brown, J.S., Royer, L. 2012. Distribution and fate of PAH and chemical dispersants in the water column following the deepwater horizon oil spill. In: Presentation at the 243rd American Chemical Society National Meeting, San Diego, CA. March 26–29, 2012.

Brown, J. S., D. Beckmann, L. Bruce, L. Cook, and S. Mudge, 2011. PAH Depletion Ratios Document the Rapid Weathering and Attenuation of PAHs in Oil Samples Collected after the Deepwater Horizon: 2011 International Oil Spill Conference, Portland, Oregon. In International Oil Spill Conference Proceedings (IOSC), vol. 2011, no. 1, p. Abs336. American Petroleum Institute, 2011.

Bryden, H.L. 1973. New polynomials for thermal expansion, adiabatic temperature gradient, and potential temperature of sea water. Deep-Sea Research 20: 401-408.

Camilli, R., C. M. Reddy, D. R. Yoerger, B. a. S. Van Mooy, M. V. Jakuba, J. C. Kinsey, C. P. Mcintyre, S. P. Sylva and J. V. Maloney. 2010. Tracking hydrocarbon plume transport and biodegradation at Deepwater Horizon. Science 330:201-204.

Chassignet, E.P., H.E. Hurlburt, E.J. Metzger, O.M. Smedstad, J.A. Cummings, G.R. Halliwell, R. Bleck, R. Baraille, A.J. Wallcraft, C. Lozano, H.L. Tolman, A. Srinivasan, S. Hankin, P. Cornillon, R. Weisberg, A. Barth, R. He, F. Werner, and J. Wilkin. 2009. US GODAE: Global ocean prediction with the HYbrid Coordinate Ocean Model (HYCOM). Oceanography 22(2):64–75, http://dx.doi.org/10.5670/oceanog.2009.39.

Chao, Y., R. He, J. Farrara, and C. Zhang, 2014. ROMS Hydrodynamic Modeling. Report to NOAA OR&R NRDA program, June 5, 2014, 64p.

Chao, Y., Li, Z., Farrara, J. D., McWilliams, J. C., Bellingham, J., Capet, X., Chavez, F., Choi, J. K., Davis, R., Doyle, J. Frantaoni, D., Li, P. P., Marchesiello, P., Moline, M. A., Paduan, J., Ramp, S., 2009. Development, implementation and evaluation of a data-assimilative ocean forecasting system off the central California coast. Deep-Sea Research II, 56, 100-126, doi:10.1016/j.dsr2.2008.08.011.

Chan, G., A. Chow and E. E. Adams. 2014. Effects of droplet size on intrusion of sub-surface oil spills. Environmental Fluid Mechanics:1-15.

Csanady, G. T. 1973. Turbulent Diffusion in the Environment, D. Reidel Publishing Company, Dordrecht, Holland.

Danek, L. J., and Tomlinson, M. S., 1980, Currents and hydrography of the Buccaneer Field and adjacent waters, in: Jackson, W. B., and Wilkens E. P. (eds.), Environmental Assessment of the Buccaneer Gas and Oil Field in the Northwestern Gulf of Mexico, 1975-1980, Vol. VI. NOAA Technical Memorandum NMFS-SEFC-40, 33 pp. Available from: NTIS, Springfield, Virginia.

Davis, C. S. and N. C. Loomis. 2014. Deepwater Horizon Oil Spill (DWHOS) Water Column Technical Working Group Image Data Processing Plan: Holocam, Description of data processing methods used to determine oil droplet size distributions from in situ holographic imaging during June 2010 on cruise *M/V Jack Fitz 3*. Cabell S. Davis, Woods Hole Oceanographic Institution; Nick Loomis, MIT/WHOI Joint Program in Oceanography. 15 pages + Appendix.

Diercks, A. R., R. C. Highsmith, V. L. Asper, D. Joung, Z. Zhou, L. Guo, A. M. Shiller, S. B. Joye, A. P. Teske, N. Guinasso, T. L. Wade and S. E. Lohrenz. 2010. Characterization of subsurface polycyclic aromatic hydrocarbons at the Deepwater Horizon site. Geophys. Res. Lett. 37, L20602:1-6.

Di Toro, D.M., J.A. McGrath and D.J. Hansen. 2000. Technical basis for narcotic chemicals and polycyclic aromatic hydrocarbon criteria. I. Water and tissue. Environmental Toxicology and Chemistry 19(8): 1951-1970.

D'Sa, E. J. and D. S. Ko. 2008. Short-term influences on suspended particulate matter distribution in the northern Gulf of Mexico: satellite and model observations. Sensors 8: 4249-4261.

D'Sa, E. J., R.L. Miller and B.A. McKee. 2007. Suspended particulate matter dynamics in coastal waters from ocean color: application to the northern Gulf of Mexico. Geophysical Research Letters 34: 6.

Forth, H., J. Morris, C. Lay, J. Lipton and C. Mitchelmore. 2015a. Characterization of oil and water accommodated fractions used to conduct aquatic toxicity testing in support of the Deepwater Horizon Natural Resource Damage Assessment. DWH NRDA Toxicity Technical

Working Group Report. Prepared for National Oceanic and Atmospheric Administration by Abt Associates, Boulder, CO. August.

Forth, H.P., J.M. Morris, and D. Cacela. 2015b. Explanation of Analytes Included in the Total Polycyclic Aromatic Hydrocarbon Sums Used by the Deepwater Horizon Natural Resource Damage Assessment Toxicity Group. DWH NRDA Toxicity Technical Working Group Report. Prepared for National Oceanic and Atmospheric Administration by Abt Associates, Boulder, CO. August.

French, D., M. Reed, K. Jayko, S. Feng, H. Rines, S. Pavignano, T. Isaji, S. Puckett, A. Keller, F. W. French III, D. Gifford, J. McCue, G. Brown, E. MacDonald, J. Quirk, S. Natzke, R. Bishop, M. Welsh, M. Phillips and B.S. Ingram. 1996. The CERCLA type A natural resource damage assessment model for coastal and marine environments (NRDAM/CME), Technical Documentation, Vol. I - V. Final Report, submitted to the Office of Environmental Policy and Compliance, U.S. Dept. of the Interior, Washington, DC, April, 1996; Available from National Technical Information Service, 5285 Port Royal Road, Springfield, VA 22161, PB96-501788.

French, D.P. and H. Rines. 1997. Validation and use of spill impact modeling for impact assessment. In: Proceedings, 1997 International Oil Spill Conference, American Petroleum Institute Publication No. 4651, Washington, DC, pp-829-834.

French, D.P., H. Rines and P. Masciangioli. 1997. Validation of an Orimulsion Spill Fates Model Using Observations from Field Test Spills. In: Proceedings of the Twentieth Arctic and Marine Oilspill Program (AMOP) Technical Seminar, Emergencies Science Division, Environment Canada, Ottawa, ON, pp. 933-961.

French McCay, D.P. 2002. Development and Application of an Oil Toxicity and Exposure Model, OilToxEx, Environmental Toxicology and Chemistry, 21:10, pp. 2080-2094.

French McCay, D.P. 2003. Development and Application of Damage Assessment Modeling: Example Assessment for the North Cape Oil Spill. Marine Pollution Bulletin, 47 (9-12), pp. 341-359.

French McCay, D.P. 2004. Oil Spill Impact Modeling: Development and Validation. Environmental Toxicology and Chemistry, 23 (10), pp. 2441-2456.

French McCay, D.P. 2009. State-of-the-Art and Research Needs for Oil Spill Impact Assessment Modeling. In Proceedings of the 32nd AMOP Technical Seminar on Environmental Contamination and Response, Emergencies Science Division, Environment Canada, Ottawa, ON, Canada, pp. 601-653.

French McCay, D.P., and J.J. Rowe. 2004. Evaluation of Bird Impacts in Historical Oil Spill Cases Using the SIMAP Oil Spill Model. In Proceedings of the 27th Arctic and Marine Oil Spill Program (AMOP) Technical Seminar, Emergencies Science Division, Environment Canada, Ottawa, ON, Canada, pp. 421-452.

French McCay, D., N. Whittier, S. Sankaranarayanan, J. Jennings, and D. S. Etkin. 2004. Estimation of Potential Impacts and Natural Resource Damages of Oil. J. Hazardous Materials 107/1-2:11-25.

French McCay, D.P., N. Whittier, C. Dalton, J.J. Rowe, and S. Sankaranarayanan. 2005. Modeling fates and impacts of hypothetical oil spills in Delaware, Florida, Texas, California, and Alaska waters, varying response options including use of dispersants. In: Proceedings, International Oil Spill Conference, May 2005, Paper 399, American Petroleum Institute, Washington, DC.

French McCay, D.P, C. Mueller, K. Jayko, B. Longval, M. Schroeder, J.R. Payne, E. Terrill, M. Carter, M. Otero, S. Y. Kim, W. Nordhausen, M. Lampinen, and C. Ohlmann. 2007. Evaluation of Field-Collected Data Measuring Fluorescein Dye Movements and Dispersion for Dispersed Oil Transport Modeling. In: Proceedings of the 30th Arctic and Marine Oil Spill Program (AMOP) Technical Seminar, Emergencies Science Division, Environment Canada, Ottawa, ON, Canada, pp.713-754.

French McCay, D., J. Rowe, R. Balouskus, A. Morandi, M.C. McManus, 2015. Technical Reports for Deepwater Horizon Water Column Injury Assessment – WC_TR.28: Injury quantification for planktonic fish and invertebrates in estuarine, shelf and offshore waters. RPS ASA, South Kingstown, RI, USA, August 2015.

Garcia, H. E., R. A. Locarnini, T. P. Boyer, J. I. Antonov, O. K. Baranova, M. M. Zweng, and D. R. Johnson. 2010a. World Ocean Atlas 2009, Volume 3: Dissolved Oxygen, Apparent Oxygen Utilization, and Oxygen Saturation. S. Levitus, Ed. NOAA Atlas NESDIS 70, U.S. Government Printing Office, Washington, D.C., 344 pp.

Garcia, H. E., R. A. Locarnini, T. P. Boyer, J. I. Antonov, M. M. Zweng, O. K. Baranova, and D. R. Johnson. 2010b. World Ocean Atlas 2009, Volume 4: Nutrients (phosphate, nitrate, silicate). S. Levitus, Ed. NOAA Atlas NESDIS 71, U.S. Government Printing Office, Washington, D.C., 398 pp.

Grennan, M., S. Zamorski, L. Decker, M. Horn, and Y. Kim, 2015. Technical Reports for Deepwater Horizon Water Column Injury Assessment – FE_TR.39: Volume II. Water Column CTD and Sensor Data from the Deepwater Horizon Oil Spill. RPS ASA, South Kingstown, RI, USA, August 2015.

Hazen, T. C., E. A. Dubinsky, T. Z. Desantis, G. L. Andersen, Y. M. Piceno, N. Singh, J. K. Jansson, A. Probst, S. E. Borglin, J. L. Fortney, W. T. Stringfellow, M. Bill, M. E. Conrad, L. M. Tom, K. L. Chavarria, T. R. Alusi, R. Lamendella, D. C. Joyner, C. Spier, J. Baelum, M. Auer, M. L. Zemla, R. Chakraborty, E. L. Sonnenthal, P. D'haeseleer, H. Y. N. Holman, S. Osman, Z. Lu, J. D. Van Nostrand, Y. Deng, J. Zhou and O. U. Mason. 2010. Deep-sea oil plume enriches indigenous oil-degrading bacteria. Science 330:204-208.

Hines, A.L. and R.N. Maddox. 1985. Mass Transfer Fundamentals and Application. Prentice-Hall, Inc., Englewood Cliffs, New Jersey, 542p.

Horn, M., M. Grennan, L. Decker, S. Zamorski, D. French McCay, and Z. Li, 2015a. Technical Reports for Deepwater Horizon Water Column Injury Assessment –Volume I. Water Column Chemistry Data from the Deepwater Horizon Blowout. RPS ASA, South Kingstown, RI, USA, August 2015.

Horn, M., D. French McCay, J. Payne, W. Driskell, Z. Li, M. Grennan, L. Decker, S. Zamorski, 2015b. Technical Reports for Deepwater Horizon Water Column Injury Assessment –Volume III. Water Column Chemical and Physical Data from the Deep Water Horizon Blowout. RPS ASA, South Kingstown, RI, USA, August 2015.

Hyun, K. H. and R. He. 2010. Coastal upwelling in the South Atlantic Bight: A revisit of the 2003 cold event using long term observations and model hindcast solutions. Journal of Marine Systems 83(1–2):1-13.

JAG. 2010. Joint Analysis Group (JAG) Review of R/V Brooks McCall Data to Examine Subsurface Oil (http://www.ncddc.noaa.gov/activities/healthy-oceans/jag/reports/).

Jernelov, A. and O. Linden. 1981. Ixtoc I: A case study of the world's largest oil spill. Ambio 10(6):299-306.

Jose, F., Stone, G.W., Kobashi, D., SiadatMousavi, S.M., and L. A. Baozhu, 2009. Hydrodynamic Response of a Transgressive Shoal to the Proposed Mining for Restoring Adjacent Beaches and Barriers: Sabine Bank off Louisiana-Texas Coast, United States. Coastal Dynamics, Paper # 146.

Jones, R.K. 1997. A Simplified Pseudo-Component of Oil Evaporation Model. In Proceedings of the 20th Arctic and Marine Oil Spill Program (AMOP) Technical Seminar, Environment Canada, pp. 43-61.

Joye, S., I.R. MacDonald, I. Leifer, and V. Asper, 2011. Magnitude and Oxidation Potential of Hydrocarbon Gases Released from the BP Oil Well Blowout. Nature Geoscience, Letters, published online 13 February 2011.

Kessler, J. D., D. L. Valentine, M. C. Redmond, M. Du, E. W. Chan, S. D. Mendes, E. W. Quiroz, C. J. Villanueva, S. S. Shusta, L. M. Werra, S. A. Yvon-Lewis and T. C. Weber. 2011. A persistent oxygen anomaly reveals the fate of spilled methane in the deep Gulf of Mexico Science 331:312-315.

Kirstein, B.E., J.R. Clayton, C. Clary, J.R. Payne, D. McNabb, Jr., G. Fauna and R. Redding. 1987. Integration of Suspended Particulate Matter and Oil Transportation Study. Minerals Management Service, OCS Study MMS87-0083, Anchorage, Alaska, 216p.

Kolpack, R.L., Plutchak, N.B. and R. W. Stearns. 1977. Fate of oil in a water environment - Phase II, a Dynamic model of the mass balance for released oil. University of Southern California, prepared for American Petroleum Institute, API Publication 4313, Washington, D.C.

Kujawinski, E. B., M. C. Kido Soule, D. L. Valentine, A. K. Boysen, K. Longnecker and M. C. Redmond. 2011. Fate of Dispersants Associated with the Deepwater Horizon Oil Spill. Environmental Science & Technology 45(4):1298-1306.

Kullenberg, G. (ed.) 1982. Pollutant transfer and transport in the sea. Volume I. CRC Press, Boca Raton, Florida. 227 p.

Lehr, W., Bristol, S., Possolo, A. et al. 2010. Oil budget calculator, Deepwater Horizon, Technical Documentation. A report to the national incident command. The Federal Interagency Solutions Group, Oil Budget Calculator Science and Engineering Team, http://www.restorethegulf.gov/sites/default/files/documents/pdf/OilBudgetCalc_Full_HQ-Print_111110.pdf, November 2010. (Accessed on April 1, 2012).

Li, Z., Chao, Y., McWilliams, J. C., Ide, K., 2008a. A three-dimensional variational data assimilation scheme for the regional ocean modeling system. Journal of Atmospheric and Oceanic Technology 25(11): 2074-2090.

Li, Z., Chao, Y., McWilliams, J. C., Ide, K., 2008b. A three-dimensional variational data assimilation scheme for the Regional Ocean Modeling System: Implementation and basic experiments. Journal of Geophysical Research C: Oceans 113(5), C05002, doi:10.1029/2006JC004042.

Li, Z., A. Bird, J.R. Payne, N. Vinhateiro, Y. Kim, C. Davis and N. Loomis, 2015. Technical Reports for Deepwater Horizon Water Column Injury Assessment – Volume IV. Oil Particle Data from the Deepwater Horizon Oil Spill. RPS ASA, South Kingstown, RI, USA, August 2015.

Lindo-Atichati, D., C. B. Paris, M. Le Hénaff, M. Schedler, A. G. Valladares Juárez and R. Müller. 2014. Simulating the effects of droplet size, high-pressure biodegradation, and variable flow rate on the subsea evolution of deep plumes from the Macondo blowout. Deep Sea Research Part II: Topical Studies in Oceanography (0).

Locarnini, R. A., A. V. Mishonov, J. I. Antonov, T. P. Boyer, H. E. Garcia, O. K. Baranova, M. M. Zweng, and D. R. Johnson. 2010. World Ocean Atlas 2009, Volume 1: Temperature. S. Levitus, Ed. NOAA Atlas NESDIS 68, U.S. Government Printing Office, Washington, D.C., 184 pp

Mackay, D. and P.J. Leinonen. 1977. Mathematical model of the behavior of oil spills on water with natural and chemical dispersion. Prepared for Fisheries and Environment Canada. Economic and Technical Review Report EPS-3-EC-77-19, 39p.

Mackay, D., S. Paterson and K. Trudel. 1980. A mathematical model of oil spill behavior. Department of Chemical and Applied Chemistry, University of Toronto, Canada, 39p.

Mackay, D., W.Y. Shiu, and K.C. Ma. 1992. Illustrated Handbook of Physical-Chemical Properties and Environmental Fate for Organic Chemicals, Vol. I-IV. Lewis Publishers, Inc, Chelsea, Michigan.

Mackay D, Shiu WY, Ma K-C & Lee SC, 2006a. Handbook of Physical-Chemical Properties and Environmental Fate for Organic Chemicals. Vol. I, Introduction and Hydrocarbons. CRC Press, Taylor & Francis Group.

Mackay D, Shiu WY, Ma K-C & Lee SC, 2006b. Handbook of Physical-Chemical Properties and Environmental Fate for Organic Chemicals. Vol. IV, Nitrogen and Sulfur Containing Compounds and Pesticides. CRC Press, Taylor & Francis Group.

McKenna, A.M., R.K. Nelson, C.M. Reddy, J.J. Savory, N.K. Kaiser, J.E. Fitzsimmons, A.G. Marshall, and R.P. Rodgers. 2013. Expansion of the Analytical Window for Oil Spill Characterization by Ultrahigh Resolution Mass Spectrometry: Beyond Gas Chromatography. Environmental Science and Technology, pp. 7530-7539.

McNutt M., R. Camilli,G. Guthrie G, et al. 2011. Assessment of Flow Rate Estimates for the Deepwater Horizon / Macondo Well Oil Spill. Flow Rate Technical Group report to the National Incident Command, Interagency Solutions Group, March 10, 2011.

Meade, R. H. 1995. Setting: Geology, Hydrology, Sediments, and Engineering of the Mississippi River. In: Contaminants in the Mississippi River U.S. Geological Survey Circular 1133 Reston, Virginia, 1995. Edited by R. H. Meade. Available Online http://pubs.usgs.gov/circ/circ1133/geosetting.html (Accessed on December 20, 2012).

Montagna PA, Baguley JG, Cooksey C, Hartwell I, Hyde LJ, et al. 2013. Deep-Sea Benthic Footprint of the Deepwater Horizon Blowout. PLoS ONE 8(8): e70540. doi: 10.1371/journal.pone.0070540

Morris, J.M., C.R. Lay, H.P. Forth, D. Cacela, and J. Lipton. 2015b. Use of Bioassay Data in Field Exposure and Toxicity Modeling. DWH NRDA Toxicity Technical Working Group Report. Prepared for National Oceanic and Atmospheric Administration by Abt Associates, Boulder, CO.

Morris, J.M., C.R. Lay, H.P. Forth, D. Cacela, and J. Lipton. 2015b. Use of Bioassay Data in Field Exposure and Toxicity Modeling. DWH NRDA Toxicity Technical Working Group Report. Prepared for National Oceanic and Atmospheric Administration by Abt Associates, Boulder, CO.

Mulcahy, R, 2010. Water Column Injury Ephemeral Data Collection: ADCP Monitoring Plan (M/V Bunny Bordelon) (May 26, 2010). Originated as a Requirement by D. French McCay, Y. Kim, and Laurie Sullivan, 2010. Deepwater Horizon NRDA > Administrative Record > Pre-assessment -- Water Column: http://www.doi.gov/deepwaterhorizon/adminrecord/Pre-assessment-Water-Column.cfm

North, E. W., E. E. Adams, Z. Schlag, C. R. Sherwood, R. He, K. H. Hyun and S. A. Socolofsky. 2011. Simulating Oil Droplet Dispersal From the Deepwater Horizon Spill With a Lagrangian Approach. Monitoring and Modeling the Deepwater Horizon Oil Spill: A Record-Breaking Enterprise. American Geophysical Union, Pp. 217-226.

North, E. W., E. E. Adams, A. Thessen, E. , Z. Schlag, R. He, S. Socolofsky, A., S. Masutani, M. and S. Peckham, D. . 2015. The influence of droplet size and biodegradation on the transport of subsurface oil droplets during the Deepwater Horizon spill: a model sensitivity study. Environmental Research Letters 10(2):024016.

Okubo, A. and R.V. Ozmidov. 1970. Empirical dependence of the coefficient of horizontal turbulent diffusion in the ocean on the scale of the phenomenon in question. Atmospheric and Ocean Physics 6(5):534-536.

Okubo, A. 1971. Oceanic diffusion diagrams. Deep-Sea Research 8:789-802.

Passow, U. 2014. Formation of rapidly-sinking, oil-associated marine snow. Deep Sea Research Part II: Topical Studies in Oceanography (0).

Passow, U., K. Ziervogel, V. Asper and A. Diercks. 2012. Marine snow formation in the aftermath of the Deepwater Horizon oil spill in the Gulf of Mexico. Environmental Research Letters 7.

Patton, J. S., M. W. Rigler, P. D. Boehm and D. L. Fiest. 1981. Ixtoc 1 oil spill: flaking of surface mousse in the Gulf of Mexico. Nature 290(5803):235-238.

Payne, J.R. and G.D. McNabb Jr. 1984. Weathering of Petroleum in the Marine Environment. Marine Technology Society Journal 18(3):24-42.

Payne, J.R., B.E. Kirstein, G.D. McNabb, Jr., J.L. Lambach, R. Redding R.E. Jordan, W. Hom, C. deOliveria, G.S. Smith, D.M. Baxter, and R. Gaegel. 1984. Multivariate analysis of petroleum weathering in the marine environment – sub Arctic. Environmental Assessment of the Alaskan Continental Shelf, OCEAP, Final Report of Principal Investigators, Vol. 21 and 22, Feb. 1984, 690p.

Payne, J.R., B.E. Kirstein, J.R. Clayton, Jr., C. Clary, R. Redding, G.D. McNabb, Jr., and G. Farmer. 1987. Integration of suspended particulate matter and oil transportation study. Final Report. Minerals Management Service, Environmental Studies Branch, Anchorage, AK. Contract No. 14-12-0001-30146. 216 p.

Payne, J.R., and W.B. Driskell, 2015a. 2010 DWH Offshore Water Column Samples—Forensic Assessments and Oil Exposures. PECI Technical Report to the Trustees in support of the pDARP.

Payne, J.R., and W.B. Driskell, 2015b. Forensic Fingerprinting Methods and Classification of DWH Offshore Water Samples. PECI Technical Report to the Trustees in support of the pDARP.

Payne, J.R., and W.B. Driskell, 2015c. Dispersant effects on waterborne oil profiles and behavior. PECI Technical Report to the Trustees in support of the pDARP.

Payne, J.R., and W.B. Driskell, 2015d. Offshore adaptive sampling strategies. PECI Technical Report to the Trustees in support of the pDARP.

Reddy, C.M., J. S. Arey, J. S. Seewald, S. P. Sylva, K. L. Lemkau, R. K. Nelson, C. A. Carmichael, C. P. McIntyre, Judith Fenwick, G. T. Ventura, B. A. S. Van Mooy, and R. Camilli, 2011. Composition and fate of gas and oil released to the water column during the Deepwater Horizon oil spill. Proceedings of National Academy of Sciences PNAS early edition: 1-6. www.pnas.org/cgi/doi/10.1073/pnas.1101242108.

Reddy, C. M., J. S. Arey, J. S. Seewald, S. P. Sylva, K. L. Lemkau, R. K. Nelson, M. a. S. Van Mooy and R. Camilli. 2012. Composition and fate of gas and oil released to the water column during the Deepwater Horizon oil spill. Proceedings of National Academy of Sciences 109(5):20229-20234.

Ryerson T. B., R. Camilli, J. D. Kessler, E. B. Kujawinski , C. M. Reddy ,D. L. Valentine, E. Atlas, D. R. Blake, J. de Gouwa, S. Meinardi, D. D. Parrish, J. Peischl, J. S. Seewald, and C. Warneke, 2011. Chemical data quantify Deepwater Horizon hydrocarbon flow rate and environmental distribution, Proceedings of the National Academy of Sciences, www.pnas.org/cgi/doi/10.1073/pnas.1110564109.

Ryerson, T. B., R. Camilli, J. D. Kessler, E. B. Kujawinski, C. M. Reddy, D. L. Valentine, E. Atlas, D. R. Blake, J. De Gouw, S. Meinardi, D. D. Parrish, J. Peischl, J. S. Seewald and C. Warneke. 2012. Chemical data quantify Deepwater Horizon hydrocarbon flow rate and environmental distribution. Proceedings of the National Academy of Sciences 109(50):20246-20253.

Salisbury, J. E., J.W. Campbell, E. Linder, L.D. Meeker, F.E. Muller-Karger and C.J. Vorosmarty. 2004. On the seasonal correlation of surface particle fields with wind stress and Mississippi discharge in the northern Gulf of Mexico. Deep-Sea Research II 51: 1187-1203.

Schmitz Jr., W.J., D.C. Biggs, A. Lugo-Fernandez, L.-Y. Oey, and W. Sturges. 2005. A Synopsis of the Circulation in the Gulf of Mexico and on its Continental Margins. In W. Sturges and A. Lugo-Fernandez, Circulation in the Gulf of Mexico: Observations and Models (pp. 11-29). Washington, D.C., United States: American Geophysical Union.

Socolofsky, S. A. and G. H. Jirka, 2005. Environmental Fluid Mechanics. Part I: Mass Transfer and Diffusion. Engineering – Lectures. Publisher: Texas A&M University 2005, 184 p.

Socolofsky, S. A., E. E. Adams and C. R. Sherwood. 2011. Formation dynamics of subsurface hydrocarbon intrusions following the Deepwater Horizon blowout. Geophys. Res. Lett. 38(9):L09602.

Spaulding, M.S., D. Mendelsohn, D. Crowley, Z. Li, and A. Bird, 2015. Technical Reports for Deepwater Horizon Water Column Injury Assessment – WC_TR.13: Application of OILMAP DEEP to the Deepwater Horizon Blowout. RPS ASA, 55 Village Square Drive, South Kingstown, RI 02879.

Spier, C., W. T. Stringfellow, T. C. Hazen and M. Conrad. 2013. Distribution of hydrocarbons released during the 2010 MC252 oil spill in deep offshore waters. Environmental Pollution 173(0):224-230.

Stiver, W. and D. Mackay, 1984. Evaporation rate of oil spills of hydrocarbons and petroleum mixtures. Environmental Science and Technology 18: 834-840.

Stout, S.A., 2015a. Physical and chemical properties of the fresh MC252 Macondo-1 well crude oil. NewFields Technical Report to the Trustees in support of the pDARP.

Stout, S.A., 2015b. Bulk chemical and physical properties of fresh and weathered Macondo crude oil. NewFields Technical Report to the Trustees in support of the pDARP.

Stout, S.A., 2015c. Range in composition and weathering among floating Macondo oils during the Deepwater Horizon oil spill. NewFields Technical Report to the Trustees in support of the pDARP.

Stout, S.A., 2015d. Chemical evidence for the prescence and distribution of Macondo oil in deep-sea sediments following the Deepwater Horizon oil spill. Newfields Technical Report to the Trustees in support of the pDARP

Stout, S., S. Rouhani, B. Liu, and J. Oehrig, 2015. Spatial Extent ("Footprint") and volume of Macondo oil found on the deep-sea floor following the Deepwaer Horizion Oil Spill. Newfields Technical Report to the Trustees in support of the pDARP.

Travers, C., H. Forth, M. Rissing, and D. Cacela. 2015a. Polycyclic Aromatic Hydrocarbon Concentrations in the Upper Water Column During the Deepwater Horizon Oil Spill. DWH NRDA Water Column Technical Working Group Report. Prepared for National Oceanic and Atmospheric Administration by Abt Associates, Boulder, CO. August

Travers, C., C. Wobus and J. Morris. 2015b. Mortality Estimates of Invertebrates and Early Life Stage Fish and Other Injury Metrics in the Upper Mixed Layer of the Water Column during the Deepwater Horizon Oil Spill. DWH NRDA Water Column Technical Working Group Report. Prepared for National Oceanic and Atmospheric Administration by Abt Associates, Boulder, CO. August.

Valentine, D. L. K., J.D.; Redmond, M.C.; Mendes, S.D.; Heintz, M.B.; Farwell, C.; Hu, L.; Kinnaman, F.S.; Yvon-Lewis, S.; Du, M.; Chan, E.W.; Tigreros, F.G.; Villanueva, C.J. 2010. Propane respiration jump-starts microbial response to a deep oil spill. Science 330:208-211.

Valentine, D. L., G. B. Fisher, S. C. Bagby, R. K. Nelson, C. M. Reddy, S. P. Sylva, and M. A. Woo, 2014. Fallout plume of submerged oil from Deepwater Horizon. PNAS vol. 111, No. 45, pp. 15906–15911, doi: 10.1073/pnas.1414873111.

USDC, 2015. The US District Court for Eastern District of Louisiana, Case 2:10-md-02179-CJB-SS Document 14021 Filed 01/15/15, Findings of fact and conclusions of law phase two trial. Pp 1-44. (http://www2.epa.gov/sites/production/files/2015-01/documents/phase2ruling.pdf)

Zahed, M. A., H. A. Aziz, M. H. Isa, L. Mohajeri, S. Mohajeri and S. R. M. Kutty. 2011. Kinetic modeling and half-life study on bioremediation of crude oil dispersed by Corexit 9500. Journal of Hazardous Materials 185(2-3):1027-1031.

Ziervogel, K., L. Mckay, B. Rhodes, C. L. Osburn, J. Dickson-Brown, C. Arnosti and A. Teske. 2012. Microbial Activities and Dissolved Organic Matter Dynamics in Oil-Contaminated Surface Seawater from the Deepwater Horizon Oil Spill Site. PLoS ONE 7(4):e34816.

Ziervogel, K. and C. Arnosti. 2014. Enhanced protein and carbohydrate hydrolyses in plume-associated deepwaters initially sampled during the early stages of the Deepwater Horizon oil spill (In Press). Deep Sea Research Part II: Topical Studies in Oceanography, 2013; DOI: 10.1016/j.dsr2.2013.09.003

Technical Reports for Deepwater Horizon Water Column Injury Assessment

WC_TR.14: Modeling Oil Fate and Exposure Concentrations in the Deepwater Plume and Rising Oil Resulting from the Deepwater Horizon Oil Spill

Appendix A. Oil Fate Model Algorithms

Authors: Deborah French McCay, Katherine Jayko, Zhengkai Li, Matthew Horn, Yong Kim, Tatsu Isaji, Deborah Crowley, Malcolm Spaulding, Lauren Decker, Cathleen Turner, Stefanie Zamorski, Jeremy Fontenault, Rachel Shmookler, and Jill Rowe

Revised: September 29, 2015
Project Number: 2011-144
RPS ASA, 55 Village Square Drive, South Kingstown, RI 02879

Table of Contents

List of Figures

List of Tables

A.1 Chemical Characterization of Oil in the SIMAP Oil Fate Model

Oil is a mixture of hydrocarbons of varying physical, chemical, and toxicological characteristics. Thus, oil hydrocarbons have varying fates and effects on aquatic organisms. In the model, oil is represented by multiple component categories, and the fate of each component is tracked separately. The "pseudo-component" approach (Payne et al., 1984; Payne et al., 1987; French et al., 1996;Jones, 1997; Lehr et al., 2000) is used, where chemicals in the oil mixture are grouped by physical-chemical properties, and the resulting component category behaves as if it were a single chemical with characteristics typical of the chemical group.

The SIMAP fates model focuses on tracking the lower molecular weight aromatic (and other soluble) compounds divided into chemical groups (components) based on volatility, solubility, and hydrophobicity. Compounds having octanol-water partition coefficients (K_{ow}) < 10^6 ($\log(K_{ow})<6$) are considered soluble in water: low molecular weight aromatics (i.e., monoaromatic and polycyclic aromatic hydrocarbons, MAHs and PAHs) and short-chain or cyclic alkanes. In the model, the oil is treated as comprising pairs of aliphatic and aromatic components. The standard (default) number of components used in SIMAP is 8, as defined in Table A-1; however, a 19-component model has been implemented in the present model (Tables A-2 to A-6; properties are in Appendix B). Note that the breakout into components is operationally defined; soluble and semi-soluble compounds with $\log(K_{ow})<6$ may include aromatics as well as polar, cyclic or other soluble hydrocarbon compounds; whereas the aliphatic group includes compounds that are volatile but not soluble. Thus, the names "aromatic" and "aliphatic" characterize most of the compounds but members of the classifications are not exclusively these chemical types.

All but the residual components, representing non-volatile aromatics and aliphatics, evaporate at rates specific to the component. Solubility is strongly correlated with volatility, and the solubility of aromatics is higher than aliphatics of the same volatility. The MAHs are the most soluble, the 2-ring PAHs are less soluble, and the 3-ring PAHs slightly soluble (Mackay , et al., 2006). Both the solubility and toxicity of the non-aromatic hydrocarbons are much less than for the aromatics. Dissolution of essentially non-soluble hydrocarbons is not evaluated in the model. Dissolved concentrations are calculated only for each of the soluble and semi-soluble "aromatic" components.

Table A-1: Definition of four distillation cuts and the eight components (one aliphatic and one aromatic for each of the 4 distillation cuts) used as the default in the SIMAP model (MAHs = Mono-aromatic Hydrocarbons; BTEX = Benzene + Toluene + Ethylbenzene + Xylene; PAHs = Polycyclic Aromatic Hydrocarbons).

Characteristic	Volatile and Highly Soluble	Semi-volatile and Soluble	Low Volatility and Slightly Soluble	Residual (non-volatile and very low solubility)
Distillation cut	1	2	3	4
Boiling Point (°C)	<180	180 - 265	265 - 380	>380
Molecular Weight	50 - 125	125 - 168	152 - 215	>215
Log(K_{ow})	2.1-3.7	3.7-4.4	3.9-5.6	>5.6
Aliphatic components: Number of Carbons	volatile aliphatics: C4 – C10	semi-volatile aliphatics: C10 – C15	low-volatility aliphatics: C15 – C20	non-volatile aliphatics: >C20
Aromatic component name: included compounds	MAHs: BTEX, MAHs to C3-benzenes	2 ring PAHs: C4-benzenes, naphthalene, C1-, C2-naphthalenes	3 ring PAHs: C3-, C4-naphthalenes, 3-4 ring PAHs with log(K_{ow}) <5.6	≥4 ring aromatics: PAHs with log(K_{ow}) >5.6 (very low solubility)

Table A-2: Definition of distillation cuts and the 19 components used in the in the present model application for deep water releases. (The residual aromatics and aliphatics are treated as a combined component 19; solubility defined under NIST Standard Conditions of 15°C and 14.7 psi)

All hydrocarbons	AR or AL Component #	Soluble and semi-solubles (AR components)	Non-soluble aliphatics (AL components)	Boiling Point (°C) for non-solubles
Volatiles	1	MAHs (BTEX & styrene)	Volatile aliphatics	< 150
	2	C3-benzenes	Volatile aliphatics	150-180
Semi-volatiles	3	C4-benzenes	Semi-volatile aliphatics	180-200
	4	Decalins	Semi-volatile aliphatics	200-230
	5	C0-C2 Naphthalenes & C0-C2 Benzothiophenes	Semi-volatile aliphatics	230-280
Low Volatility	6	C3-C4 Naphthalenes & C3-C4 Benzothiophenes	Low volatility aliphatics	280-300
	7	Fluorenes & C0-C1 phenanthrenes & dibenzothiophenes	Low volatility aliphatics	300-354
	8	4-ring PAHs & C2-C3 phenanthrenes & dibenzothiophenes	Low volatility aliphatics	354-380
High Volatility Aliphatics	9	Highly Volatile and Soluble Non-aromatic VOCs (Alkanes, Isoalkanes, Cycloalkanes)	(component to track dispersant indicators; not used)	<180
Residual (non-volatile)	19	High molecular weight aromatics	High molecular weight aliphatics	>380

Table A-3: Some properties of the 19-component model used in the present model application for deep water releases. [Other properties and properties of individual compounds are in Appendix B.]

Code	Group	Includes	Log (Kow)	Vapor Pressure (1 atm, 20°C)
AR1	BTEX	BTEX, styrene	2.91	3.40E-02
AR2	C3-benzenes	C3-benzenes	3.71	3.32E-03
AR3	C4-benzenes	C4-benzenes	4.02	1.52E-03
AR4	Decalins	cis/trans decalin to C4-decalin	4.89	7.27E-04
AR5	C0-C2 Naphthalenes & C0-C2 Benzothiophenes	C0-C2 Naphthalenes, C0-C2 Benzothiophenes, biphenyl, acenaphthene, acenaphthylene	4.02	8.04E-05
AR6	C3-C4 Naphthalenes & C3-C4 Benzothiophenes	C3-C4 Naphthalenes, C3-C4 Benzothiophenes, dibenzofuran	5.08	5.48E-06
AR7	Fluorenes & C0-C1 phenanthrenes & dibenzothiophenes	C0-C3 Fluorenes, C0-C1 phenanthrenes, C0-C1 dibenzothiophenes	5.02	8.36E-07
AR8	4-ring PAHs & C2-C3 phenanthrenes & dibenzothiophenes	C0-C2 pyrenes, C0-C2 fluoranthenes, C2-C3 dibenzothiophenes, C2-C3 phenanthrenes, chrysene, triphenylene	5.50	1.05E-07
AR9	Soluble alkanes	Low mol.wt. Alkanes, Isoalkanes, Cycloalkanes	3.65	1.76E-01
AL1	Aliphatics: BP < 150	(unmeasured compounds)	3.49	9.12E-02
AL2	Aliphatics: BP 150-180	(unmeasured compounds)	5.05	4.43E-03
AL3	Aliphatics: BP 180-200	C11 Alkanes	6.94	5.72E-04
AL4	Aliphatics: BP 200-230	C12 Alkanes	7.24	1.76E-04
AL5	Aliphatics: BP 230-280	C13-C16 Alkanes	7.37	2.77E-05
AL6	Aliphatics: BP 280-300	C17-C18 Alkanes	8.53	1.43E-06
AL7	Aliphatics: BP 300-350	C19-C20 Alkanes	10.10	1.33E-07
AL8	Aliphatics: BP 350-380	C21-C23 Alkanes	13.00	5.03E-11
AL9	Dispersant	(dispersant on oil droplets)	3.00	6.00E-02
Residual	Residual	Other non-volatile, non-soluble hydrocarbons	> 6.0	

* Dispersant concentration in oil droplets for treated oil.

Table A-4: Compounds in soluble aromatic components ("AR1" through "AR8") of the 19-component model used in the present model application for deep water releases.

Aromatic Hydrocarbon Name(s)	Type	Component #	Component Name
Benzene	MAH	AR1	BTEX + Styrene
Toluene	MAH	AR1	BTEX + Styrene
Ethylbenzene	MAH	AR1	BTEX + Styrene
Xylenes-p	MAH	AR1	BTEX + Styrene
Xylenes-m	MAH	AR1	BTEX + Styrene
Xylenes-o	MAH	AR1	BTEX + Styrene
styrene	MAH	AR1	Styrene
propylbenzenes-iso	MAH	AR2	C3-Benzene
propylbenzenes	MAH	AR2	C3-Benzene
Trimethlybenzenes-1,3,5	MAH	AR2	C3-Benzene
ethyl-methylbenzenes (cumene) & trimethylbenzenes	MAH	AR2	C3-Benzene
Trimethlybenzenes-1,2,4	MAH	AR2	C3-Benzene
Trimethlybenzenes-1,2,3	MAH	AR2	C3-Benzene
methylstyrenes	MAH	AR2	C3-Benzene
butylbenzenes	MAH	AR3	C4-Benzene
tetralin	MAH	AR3	C4-Benzene
tetramethlybenzenes	MAH	AR3	C4-Benzene
cis-Decalin	cycloalkane	AR4	C0-2 Decalin
trans-Decalin	cycloalkane	AR4	C0-2 Decalin
C1-Decalins	cycloalkane	AR4	C0-2 Decalin
C2-Decalins	cycloalkane	AR4	C0-2 Decalin
C3-Decalins	cycloalkane	AR4	C3-4 Decalin
C4-Decalins	cycloalkane	AR4	C3-4 Decalin
Benzo(b)thiophene	2-ring hetero-cyclic PAH	AR5	C0-2, 2-ring PAH
naphthalene	2-ring PAH	AR5	C0-2, 2-ring PAH
C1-naphthalenes	2-ring PAH	AR5	C0-2, 2-ring PAH
C2-naphthalenes	2-ring PAH	AR5	C0-2, 2-ring PAH
acenaphthene	2-ring PAH	AR5	2.5-ring PAH
C1-Benzothiophenes	2-ring hetero-cyclic PAH	AR5	C0-2, 2-ring PAH
biphenyl	PAH	AR5	C0-2, 2-ring PAH
C2-Benzothiophenes	2-ring cyclic	AR5	C0-2, 2-ring PAH
acenaphthylene	PAH	AR5	2.5-ring PAH
dibenzofuran	PAH	AR6	2.5-ring PAH
C3-naphthalenes	PAH	AR6	C3,4 2-ring PAH
C3-Benzothiophenes	2-ring cyclic	AR6	C3,4 2-ring PAH
C4-naphthalenes	PAH	AR6	C3,4 2-ring PAH
C4-Benzothiophenes	2-ring cyclic	AR6	C3,4 2-ring PAH
Fluorene	PAH	AR7	2.5-ring PAH
dibenzothiophene	PAH	AR7	3-ring PAH
C1-fluorenes	PAH	AR7	2.5-ring PAH
C2-fluorenes	PAH	AR7	2.5-ring PAH
C3-fluorenes	PAH	AR7	2.5-ring PAH
C1-dibenzothiophene	PAH	AR7	C0-1 3-ring PAH
phenanthrene/anthracene	PAH	AR7	C0-1 3-ring PAH
C1-phenanthrenes/anthracenes	PAH	AR7	C0-1 3-ring PAH
C2-phenanthrenes/anthracenes	PAH	AR8	C2 3-ring PAH
C2-dibenzothiophene	PAH	AR8	C2 3-ring PAH
C3-phenanthrenes/anthracenes	PAH	AR8	C3 3-ring PAH
C3-dibenzothiophene	PAH	AR8	C3 3-ring PAH
pyrene	PAH	AR8	4-ring PAH
C1-Fluoranthenes/pyrenes	PAH	AR8	4-ring PAH

Aromatic Hydrocarbon Name(s)	Type	Component #	Component Name
C2-Fluoranthenes/pyrenes	PAH	AR8	4-ring PAH
fluoranthene	PAH	AR8	4-ring PAH
Chrysene + Triphenylene	PAH	AR8	4-ring PAH

Table A-5: Compounds in the soluble aliphatic component ("AR9") of the 19-component model used in the present model application for deep water releases.

Soluble Paraffins & Isoparaffins	Type	Component #	Component Name
Cyclopentane	Naphthene (cycloalkane)	AR9	cyclic alkane
Isopentane	Isoparaffin (Isoalkane)	AR9	branched alkane
Pentane	Paraffin (n-alkane)	AR9	normal alkane
Cyclohexane	Naphthene (cycloalkane)	AR9	cyclic alkane
Methylcyclopentane	Naphthene (cycloalkane)	AR9	cyclic alkane
2,3-Dimethylbutane	Isoparaffin (Isoalkane)	AR9	branched alkane
2-Methylpentane	Isoparaffin (Isoalkane)	AR9	branched alkane
3-Methylpentane	Isoparaffin (Isoalkane)	AR9	branched alkane
Hexane	Paraffin (n-alkane)	AR9	normal alkane
Methylcyclohexane	Naphthene (cycloalkane)	AR9	cyclic alkane
1-Heptene / 1,2-DMCP (trans)	Naphthene (cycloalkane)	AR9	cyclic alkane
2,2-Dimethylpentane	Isoparaffin (Isoalkane)	AR9	branched alkane
2,4-Dimethylpentane	Isoparaffin (Isoalkane)	AR9	branched alkane
2-Methylhexane	Isoparaffin (Isoalkane)	AR9	branched alkane
Heptane	Paraffin (n-alkane)	AR9	normal alkane
2,3-Dimethylpentane	Isoparaffin (Isoalkane)	AR9	branched alkane
3-Methylhexane	Isoparaffin (Isoalkane)	AR9	branched alkane
2-Methylheptane	Isoparaffin (Isoalkane)	AR9	branched alkane
2,3,4-Trimethylpentane	Isoparaffin (Isoalkane)	AR9	branched alkane
2,2,3-Trimethylpentane	Isoparaffin (Isoalkane)	AR9	branched alkane
2,5-Dimethylhexane	Isoparaffin (Isoalkane)	AR9	branched alkane
2,4-Dimethylhexane	Isoparaffin (Isoalkane)	AR9	branched alkane
2,3,3-Trimethylpentane	Isoparaffin (Isoalkane)	AR9	branched alkane
2,3-Dimethylhexane	Isoparaffin (Isoalkane)	AR9	branched alkane
3-Ethylhexane	Isoparaffin (Isoalkane)	AR9	branched alkane
3-Methylheptane	Isoparaffin (Isoalkane)	AR9	branched alkane
Octane	Paraffin (n-alkane)	AR9	normal alkane
Nonane	Paraffin (n-alkane)	AR9	normal alkane
Decane	Paraffin (n-alkane)	AR9	normal alkane

Table A-6: Compounds representative of the insoluble components of the 19-component model used in the present model application for deep water releases: Insoluble aliphatic hydrocarbons categorized as volatile components "AL1" through "AL8" and the non-volatile component "residual".

Aliphatic Hydrocarbon Name(s)	C#	Component #	Component Name
[alkanes and iso alkanes in AR9]	6	AL1	C4-C6
[alkanes and iso alkanes in AR9]	7	AL1	C7-C8
[alkanes and iso alkanes in AR9]	8	AL1	C7-C8
[n-Nonane in AR9]	9	AL2	C9-C10
[n-Decane in AR9]	10	AL2	C9-C10
n-Undecane	11	AL3	C11-C12
n-Dodecane	12	AL4	C11-C12
n-Tridecane	13	AL5	C13-C16
n-Tetradecane	14	AL5	C13-C16
2,6,10-Trimethyldodecane	15	AL5	C13-C16
2,6,10-Trimethyltridecane	16	AL5	C13-C16
n-Hexadecane	16	AL5	C13-C16
n-Pentadecane	17	AL6	C17-C18
Norpristane	18	AL6	C17-C18
n-Heptadecane	17	AL6	C17-C18
n-Octadecane	18	AL6	C17-C18
Pristane	19	AL7	C19-C20
Phytane	20	AL7	C19-C20
n-Nonadecane	19	AL7	C19-C20
n-Eicosane	20	AL7	C19-C20
n-Heneicosane	21	AL8	C21-C23
n-Docosane	22	AL8	C21-C23
n-Tricosane	23	AL8	C21-C23
n-Tetracosane	24	Residual	C23+
n-Pentacosane	25	Residual	C23+
n-Hexacosane	26	Residual	C23+
n-Heptacosane	27	Residual	C23+
n-Octacosane	28	Residual	C23+
n-Nonacosane	29	Residual	C23+
n-Triacontane	30	Residual	C23+
n-Hentriacontane	31	Residual	C23+

Aliphatic Hydrocarbon Name(s)	C#	Component #	Component Name
n-Dotriacontane	32	Residual	C23+
n-Tritriacontane	33	Residual	C23+
n-Tetratriacontane	34	Residual	C23+
n-Pentatriacontane	35	Residual	C23+
n-Hexatriacontane	36	Residual	C23+
n-Heptatriacontane	37	Residual	C23+
n-Octatriacontane	38	Residual	C23+
n-Nonatriacontane	39	Residual	C23+
n-Tetracontane	40	Residual	C23+

An alternative approach, treating oil as a single compound with empirically-derived rates (e.g., Mackay et al., 1980a,b; Stiver and Mackay, 1984), does not provide sufficient resolution or accuracy for environmental effects analyses because the effects to water column organisms are determined by availability and uptake rates of MAHs, PAHs, and other soluble hydrocarbons, which have specific properties that differ from the other volatile and insoluble compounds. The model has been validated in predicting dissolved concentrations, supporting the appropriateness of the components-based approach (French McCay, 2002; French McCay, 2003).

The lower molecular weight aromatics (and other soluble hydrocarbons) dissolve from the whole oil, are adsorbed to suspended particulate matter (SPM), and are partitioned between the dissolved phase and SPM in the water column according to equilibrium partitioning theory (French , et al., 1996; Payne et al., 2003; French McCay, 2004). The residual fractions in the model are composed of non-volatile and insoluble compounds that remain in the “whole oil” that spreads, is transported on the water surface, strands on shorelines, and disperses in the water column as oil droplets or remains on or near the surface as tar balls.

A.2 Oil Fate Algorithms Applicable to Modeling Rising Oil and the Deep Plume

As SIMAP was used to model the rising oil up to a depth of 20m and the deep plume, and not to model the surfaced oil's fate and transport, this section describes algorithms used for modeling oil fate below 20m. The oil fate model estimates the distribution and mass of oil in the water column and on the sediments through time. Processes simulated by the physical fates modeling include oil droplet transport and dispersion, dissolution of soluble components into the water column, partitioning of oil between water and suspended particulate matter (SPM), sedimentation of oil droplets, and degradation.

A.2.1 Subsurface Transport

Spillets are moved in three dimensions over time. For each model time step, the new vector position of the spillet center is calculated from the old plus the vector sum of east-west, north-south, and vertical components of advective and diffusive velocities multiplied by the time step for model computations:

$$X_{t+1} = X_t + \Delta t\,(U_t + D_t + R_t)$$

Eq 1

where X_t is the vector position at time t, X_{t+1} is the vector position the next time step, Δt is the time step, U_t is the sum of all the advective (current) velocity components in three dimensions at time t (model inputs), D_t is the sum of the randomized diffusive velocities in three dimensions at time t, and R_t is the rise or sinking velocity of whole oil droplets in the water column. The magnitudes of the components of D_t are scaled by horizontal and vertical diffusion coefficients (Okubo and Ozmidov, 1970; Okubo, 1971). R_t is computed by Stoke's law, where velocity is related to the difference in density between the particle (i.e., droplet) and the water, and to the particle diameter.

A.2.1.1 Diffusion by Random Walk

A random walk dispersion process adds horizontal velocity to account for the advective dispersive processes below the scale of resolution of the input current field. For a discussion of these dispersive processes see Okubo (1980).

The dispersion velocities, u_{dd}, v_{dd}, and w_{dd}, (m/sec), in the east, north, and vertical directions, respectively, can be defined (Bear and Verruijt, 1987) as

$$u_{dd} = \gamma\sqrt{\frac{2D_x}{\Delta t}}$$

Eq 2

$$v_{dd} = \gamma\sqrt{\frac{2D_y}{\Delta t}}$$

Eq 3

$$w_{dd} = \gamma\sqrt{\frac{2D_z}{\Delta t}}$$

Eq 4

where

D_x - horizontal dispersion coefficient in east-west direction (m^2/sec)
D_y - horizontal dispersion coefficient in north-south direction (m^2/sec)
D_z - vertical dispersion coefficient (m^2/sec)
Δt - time step (sec)
γ - random number (-1 to +1)

D_x and D_y are usually ~equal, and are treated as such in the model. Values by one-or-more vertical layer(s) of the water column (with an option of using a spatial time-varying grid) are inputs to the model.

A cloud of subsurface oil droplets represented as a spillet spreads by turbulent diffusion. The radius of the cloud is estimated as the dispersive distance, D_d, defined as 2 standard deviations of a Gaussian-shaped spread of mass, which increases over time since release, t_a:

$$D_d = 2\sqrt{2\,D_{xy}\,t_a}$$

Eq 5

where D_{xy} is the horizontal spreading dispersion coefficient in the east-west and north-south directions (m^2/sec).

A.2.1.2 Droplet Rise Velocity

For small droplet sizes (less than 1 mm) the rise velocity is calculated by Stokes law:

$$W_d = gd^2(1-\Delta)/18v$$

Eq 6

where, W_d - rise velocity (m/sec), d- droplet diameter (m), g- gravity (m/sec^2), Δ - ratio of oil to water density (dimensionless, typical values range from 0.75 to 0.95), v – kinematic viscosity of water (m^2/sec).

Kinematic viscosity of water as a function of temperature was fitted to the data in Lindeburg (2003) as follows:

$$\nu_t = a_v - b_v t + c_v t^2$$

If S>0, then $\nu_t = \nu_t + 1.55 \times 10^{-9}(S - 35)$

Eq 7

where v_t is the kinematic viscosity of water at temperature t (in °C), and a_v, b_v and c_v are coefficients. This equation was fitted to the seawater (salinity, S = 35 ppt) kinematic viscosity data in the range of 0 to 50°C, as reported in "Properties of Water at Atmospheric Pressure, Appendix 14.B" of Lindeburg (2003), obtaining the following coefficient values:

Saltwater (salinity > 0 ppt): a_v = 1.79 x 10^{-6}, b_v = 4.53 x 10^{-8}, c_v = 4.40 x 10^{-10}

The density of seawater is obtained through a linear interpolation for a small range of S by the following equation (Fisher et al., 1979):

$$\sigma_t(T,S) \approx \sigma_t(T,S_0) + \frac{\partial \sigma_t}{\partial S}(T,S_0)[S - S_0]$$

In SIMAP Spill model code, a 24-parameter equation of state for seawater that was established for use in the open ocean has been adopted from (Chen and Millero, 1977). The equation of state of seawater is in the form:

$$\boldsymbol{V^P = V^0 - V^0 P/(K^0 + AP + BP^2)}$$ Eq 8

Where, V^P and V^0 are the specific volumes of seawater at applied pressure P and atmospheric pressure (0), respectively. V^0, K^0, A, and B are all salinity (S in ppt) and temperature (t in °C) dependent parameters. The constants of Equation (8) are given by:

$$V^0 = 1/d^0$$

$$\begin{aligned} d^0 = {} & 1.0281045 - 5.35633 \times 10^{-5} t - 6.78195 \times 10^{-6} t^2 \\ & + 7.0517 \times 10^{-8} t^3 - 8.4794 \times 10^{-10} t^4 + 5.057 \times 10^{-12} t^5 \\ & + (8.0792 \times 10^{-4} - 3.2481 \times 10^{-6} t + 6.423 \times 10^{-8} t^2 - 6.490 \times 10^{-10} t^3) \\ & \times (S - 35) + 2.045 \times 10^{-7} (S - 35)^2 \end{aligned}$$

$$\begin{aligned} K^0 = {} & 21585.72 + 132.5657t - 2.0860t^2 + 8.7648 \times 10^{-3} t^3 \\ & + (56.928 - 0.2975t)(S - 35) \end{aligned}$$

$$\begin{aligned} A = {} & 3.40075 - 7.6371 \times 10^{-3} t + 2.9651 \times 10^{-4} t^2 \\ & + (2.287 \times 10^{-3} - 3.255 \times 10^{-4} t)(S - 35) \end{aligned}$$

$$B = 2.211 \times 10^{-5}.$$

For droplet sizes larger than or equal to 1 mm, the drag coefficient of flow around the droplet is calculated by the following equation (White, 2005):

$$C_D = \frac{24}{Re} + \frac{6}{1 + \sqrt{Re}} + 0.4$$

Eq 9

where Re is the Reynolds Number, calculated as the product of rise velocity and droplet diameter divided by the kinematic viscosity of ambient seawater. Eq. 9 has an accuracy within 10% of error for the wide range of Re from 0 to $2x10^5$. The rise velocity is then calculated by:

$$W_d = \sqrt{\frac{4dg(1-\Delta)}{3 * C_D}}$$

Eq 10

The rise velocity is calculated using an iterative approach which refines the drag coefficient and vertical velocity until the calculated velocity changes less than a tolerance. To initialize this calculation, the terminal velocity of small droplets (d ≤ 1 mm) is estimated based on Eq. 6; and the velocity of larger droplets is based on Eq. 10. Droplets with diameters from 1 mm to 1 cm are given an initial drag coefficient of 1.0 while those greater than 1 cm start with a drag coefficient of 0.45.

A.2.2 Changes in Physical Properties

Temperature and weathering which changes the oil's chemical composition affect the viscosity and density of the oil. The chemical composition of the volatile fraction (taken as the volatile and semi-volatile fraction of the oil, that portion distilled at <380°C in SIMAP) changes due to dissolution of the soluble or semi-soluble components and degradation.

A.2.2.1 Viscosity Changes with Temperature

Viscosity is a function of temperature and state of weathering of the oil. SIMAP uses the algorithm of Mackay et al. (1982), an Arrhenius equation, to estimate the change in viscosity (μ_{temp}, cp) due to temperature (T, in degrees K),

$$\mu_{temp} = \mu_o exp\left[C_{temp}\left(\frac{1}{T} - \frac{1}{T_o}\right)\right]$$

Eq 11

where, μ_o - the viscosity (cp) of the fresh oil at a reference temperature T_o (K) and C_{temp} is a temperature correction factor, which is constant for each oil type. C_{temp} can be estimated by E_a/R, where E_a is the activation energy (J/mol) and R is the universal gas constant (8.314 J/mol-K). Luo and Gu (2007) reported that E_a is dependent on the asphaltene fraction of the oil, hence explaining a higher C_{temp} coefficient for heavy fuel oil than medium and light crude oils. The oil temperature, *T*, is not usually available so the model approximates it as the temperature of the surrounding water.

Viscosities of Deepwater Horizon (DWH) MC252 oil were reported by Belore et al. (2011), Stout (2015), and SL Ross (2010). The temperature coefficient without evaporation or dissolution of volatile and soluble components was estimated using the Stout (2015) data for viscosity at 30°C, 4.503 cp, and at 15°C, 7.145 cp; such that C_{temp} = 2088.535.

A.2.2.2 Viscosity Changes with Weathering

The effect of the loss of volatile and soluble fractions on dynamic viscosity, μ (cp), is given as

$$\mu = \mu_{temp} * \exp(C_{evap} * F_v)$$

Eq 12

where μ_{temp} – oil starting dynamic viscosity corrected to the ambient temperature (cP); C_{evap} – constant; *Fv* - fraction of initially-released oil mass lost to evaporation, dissolution, and degradation. In the present application the losses are due to dissolution and degradation, and so the constant C_{evap} is termed the weathering coefficient herein.

The DWH MC252 oil weathering data reported by Belore et al. (2011) and SL Ross (2010) can be used to estimate C_{evap} for the DWH source oil. The weathering coefficient was estimated as C_{evap} = 6.3224 for the evaporation test data of Belore et al. (2011), and C_{evap} = 7.0787 for the lab test reported by SL Ross (2010).

To generalize the model for oil conditions of varying initial volatile content, the rate of change of viscosity with weathering (by loss of volatile and soluble fractions) is expressed as follows:

$$\mu = \mu_o * \exp(C'_{evap} * F_v / F_{bp350})$$

Eq 13

where C'_{evap} = 4.6077 (Figure A-1) is the coefficient of viscosity increment as a result of fraction of the oil evaporated (in a laboratory test, or of total volatiles lost in the environment) that is normalized by F_{bp350} , the fraction of the initial oil distilled at < 350°C (i.e., ~ the volatile and semi-volatile fraction of the un-weathered oil). The estimate of C'_{evap}/F_{bp350} = 7.68 for the MC252 oil based on SL Ross (2010) lab test data is close to the C_{evap} value (7.08) that is obtained from a direct fit of the Fv to the viscosity data. The generalized algorithm (Eq. 13) is used in SIMAP, where the sum of all volatile components is used for F_{bp350}.

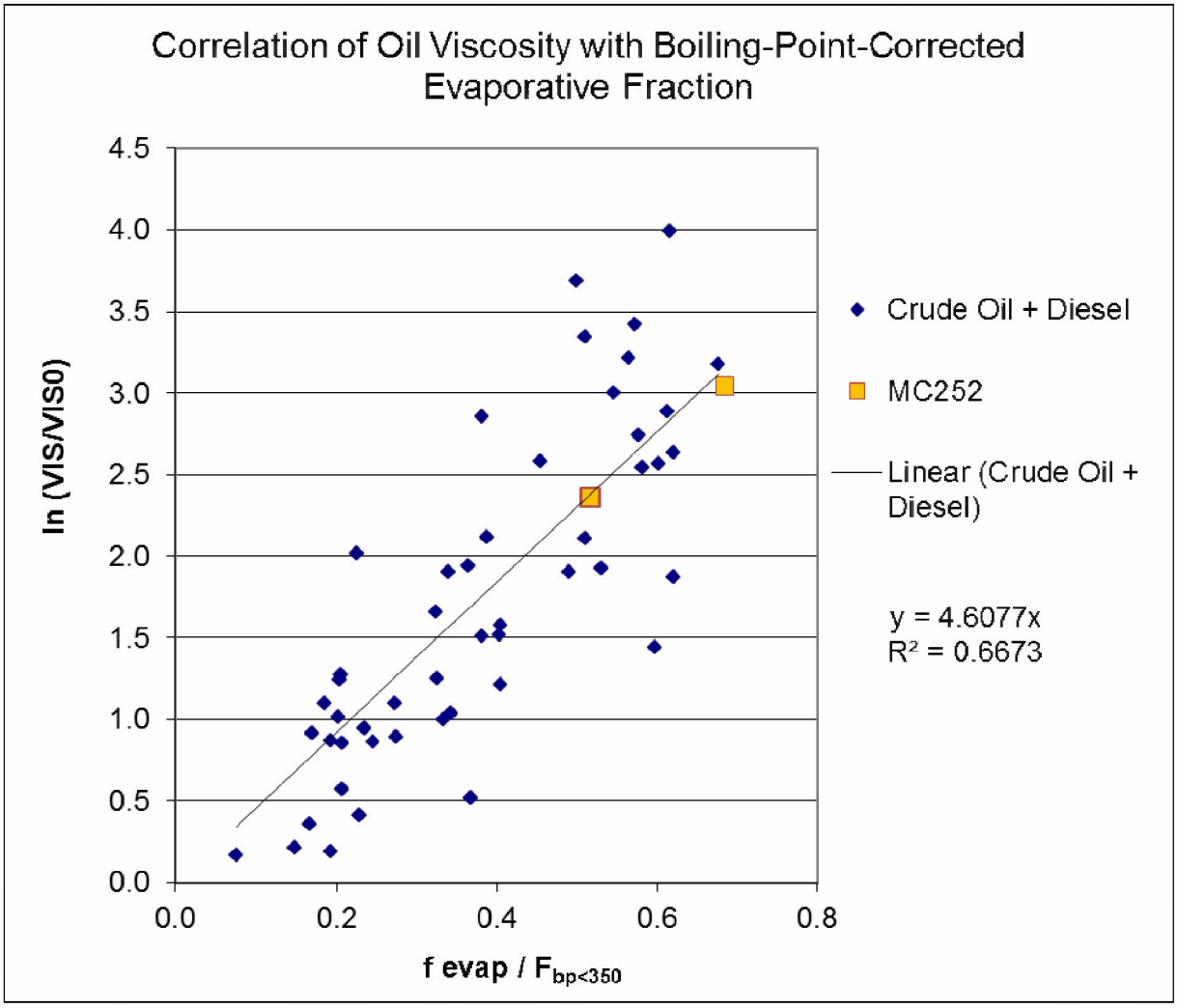

Figure A-1: Correlation of oil viscosity increase (μ/μ_o) and the evaporated fraction (in a weathering experiment) normalized by the volatile fraction of the un-weathered oil. Data sources: Environment Canada spills oil properties databases (http://www.etc-cte.ec.gc.ca/databases/OilProperties /oil_prop_e.html); MC252 data from Belore et al. (2011) indicate 31% and 41% evaporation at 15°C, corresponding to the x-axis values of 0.52 and 0.68, respectively, after normalization by the source oil's 60% fraction boiled at <350°C.

A.2.2.3 Density Changes with Temperature and Weathering

The combined effect of temperature and of loss of the volatile and soluble fractions on oil density is modeled (using the formulation in Lehr et al., 2002) as:

$$\rho = \rho_o\left[1 - k_{temp}(T - T_o)\right]\left(1 + k_{evap}F_v\right)$$

Eq 14

where: ρ_o is the source oil density, T is ambient temperature (K), T_o is the reference temperature (K) , and F_v is the fraction of the oil lost to (evaporation,) dissolution and degradation.

The coefficients k_{temp} and k_{evap} are empirically fitted constants that will vary somewhat for different oils. ADIOS (Lehr et al., 2002) reported values are 0.008 K^{-1} and 0.18, respectively; however, the 0.008 K^{-1} value appears to be in error. The average and standard deviation of regressions using data for 22 oils from the Environment Canada database yielded 0.00084 K^{-1} +/- 0.00012 for k_{temp} and 0.18 for k_{evap}. Based on MC-252 oil data reported by Leirvik et al. (2010), SL Ross (2010), and Belore et al. (2011), estimates of k_{temp} = 0.0008/K and k_{evap} = 0.160 were made for the DWH source oil (Figure A-2). As the MC-252 data were aligned with the regression for oils generally, the regression using the 22 oils from the Environment Canada database is used in SIMAP.

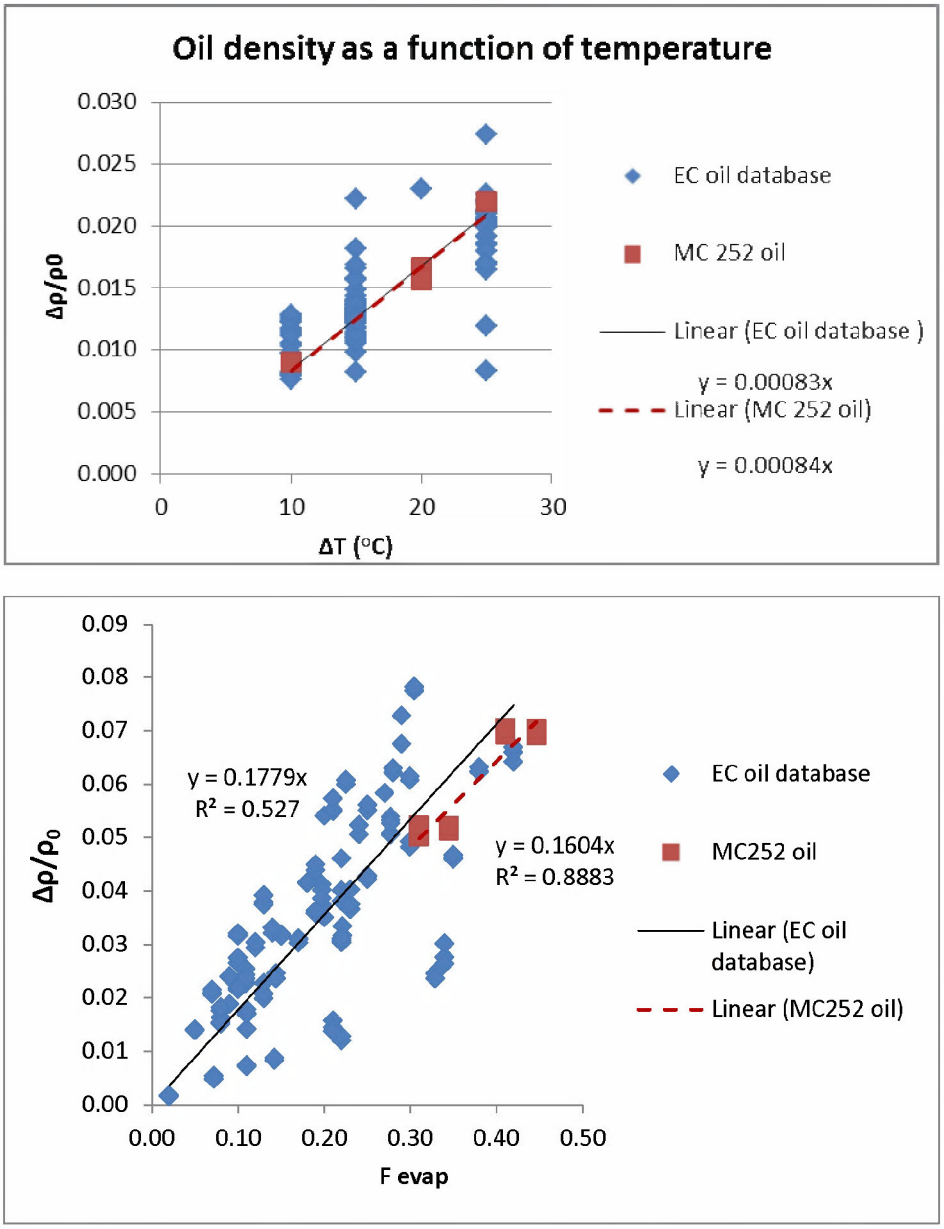

Figure A-2: Estimation of density change with temperature (upper panel) and with the fraction of evaporation (lower panel) for 22 oils in the Environment Canada database http://www.etc-cte.ec.gc.ca/databases/OilProperties/oil_prop_e.html, and MC252 oil (Belore et al., 2011; SL Ross, 2010)

A.2.3 Dissolution

Dissolution is the process by which soluble hydrocarbons (most of which are aromatics) enter the water from subsurface oil droplets. The lower molecular weight hydrocarbons tend to be both more volatile and more soluble than those of higher molecular weight. Dissolution can be significant from subsurface droplets due to the lack of atmospheric exposure (and loss to the

atmosphere) and the high surface area per unit of volume of oil when in small as opposed to large droplets.

The dissolution algorithm of Mackay and Leinonen (1977), which is based on Raoult's Law, was developed in French et al. (1996) and is used in SIMAP for dissolution. The droplet (spillet) is treated as a sphere, with a mass flux (Hines and Maddox, 1985) related to solubility and temperature. It assumes a well-mixed layer with most of the resistance to mass transfer lying in a hypothetical stagnant region close to the oil.

The dissolution rate, dN_{id}/dt (mol/sec), is defined as

$$d\,N_{id}\,/dt \;=\; K_{id}\,[\,e_{\,i}x_i\,C_{\,i}^{\,s} - \;C_i^w]\,A$$

Eq 15

where N_{id} - dissolved mass (mol) of component i, i - i^{th} oil component, A - surface area of oil (cm^2), K_{id} - dissolution mass transfer coefficient (cm/sec) of component i, e_i - solubility enhancement factor of component i (component solubility is usually greater in a mixture), x_i - oil phase mole fraction of component i, C_i^s - pure component solubility (mol/cm^3) of component i, C_i^w - actual concentration of component i in the water phase (mol/cm^3). The value of C_i^w is analyzed locally at the spillet's location.

The enhancement factor of a supercritical compound (i.e., melting point of pure compound is above ambient temperature (25°C), but is present in the mixture of compounds such as crude oil because of the co-solvent effect of other liquid state compounds) can be calculated using the following equation (Yalkowsky, 1979; Di Toro et al., 2007):

$$e_i \;=\; \frac{S_L}{S_S} = \exp[\frac{\Delta S_m}{R} * \left(\frac{T_m}{T} - 1\right)]$$

Eq 16

where T_m is the melting point (Kelvin) of the pure compound; T is the ambient temperature (e.g., 298.15K); ΔS_m is the entropy of fusion, which is about 56.5 J/mol-K for compounds with rigid structure; and R is the universal gas constant (8.3145 J/mol-K).

The pure component solubility, C_i^s, is defined (Payne et al., 1984) as:

$$C_i^s \;=\; C_i^o \,/\, P_i$$

Eq 17

where Pi - oil-water partitioning coefficient for component i, and C_i^o - component concentration in oil phase (mol/cm^3).

The dissolution mass transfer coefficient, K_{id} (m/sec) for subsurface spherical droplets (Hines and Maddox, 1985) is

$$K_{id} \;=\; Sh_i D_{ABi} \,/\, d$$

Eq 18

where Sh_i - Sherwood number for component i, d - diameter of the droplet (m), and D_{ABi} - diffusion coefficient at 25°C (m^2/sec) for component i.

Diffusivities of the aromatic pseudo-components were estimated using the Hayduk and Laudie (1974) method described in Lyman et al. (1982).

$$D_{ABi} = 13.26 \times 10^{-5} / [\mu_w^{1.14} V'^{0.589}_{B,i}]$$

Eq 19

where: μ_w - (absolute) viscosity of water at 25°C (cP), and $V'_{B,i}$ - Le Bas molar volume (cm^3/mole).

$$\mu_w = exp(-24.71 + (4209/T) + 0.04527\,T - 0.00003376\,T^2)$$

Eq 20

The Sherwood number, Sh_i, in this case is

$$Sh_i = 2 + 0.347\,Sc_i^{0.31}\,Re_d^{0.62}$$

Eq 21

where Re_d - Reynolds number based on droplet diameter (m) and Sc_i - Schmidt number for component i. The Reynolds number is defined as

$$Re_d = Wd/\nu$$

Eq 22

where W - rise velocity acting on the oil droplet (m/sec).

The Schmidt number is defined as

$$Sc_i = \nu/D_{ABi}$$

Eq 23

where ν - kinematic viscosity of water (m^2/sec).

A.2.4 Adsorption and Sedimentation

Algorithms for adsorption and sedimentation follow those described in French et al. (1996). Aromatics dissolved in the water column are to some extent carried to the sediments by adsorption to suspended particulates, and subsequent settling. The ratio of adsorbed (C_a) to dissolved (C_{dis}) concentrations is computed from standard equilibrium partitioning theory as

$$C_a / C_{dis} = K_{oc}\,C_{ss}$$

Eq 24

K_{oc} is a dimensionless partition coefficient and C_{ss} is the concentration of suspended particulate matter (SPM) in the water column expressed as mass of particulate per volume of water (mg/L). In typical coastal waters, the concentration of total suspended solids is on the order of 10 mg/L (Kullenberg, 1982); less in offshore waters. In SIMAP the SPM concentration is specified as a

model input. At a total suspended solid (SPM) concentration of 10 mg/L or lower, most of the soluble and semi-soluble hydrocarbons are in the dissolved form.

When the K_{oc} value is not directly measured, it can be calculated based on an equation reported by Di Toro et al. (1991):

$$log(k_{oc}) = 0.983 * log(k_{ow}) + 0.00028$$

Eq 25

Sedimentation of oil droplets occurs when the specific gravity of oil combined with particulates increases over that of the surrounding water. Several processes may act on subsurface oil droplets and floating oil to increase density: weathering (evaporation, dissolution and emulsification), adhesion or sorption onto suspended particles or detrital material, and incorporation of sediment into oil during interaction with suspended particulates, bottom sediments, and shorelines. Rates of sedimentation depend on the concentration of suspended particulates and the rates of particulate flux into and out of an area. In areas with high suspended particulate concentrations, rapid dispersal and removal of oil is found due to sorption and adhesion (Payne and McNabb, 1984; Payne et al., 2003).

Kirstein et al. (1985) and Payne et al. (1987) used a reaction term to characterize the water column interactions of oil and suspended particulates. The reaction term represents the collision of oil droplets and suspended matter, and both oiled and unoiled particulates are accounted for. The model formulation developed by Kirstein et al. (1985) is used to calculate the volume of oil adhered to particles. Table A-7 provides the model parameters needed.

The model formulation used by Kirstein et al. (1985) is as follows:

$$\dot{V_A} = \frac{dV_A}{dt} = K_{op} C_o C_p$$

Eq 26

where, V_A - volume of oil adsorbed to particulates in the water column (m^3/sec), t - time (sec), C_o - concentration of oil (m^3 oil/m^3 water), C_P - concentration of particulates (total, including oil adhered to particulates) (g/m^3), K_{op} - rate constant for the reaction.

The rate of adsorption of entrained oil (m^3/sec) by sediment particles, V_A, was expressed by Kolpack et al. (1977) as:

$$\dot{V_A} = \frac{dV_A}{dt} = 1.4 \times 10^{-12} C_{sed}(1 - 0.023S)$$

Eq 27

where C_{sed} - sediment load (g/m^3), suspended sediment concentration in the water; S - salinity of water (ppt).

This formulation was developed assuming an oil-to-sediment ratio of 0.5 cm^3/g (as a constant). Thus, the general formula is,

$$V_A = K_{op} C_o C_{sed} (1 - \alpha_s S)$$

Eq 28

Table A-7. Adsorption and sedimentation model parameters based on physical properties and empirical data from the literature.

Parameter	Description	Units	Values	Source
K_{op}	Adhesion rate to suspended sediments	(m^3/hr) / (g/m^3)	0.010080	Kolpack et al. (1977)
α_s	Adhesion salinity coefficient	1/ppt	0.023	Kolpack et al. (1977)

In the case where the oil mass is larger than the adhered sediment (i.e., the sediment has been incorporated into the oil) the buoyancy of the oil droplet will control its settling or rise rate. The Stoke's law formulation is used to adjust vertical position of these particles. If the mass of adhered droplets is small relative to the mass of the sediment it has adhered to, the sediment settling velocity will control the fate of the combined particulate.

A.2.5 Degradation

Degradation may occur as the result of photolysis, which is a chemical process energized by ultraviolet light from the sun, and by biological (microbial) breakdown, termed biodegradation. For oil below 20m into the water column, degradation is primarily microbial. A first-order decay algorithm is used, with degradation rates specified for the whole oil as well as for the individual hydrocarbon components. See Appendix C (Review of Degradation Rates of Crude Oil and Hydrocarbons in Seawater) for data used to estimate the degradation rates used.

Using a first-order decay algorithm, the degradation rate (g/day) can be defined as,

$$R_{h,i} = \frac{dM_{h,i}}{dt} = -K_{h,i} C_{h,i} * V_i$$

Eq 29

where

h : hydrocarbon compound (or compound group (i.e., “component”);

i : environmental compartment (water column, in this application);

$R_{h,i}$: loss rate of the mass of compound (or compound group) h in oil through degradation in environmental compartment i (g/day);

$M_{h,i}$: mass of compound (or compound group) h in oil subjected to degradation in environmental compartment i (g);

$K_{h,i}$: 1st order degradation constant for compound (or compound group) h in environmental compartment i (1/day);

$C_{h,i}$: Aqueous phase concentration of compound (or compound group) h in the environmental compartment i (g/m^3); this is either the solubility saturated concentration or the aqueous phase concentration of compound (or compound group) h calculated

based on the partitioning from oil phase and the seawater; the smaller of the two determines the compound (or compound group) h that is available (bioavailability) for biodegradation; and

V_i : The total volume of the environmental compartment i (m^3).

The degradation constant, K_{hi}, may include all degradation processes. Distinct values of K_i may be specified for whole oil and specific constituent groups (n-alkanes, aromatics, etc.) in each compartment.

A.3 References

Bear, J. and A. Verruijt. 1987. Modeling groundwater flow and pollution with computer programs for sample cases, Kluwer Academic Publishers.

Belore, R.C., B.K. Trudel and J. Morrison. 2011. Weathering, emulsification, and chemical dispersibility of Mississippi Canyon 252 crude oil: Field and Laboratory studies.

Chen, C.-T. and F. J. Millero. 1977. Precise equation of state of seawater for oceanic ranges of salinity, temperature and pressure. Deep-Sea Research 24(4):365-369.

Di Toro, D. M., J. A. Mcgrath and W. A. Stubblefield. 2007. Predicting the toxicity of neat and weathered crude oil: toxic potential and the toxicity of saturated mixtures. *Environmental toxicology and chemistry* 26(1):24-36.

Di Toro, D. M., C. S. Zarba, D. J. Hansen, W. J. Berg, R. C. Swartz, C. E. Cowan, S. P. Parlou, H. E. Allen, N. A. Thomas and P. R. Paquin. 1991. Technical basis for establishing sediment quality criteria for nonionic organic chemicals using equilibrium partitioning. Environmental Toxicology and Chemistry 10:1541-1583.

French, D., M. Reed, K. Jayko, S. Feng, H. Rines, S. Pavignano, T. Isaji, S. Puckett, A. Keller, F. W. French Iii, D. Gifford, J. Mccue, G. Brown, E. Macdonald, J. Quirk, S. Natzke, R. Bishop, M. Welsh, M. Phillips and B. S. Ingram. 1996. The CERCLA Type A Natural Resource Damage Assessment Model for Coastal and Marine Environments (NRDAM/CME), Technical Documentation, Vol. I -VI, Final Report, submitted to the Office of Environmental Policy and Compliance, U.S. Dept. of the Interior, Washington, D.C., Contract No. 14-0001-91-C-11. April, 1996.

French McCay, D.P. 2002. Development and application of an oil toxicity and exposure model, OILTOXEX. *Environment Toxicology and Chemistry* 21: 2080-2094.

French McCay, D.P. 2003. Development and application of damage assessment modeling: example assessment for the North Cape oil spill. *Marine Pollution Bulletin* 47: 341-359.

French McCay, D.P. 2004. Oil spill impact modeling: Development and validation. *Environmental Toxicology and Chemistry* 23: 2441-2456.

Hayduk, W. and H. Laudie. 1974. Prediction of diffusion coefficients for nonelectrolytes in dilute aqueous solutions, *Am. Inst. Chem. Eng. J.*, 20: 611–615

Hines, A.L. and R.N. Maddox, 1985. Mass transfer fundamentals and application, Prentice-Hall, Inc., Englewood Cliffs, New Jersey, 542p.

Jones, R. K. 1997. A simplified pseudo-component of oil evaporation model. In: Proceedings of the 20th Arctic and Marine Oil Spill Program (AMOP) Technical Seminar, Environment Canada, pp43-61

Kirstein, B.E., J.R. Clayton, C. Clary, J.R. Payne, D. McNabb, Jr., G. Farmer and R. Redding. 1985 Integration of suspended particulate matter and oil transportation study. Minerals Management Service, Anchorage, Alaska.

Kolpack, R.L., Plutchak, N.B. and R. W. Stearns. 1977. Fate of oil in a water environment - Phase II, a Dynamic model of the mass balance for released oil. University of Southern California, prepared for American Petroleum Institute, API Publication 4313, Washington, D.C.

Kullenberg, G. (ed.), 1982. Pollutant transfer and transport in the sea. Volume I. CRC Press, Boca Raton, Florida. 227 p.

Lehr, W., R. Jones, M. Evans, D. Simecek-Beatty and R. Overstreet. 2002. Revisions of the ADIOS oil spill model. Environmental Modelling & Software 17(2):189-197.

Lehr, W. J., D. Wesley, D. Simecek-Beatty, R. Jones, G. Kachook and J. Lankford. 2000. Algorithm and interface modifications of the NOAA oil spill behavior model. Proceedings of the 23rd Arctic and Marine Oil Spill Program (AMOP) Technical Seminar, Vancouver, BC, Environmental Protection Service, Environment Canada, pp. 525-539.

Leirvik, F., P. S. Daling, B. K. Trudel and B. Parscal. 2010. Assessment of dispersibility of DWH oil at different stages of weathering. Cruise report. SINTEF Materials and Chemistry, Marine Environmental Technology. 24 pages.

Lindeburg, M.R. 2003. Environmental Engineering Reference Manual for the PE Exam. Professional Publications, Inc. Belmont, CA.

Luo, P. and Y Gu. 2007. Effects of asphaltene content on the heavy oil viscosity at different temperatures. Fuel. 86: 1069-1078.

Lyman, C.J., W.F. Reehl, and D.H. Rosenblatt, 1982. Handbook of Chemical Property Estimation Methods. McGraw-Hill Book Co., New York, 960p.

Mackay, D. and P.J. Leinonen, 1977. Mathematical model of the behavior of oil spills on water with natural and chemical dispersion. Prepared for Fisheries and Environment Canada. Economic and Technical Review Report EPS-3-EC-77-19, 39p.

Mackay, D., I. Buist, R. Mascarenhas, and S. Paterson. 1980a. Oil spill processes and models. Environmental Emergency Branch, Department of Fisheries and Environment, Environment Canada, Ottawa, Canada, Report EE-8, 91p.

Mackay, D., S. Paterson and K. Trudel. 1980b. A mathematical model of oil spill behavior. Department of Chemical and Applied Chemistry, University of Toronto, Canada, 39p. .

Mackay, D., W.Y. Shiu, K. Hossain, W. Stiver, D. McCurdy and S. Peterson. 1982. Development and calibration of an oil spill behavior model, Report No. CG-D-27-83, U.S. Coast Guard, Research and Development Center, Groton, Connecticut, 83p.

Mackay, D., W.Y. Shiu, K-C. Ma and S.C. Lee. 2006. *Handbook of Physical-Chemical Properties and Environmental Fate for Organic Chemicals. Vol. I, Introduction and Hydrocarbons*. CRC Press, Taylor & Francis Group.

Stout, S.A., 2015. Bulk chemical and physical properties of fresh and weathered Macondo crude oil. NewFields Technical Report TR03 to the Trustees in support of the pDARP.
Okubo, A. 1971. Oceanic diffusion diagrams. *Deep-Sea Research* 8: 789-802.

Okubo, A. and R.V. Ozmidov. 1970. Empirical dependence of the coefficient of horizontal turbulent diffusion in the ocean on the scale of the phenomenon in question. *Atmospheric and Ocean Physics* 6: 534-536.

Okubo, A., 1980. Di¤usion and Ecological Problems: Mathematical Models. Springer,Berlin 254p.

Payne, J.R., B.E. Kirstein, J.R.J. Clayton, C. Clary, R. Redding, G.D.J. McNabb and G. Farmer. 1987. Integration of suspended particulate matter and oil transportation study. Final Report. Minerals Management Service, Environmental Studies Branch, Anchorage, AK. Contract No. 14-12-0001-30146. 216 p).

Payne, J. R., B. E. Kirstein, G. D. Mcnabb, J. L. Lambach, R. Redding, R. E. Jordon, W. Horn, C. Oliveira, G. S. Smith, D. M. Baxter and R. Geagel. 1984. Multivariate analysis of petroleum weathering in the marine environment--subarctic. Vol I and II. In: Environmental Assessment of the Alaskan Continental Shelf, Final report to Principal Investigators, US Dept of Commerce, NOAA/OCSEAP Final Report 21 and 22.

Payne, J. R., and D. McNabb Jr. 1984. Weathering of petroleum in the marine environment. Marine Technology Society Journal, 18(3): 24-42.

Payne, J.R., J.R. Clayton, Jr., and B.E. Kirstein. 2003. Oil/suspended partiiculate material interacitons and sedimentation. Spill Science & Technology Bulletin, 8(2): 201-221.

Stiver, W and D. Mackay. 1984. Evaporation rate of oil spills of hydrocarbons and petroleum mixtures. *Environmental Science and Technology* 18: 834-840.

Stout, S.A. 2015. Detailed chemical characteristics of fresh Macondo crude oil. NewFields Technical Report to the Trustees in support of the PDARP.

SL Ross. 2010. Spill related Properties of MC252 crude oil sample ENT-052210-178. Report submitted to BP by SL Ross Environmental Research Ltd. July 2010. 25 pages

White, F.M. 2005 Viscous Fluid Flow, 3rd ed. McGraw-Hill

Yalkowsky, S. H. 1979. Estimation of Entropies of Fusion of Organic Compounds. Industrial & Engineering Chemistry Fundamentals 18(2):108-111.

Technical Reports for Deepwater Horizon Water Column Injury Assessment

WC_TR.14: Modeling Oil Fate and Exposure Concentrations in the Deepwater Plume and Rising Oil Resulting from the Deepwater Horizon Oil Spill

Appendix B. Physical-Chemical Properties of the Source Oil

Authors: Deborah French McCay, Katherine Jayko, Zhengkai Li, Matthew Horn, Yong Kim, Tatsu Isaji, Deborah Crowley, Malcolm Spaulding, Lauren Decker, Cathleen Turner, Stefanie Zamorski , Jeremy Fontenault, Rachel Shmookler, and Jill Rowe

Revised: September 29, 2015
Project Number: 2011-144
RPS ASA 55 Village Square Drive, South Kingstown, RI 02879

Table of Contents

List of Tables

B.1 Introduction

This appendix summarizes the use of the physical and chemical properties of fresh MC252 Macondo-1 Well crude oil (Stout 2015 a, b) to define model inputs to the SIMAP oil fates model. The 'pseudo-component' (component) approach is used in the evaluation and modeling of physical-chemical processes describing the transfer and transformation rates of hydrocarbons in oil. The properties of each component are derived by weighted averages of properties of the group of chemicals included in the component. The physical properties and chemical composition of the oil taken as a whole alters as it undergoes weathering processes in the environment. By modeling individual components, as done in SIMAP's oil fate model, the changes in bulk oil properties with weathering are simulated.

B.2 Properties of Unweathered Source Oil

The physical analyses conducted by Stout (2015b) indicate that the MC252 Macondo-1 source oil had a density of 0.8483 g/ml at 15°C and 0.8372 at 30°C. These data were used as inputs to the model, establishing the density-temperature relationship (see Appendix A, Section A.2.2.3). The dynamic viscosity of the fresh oil at 15°C was 7.145 cP and at 35°C was 4.503 cP. The oil-water interfacial and surface tensions of the fresh oil at 20°C were 0.01963 and 0.00343 N/m, respectively.

Based on measurements by Stout (2015a,b) the fresh MC252 Macondo-1 source oil: (1) was a light (ρ = 0.8483 g/ml @ 15°C), low viscosity (7.145 cP @ 15°C) paraffinic crude oil; and (2) contained approximately 13.5 wt% volatiles (C5-C9), 68.1 wt% semi-volatiles (C9-C44), and 18.4 wt% non-volatiles (above C44). The volatiles were mostly aliphatic hydrocarbons, although volatile aromatic hydrocarbons comprised 3.16 wt% of the oil, including 1.9 wt% total BTEX (19,124 µg/goil). The semi-volatiles included total PAHs (TPAH, i.e., sum of all analytes from naphthalene to benzo[g,h,i]perylene) at 1.33 wt% of the oil, with the C0-C4 naphthalenes (0.76 wt%), comprising more than half of the TPAH.

Saturates, Aromatics, Resins, and Asphaltenes (SARA) analysis by Stout (2015b) of the C15+ topped oil showed that it was comprised of approximately 49.0 wt% aliphatic hydrocarbons, 41.8 wt% aromatic hydrocarbons, 9.0 wt% NSO-bearing resins, and only 0.24 wt% asphaltenes. Topping at 60°C for 24 hours removed volatiles of carbon chain length up to C15, which is equivalent to an evaporative loss of 45% of the original oil mass. Therefore, the unweathered source oil would have had even lower concentrations of resins and asphaltene.

B.3 Modeled Component Groups and Physical-Chemical Properties

Table B-1 lists the definition of the 19 pseudo-components in current application of the SIMAP oil fates model. The soluble and semi-soluble compounds, consisting of low molecular weight aromatics and alkanes, are included in components defined by ranges of the octanol-water partition coefficient (K_{ow}), a measure of hydrophobicity. The non-soluble compounds are

included in the volatile aliphatic and residual components, defined by boiling point (BP) ranges. Table B-2 defines codes used and summarizes the compounds included in each component.

Table B-1. The 19 pseudo-components modeled in the SIMAP oil fates model [including definition of volatile aliphatic hydrocarbons (HCs) by boiling range in 9 distillation cuts, 9 soluble/semi-soluble and volatile/semi-volatile components defined by log(K_{ow}) range, 8 insoluble and volatile/semi-volatile aliphatic components, 1 dispersant constituent component, and 1 residual oil component].

AR or AL	All HCs	Soluble and semi-soluble HCs (AR Components)		Non-soluble aliphatic HCs (AL Components)	
Compo-nent #	Volatility	Compounds	Range of log(K_{ow})	Compounds	Boiling Point Range (°C)
1	Volatiles	MAHs (BTEX)	1.9-2.8	Volatile aliphatics	< 150
2		C3-benzenes	2.8-3.6	Volatile aliphatics	150-180
3	Intermediate Volatility	C4-benzenes	3.1-3.8	Semi-volatile aliphatics	180-200
4		Decalins	4.1-6.0	Semi-volatile aliphatics	200-230
5		C0-C2 Naphthalenes	2.3-4.3	Semi-volatile aliphatics	230-280
6	Semi-Volatile	C3-C4 Naphthalenes	4.2-5.20	Low volatility aliphatics	280 - 300
7		Fluorenes & C0-C1 3-ring PAHs	4.0-5.6	Low volatility aliphatics	300-350
8		4-ring PAHs & C2-C3 3-ring PAHs	4.9-6.0	Low volatility aliphatics	350-380
9	Highly Volatile and Soluble Aliphatics	Low MW Alkanes, Isoalkanes, Cycloalkanes	2.3-5.6	N.A. (Used for Dispersant Indicators)	<180
Residual (19)	Residual (non-volatile)	High MW PAHs	>6.0	High molecular weight aliphatics	>380

Table B-2. Code designations and included compounds for the 19 pseudo-components. [BP = boiling point].

Code	Group	Includes
AR1	BTEX	BTEX, styrene
AR2	C3-benzenes	C3-benzenes (Trimethlybenzenes, propylbenzenes, ethyl-methylbenzenes, cumene & trimethylbenzenes, and Methyl-thiophene)
AR3	C4-benzenes	C4-benzenes (butylbenzenes, tetramethlybenzenes, tetralin)
AR4	Decalins	cis/trans decalin to C4-decalin
AR5	C0-C2 Naphthalenes	C0-C2 Naphthalenes, C0-C2 Benzothiophenes, biphenyl, acenaphthene, acenaphthylene
AR6	C3-C4 Naphthalenes	C3-C4 Naphthalenes, C3-C4 Benzothiophenes, dibenzofuran
AR7	Fluorenes & C0-C1 3-ring PAHs	C0-C3 Fluorenes, C0-C1 dibenzothiophenes, C0-C1 phenanthrenes
AR8	4-ring PAHs & C2-C3 3-ring PAHs	C0-C2 pyrenes & fluoranthenes, C2-C3 dibenzothiophenes, C2-C3 phenanthrenes, chrysene
AR9	Soluble alkanes	Low molecular weight Alkanes, Isoalkanes, Cycloalkanes
AL1	Aliphatics: BP < 150	Unmeasured compounds, using the properties of C6-C8 alkanes (n-hexane, n-heptane, n-octane)
AL2	Aliphatics: BP 150-180	Measured and unmeasured compounds, using the properties of C9-C10 alkanes (n-Nonane, and n-Decane)
AL3	Aliphatics: BP 180-200	Measured and unmeasured compounds, using the properties of C11 alkanes (n-Undecane)
AL4	Aliphatics: BP 200-230	Measured and unmeasured compounds, using the properties of C12 alkanes (n-Dodecane)
AL5	Aliphatics: BP 230-280	Measured and unmeasured compounds, using the properties of measured C13-C16 alkanes
AL6	Aliphatics: BP 280-300	Measured and unmeasured compounds, using the properties of measured C17-C18 alkanes
AL7	Aliphatics: BP 300-350	Measured and unmeasured compounds, using the properties of measured C19-C20 alkanes
AL8	Aliphatics: BP 350-380	Measured and unmeasured compounds, using the properties of measured C21-C23 alkanes
AL9	Dispersant indicator(s)	Dispersant indicator(s) on oil droplets
Residual	Residual	Other non-volatile, non-soluble hydrocarbons

The mass concentrations of the eight aromatic components (AR1 - AR8) and the soluble aliphatic component (AR9) were computed using the source oil sample concentrations reported by Stout (2015a). The mass concentrations of the eight non-soluble aliphatic components (AL1 - AL8) were based on measured weight fractions of the boiling curve reported by Stout (2015b), using the boiling point ranges listed in Table B-1. For components AL1 and AL2, all of the measured compounds are soluble, and so their mass concentrations were included in component AR9. Thus, AL1 and AL2 represent unmeasured compounds in their respective

boiling ranges. Component AL9 is reserved for tracking dispersant component(s); this component was not included in model runs reported herein.

Tables B-3 to B-5 list the chemical-specific properties and other input parameters used to model the oil. Values used for each individual component (AR1-AR9 and AL1-AL9) were calculated as mass fraction-weighted average values of the included compounds using the data in Table B-3 to B-5 and the measured concentrations in MC252 source oil from Stout (2015a,b).

The values of molecular weight (MW), vapor pressure (VP), melting point (MP), boiling point (BP), solubility (SL), K_{OW}, K_{oc}, and the Le Bas molar volume (V'B, cm^3/mol) of each hydrocarbon included in the components are taken, whenever available, from the Handbook of Physical-Chemical Properties and Environmental Fate for Organic Chemicals (Mackay et al. 2006a,b). If K_{oc} was not available, it was calculated from K_{ow} using the regression developed by DiToro et al. (1991).

The parameter values of the following individual compounds are taken from Mackay et al. (2006a,b): AR Groups, Benzene, Toluene, Ethylbenzene, Xylenes-p, Xylenes-m, Xylenes-o, styrene, propylbenzenes-iso, propylbenzenes, Trimethlybenzenes-1,3,5, ethyl-methylbenzenes (cumene), Trimethlybenzenes-1,2,4 (& general), Trimethlybenzenes-1,2,3, methylstyrenes, Other C3-benzenes (Indane), butylbenzenes, tetralin, tetramethylbenzenes, Other C4-benzenes (cymenes), C5-benzenes, cis-Decalin, trans-Decalin, C1-Decalins, C2-Decalins, Benzo(b)thiophene, naphthalene, C1-naphthalenes, C2-naphthalenes, acenaphthene, biphenyl, acenaphthylene, C3-naphthalenes, Fluorene, dibenzothiophene, phenanthrene/anthracene, C1-phenanthrenes/anthracenes, pyrene, fluoranthene, Chrysene, and Triphenylene; AL Groups, n-Hexane, n-Heptane, n-Octane, n-Nonane, n-Decane, n-Undecane, n-Dodecane, n-Tridecane, n-Tetradecane, n-Hexadecane, n-Pentadecane, Norpristane, n-Heptadecane, n-Octadecane, Pristane, Phytane, n-Nonadecane, n-Eicosane, n-Heneicosane, n-Docosane, n-Tricosane; and the AR9 Group, Cyclopentane, Isopentane, Pentane, Cyclohexane, Methylcyclopentane, 2,3-Dimethylbutane, 2-Methylpentane, 3-Methylpentane, Hexane, Methylcyclohexane, 2,2-Dimethylpentane, 2,4-Dimethylpentane, Heptane, 3-Methylhexane, 2-Methylheptane, 2,3,4-Trimethylpentane, 2,2,3-Trimethylpentane, 2,3,3-Trimethylpentane, 2,3-Dimethylhexane, 3-Ethylhexane, 3-Methylheptane, Octane, Nonane, Decane.

Used as an alternative source of reference, the EPI (Estimation Programs Interface) Suite™ v.4.11 (Nov 2012) (available online at URL: http://www.epa.gov/oppt/exposure/pubs/episuite.htm) is a Windows®-based suite of physical/chemical property and environmental fate estimation programs developed by the EPA's Office of Pollution Prevention Toxics and Syracuse Research Corporation (SRC). KOWWIN™, MPBPWIN™, KOCWIN™, and WSKOWWIN™ were run to estimate the Kow, Koc, MP, BP, and water solubility values if acceptable measured values are not available from literature (as reviewed by Mackay et al. (2006a,b). The parameter values of the following compounds are estimated by using the US EPA EPI suite software (2012): AR Group, C3-Decalins, C4-Decalins, C1-Benzothiophenes, C2-Benzothiophenes, dibenzofuran, C3-Benzothiophenes, C4-naphthalenes, C4-Benzothiophenes, C1-fluorenes, C2-fluorenes, C3-fluorenes, C1-dibenzothiophene, C2-phenanthrenes/anthracenes, C2-dibenzothiophene, C3-phenanthrenes/anthracenes, C3-dibenzothiophene, C1-Fluoranthenes/pyrenes, and C2-Fluoranthenes/pyrenes; AL Groups, 2,6,10-Trimethyldodecane, and 2,6,10-Trimethyltridecane; and AR9 Group, 1-Heptene / 1,2-DMCP (trans), 2-Methylhexane, 2,3-Dimethylpentane, 2,5-Dimethylhexane, and 2,4-Dimethylhexane.

The diffusion coefficient (D_{AB}) at 25°C is calculated from the Le Bas molar volume, V'B using the Hayduk and Laudie (1974) method (see details for this method in Appendix A of this report).

The solubility enhancement factor (Enhanc) is the fugacity ratio, due to the vapor pressure and solubility enhancement caused by the difference of evaporation and dissolution from the solid state of pure compounds and the liquid state of the same compounds present in mixtures such as in crude oil. The enhancement factors for the PAH components AR5 to AR8 were estimated based on Yalkowsky's (1979) method described in detail in Appendix A. The enhancement factors for AR1 to AR4 and AR9 were assumed 1.0 (i.e., no enhancement). Biodegradation rates of each component are reviewed and compiled in a separate Appendix (C, biodegradation rates).

Table B-3. Parameters for each hydrocarbon included in the soluble and semi-soluble aromatic components AR1-AR8. Those chemicals where parameters were obtained from the EPI Suite are identified by "EPI" following the chemical name. Parameters for the other chemicals were obtained from Mackay et al. (2006a,b). [ENH = Enhancement Factor; Note E-01 = x 10^{-1}, E-02 = x 10^{-2}, etc.]

Aromatic Name(s)	Type	Component Grouping	Structure	MW (g/mol)	Log(K_{ow})	Log(K_{oc})*	VP (@25 °C)	MP (°C)	BP (°C)	Solubility (25°C) (mg/L)	MC252 Content (mg/kg)#	(D_{AB}) at 25°C	ENH
Benzene	MAH	**AR1**	BTEX + Styrene	78.1	2.13	1.92	1.23. E-01	5.49	80.09	1780	2351	1.0291E-05	1
Toluene	MAH	**AR1**	BTEX + Styrene	92.1	2.69	2.00	3.79. E-02	-94.95	110.63	515	6495	9.10426E-06	1
Ethyl-benzene	MAH	**AR1**	BTEX + Styrene	106.2	3.13	2.41	1.33. E-02	-94.96	136.2	152	1274	8.22654E-06	1
Xylenes-p	MAH	**AR1**	BTEX + Styrene	106.2	3.35	2.42	1.17. E-02	13.25	138.37	180	3288	8.22654E-06	1
Xylenes-m	MAH	**AR1**	BTEX + Styrene	106.2	3.19	2.33	1.11. E-02	-47.8	139.12	187.5	3288	8.22654E-06	1
Xylenes-o	MAH	**AR1**	BTEX + Styrene	106.2	3.15	2.35	8.80. E-03	-25.5	144.5	220	2428	8.22654E-06	1
styrene	MAH	**AR1**	Styrene	104.2	3.05	2.71	7.97. E-03	-30.65	145	250	0	8.49313E-06	1
Iso-propyl-benzenes	MAH	**AR2**	C3-Benzene	120.2	3.63	3.57*	6.11. E-03	-96.02	152.41	56	341	7.54513E-06	1
Propyl-benzenes	MAH	**AR2**	C3-Benzene	120.2	3.63	2.87	4.50. E-03	-96.02	159.24	55	564	7.54513E-06	1
Trimethly-benzenes-1,3,5	MAH	**AR2**	C3-Benzene	120.2	3.78	2.82	3.60. E-03	-44.7	164.74	50	1182	7.54513E-06	1
ethyl-methyl-benzenes (cumene)	MAH	**AR2**	C3-Benzene	120.2	3.63	3.57*	3.30. E-03	-79.83	165.2	94.9	2831	7.51793E-06	1
Trimethly-benzenes-1,2,4 (& general)	MAH	**AR2**	C3-Benzene	120.2	3.78	3.28	2.71. E-03	-43.77	169.38	56	2847	7.54513E-06	1

Aromatic Name(s)	Type	Com-ponent Group-ing	Structure	MW (g/mol)	Log(K_{ow})	Log(K_{oc})*	VP (@25 °C)	MP (°C)	BP (°C)	Solu-bility (25°C) (mg/L)	MC252 Content (mg/kg)#	(D_{AB}) at 25°C	ENH
Trimethly-benzenes-1,2,3	MAH	**AR2**	C3-Benzene	120.2	3.66	2.8	2.17. E-03	-25.4	176.1	69	0	7.54513E-06	1
Methyl-styrenes	MAH	**AR2**	C3-Benzene	118.2	3.35	3.29*	1.32. E-03	-34.1	172.8	89	0	7.75499E-06	1
Other C3-benzenes (Indane)	MAH	**AR2**	C3-Benzene	118.2	3.47	3.41*	1.40. E-03	-14.81	179.64	109	72	7.54513E-06	1
Butyl-benzenes	MAH	**AR3**	C4-Benzene	134.2	4.12	3.4	1.33. E-03	-87.85	183.31	15	457	6.99728E-06	1
tetralin	MAH	**AR3**	C4-Benzene	132.2	3.83	3.77*	5.26. E-04	-35.7	207.6	14.94	0	7.16775E-06	1
Tetramethyl-benzenes	MAH	**AR3**	C4-Benzene	134.2	4.10	3.12	5.24. E-04	-23.7	190.74	27.88	198	6.99728E-06	1
Other C4-benzenes (cymenes)	MAH	**AR3**	C4-Benzene	134.2	4.00	3.93*	1.61. E-03	-28.15	178.34	12.7	3967	6.99728E-06	1
C5-benzenes	MAH	**AR3**	C5-Benzene	148.3	4.50	4.42*	3.62. E-04	-75	205.4	5.048	52	6.54500E-06	1
cis-Decalin	Cyclo-alkane	**AR4**	C0-2 Decalin	138.3	4.20	4.13*	1.33. E-03	-42.9	195.77	0.889	0	7.00174E-06	1
trans-Decalin	Cyclo-alkane	**AR4**	C0-2 Decalin	138.3	4.20	4.13*	1.24. E-03	-30.4	187.27	0.889	779	7.00174E-06	1
C1-Decalins	Cyclo-alkane	**AR4**	C0-2 Decalin	152.3	4.61	4.53*	9.00. E-04	-21.1	194.1	0.51	1174	6.08334E-06	1
C2-Decalins	Cyclo-alkane	**AR4**	C0-2 Decalin	166.3	5.07	4.98*	5.76. E-04	-0.76	203.53	0.8741	966	6.08334E-06	1
C3-Decalins (EPI)	Cyclo-alkane	**AR4**	C3-4 Decalin	180.3	5.40	5.31*	2.96. E-04	6.78	217.33	0.3296	436	5.68695E-06	1
C4-Decalins (EPI)	Cyclo-alkane	**AR4**	C3-4 Decalin	194.4	6.01	5.91*	9.69. E-05	1.67	239.87	0.09928	431	5.10836E-06	1

Aromatic Name(s)	Type	Com-ponent Group-ing	Structure	MW (g/mol)	Log(K_{ow})	Log(K_{oc})*	VP (@25 °C)	MP (°C)	BP (°C)	Solu-bility (25°C) (mg/L)	MC252 Content (mg/kg)#	(D_{AB}) at 25°C	ENH
Benzo(b)-thiophene	2-ring hetero-cyclic PAH	**AR5**	C0-2, 2-ring PAH	134.2	3.12	2.30	2.64. E-04	32	221	130	7	8.44832E-06	1.17
naphthalene	2-ring PAH	**AR5**	C0-2, 2-ring PAH	128.2	3.37	3.11	1.07. E-04	80.26	217.9	31	964	7.98775E-06	3.51
C1-naph-thalenes	2-ring PAH	**AR5**	C0-2, 2-ring PAH	142.2	3.87	3.36	8.85. E-05	-30.43	244.7	26.5	2106	7.35501E-06	1
C2-naph-thalenes	2-ring PAH	**AR5**	C0-2, 2-ring PAH	156.2	4.38	4.31*	6.95. E-05	-6	263	6.4	2259	6.84151E-06	1
Acenaph-thene	2-ring PAH	**AR5**	2.5-ring PAH	154.2	3.92	3.38	4.02. E-05	93.4	279	3.8	21	7.27209E-06	4.72
C1-Benzo-thiophenes (EPI)	2-ring hetero-cyclic PAH	**AR5**	C0-2, 2-ring PAH	148.2	3.65	3.59*	2.30. E-05	53.47	258.13	29.7	33	5.1494E-06	1.91
biphenyl	PAH	**AR5**	C0-2, 2-ring PAH	154.2	4.70	3.4	1.27. E-05	68.93	256.1	4.37	204	7.00174E-06	2.71
C2-Benzo-thiophenes (EPI)	2-ring cyclic	**AR5**	C0-2, 2-ring PAH	162.3	4.17	4.10*	9.71. E-06	62.4	274.74	10.2	31	4.99701E-06	2.34
Acenaph-thylene	PAH	**AR5**	2.5-ring PAH	152.2	4.00	3.83	8.93. E-06	91.8	280	16.1	9	7.46166E-06	4.55
Dibenzo-furan (EPI)	PAH	**AR6**	2.5-ring PAH	168.2	4.27	4.20*	9.40. E-06	72.52	296.63	2.2217	30	5.25507E-06	4.72
C3-naphtha-lenes	PAH	**AR6**	C3,4_2-ring PAH	170.2	5.00	4.92*	6.72. E-06	63	285	2.1	1597	6.41451E-06	2.37
C3-Benzo-thiophenes (EPI)	2-ring cyclic	**AR6**	C3,4_2-ring PAH	176.3	4.66	4.58*	4.26. E-06	76.44	290.45	3.69	48	4.86194E-06	3.21
C4-naphthalene s (EPI)	PAH	**AR6**	C3,4_2-ring PAH	184.3	5.30	5.21*	2.84. E-06	71.98	298.06	1.393	721	4.99683E-06	2.37

Aromatic Name(s)	Type	Com-ponent Group-ing	Structure	MW (g/mol)	Log(K_{ow})	Log(K_{oc})*	VP (@25 °C)	MP (°C)	BP (°C)	Solu-bility (25°C) (mg/L)	MC252 Content (mg/kg)#	(D_{AB}) at 25°C	ENH
C4-Benzo-thiophenes (EPI)	2-ring cyclic	**AR6**	C3,4_2-ring PAH	190.3	5.18	5.09*	1.94. E-06	90.13	305.25	1.852	37	4.74254E-06	4.39
Fluorene	PAH	**AR7**	2.5-ring PAH	166.2	4.18	4.11*	4.67. E-06	114.77	295	1.9	150	6.92905E-06	7.67
dibenzothiophene	PAH	**AR7**	3-ring PAH	184.3	4.34	4.00	2.64. E-06	98.2	332.5	1.7	53	5.98423E-06	5.27
C1-fluorenes (EPI)	PAH	**AR7**	2.5-ring PAH	180.2	4.97	4.89*	1.34. E-06	85	307.25	1.09	308	4.68873E-06	3.90
C2-fluorenes (EPI)	PAH	**AR7**	2.5-ring PAH	194.3	5.20	5.11*	8.35. E-07	88.45	321.03	0.1571	404	7.00398E-06	4.22
C3-fluorenes (EPI)	PAH	**AR7**	2.5-ring PAH	208.3	5.70	5.60*	5.07. E-07	94.39	330.26	0.066173	286	6.30088E-06	4.83
C1-dibenzo-thiophene (VP EPI system)	PAH	**AR7**	C0-1_3-ring PAH	198.3	4.86	4.78*	2.21. E-07	112.15	345.61	0.34	153	6.85625E-06	7.23
Phenan-threne/ anthracene	PAH	**AR7**	C0-1_3-ring PAH	178.2	4.57	4.28	1.97. E-07	99.24	340	1.1	310	6.74475E-06	5.39
C1-phenan-threnes/ anthracenes	PAH	**AR7**	C0-1_3-ring PAH	192.3	5.12	5.03*	1.86. E-07	123	354	0.187	676	6.69476E-06	9.25
C2-phenan-threnes/ anthracenes (EPI)	PAH	**AR8**	C2_3-ring PAH	206.3	5.25	5.16*	1.60. E-07	187	360	0.056	657	6.29081E-06	39.52
C2-dibenzo-thiophene (VP EPI)	PAH	**AR8**	C2_3-ring PAH	212.3	5.33	5.24*	1.17. E-07	117.18	357.21	0.078	197	4.37187E-06	8.10
C3-phenan-threnes/ anthracenes (EPI)	PAH	**AR8**	C3_3-ring PAH	220.3	5.92	5.82*	8.48. E-08	115.59	363.09	0.02653	381	6.35185E-06	7.82

Aromatic Name(s)	Type	Com-ponent Group-ing	Structure	MW (g/mol)	Log(K_{ow})	Log(K_{oc})*	VP (@25 °C)	MP (°C)	BP (°C)	Solu-bility (25°C) (mg/L)	MC252 Content (mg/kg)#	(D_{AB}) at 25°C	ENH
C3-dibenzothiophene (EPI)	PAH	**AR8**	C3_3-ring PAH	226.3	5.81	5.71*	6.19.E-08	128.21	368.81	0.017	146	6.31775E-06	10.41
pyrene	PAH	**AR8**	4-ring PAH	202.3	5.18	4.92	3.39.E-08	150.62	404	0.132	16	6.36046E-06	17.31
C1-Fluoranthenes/ pyrenes (EPI: methyl-fluoranthene)	PAH	**AR8**	4-ring PAH	216.3	5.29	5.20*	2.75.E-08	132.34	383.45	0.05838	80	6.42158E-06	3.33
C2-Fluoranthenes/ pyrenes (EPI)	PAH	**AR8**	4-ring PAH	230.1	5.56	5.47*	1.44.E-08	137.84	395.05	0.01675	130	6.38646E-06	12.95
Fluoranthene	PAH	**AR8**	4-ring PAH	202.3	5.22	5.13*	6.67.E-09	110.19	384	0.26	4	6.36046E-06	6.91
Chrysene + Triphenylene (mean)	PAH	**AR8**	4-ring PAH	228.3	5.55	5.46	2.02.E-09	227	436	0.0225	56	6.36909E-06	97.98

* log Koc = 0.983 log Kow + 0.00028 (Di Toro et al 1991)

Table B-4. Parameters for each hydrocarbon included in the soluble and semi-soluble aliphatic component AR9. Those chemicals where parameters were obtained from the EPI Suite are identified by "EPI" following the chemical name. Parameters for the other chemicals were obtained from Mackay et al. (2006a,b).

Paraffins, Isoparaffins, and Naphthenes	Type	Structure	Molecular Weight (g/mol)	Log(K_{ow})	Log(K_{oc})*	VP (@25°C)	Melting Point (°C)	Boiling Point (°C)	Solubility (25°C) (mg/l)	VB (cm^3/mol)	MC252 Content (mg/kg)	(D_{AB}) at 25°C
Cyclopentane	Naphthene (cycloalkane)	cyclic alkane	70.1	3.00	2.95*	4.18.E-01	-94.96	136	156	99.5	1272	1.00×10^{-5}
Isopentane	Isoparaffin (Isoalkane)	branched alkane	72.1	2.47	2.43*	9.05.E-01	-159.77	28	48.5	118.4	6244	9.06×10^{-6}
Pentane	Paraffin (n-alkane)	normal alkane	72.1	3.39	3.33*	6.92.E-01	-129.7	36	40.6	118.4	9385	9.06×10^{-6}
Cyclohexane	Naphthene (cycloalkane)	cyclic alkane	84.2	3.44	2.68	1.29.E-01	6.59	81	58	118.2	5688	9.07×10^{-6}
Methyl-cyclopentane	Naphthene (cycloalkane)	cyclic alkane	86.2	3.37	3.31*	1.81.E-01	-142.42	72	43	121.7	5603	8.91×10^{-6}
2,3-Dimethylbutane	Isoparaffin (Isoalkane)	branched alkane	86.2	3.42	3.36*	3.09.E-01	-128.1	58	21	140.6	930	8.19×10^{-6}
2-Methylpentane	Isoparaffin (Isoalkane)	branched alkane	86.2	3.23	3.18*	2.79.E-01	-153.6	60	13.7	140.6	5480	8.19×10^{-6}
3-Methylpentane	Isoparaffin (Isoalkane)	branched alkane	86.2	3.18	2.35	2.50.E-01	-162.9	63	12.9	140.6	3560	8.19×10^{-6}
Hexane	Paraffin (n-alkane)	normal alkane	86.2	3.00	2.95*	0.1992	-95.35	69	9.5	140.6	12572	8.19×10^{-6}
Methylcyclohexane	Naphthene (cycloalkane)	cyclic alkane	98.2	3.61	3.55*	6.08.E-02	-126.6	101	15.1	140.4	18561	8.19×10^{-6}
1-Heptene / 1,2-DMCP (trans) (EPI)	Naphthene (cycloalkane)	cyclic alkane	98.2	3.52	3.46*	6.21.E-02	-77.23	98	33.92	162.8	3568	7.51×10^{-6}
2,2-Dimethylpentane	Isoparaffin (Isoalkane)	branched alkane	100.2	3.62	3.56*	1.38.E-01	-123.7	79	4.9	162.8	263	7.51×10^{-6}
2,4-Dimethylpentane	Isoparaffin (Isoalkane)	branched alkane	100.2	3.66	3.60*	1.30.E-01	-119.5	80	4.2	162.8	643	7.51×10^{-6}
2-Methylhexane (EPI)	Isoparaffin (Isoalkane)	branched alkane	100.2	3.71	3.65*	8.68.E-02	-118.2	90	2.54	162.8	3944	7.51×10^{-6}

Paraffins, Isoparaffins, and Naphthenes	Type	Structure	Molecular Weight (g/mol)	Log(K_{ow})	Log(K_{oc}) *	VP (@25°C)	Melting Point (°C)	Boiling Point (°C)	Solubility (25°C) (mg/l)	VB (cm^3/ mol)	MC252 Content (mg/kg)	(D_{AB}) at 25°C
Heptane	Paraffin (n-alkane)	normal alkane	100.2	3.50	3.44*	0.0552	-90.55	98	2.93	162.8	13461	7.51 x10^{-6}
2,3-Dimethylpentane (EPI)	Isoparaffin (Isoalkane)	branched alkane	100.2	3.63	2.8	9.07.E-02	-104.71	66	5.25	162.8	1234	7.51 x10^{-6}
3-Methylhexane	Isoparaffin (Isoalkane)	branched alkane	100.2	3.71	3.65*	8.09.E-02	-119	91	4.95	162.8	3902	7.51 x10^{-6}
2-Methylheptane	Isoparaffin (Isoalkane)	branched alkane	114.2	4.20	3.11	6.78.E-02	-105	99	7.965	185.0	4946	6.96 x10^{-6}
2,3,4-Trimethylpentane	Isoparaffin (Isoalkane)	branched alkane	114.2	4.09	4.02*	6.49.E-02	-107.3	99	9.91	185.0	130	6.96 x10^{-6}
2,2,3-Trimethylpentane	Isoparaffin (Isoalkane)	branched alkane	114.2	4.09	4.02*	4.22.E-02	-112.2	110	9.91	185.0	45	6.96 x10^{-6}
2,5-Dimethylhexane (EPI)	Isoparaffin (Isoalkane)	branched alkane	114.2	4.12	4.05*	3.91.E-02	-91	109	9.204	185.0	616	6.96 x10^{-6}
2,4-Dimethylhexane (EPI)	Isoparaffin (Isoalkane)	branched alkane	114.2	4.12	4.05*	3.91.E-02	-91.83	91	9.204	185.0	803	6.96 x10^{-6}
2,3,3-Trimethylpentane	Isoparaffin (Isoalkane)	branched alkane	114.2	4.09	4.02*	3.55.E-02	-100.9	115	9.91	185.0	58	6.96 x10^{-6}
2,3-Dimethylhexane	Isoparaffin (Isoalkane)	branched alkane	114.2	4.12	4.05*	3.08.E-02	-91.83	116	9.204	185.0	530	6.96 x10^{-6}
3-Ethylhexane	Isoparaffin (Isoalkane)	branched alkane	114.2	4.20	4.13*	2.63.E-02	-80.1	119	7.965	185.0	354	6.96 x10^{-6}
3-Methylheptane	Isoparaffin (Isoalkane)	branched alkane	114.2	4.20	3.36	2.58.E-02	-100	118	7.965	185.0	2776	6.96 x10^{-6}
Octane	Paraffin (n-alkane)	normal alkane	114.2	4.00	3.93*	0.0187	-56.82	126	0.66	185.0	12028	6.96 x10^{-6}
Nonane	Paraffin (n-alkane)	normal alkane	128.3	4.50	4.42*	0.00623	-53.46	151	0.22	207.2	8700	6.51 x10^{-6}
Decane	Paraffin (n-alkane)	normal alkane	142.3	5.67	5.57	0.00238	-29.6	174	0.016	229.4	5895	6.13 x10^{-6}

* log Koc = 0.983 log Kow + 0.00028 (Di Toro et al 1991)

Table B-5. Parameters for each hydrocarbon included in the non-soluble and volatile aliphatic components. Those chemicals where parameters were obtained from the EPI Suite are identified by "EPI" following the chemical name. Parameters for the other chemicals were obtained from Mackay et al. (2006a,b).

Aliphatic Name(s)	C#	Component Grouping	Molecular Weight (g/mole)	Log(K_{ow})	Log(K_{oc})**	VP (@25°C)	Melting Point (°C)	Boiling Point (°C)	Solubility (25°C)	MC252 Content (mg/kg)**
n-Hexane, representative (in AR9)	6	**AL1**	86.18	3.00	2.95	0.1992	-95.35	68.73	9.5	12572
n-Heptane, representative (in AR9)	7	**AL1**	100.20	3.50	3.44	0.0552	-90.55	98.4	2.93	13461
n-Octane, representative (in AR9)	8	**AL1**	114.23	4.00	3.93	0.0187	-56.82	125.67	0.66	12028
n-Nonane	9	**AL2**	128.26	4.50	4.42	0.00623	-53.46	150.82	0.22	10080
n-Decane	10	**AL2**	142.29	5.67	5.57	0.00238	-29.6	174.15	0.016	8867
n-Undecane	11	**AL3**	156.31	6.94	6.82	0.0005718	-25.5	195.9	0.0044	8509
n-Dodecane	12	**AL4**	170.34	7.24	7.12	0.000176	-9.57	216.32	0.0084	7613
n-Tridecane	13	**AL5**	184.37	6.65	6.54	0.0000573	-5.4	235.47	0.00104	7022
n-Tetradecane	14	**AL5**	198.39	7.20	7.08	0.0000156	5.82	253.58	0.0069	6248
2,6,10-Trimethyldodecane (EPI)	15	**AL5**	212.42	7.49	7.36	4.86842E-05	-19.8	249.134	0.004421	1403
2,6,10-Trimethyltridecane (EPI)	16	**AL5**	226.45	7.98	7.84	1.84211E-05	18	266.871	0.0069	2265
n-Hexadecane	16	**AL5**	226.45	8.25	8.11	0.00000092	18.12	286.86	0.00628	5231
n-Pentadecane	17	**AL6**	212.42	7.72	7.59	0.00000311	9.95	270.6	7.60E-05	6312
Norpristane	18	**AL6**	254.50	8.92	8.77	0.00000092	28.2	316.3	0.0075	1609
n-Heptadecane	17	**AL6**	240.47	8.92	8.77	0.000000253	21	302	0.00775	4385

Aliphatic Name(s)	C#	Component Grouping	Molecular Weight (g/mole)	Log(K_{ow})	Log(K_{oc})**	VP (@25°C)	Melting Point (°C)	Boiling Point (°C)	Solubility (25°C)	MC252 Content (mg/kg)**
n-Octadecane	18	**AL6**	254.50	9.32	9.16	0.00000013	29	302	0.00775	3565
Pristane	19	**AL7**	268.54	9.32	9.16	0.000000253	33	296	0.00775	2919
Phytane	20	**AL7**	282.55	10.39	10.21	0.00000013	37	317	1.68E-05	1568
n-Nonadecane	19	**AL7**	268.53	10.39	10.21	0.00000013	33	330	2.97E-05	3190
n-Eicosane	20	**AL7**	282.55	10.39	10.21	2.09E-08	37	343	0.0019	2993
n-Heneicosane	21	**AL8**	296.58	13.00	12.78	5.03E-11	41	357	5.80E-10	2503
n-Docosane	22	**AL8**	310.61	13.00	12.78	5.03E-11	42	380	5.80E-10	2369
n-Tricosane	23	**AL8**	324.63	13.00	12.78	5.03E-11	49	380	5.80E-10	1859

** log Koc = 0.983 log Kow + 0.00028 (Di Toro et al 1991) for all chemicals

B.4 Oil Fates Model Inputs

Based on the preceding review of MC252 source oil physical-chemical properties and the characteristics of the source oil compositional compounds, the following oil properties and component group physical-chemical properties were used as input parameters for the oil fates model simulations. Table B-6 lists the physical properties taken from Stout (2015b). The component parameters were based on the detailed characterization of the source oil (described in Stout 2015b), and the constituents in each component were used to calculate the mass-weighted parameters. Tables B-7 to B-9 list the mass-weighted mean values of the physical chemical parameters for the eight soluble/semi-soluble aromatic components, the soluble aliphatics component (AL9), and the eight insoluble aliphatic components of the fresh MC252 Macando-1 source oil that are tracked separately in the model. Table B-7 lists the component fractions of the source oil and their molecular weight, vapor pressure, melting point, and boiling point, which are used for each aromatic and aliphatic component of the MC252 oil in the model. Table B-8 lists the total aromatic volatile fraction, total aliphatic volatile fraction, and total volatile fractions of the MC252 oil. Table B-9 gives a summary of the dissolution parameters of the soluble components that are used in the model, i.e., solubility, log K_{OW}, organic carbon partition coefficient, diffusivity coefficient, and solubility enhancement factor.

Table B-6. List of source oil physical properties as input parameters to the model

Density (g/cm^3) @ 30.0^{o}C	0.8372
Density (g/cm^3) @ 15.6^{o}C	0.83976
Viscosity (cP) @ 30.0^{o}C	4.503
Viscosity (cP) @ 15.0^{o}C	7.145
Surface Tension (dyne/cm)	3.43
Interfacial Tension (dyne/cm)	19.63
Pour Point (^{o}C)	-28.0
Resin Content (%)	10.10
Asphaltene Content (%)	0.27

Table B-7. Chemical properties of each component as input parameters to the model.

Component	Fraction of Total	Molecular Weight (g/mol)	Vapor Pressure at 25°C	Melting Point (°C)	Boiling Point (°C)
AR1	0.019124	98.0	0.03400	-47.0	123.0
AR2	0.007836	120.2	0.33200×10^{-2}	-63.0	166.0
AR3	0.004674	134.4	0.15200×10^{-2}	-34.0	180.0
AR4	0.003786	161.0	0.72700×10^{-3}	-12.0	203.0
AR5	0.005634	146.0	0.80400×10^{-4}	4.0	248.0
AR6	0.002434	174.8	0.54800×10^{-5}	66.0	289.0
AR7	0.002339	189.7	0.83600×10^{-6}	104.0	333.0
AR8	0.001667	215.0	0.10500×10^{-6}	152.0	368.0
AR9	0.133190	98.7	0.17600	-99.0	93.0
AL1	0.006923	100.0	0.09120	-81.0	97.0
AL2	0.060913	134.8	0.44300×10^{-2}	-42.0	162.0
AL3	0.034279	156.3	0.57200×10^{-3}	-26.0	196.0
AL4	0.053814	170.3	0.17600×10^{-3}	-10.0	216.0
AL5	0.095099	204.3	0.27700×10^{-4}	5.0	257.0
AL6	0.036292	233.9	0.14300×10^{-5}	19.0	291.0
AL7	0.092923	274.5	0.13300×10^{-6}	35.0	322.0
AL8	0.049473	309.3	0.50300×10^{-10}	43.0	371.0
AL9	0.000000	200.0	0.06000	0.0	0.0

Table B-8. Aromatic, aliphatic and total volatile fractions of MC252 Oil used in the model.

Component Group	Fraction by Weight
Total Fraction of AR1 – AR9 Volatiles	0.18068
Total Fraction of AL1 – AL8 Volatiles	0.42972
Total Fraction Volatiles (sum)	0.6104

Table B-9. Dissolution parameters used for soluble components in the model.

Component	Solubility at 25°C (mg/L)	Log (K_{OW})	Organic Carbon Solubility Partition Coefficient (particulate/ dissolved)	Diffusivity Coefficient at 25°C (cm^2/sec)	Enhance-ment Factor
AR1	495.0	2.91	726	8.8×10^{-6}	1.0
AR2	69.56	3.71	4438	7.5×10^{-6}	1.0
AR3	13.48	4.02	8952	7.0×10^{-6}	1.0
AR4	0.613	4.89	64143	6.1×10^{-6}	1.0
AR5	18.37	4.02	8952	7.2×10^{-6}	1.5
AR6	1.919	5.08	98610	5.9×10^{-6}	2.5
AR7	0.561	5.02	86088	6.5×10^{-6}	6.3
AR8	0.046	5.50	255141	6.1×10^{-6}	23.9
AR9	17.18	3.65	3875	7.8×10^{-6}	1.0

B.5 References

EPI. 2012. Estimation Programs Interface Suite™ v.4.11 (Nov 2012) is a Windows®-based suite of physical/chemical property and environmental fate estimation programs developed by the EPA's Office of Pollution Prevention Toxics and Syracuse Research Corporation (SRC). KOWWIN™, MPBPWIN™, KOCWIN™, and WSKOWWIN™ were run to estimate the Kow, Koc, MP, BP, and water solubility values if acceptable measured values are not available from literature. Available online at: http://www.epa.gov/oppt/exposure/pubs/episuite.htm

Hayduk, W. and H. Laudie. 1974. Prediction of diffusion coefficients for nonelectrolytes in dilute aqueous solutions, Am. Inst. Chem. Eng. J., 20: 611–615

Mackay, D., W. Y. Shiu, K.-C. Ma and S. C. Lee. 2006a. Handbook of Physical-Chemical Properties and Environmental Fate for Organic Chemicals. Vol. I, Introduction and Hydrocarbons. CRC Press, Taylor & Francis Group. 925 pp. Available online (Accessed on August 24, 2015) http://files.rushim.ru/books/spravochniki/mackay1.pdf

Mackay, D., W. Y. Shiu, K.-C. Ma and S. C. Lee. 2006b. Handbook of Physical-Chemical Properties and Environmental Fate for Organic Chemicals. Vol. IV, Nitrogen and Sulfur Containing Compounds and Pesticides. CRC Press, Taylor & Francis Group. 993 pp. Available online (Accessed on August 24, 2015) http://files.rushim.ru/books/spravochniki/mackay4.pdf

Stout, S.A., 2015a. Physical and chemical properties of the fresh MC252 Macondo-1 well crude oil. NewFields Technical Report to the Trustees in support of the PDARP.

Stout, S.A., 2015b. Bulk chemical and physical properties of fresh and weathered Macondo crude oil. NewFields Technical Report to the Trustees in support of the PDARP.

Yalkowsky, S. H. 1979. Estimation of Entropies of Fusion of Organic Compounds. Industrial & Engineering Chemistry Fundamentals 18(2):108-111.

Technical Reports for Deepwater Horizon Water Column Injury Assessment

WC_TR.14: Modeling Oil Fate and Exposure Concentrations in the Deepwater Plume and Rising Oil Resulting from the Deepwater Horizon Oil Spill

Appendix C. Review of Biodegradation Rates of Crude Oil and Hydrocarbons in Seawater

Authors: Deborah French McCay, Katherine Jayko, Zhengkai Li, Matthew Horn, Yong Kim, Tatsu Isaji, Deborah Crowley, Malcolm Spaulding, Lauren Decker, Cathleen Turner, Stefanie Zamorski, Jeremy Fontenault, Rachel Shmookler, and Jill Rowe

Appendix C: Prepared by Zhengkai Li, RPS ASA

Revised: September 29, 2015
Project Number: 2011-144
RPS ASA 55 Village Square Drive, South Kingstown, RI 02879

Table of Contents

List of Figures

List of Tables

Executive Summary

The objective of this literature review is to evaluate biodegradation of petroleum hydrocarbons in the environment; the emphasis is put on reviewing available biodegradation rates of individual hydrocarbon compounds or component groups in seawater.

Most of the laboratory and field studies on hydrocarbon biodegradation rates used first-order degradation kinetics to evaluate their data; many of them included a separate parameter of a lag phase prior to the onset of biodegradation. The lag phases varied among hydrocarbon compounds or groups and different studies; generally, degradation of aromatics has a longer lag phase than aliphatics. Some biodegradation data are unable to be fit using the first-order rate equation, meaning that other more complex models might be needed to fully explain the data (Yassine et al., 2013).

The hydrocarbon "pseudo-component" approach (as used in modeling of the evaporation and dissolution processes within the SIMAP oil fate model) is used to describe the biodegradation rates of hydrocarbons in seawater. The oil component properties (OCP) and degradation rates developed herein are summarized by each of AR and AL components. Of these components, AR1 to AR8 are soluble aromatics (AR), AR9 is soluble alkanes, AL1 to AL8 are non-soluble aliphatic fractions, and, lastly, a residual component is made up of non-volatile compounds.

Among the hydrocarbon groups, n-alkanes have faster degradation rates than branched and cyclic compounds, and alkanes also have different rates from the mono-ring and polycyclic aromatic hydrocarbons; therefore, the biodegradation rates obtained from the analyses of groups of similar molecular-weight alkanes within separate boiling – cut based fractions are more suitable estimates of the AL component's degradation rates than the estimates from the average of a few selected n-alkane rates.

Both AR and AL component rates estimated from low oil concentration lab studies, which have been designed to represent well-dispersed and diluted oil in the water column, are always much higher than rates obtained from other experiments tested at high oil concentrations. It is important to differentiate the biodegradation of oil dispersed in the water column from the loss rates of surface floating oil or from the degradation rates in sediments, as the hydrocarbon degradation processes in different environmental compartments may follow different kinetics and pathways.

Table C-Ex-1 summarizes the first-order degradation rates and half-lives of AR1-9, AL1-8, and Residual biodegradation in the water column; the large standard deviations of half-lives of AR6-8 (the less soluble aromatics, primarily 3-ring PAHs) indicate high uncertainties in the estimates. Biodegradation rates of aromatics, especially the sparingly soluble high molecular weight PAH compounds, are dependent on the dissolution rates, and consequently on the extent of dispersion. Therefore, it is important to consider the effects of dispersed oil droplet size distribution on the dissolution and biodegradation of oil in the water column.

Table C-Ex-1: Summary of degradation rates of AR1-9, AL1-8, and Residual in seawater *

Component Group	First-order rate (day^{-1})	Half-Life (days)
AR1	0.23	3.0
AR2	0.29	2.4
AR3	0.28	2.5
AR4	0.06	11.6
AR5	0.28	2.5
AR6	0.18	3.9
AR7	0.15	4.6
AR8	0.10	6.9
AR9	0.17	4.1
AL1	0.24	2.9
AL2	0.12	5.8
AL3	0.06	11.6
AL4	0.06	11.6
AL5	0.06	11.6
AL6	0.05	13.9
AL7	0.04	17.3
AL8	0.04	17.3
Residual	0.02	34.7

* AR1-8 are sparingly soluble aromatics and AR9 is semi-soluble aliphatics, while AL1-8 are insoluble aliphatics.

C1. Introduction

Oils spilled at sea eventually are altered in their chemical compositions and physical-chemical properties through a variety of weathering and sedimentation processes including evaporation, dissolution, dispersion, emulsification, biodegradation, photooxidation, sedimentation, and shoreline interactions. These changes usually take place at different time scales and result in amendment of the distribution of oil components in the environmental compartments, such as water column, surface layer, atmosphere, or sediments (Figure C-1). Among these weathering processes, biodegradation and photo-oxidation are the two main processes known to cause transformation of hydrocarbons into other molecules in the environment. Biodegradation is a major process controlling weathering and the ultimate removal of hydrocarbons entering the marine environment (NRC, 2003). Biodegradation occurs from the uptake and consumption of hydrocarbons as carbon and energy sources by microorganisms for their growth and reproduction. Biodegradation refers to both incorporation of substrates into biomass and mineralization to simple compounds and constituent nutrients. Photo-oxidation of oil is abiotic decomposition of hydrocarbon components through auto-oxidation induced by sunlight. The focus of this Appendix is to review biodegradation with emphasis on the biodegradation rates of petroleum hydrocarbons in marine aquatic environments.

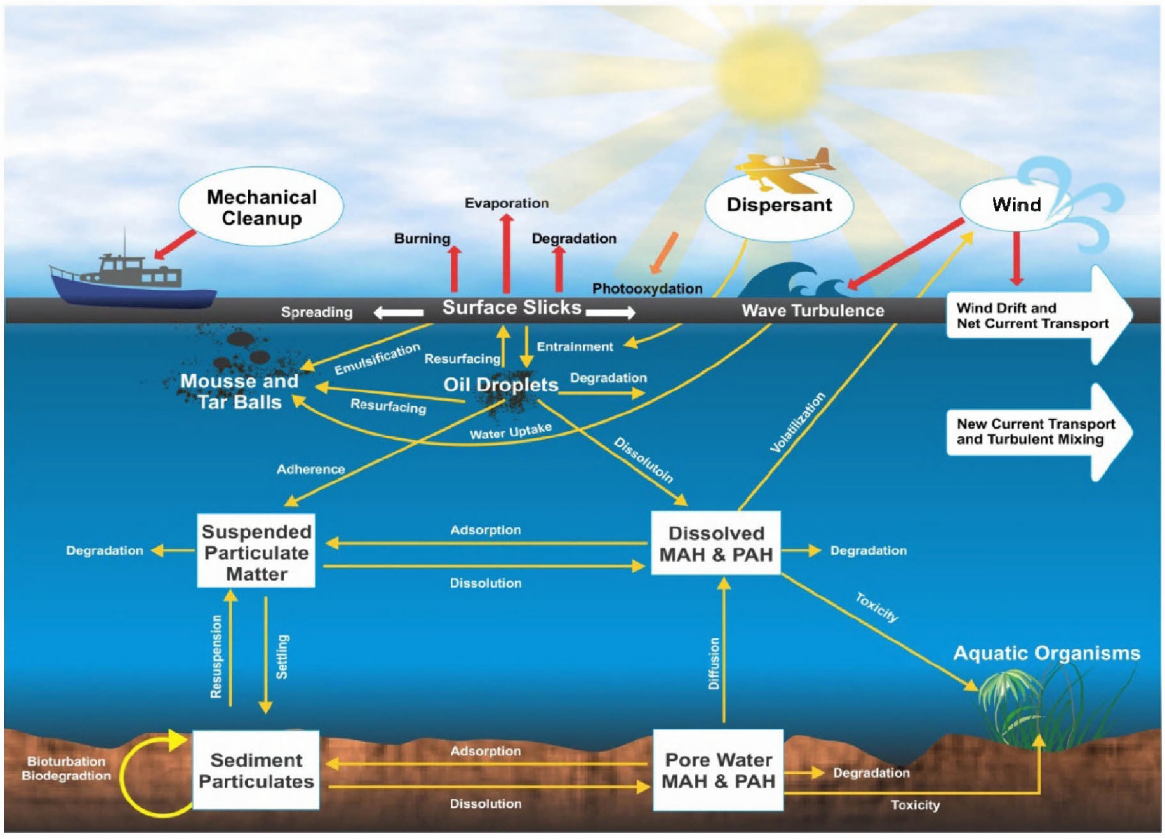

Figure C-1. Fate processes (including photooxidation and biodegradation) of oil spilled at sea (RPS ASA 2010).

C2. Biodegradation of Crude Oil and Petroleum Products in the Marine Environment

Bacterial degradation of crude oil and petroleum products is an interfacial phenomenon due to the hydrophobic nature of the hydrocarbons (Figure C-2). In oil degradation consortia, some microorganisms can produce bio-surfactants that enhance dissolution of hydrocarbon compounds (Banat 1995; Desai et al.,1997; Ron and Rosenberg, 2002; Rahman and Gakpe, 2008; Ward, 2010), other microbes can weather minerals to release phosphate and degrade oil (Head et al., 2006). While primary oil degraders compete for limiting nutrients (such as nitrogen and phosphate), secondary consumers feed on metabolites and can recycle nutrients (Head et al., 2006).

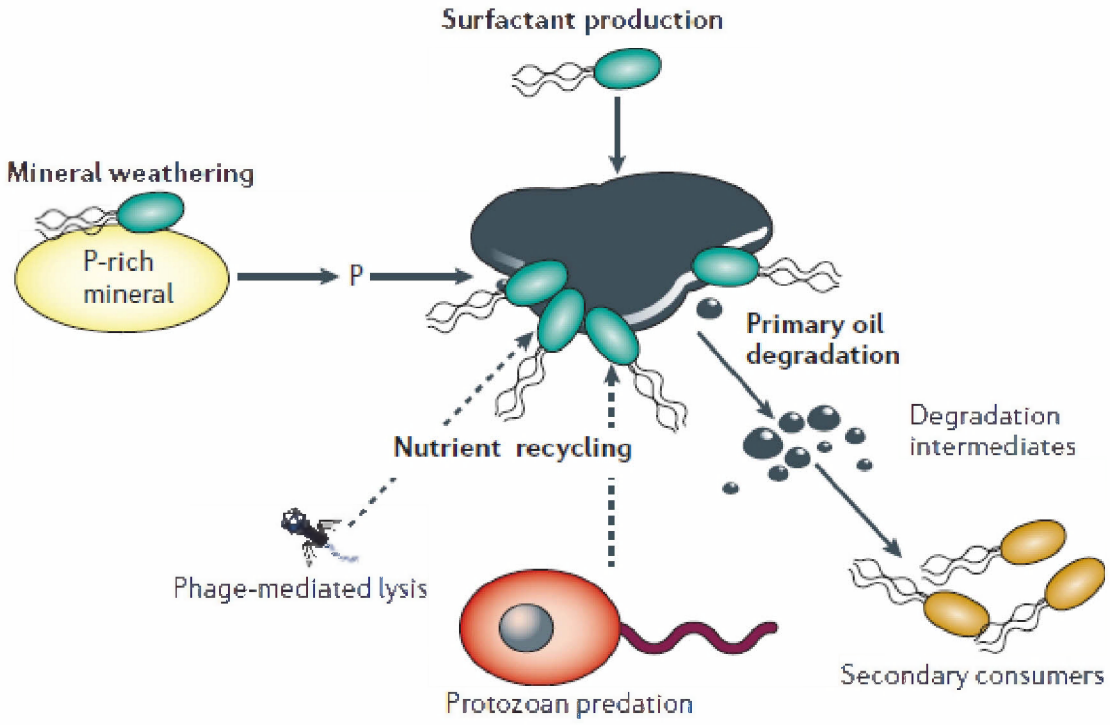

Figure C-2. Microbial oil degradation consortia involve more biological components than just the microorganisms that directly attack oil (the primary oil degraders); the primary oil degraders (green) interact with these components. Solid arrows indicate material fluxes, and broken arrows indicate direct interactions (for example, lysis by phage and predation by protozoa) (Head et al., 2006).

Ziervogel et al. (2012) showed that the microbial dynamics and carbon flux in oil-contaminated surface waters sampled near the Deep water horizon (DWH) spill site were greatly influenced by the activities of microbes associated with macroscopic oil aggregates. In roller bottle microcosms set up in the lab with oil-amended water, rapid formation of oil aggregates was observed that were similar in size and appearance compared to oil aggregates observed in surface waters near the spill site. Oil aggregates that formed in roller bottles were densely colonized by heterotrophic bacteria, exhibiting high rates of enzymatic activity (lipase hydrolysis)

indicative of oil degradation. Ambient waters surrounding aggregates also showed enhanced microbial activities not directly associated with primary oil degradation (b-glucosidase; peptidase), as well as a twofold increase in dissolved organic carbon (DOC) and concurrent changes in fluorescence properties of colored dissolved organic matter (CDOM), suggesting an increase in oil-derived, aromatic hydrocarbons in the DOC pool. Edwards et al. (2011) collected surface water samples at stations near the DWH site within and outside the slicks. They examined community respiration rates, lipase enzyme activities, microbial abundances, and microbial biomass to delineate the microbial community response to the introduction of crude oil. Although they observed no increase in microbial abundances or biomass within the slick, microbes within the surface slick showed higher of alkaline phosphatase activity rates, microbial respiration, and lipase activity. Amendments with inorganic nutrients led to increased respiration and bacterial biomass.

C.2.1 Degradation of oil and dispersants in the deep sea

Biodegradation of oil hydrocarbons in the deep sea have been studied by the following three different approaches: (A) characterization of the microbial community structure and function, (B) assessing the hydrocarbon chemistry, and (C) modeling biodegradation by using numerical simulation.

C.2.1.1 Microbial community structure and function

Hazen et al. (2010) reported the Deepwater Horizon oil spill resulted in a deep-sea hydrocarbon plume (layer enriched with oil hydrocarbons at ~1,100-1,300 m) that affected both microbial cell densities and composition. Hazen et al. (2010) detected using Phylochip analysis, at the early spill stage, a bloom of uncultured and uncharacterized members of the order *Oceanospirillales* in the γ-Proteobacteria; these members were significantly enriched relative to background deep seawater with no oil. Hazen et al. (2010) showed with GeoChip functional array analysis that microbial community functional composition and structure were considerably different between oil-plume and non-plume control samples. Many of the genes involved in hydrocarbon degradation were significantly increased in oil plume samples. Based on these results, Hazen et al. (2010) suggested that a variety of hydrocarbon-degrading populations exist in the deep-sea plume and that the microbial communities appeared to be undergoing rapid dynamic adaptation in response to oil to carry out intrinsic bioremediation of oil contaminants in the deep sea.

Mason et al. (2012) further determined the functional role of the *Oceanospirillales* and other active members of the indigenous microbial community using a deep sequencing technique for evaluating community DNA and RNA, as well as single-cell genomics. Shotgun metagenomic and metatranscriptomic sequencing revealed that genes for motility, chemotaxis and aliphatic hydrocarbon degradation were significantly enriched and expressed in the hydrocarbon plume samples compared with uncontaminated seawater collected from plume depth. In contrast, although genes coding for degradation of mono-aromatic compounds, such as benzene, toluene, ethylbenzene, total xylenes, and polycyclic aromatic hydrocarbons, were identified in the metagenomes, they were expressed at low levels, or not at all based on analysis of the metatranscriptomes. Isolation and sequencing of two *Oceanospirillales* single cells revealed that both cells possessed genes coding for n-alkane and cycloalkane degradation. Specifically, the near-complete pathway for cyclohexane oxidation in the *Oceanospirillales* single cells was elucidated and supported by both metagenome and metatranscriptome data. The draft genome also included genes for chemotaxis, motility and nutrient acquisition strategies that were also

identified in the metagenomes and metatranscriptomes. These data point towards a rapid response of members of the *Oceanospirillales* to aliphatic hydrocarbons in the deep sea.

Lu et al. (2012) assessed the dynamic changes of microbial communities in response to the DWH oil spill; microbial community functional composition and structure were analyzed using functional gene arrays (GeoChip 4.0). Their results showed that the microbial community functional composition and structure were dramatically altered in a deep-sea oil plume resulting from the spill. A variety of metabolic genes involved in both aerobic and anaerobic hydrocarbon degradation were highly enriched in the plume compared with those outside the plume. A substantial number of genes involved in hydrocarbon degradation were detected in the oil plume samples (Hazen et al., 2010), especially those involved in degrading alkanes, alkynes and cycloalkanes, BTEX and related aromatics, chlorinated aromatics, heterocyclic aromatics, nitroaromatics, polycyclic aromatics and aromatic carboxylic acids. GeoChip analysis also detected many aerobic PAH degradation genes from a variety of microorganisms. PAH degradation genes were more abundant in the plume samples, while some were unique to the plume samples. The gene bbs (beta-oxidation of benzylsuccinate) for anaerobic toluene degradation was also enriched in plume samples. Various other microbial functional genes that are relevant to carbon, nitrogen, phosphorus, sulfur and iron cycling, metal resistance and bacteriophage replication were also enriched in the plume.

Redmond and Valentine (2011) reported that microbial communities present in the Gulf of Mexico rapidly responded to the Deepwater Horizon oil spill. While an initial report after the Deepwater Horizon spill showed that, in late May, an uncultivated group of *Oceanospirillales* were dominant in plume samples (Hazen et al., 2010), in June, plume samples were dominated by two different groups of γ-proteobacteria, *Colwellia* and *Cycloclasticus* (Valentine et al., 2010), and by September (after the well was capped in mid-July), these groups were much less abundant and plumes were dominated by methylotrophs (*Methylococcaceae*, *Methylophaga*, and *Methylophilaceae*), Flavobacteria, and Rhodobacterales (Kessler et al., 2011). None of the deep water plume enriched microbial community members, *Oceanospirillales, Colwellia,* and *Cycloclasticus,* were abundant in surface oil slick samples. Redmond and Valentine (2011) suggested temperature might have played a significant role in determining which members of the microbial community responded to the Deepwater Horizon spill. The *Colwellia*, a psychrophile, much more abundant in oil-degrading enrichment cultures incubated at 4°C than at room temperature, incorporated ^{13}C-benzene as well as ^{13}C- ethane and ^{13}C- propane in stable isotope probing experiments. The abundance of *Colwellia* in crude oil enrichments without natural gas suggested that it had the ability to consume a wide range of hydrocarbon compounds or their degradation products. Redmond and Valentine (2011) suggested that *Flavobacteria* might have been secondary consumers of methane, oil, or cellular decay products, for a number of reasons: *Flavobacteria* are abundant in the ocean, are often associated with the degradation of high molecular weight dissolved organic carbon compounds, several methanol-oxidizing strains of Flavobacterium have been isolated and they have often been observed in ^{13}C-labeled DNA from methane SIP studies.

Dubinsky et al. (2013) highlighted the succession of hydrocarbon-degrading bacteria before, during and after the Deepwater Horizon spill in the water column. Early in the spill unmitigated flow from the wellhead resulted in relatively high proportions of *n*-alkanes and cycloalkanes at depth and corresponded with dominance by *Oceanospirillaceae* and *Pseudomonas*. After partial capture of oil and gas began on June 04, an additional amount of recovery starting June 11, and the continual application of subsea dispersants, measured particulate petroleum hydrocarbons decreased, the relative fraction of aromatic hydrocarbons increased, and *Colwellia*,

Cycloclasticus and *Pseudoalteromonas* increased in dominance. Enrichment of *Methylomonas* coincided with positive shifts in the δ13C values of methane in the plume and indicated significant methane oxidation occurred earlier than previously reported. Anomalous oxygen depressions persisted at plume depths for over six weeks after in the oil release ceased and were likely caused by common marine heterotrophs associated with degradation of high-molecular-weight organic matter, including *Methylophaga*. Payne and Driskell (2015c) noted DO sags in CTD casts in November and possibly December 2010.

Kimes et al. (2014) found similar successional changes in indigenous microbial community composition in the water column and surface water, as well as in deep-sea sediments and coastal sediments and sands. The authors stated that while aerobic microbial degradation of hydrocarbons is the predominant metabolic pathway of hydrocarbons in seawater, anaerobic biodegradation is also important in marine ecosystems especially marine sediments. The formed oxygenated hydrocarbons appear to be recalcitrant and more research is warranted to increase understanding the microbial metabolism and environmental fate and toxicity of this weathered, oxygenated fraction of oil that may persist after a spill.

C.2.1.2 Hydrocarbon and dispersant chemistry data

Hazen et al. (2010) reported rapid biodegradation of oil in the deep sea hydrocarbon plume resulting from the DWH spill based on tracking concentrations of C_{13}-C_{26} n-alkanes. Source oil degradation experiments were conducted to investigate degradation of C_{13}-C_{26} n-alkanes in the plume.

Studies of Kessler et al. (2011) and Valentine et al. (2010) documented fast depletion of short-chain alkanes (namely ethane, propane, and butane), and found that the degradation was correlated to the anomaly of the dissolved oxygen at the plume depth. Du and Kessler (2012) investigated 1,316 dissolved oxygen profiles measured from 11 May until 20 September 2010 to study the spatial and temporal variability of the bulk hydrocarbon respiration in deep and intermediate plumes. Based on the cumulative loss of dissolved oxygen, which peaked from 14 August through 18 September at value of 18.9 ± 3.8 Gmol, the authors estimated that the ratio of the total mass of oil and gas released to the plume layer to the total mass into the environment was 38%. The analyses suggest that the highest hydrocarbon respiration rates reached 1.54 Gg/day of dissolved hydrocarbon and 2.16 Gg/day of both dissolved and trapped particulate hydrocarbon, corresponding to first-order degradation rates of approximately 0.275 d^{-1} and 0.368 d^{-1}, respectively (i.e., half-lives of 2.52 and 1.88 d, respectively).

Camilli et al. (2010) and Reddy et al. (2012) tracked the DWH hydrocarbon plume, especially the dissolved hydrocarbon components mono-ring aromatic compounds (i.e. BTEX). They discussed much lower degradation rates for BTEXs than the rates commonly published in coastal and marine environments (Rontani et al., 1985; van der Linden, 1978; Prince et al., 2007). Based on their conclusion that no systematic spatial trends were shown for the absolute and relative abundance of BTEX compounds, Reddy et al. (2012) suggested that negligible biodegradation occurred during transport of BTEX in the plume. Taken together with the interpretation of results of Valentine et al. (2010) on the respiration of volatile hydrocarbons and those of Camilli et al. (2010) on the overall respiration rate of hydrocarbons, Reddy et al. (2012) suggested that the degradation of soluble hydrocarbons had a half-life on the order of 1 month. Reddy et al. (2012) concluded that although biodegradation might have been an important process, the ultimate fate of the water-soluble petroleum hydrocarbons in the deep water plume

was unknown. However, Payne and Driskell (2015a, Figure 4), showed a clear decline in plume depth benzene and ethylbenzene concentrations with distance from the wellhead out to 10 km and the xylenes persisting out to 20 km. These data suggest that biodegradation was occurring.

Bælum et al. (2012) enriched and isolated indigenous hydrocarbon degrading bacteria from deep and uncontaminated Gulf of Mexico waters with MC252 oil and Corexit 9500 dispersant. Incubation was conducted at 5°C for 20 days to determine CO_2 production, hydrocarbon degradation, and the microbial community composition. They observed 60% and 25% of the dissolved oil degraded over the 20 days with and without dispersant, respectively. In addition, the hydrocarbons in Corexit 9500 degraded by about 50% in that time period. *Colwellia* and *Oceanospirillales* increased in abundance during incubation. Flocs formed during incubations with oil in the presence and absence of dispersant was found to be comprised of oil, carbohydrates and biomass; *Colwellia* was the dominant bacteria in the flocs. The non-hydrocarbon components of the chemical dispersant, dioctylsulfosuccinate (DOSS) were shown to degrade at linear rate and with more than 60% of the initial mass removed after 20 days. The other non-hydrocarbon components, glycols, however, were more persistent, with less than 5% removal within 20 days of their degradation experiment.

Kujawinski et al. (2011) published data on deep water samples that contained very low concentrations of anionic surfactant, dioctyl sodium sulfosuccinate (DOSS) which is a constituent of the dispersant Corexit 9500, and evaluated long-term (up to 74 days) horizontal transport of DOSS in the subsurface plume. They reported that the observed DOSS concentrations in the DWH surrounding water masses were similar to those predicted based on dilution for a given distance. Although it was possible that biodegradation or sedimentation was also contributing to the decrease of DOSS concentration in these water masses, given the variability in DOSS release rates at the wellhead, Kujawinski et al. (2011) concluded that the most significant factor that caused a decrease in DOSS concentration at depth would have been from dilution.

Campo et al. (2013) assessed persistence of the DOSS surfactant in Corexit 9500 dispersant with and without the dispersed South Louisiana crude (SLC) oil in laboratory microcosms at two temperature conditions, 25°C and 5°C. The study was conducted using two oil-degrading cultures isolated from the Gulf of Mexico, one from the surface (meso-culture) and the other from the area of the Macondo well (cryo-culture at a depth of 1240 m deep). Each culture was enriched with SLC, the former at 25°C, and the later at 5°C. The results indicated that alkanes and aromatics were degraded rapidly and completely at 25°C. The alkanes and aromatic compounds were also degradable at 5°C, but at much slower rate for alkanes, with various lengths of lag phases, and a remaining residual of iso-alkanes, long-chain alkanes (C_{30-35}) and the 4-ring PAHs after 6 weeks degradation experiment. The 2 to 3 ring PAHs, however, were degraded even faster at 5°C than 25°C. Rapid DOSS degradation was also observed in the microcosms incubated at 25°C, but the onset of DOSS removal was much slower at 5°C, with a 28-d lag phase, and was incomplete in the replicated microcosms.

C.2.1.3 Biodegradation byproducts chemistry data

Ziervogel and Arnosti (2013) discussed that oil spilled in the ocean can be biodegraded through a cascade of microbial processes, including direct degradation of petroleum-derived hydrocarbons, as well as subsequent degradation of transformation byproducts and exopolymeric substances (EPS) that are produced by microbes to emulsify hydrocarbons and facilitate access to oil. The authors measured carbohydrate and peptide hydrolase activities as

indicators of the degradation of high molecular weight organic matter, including EPS substrates. Deepwater associated with the hydrocarbon plume revealed higher peptidase activity compared to non-plume deepwater samples. Enzymatic hydrolysis of carbohydrates, measured by the means of exo-acting enzyme activity (β -glucosidase), was also more rapid inside compared to outside the deepwater plume. Hydrolysis rates and patterns of endo-acting polysaccharide hydrolases, measured by means of distinct polysaccharide substrates in longer-term incubations, demonstrated more rapid plume-associated hydrolysis of two (laminarin and xylan) of the three substrates hydrolyzed in deep waters. These results indicate that microbial communities associated with the deepwater plume exhibited 'primed' responses to addition of specific substrates, which may structurally resemble components found in bacterial EPS and oil degradation byproducts. Bacterial transformation of oil-degradation byproducts thus likely contributed to microbial growth and respiration measured inside the deepwater plume.

Lin and Guo (2015) collected samples from the northern Gulf of Mexico during October 2010 and October 2011 to examine the abundance, spatial and vertical distributions, and partitioning of carbohydrates (CHO) among monosaccharides (MCHO), HCl-hydrolysable polysaccharides (HCl-PCHO), and dilute-HCl-resistant polysaccharides (HR-PCHO). Elevated deepwater HR-PCHO abundance and TCHO/DOC ratio at some stations likely resulted from enhanced microbial production of exopolysaccharides due to the presence of oil components after the Deepwater Horizon oil spill.

Aeppli et al. (2012) documented that oil weathering after the Deepwater Horizon disaster led to the formation of oxygenated residues.

C.2.1.4 Numerical model simulation of biodegradation

Adcroft et al. (2010) reported simulations of underwater plumes of dissolved oil in the Gulf of Mexico, and used a temperature-dependent (Q_{10} = 3) decay time scale as 12 days x $3^{-(T-20)/10}$. Based on this equation, the first-order degradation rate that was used by the authors was about 0.016 d^{-1} at 5°C and 0.14 d^{-1} at 25°C. These rates are taken from the lab study values reported by other investigators at different temperature conditions (Atlas, 1981; Venosa and Holder, 2007).

Valentine et al. (2012) developed a coupled physical-metabolic model to assess the effect of mixing processes on these deep ocean bacterial communities and their capacity for hydrocarbon and oxygen use. They described their biodegradation by considering exponential growth of bacteria from seed populations present at low abundance; asserting that current oscillations and mixing processes played a critical role in distributing hydrocarbons and associated bacterial blooms within the northeast Gulf of Mexico. The authors proposed that the mixing processes also accelerated hydrocarbon degradation through an auto-inoculation effect, where water masses, in which the hydrocarbon irruption had caused blooms, later returned to the spill site with hydrocarbon-degrading bacteria persisting at elevated abundance. The hydrocarbon biodegradation and the microbial population growth rates were simulated using first-order rate coefficients for individual compounds, including short-chain-length n- and cyclo-alkanes, 1- and 2- ring aromatics, and whole oil. The doubling time of the microbial population was derived from the literature, ranging from 0.75-1.5 days for alkanes, 3 days for aromatics, and 1-5 days for oil as a function of the number of carbons.

North et al. (2015) conducted a sensitivity study to evaluate the influence of assumed initial droplet size distribution and biodegradation rates on the subsurface transport and fate of oil droplets from the Deepwater Horizon oil spill. The biodegradation rates of whole oil droplets

were assumed to be at Hazen et al. (2010) estimated rates for C13-26 n-alkanes degradation, with a mean half-life of 3.05 day, and a range between 1.2 d and 6.1 d. Simulation of subsurface oil transport and fate processes were performed with these three different biodegradation rates plus a non-degradation control, and 5 different initial droplet diameter (10, 30, 50, 100, and 300 µm). Simulations were conducted with an assumption of 17.4% of released oil remained in the subsurface intrusion layer, with 5.8% each for the masses in 10, 30, and 50 µm droplets. The author's simulation results indicated that including biodegradation rates (with accompanying decrease in droplet size as the oil degraded) resulted in an increased depth range of the vertical distribution of oil droplets, decreased footprint of horizontal distribution ranges, and several orders of magnitude reduction of oil mass in the water column. Nevertheless, the authors themselves also pointed out that their prediction was highly likely an over-prediction of transport of oil to far locations because other fate processes (such as dissolution) were not included in the model parameterization.

C3. Factors affecting biodegradation rates

The hydrocarbon biotransformation rates are dependent on the accessibility of substrates to microbes. The hydrocarbon compounds could either be available as dissolved compounds in the aqueous phase or accessible at the surfaces of particles. Likewise, the hydrocarbon degraders are either bundled with particulates as agglomerates or present as free swimmers in the aquatic environments (Chang et al., 2009; Southam et al., 2001). Biodegradation rates of oil and hydrocarbon compounds are also dependent on oil chemical composition and various environmental conditions. When chemical dispersants are applied to surface oil slicks or at the subsurface oil release to disperse oil into smaller droplets, the oil can be dispersed into oil droplets due to the mixing energy of breaking waves, or by turbulence at a subsurface release location. Therefore, chemical dispersant is anticipated to enhance the biodegradation rate of oil.

Factors determining petroleum degradation rates in seawater fall into three broad categories: (A) oil constituents (e.g., concentration, composition, properties, and weathering), (B) microorganisms (e.g., community structure, function, activities), and (C) environmental conditions (e.g., temperature, pressure, dissolved oxygen, and nutrients) (NRC, 2003).

C.3.1 Oil constituents

Most petroleum hydrocarbons are biodegradable but different hydrocarbon components degrade at varying rates (Stout and Wang, 2007). The normal n-alkanes in the range of C_{10}-C_{22} are the most readily and frequently utilized hydrocarbon substrates (Belhaj et al., 2002; NRC, 2003); low molecular weight aromatics such as benzene, toluene, ethylene, and xylenes (BTEX) are also readily biodegradable by marine organisms (Cho et al., 2007; Krumholz et al., 1996; Van Hamme et al., 2003). The C_5-C_{10} homologues (e.g., pentane, hexane, heptane, octane, nonane, and decane) have been shown to be inhibitory to the majority of hydrocarbon degraders (Bartha and Atlas, 1977); as solvents, these homologues tend to disrupt lipid membrane structures of microorganisms; similarly, the mono-cycloaliphatic compounds (cyclopentane, cyclohexane, and cycloheptane) have a strong solvent effect on lipid membranes and are toxic to hydrocarbon degrading microorganisms (Leahy and Colwell, 1990). However, as physical weathering at the surface affects constituents with a boiling point ≤ 250°C (e.g., *n*-C14 alkanes), the effect of pressure in the deep ocean environment can result in greater solubility, reduced oil droplet sizes and reduced degassing of these compounds (Harayama et al., 1999; Newfields, 2012). Biodegradation of longer alkanes occurs at rates that exceed their

respective dissolution rates, and are a function of hydrocarbon surface area available for emulsification or physical attachment by microbes (Leahy and Colwell, 1990). Long chain alkanes in the C_{20}-C_{40} range are highly hydrophobic (including C_{18} and longer paraffin waxes that are solid at ambient temperature) and adversely influence their biodegradation (Wentzel et al., 2007). The isoalkanes, cycloalkanes, and high molecular weight aromatics are degraded more slowly. High molecular weight cycloparaffinic and asphaltenic petroleum compounds are biodegraded at extremely slow rates.

C.3.2 Microorganisms

Microorganisms (bacteria, yeast, and fungi) are important in the degradation of petroleum in surface films, slicks, the water column, and sediments. A wide variety of bacterial and fungal genera exhibit the capacity to degrade hydrocarbons in marine environments (Atlas, 1984; Head et al., 2006; Leahy and Colwell, 1990; Zobell, 1973). Bacteria are distributed ubiquitously from tropical environments to the extremely cold regions in Antarctic and Arctic (Head et al., 2006; Venosa and Zhu, 2003). While normally present in very small numbers in pristine environments, oil-degrading microbes can multiply rapidly upon the exposure to oil (Atlas 1995b; Brakstad et al., 2008; Harayama et al., 2004). In environments with chronic exposure to hydrocarbon pollutants, elevated numbers and predominance of oil-degrading microorganisms have been documented (Atlas 1995a; Macnaughton et al., 1999; Whyte et al., 2002).

Petroleum hydrocarbon compounds are degraded by a variety of microorganisms, some may attack more specific groups of hydrocarbons (e.g., alkanes or aromatics) while others may degrade a broad range of compounds (e.g., both alkanes and aromatics) (Bartha and Atlas, 1977). In some cases syntrophic processes (which require co-location of two or more taxa with complementary metabolic requirements) must occur (McGenity et al., 2012). Various hydrocarbon components may also influence each other's degradation through the phenomena of co-metabolism or *diauxie* (NRC, 2003). In the first case, a normally refractory hydrocarbon may be degraded in the presence of a second readily degradable hydrocarbon; in the second case, however, the presence of a more easily utilized hydrocarbon represses enzyme induction needed for metabolism of the other hydrocarbon; rather than metabolizing the two available substrates simultaneously, microbial cells commonly consume them in a sequential pattern, resulting in two separate growth phases. Co-metabolism plays an important role in oil biodegradation and may require microbial consortia (or syntrophic interspecies cooperation) (Bauer and Capone 1988; Head et al., 2006; Mcinerney et al., 2008). Many complex branched, cyclic, and aromatic hydrocarbons, which otherwise would not be biodegraded individually, can be oxidized through co-metabolism in an oil mixture due to the abundance of other substrates that can be metabolized easily within the oil (Atlas, 1981). Selective degradation and utilization result in relative enrichment of a slow-degrading chemical fraction (such as high molecular weight PAHs) over faster-degrading factions (such as shorter length alkanes) (Atlas and Bragg, 2009). However, an opposite trend was observed by Payne and Driskell (2015c), who noted abiotic dissolution of PAH and inhibited n-alkane biodegradation in dispersant-mediated oil at depth within 2-5 km of the wellhead. Three mechanisms are recognized by which microorganisms take up hydrocarbons prior to metabolic transformation (NRC 2005): (1) transport of aqueous-phase substrates through membrane transport mechanisms (e.g., passive diffusion, active transport); (2) direct contact with non-aqueous-phase liquids or solids followed by incorporation into cell membranes or intracellular vesicles; and (3) uptake of water-accommodated fraction of hydrocarbons that are present in surfactant micelles. Microbial uptake of semi-volatile PAH, such as naphthalene and phenanthrene, has been shown to occur

by transport of aqueous-phase (i.e., dissolved phase) molecules, whereas direct attachment to non-aqueous phase liquid droplets is essential for growth of certain alkane degraders. Some other hydrocarbon degraders produce biological emulsifying agents that enhance substrate transport and subsequent degradation of hydrocarbons. In addition, the fatty acid moieties of bio-surfactants promote the growth of microorganisms on the surface of oil droplets and facilitate oil removal from contaminated marine sediments (Saeki et al., 2009).

C.3.3 Environmental conditions

Environmental conditions vary widely in different regions of the aquatic areas (e.g., temperature, hydrostatic pressure, dissolved oxygen, nutrients, pH, salinity, and the abundance of hydrocarbon degraders and their substrate range) all potentially have effects on oil biodegradation rates.

C.3.1.1 Temperature:

Temperature affects both the properties of spilled oil and the density and activity of microorganisms (Atlas, 1981; Leahy and Colwell, 1990). Although hydrocarbon biodegradation can occur over a wide range of temperatures, the rate of biodegradation generally decreases with decreasing temperature. The effect of temperature on bacterial degradation is generally considered with the Q_{10} rule (Atlas and Bartha, 1972a; Tchobanoglous et al., 2002).

$$Q_{10} = (k_2/k_1)^{10/\Delta T}$$

The Q_{10} relationship is related to the Arrhenius equation and is the ratio of a first-order rate constant at a specific temperature to the rate constant at a temperature 10°C lower, where k_1 and k_2 are the rate constants calculated at temperature T_1 and T_2 and ΔT is the change in temperature from T_2 to T_1. A general rule-of-thumb is that the reaction rates double for every 10 degrees Kelvin rise; therefore the expected Q_{10} value is 2. NRC (2003) cited Gibbs et al. (1975) and Gibbs and Davis (1976) Q_{10} value of 2.7 for hydrocarbon biodegradation.

Bagi et al. (2013) reviewed oil biodegradation rates at various temperatures in marine environments and calculated a total of 32 Q_{10} values, ranging from 1.1 to 16.2. The mean, mode and median value of the frequency distribution of these Q_{10} values were found to be 2.8, 2.5, and 2.0, respectively. Possible reasons for the variability of Q_{10} values were attributed to bioavailability effect of different substrates, temperature effect on biomass and specific metabolic activity, and other experimental factors. Bagi et al. (2013) concluded that because biodegradation rates predicted with calculations using temperature compensation approaches involve great uncertainty, it is desirable to develop coupled physical-metabolic-ecological models in order to better describe the complex microbial ecosystems established around marine oil biodegradation.

C.3.1.2 Pressure

High pressure may influence the degradation of oil by affecting both microbial community composition and enzyme activity (Fang et al., 2010). Schedler et al. (2014) investigated the effects of high pressure on bacterial biodegradation of crude oil and its components. Both hydrocarbon degradation and growth of model oil-degrading strains were studied using high-pressure reactors with pressure ranging from 0.1-15 MPa. Schedler et al. (2014) reported that alkane degraders grew well on n-alkanes at high pressure, although at slightly decreased growth rate; the aromatic hydrocarbon degraders also grew well at pressure up to 8.8 MPa, with growth decreased as pressure further increased. However, conversion of naphthalene PAH

was complete under both ambient pressure and high pressures up to 12 MPa, and slightly reduced when pressures were further increased to 13 MPa. Similarly, Schwarz et al. (1974; 1975) conducted studies of the effects of hydrostatic pressure on hydrocarbon biodegradation. They tested degradation of tetradecane, hexadecane, and a mixed hydrocarbon substrate by a mixed culture of deep-sea sediment bacteria and found that at 20°C and 25°C under 500atm biodegradation was only moderately delayed as compared to under 1atm; at 4°C, however, 94% of the hexadecane was utilized after a 40-week incubation under conditions of high pressure, as compared with only 8 weeks (to reach 94% degraded) at ambient pressure.

An indirect pressure effect on biodegradation of hydrocarbons, particularly PAHs, is the potentially enhanced bioavailability under high pressure and high temperature reservoir conditions. In such environment, increased fraction of otherwise sparingly soluble PAHs such as phenanthrene and fluoranthene could be partitioned into the gas phase rather than the liquid phase (Zick, 2013). After the gas phase was released to the ambient seawater, gases are dissolved into the ambient seawater as the mixture of oil and gas rise to the trapping depth of the plume. After the gases are removed through dissolution, other hydrocarbon compounds inside the gas phase would likely be transported directly from the gas phase to the ambient seawater aqueous phase as well, and become bioavailable for the degradation of microorganisms. Increased aqueous solubility, vapor pressure, and Henry's law constant of PAHs have been documented (Abou-Naccoul et al., 2014). And rapid extraction of solid phase PAH contaminants by pressurized compression-decompression cycles has been developed as a new engineering approach for extraction of PAHs from contaminated soils and sediments (Anitescu and Tavlarides, 2006; Hong and Nakra, 2009).

C.3.1.3 Dissolved oxygen

Molecular oxygen is both an essential reactant in the initial activation of hydrocarbons under aerobic conditions and the most energetically favorable terminal electron acceptor for microbial growth (Diaz, 2004; Prince and Walters, 2007). Hence in the mixing layer and upper water column wherever dissolved oxygen is available, aerobic catabolism of hydrocarbons is usually the preferred biochemical pathway (Leahy and Colwell, 1990). The initial steps in the aerobic catabolism of aliphatic, cyclic, and aromatic hydrocarbons by bacteria and fungi involve the oxidation of the substrate by oxygenases, for which molecular oxygen is required (Leahy and Colwell, 1990).

Monitoring of dissolved oxygen concentrations was a priority for the water quality monitoring program during DWH oil spill emergency response phase (e.g., JAG report Review of *R/V Brooks McCall* Data to Examine Subsurface Oil). There was concern over the possibility of hypoxia due to rapid microbial respiration of oil hydrocarbons and other organic materials in subsurface waters. Hypoxia occurs when dissolved oxygen (DO) becomes lower than 2 mg L^{-1} (63 µmol O_2 dm^{-3}) in coastal waters (Diaz and Rosenberg, 2008). The field monitoring data of dissolved oxygen in the water column does not show the existence of hypoxia induced by subsurface plume respiration (JAG 2010). Nevertheless, the subsurface DO profiles provided extensive datasets to estimate the extent of hydrocarbon biodegradation in the water column (Camilli et al., 2010; Du and Kessler, 2012; Edwards et al., 2011; Kessler, 2011; Reddy et al., 2012; Redmond and Valentine, 2011; Ryerson et al., 2012; Valentine, 2010).

Biodegradation of hydrocarbons can proceed under both aerobic and anaerobic conditions (Prince and Walters, 2007). Oxygen may become limiting in subsurface sediments and anoxic zones of the water column, under which circumstances the anaerobic biodegradation of

hydrocarbons may be important (Botton and Parsons, 2006; Krumholz et al., 1996; Lovley, 2000). Although there appears to be the apparent preference for degradation of alicyclic compounds under anaerobic biodegradation (Prince and Walters, 2007), the degradation rates of hydrocarbons under anaerobic conditions are usually orders-of-magnitude lower than under aerobic conditions (NRC, 2003 references therein).

C.3.1.4 Nutrients

The release of hydrocarbons into aquatic environments that contain low concentrations of inorganic nutrients often produces a situation with exceedingly high carbon/nitrogen or carbon/phosphorus ratios that is unfavorable for microbial growth (Atlas, 1984; Leahy and Colwell, 1990). There is evidence that the availability of nitrogen and phosphorous limits the biodegradation of hydrocarbons in estuarine water and sediment, seawater (Atlas and Bartha, 1972b), and marine sediment (Leahy and Colwell, 1990).

Bioremediation of hydrocarbon pollutants in beach shorelines, freshwater and saltwater marshes with amendment of nutrients has been investigated (Boufadel et al., 1999; Braddock et al., 1997; Fernãndez-Ãlvarez et al., 2006; Garcia-Blanco et al., 2007; Jimenez et al.,2006; Macnaughton et al., 1999; Venosa et al., 2002; Venosa et al., 1996; Wrenn et al., 1997). Theoretically, approximately 150 mg of nitrogen and 30 mg of phosphorus are utilized in the conversion of 1 g of hydrocarbon to cell materials (Rosenberg and Ron, 1996). Various values of the optimal nitrogen concentration (ranging from 1.5 to 25 mg N/L) have been reported for supporting near maximal biodegradation of hydrocarbons and oils in laboratory microcosms studies (Venosa et al., 2002). Adding nutrients, however, may not always enhance hydrocarbon biodegradation. A field trial of hydrocarbon bioremediation in freshwater wetlands concluded that dissolved oxygen rather than nutrients was the limiting factor for effective biodegradation of hydrocarbon contaminants, and therefore natural attenuation was recommended as the optimum approach for the restoration of the system (Venosa et al., 2002). In a contaminated shoreline area of the Prince William Sound, pockets of highly weathered petroleum hydrocarbons were found in the presence of high concentrations of nutrients, indicating that other factors would have to be limiting factor for the lingering oil after the contamination event (Atlas & Bragg, 2009; Boufadel et al., 2010; Venosa et al., 2010). Conversely, at hydrocarbon concentrations representative of spilled petroleum hydrocarbons in an open marine environment after application of chemical dispersants, the biodegradation rate suggested that biodegradation was not limited by inorganic nutrients in seawater (Lee et al., 2013; Prince et al., 2013).

Shiller and Joung (2012) examined correlated depletions of nitrate, phosphate and oxygen in the submerged Deepwater Horizon plumes and conclude that a substantial portion of hydrocarbons in these plumes was converted to biomass, contrasting with nutrient-limited surface waters where other work has suggested hydrocarbon-induced microbial growth to have been minimal.

C4. Degradation algorithm and rate coefficients in existing models

Fate algorithms depicting degradation of oil in seawater are important in quantifying oil spill behavior and oil fate in models. The most frequently used model to describe biodegradation rate

of oil is the first-order degradation equation. The degradation rate is based on the removal rate of either the whole oil, or the individual hydrocarbon components of oil.

In environments with low and relatively constant biomass, like seawater, degradation rates are often determined by first-order rate kinetics (Battersby, 1990; Brakstad et al., 2008), which is convenient for use in numerical models (e.g., SIMAP) and commonly used in many laboratory and field studies (Chen et al., 2008; Venosa and Holder 2007; Venosa et al., 1996; Zahed et al., 2011). Stewart et al. (1993) reviewed degradation rates of oil at different concentrations over several orders of magnitude and found when temperature-corrected degradation rates from all systems are plotted versus initial oil concentration on a logarithmic scale, the slope of the regressed line approached unity, indicating that the process can be interpreted as first-order with respect to oil concentration.

According to the first-order decay algorithm, the degradation rate (g/L/d) is given as,

$$R_{h,i} = \frac{dC_{h,i}}{dt} = -k_{h,i}C_{h,i} \qquad \text{Eq 1}$$

where

h: hydrocarbon compound (or compound group (i.e., "component"), such as AR1-3, AL1-3, and residual);
i: environmental compartment (water or shoreline surface, upper and lower water column, and sediments);
$R_{h,i}$: loss rate of the mass of compound (or compound group) h in oil through degradation in environmental compartment i ($g \cdot m^{-3} \cdot d^{-1}$);
$k_{h,i}$: 1st order degradation constant for compound (or compound group) h in environmental compartment i (d^{-1});
$C_{h,i}$: Aqueous phase concentration of compound (or compound group) h in the environmental compartment i ($g \cdot m^{-3}$).

Half life ($\lambda_{h,i}$) of a component is calculated from the degradation constant using:

$$\lambda_{h,i} = 0.693/ k_{h,i.}$$

The degradation constant, K_{hi}, may include all degradation processes. Distinct values of K_i may be specified for whole oil and specific constituent groups (n-alkanes, aromatics, etc.) in each compartment. For dissolved compounds, the disappearance rates of the component group hydrocarbon concentrations may be used to estimate the degradation rates. Degradation of particulate oil requires colonization by the microbes and extracellular surfactant transfer of individual compounds into the cells. These complex processes are combined into a single rate constant for input to the model.

Table C-1 lists the degradation rate coefficients of whole oil and the aromatic components in various environment compartments used in the NRDAM/CME Type A oil fate model (French McCay et al., 1996) and early versions of SIMAP. In this appendix, updated model inputs are developed.

Similarly, the Oil Spill Contingency and Response (OSCAR) model employs degradation coefficients (Table C-2) for individual component or component groups (Reed et al., 2001).

Brakstad and Faksness (2000) determined biodegradation of oil compounds in water-accommodated fractions (WAFs) and dispersed oils after discharge into seawater in the project "Advances Management of Oil Spills (AMOS)". WAFs in seawater were generated by careful stirring in flasks according to a procedure established by the "Chemical Response to Oil Spills: Ecological Effect Research Forum (CROSERF)", with subsequent separation from the oil phase. Primary biodegradation of selected oil components were measured as transformation by GC-FID and GC-MS analysis in both WAFs and dispersed oils during a period of 7 days (WAFs) or 14 days (dispersed oils), and transformation rates were calculated after corrections for abiotic disappearance. Biodegradation was determined for various oils, for fresh and weathered oil, and for oil treated with a chemical dispersant. The degradation data were included in the OSCAR spill simulation model (Reed et al., 2001) for computation of behavior and fates of oil spills.

Table C-1: Degradation rate coefficients for whole oil and aromatics in different environmental compartments in NRDAM/CME Type A fate model (French-McCay, et al., 1996).

Degradation rate	Description	Unit	Value	Source of information
Degradation rate for whole oil in water	Instantaneous degradation rate for whole oil in water	1/day	0.01	French McCay et al., 1996
Degradation rate for whole oil in sediments	Instantaneous degradation rate for whole oil in sediments	1/day	0.001	French McCay et al., 1996
Degradation rate for whole oil on surface	Instantaneous degradation rate for whole oil on surface exposed to air	1/day	0.01	French McCay et al., 1996
Degradation rate for aromatics in water	Instantaneous degradation rate for aromatics in water	1/day	0.04	French McCay et al., 1996
Degradation rate for aromatics in sediments	Instantaneous degradation rate for aromatics in sediments	1/day	0.004	French McCay et al., 1996

Table C-2: Degradation rate coefficients of individual components or component groups in OSCAR (Reed et al., 2001).

No	Chemical component or component group	Transformation rates WAF (d^{-1})	Transformation rates aerobic sediments (d^{-1})	Transformation rates droplets (d^{-1})	Vapor pressure (atm)	Solubility (mg/l)
1	C1-C4 gasses	1.00E+00	1.00E+00	1.00E-01	2.96E+01	4.00E+00
2	C5-saturates (n-/iso-/cyclo)	2.88E-01	1.00E-01	1.00E-01	6.27E-01	9.50E+00
3	C6-saturates (n-/iso-/cyclo)	2.48E-01	1.00E-01	1.00E-01	1.90E-01	3.25E+00
4	Benzene	2.66E-01	1.00E-01	1.00E-01	1.29E-01	1.78E+03
5	C7-saturates (n-/iso-/cyclo)	2.67E-01	1.00E-01	1.00E-01	8.70E-02	9.00E+00

No	Chemical component or component group	Transformation rates WAF (d^{-1})	Transformation rates aerobic sediments (d^{-1})	Transformation rates droplets (d^{-1})	Vapor pressure (atm)	Solubility (mg/l)
6	C1-Benzene (Toluene)	4.62E-01	1.00E-01	1.00E-01	3.83E-02	5.12E+02
7	C8-saturates (n-/iso-/cyclo)	2.67E-01	1.00E-01	1.00E-01	2.86E-02	4.35E+00
8	C2-Benzene (xylenes)	4.33E-01	1.00E-01	1.00E-01	1.06E-02	1.75E+02
9	C9-saturates (n-/iso-/cyclo)	2.67E-01	1.00E-01	1.00E-01	7.76E-03	2.05E-01
10	C3-Benzene	4.33E-01	1.00E-01	1.00E-01	4.30E-03	5.75E+01
11	C10-saturates (n-/iso-/cyclo)	2.00E-01	7.30E-03	1.02E-01	1.68E-03	1.00E-04
12	C4-Benzenes	3.85E-01	1.00E-01	1.00E-01	1.19E-03	1.25E+01
13	C11-C12	2.00E-01	7.70E-03	8.25E-02	4.90E-04	1.00E-04
14	Phenols (C0-C4 alkylated)	2.00E-01	8.94E-02	1.00E-02	2.93E-04	5.10E+04
15	Naphthalenes (C0-C1 alkylated)	6.30E-01	4.00E-02	1.73E-01	1.32E-04	2.75E+01
16	C13-C14	2.00E-01	6.70E-02	7.37E-02	5.88E-05	1.00E-04
17	UCM C10-C36	1.17E-01	1.00E-03	1.00E-02	4.45E-05	1.50E+02
18	Naphthalenes (C2-C3 alkylated)	4.95E-01	3.60E-02	6.08E-02	1.26E-05	5.50E+00
19	C15-C16	2.00E-01	3.90E-03	7.07E-02	7.80E-06	1.00E-04
20	PAH 1 (3 rings, non-alkylated)	4.62E-01	2.54E-02	6.60E-03	3.11E-06	3.65E+00
21	C17-C18	2.00E-01	4.90E-03	7.07E-02	1.20E-06	1.00E-04
22	C19-C20	2.00E-01	4.00E-03	6.35E-02	1.97E-07	1.00E-05
23	C21-C25	2.00E-01	4.10E-03	6.47E-02	1.82E-08	1.00E-06
24	PAH 2 (3 rings-alkylated, 4-5+ rings)	4.08E-01	1.80E-03	1.00E-03	1.72E-09	1.01E-01
25	C25+ (Total)	2.00E-01	3.30E-03	3.76E-02	1.14E-09	1.00E-06

C5. US EPA EPI Suite Environmental fate estimation programs hydrocarbon first-order degradation rates

The US Environmental Protection Agency (EPA) Office of Pollution Prevention Toxics and Syracuse Research Corporation have developed the Estimation Program Interface (EPI) Suite – a Windows-based suite of physical/chemical property and environmental fate estimation programs (http://www.epa.gov/oppt/exposure/pubs/episuitedl.htm). In EPI Suite, BioHCwin was developed to estimate biodegradation half-life for compounds containing only carbon and hydrogen, i.e., petroleum hydrocarbons. The methodology of BioHCwin is described in Howard et al. (2005). BioHCwin is a predictive model for determining quantitative primary biodegradation

half-lives of individual petroleum hydrocarbons. This model uses a fragment-based approach similar to that within the Biodegradation Probability Estimation Program (BIOWIN of EPI Suite), which is a suite of seven different models currently used by the US EPA and the European Union Working Group addressing persistent, bio-cumulative, and toxic compounds as an initial persistence screen when reliable experimental biodegradation data in environmentally relevant media are not available. The biodegradation references for the studied compounds were obtained from the BIOLOG and DATALOG files of the Environmental Fate Data Base (EFDB) of the Syracuse Research Corporation (Howard et al., 1986). Preferences were given to studies run under environmentally relevant conditions (e.g., grab and field studies in which the initial test concentrations were not unrealistically high, the temperature within the environmental range, additional microorganisms were not added, and the inoculum was not pre-acclimated to hydrocarbons).

Table C-3 lists biodegradation half-lives of representative petroleum hydrocarbons included in the BioHCwin software program. There are three columns of BioHCwin estimates of each hydrocarbon compound. The first column value of the Recommended half-life of each compound was primarily biodegradation data either directly obtained from literature or calculated assuming first-order kinetics if sufficient experimental data were available (Howard et al., 2005). From the primary biodegradation data that were compiled for each hydrocarbon structure, a single recommended biodegradation half-life was chosen for use in the regression analysis. This was necessary for model development, although biodegradation rates for a single compound can easily span an order of magnitude given the variability of study designs and conditions found in the literature (Howard et al., 2005). The second column shows the value of the predicted half-life based on a linear model describing weighted coefficients from a total of 31 structural fragments. The detailed regression analysis of the model development and the derived intercept and coefficients of different fragments can be found in Howard et al. (2005). The third column lists the residual of model prediction (i.e., the difference of prediction subtracted by the recommended value); smaller residuals correspond to the better match of model prediction and the recommended experimentally-based biodegradation half-life results.

Table C-3: Biodegradation rates of individual hydrocarbon compounds in BioHCwin.

			BioHCwin	
		Recommended	Estimated	Estimation
		Half-life	Half-life	Residual
CAS No.	Hydrocarbon	days	days	days
0	1-(3'-Methylbutyl)-7-cyclohexyltetralin	162	68	94
21964498	1,13-Tetradecadiene	13	13	0
1638262	1,1-Dimethylcyclopentane	19	21	-2
488233	1,2,3,4-Tetramethylbenzene	4	4	0
526738	1,2,3-Trimethylbenzene	4	4	0
95932	1,2,4,5-Tetramethylbenzene	7	4	3
933982	1,2-Dimethyl-3-ethylbenzene	6	5	1

			BioHCwin	
		Recommended	Estimated	Estimation
583573	1,2-Dimethylcyclohexane	18	5	13
108678	1,3,5-Trimethylbenzene	3	4	-1
141935	1,3-Diethylbenzene	7	5	2
874419	1,3-Dimethyl-4-ethylbenzene	4	5	-1
2453001	1,3-Dimethylcyclopentane	4	4	0
1758889	1,4-Dimethyl-2-ethylbenzene	3	5	-2
571584	1,4-Dimethylnaphthalene	15	14	1
13849962	17alpha(H), 21beta(H)-Hopane	1000	1072	-72
53584591	17alpha(H)-22,29,30-Trisnorhopane	1000	988	12
0	18alpha(H)-22,29,30-Trisnorneohopane	1000	933	67
1074175	1-Methyl-2-n-propylbenzene	3	6	-3
620144	1-Methyl-3-ethylbenzene	3	5	-2
622968	1-Methyl-4-ethylbenzene	4	5	-1
0	1-Methyl-7-cyclohexyltetralin	18	32	-14
832699	1-Methylphenanthrene	23	24	-1
464062	2,2,3-Trimethylbutane	6	9	-3
564023	2,2,3-Trimethylpentane	7	11	-4
540841	2,2,4-Trimethylpentane	40	11	29
3522949	2,2,5-Trimethylhexane	18	13	5
75832	2,2-Dimethylbutane	19	7	12
590738	2,2-Dimethylhexane	4	9	-5
590352	2,2-Dimethylpentane	7	8	-1
1069530	2,3,5-Trimethylhexane	8	9	-1
95158	2,3-Benzothiophene	25	19	6
584941	2,3-Dimethylhexane	26	7	19
2213232	2,4-Dimethylheptane	6	8	-2
589435	2,4-Dimethylhexane	7	7	0
108087	2,4-Dimethylpentane	48	6	42
592132	2,5-Dimethylhexane	25	7	18
15869893	2,5-Dimethyloctane	2	9	-7
592278	2-Methylheptane	3	6	-3
591764	2-Methylhexane	3	5	-2
91576	2-Methylnaphthalene	14	9	5
3221612	2-Methyloctane	5	7	-2
2531842	2-Methylphenanthrene	23	24	-1

			BioHCwin	
		Recommended	Estimated	Estimation
563166	3,3-Dimethylhexane	5	9	-4
583482	3,4-Dimethylhexane	3	7	-4
619998	3-Ethylhexane	4	6	-2
617787	3-Ethylpentane	4	5	-1
589811	3-Methylheptane	3	6	-3
589344	3-Methylhexane	9	5	4
0	3-Methylindene	3	4	-1
589537	4-Methylheptane	4	6	-2
824226	4-Methylindan	2	3	-1
874351	5-Methylindan	2	3	-1
0	6-Cyclohexyltetralin	11	15	-4
2294828	9-Ethylfluorene	29	38	-9
83329	Acenaphthene	39	19	20
120127	Anthracene	123	123	0
71432	Benzene	6	5	1
56553	Benzo(a)anthracene	286	344	-58
205992	Benzo(b)fluoranthene	282	285	-3
192972	Benzo(e)pyrene	365	422	-57
191242	Benzo(ghi)perylene	562	517	45
205823	Benzo(j)fluoranthene	300	285	15
207089	Benzo(k)fluoranthene	351	285	66
56832736	Benzofluoranthene	305	285	20
92524	Biphenyl	31	31	0
191071	Coronene	733	634	99
287923	Cyclopentane	50	45	5
2292797	Diadamantane	2000	861	1139
189559	Dibenzo(a,l)pyrene	296	627	-331
132650	Dibenzothiophene	36	28	8
70021475	Dimethyldibenzothiophene	51	71	-20
28804888	Dimethylnaphthalene	15	14	1
29062984	Dimethylphenanthrene	44	38	6
0	endo, endo-Dihydrodi(norbornadiene)	1000	2350	-1350
1678917	Ethylcyclohexane	2	9	-7
0	exo-Tetrahydrodi(cyclopentadiene)	1000	752	248
206440	Fluoranthene	147	191	-44
496117	Indan	6	3	3

			BioHCwin	
		Recommended	Estimated	Estimation
95136	Indene	3	2	1
193395	Indeno(1,2,3-cd)pyrene	330	349	-19
98828	Isopropylbenzene	15	11	4
0	Methyl ethyloctane	4	10	-6
41637905	Methylchrysene	156	132	24
96377	Methylcyclopentane	4	6	-2
30995643	Methyldibenzothiophene	40	44	-4
26914170	Methylfluorene	19	24	-5
28652815	Methylphenanthrene	23	24	-1
2381217	Methylpyrene	92	109	-17
108383	m-Xylene	10	4	6
91203	Naphthalene	3	6	-3
61523340	Naphthobenzothiophene	36	41	-5
124185	n-Decane	9	9	0
112403	n-Dodecane	10	12	-2
544854	n-Dotriacontane	284	292	-8
629947	n-Heneicosane	25	47	-22
593497	n-Heptacosane	141	90	51
629787	n-Heptadecane	20	25	-5
630013	n-Hexacosane	100	78	22
544763	n-Hexadecane	17	22	-5
110543	n-Hexane	9	5	4
630035	n-Nonacosane	100	123	-23
630024	n-Octacosane	125	105	20
593453	n-Octadecane	21	29	-8
111659	n-Octane	9	6	3
25663029	Norpristane	31	35	-4
629629	n-Pentadecane	26	19	7
646311	n-Tetracosane	114	57	57
629594	n-Tetradecane	23	16	7
14167590	n-Tetratriacontane	383	397	-14
638686	n-Triacontane	175	143	32
629505	n-Tridecane	12	14	-2
630057	n-Tritriacontane	363	340	23
95476	o-Xylene	6	4	2
198550	Perylene	898	422	476
638368	Phytane	42	55	-13
1921706	Pristane	42	47	-5

			BioHCwin	
		Recommended	Estimated	Estimation
106423	p-Xylene	9	4	5
108883	Toluene	2	4	-2
28652779	Trimethylnaphthalene	24	23	1
217594	Triphenylene	378	344	34
110827	Cyclohexane	50	55	-5
527537	1,2,3,5-Tetramethylbenzene	3	4	-1
95636	1,2,4-Trimethylbenzene	4	4	0
934805	1,2-Dimethyl-4-ethylbenzene	5	5	0
2452995	1,2-Dimethylcyclopentane	4	4	0
934747	1,3-Dimethyl-5-ethylbenzene	2	5	-3
3258875	17beta(H), 21alpha(H)-Norhopane	1000	799	201
611143	1-Methyl-2-ethylbenzene	4	5	-1
90120	1-Methylnaphthalene	14	9	5
1071267	2,2-Dimethylheptane	6	11	-5
560214	2,3,3-Trimethylpentane	53	11	42
565753	2,3,4-Trimethylpentane	15	8	7
581408	2,3-Dimethylnaphthalene	15	14	1
565593	2,3-Dimethylpentane	7	6	1
2216300	2,5-Dimethylheptane	6	8	-2
609267	2-Methyl-3-ethylpentane	6	7	-1
0	2-Methylindene	3	2	1
562492	3,3-Dimethylpentane	9	8	1
2216333	3-Methyloctane	5	7	-2
644086	4-Methylbiphenyl	38	31	7
2216344	4-Methyloctane	5	7	-2
779022	9-Methylanthracene	260	197	63
208968	Acenaphthylene	38	31	7
281232	Adamantane	1000	52	948
238846	Benzo(a)fluorene	141	348	-207
50328	Benzo(a)pyrene	224	422	-198
203123	Benzo(ghi)fluoranthene	350	235	115
11095435	Benzothiophene	25	19	6
1176449	C30 Moretane [17beta(H), 21alpha(H)-Hopane]	1000	1072	-72
218019	Chrysene	378	344	34
53703	Dibenz(a,h)anthracene	420	511	-91
100414	Ethylbenzene	8	5	3

			BioHCwin	
		Recommended	Estimated	Estimation
1640897	Ethylcyclopentane	15	7	8
86737	Fluorene	44	15	29
538932	Isobutylbenzene	10	8	2
108872	Methylcyclohexane	4	7	-3
30997398	Methylfluoranthene	25	73	-48
1321944	Methylnaphthalene	6	9	-3
67526856	Methylnaphthobenzothiophene	66	16	50
629970	n-Docosane	125	42	83
112958	n-Eicosane	25	40	-15
630046	n-Hentriacontane	276	251	25
142825	n-Heptane	7	5	2
629925	n-Nonadecane	18	34	-16
111842	n-Nonane	9	7	2
629992	n-Pentacosane	121	67	54
109660	n-Pentane	5	4	1
103651	n-Propylbenzene	4	6	-2
638675	n-Tricosane	145	49	96
1120214	n-Undecane	7	10	-3
85018	Phenanthrene	42	15	27
129000	Pyrene	237	283	-46
111013	Squalane	42	333	-291
119642	Tetralin	8	1	7
30232269	Trimethylphenanthrene	83	61	22

C6. Review of Oil and hydrocarbon first-order degradation rates and half-lives in laboratory experimental studies

Several recent studies investigated the first-order degradation rates of specific components or compound groups of petroleum hydrocarbons in marine environmental conditions. In this Chapter, the key papers that reported first-order biodegradation rates of petroleum hydrocarbon compounds or compound groups are reviewed and the reported rates (either expressed in half-lives of starting compounds or the first-order rate coefficients) are tabulated, and the main experimental conditions are also described.

C.6.1 Brakstad et al. (2015)

In this study, experiments were set up to investigate the biodegradation of volatile and semi-volatile hydrocarbons and oil compound groups in oil droplets that were dispersed into different size distribution groups, one with a volume median diameter of 10 microns and the other 30 microns. Both groups were incubated at low temperature to simulate the biodegradation of well dispersed oil at subsea environment, with nominal oil concentration of 2 mg/L in natural unfiltered seawater as well as in sterile-filtered (0.2µm) seawater killed control to minimize bacterial growth. A gas chromatograph coupled to a flame ionization detector (GC-FID) was used for quantification of extracted C10–C36 saturates separated according to boiling points, termed as total petroleum hydrocarbons extractable organic carbon (TEOC), while 96 individual targeted compounds (C_{10}–C_{36} n-alkanes, decalines, phenols, 2- to 5-ring PAH) and 17a(H),21b(H)-Hopane (30ab Hopane) were analyzed in a gas chromatograph coupled to a mass spectrometer (GC–MS, operated in Selected Ion Monitoring [SIM] modus). Dispersions were acidified (pH < 2) for analyses of 87 targeted volatile organic carbon (VOC) compounds in a Purge & Trap unit coupled to a GC–MS (P&T GC–MS). The VOC and SVOC target compounds included in GC – MS analyses are shown in Table C-4.

Table C-4: Analytical target groups from GC-MS analysis of volatile and semi-volatile compounds in Brakstad et al. (2015) study.

Groups	Compounds
C5-sat	Isopentane. n-C5 (Pentane). Cyclopentane
C6-sat	2.2-Dimethylbutane. 2-methylpentane. 3-Methylpentane. 2.3-dimethylbutane. n-C6 (Hexane). Methylcyclopentane. Cyclohexane
Benzene	Benzene
C7-sat	2.4-Dimethylpentane. 2.2-Dimethylpentane. 2-Methylhexane. 2.3-Dimethylpentane. 3-methylhexane. 2-Methyl-1-Hexene. n-C7 (Heptane). cis-3-Heptene. Methylcyclohexane
C1-Ben	Toluene
C8-sat	2.2.4-Trimethylpentane. 2.2.3-Trimethylpentane. 2.4-Dimethylhexane. 2.5-dimethylhexane. ctc-1.2.4-Trimethylcyclopentane. ctc-1.2.3-Trimethylcyclopentane. 3-ethylhexane. 2.3.4-Trimethylpentane.2.3.3-Trimethylpentane. 2.3-Dimethylhexane. 4-Methylheptane. 2-Methylheptane. 3-Methylheptane. ctt-1.2.4-Trimethylcyclopentane. 1-Octene. Isopropylcyclopentane. n-C8 (Octane). trans-2-Octene. Ethylcyclohexane
C2-Ben	Ethylbenzene. m-Xylene. p-Xylene. o-Xylene.
C9-sat	2.4-Dimethylheptane. 1.1.4-Trimethylcyclohexane. ctt-1.2.4-Trimethylcyclohexane. 2.3-Dimethylheptane. 2-Methyloctane. 4-Methyloctane. 1.2.4-Trimethylcyclohexane. 1-Nonene. trans-2-Nonene. n-C9 (Nonane). Isopropylcyclohexane. Butylcyclopentane
C3-Ben	Isopropylbenzene. Propylbenzene. 1-Methyl-3-ethylbenzene. 1-Methyl-4-ethylbenzene. 1.3.5-Trimethylbenzene. 1-Methyl-2-ethylbenzene. 1.2.4-Trimethylbenzene. 1.2.3-Trimethylbenzene. Indane
C10-sat	C10 saturates based on boiling point. n-C10

Groups	Compounds
C4-Ben	Tert-butyl-Benzene. sec-butylbenzene. m-Cymene. o-Cymene. p-Cymene. 1.3-Diethylbenzene.1-Methyl-3-propylbenzene. 1.4-Diethylbenzene. 1-Methyl-2-propylbenzene. 1-Methyl-4-Propylbenzene. n-Butylbenzene. 1.2-Diethylbenzene. 1.3-Dimethyl-5-Ethylbenzene. 1.4-Dimethyl-2-Ethylbenzene. 1.2-Dimethyl-4-Ethylbenzene. 2.4-dimethylethylbenzen. 1.3-Dimethyl-2-Ethylbenzene. 1.2-Dimethyl-3-Ethylbenzene. 1.2.3.5-Tetramethylbenzene. 1.2.4.5-Tetramethylbenzene. n-Pentylbenzene. 1.2.3.4-Tetramethylbenzene
C11-12	C11-C12 saturates based on boiling point. nC11. nC12
Napht-1	Naphthalene. C1-naphthalenes
C13-14	C13-C14 saturates based on boiling point. nC13. nC14
Napht-2	C2-naphthalenes. C3-naphthalenes
C15-16	C15-C16 saturates based on boiling point. nC15. nC16
PAH-1	Benzo(b)thiophene. C1-benzo(b)thiophenes. C2-benzo(b)thiophene. C3-benzo(b)thiophenes. C4-benzo(b)thiophenes. C4-naphthalenes. Biphenyl. Acenaphthylene. Acenaphthene. Dibenzofuran. Fluorene. C1-fluorenes. C2-fluorenes. C3-fluorenes. Phenanthrene. Anthracene. C1-phenanthrenes/anthracenes. C2-phenanthrenes/anthracenes. C3-phenanthrenes/anthracenes. C4-phenanthrenes/anthracenes. Dibenzothiophene. C1-dibenzothiophenes.C2-dibenzothiophenes. C3-dibenzothiophenes. C4-dibenzothiophenes
C17-18	C17-C18 saturates based on boiling point. nC17. nC18
C19-20	C19-C20 saturates based on boiling point. nC19. nC20
C21-25	C21-C25 saturates based on boiling point; nC21. nC22. nC23. nC24. nC25
PAH-2	Fluoranthene. Pyrene. C1-fluoranthrenes/pyrenes. C2-fluoranthenes/pyrenes. C3-fluoranthenes/pyrenes. Naphthobenzothiophene. C1-Naphthobenzothiophene. C2-Naphthobenzothiophene. C3-Naphthobenzothiophene. C4-Naphthobenzothiophene. Benz(a)anthracene. Chrysene. C1-chrysenes. C2-chrysenes. C3-chrysenes. C4-chrysenes. Benzo(b)fluoranthene. Benzo(k)fluoranthene. Benzo(e)pyrene. Benzo(a)pyrene. Perylene. Indeno(1.2.3-c.d)pyrene. Dibenz(a.h)anthracene. Benzo(g.h.i)perylene. Retene. Benzo(b)fluorene
C25+	C26-C36 saturates based on boiling point. nC26. nC27. nC28. nC29. nC30. nC31. nC32. nC33. nC34. nC35. nC36

Depletion of semivolatile nC10 – nC36 alkanes and non-alkylated and alkyl-substituted decalines, naphthalenes, fluorenes, phenanthrenes, dibenzothiophenes, fluoranthenes and chrysenes were examined in the dispersions after normalization against the persistent biomarker 17a(H),21b(H)-Hopane (30ab Hopane), commonly used in biodegradation studies. VOC compounds determined by P&T GC – MS analyses could not be normalized against a biomarker, since analyses of these did not include any recalcitrant biomarker.

Figure C-3A and Tables C-5 and C-6 present the first-order rate calculations of targeted semi-volatile n-alkanes, normalized against 30ab Hopane, for the oil droplet groups with VMD of 10µm and 30µm respectively. Figure C-3B and Tables C-7 and C-8 present the first-order rate calculations of targeted semi-volatile 2- to 4-ring PAH normalized against 30ab Hopane, for the 10µm and 30µm droplets, respectively. The estimated lag-phases were not included in the calculations of first-order rate coefficients and half-lives, based on the argument that in deepwater with bacteria re-entering the spill site and causing accelerated hydrocarbon

biodegradation (Valentine et al., 2012), in the result would be a situation in which hydrocarbon-stimulated bacterial populations eventually could degrade oil compounds without a preceding lag-phase. Half-lives calculated from the rate coefficients varied from 0.6 – 5.6 days (median 1.1 days) and 1.1 – 11.1 days (median 2.5 days) for nC10 – nC30 alkanes in 10 µm and 30 µm dispersions, respectively, while corresponding data for 2- to 4-ring PAH were 0.9 – 31.9 (median 5.3 days) and 0.9 – 54.9 days (median 10.2 days).

These data clearly support the abiotic dissolution of PAH and inhibited n-alkane biodegradation observed in dispersant-mediated oil at depth by Payne and Driskell (2015c). If the observed processes in field collected samples were biologically driven, alkanes would have disappeared first followed by slower removal of the PAH. The field-collected samples may have also reflected a lag-phase due to hydrocarbon toxicity in close proximity to the wellhead. With abiotic PAH dissolution of PAH (Payne and Driskell 2015c), there was no lag-phase and the PAHs were stripped from the smaller oil droplets (with high dispersant concentrations) before microbial degradation of the alkanes occurred to an appreciable extent.

These n-alkane and PAH biodegradation data are in good agreement with results from studies with chemically dispersed oils incubated at low temperature (-1 to +8°C), in which n-alkane depletion corresponded to half-lives of 2 - 10 days, while 2- to 4-ring PAH half-lives ranged 2 - 37 days (Siron et al., 1995; Venosa and Holder, 2007; Prince et al., 2013; McFarlin et al., 2014). The n-alkane data are also in agreement with results from the DWH deepwater plume samples and laboratory studies with microbial consortia or seawater from GoM, with average n-alkane (nC13-nC26) half-lives of 1.2 – 6.1 days (Hazen et al., 2010). The PAH results are consistent with a recent study with small droplet (10 – 30 µm) dispersions of Macondo oil in GoM deepwater, in which biotransformation of 2 – 3 ring PAH appeared after 9 - 39 days of incubation, while 4 – 6 ring PAH transformation had started after 39 days of incubation (Wang et al., 2014).

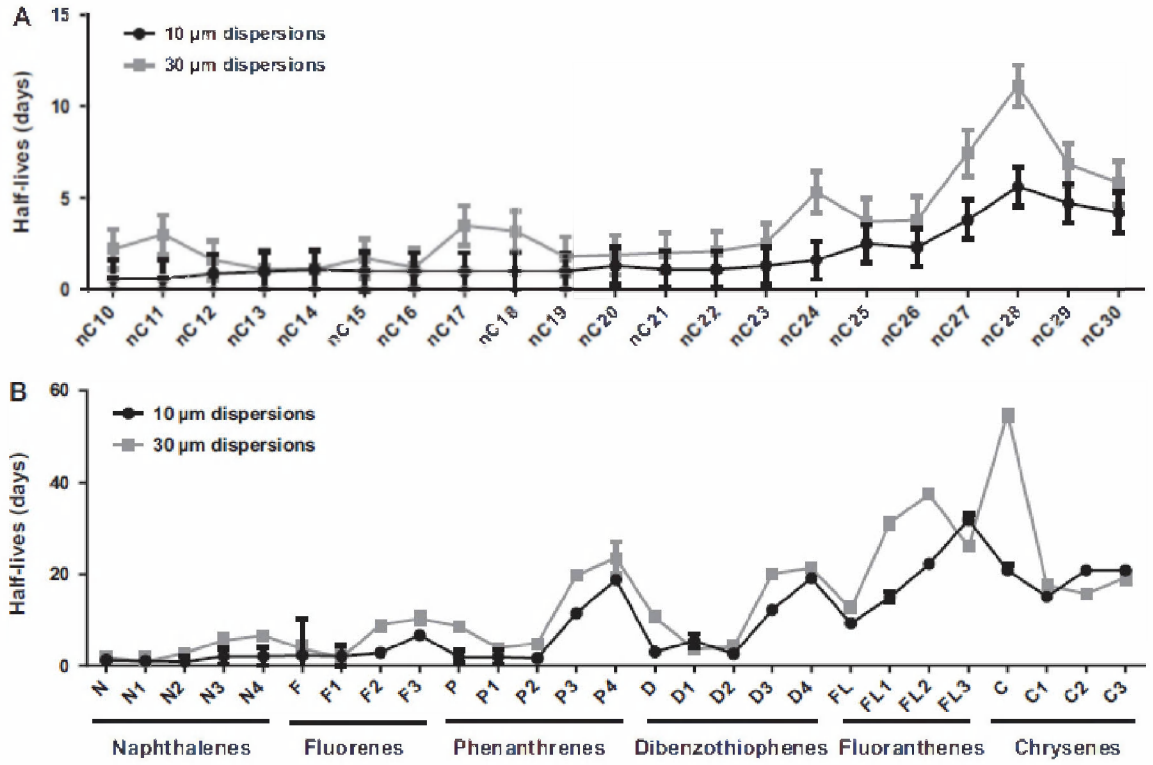

Figure C-3. Half-lives of nC10 – nC30 alkanes (A) and naphthalenes, fluorenes, phenanthrenes, dibenzothiophenes, fluoranthenes and chrysenes (B) in 10 µm and 30 µm dispersions with standard deviation errors bars of 3 replicates. Half-lives were determined from rate coefficients without lag-periods included. The numbering of the aromatic groups describes the degree of alkyl-substitution.

Table C-5: Degradation Rate Coefficients of C10-C30 n-alkanes in 10 µm Macondo oil dispersions.

Table S2A	Kinetics data for nC10-nC30 alkanes in 10 µm Macondo oil dispersions			
Groups	Lag-phase	Rate coefficient	Half-life	Half-life + lag-phase
	(days)	(day^{-1})	(days)	(days)
nC10	1.4	1.1930	0.6	2
nC11	1.9	1.0680	0.6	2.5
nC12	2.0	0.7297	0.9	2.9
nC13	2.0	0.6622	1.0	3
nC14	2.0	0.6487	1.1	3.1
nC15	1.9	0.6692	1.0	2.9
nC16	1.9	0.7227	1.0	2.9
nC17	1.9	0.7249	1.0	2.9
nC18	1.9	0.6931	1.0	2.9
nC19	1.9	0.6757	1.0	2.9

Table S2A	Kinetics data for nC10-nC30 alkanes in 10 µm Macondo oil dispersions			
Groups	Lag-phase	Rate coefficient	Half-life	Half-life + lag-phase
nC20	1.8	0.5419	1.3	3.1
nC21	1.9	0.6143	1.1	3
nC22	1.9	0.6055	1.1	3
nC23	1.9	0.5268	1.3	3.2
nC24	1.9	0.4376	1.6	3.5
nC25	1.9	0.2745	2.5	4.4
nC26	2.9	0.3031	2.3	5.2
nC27	2.0	0.1842	3.8	5.8
nC28	2.0	0.1227	5.6	7.6
nC29	10.1	0.1472	4.7	14.8
nC30	13.4	0.1653	4.2	17.6

Table C-6: Degradation Rate Coefficients of C10-C30 n-alkanes in 30 µm Macondo oil dispersions.

Table S2B *	Kinetics data for nC10-nC30 alkanes in 30 µm Macondo oil dispersions			
Groups	Lag-phase	Rate coefficient	Half-life	Half-life + lag-phase
	(days)	(day^{-1})	(days)	(days)
nC10	0.9	0.3150	2.2	3.1
nC11	1.4	0.2274	3.0	4.4
nC12	3.5	0.4289	1.6	5.1
nC13	3.6	0.6257	1.1	4.7
nC14	3.6	0.6265	1.1	4.7
nC15	3.4	0.4024	1.7	5.1
nC16	3.6	0.6004	1.2	4.8
nC17	3.5	0.1959	3.5	7.0
nC18	3.5	0.2201	3.2	6.7
nC19	3.3	0.3785	1.8	5.1
nC20	3.4	0.3661	1.9	5.3
nC21	3.3	0.3484	2.0	5.3
nC22	3.2	0.3228	2.1	5.3
nC23	3.0	0.2742	2.5	5.5
nC24	1.7	0.1307	5.3	7.0
nC25	2.8	0.1882	3.7	6.5
nC26	3.5	0.1809	3.8	7.3
nC27	1.4	0.0936	7.4	8.8
nC28	1.5	0.0626	11.1	12.6

Table S2B *	Kinetics data for nC10-nC30 alkanes in 30 µm Macondo oil dispersions			
Groups	Lag-phase	Rate coefficient	Half-life	Half-life + lag-phase
nC29	12.0	0.1022	6.8	18.8
nC30	15.0	0.119	5.8	20.8

Table C-7: Degradation Rate Coefficients of 2- to 4-ring aromatic compounds in 10 µm Macondo oil dispersions.

Table S2C	Kinetics data for 2- to 4-ring aromatic compounds in 10 µm Macondo oil dispersions			
Groups	Lag-phase	Rate coefficient	Half-life	Half-life + lag-phase
	(days)	(day^{-1})	(days)	(days)
Naphthalene	7.8	0.5665	1.2	9.0
C1-Naphthalenes	7.8	0.7061	1.0	8.8
C2-Naphthalenes	7.9	0.7855	0.9	8.8
C3-Naphthalenes	7.5	0.3539	2.0	9.5
C4-Naphthalenes	7.5	0.3504	2.0	9.5
Fluorene	7.5	0.3218	2.2	9.7
C1-Fluorenes	7.5	0.3391	2.0	9.5
C2-Fluorenes	7.6	0.2489	2.8	10.4
C3-Fluorenes	11.1	0.1055	6.6	17.7
Phenanthrene	7.5	0.3746	1.9	9.4
C1-Phenanthrenes/anthracenes	7.5	0.3574	1.9	9.4
C2-Phenanthrenes/anthracenes	11.3	0.4291	1.6	12.9
C3-Phenanthrenes/anthracenes	7.2	0.0606	11.4	18.6
C4-Phenanthrenes/anthracenes	12.0	0.0368	18.8	30.8
Dibenzothiophene	7.6	0.2405	2.9	10.5
C1-Dibenzothiophenes	7.0	0.1308	5.3	12.3
C2-Dibenzothiophenes	7.8	0.2817	2.5	10.3
C3-Dibenzothiophenes	9.9	0.0574	12.1	22.0
C4-Dibenzothiophenes	13.6	0.0363	19.1	32.7
Fluoranthene	6.7	0.0754	9.2	15.9
C1-Fluoranthenes/pyrenes	6.7	0.0465	14.9	21.6
C2-Fluoranthenes/pyrenes	13.3	0.0311	22.3	35.6
C3-Fluoranthenes/pyrenes	13.3	0.0217	31.9	45.2
Chrysene	20.0	0.0331	20.9	49.9
C1-Chrysenes	20.0	0.0463	15.0	35.0
C2-Chrysenes	20.0	0.0331	20.9	40.9
C3-Chrysenes	20.0	0.0331	20.9	40.9

Table C-8: Degradation Rate Coefficients of 2- to 4-ring aromatic compounds in 30 µm Macondo oil dispersions.

Table S2D *	Kinetics data for 2- to 4-ring aromatic compounds in 30 µm Macondo oil dispersions			
Groups	Lag-phase	Rate coefficient	Half-life	Half-life + lag-phase
	(days)	(day^{-1})	(days)	(days)
Naphthalene	7.8	0.3764	1.8	9.6
C1-Naphthalenes	7.8	0.7492	0.9	8.7
C2-Naphthalenes	7.9	0.2560	2.7	10.6
C3-Naphthalenes	8.0	0.1288	5.4	13.4
C4-Naphthalenes	6.7	0.1070	6.5	13.2
Fluorene	8.0	0.1905	3.6	11.6
C1-Fluorenes	7.6	0.3800	1.8	9.4
C2-Fluorenes	5.5	0.0787	8.8	14.3
C3-Fluorenes	11.1	0.0682	10.2	21.3
Phenanthrene	8.0	0.0812	8.5	16.5
C1-Phenanthrenes/anthracenes	7.0	0.1844	3.8	10.8
C2-Phenanthrenes/anthracenes	13.6	0.1448	4.8	18.4
C3-Phenanthrenes/anthracenes	7.2	0.0351	19.7	26.9
C4-Phenanthrenes/anthracenes	12.0	0.0294	23.6	35.6
Dibenzothiophene	5.5	0.0669	10.4	15.9
C1-Dibenzothiophenes	7.0	0.1944	3.6	10.6
C2-Dibenzothiophenes	15.6	0.1730	4.0	19.6
C3-Dibenzothiophenes	10.0	0.0344	20.1	30.1
C4-Dibenzothiophenes	13.0	0.0324	21.4	24.4
Fluoranthene	6.7	0.0561	12.4	19.1
C1-Fluoranthenes/pyrenes	6.7	0.0223	31.2	37.9
C2-Fluoranthenes/pyrenes	13.3	0.0185	37.4	50.7
C3-Fluoranthenes/pyrenes	21.8	0.0266	26.1	47.9
Chrysene	20.0	0.0126	54.9	74.9
C1-Chrysenes	20.0	0.0396	17.5	37.5
C2-Chrysenes	20.0	0.0443	15.7	35.7
C3-Chrysenes	20.0	0.0361	19.2	39.2

The resolved targeted compounds described above only cover a fraction of the oil. Comparison of TEOC concentrations (GC-FID analyses) with the targeted SVOC and VOC saturate and aromatic oil compound (GC – MS analyses) showed that the sum of the targeted compounds (n-

alkanes, 2 – 5 ring PAH, volatile C5 – C9 saturates and C0 – C5 benzenes) constituted 33.5% and 40.4% of the sum of TEOC and VOC concentration at the start of the experiment in the 10 µm and 30 µm dispersions, respectively.

Figure C-4 and Table C-9 and 10 present the calculated biotransformation rate coefficients and half-lives of 22 volatile and semi-volatile oil compound groups, representing the boiling point range described above (Table C-4), including C5 – C36 saturates and 1- to 5-ring aromatic compounds. The results showed rate coefficients of 0.0096 – 0.2665 (median 0.1692) in the 10 µm dispersions and 0.0054 – 0.2475 (median 0.0995) in the 30 µm dispersions, corresponding to half-lives of 2.8 to 72.2 days (median 4.1 days) and 2.8 to 128.3 days (median 7.2 days) in the 10 and 30 µm dispersions, respectively. The rate coefficients were generally higher for the aromatic (average of 0.175 d^{-1}) than the saturate (0.099 d^{-1}) oil compound groups, probably associated with the water-solubility of the aromatic hydrocarbons, as well as the presence of poorly biodegradable branched and cyclic alkanes in the semi-volatile saturate groups.

The saturates representing the C_{10} to C_{25+} oil compound groups are mostly unresolved complex mixtures (UCM) in the GC-FID profiles, which account for 60 – 70% of the groups and become the predominant oil fraction during the biodegradation period for UCM that is not readily susceptible to biodegradation. The UCMs were predominant in each of the saturate groups from C_{11} – C_{12} to C_{25+}, and their degradation rates decreased by increasing boiling point ranges.

The rate for the sum of the 22 oil compound groups was 0.040 d^{-1} and 0.020 d^{-1}, respectively, in the 10 µm and 30 µm oil droplet dispersions, corresponding to half-lives of 17.4 and 34.6 days. Since the sum of these groups may represent most of the oil, these numbers may be used as biotransformation rates for the oil, representing a boiling point range of 27 – 500+°C.

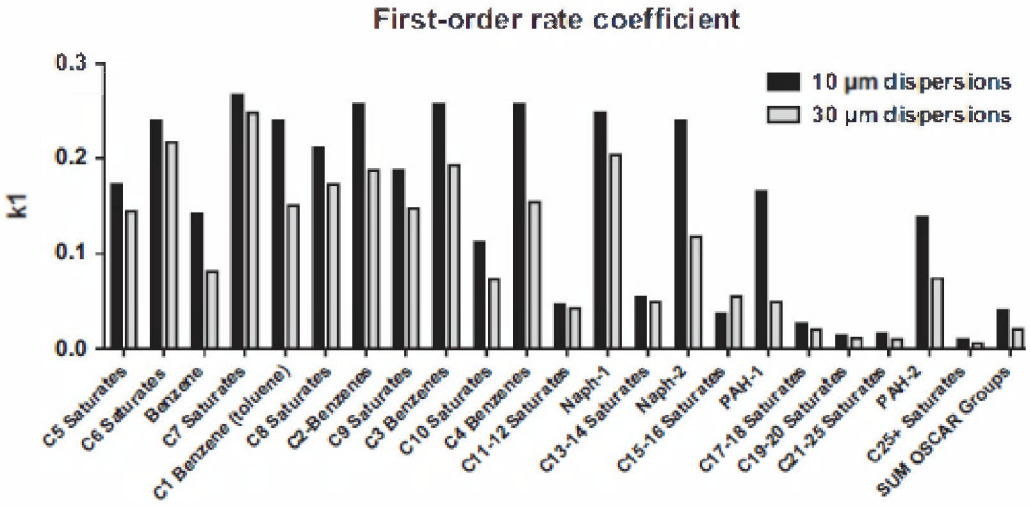

Figure C-4. First-order rate coefficients for oil compound groups of the Macondo oil in 10 and 30 µm dispersions.

Table C-9: Degradation Rate Coefficients of boiling-cut basis defined oil compound groups in 10 µm Macondo oil dispersions.

Groups	**Kinetics data for OSCAR oil compound groups in 10 µm Macondo oil dispersions**			
	Lag-phase	Rate coefficient	Half-life	Half-life + lag-phase
	(days)	(day^{-1})	(days)	(days)
C5-sat	5.0	0.1733	4.0	9.0
C6-sat	7.0	0.2390	2.9	9.9
Benzene	8.0	0.1414	4.9	12.9
C7-sat	7.0	0.2665	2.6	9.6
C1-Ben	7.0	0.2390	2.9	9.9
C8-sat	0.0	0.2100	3.3	3.3
C2-Ben	7.0	0.2567	2.7	9.7
C9-sat	0.0	0.1873	3.7	3.7
C3-Ben	7.0	0.2567	2.7	9.7
C10-sat	0.0	0.1118	6.2	6.2
C4-Ben	7.0	0.2567	2.7	9.7
C11-12	0.0	0.0462	15.0	15.0
Napht-1	7.0	0.2475	2.8	9.8
C13-14	0.0	0.0533	13.0	13.0
Napht-2	7.0	0.239	2.9	9.9
C15-16	0.0	0.0361	19.2	19.2
PAH-1	7.0	0.165	4.2	11.2
C17-18	0.0	0.0263	26.3	26.3
C19-20	0.1	0.0137	50.6	50.7
C21-25	0.0	0.0155	44.7	44.7
PAH-2	7.0	0.1386	5.0	12.0
C25+	0.1	0.0096	72.2	72.3

Table C-10: Degradation Rate Coefficients of boiling-cut basis defined oil compound groups in 30 µm Macondo oil dispersions.

Groups	Kinetics data for OSCAR oil compound groups in 30 µm Macondo oil dispersions			
	Lag-phase	Rate coefficient	Half-life	Half-life + lag-phase
	(days)	(day^{-1})	(days)	(days)
C5-sat	5.0	0.1444	4.8	9.8
C6-sat	7.0	0.2166	3.2	10.2
Benzene	8.0	0.0815	8.5	16.5
C7-sat	7.0	0.2475	2.8	9.8
C1-Ben	7.0	0.1507	4.6	11.6
C8-sat	0.0	0.1733	4.0	4.0
C2-Ben	7.0	0.1873	3.7	10.7
C9-sat	0.0	0.1474	4.7	4.7
C3-Ben	7.0	0.1925	3.6	10.6
C10-sat	0.0	0.0729	9.5	9.5
C4-Ben	7.0	0.1540	4.5	11.5
C11-12	0.0	0.0417	16.6	16.6
Napht-1	7.0	0.2038	3.4	10.4
C13-14	0.0	0.0491	14.1	14.1
Napht-2	7.0	0.1175	5.9	12.9
C15-16	0.0	0.0550	12.6	12.6
PAH-1	7.1	0.0491	14.1	21.2
C17-18	0.0	0.0196	35.4	35.4
C19-20	0.1	0.0105	66.0	66.1
C21-25	0.1	0.0099	70.0	70.1
PAH-2	17.0	0.0737	9.4	26.4
C25+	0.0	0.0054	128.3	128.3

C.6.2 Brakstad and Faksness (2000)

This study was carried out during the project "Advances Management of Oil Spills (AMOS)" to determine the biodegradation of oil compounds in the water accommodated fractions (WAF) and dispersed oils after their discharge to the seawater. WAF in seawater were generated from fresh crude Statfjord, Aquila, or Marine diesel, or Statfjord 250+^{o}C weathered crude oil in natural

seawater (collected from Norwegian Fjord) in flasks that were prepared according to the "Chemical Response to Oil Spills: Ecological Effect Research Forum (CROSERF)" standard procedure (Singer et al., 2000), with subsequent separation from the oil phase. Mechanically dispersed oils were generated and maintained by vigorous agitation. The initial oil-seawater loading ratios were 1:10,000 (i.e., a nominal oil concentration of 85 mg/L). Approximately 35 VOCs (C5-C9, including benzene, toluene, ethylbenzene and xylenes - BTEX) were analyzed by Purge and Trap GC – MS (P&T GC-MS). Approximately 60 PAH and phenol compounds were analyzed by GC-MS SIM analysis following extraction with dichloromethane (DCM). TEOC from C10 to C36 was determined by GC-FID on DCM extractions.

Figures C-5 and C-6 and Table C-11 show the group composition and concentrations in WAF and dispersed oil for a Statfjord fresh oil loaded at 1:10,000 in seawater, as well as their first-order biotransformation rates and half-lives. WAF rates were calculated for C5 to C9 saturates, BTEX, naphthalenes and PAH-compounds, for C10 to C36 TEOC, and polars, while C10 to C36 saturates/aromatics, naphthalenes and PAH were determined for dispersed oil.

The results indicate that the transformation rates are strongly dependent on the distribution between WAF and dispersed oil phases. The transformation rates differed significantly between the WAF and dispersed oil for the same compounds. While the naphthalene/PAH compounds in WAF were nearly completely transformed after 7 days of degradation, the correspondent transformation for these same compounds in the dispersed oil were only 10 to 47% after 14 days of degradation. Noteworthy is the considerably higher concentrations of the sparingly soluble compounds (such as PAH-1 and PAH-2 groups) in dispersed oil than in WAF incubation. The authors also found that introduction of a chemical dispersant in the oil had only small influence on the transformation. This lessened dispersant-mediated effect may also reflect the higher nominal oil loadings imparting a toxic or lag effect.

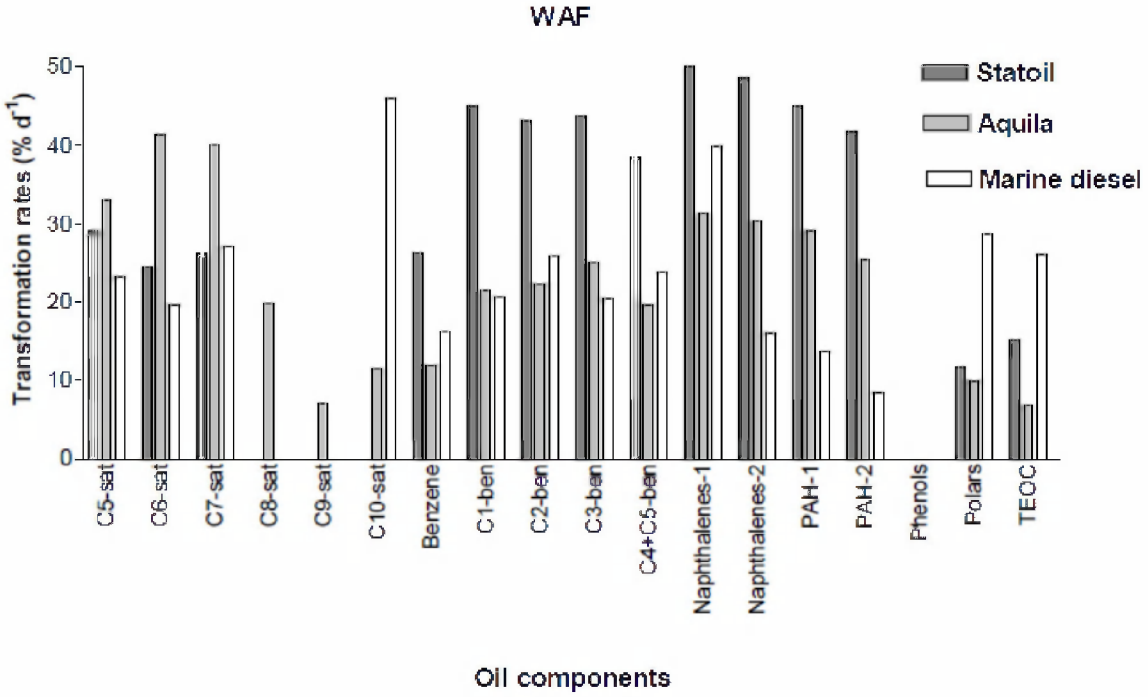

Figure C-5. Transformation rates of WAF compound groups of three fresh crude oils.

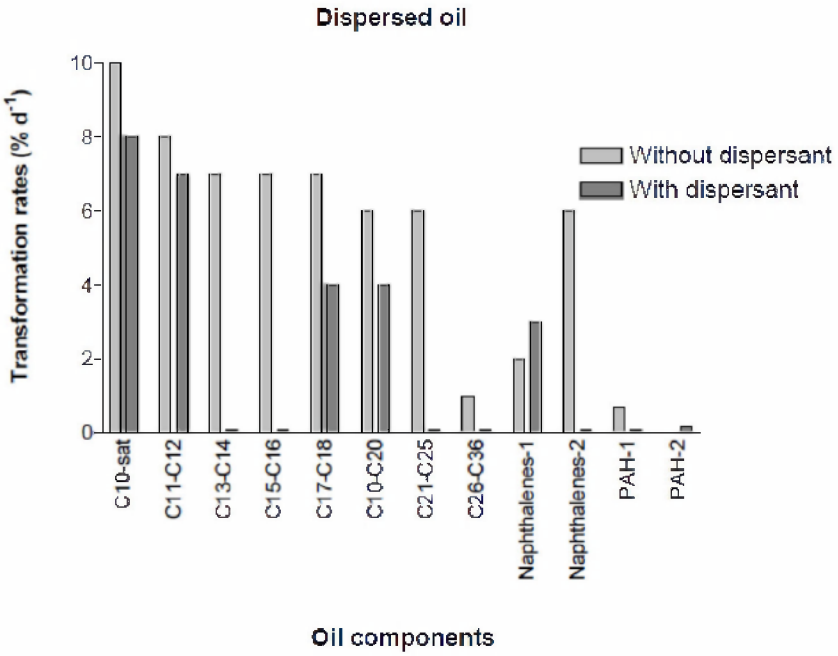

Figure C-6. Transformation rates of mechanically dispersed oil with or without a chemical dispersant.

Table C-11: Degradation Rate Coefficients of boiling-cut basis defined oil compound groups in WAF and Dispersed oil (Brakstad and Faksness, 2000).

Component group	WAF			Dispersed oil		
	Concentration (µg/L)	1st-order rate (d^{-1})	Half-life (d)	Concentration (µg/L)	1st-order rate (d^{-1})	Half-life (d)
C5-saturates	138	0.29	2.4	ND	ND	ND
C6-saturates	176	0.25	2.8	ND	ND	ND
C7-saturates	45	0.26	2.6	ND	ND	ND
C8-saturates	0.11	ND	ND	ND	ND	ND
C9-saturates	ND	ND	ND	ND	ND	ND
Benzene	349	0.26	2.6	ND	ND	ND
C1-benzenes	753	0.45	1.5	ND	ND	ND
C2-benzenes	904	0.43	1.6	ND	ND	ND

Component group	WAF			Dispersed oil		
	Concentration (µg/L)	1st-order rate (d^{-1})	Half-life (d)	Concentration (µg/L)	1st-order rate (d^{-1})	Half-life (d)
C3-benzenes	640	0.44	1.6	ND	ND	ND
C4/C5-benzenes	15	0.38	1.8	ND	ND	ND
C10-sat (GC/FID)	ND	ND	ND	732	0.10	6.8
C11-C12	ND	ND	ND	2566	0.08	8.4
C13-C14	ND	ND	ND	4497	0.07	9.4
C15-C16	ND	ND	ND	4803	0.07	9.8
C17-C18	ND	ND	ND	4724	0.07	9.9
C19-C20	ND	ND	ND	3932	0.06	10.9
C21-C25	ND	ND	ND	8113	0.06	10.7
C26-C36	ND	ND	ND	10937	0.04	[A)] 18.4
Naphthalenes 1	126	0.63	1.1	80	0.17	4.0
Naphthalenes 2	38	0.49	1.4	157	0.06	11.4
PAH-1	20	0.45	1.500	144	0.007	[A)] 105
PAH-2	1.7	0.42	1.7	198	<0.001	ND
Phenols C0-C4	5.2	ND	ND	ND	ND	ND
Polars	557	0.12	5.90	ND	ND	ND
TEOC	746	0.15	4.60	40298	0.04	[A)] 54

C.6.3 Brakstad et al. (2004) and Brakstad and Bonaunet (2006)

The objective of these studies were to establish methods for controlled studies of hydrocarbon depletion from thin oil films in cold natural seawater, and to determine biotransformation in relation to other essential depletion processes (especially dissolution) in flow-through systems rather than closed static experiments. This is based on consideration that the immiscible oil surfaces tend to be constantly washed with seawater, caused by a variety of physical and chemical processes, including wind, currents, oil weathering, film generation, and oil dispersion, and therefore new microbes are continuously contacting the oil film or droplet surfaces.

Brakstad et al. (2004) studied degradation of a paraffinic oil film (10 – 20 µm thickness) immobilized on a hydrophobic fluortex fabric in flow-through natural seawater at 6-8°C during a test period of 42 days. The seawater was collected from a depth of 90 m, and microbial characterization showed relatively larger densities of microbes on the fabric than in the corresponding seawater. Chemical analysis of hydrocarbons showed that n-alkanes decreased by 98% after 21 days as a result of biotransformation, while naphthalenes were depleted by 99-100% for the same period of time due primarily to dissolution.

A comparison of dissolution and biodegradation of oil compounds from thin oil films showed that fast dissolution of naphthalenes and non-alkylated 3-ring PAH resulted in biodegradation mainly of dissolved compounds, while negligible dissolution of n-alkanes (nC12 – nC36) resulted in biodegradation of these compounds exclusively on the oil – water interphases. For the larger PAH-compounds dissolution decreased with increasing numbers of aromatic rings and alkyl substitution, with biodegradation of these both as dissolved and as oil-associated compounds. Oil compound biodegradation involves bacterial communities in the water-phases as well as bacteria attaching the oil surfaces.

In the study of Brakstad and Bonaunet (2006), biodegradation of hydrocarbons in thin oil films was investigated in seawater at low temperatures (0 and 5°C), with a paraffinic crude oil immobilized as thin films on hydrophobic Fluortex adsorbents in nutrient-enriched or sterile seawater. Chemical and respirometric analysis of hydrocarbon depletion showed that naphthalene and other small aromatic hydrocarbons (HCs) were primarily biodegraded after dissolution to the water phase, while biodegradation of larger PAH and C10–C36 n-alkanes, including n-hexadecane, was associated primarily with the oil films. Biodegradation of PAH and n-alkanes was significant at both 0 and 5°C, but was decreased for several compounds at the lower temperature.

Table C-12 summarizes the estimated first-order biotransformation rates of the n-alkanes and branched alkanes and groups of PAH compounds from the experimental results of these studies. Figure C-7 displays the depletion of n-alkanes, naphthalenes, and other PAHs from oil-coated Fluortex adsorbents as a result of dissolution and biotransformation effects.

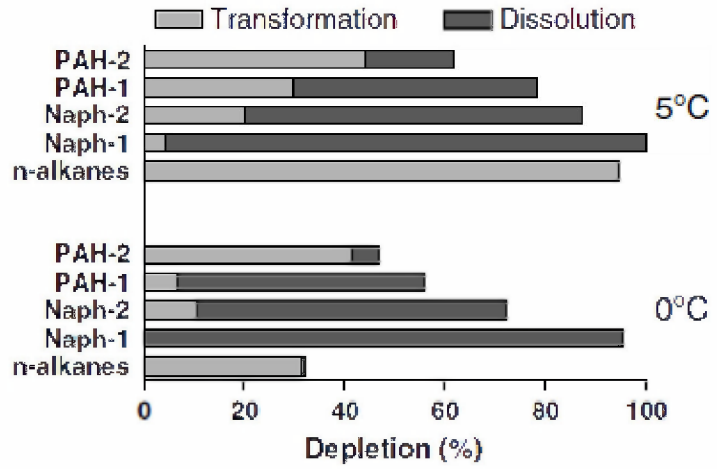

Figure C-7. Depletion of C10–C36 n-alkanes, Naph-1, Naph-2, PAH-1, and PAH-2 from oil-coated Fluortex adsorbents. The results are calculated as the distribution between dissolution and biotransformation after incubation in 56 days at 0 or 5°C.

Table C-12: Estimated first-order biodegradation rate coefficients of oil hydrocarbon compound groups in thin oil films coated on hydrophobic Fluortex adsorbents in natural-enriched seawater (Brakstad et al., 2004; Brakstad and Bonaunet, 2006).

Compound	Rate (d^{-1})	Half-life (day)
C12-C36 (n-alkanes)	0.154	4.5
Pristane	0.050	13.9
Phytane	0.043	16.0
C0- and C1- naphthalenes	0.173	4.0
C2- and C3- naphthalenes	0.154	4.5
C4-naphthalenes, biphenyl, acenaphthylene, acenaphthene, dibenzofuran, C0- to C1-fluorenes, C0- to C1-phenanthrenes/ anthracenes, C0- to C1-dibenzothiophenes	0.099	7
C2- to C3-fluorenes, C2- to C4-phenanthrenes/anthracenes, C2- to C4-dibenzothiophenes, Fluoranthrene, pyrene, C1- to C3-fluoranthrenes/pyrenes, (g,h,i)perylene, indeno(1,2,3-c,d)pyrenedibenzo(a,h)anthracene, benzobenz(a)anthracene, C0- to C4-crysenes, benzo(b,k)fluoranthene, benzo(e,a)pyrene, perylene,	0.029	24

C.6.4 Campo et al. (2013)

This is a study of biodegradation of dispersant Corexit9500 surfactant dioctyl sodium sulfosuccinate (DOSS) and dispersed South Louisiana crude oil (SLC) in laboratory experiments. The microcosms were set up using two oil-degrading bacterial cultures isolated from the Gulf of Mexico, one from the surface (25°C) and one from close to the area of the Macondo well (5°C). Chemically dispersed and mechanically dispersed oil mixtures at a nominal oil loading of around 700 mg/L were prepared using baffled beakers. These are very high loadings compared to field observed concentrations of dispersed oil. Aliquots of the composited dispersed oil suspension were then dispensed into a series of shaker flask microcosms with killed control and incubated at two different temperatures, 5°C and 25°C respectively. Dispersant alone-treatment microcosms were also prepared with a nominal DOSS concentration at 3.4 mg/L. The GC-MS analysis (following DCM extraction) of alkanes included normal and branched aliphatics ranging in carbon number from 10 to 35 as well as pristane and phytane. Aromatics included 2-, 3-, and 4-ring PAH compounds and their alkylated homologues (i.e., C0–4 -naphthalenes, C0–3 -fluorenes, C0–3 -dibenzothiophenes, C0–4 -phenanthrenes/anthracenes, C0–4 -napthbenzothiophenes, C0–2 -pyrenes, C0–4 -chrysenes). The experimental results showed that at 25°C the surface culture rapidly and completely degraded DOSS, as well as analyzed alkanes and aromatics. The deep seawater culture at 5°C metabolized the same compounds but with a lag phase of 28 d, and a remaining residual of iso-alkanes, long-chain n-alkanes (C_{30-35}), and 4-ring PAHs.

Figure C-3 and Table C-13 present the estimated first-order biodegradation rate constants for the individual hopane-normalized alkanes and PAHs at 25°C and 5°C with and without dispersant.

For n-alkanes degradation: at 25°C without dispersant, the first-order rate coefficients were about 0.4 d^{-1} for all n-alkanes measured (C10-C35), and the pristane and phytane rates were about 0.1 d^{-1}; at 5°C without dispersant, the rates ranged from less than 0.1 $d^{-1}$for shorter chain-length C10 to less than 0.05 $d^{-1}$for medium chain-length C25, and to negligible for long-chain alkanes (C30+); at 25 °C with dispersant, the rates were increased to such an extent that all the n-alkanes were completely degraded within 4d, rates unavailable to estimate, and the pristane and phytane rates were 0.5 d^{-1}; at 5°C with dispersant, the rates of n-C10-25 were about 0.3d^{-1}, n-C26-35 rates ranged 0.10- 0.02d^{-1}, in decreasing order with increasing chain length.

For PAH degradation: The rates of the two to three ring PAHs (i.e., C0–4 -naphthalenes, C0–3 -fluorenes, C0–3 -dibenzothiophenes, C0–4 -phenanthrenes/anthracenes) are around 0.05d^{-1} at 5°C without dispersant; these rates are reduced to about 0.02 d^{-1} at 25°C; treatment with dispersants seemed to have no impact on the degradation rates of these 2- to 3-ring PAHs. Higher molecular weight PAHs (i.e., C0–4 -napthbenzothiophenes, C0–2 -pyrenes, C0–4 –chrysenes) have negligible degradation rates with or without dispersants. Lack of a dispersant effect on PAH degradation rates might be due to the high nominal loadings used (and concentrations only got higher with dispersants) imparting some kind of toxic effect or lag-phase. It might also be due to the use of well dispersed oil droplets in the experiments, whether dispersed with or without dispersants, such that the dispersant effect on degradation rates would not be detected with this experimental design.

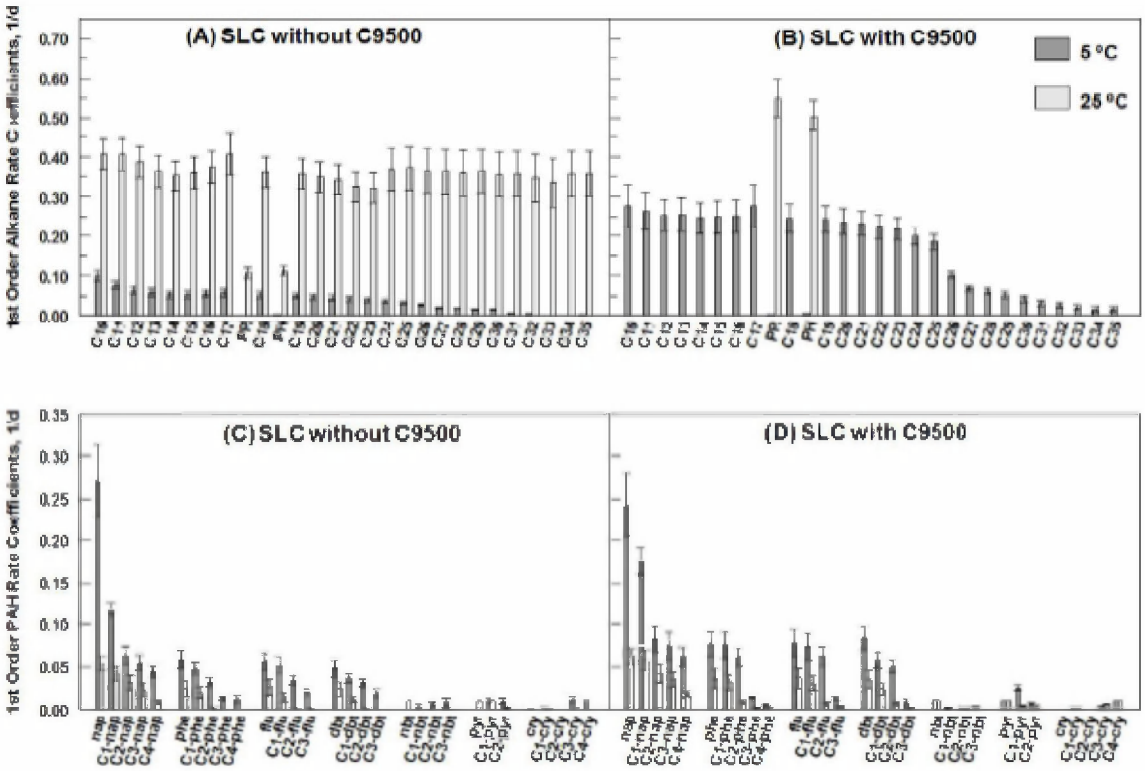

Figure C-8. First-order biodegradation rate coefficients of individual alkanes (A, B) and PAHs (C, D) at 5°C and 25°C without (A, C) and with (B, D) dispersant. Error bars are ± 1 standard deviation unit from the mean of the 3 replicates.

Table C-13: Estimated first-order biodegradation rate coefficients and half-lives of dispersed South Louisiana Crude oil hydrocarbon compound groups (Campo et al., 2013)

Compound	Rate (d^{-1})	Half-life (day)	Test conditions
C0-naphthalene	0.25	2.8	Lab study on degradation of fresh SLC crude oil dispersed in EPA baffled flask testat oil concentration level ~ 700ppm without Chemical dispersants, incubated at 5oC.
C1-naphthalene	0.10	6.9	
C2~C4-naphthalenes	0.05	13.9	
C0~C2-phenathrane2	0.05	13.9	
C3~C4-phenathranes	0.02	34.7	
C0~C2-fluorenes	0.05	13.9	
C3-fluorenes	0.02	34.7	
C0~C2-dibenzothiphenes	0.03	23.1	
C3-dibenzothiphenes	0.02	34.7	

Compound	Rate (d^{-1})	Half-life (day)	Test conditions
HMW PAHs (C0~C3-Naphthobenzothiophenes; C0~C2-pyrenes; and C0~C4-Chrysenes)	negligible	N/A	
C0-naphthalene	0.25	2.8	Dispersion of oil with Corexit 9500 (All other conditions same as above).
C1-naphthalene	0.15	4.6	
C2~C4-naphthalenes	0.05	13.9	
C0~C2-phenathrane2	0.075	9.2	
C3~C4-phenathranes	0.01	69.3	
C0~C2-fluorenes	0.05	13.9	
C3-fluorenes	0.01	69.3	
C0~C2-dibenzothiphenes	0.05	13.9	
C3-dibenzothiphenes	0.01	69.3	
HMW PAHs (C0~C3-Naphthobenzothiophenes; C0~C2-pyrenes; and C0~C4-Chrysenes)	0.01	69.3	
C0-naphthalene	0.05	13.9	Lab study on degradation of fresh SLC crude oil dispersed in EPA baffled flask testat oil concentration level ~ 700ppm without Chemical dispersants, incubated at 25°C.
C1-naphthalene	0.03	23.1	
C2~C4-naphthalenes	0.02	34.7	
C0~C2-phenathrane2	0.01	69.3	
C3~C4-phenathranes	negligible	N/A	
C0~C2-fluorenes	0.01	69.3	
C3-fluorenes	negligible	N/A	
C0~C2-dibenzothiphenes	0.01	69.3	
C3-dibenzothiphenes	negligible	N/A	
HMW PAHs (C0~C3-Naphthobenzothiophenes; C0~C2-pyrenes; and C0~C4-Chrysenes)	negligible	N/A	
C0-naphthalene	0.05	13.9	Dispersion of oil with Corexit 9500 (All other conditions same as above).
C1-naphthalene	0.05	13.9	
C2~C4-naphthalenes	0.03	23.1	
C0~C2-phenathrane2	0.02	34.7	
C3~C4-phenathranes	0.01	69.3	
C0~C2-fluorenes	0.02	34.7	
C3-fluorenes	0.01	N/A	
C0~C2-dibenzothiphenes	0.01	69.3	

Compound	Rate (d^{-1})	Half-life (day)	Test conditions
C3-dibenzothiphenes	negligible	N/A	
HMW PAHs (C0~C3-Naphthobenzothiophenes; C0~C2-pyrenes; and C0~C4-Chrysenes)	negligible	N/A	
C10	0.1	6.9	Same as above, 5°C, no dispersant
C11	0.075	9.2	
C12~C25	0.05	13.9	
C26~C32	0.01	69.3	
C33~C35	negligible	N/A	
C10	0.4	1.7	Same as above, 25°C, no dispersant
C11	0.4	1.7	
C12~C25	0.35	2.0	
C26~C32	0.35	2.0	
C33~C35	0.35	2.0	
C10	0.25	2.8	Same as above, 5°C, with dispersant Corexit 9500
C11	0.25	2.8	
C12~C25	0.20	3.5	
C26~C32	0.05	13.9	
C33~C35	0.02	34.7	

C.6.5 Hazen et al. (2010)

Hazen et al. (2010) reported rapid biodegradation in the deep sea hydrocarbon plume resulting from the DWH spill. In their field sampling program, a total of 17 samples (from 10 locations) were collected from the Gulf of Mexico during two monitoring cruises from May 27-June 2, 2010 on the R/V Brooks McCall and R/V Ocean Veritas. To estimate biodegradation rates in the plume, four data sets representing concentrations of C13-C26 n-alkanes were used. Two of the 4 data sets were field measurements from 6 sites included in Hazen et al.,(2010): BM57, BM58, BM53, BM54, OV011, and OV010. N-alkanes were not detected in any of the other field samples (i.e., from the other 4 stations of Hazen et al., 2010 study). Of these two hydrocarbon chemistry data sets, the first dataset was provided by BP and included analysis of a wide number of compounds from whole water samples, including n-alkanes. This BP data set is inclusive of all samples with the exception of OV011. The second hydrocarbon chemistry data set included concentrations of n-alkanes quantified from the neutral lipid fraction of the phospholipid fatty acid (PLFA) analysis and represents samples collected on a 0.2 µm PES filter. Both of these data sets were obtained from the same water samples taken from the associated CTD deployments from various sampling stations, but analyzed by different labs. BM53, BM54, and OV011 were considered a day 0 sampling point, and BM57, OV010 were considered intermediate points (either 1 or 3 days) and BM58 was considered the final point (either 2 or 5 days), using estimated travel times of 2 – 5 days between the day 0 and final

sampling points. This range is estimated from recorded ocean currents, with the deep water mean current speed at approximately 2 to 6 cm/s (Hamilton, 1990)

The other two data sets represent 5°C laboratory degradation studies of source oil in microcosm water collected outside the plume, with MC252 oil as the carbon source and isolates from the plume mixed as a consortium with MC252 oil. Microcosms were set up as triplicates using non-contaminated water from plume depth (OV02302) sampled June 6th 2010. 100 ml of the water was placed in 125 ml serum bottles and crude oil (MC252) was added to obtain a concentration of 100 mg/L. Bottles were closed using Teflon coated rubber stoppers and were incubated at 5°C in the dark for 20 days. Samples for analysis of hydrocarbons were taken after 0, 1, 5, and 20 days of incubation in triplicate samples.

Oil Degradation in Consortia: 2 ml of oil plume depth water (OV01003) was enriched in 18 ml bicarb buffered minimal marine medium (S*38*) amended with 0.05 g bactopeptone and 500 µL MC252 oil. From this enrichment, after four weeks, a transfer was made into fresh minimal marine media with no carbon source. After incubation for 48 h, this was used as the inoculum for the oil degradation experiment. The experiment was initiated in 45 ml minimal marine medium with 1000 mg/L MC252 oil as the sole carbon source in triplicates at 5°C. Heat killed controls were set up in parallel to account for abiotic loss of oil hydrocarbons. After mixing, samples were withdrawn for GC-MS analyses using sterile syringes after 0, 2, 5, and 8 days.

The first-order degradation rates of petroleum hydrocarbons from these four data sets (and 6 analyses) were determined to be 0.128 - 0.643 d^{-1} (as shown in Table C-14), corresponding to a half-life of 1.2 - 6.1 d (Table C-15). Owing to the coarse estimate of time and other input variables, Hazen et al.,(2010)'s data have greater uncertainty in comparison to other lab studies. Although the rate coefficients and half-lives of n-alkanes reported here are consistent with the range of others (e.g., Brakstad and Bonaunet, 2006; Venosa and Holder, 2007), it is not appropriate to represent whole oil degradation rates using the rates of the most readily degradable n-alkanes rates (see Brakstad et al., 2015; Brakstad and Faksness, 2000).

Table C-14: Estimated first-order biodegradation rate coefficients of n-alkanes of MC252 oil estimated from field measurements and microcosms data (Hazen et al., 2010).

	First order decay rate (day^{-1})					
Abbreviation	**Plume samples (2d)**	**Plume samples (5d)**	**BP data (2d)**	**BP data (5d)**	**Mixed consortia (5°C)**	**Microcosm water, (5°C)**
Average	**0.320**	**0.128**	**0.643**	**0.257**	**0.198**	**0.313**
C13 alk	0.438	0.175	0.497	0.199	0.227	0.324
C14 alk	0.46	0.184	0.506	0.202	0.197	0.304
C15 alk	0.458	0.183	0.709	0.284	0.193	0.329
C16 alk	0.432	0.173	0.344	0.138	0.193	0.31
C17 alk	0.399	0.16	0.615	0.246	0.19	0.298
C19 teralk	0.427	0.171	0.537	0.215	0.232	0.304
C18 alk	0.331	0.133	0.668	0.267	0.166	0.302
C20 teralk	0.380	0.152	0.512	0.205	0.191	0.296

	First order decay rate (day^{-1})					
Abbreviation	**Plume samples (2d)**	**Plume samples (5d)**	**BP data (2d)**	**BP data (5d)**	**Mixed consortia (5°C)**	**Microcosm water, (5°C)**
C19 alk	0.323	0.129	0.671	0.269	0.194	0.301
C20 alk	0.219	0.087	0.703	0.281	0.185	0.298
C21 alk	0.187	0.075	0.367	0.147	0.196	0.268
C22 alk	0.182	0.073	0.697	0.279	0.189	0.313
C23 alk	0.189	0.076	0.704	0.282	0.195	0.313
C24 alk	0.216	0.086	0.78	0.312	0.196	0.305
C25 alk	0.248	0.099	0.904	0.362	0.195	0.338
C26 alk	0.223	0.089	1.072	0.429	0.221	0.406

Table C-15: Estimated first-order biodegradation half-lives of n-alkanes of MC252 oil estimated from field measurements and microcosms data (Hazen et al., 2010).

	First-order decay half-life (day)					
Abbreviation	**Plume samples (2d)**	**Plume samples (5d)**	**BP data (2d)**	**BP data (5d)**	**Mixed consortia (5°C)**	**Microcosm water, (5°C)**
Average	**2.443**	**6.108**	**1.172**	**2.928**	**3.531**	**2.230**
C13 alk	1.583	3.961	1.395	3.483	3.054	2.139
C14 alk	1.507	3.767	1.370	3.431	3.519	2.280
C15 alk	1.513	3.788	0.978	2.441	3.591	2.107
C16 alk	1.605	4.007	2.015	5.023	3.591	2.236
C17 alk	1.737	4.332	1.127	2.818	3.648	2.326
C19 teralk	1.623	4.053	1.291	3.224	2.988	2.280
C18 alk	2.094	5.212	1.038	2.596	4.176	2.295
C20 teralk	1.824	4.560	1.354	3.381	3.629	2.342
C19 alk	2.146	5.373	1.033	2.577	3.573	2.303
C20 alk	3.165	7.967	0.986	2.467	3.747	2.326
C21 alk	3.707	9.242	1.889	4.715	3.536	2.586
C22 alk	3.809	9.495	0.994	2.484	3.667	2.215
C23 alk	3.667	9.120	0.985	2.458	3.555	2.215
C24 alk	3.209	8.060	0.889	2.222	3.536	2.273

	First-order decay half-life (day)					
Abbreviation	**Plume samples (2d)**	**Plume samples (5d)**	**BP data (2d)**	**BP data (5d)**	**Mixed consortia (5°C)**	**Microcosm water, (5°C)**
C25 alk	2.795	7.001	0.767	1.915	3.555	2.051
C26 alk	3.108	7.788	0.647	1.616	3.136	1.707

C.6.6 Howard et al. (2005)

In comparison to n-alkanes and PAHs, there is little data for biodegradation rates of BTEX compounds as part of a crude oil mixture. However, BTEX encompasses a group of compounds that are abundant in the DWH subsea intrusion layer as revealed by our investigation (Spaulding et al., 2015) as well as findings from other investigators (Reddy et al., 2012; Camilli et al., 2010; Payne and Driskell 2015a). In order to fill the data gap, two sets of data from indirect sources were reviewed. Table C-16 lists the data reported in BioHCWin.

Table C-16: First-order biodegradation rate coefficients and half-lives as reported in BioHCWin (Howard et al., 2005).

Compound	Rate (d^{-1})	Half-life (day)	Test conditions
Benzene	0.15	4.55	Given in USEPA BioHCWin
Toluene	0.15	4.49	
Ethylbenzene	0.14	4.97	
Xylenes	0.16	4.44	

C.6.7 Mackay et al. (2006)

Table C-17 presents the data reviewed by and provided in the Mackay et al. (2006) Handbook of physical-chemical properties of hydrocarbon compounds.

Table C-17: First-order biodegradation rate coefficients and half-lives as reported in (Mackay et al., 2006, and references therein).

Compound	Rate (d^{-1})	Half-life (day)	Test conditions
Benzene	0.1155	6	in estuarine water
	0.043-0.139	5-16	t½(aq. aerobic) = 120–384 h, based on seawater dieaway test data and river dieaway data
	0.11	6.3	k = 4.58 × 10–3 h–1 in water
	0.5	1.4	degradation in favorable aerobic environment
	0.12	5.8	k = 0.12 d–1 in river water
	0.081	8.6	in activated sludge
	0.139	5.0	t½(aerobic) = 5 d, t½(anaerobic) = 110 d in natural waters
	0.58-0.12	1.2-5.8	k = 0.58 d–1 associated with microbial population growth initially followed by a slower second phase with k = 0.12 d–1 degradation by P. aeruginosa is a two-stage process
Toluene	0.5	1.4	degradation in favorable aerobic environment
	0.073	9.5	in activated sludge
	0.03-0.173	4-22	t½(aq. aerobic) =: 96–528 h, based on an acclimated seawater dieaway test
	0.173	4.0	t½(aerobic) = 5 d, t½(anaerobic) = 110 d in natural waters
Ethylbenzene	0.0693-0.231	3-10	t½(aq. aerobic) = 72–240 h, based on unacclimated aqueous aerobic biodegradation half-life and seawater dieaway test data
	0.5	1.4	degradation in favorable aerobic environment
	0.3465	2	degradation by established microorganisms depending on body of water and its temperature
o-xylene (1,2-dimethylbenzene)	0.099	7	t½(aerobic) = 7 d, t½(anaerobic) = 180 d in natural waters
m,p-xylene (1,2-dimethylbenzene)	0.025-0.099	7-28	t½(aq. aerobic) = 168–672 h, based on aqueous screening test data and soil column study simulating an aerobic river/groundwater infiltration system

C.6.8 Prince et al. (2007)

Prince et al. (2007) studied primary biodegradation of gasoline (at about 70 mg/L) by inocula from unacclimated river water and seawater, and from a domestic sewage treatment plant at room temperature (21°C). Degradation microcosms were constructed by adding gasoline (0.7 μL) and 10 mL of aqueous inoculum in a 40 mL vial (30 mL air headspace). Based on individual hydrocarbon concentrations in the source oil, the air/water partitioning coefficient, and volume of air and water in each microcosm vial, the aqueous phase hydrocarbon concentrations were estimated. The aromatic concentrations ranged from 258 ppb (naphthalene) to 2,283 ppb (benzene). The n-alkane and iso-alkane concentrations were from 0.2 ppb (nonane) to 21 ppb (butane), and the naphthenes and olefins were from 2 ppb (cis-2-hexene) to 18 ppb (methylcyclopentane). Biodegradation rates were quantified with first-order degradation kinetics; the rate coefficients were estimated based on the loss rate of target analyte normalized by conserved internal biomarkers (hexachloroethane and hexachlorobenzene) to correct for abiotic losses. The Biodegradation was rapid and complete in all inocula, with an overall median half-live of 5 days at low levels of inorganic nutrients (Table C-18). Prince et al. (2007) observed that the larger n-alkanes and iso-alkanes, and simple and alkylated aromatic compounds were the most readily degraded compounds, followed by the smaller n-alkanes and iso-alkanes and naphthalenes; and the last compounds to be degraded were butane, iso-butane, and 2, 2-dimethylbutane, with an apparent half-life within 30 days.

Table C-18: First-order biodegradation rate coefficients and half-lives for primary biodegradation of gasoline range hydrocarbon compounds (Prince et al., 2007).

CLASS/COMPOUND	Half-life (days)		First-order rate (d^{-1})	
	Median	Mean	Median	Mean
Aromatics				
benzene	3.2	4.6	0.217	0.151
toluene (methylbenzene)	3.2	4.7	0.217	0.147
ethylbenzene	3.2	7.3	0.217	0.095
propylbenzene	3.2	5.6	0.217	0.124
1-methylethylbenzene	3.2	5.2	0.217	0.133
butylbenzene	2.3	3.3	0.301	0.210
(1-methylpropyl)benzene	3.2	5.3	0.217	0.131
(2-methylpropyl)benzene	3.2	11.8	0.217	0.059
o-xylene (1,2-dimethylbenzene)	3.2	4.5	0.217	0.154
1-ethyl-2-methylbenzene	3.2	4.5	0.217	0.154
1-methyl-2-(1-methylethyl)benzene	3.6	4.9	0.193	0.141
1-methyl-2-propylbenzene	2.0	2.3	0.347	0.301
1,2-diethylbenzene	2.8	3.1	0.248	0.224

CLASS/COMPOUND	Half-life (days)		First-order rate (d^{-1})	
	Median	Mean	Median	Mean
m-xylene (1,3-dimethylbenzene)	3.2	7.3	0.217	0.095
1-ethyl-3-methylbenzene	3.2	4.2	0.217	0.165
1-methyl-3-(1-methylethyl)benzene	3.2	4.5	0.217	0.154
1-methyl-3-propylbenzene	1.7	2.9	0.408	0.239
p-xylene (1,4-dimethylbenzene)	3.2	5.1	0.217	0.136
1-ethyl-4-methylbenzene	3.2	5.3	0.217	0.131
1-methyl-4-(1-methylethyl)benzene	2.5	3.7	0.277	0.187
1-methyl-4-propylbenzene	2.2	3.2	0.315	0.217
1,4-diethylbenzene	2.1	2.9	0.330	0.239
1,2,3-trimethylbenzene	3.2	4.6	0.217	0.151
2-ethyl-1,3-dimethylbenzene	3.2	4.9	0.217	0.141
1,2,4-trimethylbenzene	3.2	4.2	0.217	0.165
1,4-dimethyl-2-ethylbenzene	3.2	4.4	0.217	0.158
2,4-dimethyl-1-ethylbenzene	3.2	4.4	0.217	0.158
1,2-dimethyl-4-ethylbenzene	3.2	4.9	0.217	0.141
1,3,5-trimethylbenzene	3.2	4.6	0.217	0.151
1-ethyl-3,5-dimethylbenzene	1.8	2.1	0.385	0.330
1,3-dimethyl-5-(1-methylethyl)benzene	3.2	4.8	0.217	0.144
1,2,3,4-tetramethylbenzene	3.2	4.6	0.217	0.151
1,2,3,5-tetramethylbenzene	3.2	4.9	0.217	0.141
1,2,4,5-tetramethylbenzene	3.2	7.8	0.217	0.089
naphthalene	3.2	4.4	0.217	0.158
tetralin	3.2	4.6	0.217	0.151
indan	3.2	4.7	0.217	0.147
1-methylnaphthalene	3.9	5.3	0.178	0.131
2-methylnaphthalene	3.2	4.7	0.217	0.147

CLASS/COMPOUND	Half-life (days)		First-order rate (d^{-1})	
	Median	Mean	Median	Mean
5-methyltetralin	3.5	4.7	0.198	0.147
6-methyltetralin	3.2	4.5	0.217	0.154
1-methylindan	3.2	4.7	0.217	0.147
4-methylindan	3.2	4.5	0.217	0.154
5-methylindan	3.2	4.5	0.217	0.154
***n*-Alkanes**				
butane	15.0	31.8	0.046	0.022
pentane	10.7	31.3	0.065	0.022
hexane	6.5	10.2	0.107	0.068
heptane	4.5	5.7	0.154	0.122
octane	3.6	4.9	0.193	0.141
nonane	3.2	4.4	0.217	0.158
decane	3.2	3.9	0.217	0.178
undecane	2.8	3.8	0.248	0.182
dodecane	2.8	3.8	0.248	0.182
***iso*-Alkanes**				
2-methylpropane	17.1	41.7	0.041	0.017
2-methylbutane	13.0	41.2	0.053	0.017
2-methylpentane	10.4	16.7	0.067	0.042
3-methylpentane	10.1	21.3	0.069	0.033
2-methylhexane	6.6	18.7	0.105	0.037
3-methylhexane	7.5	19.3	0.092	0.036
2-methylheptane	4.8	6.0	0.144	0.116
3-methylheptane	6.5	7.1	0.107	0.098
4-methylheptane	6.5	8.1	0.107	0.086
3-ethylhexane	8.1	15.0	0.086	0.046
3-methyloctane	4.3	5.8	0.161	0.120
4-methyloctane	3.0	5.1	0.231	0.136
3-ethylheptane	3.1	7.0	0.224	0.099
3-methylnonane	3.6	4.9	0.193	0.141
4-methylnonane	3.2	4.8	0.217	0.144
5-methylnonane	3.3	5.2	0.210	0.133
3-ethyloctane	6.0	6.9	0.116	0.100

CLASS/COMPOUND	Half-life (days)		First-order rate (d^{-1})	
	Median	Mean	Median	Mean
4-ethyloctane	4.6	13.2	0.151	0.053
4-propylheptane	5.1	9.8	0.136	0.071
2,2-dimethylbutane	26.5	38.8	0.026	0.018
2,2-dimethylpentane	13.0	27.0	0.053	0.026
2,3-dimethylpentane	8.1	29.2	0.086	0.024
2,4-dimethylpentane	9.1	20.3	0.076	0.034
3,3-dimethylpentane	13.0	26.1	0.053	0.027
2,3-dimethylhexane	7.5	12.5	0.092	0.055
2,4-dimethylhexane	6.6	9.9	0.105	0.070
2,5-dimethylhexane	6.5	9.8	0.107	0.071
2,5-dimethylheptane	6.5	6.7	0.107	0.103
2,6-dimethylheptane	6.5	8.4	0.107	0.083
3,5-dimethylheptane	8.1	15.8	0.086	0.044
2,2,dimethyloctane	6.6	13.4	0.105	0.052
2,3-dimethyloctane	3.9	6.1	0.178	0.114
2,5-dimethyloctane	4.9	5.5	0.141	0.126
2,6-dimethyloctane	4.9	8.2	0.141	0.085
2,7-dimethyloctane	4.9	9.3	0.141	0.075
3,3-dimethyloctane	6.6	12.9	0.105	0.054
3,6-dimethyloctane	4.6	6.6	0.151	0.105
2,2,3-trimethylbutane	13.0	44.1	0.053	0.016
2,2,3-trimethylpentane	13.0	21.3	0.053	0.033
2,2,4-trimethylpentane	8.4	16.7	0.083	0.042
2,3,3-trimethylpentane	13.0	28.7	0.053	0.024
2,3,4-trimethylpentane	10.6	22.5	0.065	0.031
2,2,5-trimemethylhexane	8.1	15.8	0.086	0.044
2,2,4-trimethylheptane	6.5	9.6	0.107	0.072
2,2,5,5-tetramethylhexane	7.4	10.9	0.094	0.064
Naphthenes				
cyclopentane	9.1	29.5	0.076	0.023
cyclohexane	8.2	28.5	0.085	0.024
methylcyclopentane	8.1	16.0	0.086	0.043
ethylcyclopentane	6.5	10.1	0.107	0.069
methylcyclohexane	7.4	13.8	0.094	0.050

CLASS/COMPOUND	Half-life (days)		First-order rate (d^{-1})	
	Median	Mean	Median	Mean
ethylcyclohexane	6.5	8.3	0.107	0.084
propylcyclohexane	6.5	8.3	0.107	0.084
butylcyclohexane	5.2	6.4	0.133	0.108
pentylcyclohexane	3.7	5.0	0.187	0.139
hexylcyclohexane	3.2	5.4	0.217	0.128
1,1-dimethylcyclopentane	8.9	20.6	0.078	0.034
trans-1,2-dimethylcyclopentane	10.4	16.7	0.067	0.042
trans-1,3-dimethylcyclopentane	8.0	14.2	0.087	0.049
cis-1,3-dimethylcyclopentane	8.3	15.9	0.084	0.044
1,1-dimethylcyclohexane	10.4	17.3	0.067	0.040
trans-1,2-dimethylcyclohexane	8.1	20.5	0.086	0.034
trans-1,3-dimethylcyclohexane	7.7	7.9	0.090	0.088
cis-1,2-dimethylcyclohexane	7.9	13.1	0.088	0.053
cis-1,3-dimethylcyclohexane	8.1	14.5	0.086	0.048
1,1,3-trimethylcyclohexane	8.5	14.2	0.082	0.049
Olefins				
trans-2-pentene	8.6	11.0	0.081	0.063
cis-2-pentene	7.4	9.1	0.094	0.076
trans-2-hexene	5.1	6.1	0.136	0.114
cis-2-hexene	6.5	7.1	0.107	0.098
cis-3-hexene	6.5	8.4	0.107	0.083
cyclopentene	8.1	11.5	0.086	0.060
2-methyl-1-butene	10.8	21.5	0.064	0.032
2-methyl-2-butene	8.2	14.0	0.085	0.050
2-methyl-1-pentene	7.9	12.1	0.088	0.057
3-methyl-2-pentene	6.5	9.1	0.107	0.076
1-methylcyclopentene	6.5	8.1	0.107	0.086
3-methylcyclopentene	8.1	13.2	0.086	0.053
4-methylcyclopentene	8.1	12.5	0.086	0.055

C.6.9 Prince et al. (2008)

Prince et al. (2008) reported the biodegradation of a biodiesel (B20) mixture by unacclimated freshwater microorganisms. B20 fuel is a mixture of 20% soybean fatty acid methyl esters and 80% petroleum diesel. Biodegradation was rapid and essentially complete with an overall median 'half-life', at 100 ppm B20, of 6.8 days (n = 34). Using purge-and-trap (for volatile light hydrocarbons) and extraction (for less volatile compounds) methodologies, both coupled to GC/MS, and hexachloroethane and hexachlorobenzene as conserved internal markers in the B20, biodegradation of total detectable material, 76 individual analytes and eight undifferentiated groups of isomers, were calculated as half-lives. The fatty acid methyl esters, n-alkanes and iso-alkanes, and simple and alkylated aromatic compounds were the most readily degraded compounds, followed by the naphthenes. The last (identified) compounds to be degraded were ethylalkanes, trisubstituted cyclohexanes and decalins. Table C-19 summarizes the reported half-lives and alkanes, naphthenes, and aromatics of this study.

Table C-19: First-order biodegradation rate coefficients and half-lives for primary biodegradation of diesel range hydrocarbon compounds (Prince et al., 2008).

CLASS/COMPOUND	Half-lives measured by purge & trap (d)	Half-lives measured by extraction (d)	First-order degradation rates (d^{-1})
Alkanes			
Heptane	2.3		0.30
Octane	2.1		0.33
Nonane	2.1		0.33
Decane	2.1		0.33
Undecane	2.1		0.33
Dodecane	2.1		0.33
Tridecane		2.3	0.30
Tetradecane		2.3	0.30
Pentadecane		2.4	0.29
Hexadecane		2.5	0.28
Heptadecane		2.3	0.30
Octadecane		2.5	0.28
Nonadecane		2.8	0.25
Eicosane		2.8	0.25
3-Methyloctane	2.8		0.25
4-Methyloctane	2.3		0.30
2-Methylnonane	2.1		0.33
3-Methylnonane	2.1		0.33
4-Methylnonane	2.1		0.33
5-Methylnonane	4.8		0.14

CLASS/COMPOUND	Half-lives measured by purge & trap (d)	Half-lives measured by extraction (d)	First-order degradation rates (d^{-1})
2-Methyldecane	2.1		0.33
3-Methyldecane	2.1		0.33
4-Methyldecane	1.1		0.63
5-Methyldecane	2.7		0.26
2-Methylundecane	2.1		0.33
4-Methylundecane	2.1		0.33
5-Methylundecane	2.1		0.33
6-Methylundecane	2.1		0.33
3-Ethylheptane	7.2		0.10
3-Ethyloctane	6.9		0.10
4-Ethyloctane	13.9		0.05
2,5-Dimethylheptane	6.9		0.10
2,6-Dimethylheptane	5.3		0.13
3,5-Dimethylheptane	6.4		0.11
2,3-Dimethyloctane	5.3		0.13
2,5-Dimethyloctane	6.9		0.10
2,6-Dimethyloctane	4.1		0.17
2,7-Dimethyloctane	6.9		0.10
2,5-Dimethylnonane	3.9		0.18
2,6-Dimethylnonane	5.5		0.13
2-Methyl-3-ethylheptane	19.9		0.03
2,6,10,14-Tetramethyl-pentadecane (pristane)		4.3	0.16
2,6,10,14-Tetramethyl-hexadecane (phytane)		6.2	0.11
Naphthenes			
Ethylcyclohexane	6.9		0.10
Propylcyclohexane	5.5		0.13
Butylcyclohexane	2.6		0.27
Pentylcyclohexane	2.1		0.33
Hexylcyclohexane	2.1		0.33
Heptylcyclohexane		2.7	0.26

CLASS/COMPOUND	Half-lives measured by purge & trap (d)	Half-lives measured by extraction (d)	First-order degradation rates (d^{-1})
Octylcyclohexane		3.0	0.23
Nonylcyclohexane		2.8	0.25
Decylcyclohexane		3.4	0.20
Undecylcyclohexane		3.1	0.22
Dodecylcyclohexane		3.3	0.21
1,1,3-Trimethylcyclohexane	12.0		0.06
Decahydronaphthalene (decalin)	13.6		0.05
Aromatics			
1-Ring			
C3-Benzenes	4.0		0.17
C4-Benzenes	4.6		0.15
2-Ring			
Naphthalene	3.9		0.18
1-Methylnaphthalene	3.9		0.18
2-Methylnaphthalene	3.9		
C2-Naphthalenes		2.6	0.27
C3-Naphthalenes		4.2	0.17
1,2,3,4-Tetrahydro naphthalene (tetralin)	3.9		0.18
2-Methyltetralin	3.9		0.18
5-Methyltetralin	3.9		0.18
6-Methyl tetralin	3.9		0.18
Indan	3.9		0.18
1-Methylindan	3.9		0.18
4-Methylindan	3.9		0.18
5-Methylindan	3.9		0.18
Biphenyl		2.8	0.25
2-Methylbiphenyl		3.3	0.21
3-Methylbiphenyl		3.1	0.22
4-Methylbiphenyl		3.0	0.23
3-Ring			
Fluorene		2.5	0.28

CLASS/COMPOUND	Half-lives measured by purge & trap (d)	Half-lives measured by extraction (d)	First-order degradation rates (d^{-1})
Methylfluorenes		4.2	0.17
C2-Fluorenes		4.2	0.17
Phenanthrene		2.6	0.27
1-Methylphenanthrene		4.2	0.17
2-Methylphenanthrene		4.2	0.17
3-Methylphenanthrene		4.2	0.17
9-Methylphenanthrene		4.2	0.17
C2-Phenanthrenes		4.2	0.17
C3-Phenanthrenes		6.4	0.11

C.6.10 Prince et al. (2013)

Prince et al. (2013) studied degradation of slightly weathered Alaska North Slope crude oil at 8°C in un-amended seawater when oil was present at 2.5 ppm by volume. Weathering was performed by evaporation at laboratory room temperature in a hood until the oil had lost 20% of its weight. Oil present at the ppm levels is expected from a successful application of dispersants to promote entrainment and dilution of oil in the water column. The experiments were set up in multiple pairs of duplicate 5L carboys containing 10 µl of either untreated oil or dispersant treated oil in 4L seawater, and incubated in cold room for 60 days, with intermittent sacrificial sampling times on 0, 4, 6, 11, 24, and 41 days. Oil biodegradation was followed with respect to 17a(H),21b(H)-hopane as a conserved internal marker within the oil. Two-dimensional GC coupling to a flame ionization detector method was adopted, with the first column separated the oil components by boiling point, the second by polarity. This approach separates the oil into eight major classes: 3-ring aromatics, 2-ring aromatic + 1-saturated ring or 5-saturated rings, 2-ring aromatics or 4-saturated rings, 1-ring aromatic + 1-saturated ring or 3-saturated rings, 1-ring aromatic or 2-saturated rings, 1-saturated ring, alkanes, and hopanes.

Table C-20 presents the first-order degradation rates of specific components or compound groups of petroleum hydrocarbons from this lab study. The results indicated that more than 80% of the hydrocarbons of lightly weathered Alaska North Slope crude oil were degraded in 60 d at 8°C in un-amended seawater. The apparent half-life of the biodegradation was 13.8 d in the absence of dispersants and 11 d in the presence of Corexit 9500.

Table C-20: First-order biodegradation rate coefficients and half-lives from primary biodegradation of crude oil hydrocarbon compounds (Prince et al., 2013).

	Initial concentration (ppb or µg/L)	Median apparent half-life (d)	Median apparent half-life with dispersant (d)	Median apparent first-order rate (d^{-1})	Median apparent 1st-order rate with dispersant (d^{-1})
Total detectable hydrocarbons		13.8	11.0	0.050	0.063
Total saturates (m/z = 57)		15.6	11.6	0.044	0.060
17a(H),21b(H)-hopane	0.48				
Heptadecane (C17)	9.24	1.9	1.8	0.365	0.385
Pristane (C19)	4.87	4.7	3.4	0.147	0.204
Octadecane (C18)	5.48	2.5	2.2	0.277	0.315
Phytane (C20)	3.36	5.3	3.8	0.131	0.182
Triacontane (C30)	1.85	13.1	7.8	0.053	0.089
Naphthalene	1.35	2.3	1.9	0.301	0.365
C1-naphthalenes	2.96	2.0	1.7	0.347	0.408
C2-naphthalenes	3.73	1.9	1.7	0.365	0.408
C3-naphthalenes	2.88	1.9	1.8	0.365	0.385
C4-naphthalenes	1.46	2.1	1.9	0.330	0.365
Fluorene	0.20	3.1	2.6	0.224	0.267
Phenanthrene	0.56	2.6	2.2	0.267	0.315
1-Methylphenanthrene	0.36	2.8	2.4	0.248	0.289
2-Methylphenanthrene	0.27	2.9	2.5	0.239	0.277
3-Methylphenanthrene	0.22	3.0	2.6	0.231	0.267
9-Methylphenanthrene	0.41	3.5	2.5	0.198	0.277
C2-phenanthrenes	1.48	7.9	9.7	0.088	0.071
C3-phenanthrenes	1.05	18.9	22.4	0.037	0.031
C4-phenanthrenes	0.63	28.8	35.7	0.024	0.019
Dibenzothiophene	0.49	2.7	2.4	0.257	0.289
1-Methyldibenzothiophene	0.17	3.7	4.5	0.187	0.154
2/3-Methyldibenzothiophenes	0.27	3.0	3.5	0.231	0.198
4-Methyldibenzothiophene	0.51	2.8	3.5	0.248	0.198
C2-dibenzothiophenes	1.43	7.8	7.6	0.089	0.091
C3-dibenzothiophenes	1.26	19.5	21.2	0.036	0.033
C4-dibenzothiophenes	0.69	33.3	35.9	0.021	0.019
Benz[a]anthracene	0.03	26.6	17.8	0.026	0.039
Chrysene	0.10	30.8	36.2	0.023	0.019
1-Methylchrysene	0.02	14.3	14.3	0.048	0.048
2-Methylchrysene	0.02	6.3	11.2	0.110	0.062
3-Methylchrysene	0.11	27.1	36.5	0.026	0.019
4/6-Methylchrysenes	0.02	11.3	12.4	0.061	0.056
C2-chrysenes	0.25	28.1	28.5	0.025	0.024

	Initial concentration (ppb or µg/L)	Median apparent half-life (d)	Median apparent half-life with dispersant (d)	Median apparent first-order rate (d^{-1})	Median apparent 1st-order rate with dispersant (d^{-1})
Sum 16 EPA priority pollutants	2.24	4.5	4.0	0.154	0.173

C.6.11 Venosa and Holder (2007)

Venosa and Holder (2007) conducted lab experiments to study the biodegradability of oil after dispersants were applied. Two experiments were conducted: one at 20°C and the other at 5°C; in both experiments, only the dispersed oil (Fresh Prudhoe Bay Crude) fraction was investigated. Two different concentrations of dispersed oil were prepared, the dispersed oil then transferred to shaker flasks, which were inoculated with a bacterial culture and shaken on a rotary shaker at 200 rpm for several weeks. Periodically, triplicate flasks were removed and sacrificed to determine the residual oil concentration remaining at that time. Oil compositional analysis was performed by gas chromatography/mass spectrometry (GC/MS) to quantify the biodegradability. At 20°C, the first-order degradation rates of total n-alkanes were 0.17 d^{-1} without dispersant, and from 0.21 d^{-1} to 0.66 d^{-1} with dispersants; and the degradation rates of total PAHs without dispersant was 0.13 d^{-1} and from 0.15 to 0.23 d^{-1} with dispersants. At 5°C, the first-order degradation rates of total n-alkanes were 0.073 d^{-1} without dispersant, and from 0.073 d^{-1} to 0.156 d^{-1} with dispersants; and the degradation rates of total PAHs without dispersant was 0.052 d^{-1} and from 0.057 to 0.116 d^{-1} with dispersants. Based on the experimental results (Figures C-9 to C-12, Table C-21), the authors suggested that the ultimate fate of dispersed oil in the sea is rapid loss by biodegradation.

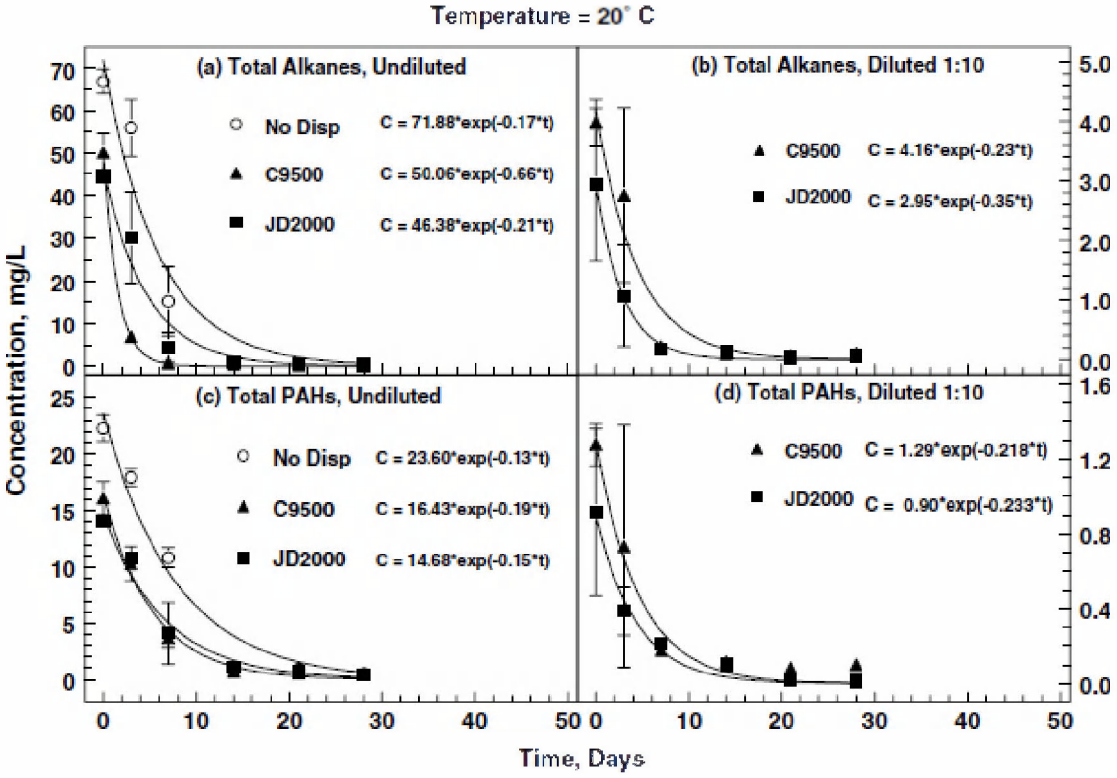

Figure C- 9. Biodegradation of total alkanes and total aromatics in crude oil either non-dispersed or dispersed by Corexit 9500 and JD2000 undiluted (a, c) and diluted 1:10 (b, d). Temperature = 20°C.

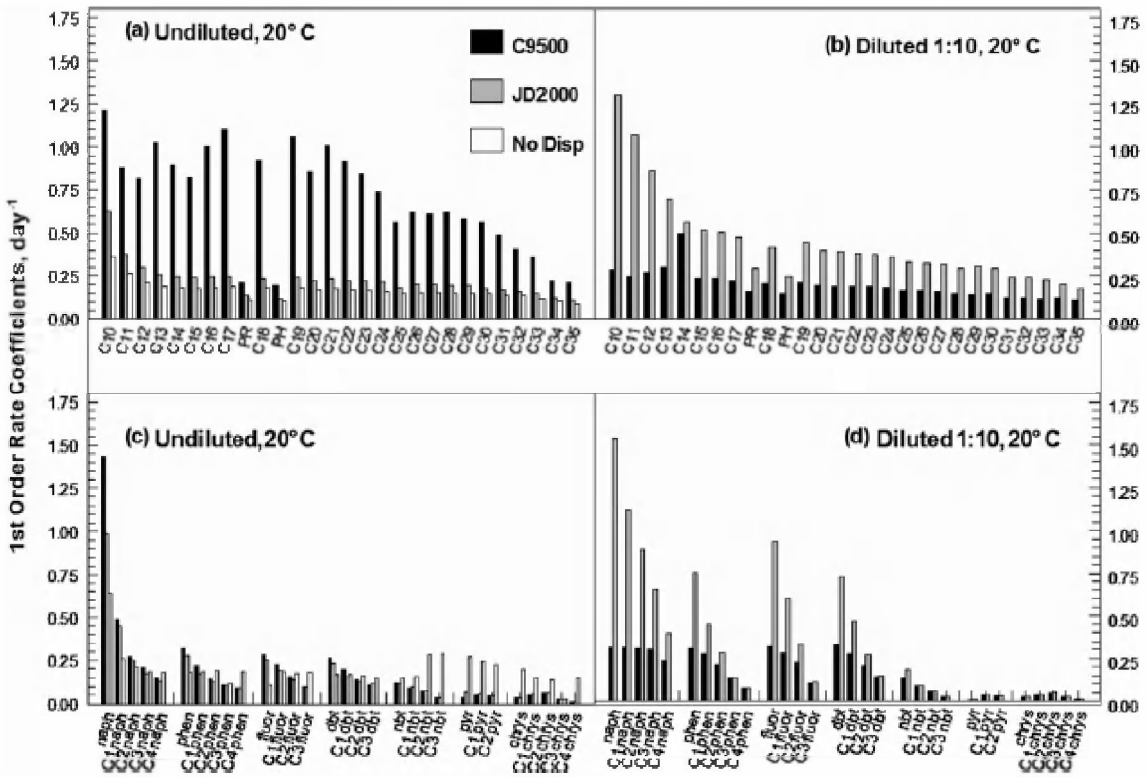

Figure C-10. First-order biodegradation rate coefficients of individual alkanes undiluted (a) and diluted 1:10 (b) and individual aromatics undiluted (c) and diluted 1:10 (d). Temperature = 20°C.

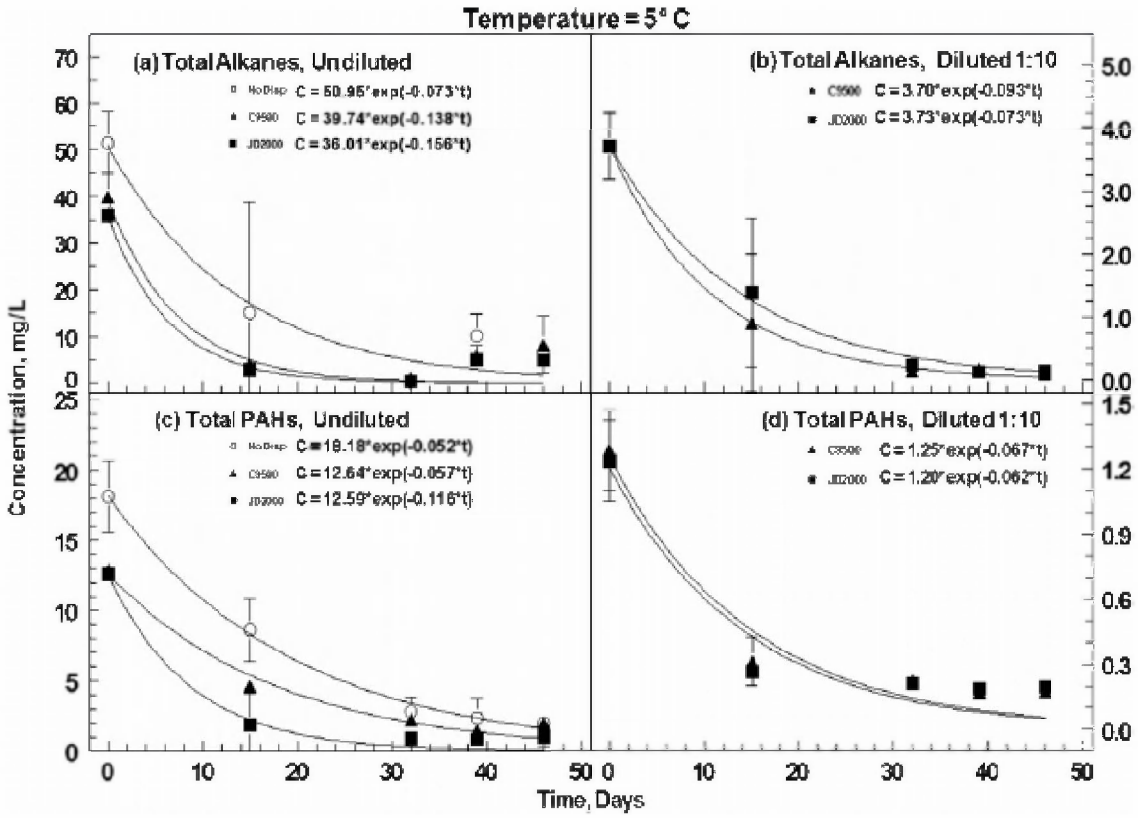

Figure C-11. Biodegradation of total alkanes and total aromatics in crude oil either non-dispersed or dispersed by Corexit 9500 and JD2000 undiluted (a, c) and diluted 1:10 (b, d). Temperature = 5°C.

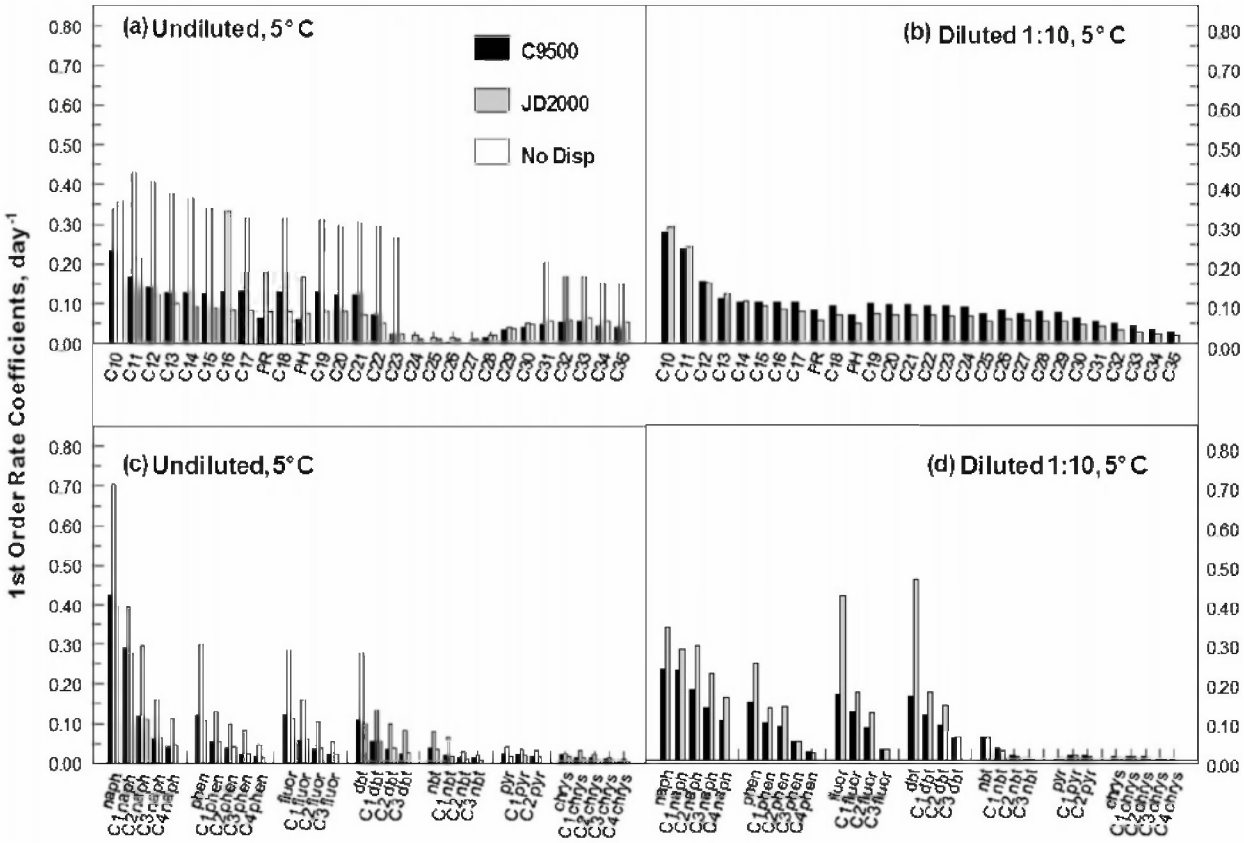

Figure C-12. First-order biodegradation rate coefficients of individual alkanes undiluted (a) and diluted 1:10 (b) and individual aromatics undiluted (c) and diluted 1:10 (d). Temperature = 5°C.

Table C-21: First-order biodegradation rate coefficients and half-lives from primary biodegradation of crude oil hydrocarbon compounds (Venosa and Holder, 2007).

Compound	Rate (d^{-1})	Half-life (d)	Test conditions
C0-naphthalene	0.4	1.7	Lab study on degradation of fresh Prudhoe Bay crude oil (ρ = 0.887 g/cm^3) that was first dispersed in EPA baffled flask test at 20°C, at two oil concentration levels (739ppm and 74 ppm). Biodegradation was then conducted at 5°C
C1-naphthalene	0.30	2.3	
C2~C4-naphthalenes	0.1	6.9	
C0~C2-phenathrane2	0.05	13.9	
C3~C4-phenathranes	0.02	34.7	
C0~C2-fluorenes	0.05	13.9	
C3-fluorenes	0.02	34.7	
C0~C2-dibenzothiphenes	0.05	13.9	
C3-dibenzothiphenes	0.02	34.7	

Compound	Rate (d^{-1})	Half-life (d)	Test conditions
HMW PAHs (C0~C3-Naphthobenzothiophenes; C0~C2-pyrenes; and C0~C4-Chrysenes)	0.01	69.3	
C0-naphthalene	1.00	0.7	Biodegradation was conducted at 20°C (All the other conditions the same as above)
C1-naphthalene	0.50	1.4	
C2~C4-naphthalenes	0.20	3.5	
C0~C2-phenathrane2	0.20	3.5	
C3~C4-phenathranes	0.10	6.9	
C0~C2-fluorenes	0.20	3.5	
C3-fluorenes	0.10	6.9	
C0~C2-dibenzothiphenes	0.20	3.5	
C3-dibenzothiphenes	0.10	6.9	
HMW PAHs (C0~C3-Naphthobenzothiophenes; C0~C2-pyrenes; and C0~C4-Chrysenes)	0.01	69.3	
C10	0.30	2.3	Lab study on degradation of fresh Prudhoe Bay crude oil (ρ = 0.887 g/cm3) that was first dispersed in EPA baffled flask test at 20°C, respectively at two oil concentration levels (739ppm and 74 ppm). Biodegradation was conducted at 5°C
C11	0.20	3.5	
C12~C25	0.10	6.9	
C26~C32	0.05	13.9	
C33~C35	0.02	34.7	
C10	0.25	2.8	Biodegradation was conducted at 25°C (All other conditions same as above)
C11	0.20	3.5	
C12~C25	0.20	3.5	
C26~C32	0.15	4.6	
C33~C35	0.10	6.9	

C.6.12 Zahed et al. (2011)

Zahed et al. (2011) studied biodegradation of oil in seawater at relatively high concentrations of oil. Erlenmeyer flasks were used as bioreactors and 250mL oil contaminated seawater was transferred to each flask at oil concentration of 100, 500, 1000 and 2000 mg/L, respectively. A reactor was treated with the biocide HgCl2 as an abiotic control to show the effect of evaporation and other physical reactions in the absence of microbial activity. A natural attenuation test was carried out for each oil concentration; the bioreactors were prepared without nutrient or microorganism supplementation. For crude oil biodegradation experiments, bioreactors were supplemented with acclimatized microorganisms and nutrients with a C:N:P ratio of 100:10:1 for each reactor. One milliliter bacterial inoculums containing 1.2×10^{7} cells/mL

were added to each bioreactor. KNO_3 and K_2HPO_4 were used as nitrogen and phosphorus sources. The dispersed crude oil experiments were performed by supplementation of Corexit 9500 at a ratio of 20:1 (w/w) crude oil to dispersant. Degradation kinetics were estimated by first-order decay rates of the concentration of total petroleum hydrocarbons following EPA Method 1664 using hexane extraction and gravimetric determination of solvent extracted material for oil and grease analysis. The results (Table C-22) indicated that dispersant application improved the crude oil biodegradation rate at the tested oil concentrations.

Table C-22: First-order biodegradation rate coefficients and half-lives from primary biodegradation of whole oil (Zahed et al., 2011).

No	Remediation strategy*	Oil Concentration ($mg \cdot L^{-1}$)	Half-life (d)	First-order degradation rate (d^{-1})
1	Natural attenuation	100	90	0.008
2	Natural attenuation	500	102	0.007
3	Natural attenuation	1000	116	0.006
4	Natural attenuation	2000	124	0.006
5	CO Bioremediation	100	31	0.022
6	CO Bioremediation	500	40	0.017
7	CO Bioremediation	1000	50	0.014
8	CO Bioremediation	2000	75	0.009
9	DCO Bioremediation	100	28	0.025
10	DCO Bioremediation	500	32	0.022
11	DCO Bioremediation	1000	38	0.018
12	DCO Bioremediation	2000	58	0.012

*Natural attenuation = no nutrients added; CO Bioremediation = Crude oil with addition of nutrients; DCO Bioremediation = Dispersed crude oil with addition of nutrients.

C7. SIMAP Boiling-Point-Cut Hydrocarbon Pseudo-component definition

The hydrocarbon "pseudo-component" approach has been used in prior evaluations and modeling of the evaporation and dissolution processes within SIMAP. Table C-23 lists the definition of the pseudo-components in the SIMAP oil fates model. Table C-24 summarizes SIMAP pseudo-component groups, constituents, concentrations, and characteristic octanol-water partition coefficients (Kow, as $\log_{10}$(Kow). The same approach is used in the following section to synthesize the biodegradation rates of hydrocarbons in seawater. The oil component properties (OCP) are summarized by each of AR and AL components, and for residual. In these components, AR1 to AR8 are soluble aromatics (AR); AR9 is soluble alkanes; AL1 to AL8 are non-soluble aliphatics fractions, whereas AL9 is reserved for modeling of surfactants.

Table C-23: SIMAP boiling-cut pseudo-component definition

AR or AL	All HCs	Soluble and semi-soluble HCs		Non-soluble aliphatic HCs	
Compo-nent #	Volatility	Compounds	Range of log(Kow)	Compounds	Boiling Point Range (°C)
1	Volatiles	MAHs (BTEX)	1.9-2.8	Volatile aliphatics	< 150
2		C3-benzenes	2.8-3.6	Volatile aliphatics	150-180
3	Intermediate Volatility	C4-benzenes	3.1-3.8	Semi-volatile aliphatics	180-200
4		Decalins	4.1-6.0	Semi-volatile aliphatics	200-230
5		C0-C2 Naphthalenes	2.3-4.3	Semi-volatile aliphatics	230-280
6	Semi-Volatile	C3-C4 Naphthalenes	4.2-5.2	Low volatility aliphatics	280 - 300
7		Fluorenes & C0-C2 3-ring PAHs	4.0-5.6	Low volatility aliphatics	300-350
8		4-ring PAHs & C2-C3 3-ring PAHs	4.9-6.0	Low volatility aliphatics	350-380
9	Highly Volatile and Soluble Aliphatics	Alkanes, Isoalkanes, Cycloalkanes	2.3-5.6	N.A. (Used for Dispersant Indicators)	<180
Residual	Residual (non-volatile) Component 19	High MW PAHs	>6.0	High molecular weight aliphatics	>380

Table C-24: SIMAP pseudo-component groups, constituents, concentrations, and log (Kow).

Code	Group	Includes	g/g of MC252 source oil	Log (Kow)
AR1	BTEX	BTEX, styrene	0.019	2.91

Code	Group	Includes	g/g of MC252 source oil	Log (Kow)
AR2	C3-benzenes	C3-benzenes	0.008	3.71
AR3	C4-benzenes	C4-benzenes	0.005	4.02
AR4	Decalins	cis/trans decalin to C4-decalin	0.004	4.89
AR5	C0-C2 Naphthalenes	C0-C2 Naphthalenes, C0-C2 Benzothiophenes, biphenel, acenaphthene, acenaphthylene	0.006	4.02
AR6	C3-C4 Naphthalenes	C3-C4 Naphthalenes, C3-C4 Benzothiophenes, dibenzofuran	0.002	5.08
AR7	Fluorenes & C0-C2 3-ring PAHs	C0-C3 Fluorenes, C0-C1 dibenzothiophenes, C0-C1 phenanthrenes	0.002	5.02
AR8	4-ring PAHs & C2-C3 3-ring PAHs	C0-C2 pyrenes & fluoranthenes, C2-C3 dibenzothiophenes, C2-C3 phenanthrenes, chrysene	0.002	5.50
AR9	Soluble alkanes	Low mol.wt. Alkanes, Isoalkanes, Cycloalkanes	0.133	3.65
AL1	Aliphatics: BP < 150	(unmeasured compounds)	0.007	3.49
AL2	Aliphatics: BP 150-180	(unmeasured compounds)	0.061	5.05
AL3	Aliphatics: BP 180-200	C11 Alkanes	0.034	6.94
AL4	Aliphatics: BP 200-230	C12 Alkanes	0.054	7.24
AL5	Aliphatics: BP 230-280	C13-C16 Alkanes	0.095	7.37
AL6	Aliphatics: BP 280-300	C17-C18 Alkanes	0.036	8.53
AL7	Aliphatics: BP 300-350	C19-C20 Alkanes	0.093	10.10

Code	Group	Includes	g/g of MC252 source oil	Log (Kow)
AL8	Aliphatics: BP 350-380	C21-C23 Alkanes	0.049	13.00
AL9	Dispersant	(dispersant on oil droplets)	0.000	3.00
Residual	Residual	Other non-volatile, non-soluble hydrocarbons	0.390	> 6.0

C8. Degradation rates of hydrocarbon components in seawater

C.8.1 Summary of degradation rates of AR1-9 hydrocarbon components in seawater

Tables C-25 to C-33 display the first-order degradation rate constants and half-lives of the nine soluble and semi-soluble "aromatic" fractions (AR1 through AR9, each table represents one component) that are simulated in the model. Table C-34 summarizes the degradation rates used in the oil fate model.

Table C-25: Degradation rates of AR1 (BTEX, styrene) in sea water.

References	Compounds	Summary half-life (d)	Summary Rate (d^{-1})
Brakstad et al., 2015	Benzene (drop median size 10 um)	4.9	0.141429
	Toluene (10um)	2.9	0.238966
	ethylbenzene; o-,m-,p-xylene (10um)	2.7	0.256667
	Benzene (drop median size 30 um)	8.5	0.081529
	Toluene (30um)	4.6	0.150652
	ethylbenzene; o-,m-,p-xylene (30um)	3.7	0.187297
Brakstad and Faksness, 2000	Benzene (WAF)	2.6	0.266538
	Toluene (WAF)	1.5	0.462000
	ethylbenzene; o-,m-,p-xylene (WAF)	1.6	0.433125

References	Compounds	Summary half-life (d)	Summary Rate (d^{-1})
Howard, 2005	Benzene (synthesized from literature)	4.6	0.152308
	Toluene (literature)	4.5	0.154343
	Ethylbenzene (literature)	5.0	0.139437
	Xylenes (literature)	4.4	0.156081
Mackay et al., 2006 (When half-lives are given in a range, the geometric mean of the upper and lower bound values is used)	benzene (literature)	6.0	0.115500
		8.9	0.077480
		6.3	0.110000
		1.4	0.500000
		5.8	0.120000
		8.6	0.080581
		5.0	0.138600
		2.6	0.262681
	Toluene (literature)	1.4	0.500000
		9.5	0.072947
		9.4	0.073874
		4.0	0.173250
	Ethylbenzene (literature)	5.5	0.126524
		1.4	0.500000
		2.0	0.346500
	o-xylene (1,2-dimethylbenzene) (literature)	7.0	0.099000
	m,p-xylene (1,2-dimethylbenzene) (literature)	14.0	0.049500
Prince et al., 2007	benzene (as in ~70 ppm gasoline in fresh/sea/sewage water)	3.2	0.216563
	toluene (methylbenzene)	3.2	0.216563
	ethylbenzene	3.2	0.216563
	o-xylene (1,2-dimethylbenzene)	3.2	0.216563
	m-xylene (1,3-dimethylbenzene)	3.2	0.216563
	p-xylene (1,4-dimethylbenzene)	3.2	0.216563

Table C-26: Degradation rates of AR2 (C3-benzenes) in seawater.

References	Compounds	Summary half-life (d)	Summary Rate (d^{-1})
Brakstad et al., 2015 (median sizes of 10 and 30 um droplets)	Isopropylbenzene. Propylbenzene. 1-Methyl-3-ethylbenzene. 1-Methyl-4-ethylbenzene. 1.3.5-Trimethylbenzene. 1-Methyl-2-ethylbenzene. 1.2.4-Trimethylbenzene. 1.2.3-Trimethylbenzene. Indane (droplet median diameter = 10 um)	2.7	0.256667
	Isopropylbenzene. Propylbenzene. 1-Methyl-3-ethylbenzene. 1-Methyl-4-ethylbenzene. 1.3.5-Trimethylbenzene. 1-Methyl-2-ethylbenzene. 1.2.4-Trimethylbenzene. 1.2.3-Trimethylbenzene. Indane (droplet median diameter = 30 um)	3.6	0.192500
Brakstad and Faksness, 2000	Propylbenzene, 1-methyl-3-ethylbenzene, 1-methyl-4-ethylbenzene, 1-methyl-2-ethylbenzene, 1,3,5-trimethylbenzene, 1,2,4-trimethylbenzene, 1,2,3-trimethylbenzene	1.6	0.433125
Prince et al., 2007 (~70 ppm gasoline in fresh/sea/sewage water, authors' reported median values)	propylbenzene	3.2	0.216563
	1-methylethylbenzene	3.2	0.216563
	1-ethyl-2-methylbenzene	3.2	0.216563
	1-methyl-2-(1-methylethyl)benzene	3.6	0.192500
	1-ethyl-3-methylbenzene	3.2	0.216563
	1-ethyl-4-methylbenzene	3.2	0.216563
	1,2,3-trimethylbenzene	3.2	0.216563
	1,2,4-trimethylbenzene	3.2	0.216563
	1,3,5-trimethylbenzene	3.2	0.216563

Table C-27: Degradation rates of AR3 (C4-benzenes) in seawater.

References	Compounds	Summary half-life (d)	Summary Rate (d^{-1})
Brakstad et al., 2015 (10 um or 30 um)	Tert-butyl-Benzene. sec-butylbenzene. m-Cymene. o-Cymene. p-Cymene. 1.3-Diethylbenzene.1-Methyl-3-propylbenzene. 1.4-Diethylbenzene. 1-Methyl-2-propylbenzene. 1-Methyl-4-Propylbenzene. n-Butylbenzene. 1.2-Diethylbenzene. 1.3-Dimethyl-5-Ethylbenzene. 1.4-Dimethyl-2-Ethylbenzene. 1.2-Dimethyl-4-Ethylbenzene. 2.4-dimethylethylbenzen. 1.3-Dimethyl-2-Ethylbenzene. 1.2-Dimethyl-3-Ethylbenzene. 1.2.3.5-Tetramethylbenzene. 1.2.4.5-Tetramethylbenzene. n-Pentylbenzene. 1.2.3.4-Tetramethylbenzene (droplet median diameter 10 um)	2.7	0.256667
	(same as above, except droplet median diameter 30 um)	4.5	0.154000
Brakstad and Faksness, 2000	n-butylbenzene, 1,2,4,5-tetramethylbenzene, n-pentylbenzene (WAF)	1.8	0.385000
Prince et al., 2007	butylbenzene	2.3	0.301304
	(1-methylpropyl)benzene	3.2	0.216563
	(2-methylpropyl)benzene	3.2	0.216563
	1-methyl-2-propylbenzene	2.0	0.346500
	1,2-diethylbenzene	2.8	0.247500
	1-methyl-3-(1-methylethyl)benzene	3.2	0.216563
	1-methyl-3-propylbenzene	1.7	0.407647
	1-methyl-4-(1-methylethyl)benzene	2.5	0.277200
	1-methyl-4-propylbenzene	2.2	0.315000
	1,4-diethylbenzene	2.1	0.330000
	2-ethyl-1,3-dimethylbenzene	3.2	0.216563
	1,4-dimethyl-2-ethylbenzene	3.2	0.216563
	2,4-dimethyl-1-ethylbenzene	3.2	0.216563
	1,2-dimethyl-4-ethylbenzene	3.2	0.216563

References	Compounds	Summary half-life (d)	Summary Rate (d^{-1})
	1-ethyl-3,5-dimethylbenzene	1.8	0.385000
	1,3-dimethyl-5-(1-methylethyl)benzene	4.8	0.144375
	1,2,3,4-tetramethylbenzene	3.2	0.216563
	1,2,3,5-tetramethylbenzene	3.2	0.216563
	1,2,4,5-tetramethylbenzene	3.2	0.216563

Table C-28: Degradation rates of AR4 (cis/trans decalin to C4-decalin) in sea water

References	Compounds	Summary half-life (d)	Summary Rate (d^{-1})
Prince, 2008	Decahydronaphthalene (decalin)	13.6	0.050956
Brakstad et al., 2015 (10um and 30 um droplets)	C10- saturates (10 um droplets)	6.2	0.111774
	C11-12- saturates (10 um droplets)	15.0	0.046200
	C10- saturates (30 um droplets)	9.5	0.072947
	C11-12- saturates (30 um droplets)	16.6	0.041747

Table C-29: Degradation rates of AR5 (C0-C2 Naphthalenes, C0-C2 Benzothiophenes, biphenyl, acenaphthene, acenaphthylene) in sea water.

References	Compounds	Summary half life (d)	Summary Rate (d^{-1})
Brakstad et al., 2015	Naphthalene. C1-naphthalenes (10 um droplets)	2.8	0.247500
	C2-naphthalenes. C3-naphthalenes (10 um droplets)	2.9	0.238966
	Naphthalene. C1-naphthalenes (30 um droplets)	3.4	0.203824
	C2-naphthalenes. C3-naphthalenes (30 um droplets)	5.9	0.117458
Brakstadand Faksness, 2000	Naphthalene. C1-naphthalenes (WAF)	1.1	0.630000
	C2-naphthalenes. C3-naphthalenes (WAF)	1.4	0.495000
	Naphthalene. C1-naphthalenes (dispersed droplets)	4.0	0.173250

References	Compounds	Summary half life (d)	Summary Rate (d^{-1})
	C2-naphthalenes. C3-naphthalenes (dispersed droplets)	11.4	0.060789
Brakstad et al., 2004	Naphthalene. C1-naphthalenes (oil film coated on fabrics)	4.0	0.173250
	C2-naphthalenes. C3-naphthalenes (oil film coated on fabrics)	4.5	0.154000
Campo et al., 2013	C0-naphthalene (SLC dispersed in EPA BFT without dispersant; 5°C)	2.8	0.249947
	C1-naphthalene (SLC dispersed in EPA BFT without dispersant; 5°C)	6.9	0.099979
	C0-naphthalene (SLC dispersed in EPA BFT with dispersant; 5°C)	2.8	0.249947
	C1-naphthalene (SLC dispersed in EPA BFT with dispersant; 5°C)	4.6	0.149968
	C0-naphthalene (SLC dispersed in EPA BFT without dispersant; 25°C)	13.9	0.049989
	C1-naphthalene (SLC dispersed in EPA BFT without dispersant; 25°C)	23.1	0.029994
	C0-naphthalene (SLC dispersed in EPA BFT with dispersant; 25°C)	13.9	0.049989
	C1-naphthalene (SLC dispersed in EPA BFT with dispersant; 25°C)	13.9	0.049989
Prince et al., 2008	Naphthalene	3.9	0.177692
	1-Methylnaphthalene	3.9	0.177692
	2-Methylnaphthalene	3.9	0.177692
	C2-Naphthalenes	2.9	0.238966
	Biphenyl	2.8	0.247500
Prince et al., 2013	Naphthalene (no dispersant)	2.3	0.301304
	C1-naphthalenes (no dispersant)	2.0	0.346500

References	Compounds	Summary half life (d)	Summary Rate (d^{-1})
	C2-naphthalenes (no dispersant)	1.9	0.364737
	Naphthalene (with dispersant)	1.9	0.364737
	C1-naphthalenes (with dispersant)	1.7	0.407647
	C2-naphthalenes (with dispersant)	1.7	0.407647
Venosa and Holder, 2007	C0-naphthalene (PBC degradation at 5°C)	1.7	0.399915
	C1-naphthalene (PBC degradation at 5°C)	2.3	0.299936
	C0-naphthalene (PBC degradation at 20°C)	0.7	0.999788
	C1-naphthalene (PBC degradation at 20°C)	1.4	0.499894

Table C-30: Degradation rates of AR6 (C3-C4 Naphthalenes, C3-C4 Benzothiophenes, dibenzofuran) in sea water.

References	Compounds	Summary half-life (d)	Summary Rate (d^{-1})
Brakstad et al., 2015	C2-naphthalenes. C3-naphthalenes (10 um droplets)	2.9	0.238966
	Benzo(b)thiophene. C1-benzo(b)thiophenes. C2-benzo(b)thiophene. C3-benzo(b)thiophenes. C4-benzo(b)thiophenes. C4-naphthalenes. Biphenyl. Acenaphthylene. Acenaphthene. Dibenzofuran. Fluorene. C1-fluorenes. C2-fluorenes. C3-fluorenes. Phenanthrene. Anthracene. C1-phenanthrenes/anthracenes. C2-phenanthrenes/anthracenes. C3-phenanthrenes/anthracenes. C4-phenanthrenes/anthracenes. Dibenzothiophene. C1-dibenzothiophenes. C2-dibenzothiophenes. C3-dibenzothiophenes. C4-dibenzothiophenes (10 um droplets)	4.2	0.165000
	C2-naphthalenes. C3-naphthalenes (30 um droplets)	5.9	0.117458

References	Compounds	Summary half-life (d)	Summary Rate (d^{-1})
	Benzo(b)thiophene. C1-benzo(b)thiophenes. C2-benzo(b)thiophene. C3-benzo(b)thiophenes. C4-benzo(b)thiophenes. C4-naphthalenes. Biphenyl. Acenaphthylene. Acenaphthene. Dibenzofuran. Fluorene. C1-fluorenes. C2-fluorenes. C3-fluorenes. Phenanthrene. Anthracene. C1-phenanthrenes/anthracenes. C2-phenanthrenes/anthracenes. C3-phenanthrenes/anthracenes. C4-phenanthrenes/anthracenes. Dibenzothiophene. C1-dibenzothiophenes. C2-dibenzothiophenes. C3-dibenzothiophenes. C4-dibenzothiophenes (30 um droplets)	14.1	0.049149
Brakstad and Faksness, 2000	C2- to C3- naphthalenes (WAF)	1.4	0.495000
	C4-naphthalenes, biphenyl, acenaphthylene, acenaphthene, dibezofurane, C0- to C1-fluorenes, C0- to C1-phenanthrenes/ anthracenes, C0- to C1- dibenzothiophenes (WAF)	1.5	0.462000
	C2- to C3- naphthalenes (dispersed droplets)	11.4	0.060789
	C4-naphthalenes, biphenyl, acenaphthylene, acenaphthene, dibezofurane, C0- to C1-fluorenes, C0- to C1-phenanthrenes/ anthracenes, C0- to C1- dibenzothiophenes (dispersed droplets)	105.0	0.006600
Brakstad et al., 2004	C2- and C3- naphthalenes (oil film coated on fabrics)	4.5	0.154000

References	Compounds	Summary half-life (d)	Summary Rate (d^{-1})
	C4-naphthalenes, biphenyl, acenaphthylene, acenaphthene, dibezofurane, C0- to C1-fluorenes, C0- to C1-phenanthrenes/ anthracenes, C0- to C1-dibenzothiophenes (oil film coated on fabrics)	7.0	0.099000
Campo et al., 2013	C2~C4-naphthalenes	13.9	0.049989
	C2~C4-naphthalenes	13.9	0.049989
	C2~C4-naphthalenes	34.7	0.019996
	C2~C4-naphthalenes	23.1	0.029994
Prince et al., 2008	C3-Naphthalenes	4.2	0.165000
	Indan	3.9	0.177692
Prince et al., 2013	C3-naphthalenes	1.9	0.364737
	C4-naphthalenes	2.1	0.330000
	C3-naphthalenes	1.8	0.385000
	C4-naphthalenes	1.9	0.364737
Venosa and Holder, 2007	C2~C4-naphthalenes (PBC degradation at 5°C)	6.9	0.099979
	C2~C4-naphthalenes (PBC degradation at 20°C)	3.5	0.199958

Table C-31. Degradation rates of AR7 (C0-C3 Fluorenes, C0-C1 dibenzothiophenes, C0-C1 phenanthrenes) in sea water.

References	Compounds	Summary half- life (d)	Summary Rate (d^{-1})
Brakstad et al., 2015	Benzo(b)thiophene. C1-benzo(b)thiophenes. C2-benzo(b)thiophene. C3-benzo(b)thiophenes. C4-benzo(b)thiophenes. C4-naphthalenes. Biphenyl. Acenaphthylene. Acenaphthene. Dibenzofuran. Fluorene. C1-fluorenes. C2-fluorenes. C3-fluorenes. Phenanthrene. Anthracene. C1-phenanthrenes/anthracenes. C2-phenanthrenes/anthracenes. C3-phenanthrenes/anthracenes. C4-phenanthrenes/anthracenes. Dibenzothiophene. C1-dibenzothiophenes.C2-dibenzothiophenes. C3-dibenzothiophenes. C4-dibenzothiophenes (10 µm droplets)	4.2	0.165000
	Same as above (30 um droplets)	14.1	0.049149
Brakstad and Faksness, 2000	C4-naphthalenes, biphenyl, acenaphthylene, acenaphthene, dibezofurane, C0- to C1-fluorenes, C0- to C1-phenanthrenes/ anthracenes, C0- to C1- dibenzothiophenes (WAF)	1.5	0.462000
	C4-naphthalenes, biphenyl, acenaphthylene, acenaphthene, dibezofurane, C0- to C1-fluorenes, C0- to C1-phenanthrenes/ anthracenes, C0- to C1- dibenzothiophenes (dispersed droplets)	105.0	0.006600

References	Compounds	Summary half- life (d)	Summary Rate (d^{-1})
Brakstad et al., 2004	C4-naphthalenes, biphenyl, acenaphthylene, acenaphthene, dibezofurane, C0- to C1-fluorenes, C0- to C1-phenanthrenes/ anthracenes, C0- to C1-dibenzothiophenes (oil film coated on fabrics)	4.0	0.173250
Campo et al., 2013	C0~C2-phenathrane2 (SLC dispersed in EPA BFT without dispersant; 5°C)	13.9	0.049989
	C0~C2-fluorenes (SLC dispersed in EPA BFT without dispersant; 5°C)	13.9	0.049989
	C0~C2-dibenzothiphenes (SLC dispersed in EPA BFT without dispersant; 5°C)	23.1	0.029994
	C0~C2-phenathrane2 (SLC dispersed in EPA BFT with dispersant; 5°C)	9.2	0.074984
	C0~C2-fluorenes (SLC dispersed in EPA BFT with dispersant; 5°C)	13.9	0.049989
	C0~C2-dibenzothiphenes (SLC dispersed in EPA BFT with dispersant; 5°C)	13.9	0.049989
	C0~C2-phenathrane2 (SLC dispersed in EPA BFT without dispersant; 25°C)	69.3	0.009998
	C0~C2-fluorenes (SLC dispersed in EPA BFT without dispersant; 25°C)	69.3	0.009998
	C0~C2-dibenzothiphenes (SLC dispersed in EPA BFT without dispersant; 25°C)	69.3	0.009998
	C0~C2-phenathrane2 (SLC dispersed in EPA BFT with dispersant; 25°C)	34.7	0.019996
	C0~C2-fluorenes (SLC dispersed in EPA BFT with dispersant; 25°C)	34.7	0.019996
	C0~C2-dibenzothiphenes (SLC dispersed in EPA BFT with dispersant; 25°C)	69.3	0.009998
Prince et al., 2008	Fluorene	2.5	0.277200
	Methylfluorenes	4.2	0.165000

References	Compounds	Summary half- life (d)	Summary Rate (d^{-1})
	C2-Fluorenes	4.2	0.165000
	Phenanthrene	2.6	0.266538
	1-Methylphenanthrene	4.2	0.165000
	2-Methylphenanthrene	4.2	0.165000
	3-Methylphenanthrene	4.2	0.165000
	9-Methylphenanthrene	4.2	0.165000
Prince et al., 2013	Fluorene	3.1	0.223548
	Phenanthrene	2.6	0.266538
	1-Methylphenanthrene	2.8	0.247500
	2-Methylphenanthrene	2.9	0.238966
	3-Methylphenanthrene	3.0	0.231000
	9-Methylphenanthrene	3.5	0.198000
	C2-phenanthrenes	7.9	0.087722
Venosa and Holder, 2007	C0~C2-phenathrane2 (PBC degradation at 5°C)	13.9	0.049989
	C0~C2-fluorenes (PBC degradation at 5°C)	13.9	0.049989
	C0~C2-dibenzothiphenes (PBC degradation at 5°C)	13.9	0.049989
	C0~C2-phenathrane2 (PBC degradation at 20°C)	3.5	0.199958
	C0~C2-fluorenes (PBC degradation at 20°C)	3.5	0.199958
	C0~C2-dibenzothiphenes (PBC degradation at 20°C)	3.5	0.199958

Table C-32. Degradation rates of AR8 (C0-C2 pyrenes & fluoranthenes, C2-C3 dibenzothiophenes, C2-C3 phenanthrenes, chrysene) in sea water.

References	Compounds	Summary half- life (d)	Summary Rate (d^{-1})
Brakstad et al., 2015	Fluoranthene. Pyrene. C1-fluoranthrenes/pyrenes. C2-fluoranthenes/pyrenes. C3-fluoranthenes/pyrenes. Naphthobenzothiophene. C1-Naphthobenzothiophene. C2-Naphthobenzothiophene. C3-Naphthobenzothiophene. C4-Naphthobenzothiophene. Benz(a)anthracene. Chrysene. C1-chrysenes. C2-chrysenes. C3-chrysenes. C4-chrysenes. Benzo(b)fluoranthene. Benzo(k)fluoranthene. Benzo(e)pyrene. Benzo(a)pyrene. Perylene. Indeno(1.2.3-c.d)pyrene. Dibenz(a.h)anthracene. Benzo(g.h.i)perylene. Retene. Benzo(b)fluorene	5.0	0.138600
	Same as above (30 um droplets)	9.4	0.073723
Brakstad and Faksness, 2000	C4-naphthalenes, biphenyl, acenaphthylene, acenaphthene, dibenzofuran, C0- to C1-fluorenes, C0- to C1-phenanthrenes/ anthracenes, C0- to C1- dibenzothiophenes (WAF)	1.7	0.407647
	C4-naphthalenes, biphenyl, acenaphthylene, acenaphthene, dibenzofuran, C0- to C1-fluorenes, C0- to C1-phenanthrenes/ anthracenes, C0- to C1- dibenzothiophenes (dispersed droplets)	693.0	0.001000

References	Compounds	Summary half- life (d)	Summary Rate (d^{-1})
Brakstad et al., 2004	C2- to C3-fluorenes, C2- to C4-phenanthrenes/anthracenes, C2- to C4-dibenzothiophenes, Fluoranthrene, pyrene, C1- to C3-fluoranthrenes/pyrenes, (g,h,i)perylene, indeno(1,2,3-c,d)pyrenedibenzo(a,h)anthracene, benzobenz(a)anthracene, C0- to C4-crysenes, benzo(b,k)fluoranthene, benzo(e,a)pyrene, perylene, (oil film coated on fabrics)	24.0	0.028875
Campo et al., 2013	C3~C4-phenathranes (SLC dispersed in EPA BFT without dispersant; 5oC)	34.7	0.019996
	C3-fluorenes (SLC dispersed in EPA BFT without dispersant; 5oC)	34.7	0.019996
	C3-dibenzothiphenes (SLC dispersed in EPA BFT without dispersant; 5oC)	34.7	0.019996
	C3~C4-phenathranes (SLC dispersed in EPA BFT with dispersant; 5oC)	69.3	0.009998
	C3-fluorenes (SLC dispersed in EPA BFT with dispersant; 5oC)	69.3	0.009998
	C3-dibenzothiphenes (SLC dispersed in EPA BFT with dispersant; 5oC)	69.3	0.009998
	C3~C4-phenathranes (SLC dispersed in EPA BFT without dispersant; 25oC)	69.3	0.009998
Prince et al., 2008	C2-Phenanthrenes	4.2	0.165000
	C3-Phenanthrenes	6.4	0.108281
Prince et al., 2013	C3-phenanthrenes	4.2	0.165000
	C4-phenanthrenes	6.4	0.108281
	Dibenzothiophene	2.7	0.256667
	Chrysene	30.8	0.022500
Venosa and Holder, 2007	C3~C4-phenathranes (PBC degradation at 5oC)	34.7	0.019996
	C3-fluorenes (PBC degradation at 5oC)	34.7	0.019996
	C3-dibenzothiphenes (PBC degradation at 5oC)	34.7	0.019996

References	Compounds	Summary half- life (d)	Summary Rate (d^{-1})
	HMW PAHs (C0~C3-Naphthobenzothiophenes; C0~C2-pyrenes; and C0~C4-Chrysenes) (PBC degradation at 5oC)	69.3	0.009998
	C3~C4-phenathranes (PBC degradation at 20oC)	6.9	0.099979
	C3-fluorenes (PBC degradation at 20oC)	6.9	0.099979
	C3-dibenzothiphenes (PBC degradation at 20oC)	6.9	0.099979
	HMW PAHs (C0~C3-Naphthobenzothiophenes; C0~C2-pyrenes; and C0~C4-Chrysenes) (PBC degradation at 20oC)	69.3	0.009998

Table C-33. Degradation rates of AR9 (Low molecular weight and soluble Alkanes, Isoalkanes, Cycloalkanes) in sea water.

References	Compounds	Summary half-life (d)	Summary Rate (d^{-1})
Brakstad et al., 2015 (10 µm)	Isopentane. n-C5 (Pentane). Cyclopentane	4.0	0.173250
	2.2-Dimethylbutane. 2-methylpentane. 3-Methylpentane. 2.3-dimethylbutane. n-C6 (Hexane). Methylcyclopentane. Cyclohexane	2.9	0.238966
	2.4-Dimethylpentane. 2.2-Dimethylpentane. 2-Methylhexane. 2.3-Dimethylpentane. 3-methylhexane. 2-Methyl-1-Hexene. n-C7 (Heptane). cis-3-Heptene. Methylcyclohexane	2.6	0.266538
	2.2.4-Trimethylpentane. 2.2.3-Trimethylpentane. 2.4-Dimethylhexane. 2.5-dimethylhexane. ctc-1.2.4-Trimethylcyclopentane. ctc-1.2.3-Trimethylcyclopentane. 3-ethylhexane. 2.3.4-Trimethylpentane.2.3.3-Trimethylpentane. 2.3-Dimethylhexane. 4-Methylheptane. 2-Methylheptane. 3-Methylheptane. ctt-1.2.4-Trimethylcyclopentane. 1-Octene. Isopropylcyclopentane. n-C8 (Octane). trans-2-Octene. Ethylcyclohexane	3.3	0.210000

References	Compounds	Summary half-life (d)	Summary Rate (d^{-1})
	2.4-Dimethylheptane. 1.1.4-Trimethylcyclohexane. ctt-1.2.4-Trimethylcyclohexane. 2.3-Dimethylheptane. 2-Methyloctane. 4-Methyloctane. 1.2.4-Trimethylcyclohexane. 1-Nonene. trans-2-Nonene. n-C9 (Nonane). Isopropylcyclohexane. Butylcyclopentane	3.7	0.187297
	C10 saturates based on boiling point. n-C10	6.2	0.111774
Brakstad et al., 2015 (30 µm)	Isopentane. n-C5 (Pentane). Cyclopentane	4.8	0.144375
	2.2-Dimethylbutane. 2-methylpentane. 3-Methylpentane. 2.3-dimethylbutane. n-C6 (Hexane). Methylcyclopentane. Cyclohexane	3.2	0.216563
	2.4-Dimethylpentane. 2.2-Dimethylpentane. 2-Methylhexane. 2.3-Dimethylpentane. 3-methylhexane. 2-Methyl-1-Hexene. n-C7 (Heptane). cis-3-Heptene. Methylcyclohexane	2.8	0.247500
	2.2.4-Trimethylpentane. 2.2.3-Trimethylpentane. 2.4-Dimethylhexane. 2.5-dimethylhexane. ctc-1.2.4-Trimethylcyclopentane. ctc-1.2.3-Trimethylcyclopentane. 3-ethylhexane. 2.3.4-Trimethylpentane.2.3.3-Trimethylpentane. 2.3-Dimethylhexane. 4-Methylheptane. 2-Methylheptane. 3-Methylheptane. ctt-1.2.4-Trimethylcyclopentane. 1-Octene. Isopropylcyclopentane. n-C8 (Octane). trans-2-Octene. Ethylcyclohexane	4.0	0.173250
	2.4-Dimethylheptane. 1.1.4-Trimethylcyclohexane. ctt-1.2.4-Trimethylcyclohexane. 2.3-Dimethylheptane. 2-Methyloctane. 4-Methyloctane. 1.2.4-Trimethylcyclohexane. 1-Nonene. trans-2-Nonene. n-C9 (Nonane). Isopropylcyclohexane. Butylcyclopentane	4.7	0.147447
	C10 saturates based on boiling point. n-C10	9.5	0.072947
Brakstad and Faksness, 2000	n-pentane, iso-pentane, cyclopentane	2.4	0.288750
	n-hexane, 2-methylpentane, 3-methylpentane, methylcyclopentane, cyclohexane	2.8	0.247500

References	Compounds	Summary half-life (d)	Summary Rate (d^{-1})
	n-heptane, 3-methylhexane, 2,3-dimethylpentane, methylcyclohexane	2.6	0.266538
	C10 saturates	6.8	0.101912
Prince et al., 2007	pentane	10.7	0.064766
	hexane	6.5	0.106615
	heptane	4.5	0.154000
	octane	3.6	0.192500
	nonane	3.2	0.216563
	decane	3.2	0.216563
	undecane	2.8	0.247500
	dodecane	2.8	0.247500
	2-methylpropane	17.1	0.040526
	2-methylbutane	13.0	0.053308
	2-methylpentane	10.4	0.066635
	3-methylpentane	10.1	0.068614
	2-methylhexane	6.6	0.105000
	3-methylhexane	7.5	0.092400
	2-methylheptane	4.8	0.144375
	3-methylheptane	4.2	0.165000
	4-methylheptane	6.4	0.108281
	3-ethylhexane	8.1	0.085556
	3-methyloctane	4.3	0.161163
	4-methyloctane	3.0	0.231000
	3-ethylheptane	3.1	0.223548
	3-methylnonane	3.6	0.192500
	4-methylnonane	3.2	0.216563
	5-methylnonane	3.3	0.210000
	3-ethyloctane	6.0	0.115500
	4-ethyloctane	4.6	0.150652

References	Compounds	Summary half-life (d)	Summary Rate (d^{-1})
	4-propylheptane	5.1	0.135882
	2,2-dimethylbutane	26.5	0.026151
	2,2-dimethylpentane	13.0	0.053308
	2,3-dimethylpentane	8.1	0.085556
	2,4-dimethylpentane	9.1	0.076154
	3,3-dimethylpentane	13.0	0.053308
	2,3-dimethylhexane	7.5	0.092400
	2,4-dimethylhexane	6.6	0.105000
	2,5-dimethylhexane	6.5	0.106615
	2,5-dimethylheptane	6.5	0.106615
	2,6-dimethylheptane	6.5	0.106615
	3,5-dimethylheptane	8.1	0.085556
	2,2,dimethyloctane	6.6	0.105000
	2,3-dimethyloctane	3.9	0.177692
	2,5-dimethyloctane	4.9	0.141429
	2,6-dimethyloctane	4.9	0.141429
	2,7-dimethyloctane	4.9	0.141429
	3,3-dimethyloctane	6.6	0.105000
	3,6-dimethyloctane	4.6	0.150652
	2,2,3-trimethylbutane	13.0	0.053308
	2,2,3-trimethylpentane	13.0	0.053308
	2,2,4-trimethylpentane	8.4	0.082500
	2,3,3-trimethylpentane	13.0	0.053308
	2,3,4-trimethylpentane	10.6	0.065377
	2,2,5-trimemethylhexane	8.1	0.085556
	2,2,4-trimethylheptane	6.5	0.106615
	2,2,5,5-tetramethylhexane	7.4	0.093649
	cyclopentane	9.1	0.076154
	cyclohexane	8.2	0.084512

References	Compounds	Summary half-life (d)	Summary Rate (d^{-1})
	methylcyclopentane	8.1	0.085556
	ethylcyclopentane	6.5	0.106615
	methylcyclohexane	7.4	0.093649
	ethylcyclohexane	6.5	0.106615
	propylcyclohexane	6.5	0.106615
	butylcyclohexane	5.2	0.133269
	pentylcyclohexane	3.7	0.187297
	hexylcyclohexane	3.2	0.216563
	1,1-dimethylcyclopentane	8.9	0.077865
	trans-1,2-dimethylcyclopentane	10.4	0.066635
	trans-1,3-dimethylcyclopentane	8.0	0.086625
	cis-1,3-dimethylcyclopentane	8.3	0.083494
	1,1-dimethylcyclohexane	10.4	0.066635
	trans-1,2-dimethylcyclohexane	8.1	0.085556
	trans-1,3-dimethylcyclohexane	7.7	0.090000
	cis-1,2-dimethylcyclohexane	7.9	0.087722
	cis-1,3-dimethylcyclohexane	8.1	0.085556
	1,1,3-trimethylcyclohexane	8.5	0.081529

Table C-34: Summary of degradation rates of components AR1 through AR9 in seawater.

AR	First-order rate (d^{-1})		References
Component	mean	stdev	
AR1	0.18	0.07	Brakstad et al., 2015
	0.39	0.11	Brakstad and Faksness, 2000
	0.15	0.01	Howard et al., 2005
	0.20	0.16	Mackay et al., 2006
	0.22	0.00	Prince et al., 2007
AR2	0.22	0.05	Brakstad et al., 2015

AR	First-order rate (d^{-1})		References
Component	mean	stdev	
	0.43	N/A	Brakstad and Faksness, 2000
	0.21	0.01	Prince et al., 2007
AR3	0.21	0.07	Brakstad et al., 2015
	0.39	N/A	Brakstad and Faksness, 2000
	0.26	0.07	Prince et al., 2007
AR4	0.05	N/A	Prince et al., 2008
	0.07	0.03	Brakstad et al., 2015
AR5	0.20	0.06	Brakstad et al., 2015
	0.34	0.27	Brakstad and Faksness, 2000
	0.16	0.01	Brakstad et al., 2004
	0.12	0.09	Campo et al., 2013
	0.20	0.04	Prince et al., 2008
	0.37	0.04	Prince et al., 2013
	0.55	0.31	Venosa and Holder, 2007
AR6	0.14	0.08	Brakstad et al., 2015
	0.26	0.26	Brakstad and Faksness, 2000
	0.13	0.04	Brakstad et al., 2004
	0.04	0.01	Campo et al., 2013
	0.17	0.01	Prince et al., 2008
	0.36	0.02	Prince et al., 2013
	0.15	0.07	Venosa and Holder, 2007
AR7	0.11	0.08	Brakstad et al., 2015
	0.23	0.32	Brakstad and Faksness, 2000
	0.17	N/A	Brakstad et al., 2004
	0.03	0.02	Campo et al., 2013

AR	First-order rate (d^{-1})		References
Component	mean	stdev	
	0.19	0.05	Prince et al., 2008
	0.21	0.06	Prince et al., 2013
	0.12	0.08	Venosa and Holder, 2007
AR8	0.11	0.05	Brakstad et al., 2015
	0.20	0.29	Brakstad and Faksness, 2000
	0.03	N/A	Brakstad et al., 2004
	0.01	0.01	Campo et al., 2013
	0.14	0.04	Prince et al., 2008
	0.14	0.10	Prince et al., 2013
	0.05	0.04	Venosa and Holder, 2007
AR9	0.18	0.06	Brakstad et al., 2015
	0.23	0.08	Brakstad and Faksness, 2000
	0.12	0.05	Prince et al., 2007

C.8.2 Summary of degradation rates of AL1-8 & Residual hydrocarbon components in seawater

Tables C-35 to C-42 display the first-order degradation rate constants and half-lives of the eight aliphatic fractions (AL1-8); Table C-43 provides the rates and half-lives of the residual fraction. Table C-44 summarizes the first-order degradation rates and half-life of the AR components used as inputs to the oil fate model.

Table C-35: Degradation rates of AL1 compounds (Aliphatics: BP < 150°C) in seawater.

References	Compounds	Summary half-life (d)	Summary Rate (d^{-1})
Brakstad et al., 2015 (10 µm droplets)	Isopentane. n-C5 (Pentane). Cyclopentane	4.0	0.173250
	2.2-Dimethylbutane. 2-methylpentane. 3-Methylpentane. 2.3-dimethylbutane. n-C6 (Hexane). Methylcyclopentane. Cyclohexane	2.9	0.238966

References	Compounds	Summary half-life (d)	Summary Rate (d^{-1})
	2.4-Dimethylpentane. 2.2-Dimethylpentane. 2-Methylhexane. 2.3-Dimethylpentane. 3-methylhexane. 2-Methyl-1-Hexene. n-C7 (Heptane). cis-3-Heptene. Methylcyclohexane	2.6	0.266538
	2.2.4-Trimethylpentane. 2.2.3-Trimethylpentane. 2.4-Dimethylhexane. 2.5-dimethylhexane. ctc-1.2.4-Trimethylcyclopentane. ctc-1.2.3-Trimethylcyclopentane. 3-ethylhexane. 2.3.4-Trimethylpentane.2.3.3-Trimethylpentane. 2.3-Dimethylhexane. 4-Methylheptane. 2-Methylheptane. 3-Methylheptane. ctt-1.2.4-Trimethylcyclopentane. 1-Octene. Isopropylcyclopentane. n-C8 (Octane). trans-2-Octene. Ethylcyclohexane	3.3	0.210000
Brakstad et al., 2015 (30 µm droplets)	Isopentane. n-C5 (Pentane). Cyclopentane	4.8	0.144375
	2.2-Dimethylbutane. 2-methylpentane. 3-Methylpentane. 2.3-dimethylbutane. n-C6 (Hexane). Methylcyclopentane. Cyclohexane	3.2	0.216563
	2.4-Dimethylpentane. 2.2-Dimethylpentane. 2-Methylhexane. 2.3-Dimethylpentane. 3-methylhexane. 2-Methyl-1-Hexene. n-C7 (Heptane). cis-3-Heptene. Methylcyclohexane	2.8	0.247500
	2.2.4-Trimethylpentane. 2.2.3-Trimethylpentane. 2.4-Dimethylhexane. 2.5-dimethylhexane. ctc-1.2.4-Trimethylcyclopentane. ctc-1.2.3-Trimethylcyclopentane. 3-ethylhexane. 2.3.4-Trimethylpentane.2.3.3-Trimethylpentane. 2.3-Dimethylhexane. 4-Methylheptane. 2-Methylheptane. 3-Methylheptane. ctt-1.2.4-Trimethylcyclopentane. 1-Octene. Isopropylcyclopentane. n-C8 (Octane). trans-2-Octene. Ethylcyclohexane	4.0	0.173250
Brakstad and Faksness, 2000	n-pentane, iso-pentane, cyclopentane	2.4	0.288750
	n-hexane, 2-methylpentane, 3-methylpentane, methylcyclopentane, cyclohexane	2.8	0.247500
	n-heptane, 3-methylhexane, 2,3-dimethylpentane, methylcyclohexane	2.6	0.266538

References	Compounds	Summary half-life (d)	Summary Rate (d^{-1})
Prince et al., 2007	Hexane	6.5	0.106615
	Heptane	4.5	0.154000
	Octane	3.6	0.192500
Prince et al., 2008	Heptane	2.3	0.301304
	Octane	2.1	0.330000

Table C-36. Degradation rates of AL2 compounds (Aliphatics: BP 150-180 C) in seawater.

References	Compounds	Summary half-life (d)	Summary Rate (d^{-1})
Brakstad et al., 2015 (10 µm and 30 µm median diameter droplets)	2.4-Dimethylheptane. 1.1.4-Trimethylcyclohexane. ctt-1.2.4-Trimethylcyclohexane. 2.3-Dimethylheptane. 2-MethylOctane. 4-MethylOctane. 1.2.4-Trimethylcyclohexane. 1-Nonene. trans-2-Nonene. n-C9 (Nonane). Isopropylcyclohexane. Butylcyclopentane (10 µm droplets)	3.7	0.187297
	C10 saturates based on boiling point. n-C10 (10 µm droplets)	6.2	0.111774
	2.4-Dimethylheptane. 1.1.4-Trimethylcyclohexane. ctt-1.2.4-Trimethylcyclohexane. 2.3-Dimethylheptane. 2-MethylOctane. 4-MethylOctane. 1.2.4-Trimethylcyclohexane. 1-Nonene. trans-2-Nonene. n-C9 (Nonane). Isopropylcyclohexane. Butylcyclopentane (30 µm drop	4.7	0.147447
	C10 saturates based on boiling point. n-C10 (30 µm droplets)	9.5	0.072947
Brakstad and Faksness, 2000	C10 saturates	6.8	0.101912
Prince et al., 2007	Nonane	3.2	0.216563
	Decane	3.2	0.216563

References	Compounds	Summary half-life (d)	Summary Rate (d^{-1})
Prince et al., 2008	Nonane	2.1	0.330000
	Decane	2.1	0.330000
Venosa and Holder, 2007	C10 (5˚C)	2.3	0.299936
	C10 (25˚C)	2.8	0.249947
Campo et al., 2013	C10 (25˚C w/o dispersant)	1.7	0.405694
	C10 (5˚C w/o dispersant)	6.9	0.099824
	C10 (5˚C with dispersant)	2.5	0.276894

Table C-37: Degradation rates of AL3 compounds (Aliphatics: BP 180-200; C11 Alkanes) in seawater.

References	Compounds	Summary half-life (d)	Summary Rate (d^{-1})
Brakstad et al., 2015 (10 µm and 30 µm droplets)	C11-C12 saturates based on boiling point. nC11. nC12 (10 µm droplets)	15.0	0.046200
	C11-C12 saturates based on boiling point. nC11. nC12 (30 µm droplets)	16.6	0.041747
Brakstad and Faksness, 2000	C11-C12 total saturates + aromates	8.4	0.082500
Prince et al., 2007	Undecane	2.8	0.247500
Prince et al., 2008	Undecane	2.1	0.330000
Venosa and Holder, 2007	C11 (5˚C)	3.5	0.199958
	C11 25˚C)	3.5	0.199958
Campo et al., 2013	C11 (25˚C w/o dispersant)	1.7	0.405665
	C11 (5˚C w/o dispersant)	9.0	0.076702
	C11 (5˚C with dispersant)	2.6	0.263431

Table C-38: Degradation rates of AL4 compounds (Aliphatics: BP 200-230; C12 Alkanes) in seawater.

References	Compounds	Summary half-life (d)	Summary Rate (d^{-1})
Brakstad et al., 2015 (10 µm droplets)	C11-C12 saturates based on boiling point. nC11. nC12 (10 µm droplets)	15.0	0.046200
Brakstad et al., 2015 (30 µm droplets)	C11-C12 saturates based on boiling point. nC11. nC12 (30 µm droplets)	16.6	0.041747
Brakstad and Faksness, 2000	C11-C12 total saturates + aromates (dispersed droplets)	8.4	0.082500
Prince et al., 2007	Dodecane	3.8	0.182368
Prince et al., 2008	Dodecane	2.1	0.330000
Venosa and Holder, 2007	C12 (5˚C)	6.9	0.100435
	C12 (25˚C)	3.5	0.199958
Campo et al., 2013	C12 (25˚C w/o dispersant)	1.8	0.387044
	C12 (5˚C w/o dispersant)	11.0	0.062774
	C12 (5˚C with dispersant)	2.7	0.252693

Table C-39: Degradation rates of AL5 compounds (Aliphatics: BP 230-280; C13-16 Alkanes) in seawater.

References	Compounds	Summary half-life (d)	Summary Rate (d^{-1})
Brakstad et al., 2015 (10 µm and 30 µm droplets)	C13-C14 saturates based on boiling point. nC13. nC14 (10 µm droplets)	13.0	0.053
	C15-C16 saturates based on boiling point. nC15. nC16 (10 µm droplets)	19.2	0.036
	C13-C14 saturates based on boiling point. nC13. nC14 (30 µmdroplets)	14.1	0.049
	C15-C16 saturates based on boiling point. nC15. nC16 (30 µmdroplets)	12.6	0.055
Brakstad and Faksness, 2000	C13-C14 (dispersed droplets)	9.4	0.074
	C15-C16 (dispersed droplets)	9.8	0.071

References	Compounds	Summary half-life (d)	Summary Rate (d^{-1})
Prince et al., 2008	C13-C15	2.1	0.330
Venosa and Holder, 2007	C12-C25 (5°C)	6.9	0.100
	C12-C25 (25°C)	3.5	0.200
Campo et al., 2013	C13-15 (25°C w/o dispersant)	1.9	0.358
	C13-15 (5°C w/o dispersant)	12.6	0.055
	C13-15 (5°C with dispersant)	2.8	0.250
Hazen et al., 2010	C13 plume samples (2d)	1.6	0.438
	C13 plume samples (5d)	4.0	0.175
	C13 BP data (2d)	1.4	0.497
	C13 BP data (5d)	3.5	0.199
	C13 Mixed consortia (5oC)	3.1	0.227
	C13 Microcosm water, (5oC)	2.1	0.324
	C14 plume samples (2d)	1.5	0.46
	C14 plume samples (5d)	3.8	0.184
	C14 BP data (2d)	1.4	0.506
	C14 BP data (5d)	3.4	0.202
	C14 Mixed consortia (5oC)	3.5	0.197
	C14 Microcosm water, (5oC)	2.3	0.304
	C15 plume samples (2d)	1.5	0.458
	C15 plume samples (5d)	3.8	0.183
	C15 BP data (2d)	1.0	0.709
	C15 BP data (5d)	2.4	0.284
	C15 Mixed consortia (5oC)	3.6	0.193
	C15 Microcosm water, (5oC)	2.1	0.329

Table C-40: Degradation rates of AL6 compounds (Aliphatics: BP 280-300; C17-18 Alkanes) in seawater.

References	Compounds	Summary half-life (d)	Summary Rate (d^{-1})
Brakstad et al., 2015 (10 µm droplets)	C17-C18 saturates based on boiling point. nC17. nC18	26.3	0.026
Brakstad et al., 2015 (30 µm droplets)	C17-C18 saturates based on boiling point. nC17. nC18	35.4	0.020
Brakstad and Faksness, 2000	C17-C18	9.4	0.074
Prince et al., 2008	C17-C18	2.4	0.289
Venosa and Holder, 2007 (5°C)	C12-C25	6.9	0.100
Venosa and Holder, 2007 (25°C)	C12-C25	3.5	0.200
Campo et al., 2013 (25°C w/o dispersant)	C17-18	1.8	0.383
Campo et al., 2013 (5°C w/o dispersant)	C17-18	12.7	0.055
Campo et al., 2013 (5°C with dispersant)	C17-18	2.7	0.261
Hazen et al., 2010	C17 plume samples (2d)	1.7	0.399
	C17 plume samples (5d)	4.3	0.16
	C17 BP data (2d)	1.1	0.615
	C17 BP data (5d)	2.8	0.246
	C17 Mixed consortia (5°C)	3.6	0.19
	C17 Microcosm water, (5°C)	2.3	0.298
	C18 plume samples (2d)	2.1	0.331
	C18 plume samples (5d)	5.2	0.133
	C18 BP data (2d)	1.0	0.668
	C18 BP data (5d)	2.6	0.267
	C18 Mixed consortia (5oC)	4.2	0.166
	C18 Microcosm water, (5oC)	2.3	0.302

Table C-41: Degradation rates of AL7 compounds (Aliphatics: BP 300-350; C19-20 Alkanes) in seawater.

References	Compounds	Summary half- life (d)	Summary Rate (d^{-1})
Brakstad et al., 2015 (10 µm droplets)	C19-C20 saturates based on boiling point. nC19. nC20	50.6	0.014
Brakstad et al., 2015 (30 µm droplets)	C19-C20 saturates based on boiling point. nC19. nC20	66.0	0.011
Brakstad and Faksness, 2000	C19-C20	10.9	0.064
Brakstad et al., 2004	C12-C36	4.5	0.154
Prince et al., 2008	C19-C20	2.8	0.248
Venosa and Holder, 2007 (5°C)	C12-C25	6.9	0.100
Venosa and Holder, 2007 (25°C)	C12-C25	3.5	0.200
Campo et al., 2013 (25°C w/o dispersant)	C19-20	2.0	0.353
Campo et al., 2013 (5°C w/o dispersant	C19-20	14.4	0.048
Campo et al., 2013 (5°C with dispersant)	C19-20	2.9	0.239
Hazen et al., 2010	C19 plume samples (2d)	2.1	0.323
	C19 plume samples (5d)	5.4	0.129
	C19 BP data (2d)	1.0	0.671
	C19 BP data (5d)	2.6	0.269
	C19 Mixed consortia (5˚C)	3.6	0.194
	C19 Microcosm water, (5˚C)	2.3	0.301
	C20 plume samples (2d)	3.2	0.219
	C20 plume samples (5d)	8.0	0.087
	C20 BP data (2d)	1.0	0.703
	C20 BP data (5d)	2.5	0.281
	C20 Mixed consortia (5˚C)	3.7	0.185
	C20 Microcosm water, (5˚C)	2.3	0.298

Table C-42: Degradation rates of AL8 compounds (Aliphatics: BP 350-380; C21-23 Alkanes) in seawater.

References	Compounds	Summary half-life (d)	Summary Rate (d^{-1})
Brakstad et al., 2015 (10 µm droplets)	C21-C23 saturates based on boiling point. nC21. nC23	44.7	0.016
Brakstad et al., 2015 (30 µm droplets)	C21-C23 saturates based on boiling point. nC21. nC23	70.0	0.010
Brakstad and Faksness, 2000	C21-C23	10.7	0.065
Brakstad and Faksness, 2004	C12-C36	4.5	0.154
Prince et al., 2013	Total saturates without dispersant	15.6	0.044
	Total saturates with dispersant	11.6	0.060
Venosa and Holder, 2007 (5°C)	C12-C25	6.9	0.100
Venosa and Holder, 2007 (25°C)	C12-C25	3.5	0.200
Campo et al., 25°C w/o disp	C21-23	2.1	0.330
Campo et al., 5°C w/o disp	C21-23	16.2	0.043
Campo et al.,5°C with disp	C21-23	3.1	0.225
Hazen et al., 2010	C21 plume samples (2d)	3.7	0.187
	C21 plume samples (5d)	9.2	0.075
	C21 BP data (2d)	1.9	0.367
	C21 BP data (5d)	4.7	0.147
	C21 Mixed consortia (5˚C)	3.5	0.196
	C21 Microcosm water, (5˚C)	2.6	0.268
	C22 plume samples (2d)	3.8	0.182
	C22 plume samples (5d)	9.5	0.073
	C22 BP data (2d)	1.0	0.697
	C22 BP data (5d)	2.5	0.279
	C22 Mixed consortia (5˚C)	3.7	0.189
	C22 Microcosm water, (5˚C)	2.2	0.313

References	Compounds	Summary half-life (d)	Summary Rate (d^{-1})
	C23 plume samples (2d)	3.7	0.189
	C23 plume samples (5d)	9.1	0.076
	C23 BP data (2d)	1.0	0.704
	C23 BP data (5d)	2.5	0.282
	C23 Mixed consortia (5˚C)	3.6	0.195
	C23 Microcosm water, (5˚C)	2.2	0.313

Table C-43: Degradation rates of residual compounds (Other non-volatile, non-soluble hydrocarbons) in seawater

References	Compounds	Summary half-life (d)	Summary Rate (d^{-1})
Brakstad et al., 2015 (10 µm droplets)	C26-C36 saturates based on boiling point. nC26. nC27. nC28. nC29. nC30. nC31. nC32. nC33. nC34. nC35. nC36 (10 um droplets)	72.2	0.010
Brakstad et al., 2015 (30 µm droplets)	C26-C36 saturates based on boiling point. nC26. nC27. nC28. nC29. nC30. nC31. nC32. nC33. nC34. nC35. nC36 (30 um droplets)	128.3	0.005
Brakstad and Faksness, 2000	C26-C36 total saturates + aromates	18.4	0.038
Venosa and Holder, 2007	C26-C32 5˚C	13.9	0.05
	C33-C35 5˚C	34.7	0.02
	C26-C32 25˚C	4.6	0.15
	C33-C35 25˚C	6.9	0.10
Zahed et al., 2011 (Whole oil)	100 mg/l natural attenuation	90.0	0.008
	500 mg/l natural attenuation	102.0	0.007
	1000 mg/l natural attenuation	116.0	0.006
	2000 mg/l natural attenuation	124.0	0.006
	100 mg/l crude oil bioremediation	31.0	0.022
	500 mg/l crude oil bioremediation	40.0	0.017
	1000 mg/l crude oil bioremediation	50.0	0.014
	2000 mg/l crude oil bioremediation	75.0	0.009

References	Compounds	Summary half-life (d)	Summary Rate (d^{-1})
	100 mg/l dispersed crude oil bioremediation	28.0	0.025
	500 mg/l dispersed crude oil bioremediation	32.0	0.022
	1000 mg/l dispersed crude oil bioremediation	38.0	0.018
	2000 mg/l dispersed crude oil bioremediation	58.0	0.012
Campo et al., 2013	(5˚C droplets without dispersant) C25	1.9	0.371
	(5˚C droplets without dispersant) C26	1.9	0.364
	(5˚C droplets without dispersant) C27	1.9	0.362
	(5˚C droplets without dispersant) C28	1.9	0.359
	(5˚C droplets without dispersant) C29	1.9	0.363
	(5˚C droplets without dispersant) C30	1.9	0.356
	(5˚C droplets without dispersant) C31	1.9	0.357
	(5˚C droplets without dispersant) C32	2.0	0.346
	(5˚C droplets without dispersant) C33	2.1	0.335
	(5˚C droplets without dispersant) C34	1.9	0.357
	(5˚C droplets without dispersant) C35	1.9	0.358
	(5˚C droplets with dispersant) C25	20.7	0.033
	(5˚C droplets with dispersant) C26	25.4	0.027
	(5˚C droplets with dispersant) C27	34.0	0.020
	(5˚C droplets with dispersant) C28	36.7	0.019
	(5˚C droplets with dispersant) C29	45.3	0.015
	(5˚C droplets with dispersant) C30	45.3	0.015
	(5˚C droplets with dispersant) C31	105.8	0.007
	(5˚C droplets with dispersant) C32	151.6	0.005
	(5˚C droplets with dispersant) C33	n/a	0.000
	(5˚C droplets with dispersant) C34	n/a	0.000
	(5˚C droplets with dispersant) C35	n/a	0.000
	(25˚C droplets with dispersant) C25	3.8	0.185
	(25˚C droplets with dispersant) C26	6.8	0.103
	(25˚C droplets with dispersant) C27	10.2	0.068

References	Compounds	Summary half-life (d)	Summary Rate (d^{-1})
	(25˚C droplets with dispersant) C28	11.6	0.060
	(25˚C droplets with dispersant) C29	13.2	0.052
	(25˚C droplets with dispersant) C30	16.4	0.042
	(25˚C droplets with dispersant) C31	21.2	0.033
	(25˚C droplets with dispersant) C32	25.4	0.027
	(25˚C droplets with dispersant) C33	33.6	0.021
	(25˚C droplets with dispersant) C34	42.8	0.016
	(25˚C droplets with dispersant) C35	39.7	0.017

Table C-44: Summary of degradation rates of AL 1 through AL8 in seawater (font in blue color stands for individual compound based rates; only boiling cut based rates are used to calculate the average values in Table C-45).

AL		First-order rate (d^{-1})		References
Component	Basis	mean	stdev	
AL1	Boiling Cut	0.21	0.04	Brakstad et al., 2015
	Boiling Cut	0.27	0.02	Brakstad and Faksness, 2000
	Individual alkanes	0.15	0.04	Prince et al., 2007
	Individual alkanes	0.32	0.02	Prince et al., 2008
AL2	Boiling Cut	0.13	0.05	Brakstad et al., 2015
	Boiling Cut	0.10	N/A	Brakstad and Faksness, 2000
	Individual alkanes	0.22	0.00	Prince et al., 2007
	Individual alkanes	0.33	0.00	Prince et al., 2008
	Individual alkanes	0.27	0.04	Venosa and Holder, 2007
	Individual alkanes	0.26	0.15	Campo et al., 2013

AL		First-order rate (d^{-1})		References
Component	Basis	mean	stdev	
AL3	Boiling Cut	0.04	0.00	Brakstad et al., 2015
	Boiling Cut	0.08	N/A	Brakstad and Faksness, 2000
	Individual alkanes	0.25	N/A	Prince et al., 2007
	Individual alkanes	0.33	N/A	Prince et al., 2008
	Individual alkanes	0.20	0.00	Venosa and Holder, 2007
	Individual alkanes	0.25	0.16	Campo et al., 2013
AL4	Boiling Cut	0.04	0.00	Brakstad et al., 2015
	Boiling Cut	0.08	N/A	Brakstad and Faksness, 2000
	Individual alkanes	0.18	N/A	Prince et al., 2007
	Individual alkanes	0.33	N/A	Prince et al., 2008
	Individual alkanes	0.15	0.07	Venosa and Holder, 2007
	Individual alkanes	0.23	0.16	Campo et al., 2013
AL5	Boiling Cut	0.05	0.01	Brakstad et al., 2015
	Boiling Cut	0.07	0.00	Brakstad and Faksness, 2000
	Individual alkanes	0.33	N/A	Prince et al., 2008
	Individual alkanes	0.15	0.07	Venosa and Holder, 2007
	Individual alkanes	0.22	0.15	Campo et al., 2013
	Individual alkanes	0.33	0.15	Hazen et al., 2010

AL		First-order rate (d^{-1})		References
Component	Basis	mean	stdev	
AL6	Boiling Cut	0.02	0.00	Brakstad et al., 2015
	Boiling Cut	0.07	N/A	Brakstad and Faksness, 2000
	Individual alkanes	0.29	N/A	Prince et al., 2008
	Individual alkanes	0.15	0.07	Venosa and Holder, 2007
	Individual alkanes	0.23	0.17	Campo et al., 2013
	Individual alkanes	0.31	0.17	Hazen et al., 2010
AL7	Boiling Cut	0.01	0.00	Brakstad et al.,2015
	Boiling Cut	0.06	N/A	Brakstad and Faksness, 2000
	Individual alkanes	0.15	N/A	Brakstad et al., 2004
	Individual alkanes	0.25	N/A	Prince et al., 2008
	Individual alkanes	0.15	0.07	Venosa and Holder, 2007
	Individual alkanes	0.21	0.15	Campo et al., 2013
	Individual alkanes	0.31	0.19	Hazen et al., 2010
AL8	Boiling Cut	0.01	0.00	Brakstad et al., 2015
	Boiling Cut	0.06	N/A	Brakstad and Faksness, 2000
	Individual alkanes	0.15	N/A	Brakstad et al., 2004
	Individual alkanes	0.05	0.01	Prince et al., 2013
	Individual alkanes	0.15	0.07	Venosa and Holder, 2007

AL		First-order rate (d^{-1})		References
Component	Basis	mean	stdev	
	Individual alkanes	0.20	0.15	Campo et al., 2013
	Individual alkanes	0.26	0.18	Hazen et al., 2010
Residual	Boiling Cut	0.01	0.00	Brakstad et al., 2015
	Boiling Cut	0.04	N/A	Brakstad and Faksness, 2000
	Individual alkanes	0.08	0.06	Venosa and Holder, 2007
	Individual alkanes	0.01	0.01	Zahed et al., 2011
	Individual alkanes	0.15	0.16	Campo et al., 2013

C.8.3 Summary of Degradation Rates from All Studies –AR1-AR9, AL1-AL8 and Residual Hydrocarbon Components in Seawater

Table C-45 provides the average values of the first-order degradation rate coefficients. For this calculation, all the AR values that were summarized in Table C-34 were used in the arithmetic mean value calculation of the first-order rate coefficients; however, for the AL values, only those based on boiling-point-cut (not individual alkane) values in Table C-44 were used for the mean first-order rate coefficient value calculations – as this is more representative of the degradation rates of the total petroleum hydrocarbons in each boiling fraction in the oil. These first-order rate values (i.e., instantaneous daily degradation rates for the mass fraction of the component) are the best-estimates of the AR and AL component degradation rates in the water column based on the reviewed studies, and therefore these are used as input to the SIMAP modeling of the DWH oil spill. To put these rates on a time scale, half-lives of AR and AL components of oil were calculated based on the corresponding first-order rate coefficients. The calculated half-life values are also listed in Table C-45.

Table C-45. First-order degradation rates (instantaneous, daily) and half-lives for components of oil in the water column used as model input.

Component Group	First-order rate (day^{-1})	Half-Life (days)
AR1	0.23	3.0
AR2	0.29	2.4
AR3	0.28	2.5
AR4	0.06	11.6
AR5	0.28	2.5
AR6	0.18	3.9
AR7	0.15	4.6
AR8	0.10	6.9
AR9	0.17	4.1
AL1	0.24	2.9
AL2	0.12	5.8
AL3	0.06	11.6
AL4	0.06	11.6
AL5	0.06	11.6
AL6	0.05	13.9
AL7	0.04	17.3
AL8	0.04	17.3
Residual	0.02	34.7

C.8.4 Application of Degradation Rates in the Oil Fates Model

Based on the NRC (2005) review of the different biodegradation mechanisms for the aromatic and alkane compounds, microbial degradation acts on the dissolved phase for aromatics, but on the particulate phase for the insoluble aliphatics. Therefore, in the application of degradation rates in the oil fates model, biodegradation rates of the aromatics are calculated for the dissolved fraction, while the degradation rates of the alkanes are calculated for the dispersed particulate oil fraction.

For the soluble and semi-soluble components (AR1 to AR9), degradation within subsurface droplets in the water column are assumed negligible while in the particulate phase (i.e., negligible degradation in droplets), as degradation rates are much less than their dissolution rates. Once dissolved in the water column, the AR components degrade at the rates as given in

Table C-45. For the model application, it is a reasonable assumption that soluble and semi-soluble components degrade only in the dissolved phase.

The insoluble aliphatic components (AL1 to AL8) are present only in the droplets or floating oil; dissolution of AL1-8 are not simulated in the model because of their generally low solubility. Thus, the AL1-AL8 components degrade only in the particulate phase. This is reasonable, considering that for the insoluble alkane fraction, attachment of microorganisms to dispersed oil droplets is the main mechanism leading to degradation. Therefore, for the subsurface droplets, the degradation rates (Table C-45) are for small droplets (<200 µm in diameter, mostly <50 µm), representative of well dispersed oil entrained in the water column.

Surfactant micelles enhance uptake of water-accommodated fraction hydrocarbons into microbial cells so as to stimulate biodegradation of alkanes, and presumably also sparingly soluble PAHs. Also, a smaller droplet size distribution results in increased dissolution rates of soluble and semi-soluble aromatics, with the higher specific surface area of dispersed oil. Therefore, application chemical dispersants that effectively disperse oil into smaller droplets is expected to increase the overall biodegradation rates, under other favorable conditions that influence oil biodegradation rates.

C9. Conclusions

Degradation of hydrocarbons in seawater is an important process that influences the overall mass balance of the oil in the environment. Therefore it is necessary to incorporate the degradation rates of hydrocarbons into spill assessment models. This review synthesized available information regarding the biodegradation of oil and hydrocarbon components in the environment. Biodegradation rates of whole oil and individual hydrocarbon compounds in seawater from different experimental studies are reviewed. The biodegradation rates of different crude oil components (eight components for aromatics, one for soluble alkanes, eight for in-soluble aliphatics, and one for residuals) are synthesized (Table C-45). These degradation rates provided the basis for inputs to the SIMAP oil fate model.

C10. References

Abou-Naccoul, R., I. Mokbel, G. Bassil, J. Saab, K. Stephan and J. Jose. 2014. Aqueous solubility (in the range between 298.15 and 338.15K), vapor pressures (in the range between 10^{-5} and 80Pa) and Henry's law constant of 1,2,3,4-dibenzanthracene and 1,2,5,6-dibenzanthracene. Chemosphere 95:41-49.

Adcroft, A., R. Hallberg, J. P. Dunne, B. L. Samuels, J. A. Galt, C. H. Barker and D. Payton. 2010. Simulations of underwater plumes of dissolved oil in the Gulf of Mexico. Geophys. Res. Lett. 37(18):L18605.

Aeppli, C., C. A. Carmichael, R. K. Nelson, K. L. Lemkau, W. M. Graham, M. C. Redmond, D. L. Valentine and C. M. Reddy. 2012. Oil Weathering after the Deepwater Horizon Disaster Led to the Formation of Oxygenated Residues. Environmental Science & Technology 46(16):8799-8807.

Anitescu, G. and L. L. Tavlarides. 2006. Supercritical extraction of contaminants from soils and sediments. The Journal of Supercritical Fluids 38(2):167-180.

Atlas, R. and J. Bragg. 2009. Bioremediation of marine oil spills: when and when not – the Exxon Valdez experience. Microbial Biotechnology 2(2):213-221.

Atlas, R. M. 1981. Microbial degradation of petroleum hydrocarbons: an environmental perspective. *Microbiological Reviews* 45(1):180-209.

Atlas, R. M. 1984. *Petroleum Microbiology*. MacMillan Publishing Company. 533 pp.

Atlas, R. M. 1995a. Bioremediation of petroleum pollutants. International Biodeterioration & Biodegradation 35(1–3):317-327.

Atlas, R. M. 1995b. Petroleum biodegradation and oil spill bioremediation. Marine Pollution Bulletin 31(4-12):178-182.

Atlas, R. M. and R. Bartha. 1972a. Biodegradation of petroleum in seawater at low temperatures Canadian Journal of Microbiology 18:1851-1855.

Atlas, R. M. and R. Bartha. 1972b. Degradation and mineralization of petroleum in seawater: limitation by nitrogen and phosphorus. Biotechnology and Bioengineering 14:309-317.

Bagi, A., D. M. Pampanin, O. G. Brakstad and R. Kommedal. 2013. Estimation of hydrocarbon biodegradation rates in marine environments: A critical review of the Q10 approach. Marine Environmental Research 89(5):83-90.

Bælum, J., S. Borglin, R. Chakraborty, J. L. Fortney, R. Lamendella, O. U. Mason, M. Auer, M. Zemla, M. Bill, M. E. Conrad, S. A. Malfatti, S. G. Tringe, H.-Y. Holman, T. C. Hazen and J. K. Jansson. 2012. Deep-sea bacteria enriched by oil and dispersant from the Deepwater Horizon spill. Environmental Microbiology 14(9):2405-2416.

Banat, I. M. 1995. Biosurfactants Production and Possible Uses in Microbial Enhanced Oil-Recovery and Oil Pollution Remediation - a Review. Bioresource Technology 51(1):1-12.

Bartha, R. and R. M. Atlas. 1977. The Microbiology of Aquatic Oil Spills. In: Perlman, D.,eds. Advances in Applied Microbiology. Academic Press, Pp. 225-266.

Bauer, J. E. and D. G. Capone. 1988. Effects of co-occurring aromatic hydrocarbons on degradation of individual polycyclic aromatic hydrocarbons in marine sediment slurries. Applied and Environmental Microbiology 54(7):1649-1655.

Belhaj, A., N. Desnoues and C. Elmerich. 2002. Alkane biodegradation in Pseudomonas aeruginosa strains isolated from a polluted zone: identification of alkB and alkB-related genes. Research in Microbiology 153(6):339-344.

Botton, S. and J. R. Parsons. 2006. Degradation of BTEX compounds under iron-reducing conditions in contaminated aquifer microcosms. Environmental Toxicology and Chemistry 25(10):2630-2638.

Boufadel, M. C., P. Reeser, M. T. Suidan, B. A. Wrenn, J. Cheng, X. Du, T. H. L. Huang and A. D. Venosa. 1999. Optimal nitrate concentration for the biodegradation of n-heptadecane in a variably-saturated sand column. Environmental Technology 20(2):191-199.

Boufadel, M. C., Y. Sharifi, B. Van Aken, B. A. Wrenn and K. Lee. 2010. Nutrient and Oxygen Concentrations within the Sediments of an Alaskan Beach Polluted with the Exxon Valdez Oil Spill. Environmental Science & Technology 44(19):7418-7424.

Braddock, J. F., M. L. Ruth, P. H. Catterall, J. L. Walworth and K. A. Mccarthy. 1997. Enhancement and inhibition of microbial activity in hydrocarbon- contaminated arctic soils: Implications for nutrient-amended bioremediation. Environmental Science and Technology 31(7):2078-2084.

Brakstad, O. G., K. Bonaunet, T. Nordtug and O. Johansen. 2004. Biotransformation and dissolution of petroleum hydrocarbons in natural flowing seawater at low temperature. Biodegradation 15(5):337-346.

Brakstad, O. G. and K. Bonaunet. 2006. Biodegradation of petroleum hydrocarbons in seawater at low temperatures (0-5 degrees C) and bacterial communities associated with degradation. Biodegradation 17(1):71-82.

Brakstad, O. G. and L. G. Faksness. 2000. Biodegradation of water-accomodated fractions and dispersed oil in the seawater column. In: Society of Petroleum Engineers (SPE) International Conference on Health, Safety and Environment in Oil and Gas Exploration and Production, Staganger, Norway. International Society of Petroleum Engineers.

Brakstad, O. G., I. Nonstad, L. G. Faksness and P. J. Brandvik. 2008. Responses of microbial communities in Arctic sea ice after contamination by crude petroleum oil. Microbial Ecology 55(3):540-552.

Brakstad, O. G., T. Nordtug and M. Throne-Holst. 2015. Biodegradation of dispersed Macondo oil in seawater at low temperature and different oil droplet sizes. Marine Pollution Bulletin 93(1-2):144-152.

Camilli, R., C. M. Reddy, D. R. Yoerger, B. a. S. Van Mooy, M. V. Jakuba, J. C. Kinsey, C. P. Mcintyre, S. P. Sylva and J. V. Maloney. 2010. Tracking hydrocarbon plume transport and biodegradation at Deepwater Horizon. Science 330:201-204.

Campo, P., A. D. Venosa and M. T. Suidan. 2013. Biodegradability of Corexit 9500 and Dispersed South Louisiana Crude Oil at 5 and 25 °C. Environmental Science & Technology 47(4):1960-1967.

Chang, W. N., C. W. Liu and H. S. Liu. 2009. Hydrophobic cell surface and bioflocculation behavior of Rhodococcus erythropolis. Process Biochemistry 44(9):955-962.

Chen, J., M. H. Wong, Y. S. Wong and N. F. Y. Tam. 2008. Multi-factors on biodegradation kinetics of polycyclic aromatic hydrocarbons (PAHs) by Sphingomonas sp. a bacterial strain isolated from mangrove sediment. Marine Pollution Bulletin 57(6-12):695-702.

Cho, J., M. M. Zein, M. T. Suidan and A. D. Venosa. 2007. Biodegradability of alkylates as a sole carbon source in the presence of ethanol or BTEX. Chemosphere 68(2):266-273.

Desai, J. D. and I. M. Banat. 1997. Microbial production of surfactants and their commercial potential. Microbiology and Molecular Biology Reviews 61(1):47

Díaz, E. 2004. Bacterial degradation of aromatic pollutants: a paradigm of metabolic versatility. International Microbiology 7(3):173-180.

Diaz, R. J. and R. Rosenberg. 2008. Spreading dead zones and consequences for marine ecosystems. Science 321(5891):926-929.

Dubinsky, E. A., M. E. Conrad, R. Chakraborty, M. Bill, S. E. Borglin, J. T. Hollibaugh, O. U. Mason, Y. M. Piceno, F. C. Reid, W. T. Stringfellow, L. M. Tom, T. C. Hazen and G. L. Andersen. 2013. Succession of Hydrocarbon-Degrading Bacteria in the Aftermath of the

Deepwater Horizon Oil Spill in the Gulf of Mexico. Environmental Science & Technology 47(19):10860-10867.

Du, M. and J. D. Kessler. 2012. Assessment of the Spatial and Temporal Variability of Bulk Hydrocarbon Respiration Following the Deepwater Horizon Oil Spill. Environmental Science & Technology.

Edwards, B. R., C. M. Reddy, R. Camilli, C. A. Carmichael, K. Longnecker and B. a. S. Van Mooy. 2011. Rapid microbial respiration of oil from the Deepwater Horizon spill in offshore surface waters of the Gulf of Mexico. Environ. Res. Lett 6:1-9.

Fang J, Zhang L & Bazylinski DA (2010) Deep-sea piezosphere and piezophiles: geomicrobiology and biogeochemistry. *Trends Microbiol* **18**: 413-422.

French McCay, D., M. Reed, K. Jayko, S. Feng, H. Rines, S. Pavignano, T. Isaji, S. Puckett, A. Keller, F. W. French Iii, D. Gifford, J. Mccue, G. Brown, E. Macdonald, J. Quirk, S. Natzke, R. Bishop, M. Welsh, M. Phillips and B. S. Ingram. 1996. The CERCLA Type A Natural Resource Damage Assessment Model for Coastal and Marine Environments (NRDAM/CME), Technical Documentation, Vol. I -VI, Final Report, submitted to the Office of Environmental Policy and Compliance, U.S. Dept. of the Interior, Washington, D.C., Contract No. 14-0001-91-C-11. April, 1996.

Garcia-Blanco, S., A. D. Venosa, M. T. Suidan, K. Lee, S. Cobanli and J. R. Haines. 2007. Biostimulation for the treatment of an oil-contaminated coastal salt marsh. Biodegradation 18(1):1-15.

Gibbs, C. F. 1975. Quantitative Studies on Marine Biodegradation of Oil. I. Nutrient Limitation at 14 degrees C. Proceedings B of The Royal Society London 188(1090):61-82.

Gibbs, C. F. and S. J. Davis. 1976. The rate of microbial degradation of oil in a beach gravel column. Microbial Ecology 3(1):55-64.

Hamilton, P. 1990. Deep currents in the Gulf of Mexico. Journal of Physical Oceanography, 20: 1087-1104.

Harayama, S., Y. Kasai and A. Hara. 2004. Microbial communities in oil-contaminated seawater. Current Opinion in Biotechnology 15(3):205-214.

Harayama S., H. Kishira, Y. Kasai and K. Shutsubo. 1999. Petroleum biodegradation in marine environments. J Mol Microbiol Biotechnol, 1: 63-70.

Hazen, T. C., E. A. Dubinsky, T. Z. Desantis, G. L. Andersen, Y. M. Piceno, N. Singh, J. K. Jansson, A. Probst, S. E. Borglin, J. L. Fortney, W. T. Stringfellow, M. Bill, M. E. Conrad, L. M. Tom, K. L. Chavarria, T. R. Alusi, R. Lamendella, D. C. Joyner, C. Spier, J. Baelum, M. Auer, M. L. Zemla, R. Chakraborty, E. L. Sonnenthal, P. D'haeseleer, H. Y. N. Holman, S. Osman, Z. Lu, J. D. Van Nostrand, Y. Deng, J. Zhou and O. U. Mason. 2010. Deep-sea oil plume enriches indigenous oil-degrading bacteria. Science 330:204-208.

Head, I. M., D. M. Jones and W. F. M. Roling. 2006. Marine microorganisms make a meal of oil. Nature Reviews Microbiology 4(3):173-182.

Hong, P. K. A. and S. Nakra. 2009. Rapid extraction of sediment contaminants by pressure cycles. Chemosphere 74(10):1360-1366.

Howard, PH, Hueber AE, Mulesky BC, Crisman JS, Meylan W, Crosbie E, Gray DA, Sage GW, Howard KP, LaMacchia A, Boethling R, Troast R. 1986. BIOLOG, BIODEG, and FATE/EXPOS: New files on microbial degradation and toxicity as well as environmental fate/exposure of chemicals. *Environ Toxicol Chem* 5:977–988.

Howard, P., W. Meylan, D. Aronson, W. Stiteler, J. Tunkel, M. Comber and T. F. Parkerton. 2005. A new biodegradation prediction model specific to petroleum hydrocarbons. Environmental Toxicology and Chemistry 24(8):1847-1860.

JAG 2010. Joint Analysis Group (JAG) Review of R/V Brooks McCall Data to Examine Subsurface Oil (http://www.ncddc.noaa.gov/activities/healthy-oceans/jag/reports/).

Jimenez, N., M. Vinas, J. Sabate, S. Diez, J. M. Bayona, A. M. Solanas and J. Albaiges. 2006. The Prestige Oil Spill. 2. Enhanced Biodegradation of a Heavy Fuel Oil under Field Conditions by the Use of an Oleophilic Fertilizer. Environmental Science & Technology 40(8):2578-2585.

Kessler, J. D. V., D.L.; Redmond, M.C.; Du, M.; Chan, E.W.; Mendes, S.D.; Quiroz, E.W.; Villanueva, C.J.; Shusta, S.S.; Werra, L.M.; Yvon-Lewis, S.A.; Weber, T.C. 2011. A persistent oxygen anomaly reveals the fate of spilled methane in the deep Gulf of Mexico Science 331:312-315.

Kimes, N. E., A. V. Callaghan, J. M. Suflita and P. J. Morris. 2014. Microbial transformation of the Deepwater Horizon oil spill—past, present, and future perspectives. Frontiers in Microbiology 5:603.

Krumholz, L. R., M. E. Caldwell and S. J.M. 1996. Biodegradation of 'BTEX' hydrocarbons under anaerobic conditions. In: Crawford, R. L. and D. L. Crawford,eds. Bioremediation: Principles and Applications. Cambridge University Press, New York, NY. Pp. 61-99.

Kujawinski, E. B., M. C. Kido Soule, D. L. Valentine, A. K. Boysen, K. Longnecker and M. C. Redmond. 2011. Fate of Dispersants Associated with the Deepwater Horizon Oil Spill. Environmental Science & Technology 45(4):1298-1306.

Leahy, J. G. and R. R. Colwell. 1990. Microbial degradation of hydrocarbons in the environment. Microbiological Reviews 54(3):305-315.

Lee, K., T. Nedwed, R. C. Prince and D. Palandro. 2013. Lab tests on the biodegradation of chemically dispersed oil should consider the rapid dilution that occurs at sea. Marine Pollution Bulletin 73(1):314-318.

Lovley, D. R. 2000. Anaerobic benzene degradation. Biodegradation 11(2-3):107-116.

Lu, Z., Y. Deng, J. D. Van Nostrand, Z. He, J. Voordeckers, A. Zhou, Y.-J. Lee, O. U. Mason, E. A. Dubinsky, K. L. Chavarria, L. M. Tom, J. L. Fortney, R. Lamendella, J. K. Jansson, P. D'haeseleer, T. C. Hazen and J. Zhou. 2012. Microbial gene functions enriched in the Deepwater Horizon deep-sea oil plume. ISME J 6(2):451-460.

Macnaughton, S. J., J. R. Stephen, A. D. Venosa, G. A. Davis, Y.-J. Chang and D. C. White. 1999. Microbial Population Changes during Bioremediation of an Experimental Oil Spill. Applied and Environmental Microbiology 65(8):3566-3574.

Mackay, D., W. Y. Shiu, K.-C. Ma and S. C. Lee. 2006. Handbook of Physical-Chemical Properties and Environmental Fate for Organic Chemicals. Vol. I, Introduction and Hydrocarbons. CRC Press, Taylor & Francis Group. 925 pp. Available online (Accessed on August 24, 2015) http://files.rushim.ru/books/spravochniki/mackay1.pdf

Mason, O. U., T. C. Hazen, S. Borglin, P. S. G. Chain, E. A. Dubinsky, J. L. Fortney, J. Han, H.-Y. N. Holman, J. Hultman, R. Lamendella, R. Mackelprang, S. Malfatti, L. M. Tom, S. G. Tringe, T. Woyke, J. Zhou, E. M. Rubin and J. K. Jansson. 2012. Metagenome, metatranscriptome and single-cell sequencing reveal microbial response to Deepwater Horizon oil spill. ISME J 6(9):1715-1727.

McFarlin, K.M., Prince, R.C., Perkins, R., Leigh, M.B. 2014. Biodegradation of Dispersed Oil in Arctic Seawater at -1°C. PLoS ONE 9(1): e84297. doi:10.1371/journal.pone.0084297.

McGenity, T.J., Folwell BD, McKew BA & Sanni GO. 2012. Marine crude-oil biodegradation: a central role for interspecies interactions. *Aquat Biosyst* **8**: 10.

Newfields. 2012. Deep-sea science: Application to oil and gas exploration and development. Literature review for deep-sea oil spill fate and effects workshop. Newfields, Port Gamble, WA 98364; Section 2, Petroleum hydrocarbons and microbial communities in

deep ocean: Review of available literature. Prepared by Battelle Memorial Institute, Columbus OH 43201.

NRC. 2003. National Research Council: Oil in the Sea III: Inputs, Fates and Effects. Washington, D.C.: National Academies Press.

NRC. 2005. National Research Council: Understanding Oil Spill Dispersants: Efficacy and Effects. Washington, D.C.: National Academies Press.

Payne, J.R., and W.B. Driskell, 2015a. DRAFT 2010 DWH Offshore Water Column Samples—Forensic Assessments and Oil Exposures. PECI Technical Report to the Trustees in support of the pDARP.

Payne, J.R., and W.B. Driskell, 2015b. DRAFT Forensic Fingerprinting Methods and Classification of DWH Offshore Water Samples. PECI Technical Report to the Trustees in support of the pDARP.

Payne, J.R., and W.B. Driskell, 2015c. Dispersant effects on waterborne oil profiles and behavior. PECI Technical Report to the Trustees in support of the pDARP.

Prince, R. C., T. F. Parkerton and C. Lee. 2007. The Primary Aerobic Biodegradation of Gasoline Hydrocarbons. Environmental Science & Technology 41(9):3316-3321.

Prince, R. C. and C. C. Walters. 2007. Biodegradation of oil hydrocarbons and its implications for source identification. In: Wang, Z. and S. A. Stout,eds. Oil Spill Environmental Forensics. Elsevier, Burlington, MA. Pp. 349-379.

Prince, R. C., McFarlin, K. M., Butler, J. D., Febbo, E. J., Wang, F. C., & Nedwed, T. J. 2013. The primary biodegradation of dispersed crude oil in the sea. *Chemosphere*, *90*(2), 521-526.

Prince, R. C., Haitmanek, C., & Lee, C. C. 2008. The primary aerobic biodegradation of biodiesel B20. *Chemosphere*, *71*(8), 1446-1451.

Rahman, P. K. S. M. and E. Gakpe. 2008. Production, characterisation and applications of biosurfactants - Review. Biotechnology 7(2):360-370.

Reddy, C. M., J. S. Arey, J. S. Seewald, S. P. Sylva, K. L. Lemkau, R. K. Nelson, M. A. S. Van Mooy and R. Camilli. 2012. Composition and fate of gas and oil released to the water column during the Deepwater Horizon oil spill. Proceedings of National Academy of Sciences 109(5):20229-20234.

Redmond, M. C. and D. L. Valentine. 2011. Natural gas and temperature structured a microbial community response to the Deepwater Horizon oil spill. Proceedings of the National Academy of Sciences.

Reed, M., I. Singsaas, P. S. Daling, L.-G. Faksnes and O. G. Brakstad. 2001. Modeling the Water-Accommodated Fraction in OSCAR2000. In: IOSC, API. Pp. 1083-1091.

Ron, E. Z. and E. Rosenberg. 2002. Biosurfactants and oil bioremediation. Current Opinion in Biotechnology 13(3):249-252.

RPS ASA. 2010. SIMAP Technical Manual. Chapter 3, Physical Fates Models. Version 5.2 RPS Applied Science Associates (ASA), South Kingstown, RI

Rontani, J. F., F. Bosser-Joulak, E. Rambeloarisoa, J. C. Bertrand, G. Giusti, and R. Faure. 1985. Analytical study of Asthart crude oil asphaltenes biodegradation. Chemosphere 14:1413-1422.

Ryerson, T. B., R. Camilli, J. D. Kessler, E. B. Kujawinski, C. M. Reddy, D. L. Valentine, E. Atlas, D. R. Blake, J. De Gouw, S. Meinardi, D. D. Parrish, J. Peischl, J. S. Seewald and C. Warneke. 2012. Chemical data quantify Deepwater Horizon hydrocarbon flow rate and environmental distribution. Proceedings of the National Academy of Sciences 109(50):20246-20253.

Saeki, H., M. Sasaki, K. Komatsu, A. Miura and H. Matsuda. 2009. Oil spill remediation by using the remediation agent JE1058BS that contains a biosurfactant produced by *Gordonia sp* strain JE-1058. Bioresource Technology 100(2):572-577.

Schedler, M., R. Hiessl, A. Valladares Juárez, G. Gust and R. Müller. 2014. Effect of high pressure on hydrocarbon-degrading bacteria. AMB Express 4(1):1-7.

Schwarz, J. R., J. D. Walker and R. R. Colwell. 1974. Deep-Sea Bacteria: Growth and Utilization of Hydrocarbons at Ambient and In Situ Pressure. Applied Microbiology 28(6):982-986.

Schwarz, J., J. Walker and R. Colwell. 1975. Deep-sea bacteria: growth and utilization of n-hexadecane at in situ temperature and pressure. Canadian Journal of Microbiology 21(5):682-687.

Shiller, A. M. and D. Joung. 2012. Nutrient depletion as a proxy for microbial growth in Deepwater Horizon subsurface oil/gas plumes. Environmental Research Letters 7(4):1-4.

Singer, M. M., D. Aurand, G. E. Bragin, J. R. Clark, G. M. Coelho, M. L. Sowby and R. S. Tjeerdema. 2000. Standardization of the Preparation and Quantitation of Water-accommodated Fractions of Petroleum for Toxicity Testing. Marine Pollution Bulletin 40(11):1007-1016.

Siron, R., Pelletier, E. and Brochu, C., 1995. Environmental-Factors Influencing the Biodegradation of Petroleum-Hydrocarbons in Cold Seawater. Archives of Environmental Contamination and Toxicology, 28(4): 406-416.

Spaulding, M. L., D. Mendelsohn, D. Crowley, Z. Li and A. Bird. 2015. Draft Technical Reports for Deepwater Horizon Water Column Trustees: Application of OILMAP DEEP to the Deepwater Horizon Blowout. Date of Draft: January 30, 2015; Project No, 2011-144. RPS ASA, 55 Village Square Drive, South Kingstown, RI 02879

Stewart, P. S., D. J. Tedaldi, R. L. Aaron and E. Goldman. 1993. Biodegradation Rates of Crude Oil in Seawater. Water Environment Research 65(7):845-848.

Stout, S. A. and Z. Wang. 2007. Chemical fingerprinting of spilled or discharged petroleum - methods and factors affecting petroleum fingerprints in the environment. In: Wang, Z. and S. A. Stout,eds. Oil Spill Environmental Forensics: Fingerprinting and Source Identification. Elsevier, Burlington, MA. Pp. 1-53.

Tchobanoglous, G., F. L. Burton and D. H. Stensel. 2002. Wastewater Engineering: Treatment and Reuse, 5th Edition. MetCalf and Eddy. McGraw-Hill Science/Engineering/Math. 1848 pp.

Valentine, D. L. K., J.D.; Redmond, M.C.; Mendes, S.D.; Heintz, M.B.; Farwell, C.; Hu, L.; Kinnaman, F.S.; Yvon-Lewis, S.; Du, M.; Chan, E.W.; Tigreros, F.G.; Villanueva, C.J. 2010. Propane respiration jump-starts microbial response to a deep oil spill. Science 330:208-211.

Valentine, D. L., I. Mezic, S. Macesic, N. Crnjaric-Zic, S. Ivic, P. J. Hogan, V. A. Fonoberov and S. Loire. 2012. Dynamic autoinoculation and the microbial ecology of a deep water hydrocarbon irruption. Proceedings of the National Academy of Sciences of the United States of America 109(50):20286-20291.

Van Hamme, J. D., A. Singh and O. P. Ward. 2003. Recent Advances in Petroleum Microbiology. Microbiology and Molecular Biology Reviews 67(4):503-549.

Venosa, A. D., P. Campo and M. T. Suidan. 2010. Biodegradability of Lingering Crude Oil 19 Years after the Exxon Valdez Oil Spill. Environmental Science & Technology 44(19):7613-7621.

Venosa, A. D. and E. L. Holder. 2007. Biodegradability of dispersed crude oil at two different temperatures. Marine Pollution Bulletin 54(5):545-553.

Venosa, A. D., K. Lee, M. T. Suidan, S. Garciablanco, S. Cobanli, M. Moteleb, J. R. Haines, G. Tremblay and M. Hazelwood. 2002. Bioremediation and Biorestoration of a Crude Oil-Contaminated Freshwater Wetland on the St. Lawrence River. Bioremediation Journal 6(3):261.

Venosa, A. D., M. T. Suidan, B. A. Wrenn, K. L. Strohmeier, J. R. Haines, B. L. Eberhart, D. King and E. Holder. 1996. Bioremediation of an experimental oil spill on the shoreline of Delaware bay. Environmental Science & Technology 30(5):1764-1775.

Venosa, A. D. and X. Zhu. 2003. Biodegradation of Crude Oil Contaminating Marine Shorelines and Freshwater Wetlands. Spill Science and Technology Bulletin 8(2):163-178.

Wang, J., Sandoval, K., Ding, Y., Atlas, R., Gardinali, P.R. Biodegradation of dispersed MC252 crude oil by indigenous Gulf of Mexico microbial communities. In: Abstract of the 2014 SETAC North America 35th Annual Meeting, November 10, 2014, Vancouver, Canada.

Ward, O. P. 2010. Microbial Biosurfactants and Biodegradation. Biosurfactants. Pp. 65-74.

Wentzel, A., T. Ellingsen, H.-K. Kotlar, S. Zotchev and M. Throne-Holst. 2007. Bacterial metabolism of long-chain n-alkanes. Applied Microbiology and Biotechnology 76(6):1209-1221.

Whyte, L. G., A. Schultz, J. B. Van Beilen, A. P. Luz, V. Pellizari, D. Labbe and C. W. Greer. 2002. Prevalence of alkane monooxygenase genes in Arctic and Antarctic hydrocarbon-contaminated and pristine soils. Fems Microbiology Ecology 41(2):141-150.

Wrenn, B. A., M. T. Suidan, K. L. Strohmeier, B. L. Eberhart, G. J. Wilson and A. D. Venosa. 1997. Nutrient transport during bioremediation of contaminated beaches: Evaluation with lithium as a conservative tracer. Water Research 31(3):515-524.

Yassine, M. H., M. T. Suidan and A. D. Venosa. 2013. Microbial kinetic model for the degradation of poorly soluble organic materials. Water Research 47(4):1585-1595.

Zahed, M. A., H. A. Aziz, M. H. Isa, L. Mohajeri, S. Mohajeri and S. R. M. Kutty. 2011. Kinetic modeling and half life study on bioremediation of crude oil dispersed by Corexit 9500. Journal of Hazardous Materials 185(2-3):1027-1031.

Zick, A. A. 2013. Expert Report, U.S. v. BP Exploration & Production, Inc. et al., Equation-of-State Fluid Characterization and Analysis of the Macondo Reservoir Fluids. Prepared on behalf of the United States. Prepared by: Aaron A. Zick, Zick Technologies, Inc., 6335 SW Dolph Drive, Portland, OR. March 22, 2013.

Ziervogel, K., L. Mckay, B. Rhodes, C. L. Osburn, J. Dickson-Brown, C. Arnosti and A. Teske. 2012. Microbial Activities and Dissolved Organic Matter Dynamics in Oil-Contaminated Surface Seawater from the Deepwater Horizon Oil Spill Site. PLoS ONE 7(4):e34816.

Ziervogel, K. and C. Arnosti. 2013. Enhanced protein and carbohydrate hydrolyses in plume-associated deepwaters initially sampled during the early stages of the Deepwater Horizon oil spill. Deep Sea Research Part II: Topical Studies in Oceanography (In press).

Technical Reports for Deepwater Horizon Water Column Injury Assessment

WC_TR.14: Modeling Oil Fate and Exposure Concentrations in the Deepwater Plume and Rising Oil Resulting from the Deepwater Horizon Oil Spill

Appendix D: SIMAP Model Inputs

Authors: Deborah French McCay, Katherine Jayko, Zhengkai Li, Matthew Horn, Yong Kim, Tatsu Isaji, Deborah Crowley, Malcolm Spaulding, Lauren Decker, Cathleen Turner, Stefanie Zamorski, Jeremy Fontenault, Rachel Shmookler, and Jill Rowe

Revised: September 29, 2015
Project Number: 2011-144
RPS ASA 55 Village Square Drive, South Kingstown, RI 02879

Table of Contents

List of Figures

D.1 Geographical and Model Grid

For geographical reference, SIMAP uses a rectilinear grid to designate the location of the shoreline, the water depth (bathymetry), and the shore or habitat type. Section 4.1 in the main report describes the use of the grids by the model. Specific details of the grids used for modeling the Deepwater Horizon (DWH) oil spill are described here.

D.1.1 Basemap

The base map used defines the land-sea boundary for the modeling. The land polygon data was compiled from NOAA's ESI data: http://response.restoration.noaa.gov/esi.

The datasets used were Florida, Alabama, Mississippi, Louisiana, and Texas (though only a small part). The land polygon data were converted to a raster grid using the extent and resolution defined for the grid.

D.1.2 Grid Dimensions

- Definition of the 600-m resolution grid (95TO83W-NOF25-ALLOPEN_GT200M-SWD_600m-2.HAB)
    - Extent:
        - Top: 31°N
        - Bottom: 25°N
        - Left: 95°W
        - Right: 83°W
    - Resolution:
        - 2000 (W-E) x 1000 (N-S) cells
        - Cell Size (degrees): 0.006° x 0.006°
        - Cell size (m at wellhead) in W-E, S-N: 605.36 m x 667.94 m
        - Cell area (square meters): 404,347.53
        - Cell length if shore (meters): 635.88
    - Spatial Reference:
        - GCS_WGS_1984

D.1.3 Landward and Seaward Designations of Habitats

Within a grid, habitats are designated as landward or seaward. Landward portions are the shelf, bays and inlets, whereas seaward is the offshore portion of the grid. For all grids used in model runs, the seaward portion was set as those waters greater than 200 m deep.

- Landward/Seaward Delineation:
    - Depths less than 200 m were assigned LWD (landward) habitats
    - Depths greater than 200 m were assigned SWD (seaward) habitats

D.1.4 Preparation of Habitat Grid

The following sections describe the data sets queried and used for each of the different habitat types represented in the habitat grids.

For the 600-m resolution grid (95TO83W-NOF25-ALLOPEN_GT200M-SWD_600m-2.HAB):

1. Shoreline = ESI Data,
2. Open bottom Type = all assigned as sand bottom, and
3. Structured habitats (e.g., Submerged Aquatic Vegetation, SAV, Coral reefs, seep communities) are not mapped.

Note that in the habitat grid, subtidal habitat types were not resolved, and all areas were considered open, unstructured bottom (i.e., "sand"). Subtidal bottom types have no influence on oil fate model results; they are only used to tabulate results by habitat type. The biological density data used to evaluate exposure were from sampling in open bottom habitat (e.g., shrimp and other demersal trawls, midwater trawls and MOCNESS) and those densities were assigned to all shelf and/or all offshore areas. Thus, to determine exposure histories for all waters, all areas were designated as unstructured open water.

Some manual cleanup of the habitat grid was required after all of the processing. Some form of habitat is required between the land-water interface, so habitat information was added where missing. Since the Louisiana ESI data do not have complete shoreline coverage and do not match the shoreline exactly, the most significant cleanup was required there. Also, due to the coarse resolution of this grid, some bays and inlets were closed by habitat cells; thus, leaving no open water. Where appropriate, these areas were opened up making the habitat data match the coastline more accurately.

The habitat grid was created using NOAA's ESI data: http://response.restoration.noaa.gov/esi. ESIP polygon data were converted to a raster grid using the Maximum Combined Area method, to assign values to cells. ESIL data were also converted to a raster grid, using the Maximum Combined Length method. The resolution and extent defined for this habitat grid were used for both processes. The ESIP grid and then the ESIL grid was used to update the land base map wherever ESI data were present. A default bottom type of sand was assigned to all water cells initially.

The ESIL (lines) and ESIP (Polygon) layers were reclassified for SIMAP using the ESI codes as follows (when a feature had more than one code, the last value was used):

- ESIL:
  - 1 = Seaward Man-Made, Artificial (18)
  - 10A = Seaward Intertidal Fringing Wetland, Saltmarsh, or Mangrove (5)
  - 10B = Landward Intertidal Fringing Wetland, Saltmarsh, or Mangrove (35)
  - 10C = Landward Intertidal Fringing Wetland, Saltmarsh, or Mangrove (35)
  - 10D = Landward Intertidal Fringing Wetland, Saltmarsh, or Mangrove (35)
  - 10E = Seaward Intertidal Fringing Wetland, Saltmarsh, or Mangrove (5)
  - 1A = Seaward Intertidal Rocky Shore (1)
  - 1B = Seaward Man-Made, Artificial (18)
  - 2A = Seaward Intertidal Fringing Mud Flat (4)
  - 2B = Seaward Intertidal Fringing Mud Flat (4)
  - 3A = Seaward Intertidal Sand Beach (3)
  - 3B = Seaward Intertidal Sand Beach (3)
  - 4 = Seaward Intertidal Sand Beach (3)
  - 5 = Seaward Intertidal Gravel Beach (2)
  - 6A = Seaward Intertidal Gravel Beach (2)
  - 6B = Seaward Man-Made, Artificial (18)
  - 7 = Seaward Intertidal Fringing Mud Flat (4)

- 8A = Seaward Intertidal Rocky Shore (1)
- 8B = Seaward Man-Made, Artificial (18)
- 8C = Seaward Man-Made, Artificial (18)
- 8D = Seaward Intertidal Rocky Shore (1)
- 9 = Seaward Intertidal Fringing Mud Flat (4)
- 9A = Seaward Intertidal Fringing Mud Flat (4)
- 9B = Seaward Intertidal Fringing Wetland, Saltmarsh, or Mangrove (5)
- 9C = Seaward Intertidal Fringing Mud Flat (4)
- U = NOT USED

- ESIP:
  - 10A = Seaward Extensive Wetland, Saltmarsh, or mangrove (21)
  - 10B = Landward Extensive Wetland, Saltmarsh, or mangrove (21)
  - 10C = Landward Extensive Wetland, Saltmarsh, or mangrove (21)
  - 10D = Landward Extensive Wetland, Saltmarsh, or mangrove (21)
  - 7 = Seaward Extensive Mud Flat (20)
  - 9A = Seaward Extensive Mud Flat (20)
  - 9C = Seaward Extensive Mud Flat (20)

D.1.5 Habitat Grid Map

The 600-m resolution grid (95TO83W-NOF25-ALLOPEN_GT200M-SWD_600m-2.HAB) is shown in Figure D.1.1.

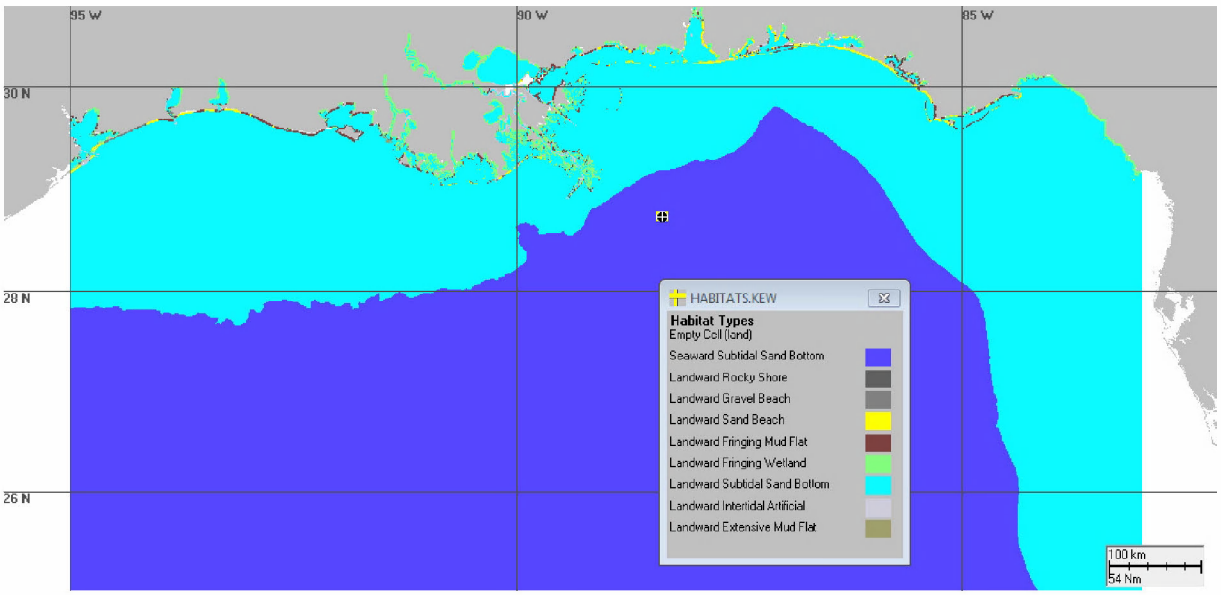

Figure D.1-1 Map of the 600 m resolution habitat grid (95TO83W-NOF25-ALLOPEN_GT200M-SWD_600m-2.HAB). (Circled cross is the DWH well site.)

D.1.6 Preparation of Depth Grid

A depth grid was created matching the extent and resolution of each habitat grid. Each subtidal (water) grid cell was assigned a depth. Depths are in meters.

Bathymetry for the Gulf of Mexico was obtained from NOAA's National Geophysical Data Center (NGDC), as follows:

http://www.ngdc.noaa.gov/mgg/coastal/crm.html

These data were downloaded in an Arc ascii format for the central, western and Florida and eastern gulf.

http://www.ngdc.noaa.gov/mgg/inundation/

These data were downloaded in an Arc ascii format for Biloxi and Panama City. Southern Louisiana was downloaded in a netCDF format and converted to Arc ascii.

http://www.ngdc.noaa.gov/mgg/inundation/vdatum/vdatum.html

Data were downloaded in an Arc ascii format for: Mobile, New Orleans, Northern Gulf Coast.

The spatial extent of each of the grids overlaps as shown in Figure D.1.2. The source bathymetry came in the following resolutions:

- Eastern, Central, Western GOM: 3 arc-second = ~0.00083°,
- Northern Gulf Coast: 1 arc second = ~0.000278°, and
- Panama City, Biloxi, Mobile, New Orleans, Southern Louisiana: 1/3 arc-second = ~0.00009°.

The base was used from the 3 arc-second datasets. The higher resolutions were used on top of that dataset.

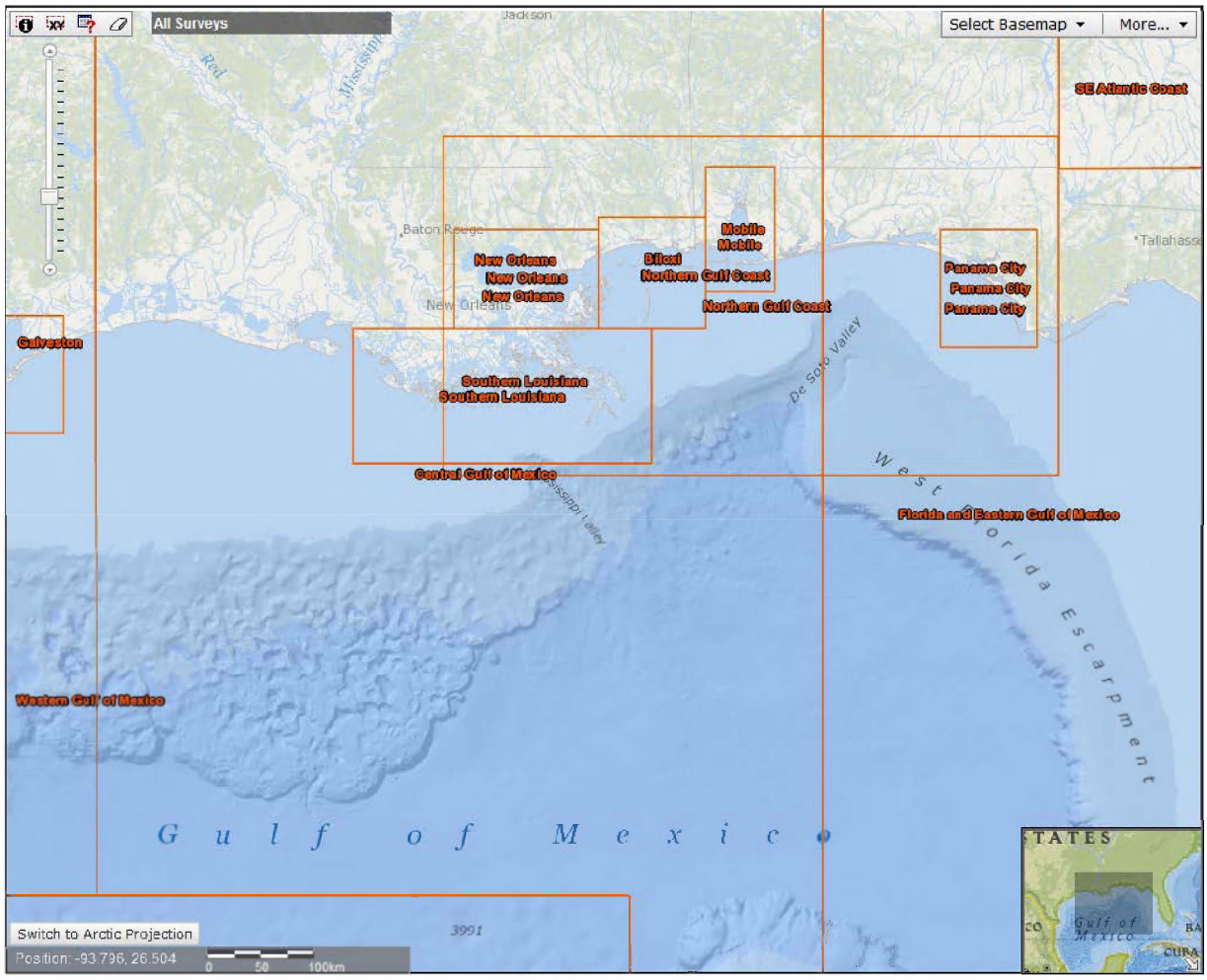

Figure D.1-2. Spatial extent of bathymetric grids available on http://maps.ngdc.noaa.gov/viewers/bathymetry/.

The habitat/depth grid for SIMAP resolution was coarser then any of the source datasets. As such, the source datasets needed to be "Resampled" down to the required resolution. Resampling reduces the cell size of each data source to the habitat grid resolution. Cell values are altered using bilinear interpolation. ArcGIS performs this by determining the new value of a cell based on a weighted distance average of the four nearest input cell centers. This procedure will cause some smoothing of the data.

After all sources were resampled to the desired cell size they were combined. In places where cells overlapped, the value was taken from the source in the following priority:

1) Panama City, Biloxi, Mobile, New Orleans, Southern Louisiana,
2) Northern Gulf Coast, and
3) Eastern, Central, Western GOM.

The higher resolution sources (other than the 3 base DEMs) were used because they provided detailed bathymetry right around the coast, specifically the Mississippi River outlet. The higher resolution data (even after resampling down) provide data for these areas.

The above bathymetry included land elevations as well as water depths. The positive elevations (land) were removed from the grid. This left a small gap in a few places along the Louisiana coast. These bathymetry datasets also indicated the depths as zero in some shallow coastal areas. The depths for these missing cells were interpolated based on surrounding depths. The result of which was that 0.1 m was assigned to the vast majority of these cells.

The 600m-resolution depth grid is shown in Figure D.1.3.

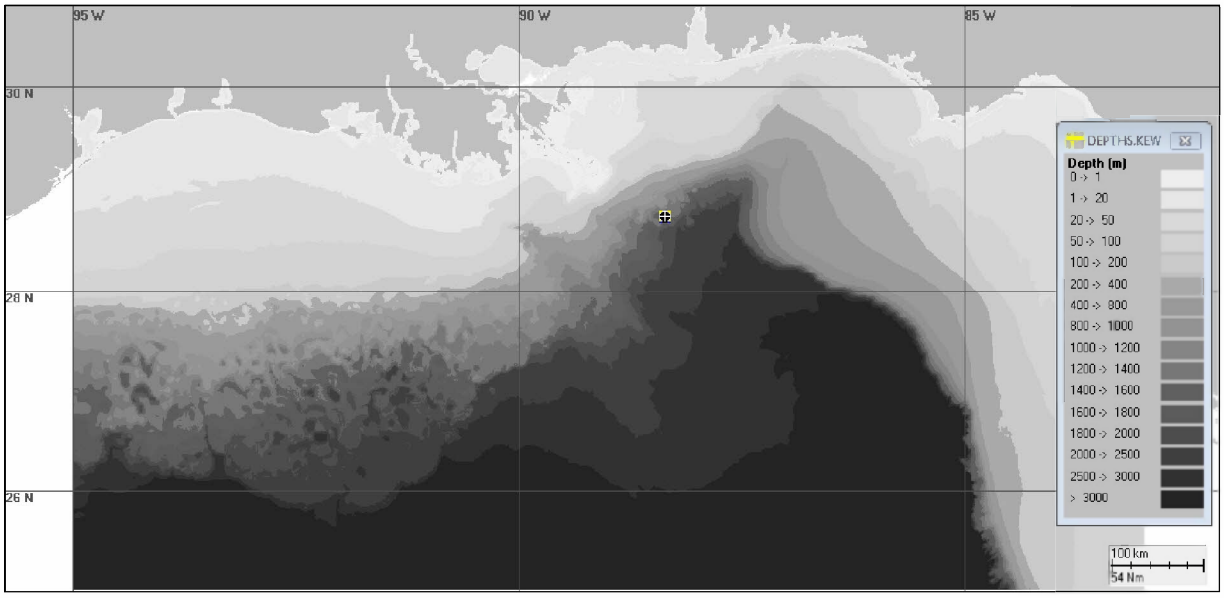

Figure D.1-3. Map of the 600-m resolution depth grid (95TO83W-NOF25-ALLOPEN_GT200M-SWD_600m-2.DEP). (Circled cross is the DWH well site.)

D.2 Water Temperature, Salinity and Density

D.2.1 Data Source and Grid Resolution

Data were obtained from the National Oceanographic Data Center (NODC) Ocean Climate Laboratory's, World Ocean Atlas, Monthly Climatology data set for the Gulf of Mexico. All data for the monthly 1/4-degree gridded data set in the NODC database as of 2013 were obtained from this url:

https://www.nodc.noaa.gov/OC5/woa13/

Data options used for temperature and salinity were:

- Objectively Analyzed mean
- 1/4° Grid
- Averaged decades
- Monthly

Downloaded on 1/19/2015 in CSV format

Data were reformatted into a text file format suitable for input to SIMAP. The extents of the grids are:

- Left = 99.000°W
- Right = 81.000°W
- Bottom = 21.000°N
- Top = 31.000°N

Since all vertical layers of each of the cells needed a value, and in some locations the atlas data did not reach the bathymetry, the value from the deepest depth where data were available was used for all depths below it. (SIMAP will not use data below the depth present in the depth grid.)

D.2.2 Temperature

Figure D.2.1 shows the resolution of the 1-4-degree grid, and the locations of three grid cells for which vertical temperature profiles are shown in Figure D.2.2.

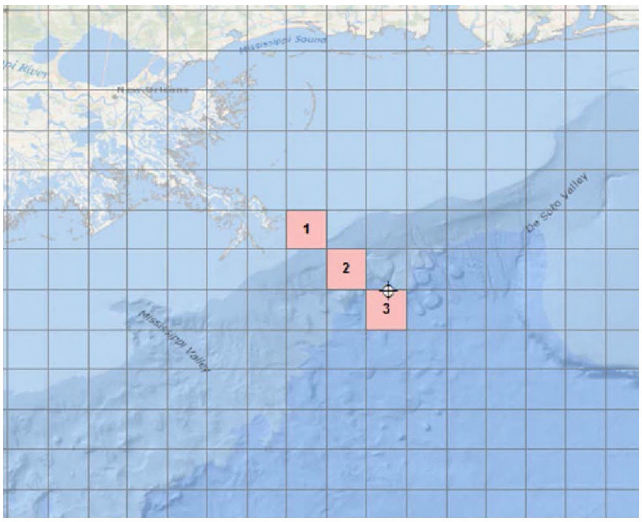

Figure D.2-1 Resolution of the 1/4-degree grid, and the locations of three grid cells for which vertical temperature profiles are shown in Figure D.2.2.

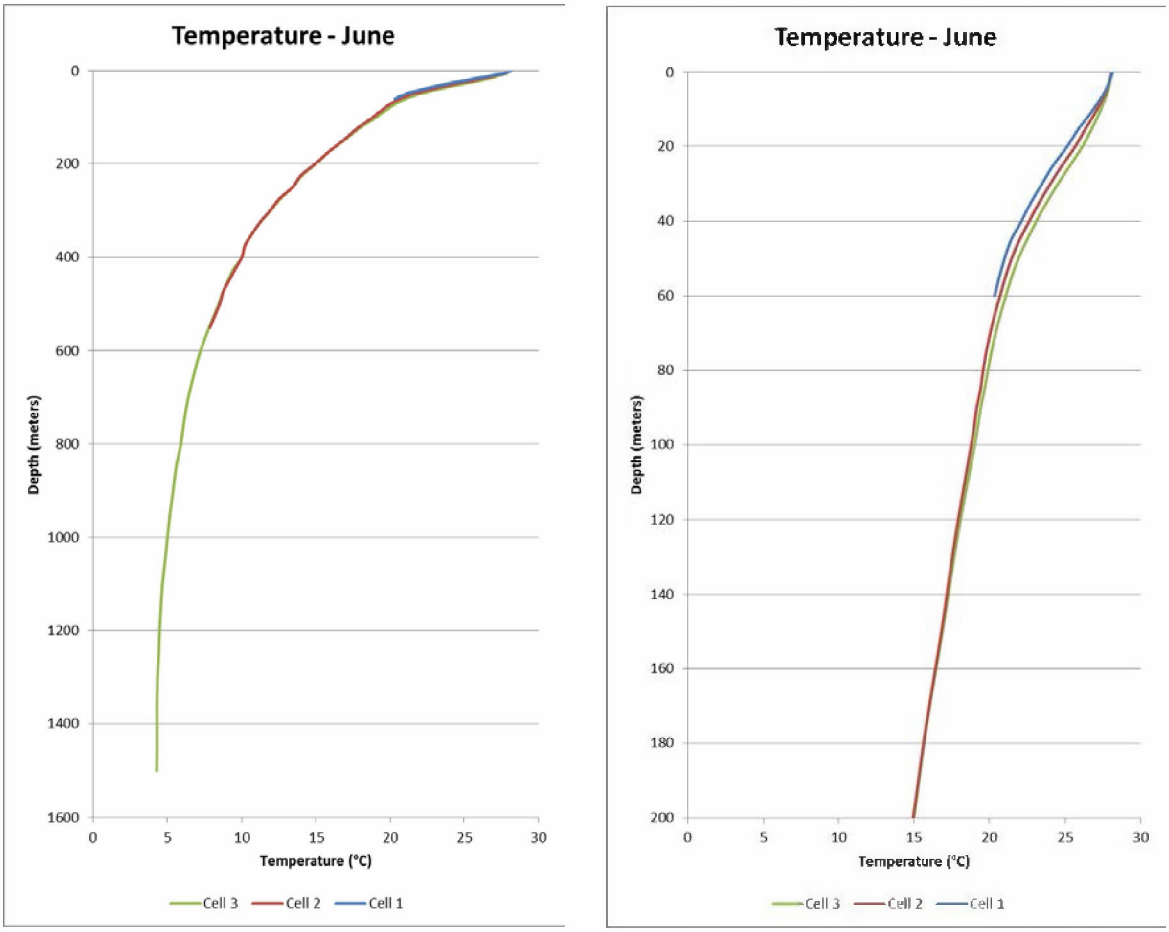

Figure D.2-2 Vertical temperature profiles for cells shown in Figure D.2.1.

Figures D.2-3 to D.2-11 show the downloaded ¼-degree 2013 NODC surface and bottom water temperature data used.

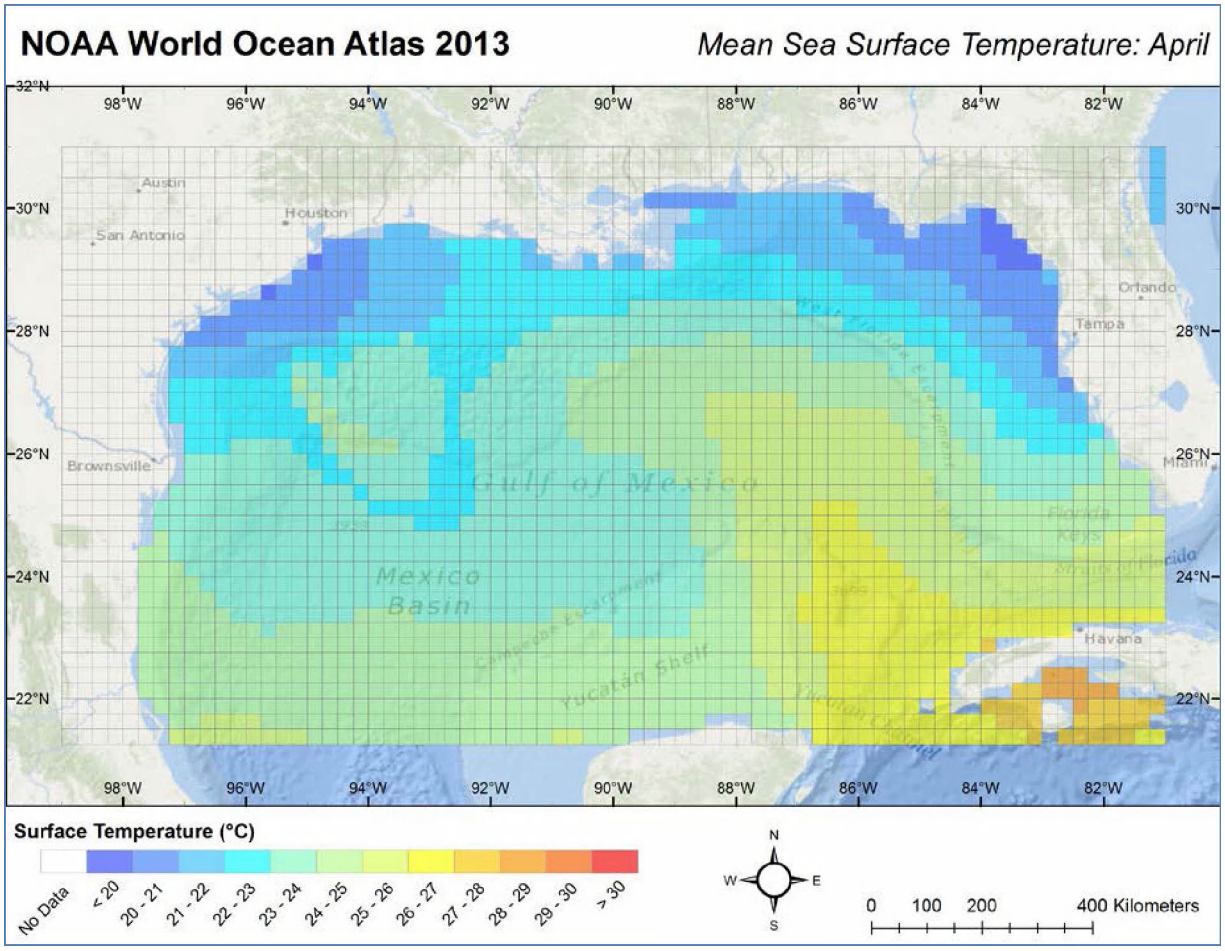

Figure D.2-3 Climatic mean surface water temperature data for April, from the NODC World Ocean Atlas (2013).

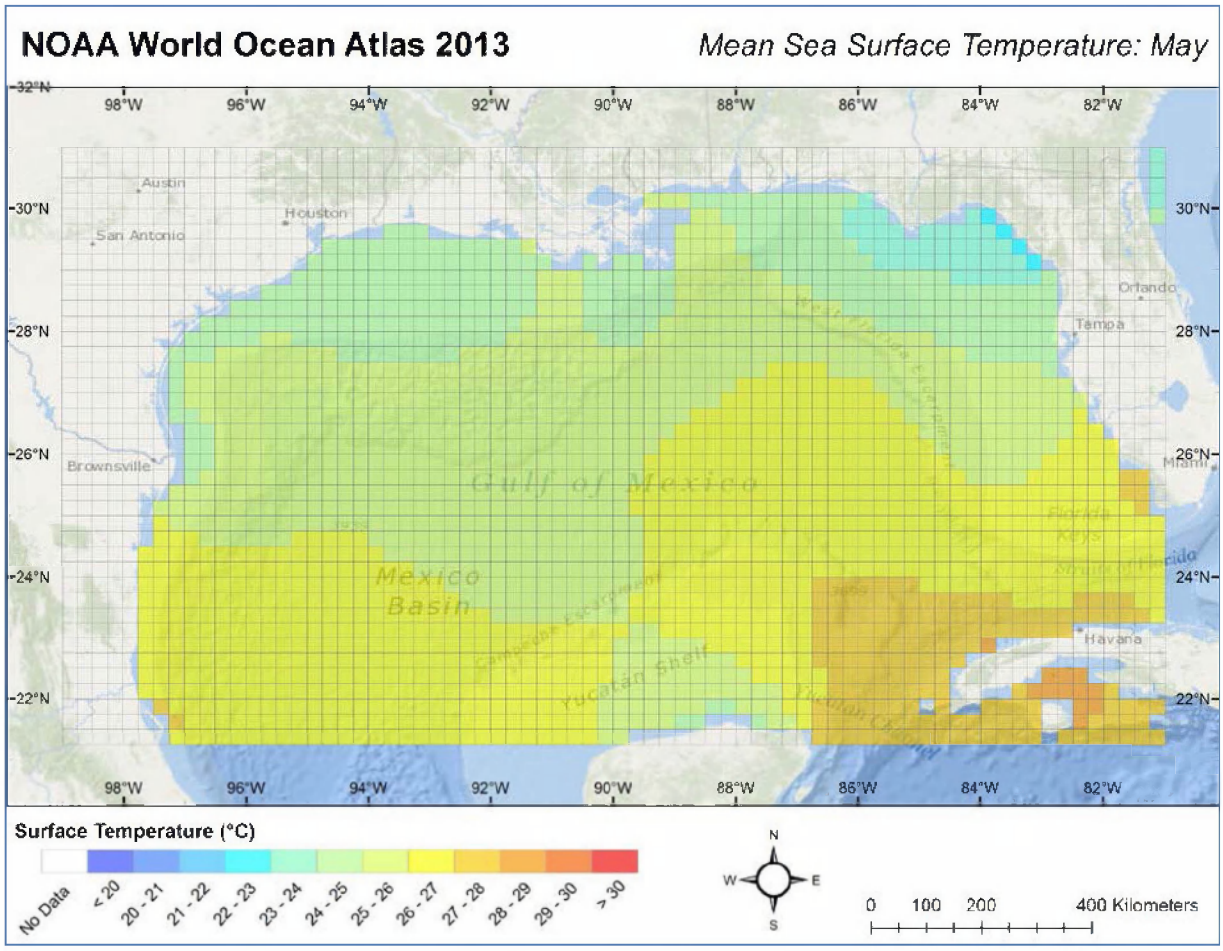

Figure D.2-4 Climatic mean surface water temperature data for May, from the NODC World Ocean Atlas (2013).

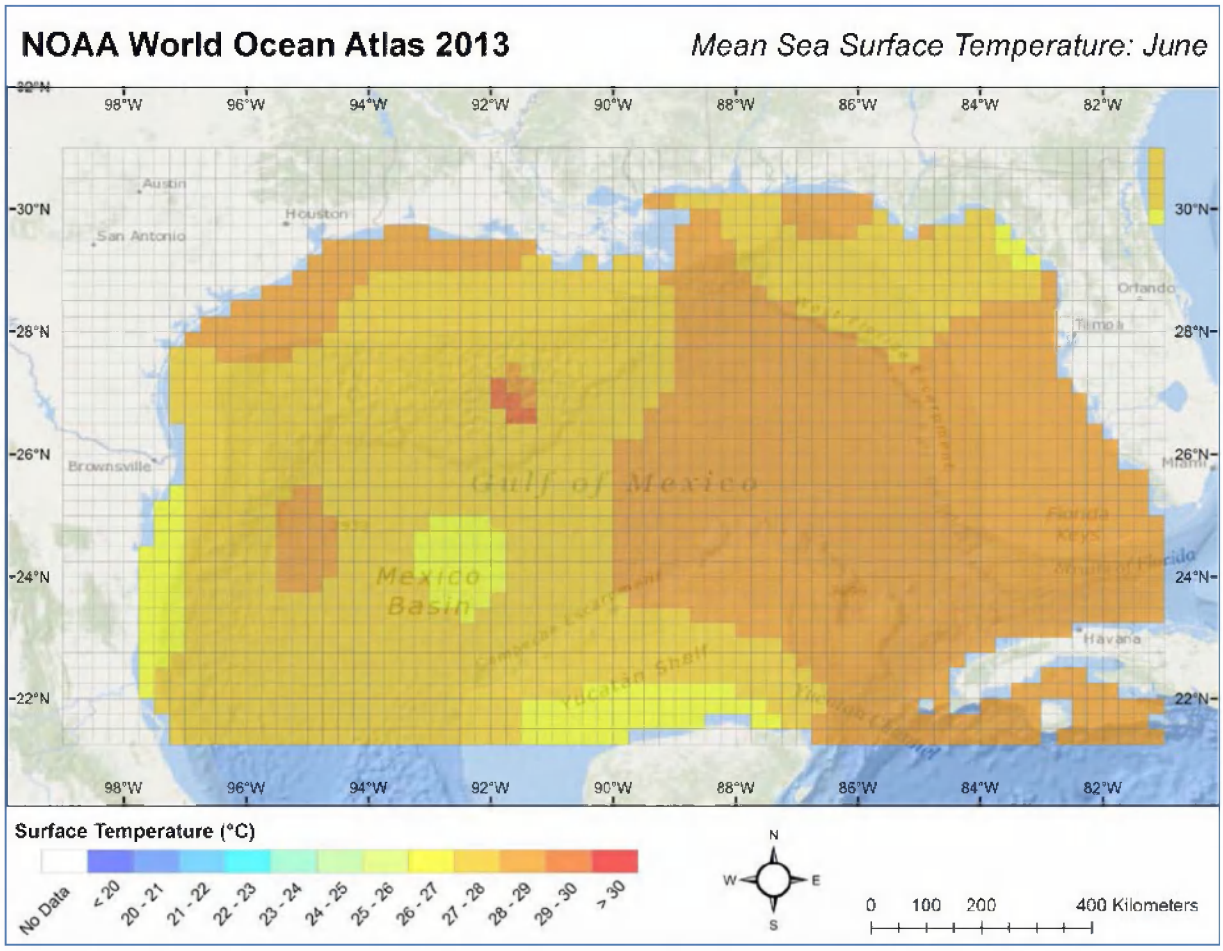

Figure D.2-5 Climatic mean surface water temperature data for June, from the NODC World Ocean Atlas (2013).

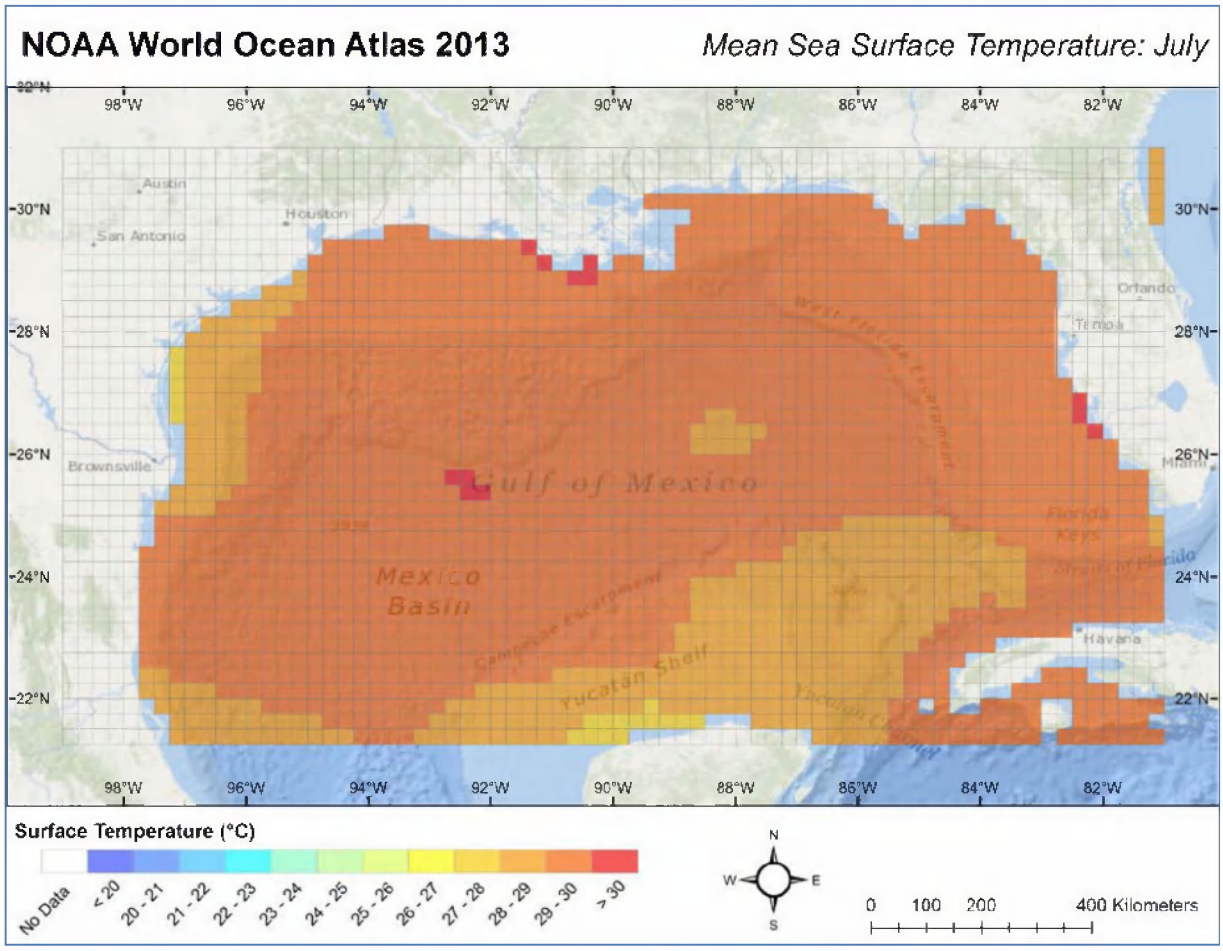

Figure D.2-6 Climatic mean surface water temperature data for July, from the NODC World Ocean Atlas (2013).

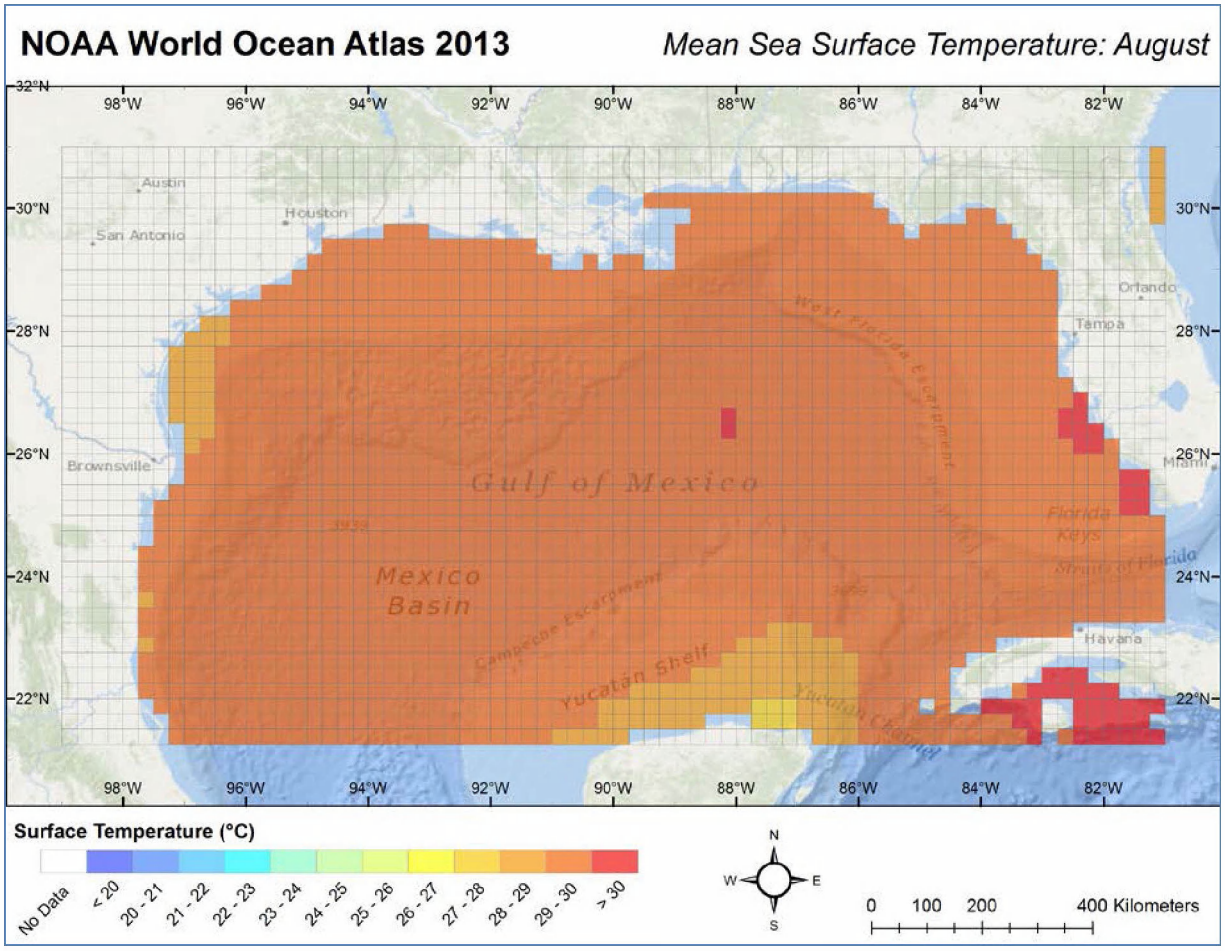

Figure D.2-7 Climatic mean surface water temperature data for August, from the NODC World Ocean Atlas (2013).

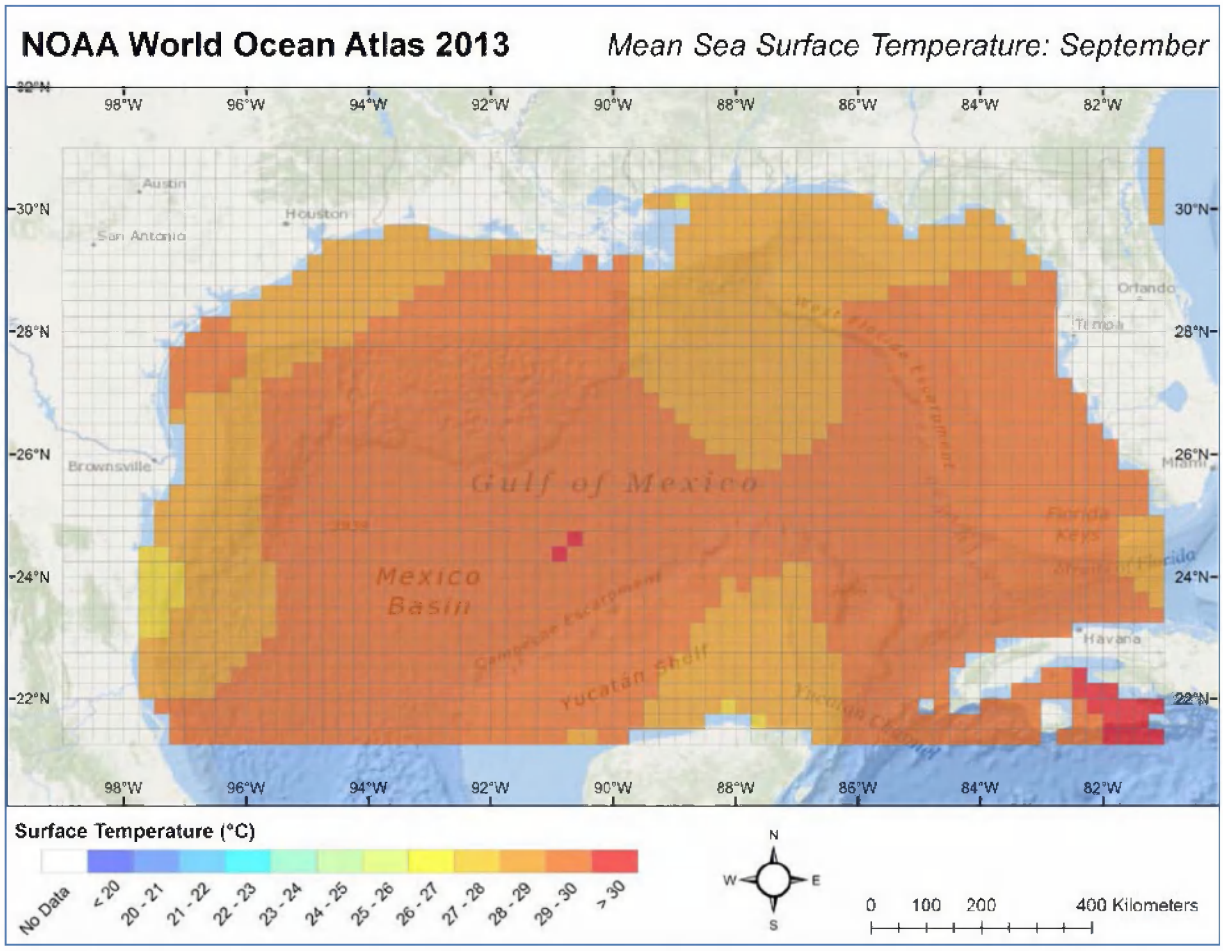

Figure D.2-8 Climatic mean surface water temperature data for September, from the NODC World Ocean Atlas (2013).

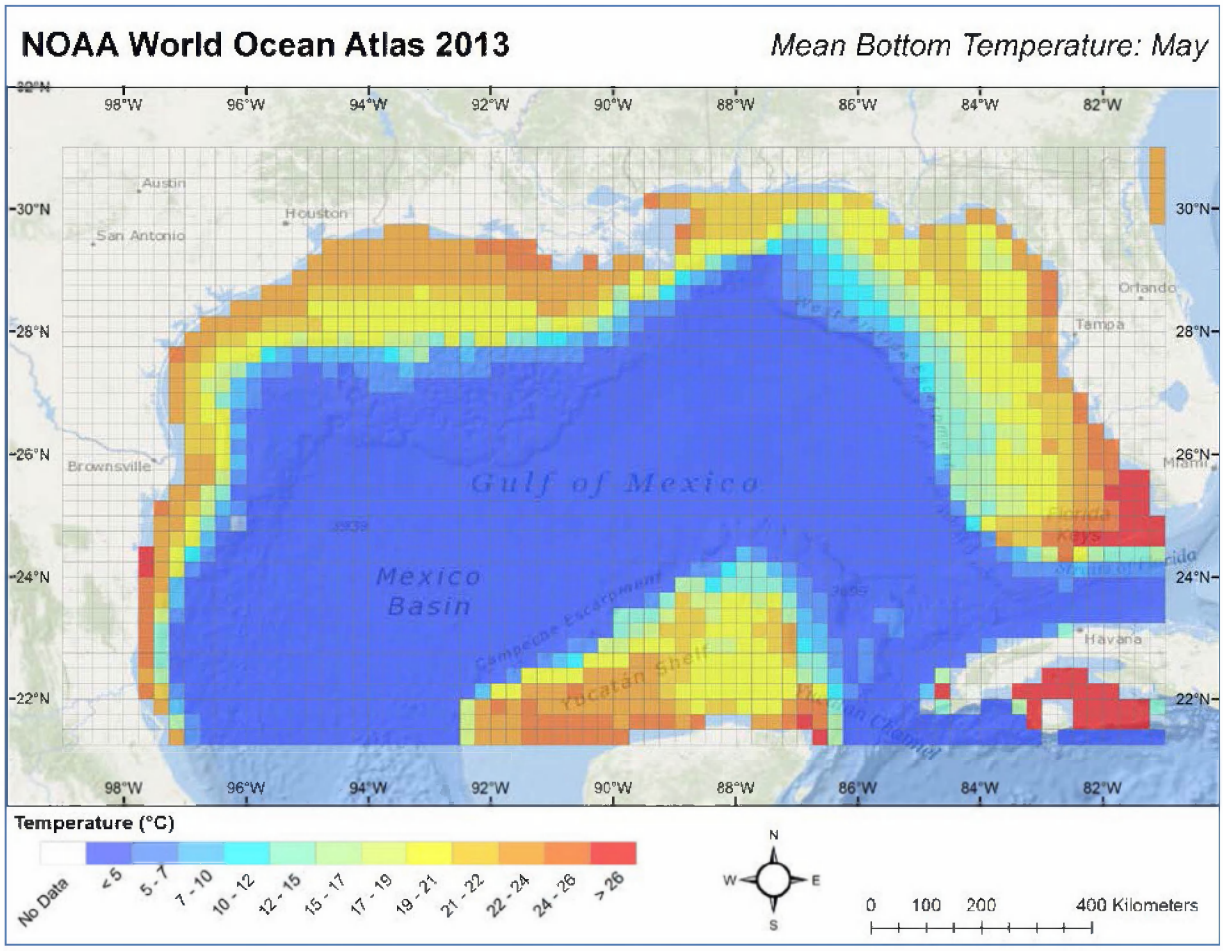

Figure D.2-9 Climatic mean bottom water temperature data for May, from the NODC World Ocean Atlas (2013).

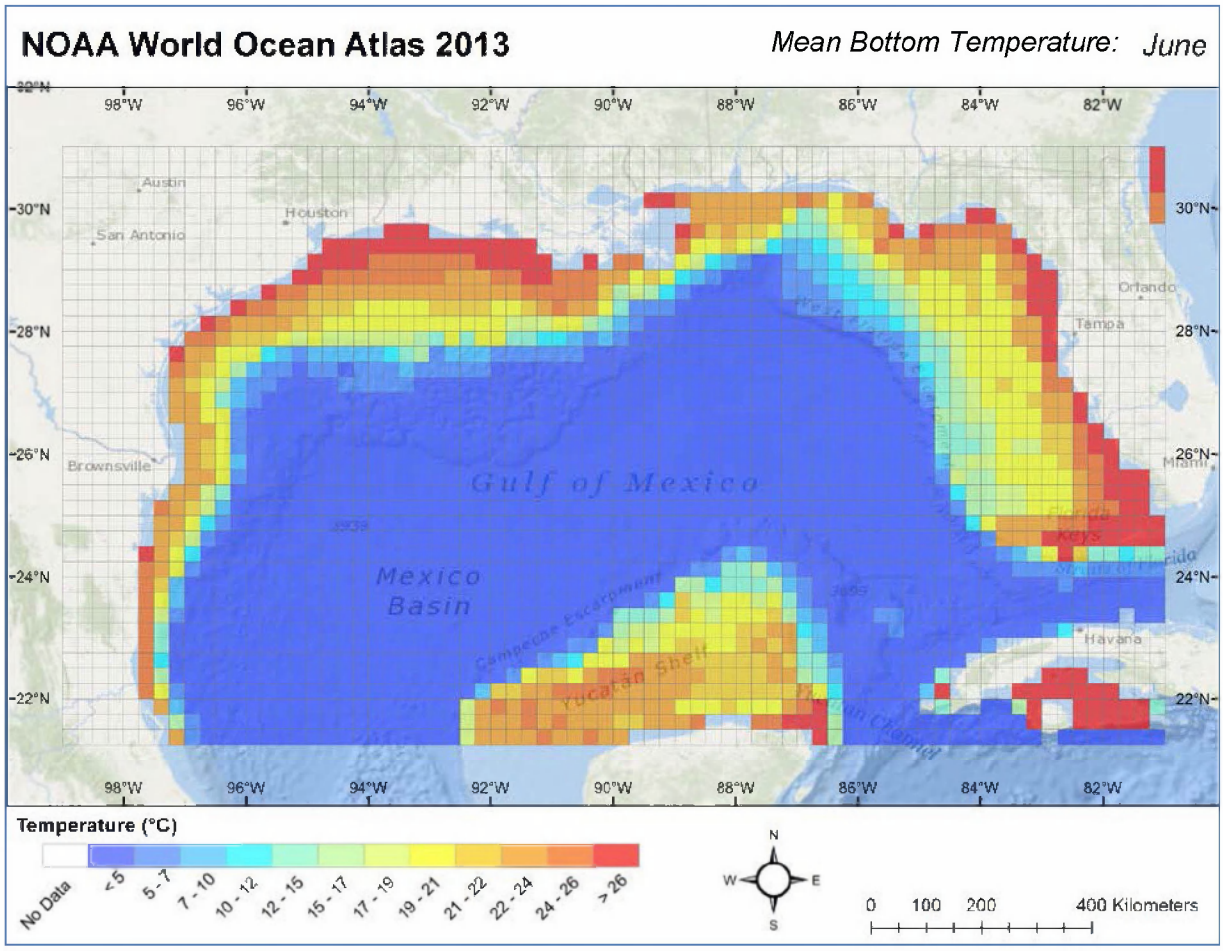

Figure D.2-10 Climatic mean bottom water temperature data for June, from the NODC World Ocean Atlas (2013).

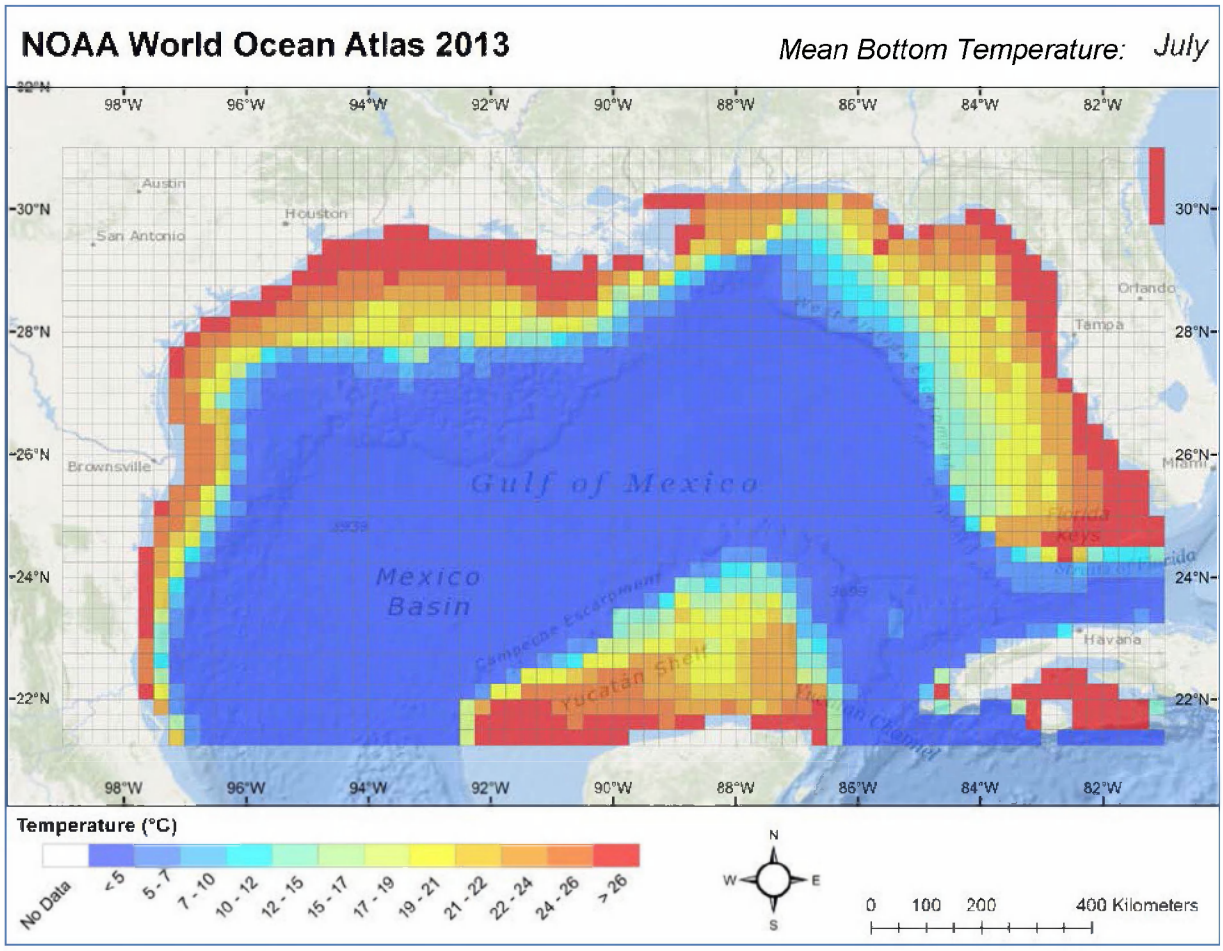

Figure D.2-11 Climatic mean bottom water temperature data for July, from the NODC World Ocean Atlas (2013).

D.2.3 Salinity

Figure D.2-12 shows vertical salinity profiles for grid cells shown in Figure D.2.2. The strong salinity gradient in the upper 20 m is typical of Mississippi plume-influenced waters near the Birds Foot.

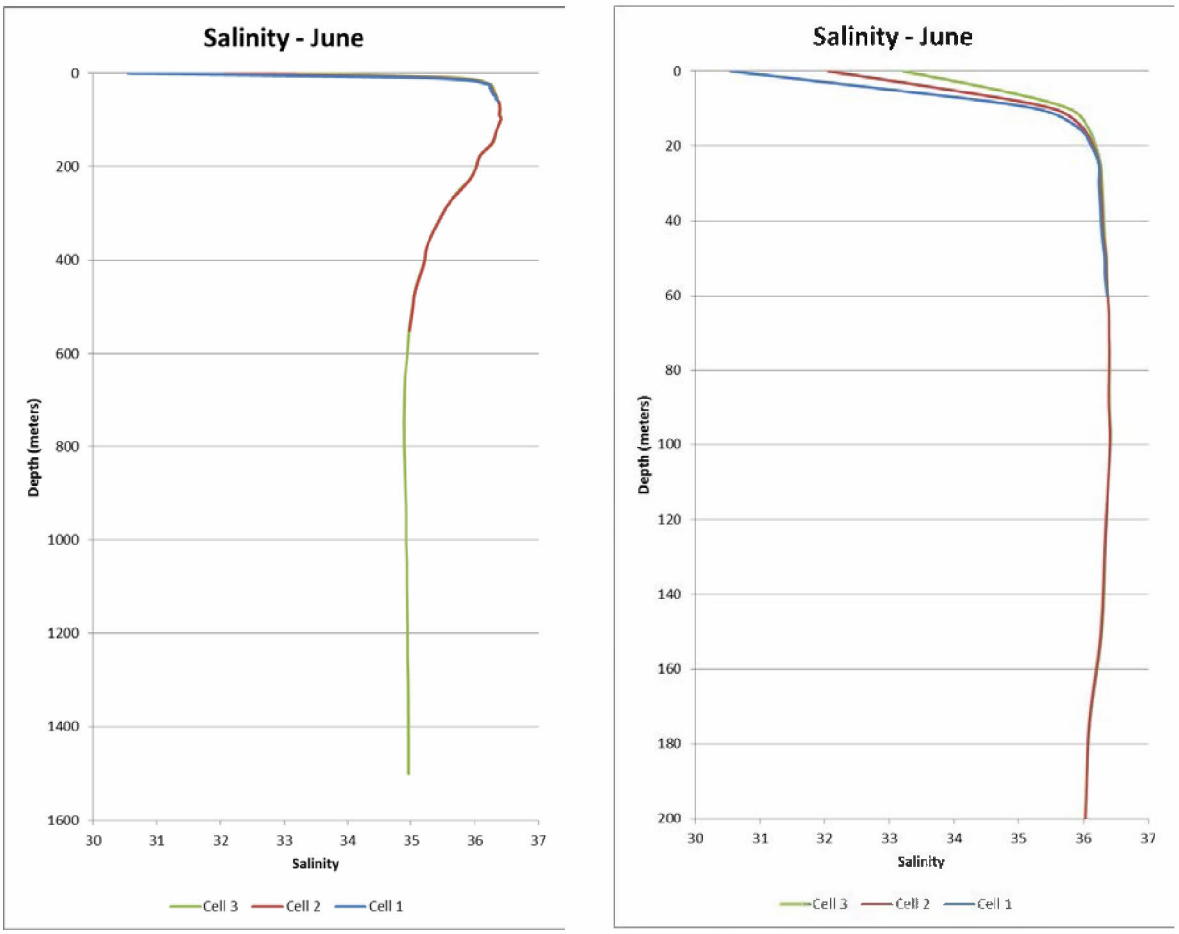

Figure D.2-12 Vertical salinity profiles for cells shown in Figure D.2.1.

Figures D.2-13 to D.2-18 show the downloaded ¼-degree NODC (2013) surface water salinity data used. The influence of river discharges is clearly seen near the Texas and Louisiana coastlines.

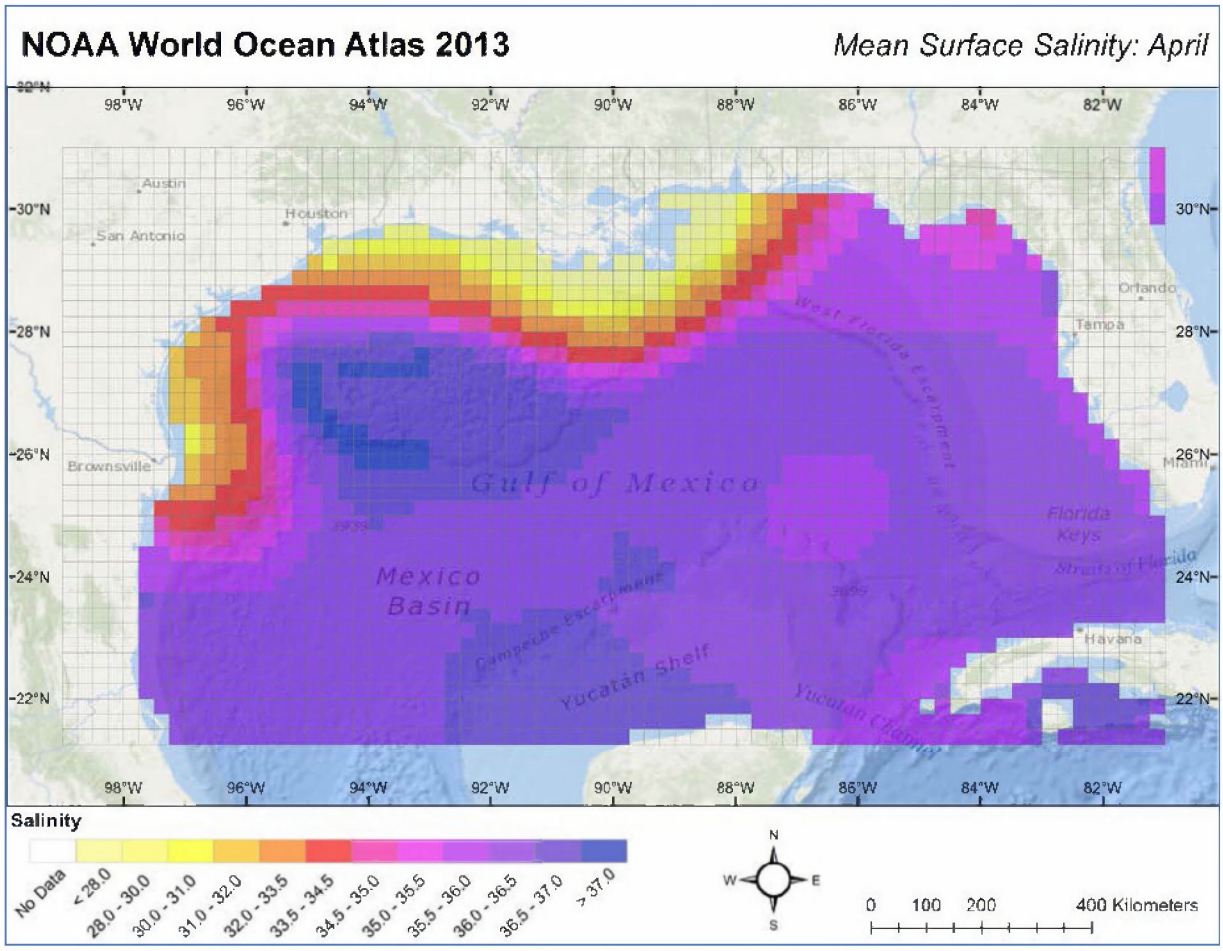

Figure D.2-13 Climatic mean surface salinity data for April, from the NODC World Ocean Atlas (2013).

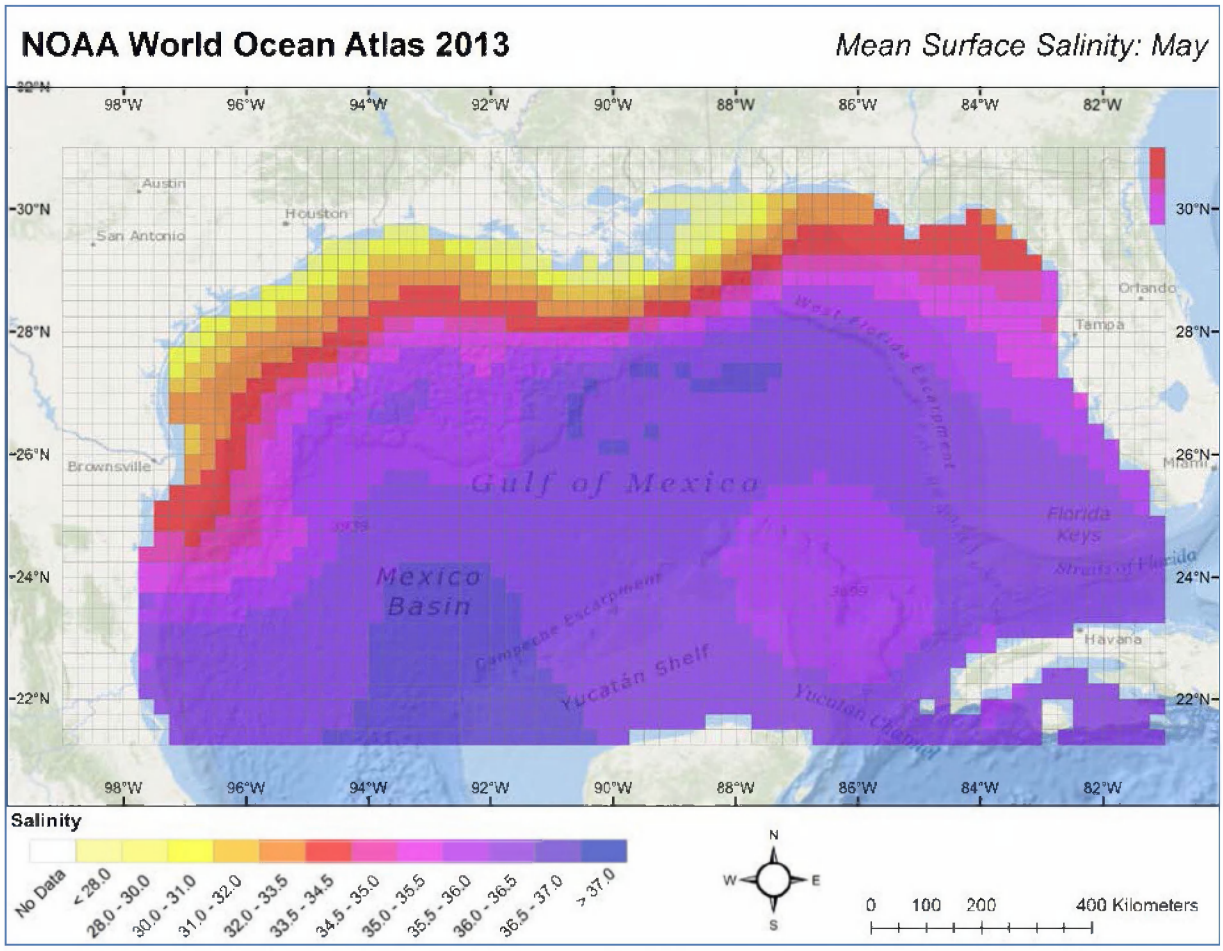

Figure D.2-14 Climatic mean surface salinity data for May, from the NODC World Ocean Atlas (2013).

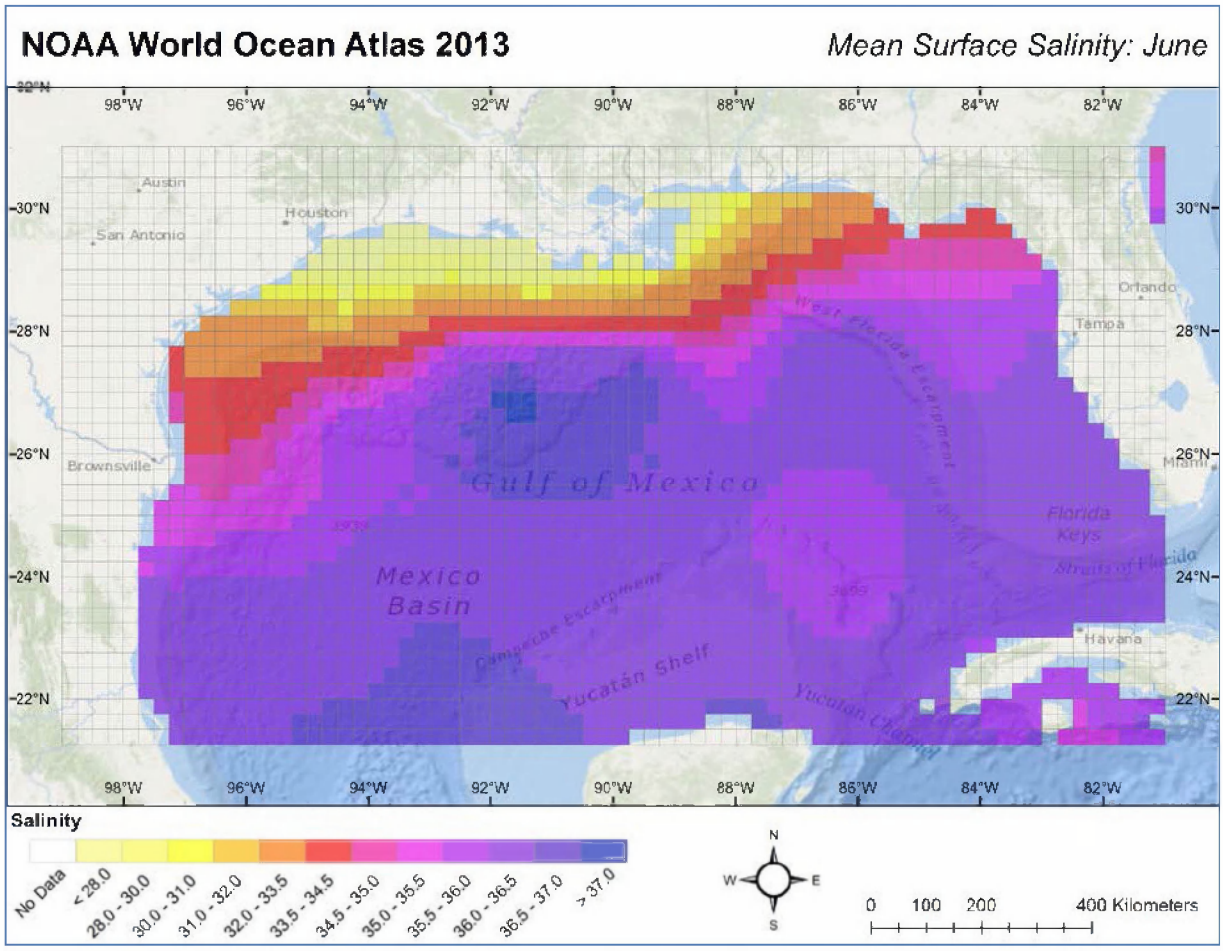

Figure D.2-15 Climatic mean surface salinity data for June, from the NODC World Ocean Atlas (2013).

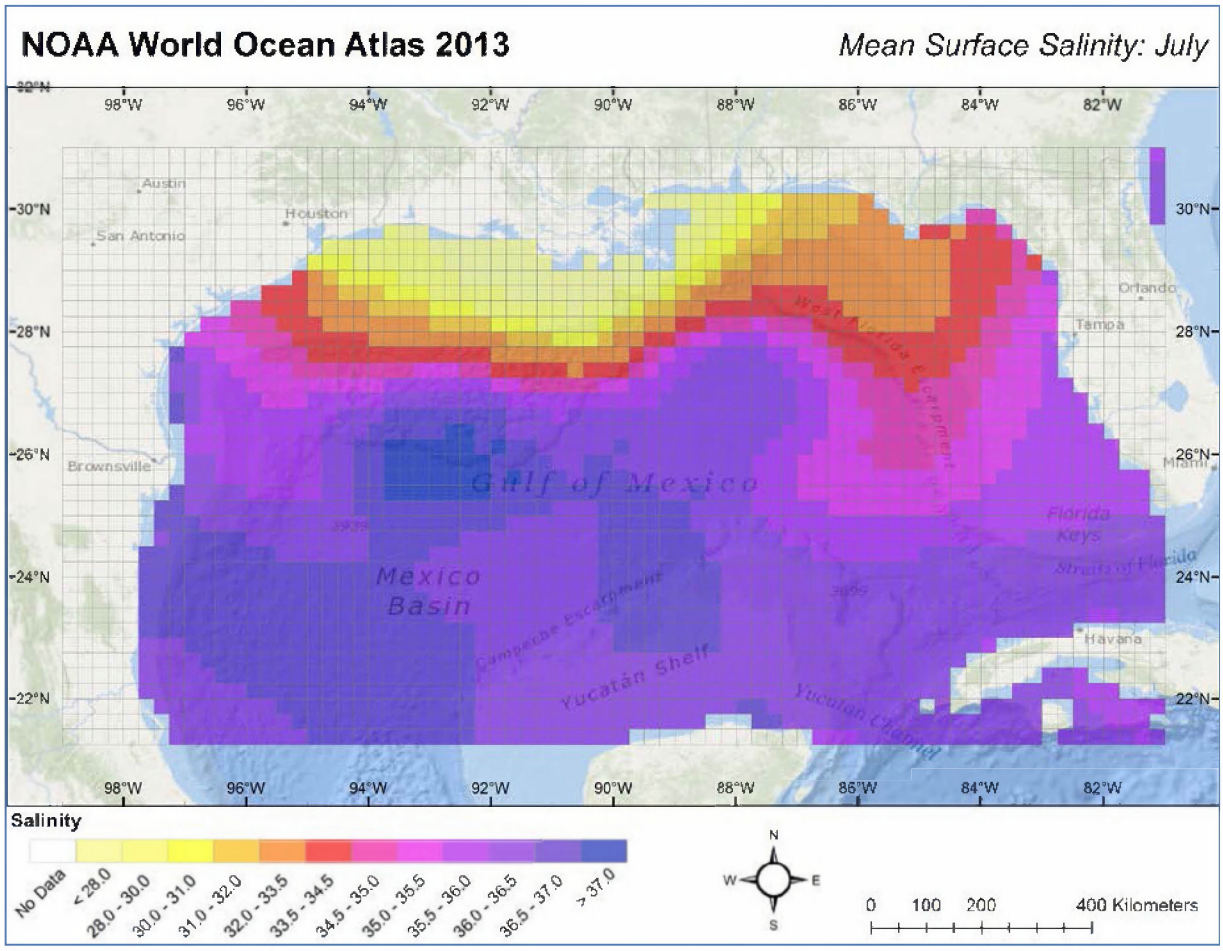

Figure D.2-16 Climatic mean surface salinity data for July, from the NODC World Ocean Atlas (2013).

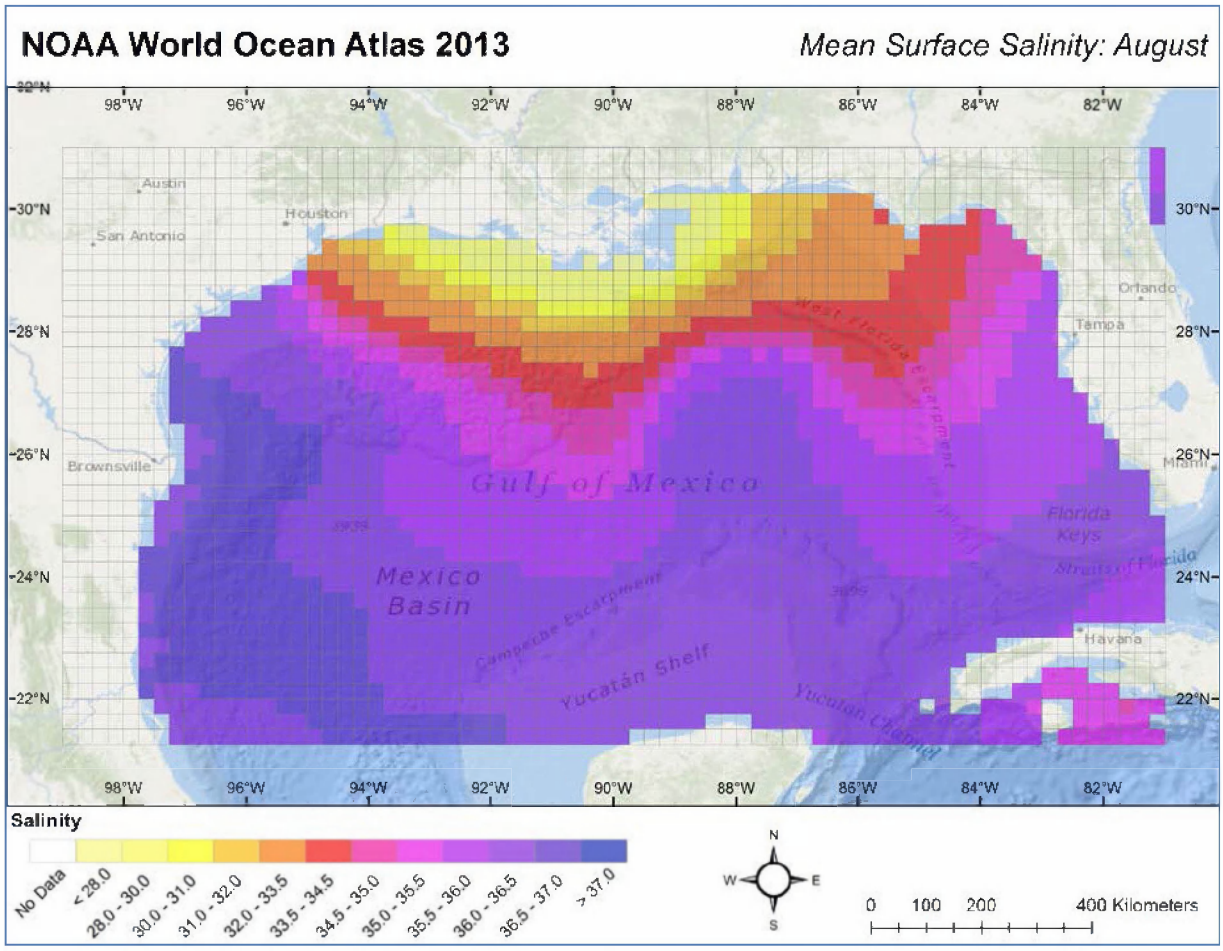

Figure D.2-17 Climatic mean surface salinity data for August, from the NODC World Ocean Atlas (2013).

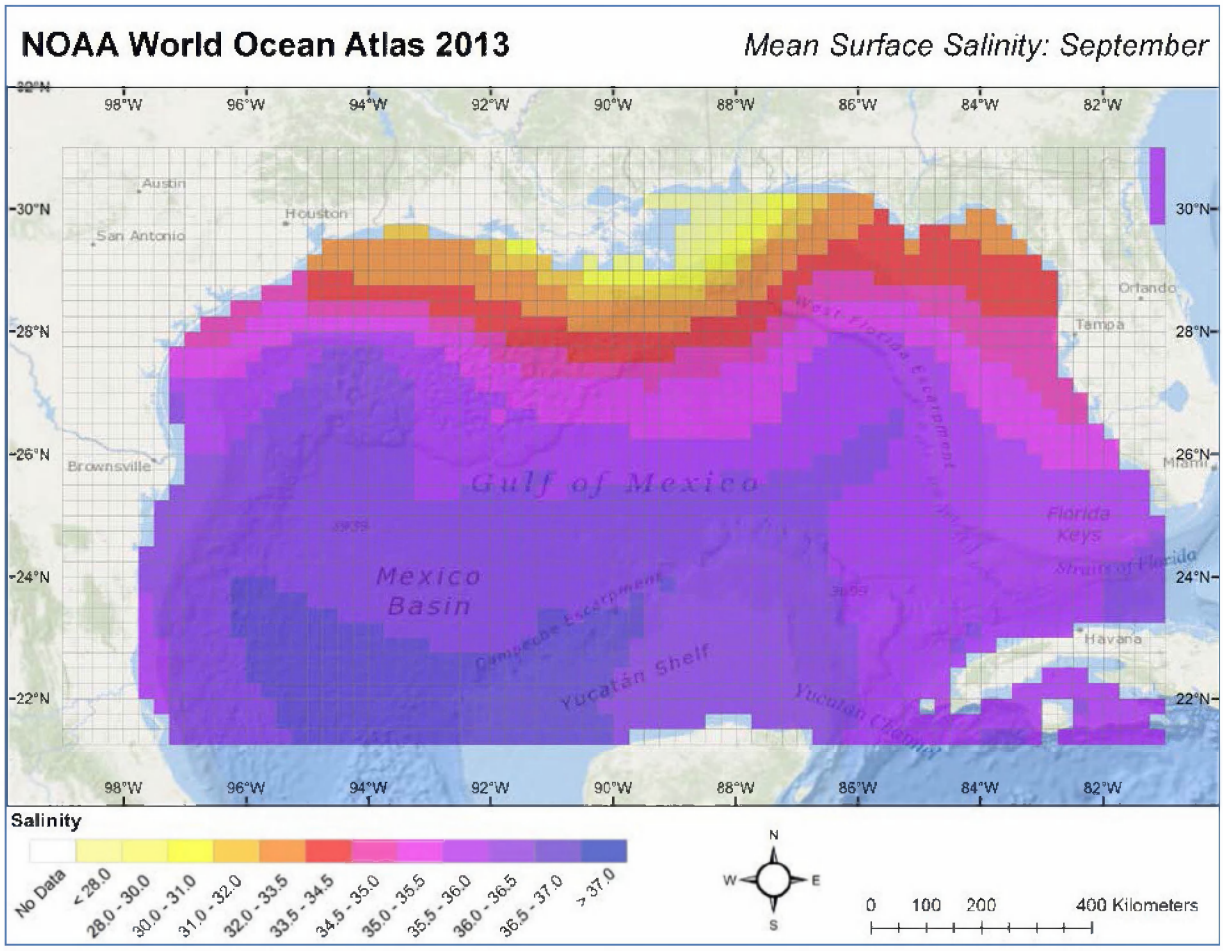

Figure D.2-18 Climatic mean surface salinity data for September, from the NODC World Ocean Atlas (2013).

D.2.4 Water Density

Figure D.2-19 shows a composite of all water density (as sigma-t) profiles based on CTD (conductivity, temperature and depth) data that have been QA/QC'd as part of the NRDA program.

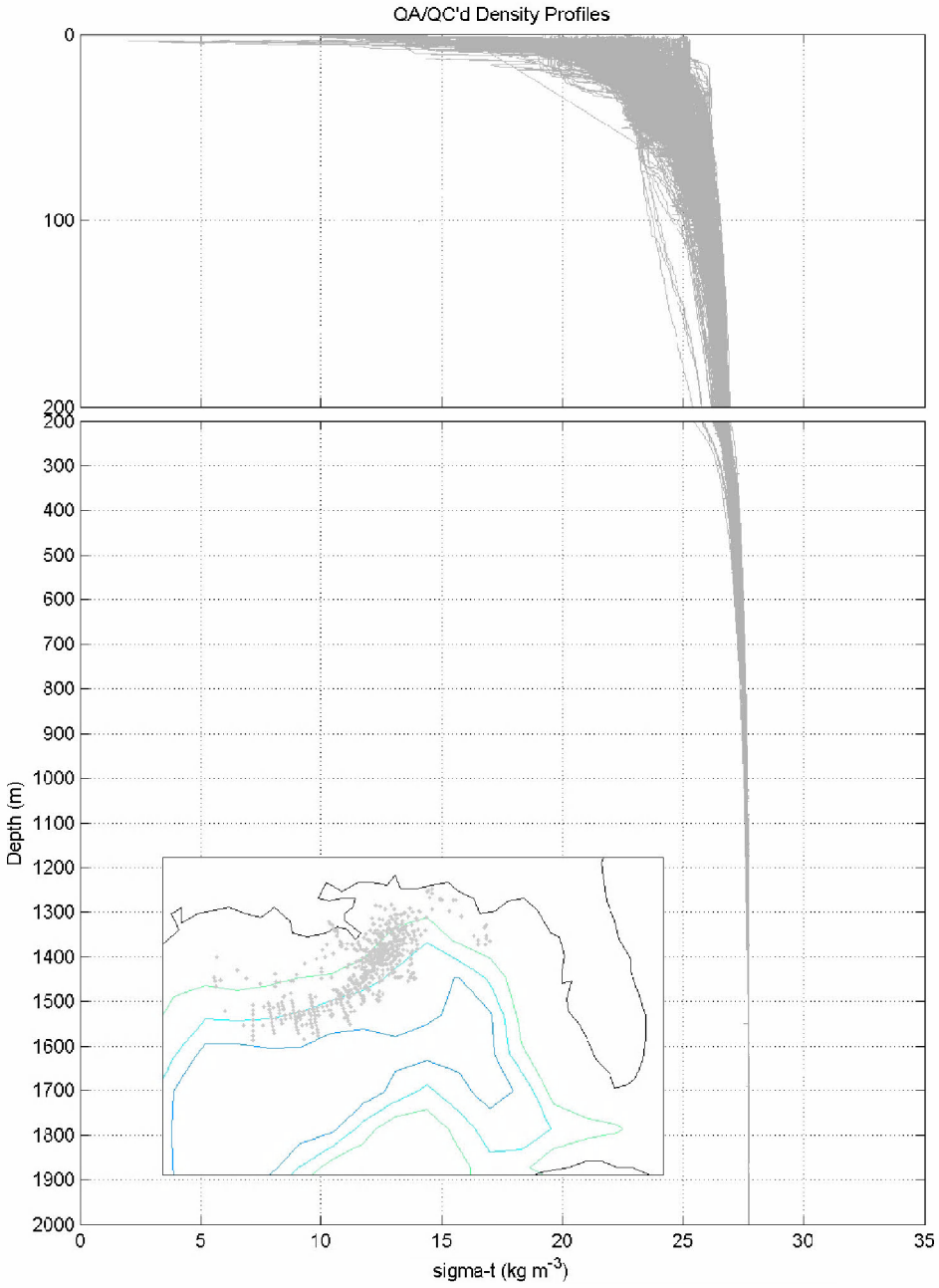

Figure D.2-19 Water density (as sigma-t) profiles based on CTD (conductivity, temperature and depth) data that have been QA/QC'd as part of the NRDA program.

DRAFT Technical Reports for Deepwater Horizon Water Column Trustees:

Modeling Oil Fate and Exposure Concentrations in the Deepwater Plume and Rising Oil Resulting from the Deepwater Horizon Oil Spill

Appendix E. Observational Data

Authors: Deborah French McCay, Katherine Jayko, Zhengkai Li, Matthew Horn, Yong Kim, Tatsu Isaji, Deborah Crowley, Malcolm Spaulding, Lauren Decker, Stefanie Zamorski, Cathleen Turner, Jeremy Fontenault, Rachel Shmookler, and Jill Rowe

Revised: September 29, 2015
Project Number: 2011-144
RPS ASA 55 Village Square Drive, South Kingstown, RI 02879

Table of Contents

List of Figures

Appendix E. Observational Data

E.1. CTD and Sensor Data for Water Column Properties and Fluorescence

Conductivity-Temperature-Depth (CTD) data were collected on nearly every cruise conducted in response to the Deepwater Horizon (DWH) oil spill in an effort to gain insight into the water column properties of the Gulf of Mexico (GOM), specifically focusing on the area around the release site. CTD and sensor (including fluorescence, dissolved oxygen, and transmissometer) data are summarized in the Technical Report by Grennan et al. (2015).

Figure E.1-1 shows vertical temperature profiles as measured by cruises in 2010 and from climatology. Typical temperatures in the upper mixed layer were 20-31ºC, in the thermocline below the mixed layer 7-20ºC, and in deep water (>800 m) 4-7ºC. Figure E.1-2 shows water density (as sigma theta) profiles for the Brooks McCall cruise data. Additional description of the data is in Grennan et al. (2015).

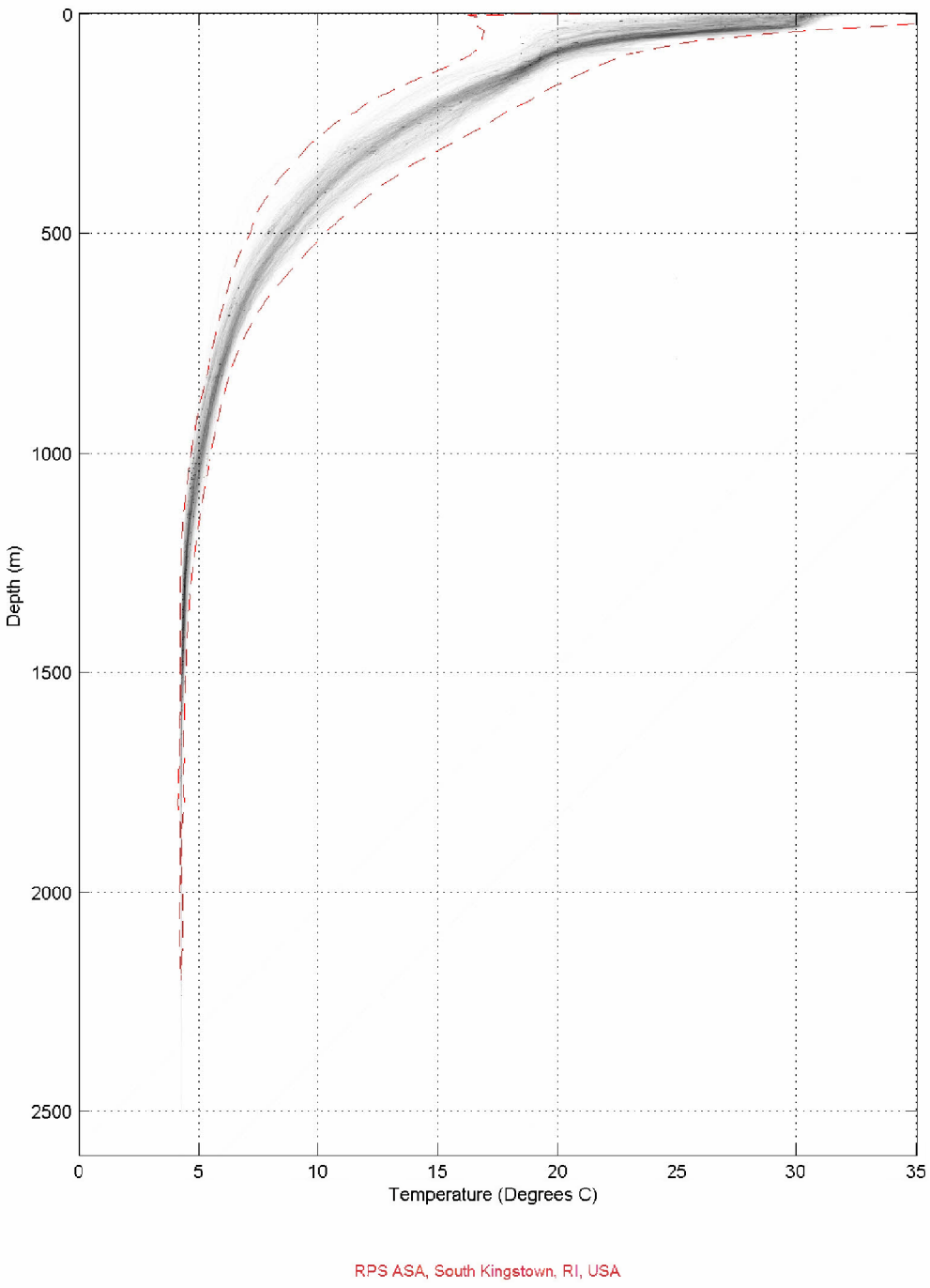

Figure E.1-1. All temperature data shown with mean climatological data +/- 3 standard deviations. The temperature data is presented in grey scale, with the more common profiles appearing darker than the less common; the yearly climatology data envelope is presented as red lines.

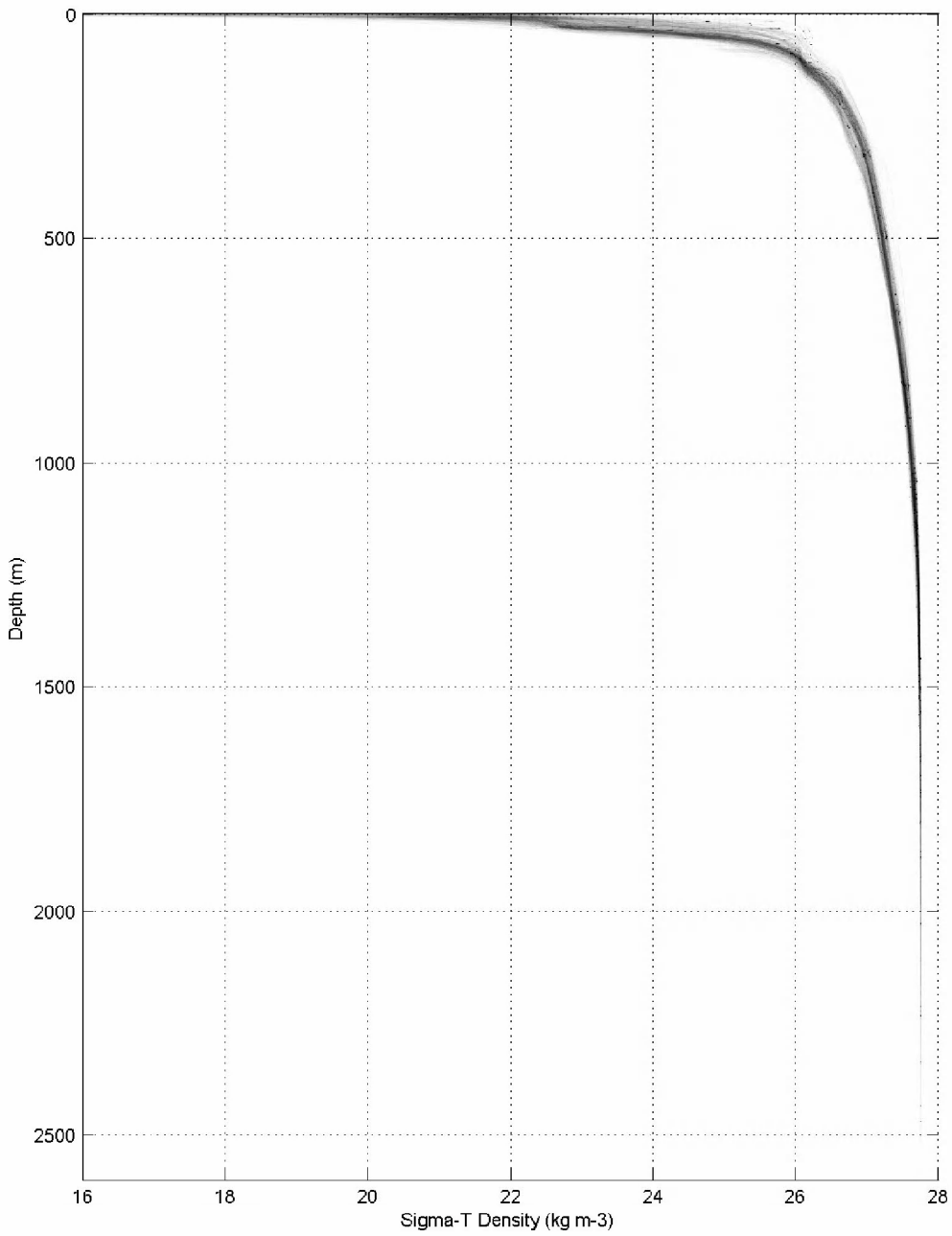

Figure E.1-2. All density profiles measured by cruises in 2010. The density data is presented in grey scale, with the more common profiles appearing darker than the less common.

There were consistently observed fluorescence anomalies, as relative high values or "peaks", at depths between approximately 1000-1300 m. Figures E.1-3 to E.1-6 summarize the observed fluorescence anomalies. Maximum anomalies occurred between roughly 1,100-1,200 m. The highest values were observed near the wellhead; the anomalies decreased as distance from the wellhead increased. Anomalies of high fluorescence values at depths of 1000-1300 m were typically associated with elevated hydrocarbon concentrations in the water column, when water samples were collected concurrently with fluorescence measurements. These fluorescence peaks were observed mainly to the southwest of the wellhead and frequently out to approximately 150 km, with Payne and Driskell (2015a) reporting a small DO sag and fluorescence anomaly at the deep-plume depth to the southwest all the way out to 412 km. Although maximum fluorescence peaks were identified within a narrow range at depth, significantly elevated fluorescence values were noted throughout large portions of profiles. Peak fluorescence values at depth typically tapered to lower values in shallower waters. It was very common to observe significantly elevated fluorescence values up to 600 m and occasionally shallower.

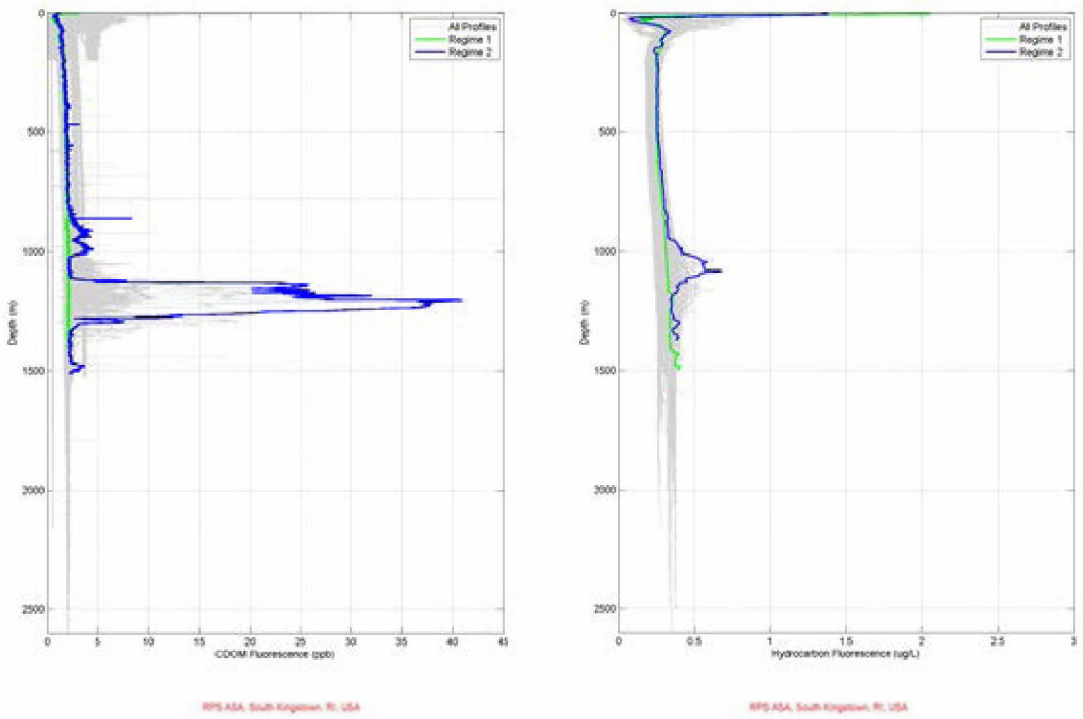

Figure E.1-3. Fluorometer data collected around the DWH spill site with two representative profiles highlighted in each. WET Labs ECO-CDOM measurements (left) are presented alongside Chelsea AquaTracka data (right). The blue line is an actual FL profile with a significant increase in signal at depth. The green line is a separate FL profile, representing a normal response at depth, in the absence of a FL anomaly. The grey lines include all of the 2010 fluorometer measurements for each specific sensor, emphasizing observed FL anomalies between roughly 1000-1300 m. Note that the calibrated units of the AquaTracka are different from that of the CDOM fluorometer. While the magnitude of the signal is lower than the CDOM in this sample, the Aquatracka is more sensitive.

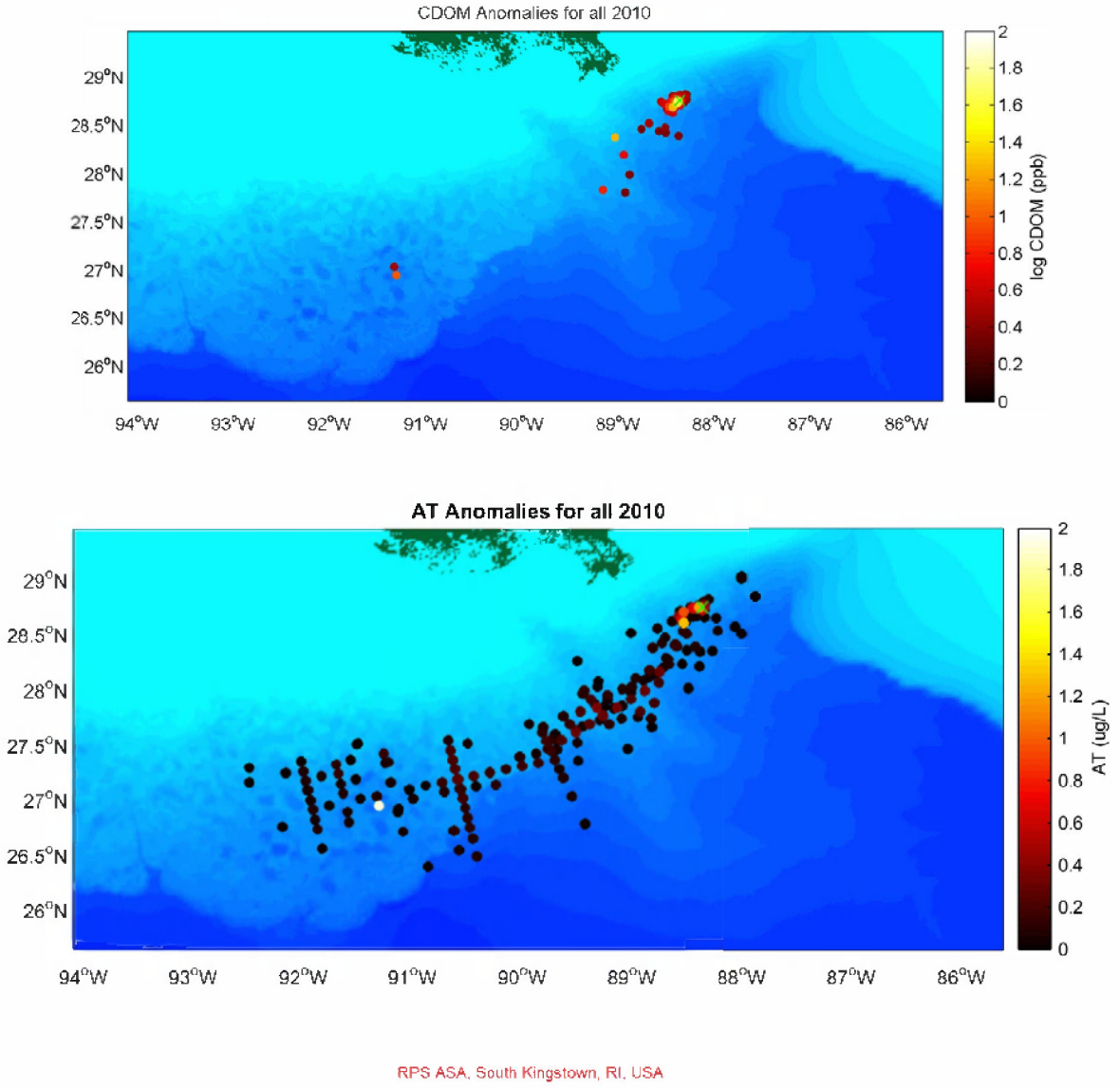

Figure E.1-4. The maximum CDOM (top) and AT (bottom) anomalies for each cast are displayed as single points in a map view. CDOM anomalies are plotted on a log-10 scale, due to the large range in reported values.

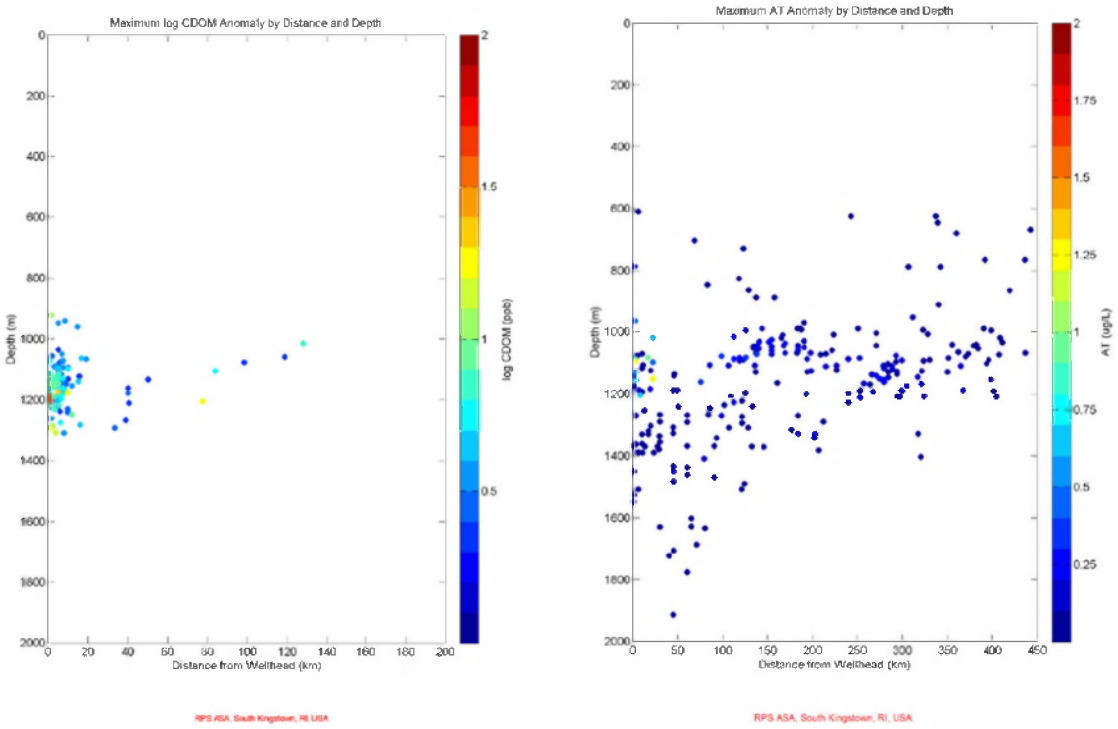

Figure E.1-5. The maximum CDOM anomalies (left) and AT anomalies (right) for each cast are displayed as a single points in a profile view. CDOM anomaly is plotted on a log-10 scale, due to the large range in reported values. Maximum FL anomalies (ppb) and corresponding depths (m) are displayed with distances from the wellhead (km).

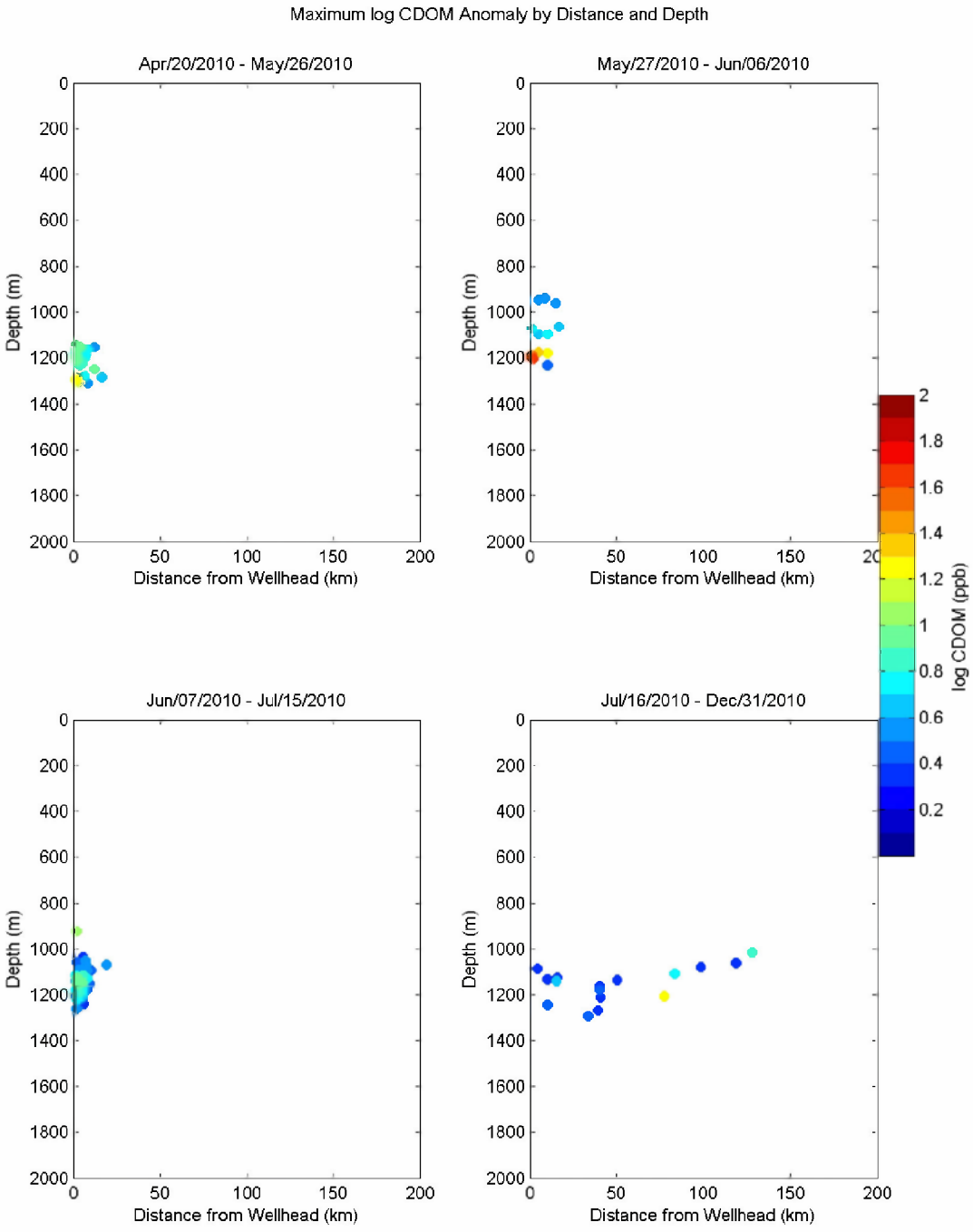

Figure E.1-6. Maximum CDOM Anomaly as a profile, broken out by date range. Log (CDOM Anomaly) (ppb) and depth (m) are displayed over the distance to the wellhead (km). Note that most samples were collected between April 20 and July 15, 2010 were within 20 km of the wellhead. More distant sampling in the far-field occurred after July 15, 2010.

There were consistent anomalous dissolved oxygen "sags" (i.e., relatively low values of dissolved oxygen in vertical profiles when compared to baseline profiles) at depths between approximately 700-1300 m. Figures E.1-7 and E.1-8 summarize the dissolved oxygen anomalies. The maximum anomalies occurred between ~1,100 and 1,200 m deep. These anomalies first increased up to approximately 50-100 km from the wellhead and then decreased as distance from the wellhead increased to approximately 350 km. Anomalies calculated greater than one standard deviation below the profile-specific-baseline were identified out to greater than 500 km from the wellhead. As distance from the wellhead increased, dissolved oxygen anomalies increased and then decreased. As sags decreased in magnitude, they frequently became slightly broader, covering larger depth ranges. These observations are indicative of microbial degradation (i.e. hydrocarbon consumption) at depth followed by mixing with surrounding waters.

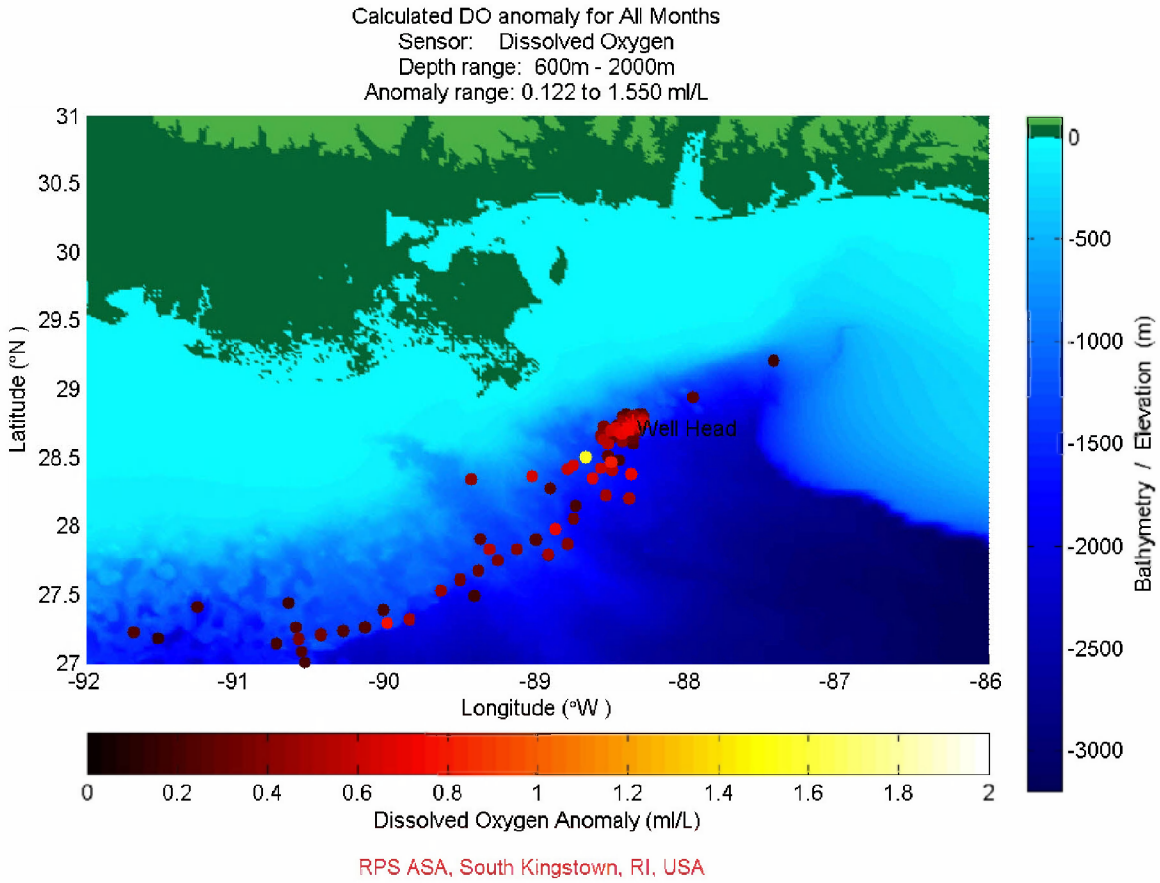

Figure E.1-7. Maximum dissolved oxygen anomaly from individual casts around the wellhead as a map view. The maximum dissolved oxygen anomaly (ml/L) for each station is displayed on the map over the investigated depth range of 600-2000 m.

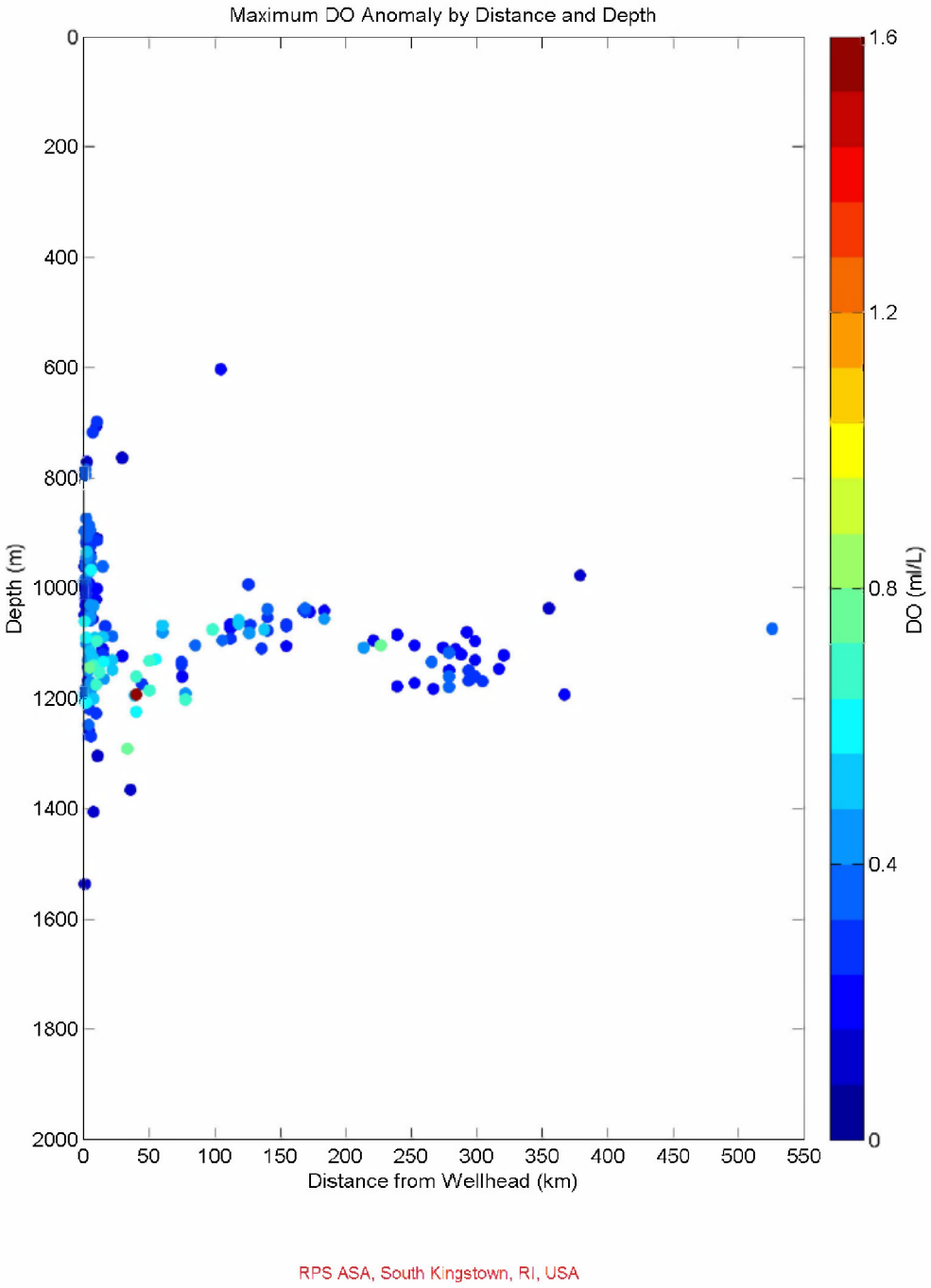

Figure E.1-8. Maximum dissolved oxygen anomaly from each individual cast as a profile view. Dissolved oxygen anomalies (ml/L) and corresponding depths (m) are displayed with distances to the wellhead (km).

E.2. Chemistry data

E.2.1. Chemistry Data Reported in the Literature

Chemistry data published in the peer-reviewed literature include oil hydrocarbons and chemical dispersant constituents that have been measured in samples collected from the subsurface intrusion plume and other depths in the water column.

E.2.1.1. Hydrocarbon Chemistry

E.2.1.1.1. Source oil hydrocarbon chemistry

Reddy et al. (2012) collected discrete source oil and gas release samples directly above the Macondo well (MW) on June 21, 2010 and analyzed oil and gas components in these samples. Analysis of selected compounds in Macondo well samples indicated that the released liquid from the wellhead included total C1-5 compounds at a concentration of 0.24 g/g, of which methane was 0.15 g/g. All the other 140 hydrocarbon compounds measured totaled 0.24 g/g. Thus, together, characterized oil and gas compounds only accounted for 0.48 g/g or slightly less than half of the total mass of released fluid. This is consistent with analyses reported by Stout (2015a and details in Appendix B)

E.2.1.1.2. Hydrocarbon chemistry in the water column

Oil-related hydrocarbon compounds were detected in the water column in the area surrounding the blowout wellhead, especially in the intrusion-layer deep plume below 1,000 m. Observations in published literature include: May 9 -16, 2010, PAHs were detected up to 13km southwest of the wellhead by Diercks et al. (2010); May 25 -June 2, 2010, BTEX and other volatiles were found in the deepwater hydrocarbon plume, also supported by CDOM (Hazen et al., 2010 Science); June 11 - 21, 2010, C_1-C_4 hydrocarbon gases were detected at depths of 800 – 1,200 m (Valentine et al., 2010, 2012); June 19-28, 2010, vertical rosette profiling including grab samples and *in situ* mass spectrometry measurements revealed elevated hydrocarbons between 1,100-1,200 m and lower concentrations of hydrocarbons between 50 - 500 m (Camilli et al., 2010).

Diercks et al. (2010) reported observations of concentrations of PAHs in subsurface waters near the DHW oil spill site. Profiles of *in situ* CDOM fluorescence and beam attenuation "indicating the presence of light-scattering dispersed oil droplets" May 9 -16, 2010 had distinct peaks at depths greater than 1,000 m. The highest intensities were close to the wellhead and the intensities decreased with increasing distance from the wellhead. Their GC/MS analyses of water samples collected at depths at which fluorescence and beam attenuation showed anomalies confirmed the presence of PAHs at concentrations up to 189 µg/L in discrete depth layers between 1,000 and 1,400 m southwest of the wellhead site and extending at least as far as 13 km. Diercks et al. (2010) noted that the PAHs in the deep plume were enriched in naphthalenes, as compared to surface samples where 3- ring PAHs were relatively enriched, a pattern consistent with water partitioning of more water soluble PAH compounds during transport to the surface.

Hazen et al. (2010) collected and analyzed 17 deep-water samples from 10 locations May 25 – June 2. They detected a deep-sea oil plume from 1,099 m – 1,219 m at distances up to 10 km

from the wellhead. In their samples, extractable hydrocarbons (e.g., n-C18) ranged from non-detectable in non-plume samples to 9.21 µg/L in the plume and volatile aromatic hydrocarbon concentrations were significantly higher in the plume (mean 139 µg/L) than in the non-plume samples.

Camilli et al. (2010) performed a subsurface sampling effort June 19 – 28, 2010 using *in situ* mass spectrometry and a rosette sampler, including three Sentry surveys conducted June 23 – 27 at depths exceeding 1,000 m. Based on mass spectra and aromatic fluorometer data, the strongest hydrocarbon readings were encountered at ~1,100-m depth, west-southwest of the well site, and a weaker signal was detected northeast of the well site. The first long-range Sentry survey—conducted as an east-northeast radial projection from the well at three separate depth intervals (1,000, 1,150, and 1,300 m)—did not encounter petroleum hydrocarbons significantly above background levels. Their mass spectrometric and fluorescence data taken ~ 4 km southwest of the leak source "confirmed a large plume at ~1,000- to 1,200-m depth, as well as a more diffuse "plume" existing between 50- and 500-m depth" (Camilli et al 2010). Hydrocarbon mixture changes in composition between the deep plume and the near surface suggested aromatic hydrocarbons in greater abundance at depth. Elevated hydrocarbon concentrations identified with the mass spectrometer on Sentry dives 2 and 3, combined with the rosette profiling data, indicate a continuous, plume as high as 200 m and in certain areas more than 2 km wide, moving with a southwestern trend for a distance of more than 35 km from its source. Approximately 27 km from the source, petroleum hydrocarbon values rapidly diminished at this 1,120-m survey depth. Sentry executed track lines at differing depths until it identified a hydrocarbon maximum at 1,160 m. Sentry's Doppler Velocimetry recorded a southwest trending current at 1,100m depth, averaging 7.8 cm/s and at 247° from the true north. The plume's horizontal stability and limited cross-sectional area increase as a function of distance from the well site suggest Lagrangian transport. The plume track is coincident with the water current direction at this depth, indicative of topographically controlled transport (German et al. 1998) along an iso-depth contour line at the continental slope. Sentry's methane m/z signal at 35km from the source was only 53% less than that at 5.8km, suggesting that plume extended considerably beyond 35km survey bound. GC analysis on mono-aromatic hydrocarbons confirmed the presence of BTEX (50 µg/L) within the plume at 16 km downrange from the wellhead, suggesting a mechanism for direct hydrocarbon transfer to the deep plume. However, DO anomaly estimates from the plume layer (±2µM) or (0.8µM O_2/d) were significantly lower than reported by Du & Kessler (2012).

Reddy et al. (2012) collected discrete water samples within a southwest trending hydrocarbon-enriched plume (that defined by Camilli et al. 2010) at a depth of 1,100 m in June 19-28, 2010. The most abundant compounds larger than C5 were BTEX, which had a plume layer concentration as high as 78 µg/L. This is consistent with the NRDA cruise data (Horn et al. 2015a,b), in which, the pre-cut (i.e., prior to Jun 3) plume layer median BTEX concentration value was 92 µg/L (range 4.5 – 228 µg/L) and the post-cut plume layer median value 60 µg/L, (range 4.9 – 176 µg/L). To quantify the relative abundance of compounds in the intrusion layer in comparison to the source release, Reddy et al. (2012) defined a benzene-normalized fractionation index (Fi) for a given compound as,

$$F_{i,benzene} = \frac{\left(\frac{c_i}{c_{benzene}}\right)_{plume}}{\left(\frac{c_i}{c_{benzene}}\right)_{source\ liquid}} \quad (1)$$

A F_i value of unity indicates the compound completely channeled into the deep water plume to the same extent as benzene, whereas a F_i value of zero indicates the compound was

completely retained in ascending oil (particles) and likely reached the sea surface (or alternatively may have sunk to the seafloor bound to particulates). Benzene was nearly absent at depths less than 1,000 m water column (Camilli et al. 2010) and very little reached the sea surface (Ryerson et al. 2011), suggesting that benzene was predominantly retained in the deep water (intrusion layer) plume. F_i values for BTEX were benzene (1.00), toluene (0.505), o-xylene (0.378), enthylbenzene (0.369), and p/m-xylene (0.359). The compound mass fractions (M_i) of BTEX in source oil (µg/g) were benzene (2300), toluene (6540), o-xylene (1880), ethylbenzene (950), and p/m-xylene (5100). These values result in combined BTEX benzene-normalized fraction index as $\sum(Fi*Mi)/\sum Mi = 50.65\%$.

Comparison of wellhead liquid and plume water sample chemistry by Reddy et al. (2012) showed that the plume was preferentially enriched with water-soluble components, indicating that dissolution played a major role in the formation of the horizontal intrusion layer plume. There was only 1 out of 20 sampling locations (with unique x, y, and z -coordinates) where benzene was found with the co-presence of n-alkanes. Uniquely, their 1,201 m depth sample at 2.3 km SW of wellhead contained significant levels of n-alkanes and other sparingly soluble compounds but was depleted in water-soluble compounds such as BTEX, suggesting that this sample might have been an 'aged' rather than a 'fresh' sample. Reddy et al. (2012) asserted that their results demonstrate that most of the C1-C3 hydrocarbons and a significant fraction of water-soluble aromatic compounds were retained in the deep water column, whereas relatively insoluble petroleum components were predominantly transported to the sea surface or deposited on the seafloor.

Ryerson et al. (2012) used airborne and subsurface chemical measurements in May – June 2010 to quantify initial hydrocarbon compositions and fate and transport processes. Note all the oil and gas phase compounds from methane to n-C42 (as opposed to oil hydrocarbons $\geq$ C5) were included in their hydrocarbon mass balance analysis. About 25% of the leaking oil and gas mixture by mass was soluble – in fact this would mainly be the gas fraction (assuming a mass ratio of [(gas+oil)/oil] = 1.31, the gas fraction is estimated as 0.31/[1.31] = ~23.7%) plus BTEX compounds (1.92%/[1.31] = 1.47% (Ryerson et al., 2012). This is based on a mass ratio of [(gas + oil)/oil] = 1.31 ± 0.08 measured at 1 atmosphere and 15.6 °C from the Woods Hole Oceanographic Institution (WHOI) sample of leaking fluid (Reddy et al 2011).

Among different environmental compartments, the evaporated mass was estimated by Ryerson et al. (2012) based on shipboard or aircraft measurements of atmospheric volatiles; as the bulk of gas phase compounds were dissolved, the evaporated fraction was mainly attributable to the volatile oil fraction. The oil slick mass at the surface was estimated by: Initial surface slick = [initial buoyant plume mass flux] – [dissolved mass flux + evaporated mass flux]. In this estimation, the initial buoyant plume mass flux was the *Slope* of Fig. S4 in Ryerson et al. (2012), estimated as follows: compound-specific atmospheric flux (kg/d) = *Slope* * compound-specific leaking fluid mass fraction (g/g), therefore the *Slope* has units of (kg leaking fluid / day). The evaporated mass flux was estimated as described above. Any compounds that are more soluble than 2-methylheptane were assumed to partition either in the intrusion layer plume as dissolved fraction or in the atmosphere as evaporated fraction, but not trapped in oil (including droplets and surface slick); so for these compounds, [dissolved] = 1 – [evaporated], and a sum of dissolved ($\sum$dissolved) provides an estimate of the fraction of compounds dissolved in plume water.

Deep sea plume intrusion layer mass was estimated by Ryerson et al. (2012) based on (1) measurements of the compound mass fraction in leaking fluids (g/g_{total}), (2) compounds above n-C6 assumed completely insoluble, methane and ethane completely soluble, and estimated

partial solubility for others, (3) total environmental release based on total integrated DO anomaly as reported by Kessler et al. (2011), scaled up with oxidation stoichiometry of hydrocarbons, and summing all characterized compound mass fractions among the total mass. In their estimation, 14.415% (=0.15*0.9610) of the total insoluble hydrocarbon mass released from wellhead (including those that were recovered) was trapped in the deep plume, where 0.15 = [(C_{10-32} n-alkane/Toluene in plume)/(C_{10-32} n-alkane/Toluene in source)] was based on the samples reported in Hazen et al. (2010) C_{10-32} n-alkane vs toluene data, with a range from 0.05 to 0.25. The value 0.9610 is the fraction of toluene dissolved in seawater samples from the deep sea.

The mass balance analysis of *oil* released on June 10, 2010 was estimated by Ryerson et al. (2012) as: Total release = 1.007×10^7 kg/d /1.31 = 7.687×10^6 kg/d (59×10^3 bbl/d); Recovered oil = 2.1×10^6 kg/d (16×10^3 bbl/d); Total environmental release = 7.687×10^6 kg/d - 2.1×10^6 kg/d = 5.587×10^6 kg/d (43×10^3 bbl/d); Oil in the deep plume = 1.09×10^6 kg/d (which is, 1.09/5.587 = 19.5% *(1±0.3)); Oil evaporated = 0.46×10^6 kg/d (which is, 0.46/5.587 = 8.23% *(1±0.5)); and oil in surface slick = 1.0×10^6 kg/d (which is, 1.0/5.587 = 17.9% *(1±0.5)).

The Ryerson et al. (2012) mass balance analysis has a number of sources of errors/uncertainties, including (1) the Kessler et al. (2011) estimated total DO Anomaly = 3.0 ~3.9×10^{10} mole O_2, (2) the Hazen et al. (2010) ratio of alkanes to toluene in the plume phase versus the ratio of alkanes to toluene in the leaking fluid phase of 0.05 ~ 0.25, being a surrogate of the droplet to dissolved phase hydrocarbons – on the premise of the co-location of the dissolved versus droplet phases. Note that in the above analysis that the tracked mass fraction would be equal to [19.5%*(1±0.3) + 8.23%*(1±0.5) + 17.9%*(1±0.5)] = 54.4% ± 18.9% of the release. In other words, nearly half of the oil mass (45.6%) was not accounted for in the analysis. The missing fraction of oil would presumably be biodegraded, suspended in the water column other than in the intrusion layer deep plume, and/or sunken to the seabed.

As an extension of Hazen et al.'s (2010) plume layer hydrocarbon data analysis, Spier et al. (2013) compiled hydrocarbon data from NOAA and BP datasets and conducted analyses to compare monitoring data with model prediction results. The NRDA data were collected in May 9 - June 28, from 16 missions, and included over 150 chemical compounds ranging from C5-C40 hydrocarbons; the BP data were from Ocean Veritas cruises 1-3 (May 27-June 10) and Brooks McCall cruises 1-8 (May 9 - June 10). After compiling and editing, 138,257 individual results remained, coming from 1967 samples, each collected at a unique location, depth, and date.

Spier et al. (2013) investigated the spatial distribution of hydrocarbons using the following three zoning strategies: (1) Two separate regions broadly defined within a 45 km radius of the well head, i.e., Region 1, the rising cone and a 250 m deep subsurface plume layer centering at 1,175 m, which were predicted to contain the majority of the subsurface hydrocarbon mass, and Region 2 all other areas within a 45 km radius of the blowout; (2) Eight directions from the wellhead, namely N, NE, E, SE, S, SW, W, and NW; and (3) Layered vertical depth intervals, including every 100m, plus 50m and 25m binning in the top 100m.

Comparison of hydrocarbons in the two broad regions indicated that Region 1 did have the highest concentrations of hydrocarbons, and Region 2 also contains substantial proportions of hydrocarbons. Vertically, contour analysis indicated the presence of hydrocarbon plumes with mid-depths of 25 m, 265 m, 865 m, and 1,175 m. After Top Hat #4 became operational (i.e., post-cut on June 3), both the sample concentration and the percentage of detectable results decreased for the 865 and 1,175 m plumes

The percentage of detectable measurements in each of Spier et al.'s (2013) identified plumes varied by direction from the wellhead, summarized as follows: A) 0.5-50 m plume - carried in all directions from the blowout, probably due to influence from surface currents and wind; B) 240-290 m plume – had the highest concentrations and the highest frequency of detectable results primarily southeast and secondarily northwest; C) 850-880 m plume - had the highest sample concentration and the highest frequency of detectable results primarily to the northwest, but was lacking data in the southeast and northeast directions; and D) 1050-1300 m plume - consistently had the highest concentration and the highest frequency of detectable results southwest and secondarily to the west of the blowout

Spier et al. (2013) also noted that chemical composition changed with respect to depth (Figure E.2-1). Most water soluble compounds such as benzene, alkylated mono-aromatics, and C5-C8 alkanes were enriched in the deep plume. Less water soluble compounds were present both in the deep water plumes and in the upper water column; C13-C22 PAHs and C9-C22 alkanes were found in both 1,175-m and 865-m plumes as well as even deeper water and near the surface; C23-C40 alkanes were found in 1,175 m and 265 m, near the surface and also in lower concentrations in the 865-m plume.

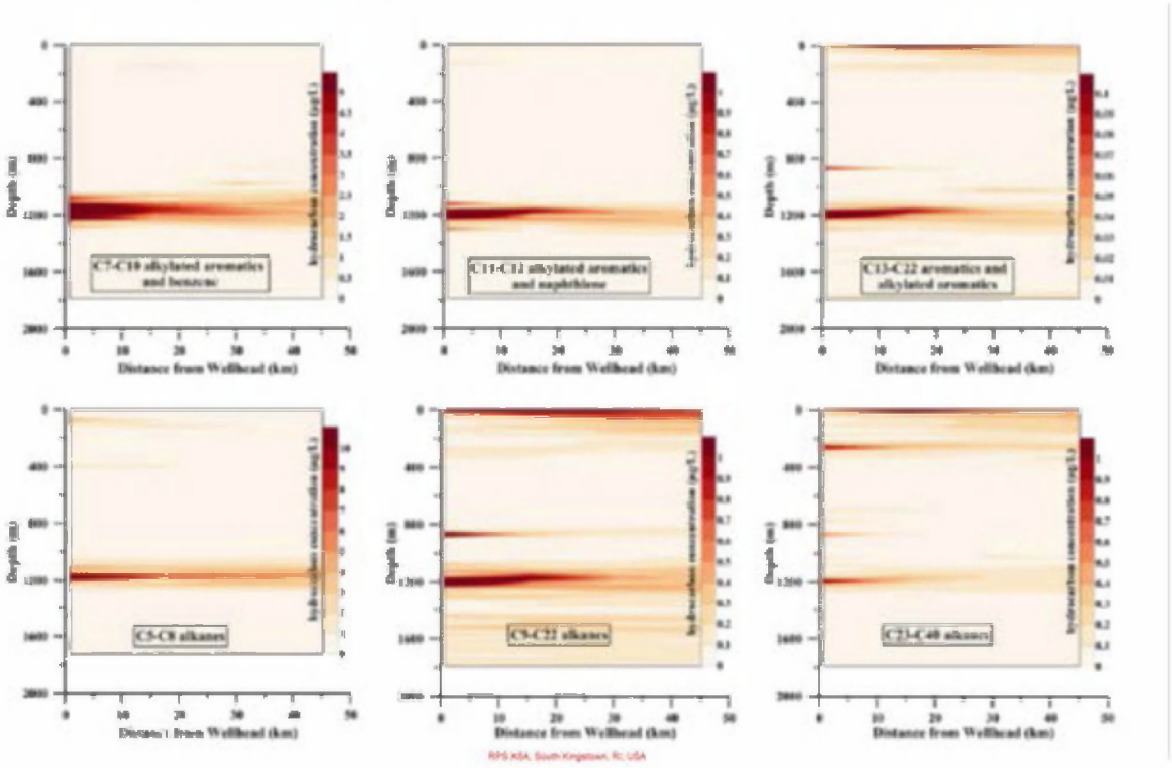

Figure E.2-1: Different hydrocarbon group concentrations in the water column, as summarized by Spier et al. (2013).

There was a statistically significant (α= 0.01) decrease in both the sample concentrations and the percent detectable results for the 865-m and 1,175-m plumes in the samples taken after the June 3 riser cut and Top Hat #4 placement. Before June 4th, the overall average sample hydrocarbon concentration was 46.1µg/L, and 17.5% of results were detectable. After Top Hat

#4 began collecting oil the overall average sample hydrocarbon concentration was reduced to 5.5µg/L on average, and 10.1% of results were above detection limits. There was overall significant increase in frequency of detects and sample concentration with higher dispersant application rates, specifically associated with less water soluble compounds including di- and polycyclic aromatics/alkylated aromatics and alkanes >C8.

From June 11 – 21, 2010, Valentine et al. (2010) investigated dissolved hydrocarbon gases at depth using chemical and isotopic surveys and on-site biodegradation studies. In the vicinity of the leaking well, propane, ethane, and methane were most abundant at depths greater than 799 m and formed plume structures with dissolved concentrations as high as 8 µM, 16 µM, and 180 µM for the three gases, respectively. Gases were orders of magnitude less concentrated at shallower depths. They also observed deep (>799 m) hydrocarbon plumes at 29 of the 31 stations (Figure 3A in Valentine et al., 2010) where methane measurements were made. In addition to the persistent plume at 1,000- to 1,200-m depth located to the southwest of the spill site, consistent with other reports (Camilli et al. 2010; Hazen et al. 2010), they also identified separate plumes at similar depths to the north and to the east, as well as a distinctive shallower plume at 800- to 1000-m depth located to the east, suggesting multiple plumes in opposing directions presumably originated at different times, and indicating complex current patterns in the area before sampling.

Propane and ethane were identified by Valentine et al. (2010) as the primary drivers of microbial respiration, accounting for up to 70% of the observed oxygen depletion in "fresh" plumes. Regression of the observed oxygen anomaly data against the propane anomaly data indicated that 58% of the oxygen anomaly can be linked to propane; 70% of the oxygen anomaly can be linked to respiration of ethane and propane together in the fresh plume; and remaining oxygen anomaly presumably derives from other HCs such as butane. Assuming that the subsurface plume contained 100% released gases and 23.6% of released oil that had been dispersed as fine droplets at the subsurface release point, Valentine et al. (2010) calculated that gases released from the DWH leak exerted a BOD in the deep plume of up to 8.3×10^{11}g O_2 for methane, 1.3×10^{11}g O_2 for ethane, 1.0×10^{11} g O_2 for propane, and 4.4×10^{11} g O_2 for oil respiration. The sum of these values, ~15×10^{11} g of O_2, provides an estimate of the maximum integrated deep-water O_2 anomaly expected from this event, with ~15% of the oxygen loss occurring in fresh plumes from respiration of propane and ethane, and ~two-thirds of the ultimate microbial productivity in deep plumes would arise from metabolism of natural gases.

The JAG Report (JAG, 2010), prepared during the spill, estimated that TPH (Total Petroleum Hydrocarbon, water-insoluble heavy saturate fraction) from GC-MS ranged between <1 - 1000 ppb, with concentrations in the subsea plume (900–1300 m) at a maximum of 485 ppb at 1.2 km from the wellhead and detectable levels extending >10 km from source. In the plume, tVOA (total volatile organic analysis; water-soluble fraction) concentrations were higher than sTPH (speciated Total Petroleum Hydrocarbon), with a maximum of 2112 ppb.

Boehm et al. (2012) reported highest concentration of total PAH (TPAH) in field chemistry samples as10–100 ppb; TPAH levels greater than 10 ppb were largely observed during the release and then close to the wellhead. Diercks et al. (2010) observed concentrations of TPAH of 189 ppb at 1,320 m depth and 29 ppb at 1160 m near the wellhead site during the release. Spier et al. (2013) reported in 422 samples from the rising cone and deep water plume, the average concentration of measured hydrocarbons in was 68.3µg/L, and more than 28% of these samples contained ≥10 µg/L benzene. In 420 samples of the plume observed at 1050–1300 m depth, the average concentration was 65.8µg/L.

E.2.1.2. Dispersant Chemistry in Subsurface Waters

Kujawinski et al. (2011) collected water samples throughout the water column on three research cruises in the Gulf of Mexico in May (27-30), June (1, 11-21), and September 2010. A total of 25 dispersant-constituent dioctyl sodium sulfosuccinate (DOSS) samples taken in May - June during the spill and 21 samples taken in September after the spill indicated that DOSS was found at elevated levels between depths of 1000 -1200 m. Kujawinski et al. (2011) concluded that DOSS was sequestered in deepwater hydrocarbon plumes at 1,000-1,200 m water depth and did not intermingle with surface dispersant applications. Kujawinski et al.'s (2011) DOSS measurements are consistent with the presence of chemically-dispersed small (<100 μm) droplets in the deep plume.

E.2.2. NRDA Water Sample Chemistry Data

During the DWH blowout and resulting spill, a variety of environmental data were collected aboard numerous ships. Discrete surface and water column samples were collected, sub-sampled, and analyzed from various vessels using NRDA protocols. While similar sampling protocols were followed, each vessel had slightly different objectives and sampling equipment. Alongside collected chemical and forensic data, concurrent and continuous measurements of dissolved oxygen and UV fluorescence were recorded.

In total, sampling on 165 cruises was conducted in support of either Response, academic or the NRDA effort. A complete summary of the 48 cruises where NRDA sampling was conducted in 2010 is presented in Figure E.2-2. The data included in this report are from samples collected in 2010, upon which physical measurements were collected concurrently with chemical samples, and where Quality Assured data were available at the time this report was prepared.

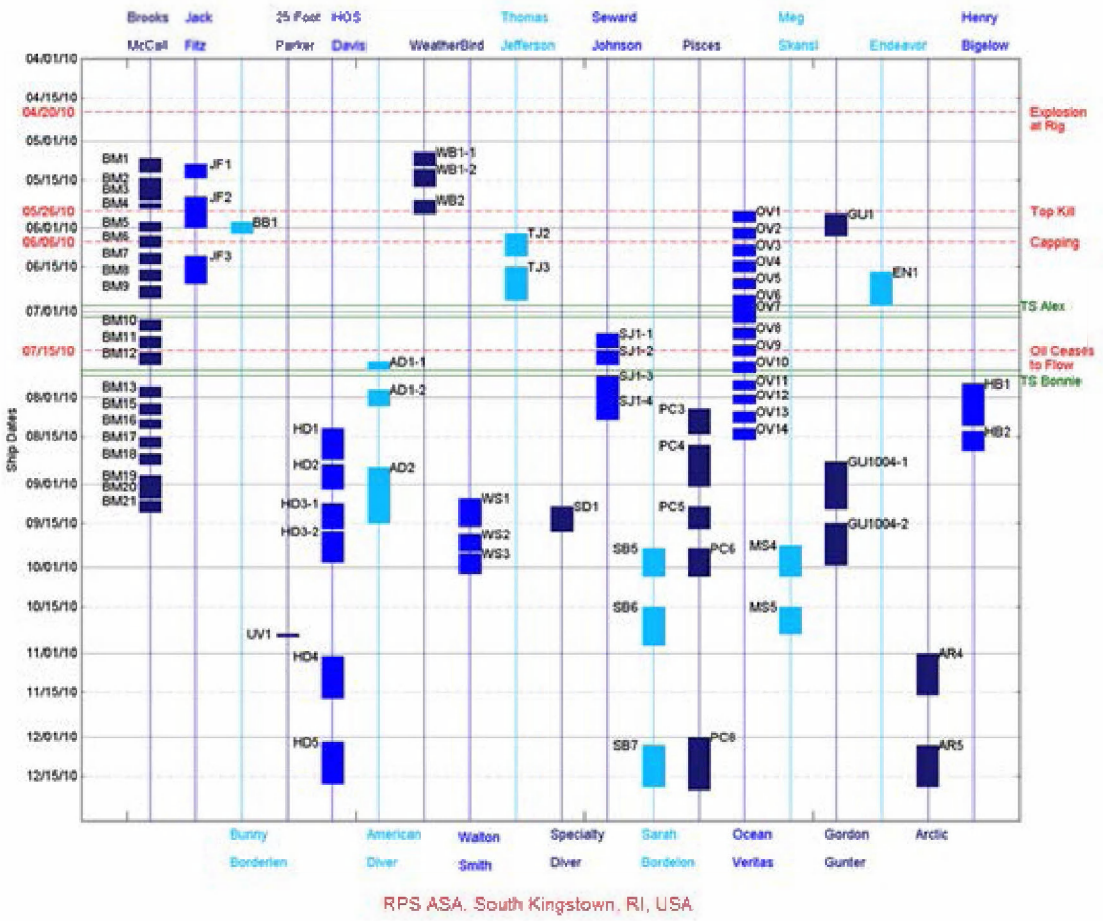

Figure E.2-2. List of 2010 cruises and associated dates where chemistry samples were collected. Important events and tropical storms have been included for reference.

Based on the analysis of the water column chemical and physical data, as well as the consideration of major events during response, four distinct periods of time are identifiable during the spill period in 2010. These are described as separate Observable Chemistry Regimes (OCR):

a. OCR 1: pre-top-kill (Apr-20 to May-26)
b. OCR 2: top-kill, riser-cutting, and initial top-hat (May-26 to June-6)
c. OCR 3: post-cut and collection (June-6 to July-15)
d. OCR 4: post-cap (after July-15) phases

In April and May, oil was released from the broken riser (at 1509 m deep) and from holes that developed at the kink in the riser pipe (at 1503 m deep). Several times during May 26-28, the spill responders attempted to fill the riser pipe with heavy drilling mud and bridging material, but the procedures did not stop the release and the well forced the mud and "junk" out of the riser. Relatively high hydrocarbon concentrations were observed during this period. During June 1-3, while the riser pipe was being cut, oil flowed freely from the riser, and this is evident in the data as elevated hydrocarbon concentrations compared to periods prior to and after this event. In

OCR 3, oil was released from the blowout preventer (BOP) at a depth of 1506 m deep from the opening of the Top Hat oil recovery installation or the gap between the Top Hat and the BOP. During OCR 4, after the release was stopped on July 15, in water hydrocarbon concentrations decreased with increasing time and space.

Sampling of the active release of oil and gas during the three phases (OCR 1-3) was focused around the wellhead (<20 km), while more extensive and broad-scale sampling into the far-field (focused to the south and southwest) did not commence until after the well shut-in was completed (OCR 4). Figures E.2-3-E.2-7 show the distribution of sampling overall and by OCR period.

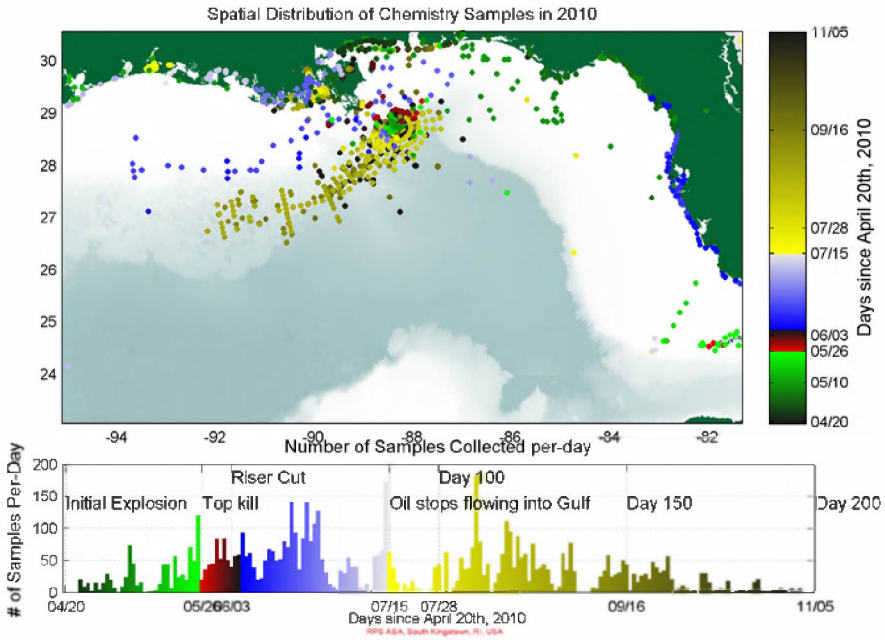

Figure E.2-3. Chemistry sampling locations throughout the Gulf of Mexico totaled 2,440 stations and nearly 14,000 discrete sampling locations (latitude, longitude, depth). Sampling locations are plotted as points with shaded colors representing date of collection. Note the four observed chemistry regimes were broken out by color.

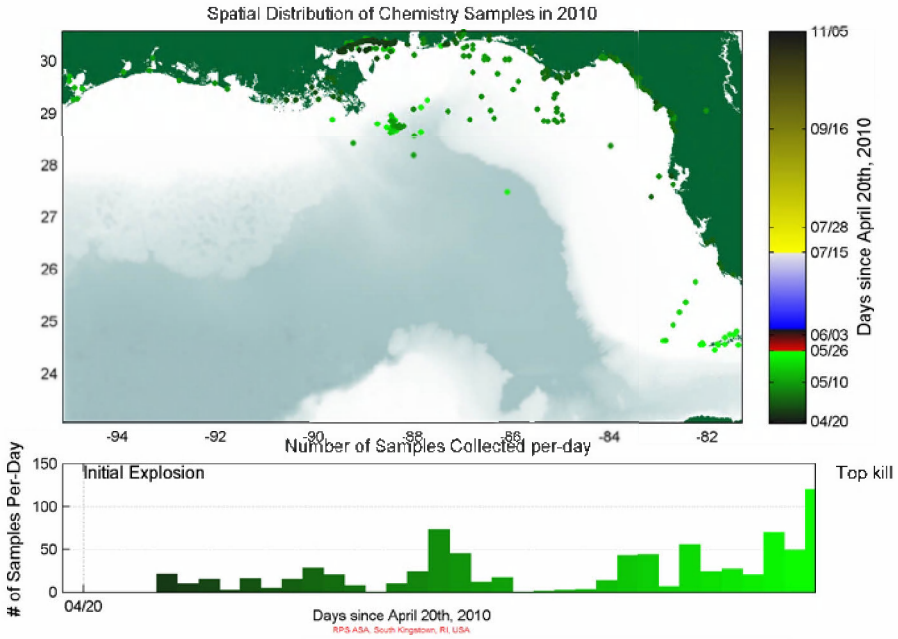

Figure E.2-4. Locations of chemistry sampling between April 20, 2010 and May 26, 2010, which encompassed the initial explosion and pre-top-kill phase.

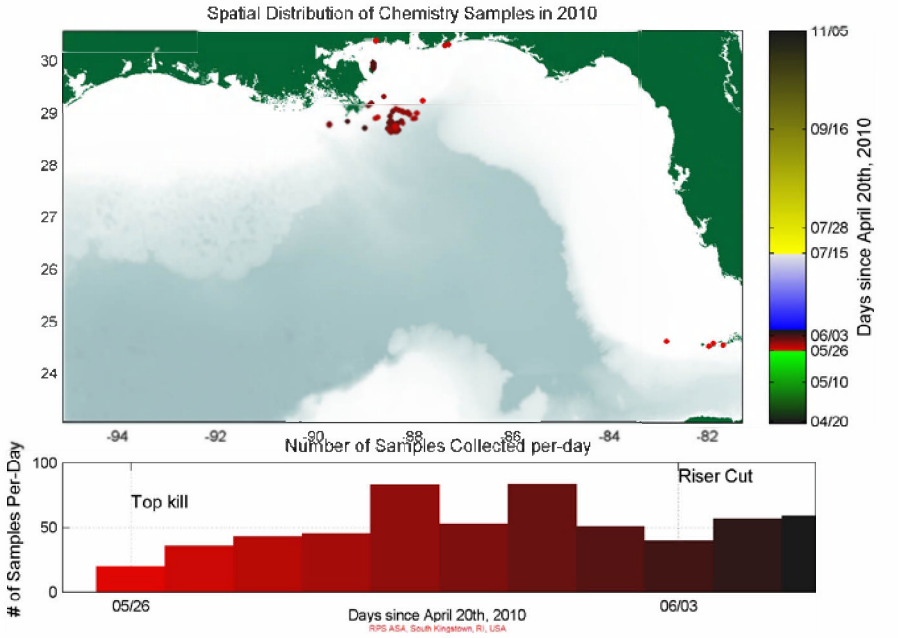

Figure E.2-5. Locations of chemistry sampling between May 26, 2010 and June 6, 2010, which encompassed top-kill, riser-cutting, and initial top-hat phase.

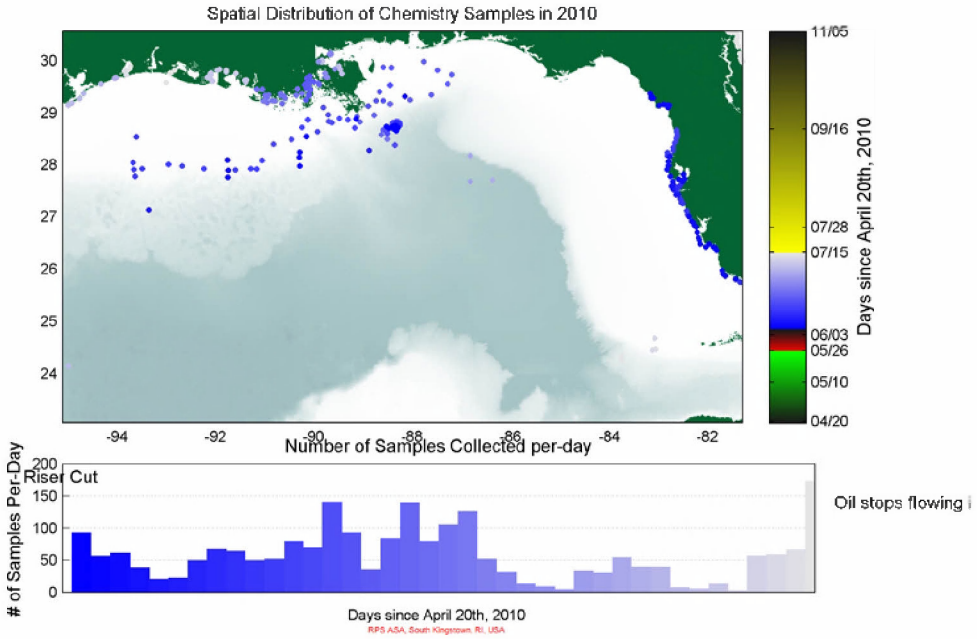

Figure E.2-6. Locations of chemistry sampling between June 6, 2010 and July 15, 2010, which encompassed the post-cut and collection phase.

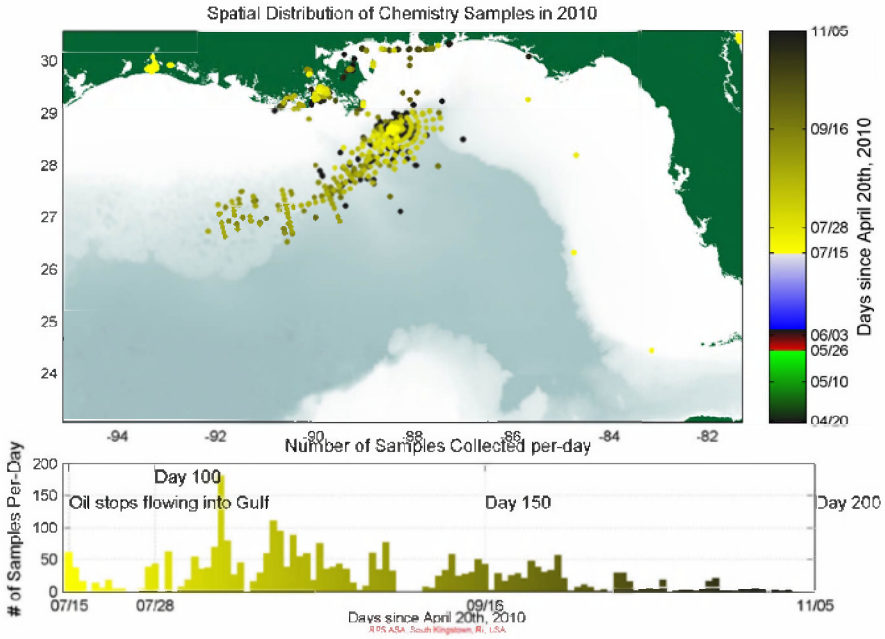

Figure E.2-7. Locations of chemistry sampling between July 15, 2010 and November 5, 2010, which encompassed the post-cap and successful shut-in phase.

Thus, discrete sampling was not continuous, nor was it evenly distributed throughout the Gulf of Mexico (GOM). The spatial and temporal pattern of chemical sampling aliases data and does not lend itself to appropriately determining the distribution of hydrocarbons throughout the GOM. The large gaps between samples in space and time likely introduce some bias in the results in such a dynamic environment. Without sampling specific locations, it is not possible to determine whether hydrocarbons were preset or absent. As an example, limited spatial sampling during June-July 2010, may inappropriately lead one to conclude that there were no hydrocarbons present greater than ~50 km from the well head. However, it is likely that there were hydrocarbons at depth and that they were merely not sampled.

Although sampling was not comprehensive in space and time, several patterns in the data may be discerned. In-water concentrations remained elevated during the blowout and the released hydrocarbons began to dissipate just after the well was contained and eventually capped. As may be seen in summary figures (Figures E.2-8 to E.2-11), the maximum hydrocarbon and dispersant concentrations occurred at the surface (<40 m) and at depths between ~1,100 and 1,200 m deep (Figure E.2-8 and Figure E.2-10). While surface observations of hydrocarbons exceeded method detection limits at some locations beyond 150 km from the wellhead (Figure E.2-8), the majority of concentrations greater than 1-10 µg/L were within approximately 50 km of the wellhead (Figure E.2-10). The highest concentrations at depth were in the BTEX group and soluble alkanes (Figure E.2-8). Elevated dispersant concentrations were identified between 1,000-1,300 m near the wellhead and between 1,100-1,200m to out beyond 150 km.

There were relatively high hydrocarbon and dispersant concentrations at depths between approximately 1,000-1,300 m. The highest observed values were near the wellhead, and the concentrations decreased as distance from the wellhead increased. In late summer and fall 2010, hydrocarbons were consistently present southwest of the wellhead, where the sampling effort was highest. Forensically identified MC252 oil was commonly observed radially within roughly 50 km of the wellhead (Figure E.2-8 and Figure E.2-10).

Elevated concentrations in excess of the method detection limits were identified throughout the water column to beyond 150 km (Figure E.2-9). Sampling in the depth range between 100-1,000 m was much more sporadic than for 1,000-1,300m. The highest concentrations at depths of 100-1000m were for the BTEX group and soluble alkanes (Figure E.2-11). The spatial extent in these intermediate waters is slightly more proximal to the wellhead, with highest concentrations observed typically within 25 km of the wellhead.

A detailed summary of the chemical analysis and data may be found in Horn et al. (2015a). A detailed summary of forensic findings may be found in Payne and Driskell (2015a,b,c) who after examining 5,332 offshore water samples identified MC252 oil in subsurface water samples as particulate-phase hydrocarbons up to 155 km from the wellhead, and as dissolved-phase as far as 267 km from the wellhead. Furthermore, based solely on dispersant indicators, fluorescence and DO features, the presence of the deep plume was detected 412 km from the wellhead. Payne and Driskell (2015c) also documented that dispersant indicators, measured for the first time in field-collected, particulate-phase oil samples at depth, document the utility of dispersant injections at the wellhead. In addition, they found that dispersant application at depth also resulted in significantly enhanced dissolution of lower-and intermediate-molecular weight PAH contributing to enhanced bioavailability to both benthic and pelagic organisms. Chemistry and sensor data are compared and synthesized in the combined chemical and physical report by Horn et al. (2015b).

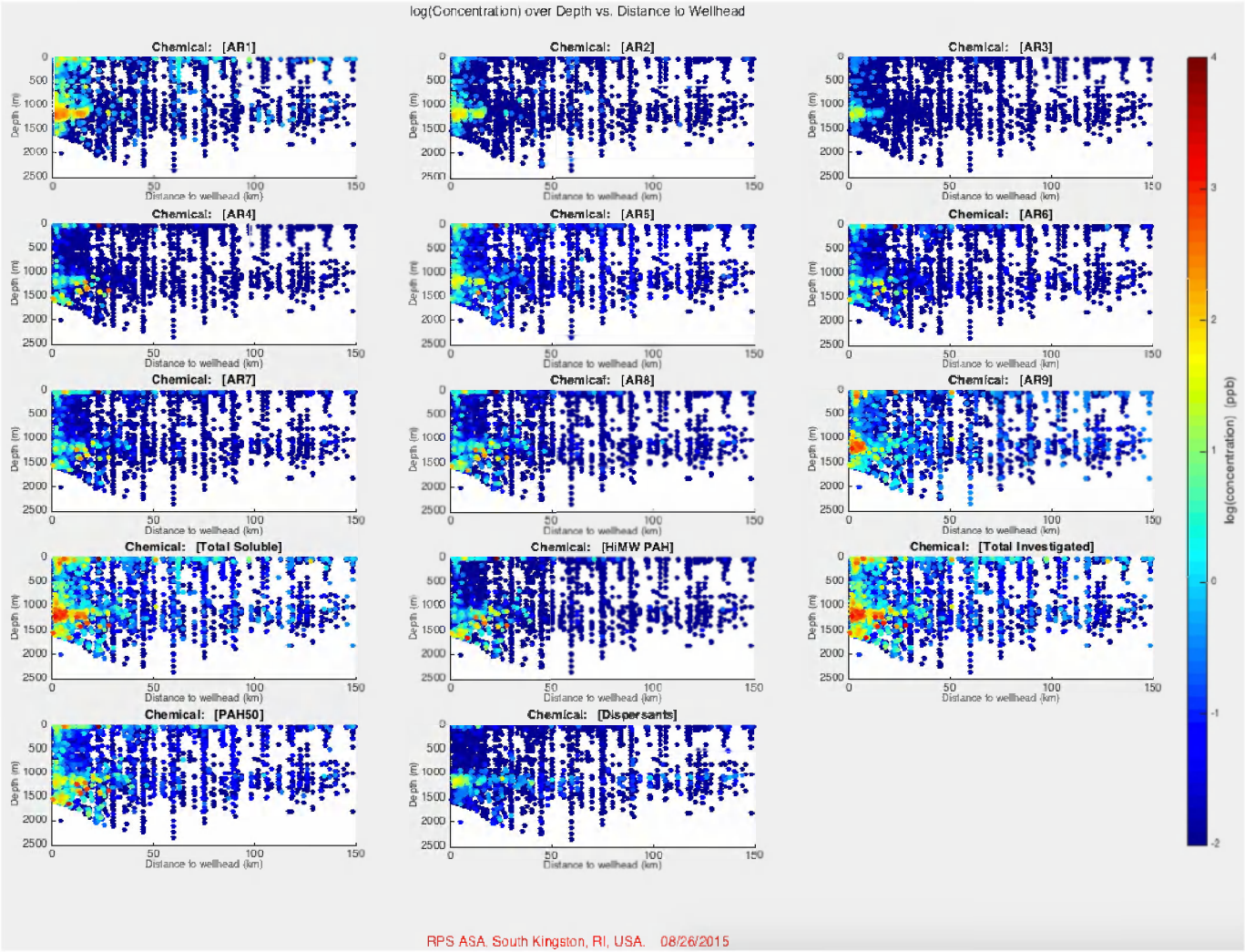

Figure E.2-8. Observed chemical concentrations (µg/L, or ppb) by grouping on a log-10 scale (color) through the full water column (0-2500 m – vertical axis) as a function of distance from the wellhead (0-150 km – horizontal axis). Note that all points represent significant hydrocarbon/dispersant concentrations, above the method detection limit for each investigated compound.

Figure E.2-9. Observed chemical concentrations (µg/L, or ppb) by grouping on a log-10 scale (color) through the water column (40-1100 m – vertical axis) as a function of distance from the wellhead (0-150 km – horizontal axis). Note that all points represent significant hydrocarbon/dispersant concentrations, above the method detection limit for each investigated compound.

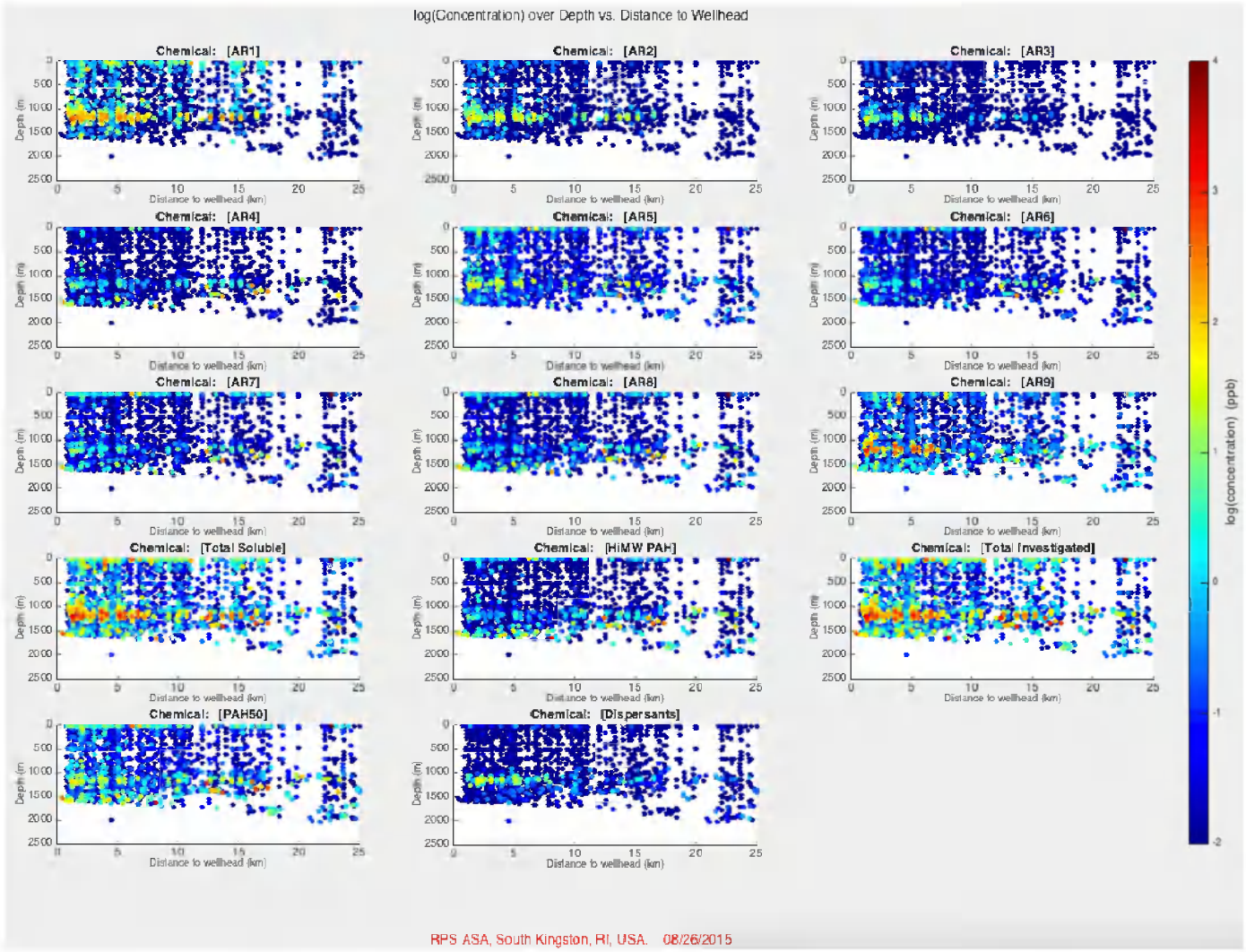

Figure E.2-10. Observed chemical concentrations (µg/L, or ppb) by grouping on a log-10 scale (color) through the full water column (0-2500 m – vertical axis) as a function of distance from the wellhead (0-25 km – horizontal axis). Note that all points represent significant hydrocarbon/dispersant concentrations, above the method detection limit for each investigated compound.

Figure E.2-11. Observed chemical concentrations (µg/L, or ppb) by grouping on a log-10 scale (color) through the water column (40-1100 m – vertical axis) as a function of distance from the wellhead (0-25 km – horizontal axis). Note that all points represent significant hydrocarbon/dispersant concentrations, above the method detection limit for each investigated compound.

E.3. Particle Data

A variety of field sampling programs have collected particle size information in the water column in the areas surrounding the DWH oil spill (See details in Li et al., 2015). The particle measurements include: (1) ROV video and camera analysis of suspended particles in the water column and sessile droplets in contact with a roughly 4 cm x 4 cm oil quantitation grid attached to the ceiling of the ROV video and camera housing on M/V *Jack Fitz* 2 (JF2) May 22-31 of 2010; (2) Holographic camera analysis of suspended particles in the water column that was performed on M/V *Jack Fitz* 3 (JF3) June 14-20 of 2010; (3) LISST-100X analysis of oil droplets or suspended particulate material (SPM) in the near-field shallow depths (within 300 m from the surface) on M/V *JF2 and JF3*; and (4) LISST-100X analysis of small particle concentrations (SPC) in the water column that was conducted on R/V *Brooks McCall* (May-August 2010) with discrete samples retrieved from the water column and at the surface.

The *JF*2 ROV dive data clearly showed particulates, including oil droplets, in the water column based on the recorded images and videos. These data indicated that (1) higher concentrations of oil droplets were present at certain depths of the water column than those at other depths; and (2) large oil droplets (>1 mm) tended to be more prevalent in the upper part of the water column.

The Holocam analysis (of 30 – 1000+ µm particles) showed the presence of round particles throughout the water column, which had count (number) median diameters around 45-50 µm. For Dives 5 & 6, increased number of category 1 (round object) and category 2 (possible oil) particles were measured both in the deep subsurface (i.e., 1,100-1,500 m) and the surface mixed layer, whereas the oil droplets were rare in the 250-850 m depth range (Davis and Loomis, 2014).

All *in situ* deployments of LISST-100X (2.5 – 500 µm detection limit) indicated presence of suspended particles throughout the water column, with relatively higher integrated particle concentrations at the surface and near the maximum deployment depth (~250 m). The particle size distributions have peaks (i.e., mode) between 300 and 400 µm.

The spill response vessel's LISST-100X analyses on the R/V *Brooks McCall* indicated that higher small particle concentrations (i.e., diameter ≤ 70 µm) were observed in the surface waters and the plume layer, in the close vicinity of the leaking wellhead.

The data reviewed in this appendix generally support the hypothesis that large droplets ascend quickly surrounding the immediate vicinity of the leaking wellhead, while a considerable number of smaller droplets remain suspended in the water column.

E.2.3. Field Data

E.2.1.3. JF2 cruise ROV video and camera imagery data on Marked Grid

Three cruises aboard the M/V *Jack Fitz* were conducted as part of the DWH oil spill NRDA program: The *Jack Fitz* 2 (May 22-31, 2010) and *Jack Fitz* 3 cruises (June 14-20, 2010) employed an ROV with a video camera to observe oil in the water column along with deploying sampling gear and collecting temperature, salinity, dissolved oxygen, fluorescence, and other sensor data (Payne and Driskell, 2015d; Li et al. 2015). The *Jack Fitz* 2 cruise deployed 17

casts/dives with the ROV; the majority of the ROV video recorded on this cruise was in color, at a resolution of 720x480. *Jack Fitz* 3 deployed nine dives, again with the majority of the ROV video recorded in color at a resolution of 720x480. (However, the majority of the *Jack Fitz* 3 video contained a video water mark which obstructed the underlying video and persisted for the duration of the recorded video. This water mark is a visibly black artifact present in more than one location on the video.)

The ROV video data starting with JF2 Dive#6 on May 24, 2010 were fitted with roughly 4 cm x 4 cm red-taped marked grid including a metal ruler with centimeter (cm) and millimeter (mm) lineation on one side as a reference scale. The oil quantitation grid (Marked Grid) was taped to the underside of the ROV housing, above and behind the camera, and during the dives the ROV was positioned to pan the camera to view the grid. The reference grid and scale next to the grid allow for visual estimations of droplet sizes in the water column, and those droplets that have collided with the grid. The grid-referenced oil droplets were identified either from the presence of visibly brown particulates in the water column, or from the sessile drops in contact (collided) with the surface of the grid. The advantage of the video over static imagery is the capability of tracking the movement of the droplets. For these droplets to be visible in this video footage, the droplet size must be greater than around 500 µm (see Li et al. 2015).

In JF2 ROV Dives 1 to 5, brown particulates indicative of oil were observed in the water column. In Dives 6-17, which were equipped with the Marked Grid, oil droplets were also observed in the water column and examined in more detail: larger droplets ($d \geq 1mm$) were found present close to the surface and smaller droplets ($d < 1mm$) were present throughout the majority of the water column at different frequencies. Certain dives (particularly Dives 8, 10, 15 and 16) contained clear boundaries between low and high droplet densities.

JF2 Dive #8 (on May 27, 2010) was located at about 3 km northwest of wellhead, and it had surveyed depths ranging from the surface to the seafloor (1,419 m). Two elevated peaks in numbers of droplets were observed: the first one was between the depths of 802 m to 1,006 m, and the second was identified between depths from 1,168 m to 1,390 m. However, brown particulates were visible throughout the water column in addition to within these two distinct peak depth intervals.

Dive #10 (on May 28, 2010) was located at approximately 4 km northwest of the wellhead and had a maximum depth of 1,444 m. A number of large droplets ($d \geq 1mm$) were observed at depths less than 261 m, and the oil droplet number density increased between 305 m and 382 m, followed by a visibly decreased yet still visible number of droplets in the water column at deeper depths, extending to the maximum depth of the dive. Figures E.3-1 and E.3-2 illustrate the captured video and camera imagery data of the dive at different depths of the water column.

Figure E.3-1: A cloud of oil droplets captured by the ROV camera of JF2 Dive#10 from about 3 m below the surface.

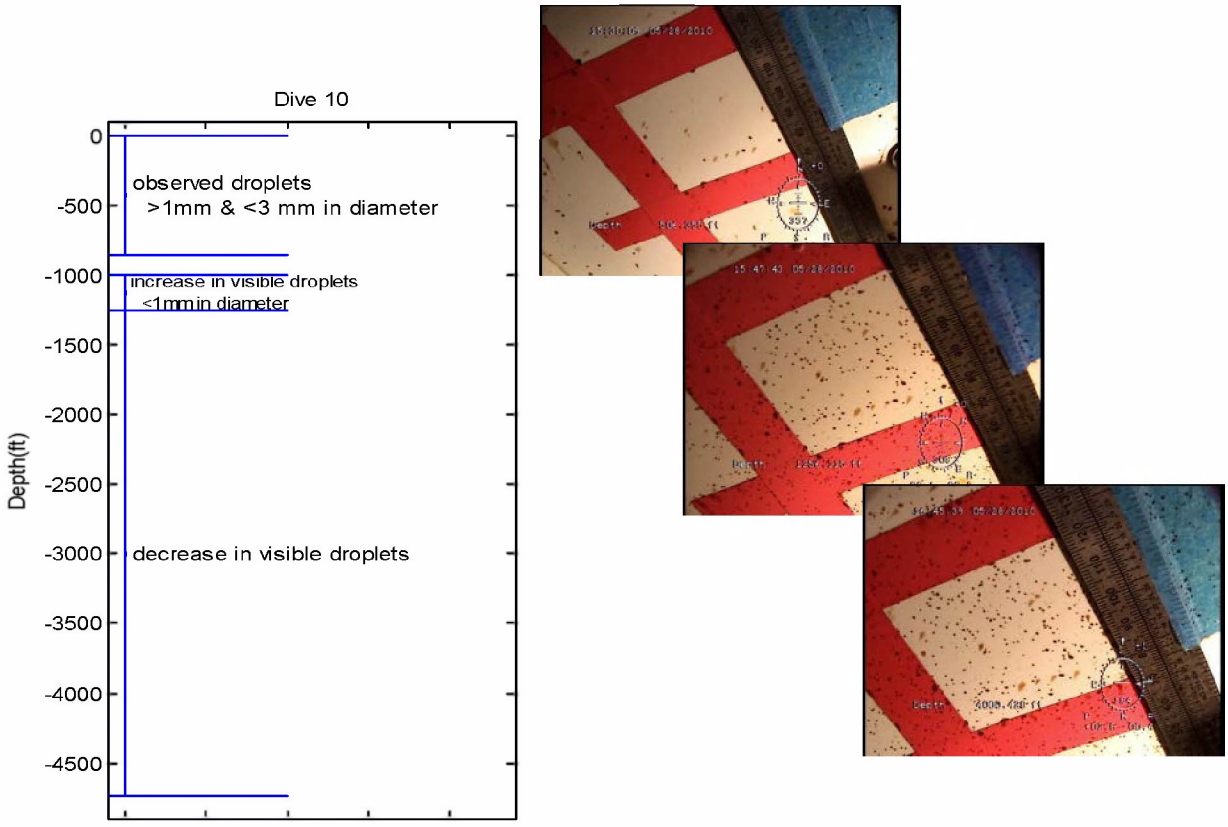

Figure E.3-2: Dive # 10 ROV video imagery data depth range (left, in feet) and representative images showing the oil droplets collided onto the roughly 4 cm x 4 cm red-tapped Marked Grid (right).

Dives #15 and 16 (on May 30, 2010) were located approximately 2 km southwest of the wellhead, with the maximum depth 1,601m for #15 and 1,212m for #16. There was very little surface oil at that location (Payne and Driskell, 2015d) and only small amounts of droplets were observed on the grid at depths less than 1,038.2 m during Dive 15, and at depths less than 990 m for Dive 16. For Dive #15, the greatest number of droplets was observed in the deep plume and on the Marked Grid in depths from 1,038 m to 1,219 m, with a large number of small droplets still readily visible in the water column until the maximum depth. For Dive#16, as the ROV descended past the depth of 990m, the amount of droplets that were visible in the water column from the forward facing camera visually increased, as were the number of droplets seen on the Marked Grid. At the maximum depth of the dive, however, the number of droplets appeared reduced. These dives clearly showed the decoupling of the deep plume from the surface manifestation of the released MC252 oil.

E.2.1.4. JF3 holographic camera imagery data

As part of the overall NOAA NRDA sampling program, a unique set of data on size distributions of oil droplets was collected and processed by Davis and Loomis (2014). On the M/V Jack Fitz 3 from June 14-20, 2010, an *in situ* digital holographic camera (Holocam) collected data from nine dives, at distances of 1-10 km from the wellhead. Among these nine dives, two were shallow dives that collected data within the upper 300 m, two dives were to 1,100 m, and the other five went deeper than 1,400 m.

During the dives, the Holocam was mounted on the front of a ROV and the unit was programmed to take an image at a set time interval over the entire dive. Objects were detected and the roundness of each detected object was used as a constraint for particle detection. Classifier truth rates (i.e., identification of particles as oil) depended on droplet size, with droplets smaller than 30 µm having too few pixels for accurate human identification and droplets larger than 150 µm much less abundant in the imaged volume. Detailed description of the data processing is presented in (Davis and Loomis, 2014).

The Holocam analysis showed that droplets (i.e., particulates defined by their roundness with a minimum diameter of 30 µm, a subset of those plotted here) were found throughout the water column with count (by number) median diameters from all the dives between 44.5-52 µm. The number-based particle size distributions at each depth generally followed lognormal number size distribution. The depth at which the peak numbers of particles were measured varied for different stations; for most dives, increased numbers of particles were measured at both the subsurface plume layer (below 1,000 m) and in the surface mixed layer.

E.2.1.5. LISST-100X SPM data

The LISST (Laser In-Situ Scattering and Transmissometry) instrument, manufactured by Sequoia Scientific Inc., uses the technique of laser diffraction to obtain size-distributions of particulate material in the water column. Processed results from the LISST instrument provide a volume concentration (µL/L) of particles in each of 32 size classes. The size classes are log-spaced over the range 2.5-500 microns (for Type-C instrument).

As part of the DWH NRDA program, a LISST-100X was deployed *in situ* on the *Jack Fitz* 2 and *Jack Fitz* 3 cruises during May and June, 2010. The instrument was attached to a descending ROV to a depth between 250 and 300 m while recording and/or transmitting nearly continuous

measurements. In general, SPM concentrations were large and variable in the upper 30-40 meters of the water column, likely due to the increased productivity and active turbulence from winds in the surface mixed layer as compared to deeper water. Below the mixed layer, SPM concentrations dropped to 50-100 ppm; then gradually increased up to the depth limits of the instrument (200-300 meters). At each individual sampling depth of the LISST data, there is a noticeable increase in SPM concentrations in the 300-400 µm range; in other words the mode of particle size distribution is approximately between 300 and 400 µm. It was not possible to identify oil droplets within these observations of SPM.

E.2.1.6. LISST-100X SPC data

The R/V *Brooks McCall* (and its alternative R/V *Ocean Veritas*) was dispatched at the request of BP and US Environment Protection Agency (EPA) to meet the US EPA Directive to monitor subsurface dispersant use (http://www.epa.gov/bpspill/dispersants/subsurface-dispersant-summary-final.pdf). The period of data analyzed in this report extends from May 8 to August 24, 2010. The monitoring program (including *Brooks McCall* and *Ocean Veritas*) collected a total of 3,197 water samples from 404 stations at depths down to 2,000 m (http://www.nodc.noaa.gov/General/DeepwaterHorizon/ships.html).

The measured small particle concentrations (SPC, i.e., d ≤ 70 µm) were plotted as a function of sampling depth below the sea surface, sampling distance from the wellhead, and the sampling date. All samples with high SPC (≥ 2.4 µl/L) were found at the surface, where the maximum was 14.2 µl/L. In comparison, the maximum SPC observed at the subsurface was 2.4 µl/L. All samples with SPC > 4.0 µl/L were within 15 km of the wellhead.

Results are included in the Joint Analysis Group (JAG) report (JAG, 2010) on the Review of R/V *Brooks McCall* Data to Examine Subsurface Oil. The plots illustrate the vertical profiles of fluorescence and oxygen measurements from CTD casts at stations with LISST-100X and laboratory analytical data from Niskin bottle samples. The JAG report concluded that: "Taken as a whole, fluorometry, TPH, and VOA measurements indicate that the anomaly observed near the wellhead is consistent with oil associated with the spill site, this signal decreases with distance from the source, and it decreases towards the southwest beyond 10 km within the area sampled. ……The water sample analysis for dispersed oil particles in the range of 2.5-60 µm using the LISST shows a correspondence with peaks in the *in-situ* fluorescence. See in particular stations B45-46, and B48-50."

E.2.4. Summary of the field observation particle data

Li et al. (2015) has compiled four sets of data that have been collected during the DWH oil spill time period: ROV video and camera imagery, the ROV holographic camera, the LISST-100X suspended particulate materials data, and the LISST-100X small particle concentration data. The discrete sampling methods for the LISST-100X analysis of small particle concentration (SPC) were not suitable for quantifying the entire droplet size distribution using a device meant for *in situ* deployment. Specifically, when discrete aliquots were pulled from GoFlo or Niskin bottles, and they were examined with a bench-top LISST on the vessel, the samples placed in the cuvettes were fraught with degassing bubbles and rapidly rising oil droplets confounding the analysis. That is one reason why *in situ* LISST measurements were utilized on the *Jack Fitz* cruises; however, this approach was depth limited (to the upper 250-300 m of the water column) because of instrumental constraints.

All *Jack Fitz* 2 ROV video data show particulates identifiable as oil in the water column. Several *Jack Fitz* 2 dives show that higher concentrations of oil droplets are present in certain depth ranges in the water column than other depths. The dive profiles also indicate large droplets (>1 mm) are more prevalent in the upper part of the water column.

Digital Holocam data were obtained by Davis and Loomis (2014) as part of the deployment of ROV in the water column during the *Jack Fitz* 3 NRDA monitoring program. The digital holographic camera data were collected in real time and *in situ* from nine different dives, including seven deep dives reaching depths of more than 1,000 m. The final results are reported as the number of round particles in the water column per size interval at each of the different depth intervals. These data clearly demonstrate the presence of round particles throughout the water column, and indicate some depths have higher numbers of particles than other depths.

In summary, during the DWH blowout release, a considerable amount of oil may have been dispersed as oil droplets into the water column. Some of these smaller droplets may have remained in the water column for an extended period of time because of their slow rise-times, while other larger droplets would have risen to the surface. The data reviewed generally support the hypothesis that large droplets rose quickly surrounding the immediate vicinity of the leaking wellhead, intermediate sized droplets extended further afield in the mid water column as they continued to rise, and a considerable number of small droplets remained suspended in the water column.

E.4. Oil Weathering

E.2.5. Weathering Processes

The oil weathering processes include or are influenced by spreading, evaporation, dissolution, emulsification, natural entrainment, chemical dispersion, biodegradation, and photo-oxidation. Weathering processes occurring as the oil droplets rose include dissolution and biodegradation.

The boiling cut curve of MC252 source oil indicated 61% of the mass was volatile and semi-volatile (Stout 2015a). SL Ross (Belore et al. 2011) concluded that the majority of the oil emulsion samples collected in the field had parent oil densities that would indicate that in excess of 55% of the initial oil volume had been lost through dissolution or evaporation prior to the sampling. SINTEF's (2010) field samples of emulsions were estimated to have 44-50% evaporative or dissolution loss. The field samples in the SINTEF study were collected 10-17 nautical miles (18.5-31.5 km) from the wellhead. Degree of weathering was not evaluated for oil samples taken close to the wellhead above the rising oil that might indicate the degree of loss through dissolution alone.

In the subsurface release of the DWH spill, depletion of soluble compounds such as BTEX and naphthalene in the water column before the oil surfaced has been attributed to dissolution (Payne and Driskell 2015a).

Microbial community shift was reported by Dubinsky et al. (2013). Once partial capture at the wellhead began, the plume microbial community structure changed significantly: The dominant species changed from alkane-degraders to aromatics-degraders, which was associated with a sharp decline in petroleum hydrocarbons, and an increase in the relative amount of BTEX and other soluble hydrocarbons in the plume.

E.2.6. MC252 Oil Weathering Data

Daling et al. (2014) reviewed literature asserting that MC252 crude oil droplets arriving on the sea surface would have already lost some of the original oil components by dissolution into the water during the ascent from 1,500 m water depth. They estimated this loss was ~15% before the oil rose to form surface slick, comprised of: saturates < C_7 representing 10–12 wt % of the stabilized crude oil, BTEX's representing 3 wt % of the crude oil, and C-3-Benzenes (1.5 wt % of the crude oil). Additionally, they estimated about 18% of the total PAH's representing 1.1 wt % of the total oil corresponding to about 0.2 wt % of the crude oil (Brown et al., 2011), would have been lost to the water before the oil surface.

Chemical measurements of floating oil and surface waters indicate that some of the PAHs remained in the larger oil droplets when they reached the surface; floating oil and surface water samples were observed to be enriched with 3- and 4-ring PAHs (Diercks et al. 2010, Spier et al. 2013; Stout 2015c, Payne and Driskell 2015a, b).

E.5. References

Belore, R. C., B. K. Trudel and J. Morrison. 2011. Weathering, emulsification, and chemical dispersibility of Mississippi Canyon 252 crude oil: Field and Laboratory studies. In: 2011 International Oil Spill Conference, IOSC 2011.

Boehm, P.D., Murray, K.J., Brown, J.S., Royer, L. 2012. Distribution and fate of PAH and chemical dispersants in the water column following the deepwater horizon oil spill. In: Presentation at the 243rd American Chemical Society National Meeting, San Diego, CA. March 26–29, 2012.

Brown, J. S., D. Beckmann, L. Bruce, L. Cook, and S. Mudge. "PAH Depletion Ratios Document the Rapid Weathering and Attenuation of PAHs in Oil Samples Collected after the Deepwater Horizon: 2011 International Oil Spill Conference, Portland, Oregon." In *International Oil Spill Conference Proceedings (IOSC)*, vol. 2011, no. 1, p. Abs336. American Petroleum Institute, 2011.

Camilli, R., C. M. Reddy, D. R. Yoerger, B. a. S. Van Mooy, M. V. Jakuba, J. C. Kinsey, C. P. Mcintyre, S. P. Sylva and J. V. Maloney. 2010. Tracking hydrocarbon plume transport and biodegradation at Deepwater Horizon. Science 330:201-204.

Daling, P. S., F. Leirvik, I. K. Almås, P. J. Brandvik, B. H. Hansen, A. Lewis and M. Reed. 2014. Surface weathering and dispersibility of MC252 crude oil. Marine Pollution Bulletin 87(1-2):300-310.

Davis, C. S. and N. C. Loomis. 2014. Deepwater Horizon Oil Spill (DWHOS) Water Column Technical Working Group Image Data Processing Plan: Holocam, Description of data processing methods used to determine oil droplet size distributions from in situ holographic imaging during June 2010 on cruise M/V Jack Fitz 3. Cabell S. Davis, Woods Hole Oceanographic Institution; Nick Loomis, MIT/WHOI Joint Program in Oceanography. 15 pages + Appendix.

Diercks, A. R., R. C. Highsmith, V. L. Asper, D. Joung, Z. Zhou, L. Guo, A. M. Shiller, S. B. Joye, A. P. Teske, N. Guinasso, T. L. Wade and S. E. Lohrenz. 2010. Characterization of subsurface polycyclic aromatic hydrocarbons at the Deepwater Horizon site. Geophys. Res. Lett. 37, L20602:1-6.

Du, M. and J. D. Kessler. 2012. Assessment of the Spatial and Temporal Variability of Bulk Hydrocarbon Respiration Following the Deepwater Horizon Oil Spill. Environmental Science & Technology 46(19):10499-10507. Dubinsky, E. A., M. E. Conrad, R. Chakraborty, M. Bill, S. E. Borglin, J. T. Hollibaugh, O. U. Mason, Y. M. Piceno, F. C. Reid, W. T. Stringfellow, L. M. Tom, T. C. Hazen and G. L. Andersen. 2013. Succession of Hydrocarbon-Degrading Bacteria in the Aftermath of the Deepwater Horizon Oil Spill in the Gulf of Mexico. Environmental Science & Technology 47(19):10860-10867.

Grennan, M., S. Zamorski, L. Decker, M. Horn, and Y. Kim, 2015. Technical Reports for Deepwater Horizon Water Column Injury Assessment – FE_TR.39: Volume II. Water Column CTD and Sensor Data from the Deepwater Horizon Oil Spill. RPS ASA, South Kingstown, RI, USA, August 2015.

Hazen, T. C., E. A. Dubinsky, T. Z. Desantis, G. L. Andersen, Y. M. Piceno, N. Singh, J. K. Jansson, A. Probst, S. E. Borglin, J. L. Fortney, W. T. Stringfellow, M. Bill, M. E. Conrad, L. M. Tom, K. L. Chavarria, T. R. Alusi, R. Lamendella, D. C. Joyner, C. Spier, J. Baelum, M. Auer, M. L. Zemla, R. Chakraborty, E. L. Sonnenthal, P. D'haeseleer, H. Y. N. Holman, S. Osman, Z. Lu, J. D. Van Nostrand, Y. Deng, J. Zhou and O. U. Mason. 2010. Deep-sea oil plume enriches indigenous oil-degrading bacteria. Science 330:204-208.

Horn, M., M. Grennan, L. Decker, S. Zamorski, D. French McCay, and Z. Li, 2015a. Technical Reports for Deepwater Horizon Water Column Injury Assessment – FE_TR.38: Volume I. Water Column Chemistry Data from the Deepwater Horizon Blowout. RPS ASA, South Kingstown, RI, USA, August 2015.Horn, M., D. French McCay, J. Payne, W. Driskell, Z. Li, M. Grennan, L. Decker, S. Zamorski, 2015b. Technical Reports for Deepwater Horizon Water Column Injury Assessment – FE_TR.40: Volume III. Water Column Chemical and Physical Data from the Deep Water Horizon Blowout. RPS ASA, South Kingstown, RI, USA, August 2015.

JAG. 2010. Joint Analysis Group (JAG) Review of R/V Brooks McCall Data to Examine Subsurface Oil (http://www.ncddc.noaa.gov/activities/healthy-oceans/jag/reports/).

Kessler, J. D., D. L. Valentine, M. C. Redmond, M. Du, E. W. Chan, S. D. Mendes, E. W. Quiroz, C. J. Villanueva, S. S. Shusta, L. M. Werra, S. A. Yvon-Lewis and T. C. Weber. 2011. A persistent oxygen anomaly reveals the fate of spilled methane in the deep Gulf of Mexico Science 331:312-315.

Kujawinski, E. B., M. C. Kido Soule, D. L. Valentine, A. K. Boysen, K. Longnecker and M. C. Redmond. 2011. Fate of Dispersants Associated with the Deepwater Horizon Oil Spill. Environmental Science & Technology 45(4):1298-1306.

Li, Z., A. Bird, J.R. Payne, N. Vinhateiro, Y. Kim, C. Davis and N. Loomis, 2015. Technical Reports for Deepwater Horizon Water Column Injury Assessment – FE_TR.41: Volume IV. Oil Particle Data from the Deepwater Horizon Oil Spill. RPS ASA, South Kingstown, RI, USA, August 2015.

Payne, J.R. and W.B. Driskell, 2015a. 2010 DWH offshore water column samples—Forensic assessments and oil exposures. PECI Technical Report to the Trustees in support of the PDARP.

Payne, J.R. and W.B. Driskell, 2015b. Forensic fingerprinting methods and classification of DWH offshore water samples. PECI Technical Report to the Trustees in support of the PDARP.

Payne, J.R. and W.B. Driskell, 2015c. Dispersant effects on waterborne oil profiles and behavior. PECI Technical Report to the Trustees in support of the PDARP.

Payne, J.R. and W.B. Driskell, 2015d. Offshore adaptive sampling strategies. PECI Technical Report to the Trustees in support of the PDARP.

Reddy, C. M., J. S. Arey, J. S. Seewald, S. P. Sylva, K. L. Lemkau, R. K. Nelson, M. a. S. Van Mooy and R. Camilli. 2012. Composition and fate of gas and oil released to the water column during the Deepwater Horizon oil spill. Proceedings of National Academy of Sciences 109(5):20229-20234.

Ryerson, T. B., K. C. Aikin, W. M. Angevine, E. L. Atlas, D. R. Blake, C. A. Brock, F. C. Fehsenfeld, R. S. Gao, J. A. De Gouw, D. W. Fahey, J. S. Holloway, D. A. Lack, R. A. Lueb, S. Meinardi, A. M. Middlebrook, D. M. Murphy, J. A. Neuman, J. B. Nowak, D. D.

Parrish, J. Peischl, A. E. Perring, I. B. Pollack, A. R. Ravishankara, J. M. Roberts, J. P. Schwarz, J. R. Spackman, H. Stark, C. Warneke and L. A. Watts. 2011. Atmospheric emissions from the Deepwater Horizon spill constrain air-water partitioning, hydrocarbon fate, and leak rate. Geophys. Res. Lett. 38(7):L07803.

Ryerson, T. B., R. Camilli, J. D. Kessler, E. B. Kujawinski, C. M. Reddy, D. L. Valentine, E. Atlas, D. R. Blake, J. De Gouw, S. Meinardi, D. D. Parrish, J. Peischl, J. S. Seewald and C. Warneke. 2012. Chemical data quantify Deepwater Horizon hydrocarbon flow rate and environmental distribution. Proceedings of the National Academy of Sciences 109(50):20246-20253.

Spier, C., W. T. Stringfellow, T. C. Hazen and M. Conrad. 2013. Distribution of hydrocarbons released during the 2010 MC252 oil spill in deep offshore waters. Environmental Pollution 173:224-230.

Stout, S.A., 2015a. Physical and chemical properties of the fresh MC252 Macondo-1 well crude oil. NewFields Technical Report to the Trustees in support of the pDARP.

Stout, S.A., 2015b. Bulk chemical and physical properties of fresh and weathered Macondo crude oil. NewFields Technical Report to the Trustees in support of the pDARP.

Stout, S.A., 2015c. Range in composition and weathering among floating Macondo oils during the Deepwater Horizon oil spill. NewFields Technical Report to the Trustees in support of the pDARP.

Valentine, D. L., J. D. Kessler, M. C. Redmond, S. D. Mendes, M. B. Heintz, C. Farwell, L. Hu, F. S. Kinnaman, S. Yvon-Lewis, M. Du, E. W. Chan, F. G. Tigreros and C. J. Villanueva. 2010. Propane respiration jump-starts microbial response to a deep oil spill. Science 330:208-211.

Valentine, D. L., I. Mezic, S. Macesic, N. Crnjaric-Zic, S. Ivic, P. J. Hogan, V. A. Fonoberov and S. Loire. 2012. Dynamic autoinoculation and the microbial ecology of a deep water hydrocarbon irruption. Proceedings of the National Academy of Sciences of the United States of America 109(50):20286-20291.

Technical Reports for Deepwater Horizon Water Column Injury Assessment

WC_TR.14: Modeling Oil Fate and Exposure Concentrations in the Deepwater Plume and Rising Oil Resulting from the Deepwater Horizon Oil Spill

Appendix F. Model Results

Authors: Deborah French McCay, Katherine Jayko, Zhengkai Li, Matthew Horn, Yong Kim, Tatsu Isaji, Deborah Crowley, Malcolm Spaulding, Lauren Decker, Cathleen Turner, Stefanie Zamorski, Jeremy Fontenault, Rachel Shmookler, and Jill Rowe

Revised: September 29, 2015
Project Number: 2011-144
RPS ASA 55 Village Square Drive, South Kingstown, RI 02879

Table of Contents

List of Figures

List of Tables

F.1 Introduction

This appendix provides figures that illustrate the results of oil fate model runs using SIMAP. The discussion of these results is in the main report in Section 6. Table F-1 lists the time domains of events, useful when evaluating model results.

Table F-1. Time domains used for the evaluation of model results.

Period	Events	Time	
		Start Time	End Time
OCR1	pre-top-kill	4/22/2010	5/26/2010
OCR2	top-kill, riser-cutting, and initial top-hat	5/26/2010	6/6/2010
OCR3	post-cut and collection	6/6/2010	7/15/2010
OCR4	post-cap	7/15/2010	9/30/2010

F.2 Static Cone Simulation

Figures F.2-1 to F.2-40 provide snapshots of the vertical concentration distributions in plane view looking north produced by the Static Cone simulation typical of each month (April 26, May 17, Jun 16, and July 15). April 26 and May 17 are during OCR1, June 16 is in OCR3, and July 15 is at the transition from OCR3 to OCR4 (Table F-1). Each figure also shows a top-down view mapping the vertical maximum concentration in the water column in horizontal space, with an associated west-east cross-section through the center of the inverted cone. The kilometer scale along the horizontal axis in the cross-section depicts distance from west to east along the blue line in the map part of the figure. The vertical axis of the cross-sections shows depth in meters from the surface. The bathymetry appears in the cross-section, indicating the locations of domes to the west and east of the wellhead. The grey box in the map view is a 50 km x 50 km box centered on the wellhead. Concentrations are in mg/m^3 (= μg/L, ~ppb).

Note that the total hydrocarbon concentrations in droplets predicted by the model are based on the full mass of the release, much of which cannot be chemically measured in water samples. Thus the modeled total hydrocarbon concentration is not comparable to a total petroleum hydrocarbon measurement. For this reason, model-predicted concentrations of the soluble and semi-soluble hydrocarbons, i.e., of the AR components, are of interest and may be compared to field sample measurements.

In this appendix, there are 10 figures for each of the 4 dates, one for each of the 9 soluble/semi-soluble components and the total of all soluble and semi-soluble components. Each figure is a pair showing concentrations in the particulate (i.e., droplet, top) and dissolved (bottom) phases.

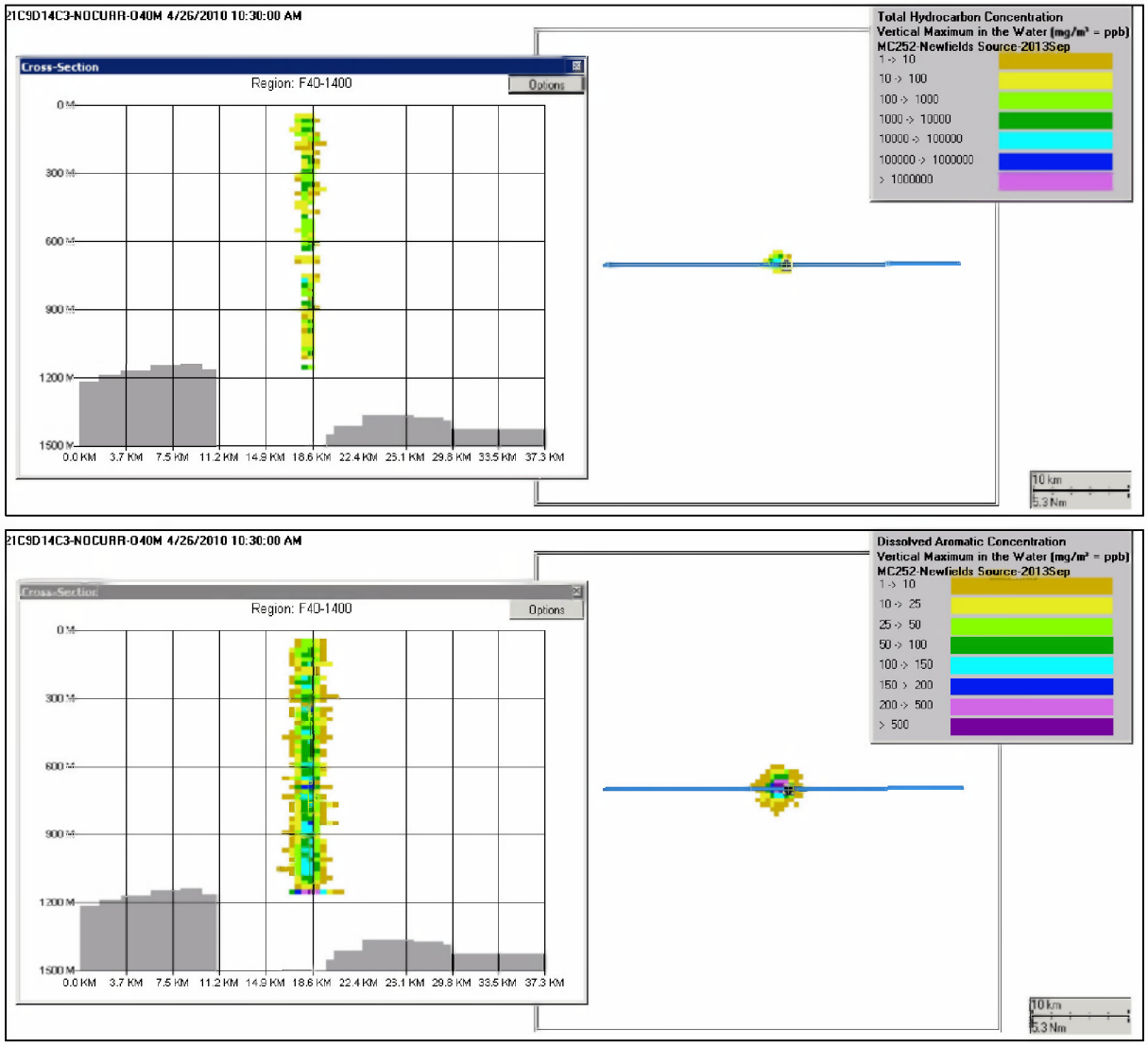

Figure F.2-1. Concentrations produced by the Static Cone simulation on April 26 – total hydrocarbons (μg/L) in droplets (top) and in the dissolved phase (bottom).

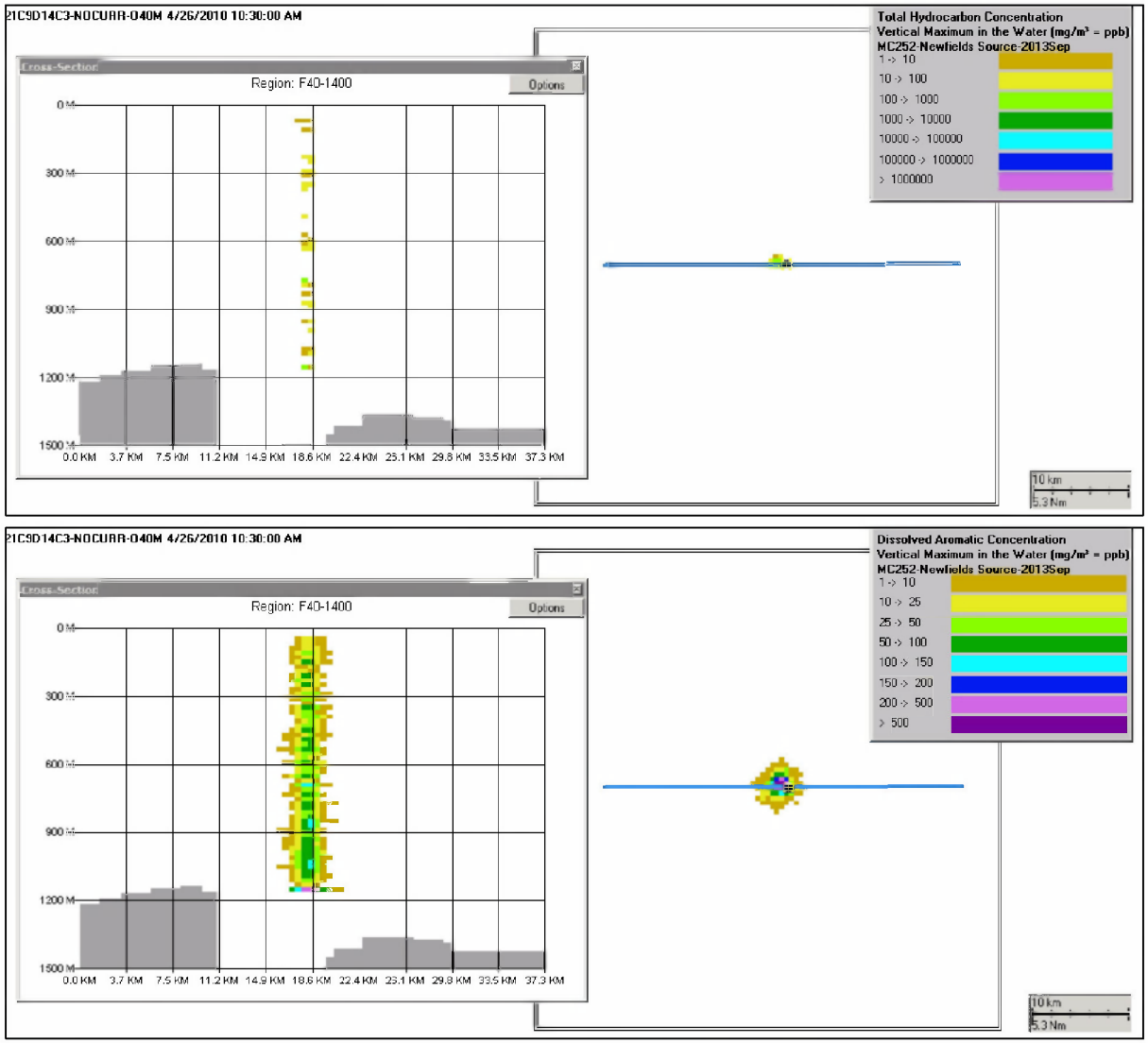

Figure F.2-2. Concentrations produced by the Static Cone simulation on April 26 – AR1 component (BTEX, µg/L) in droplets (top) and in the dissolved phase (bottom).

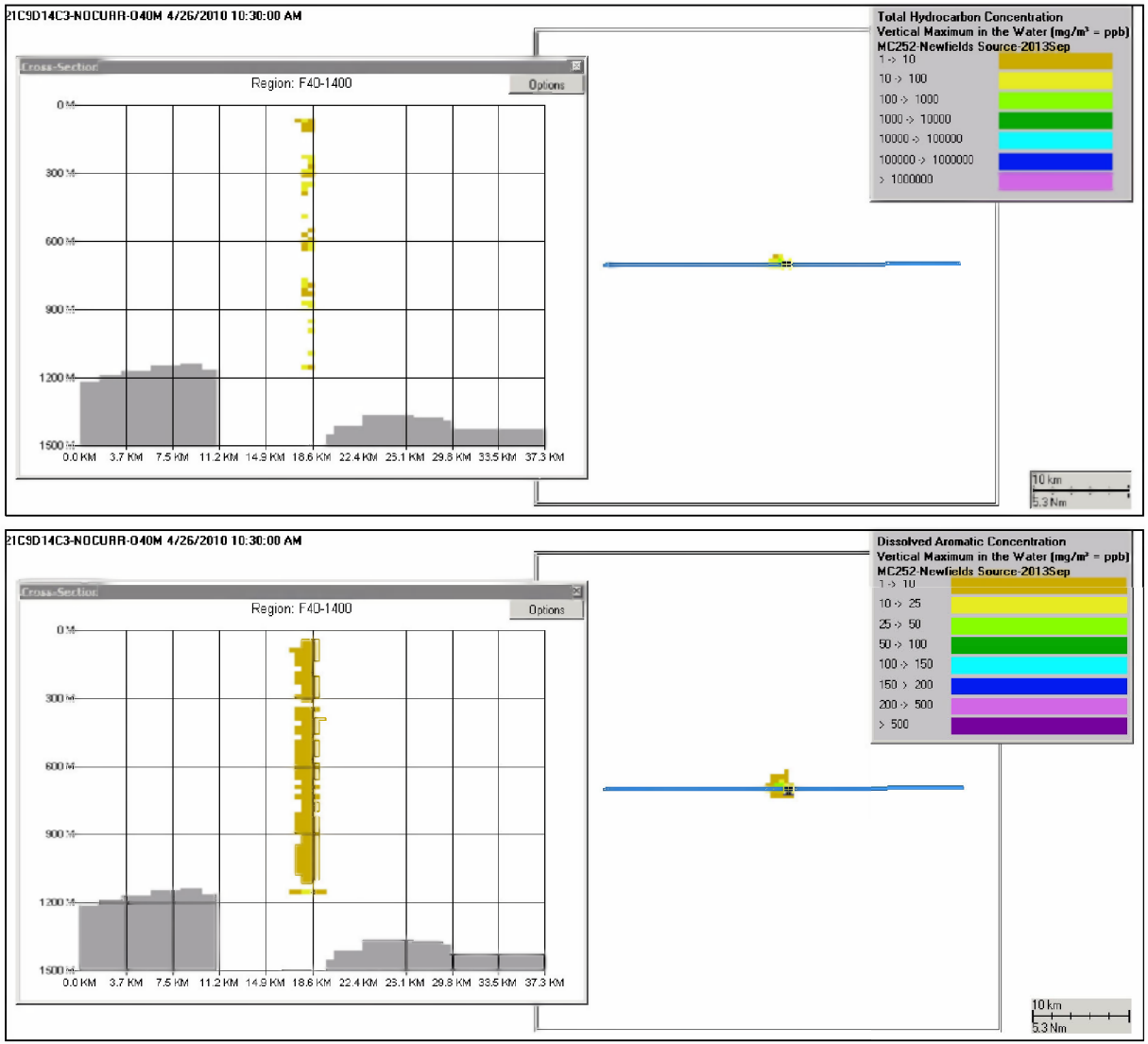

Figure F.2-3. Concentrations produced by the Static Cone simulation on April 26 – AR2 component (C3-benzenes, μg/L) in droplets (top) and in the dissolved phase (bottom).

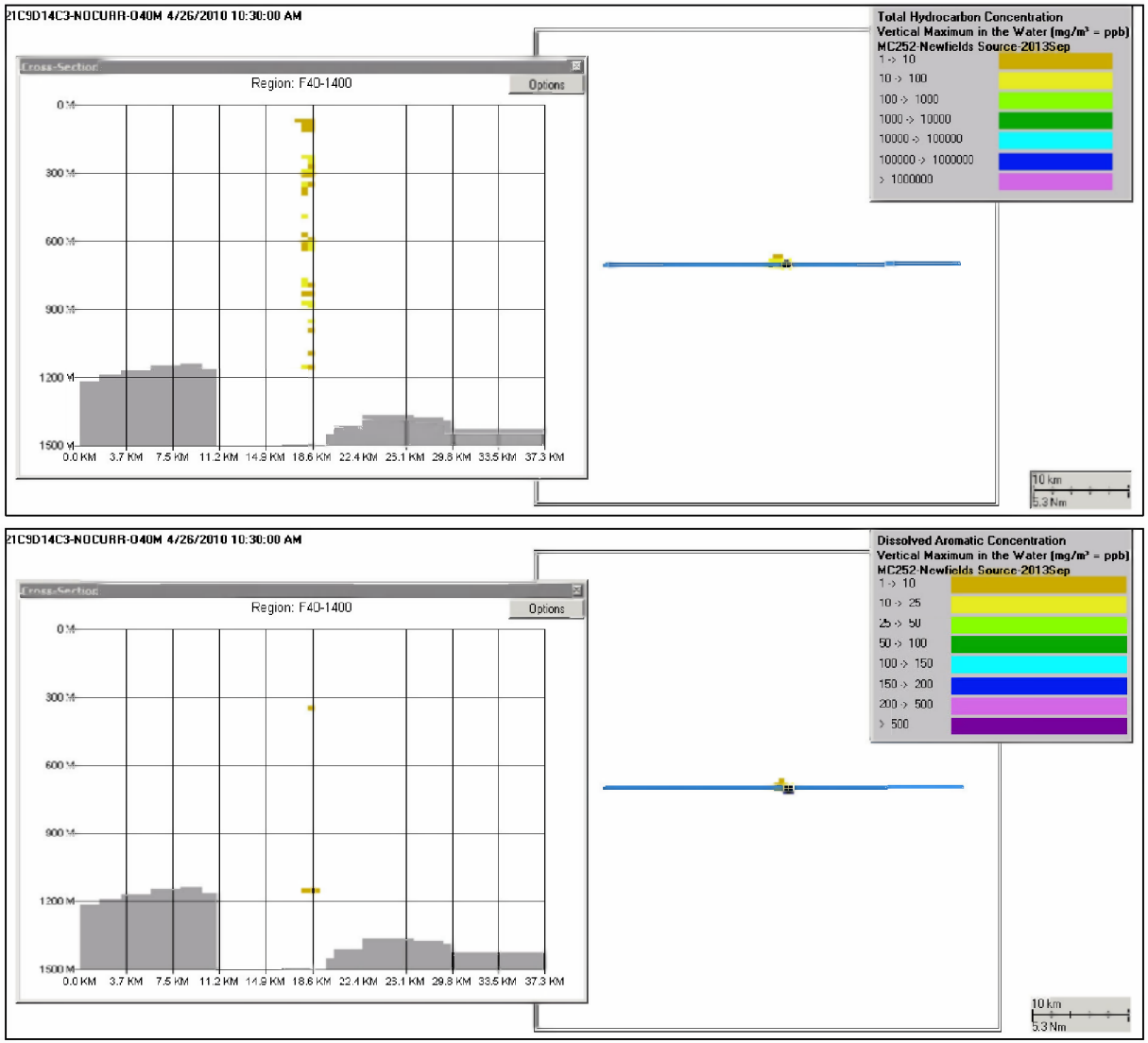

Figure F.2-4. Concentrations produced by the Static Cone simulation on April 26 – AR3 component (C4-benzenes, µg/L) in droplets (top) and in the dissolved phase (bottom).

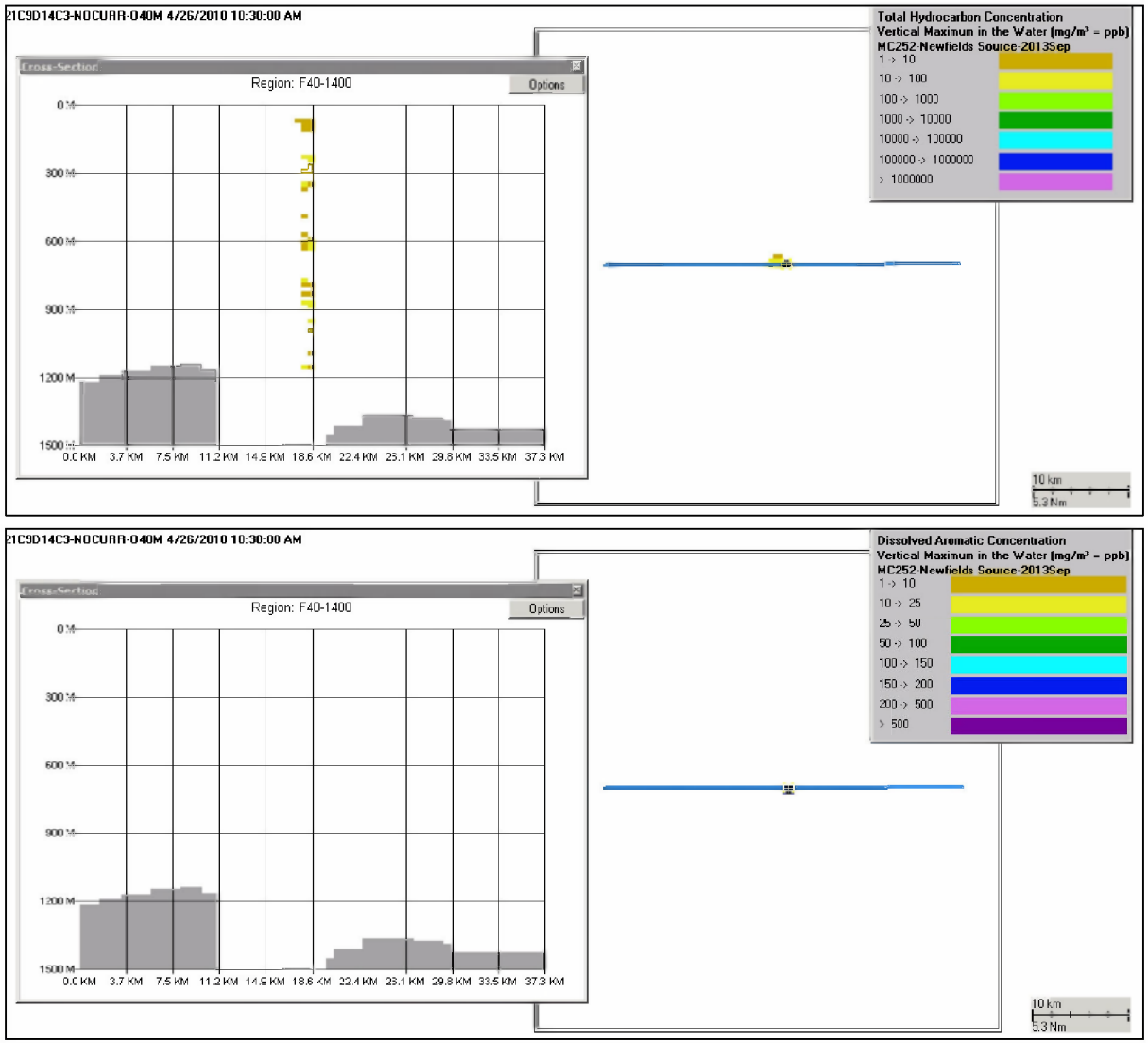

Figure F.2-5. Concentrations produced by the Static Cone simulation on April 26 – AR4 component (decalins, μg/L) in droplets (top) and in the dissolved phase (bottom).

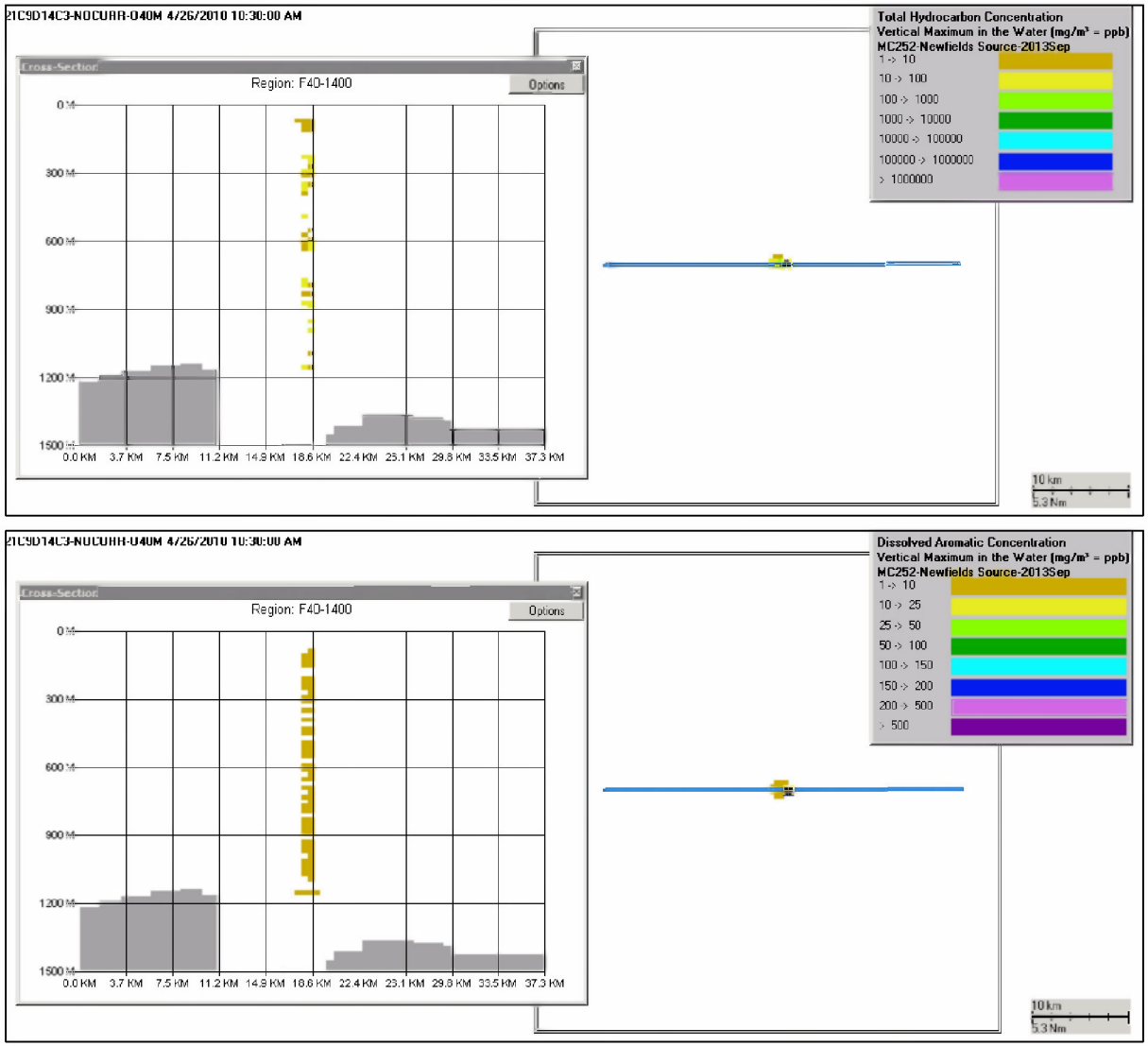

Figure F.2-6. Concentrations produced by the Static Cone simulation on April 26 – AR5 component (C0-C2 naphthalenes, μg/L) in droplets (top) and in the dissolved phase (bottom).

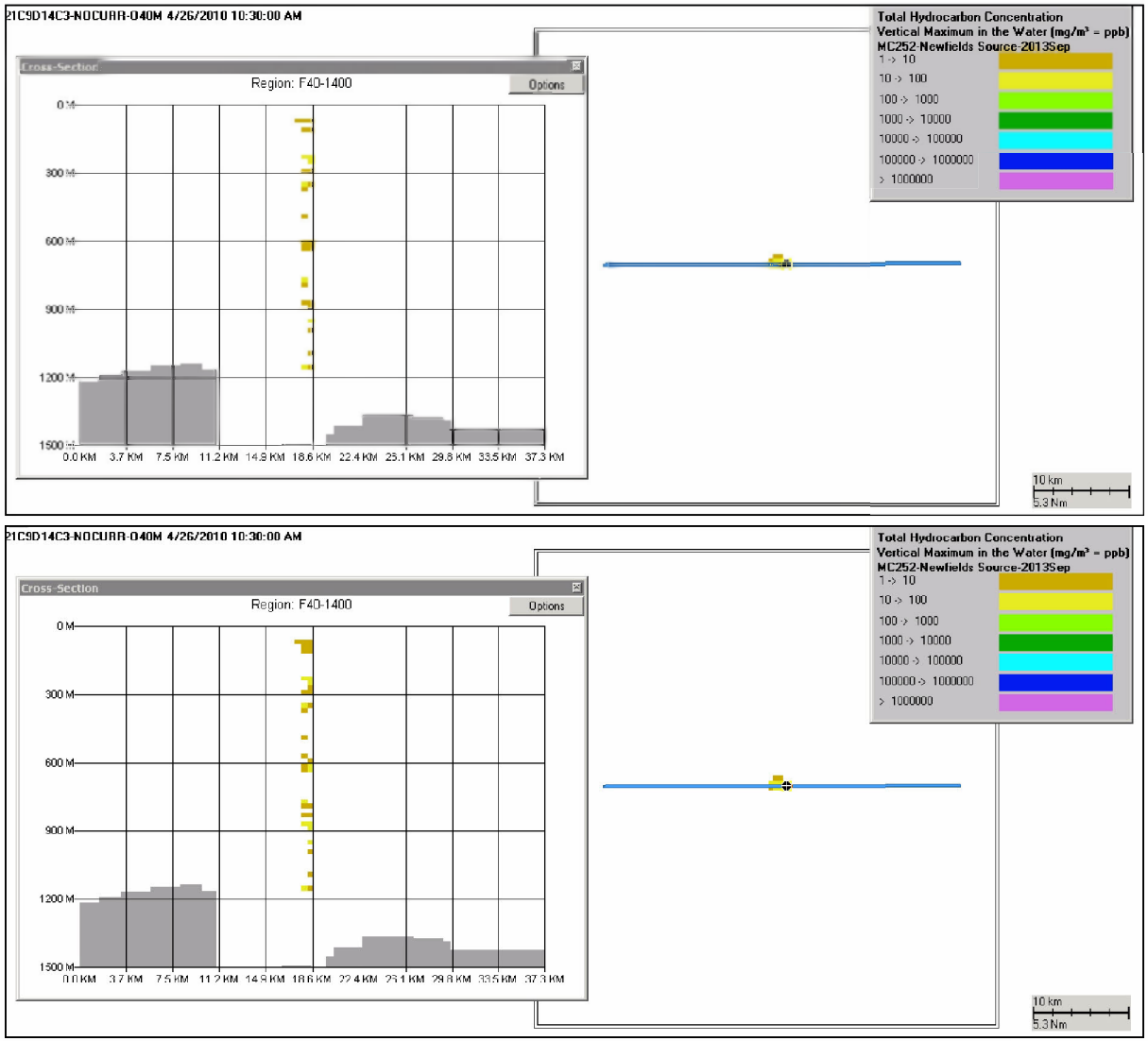

Figure F.2-7. Concentrations produced by the Static Cone simulation on April 26 – AR6 component (C3-C4 naphthalenes, µg/L) in droplets (top) and in the dissolved phase (bottom).

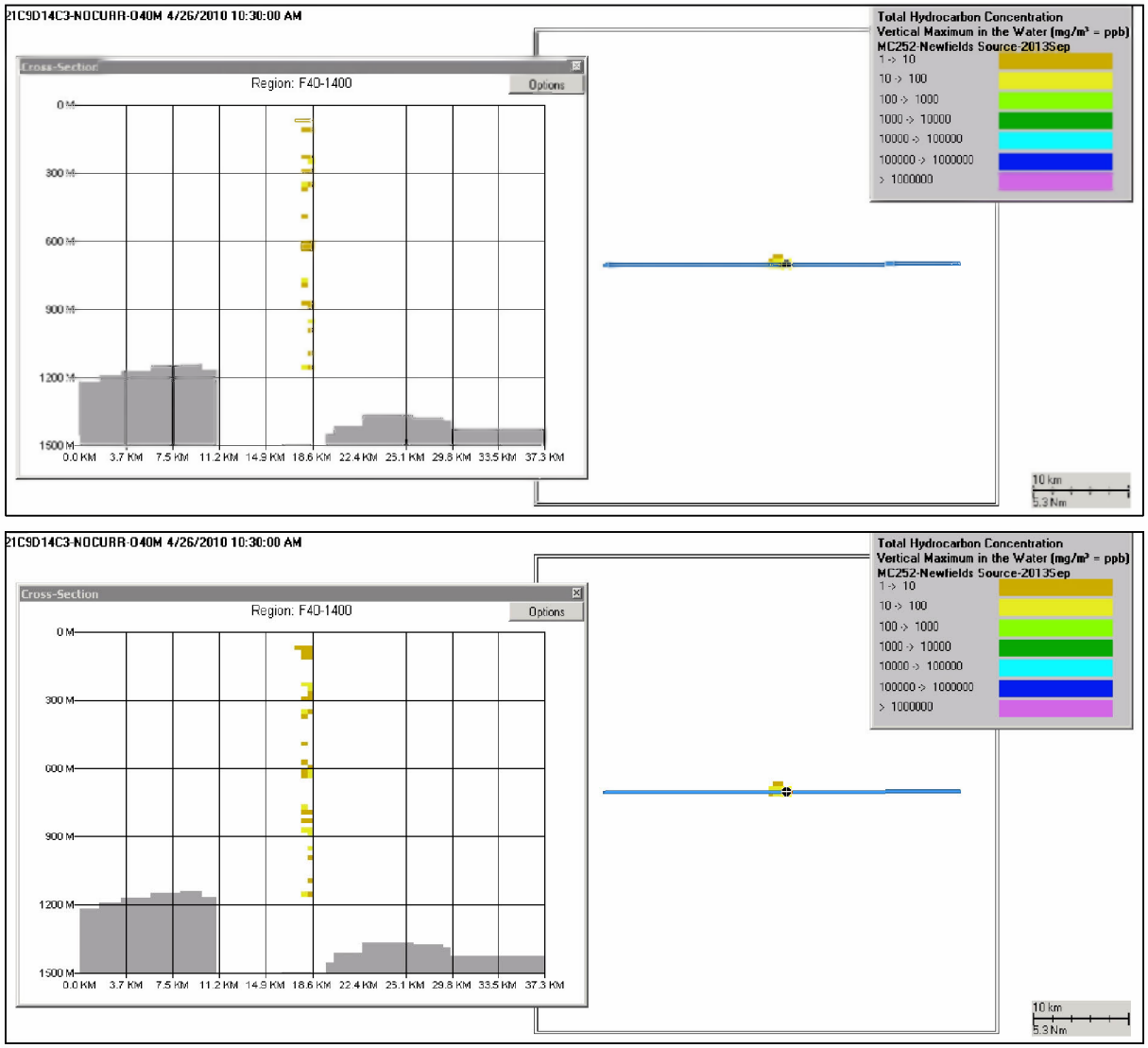

Figure F.2-8. Concentrations produced by the Static Cone simulation on April 26 – AR7 component (fluorenes & C0-C1 3-ring PAHs, µg/L) in droplets (top) and in the dissolved phase (bottom).

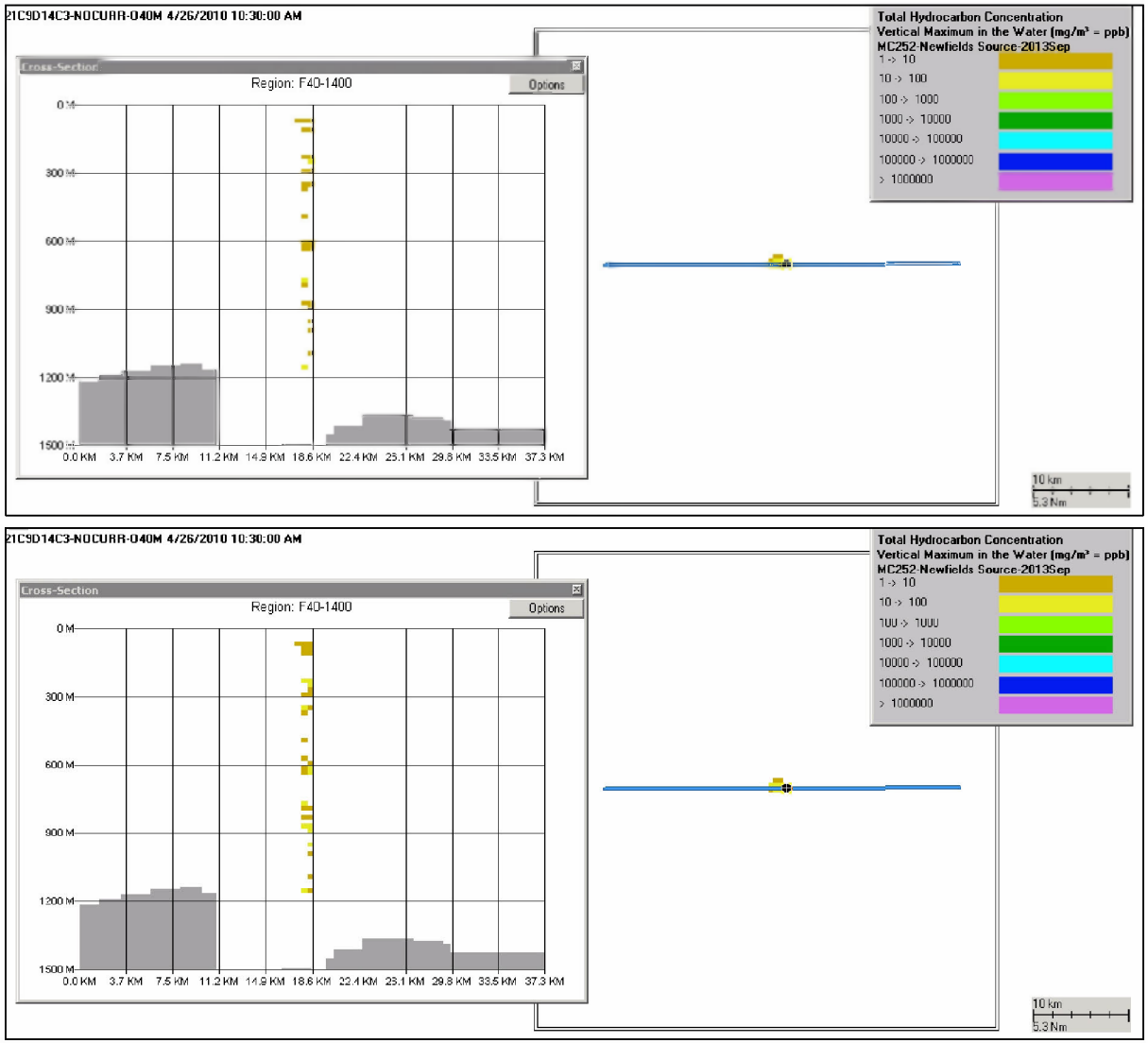

Figure F.2-9. Concentrations produced by the Static Cone simulation on April 26 – AR8 component (4-ring PAHs & C2-C3 3-ring PAHs, μg/L) in droplets (top) and in the dissolved phase (bottom).

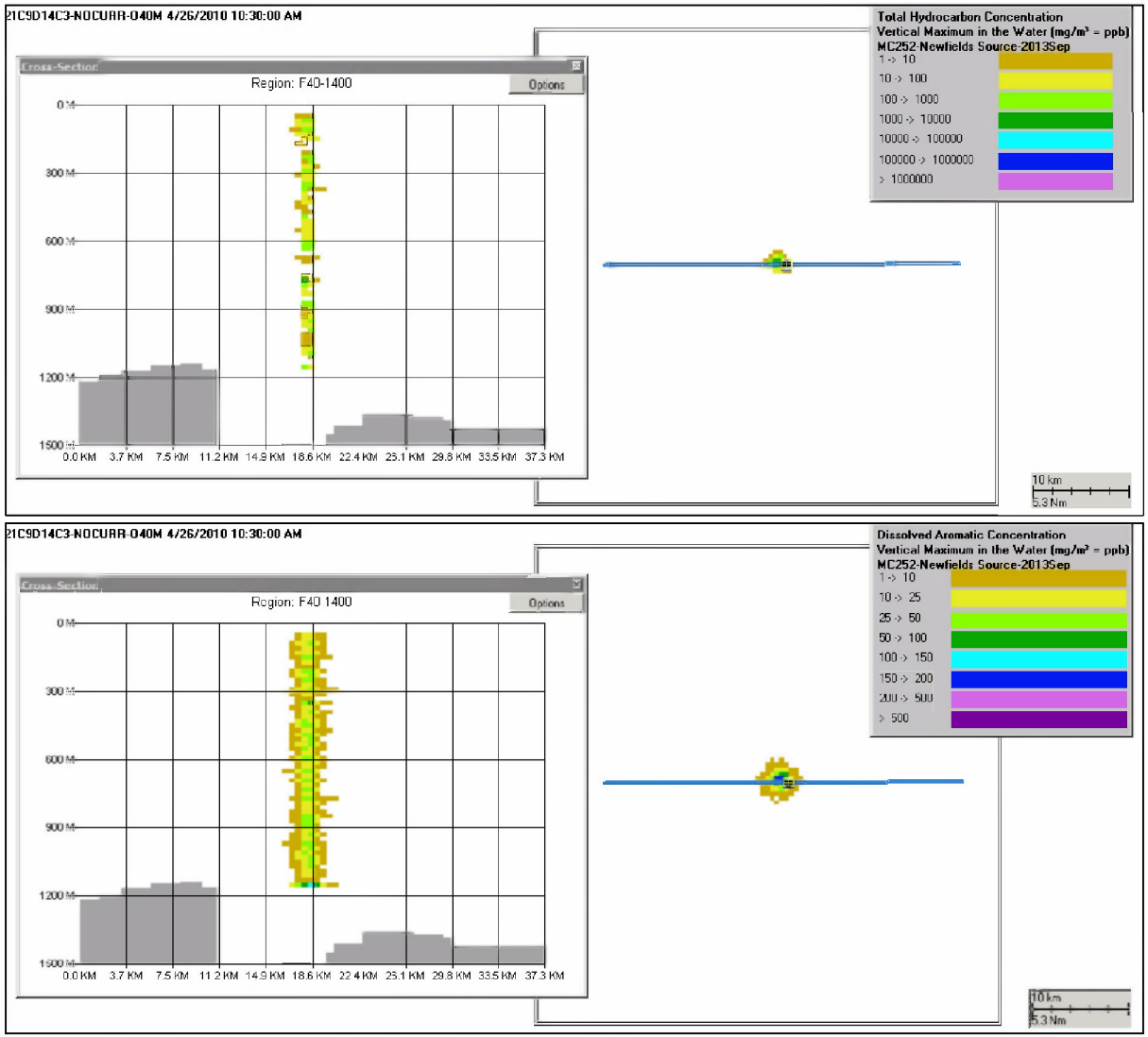

Figure F.2-10. Concentrations produced by the Static Cone simulation on April 26 – AR9 component (low molecular weight alkanes, isoalkanes, cycloalkanes, μg/L) in droplets (top) and in the dissolved phase (bottom).

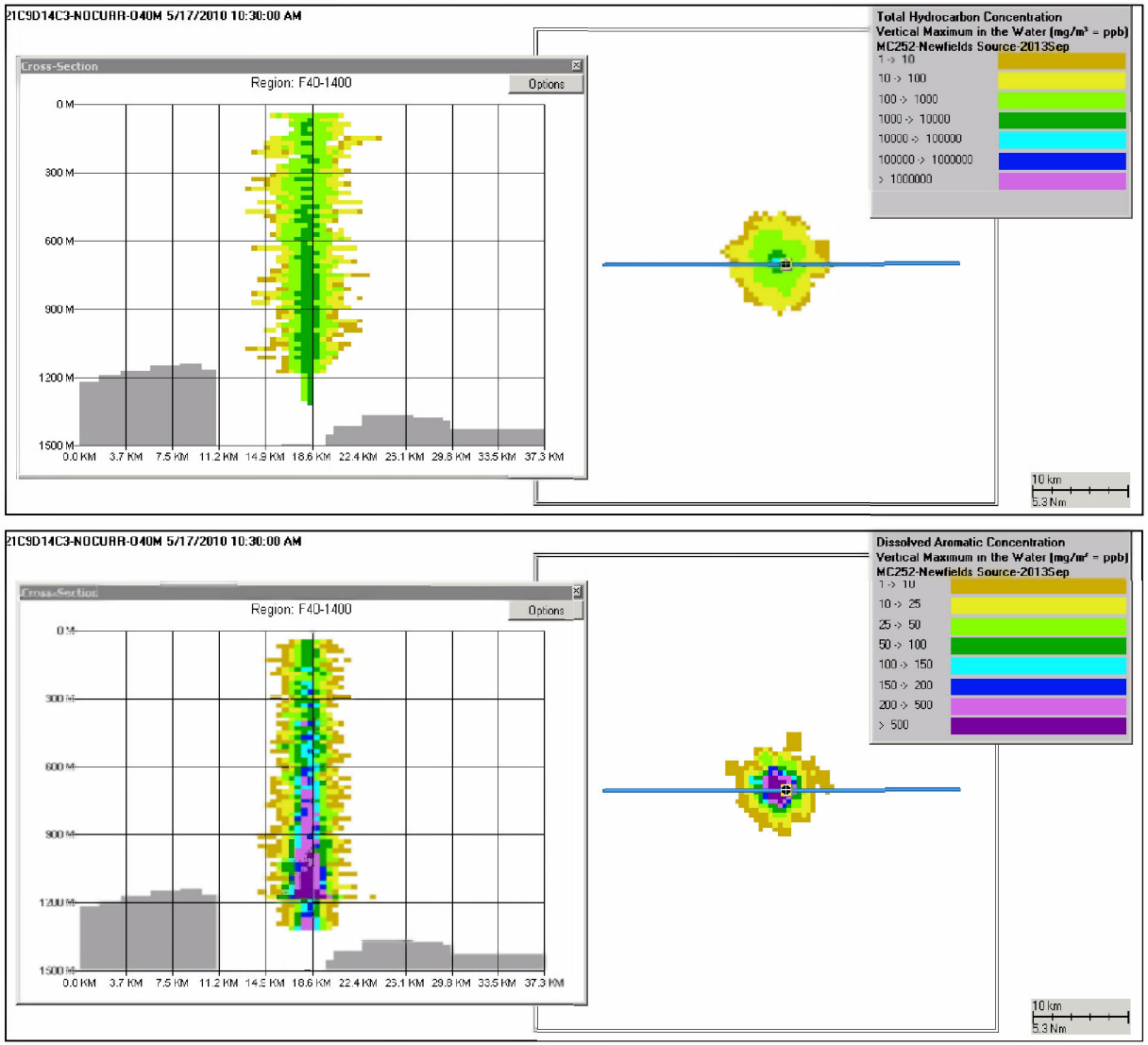

Figure F.2-11. Concentrations produced by the Static Cone simulation on May 17 – total hydrocarbons (μg/L) in droplets (top) and in the dissolved phase (bottom).

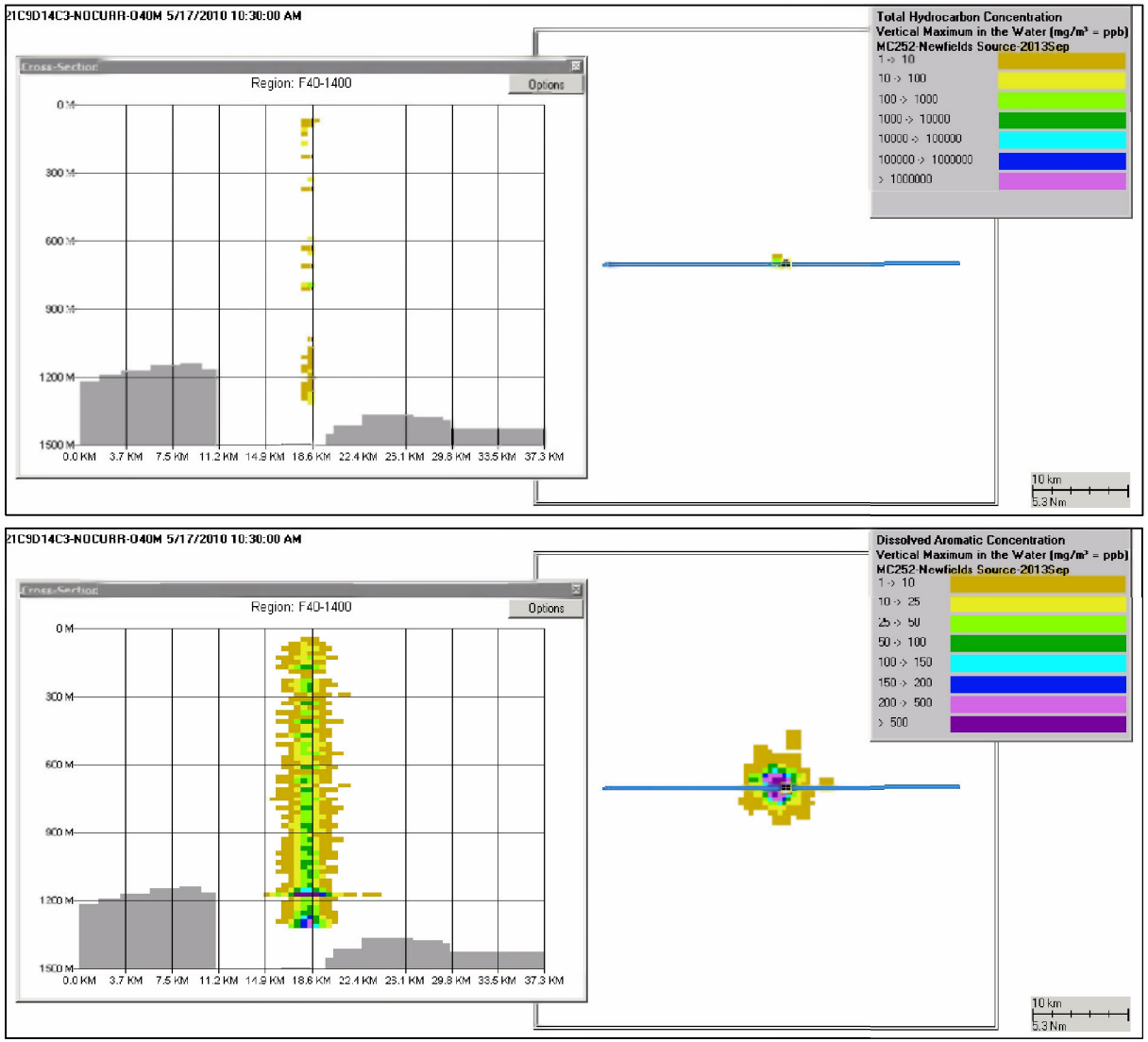

Figure F.2-12. Concentrations produced by the Static Cone simulation on May 17 – AR1 component (BTEX, µg/L) in droplets (top) and in the dissolved phase (bottom).

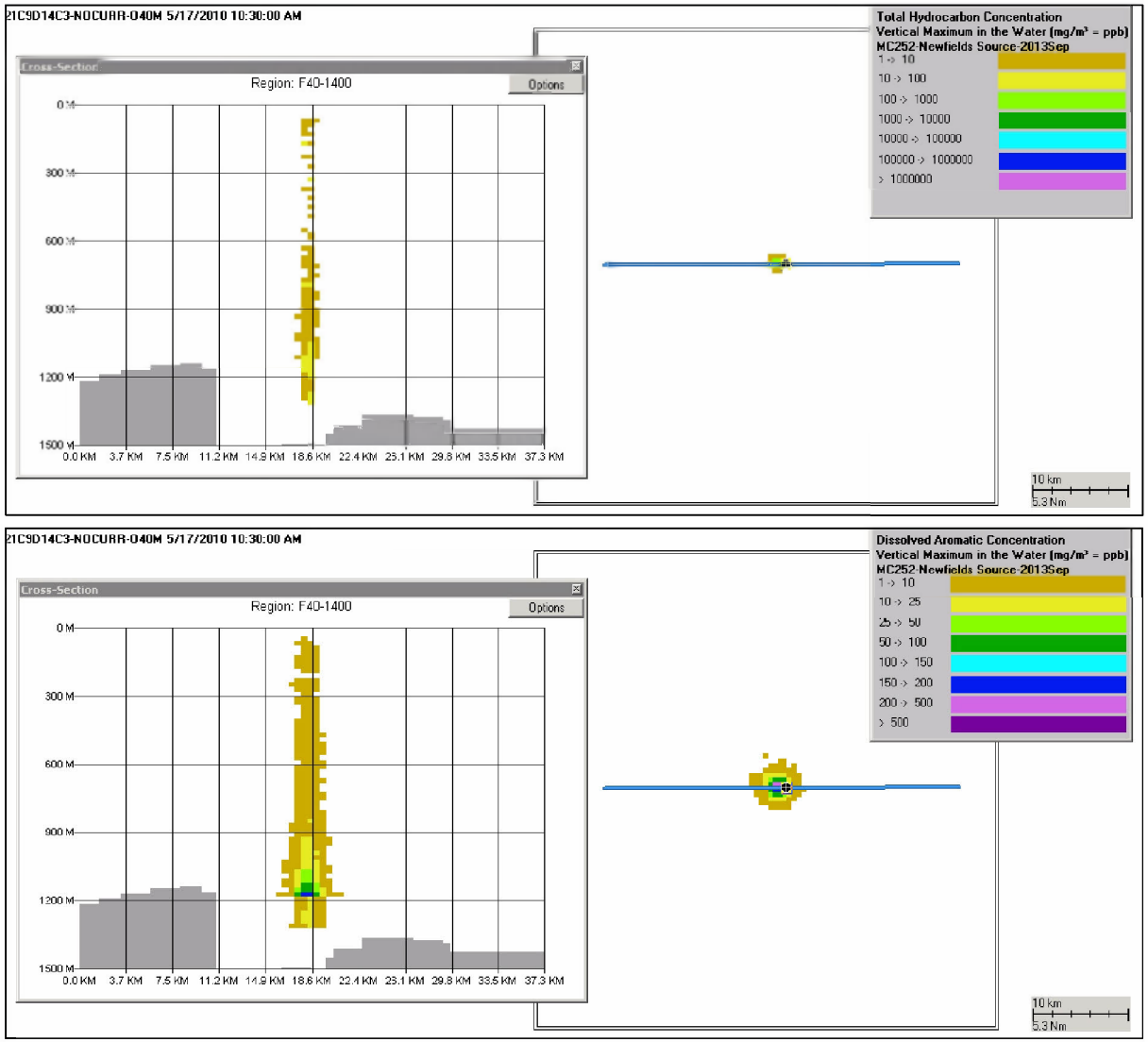

Figure F.2-13. Concentrations produced by the Static Cone simulation on May 17 – AR2 component (C3-benzenes, μg/L) in droplets (top) and in the dissolved phase (bottom).

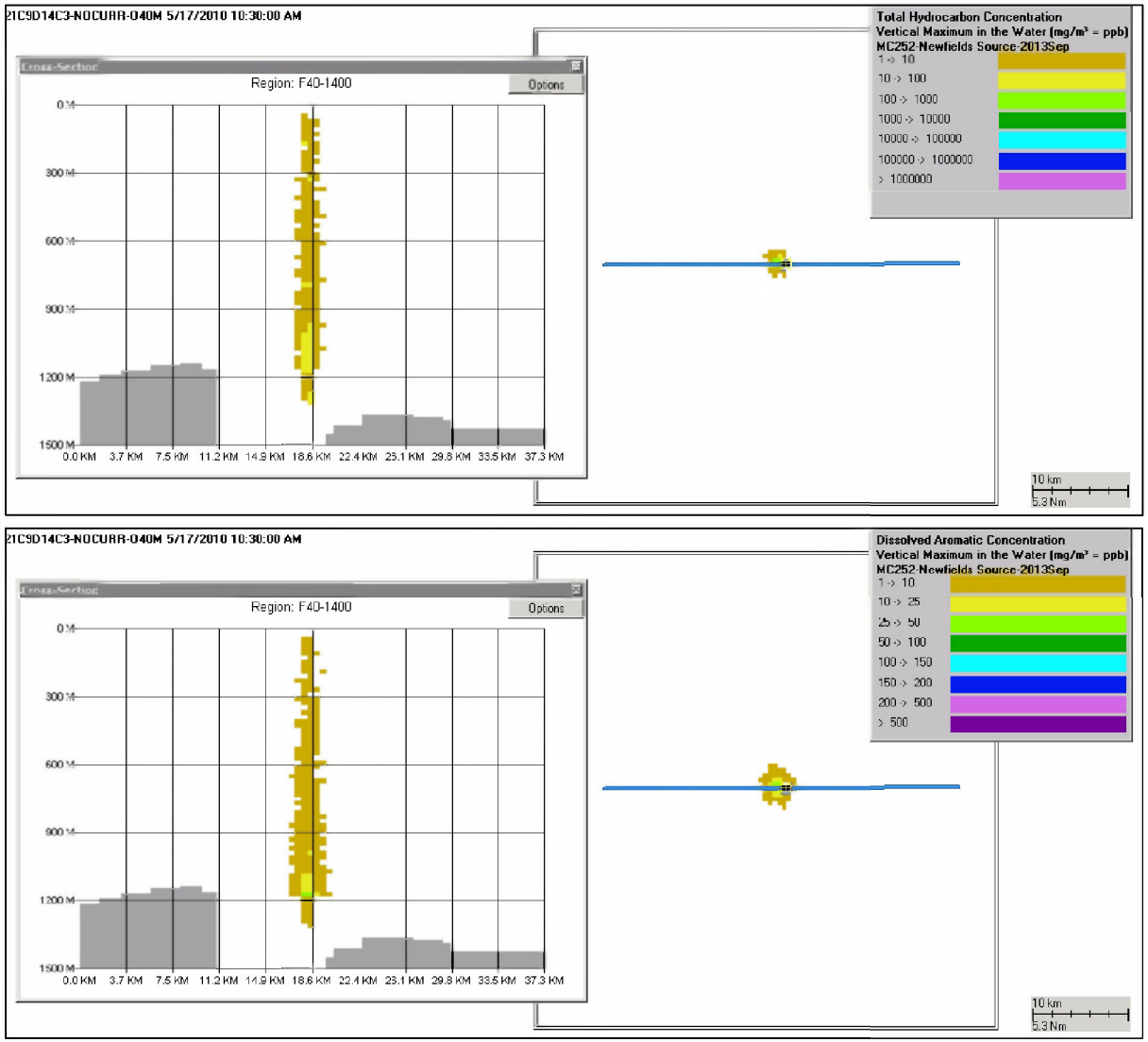

Figure F.2-14. Concentrations produced by the Static Cone simulation on May 17 – AR3 component (C4-benzenes, μg/L) in droplets (top) and in the dissolved phase (bottom).

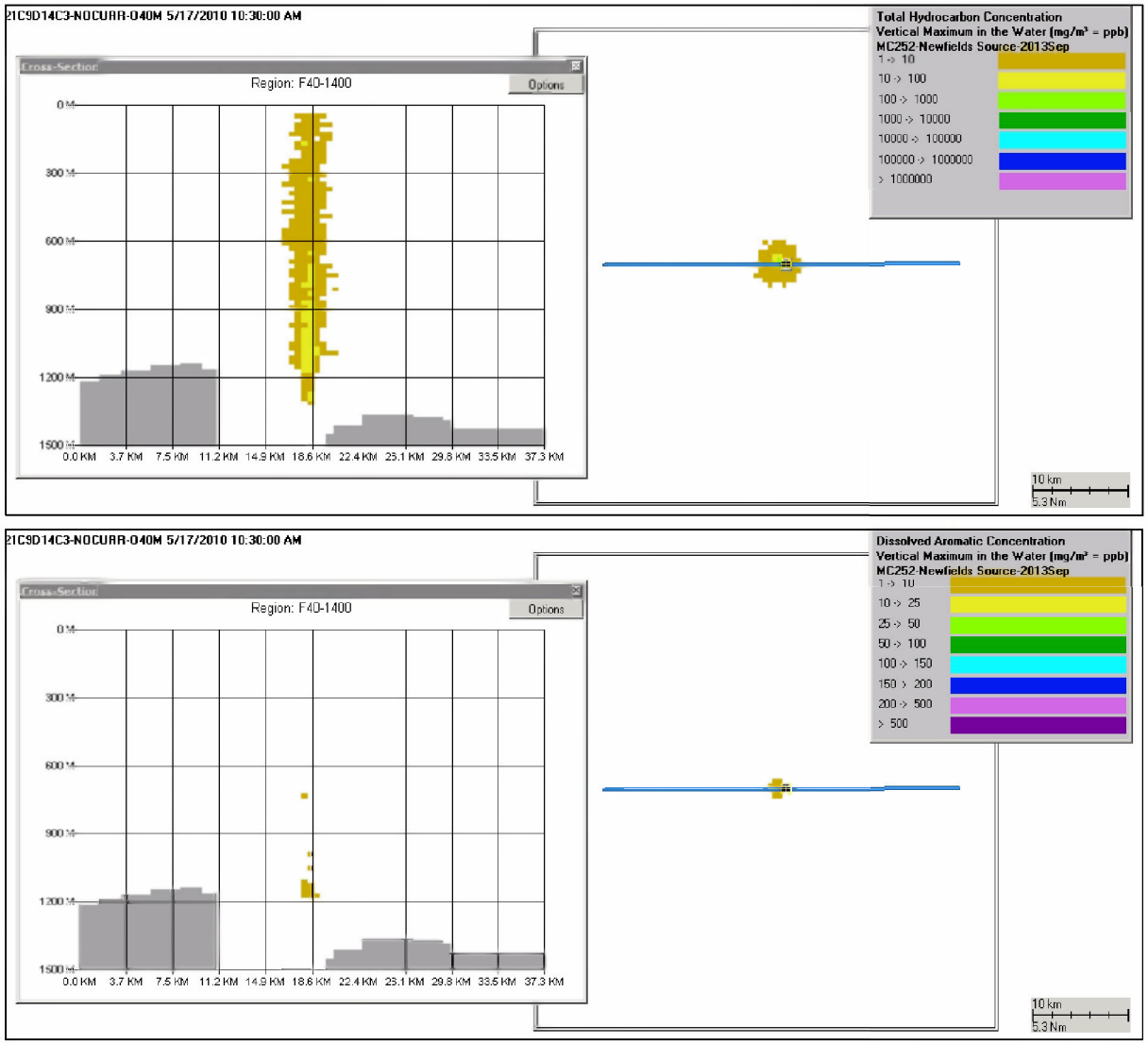

Figure F.2-15. Concentrations produced by the Static Cone simulation on May 17 – AR4 component (decalins, μg/L) in droplets (top) and in the dissolved phase (bottom).

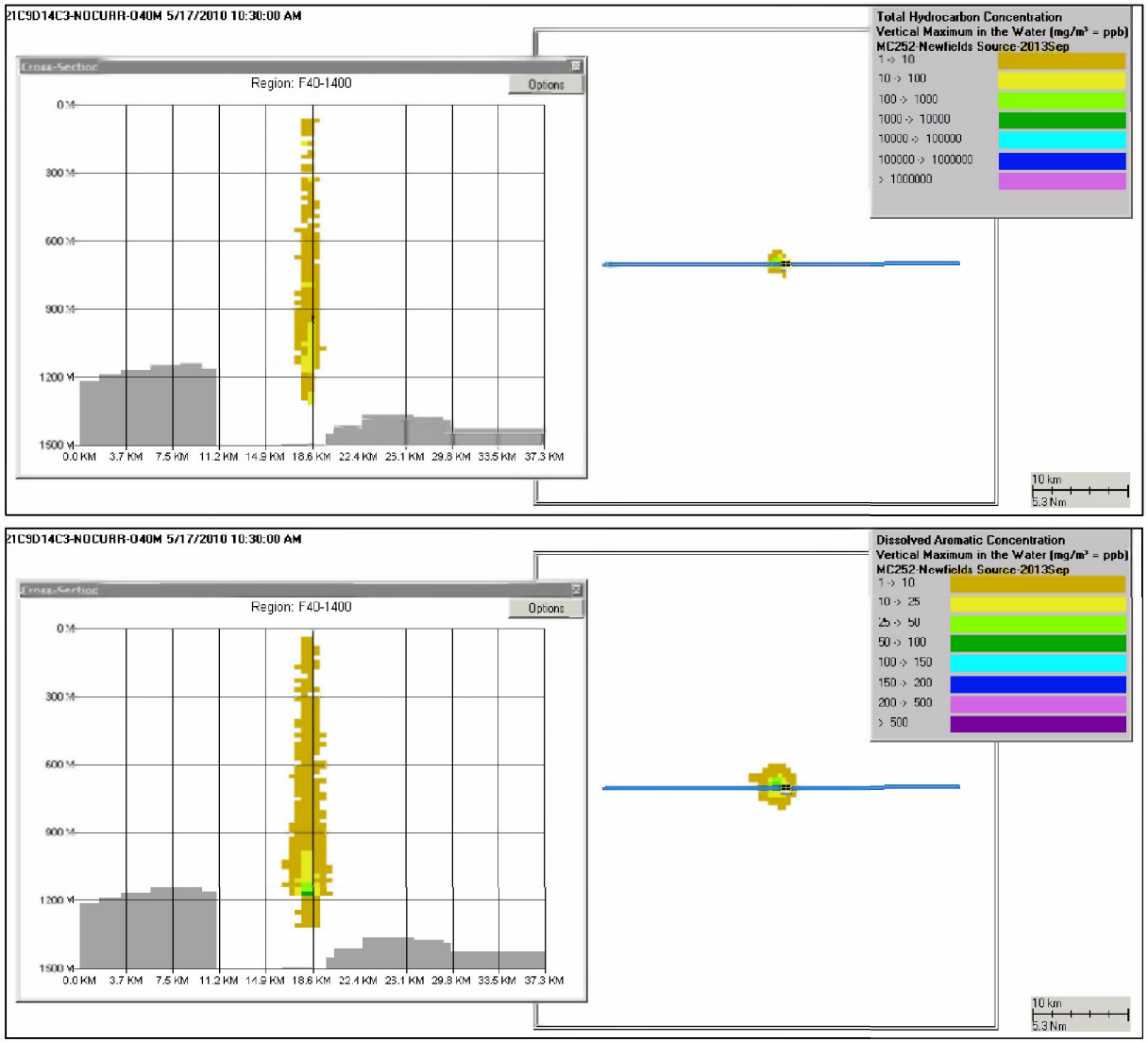

Figure F.2-16. Concentrations produced by the Static Cone simulation on May 17 – AR5 component (C0-C2 naphthalenes, μg/L) in droplets (top) and in the dissolved phase (bottom).

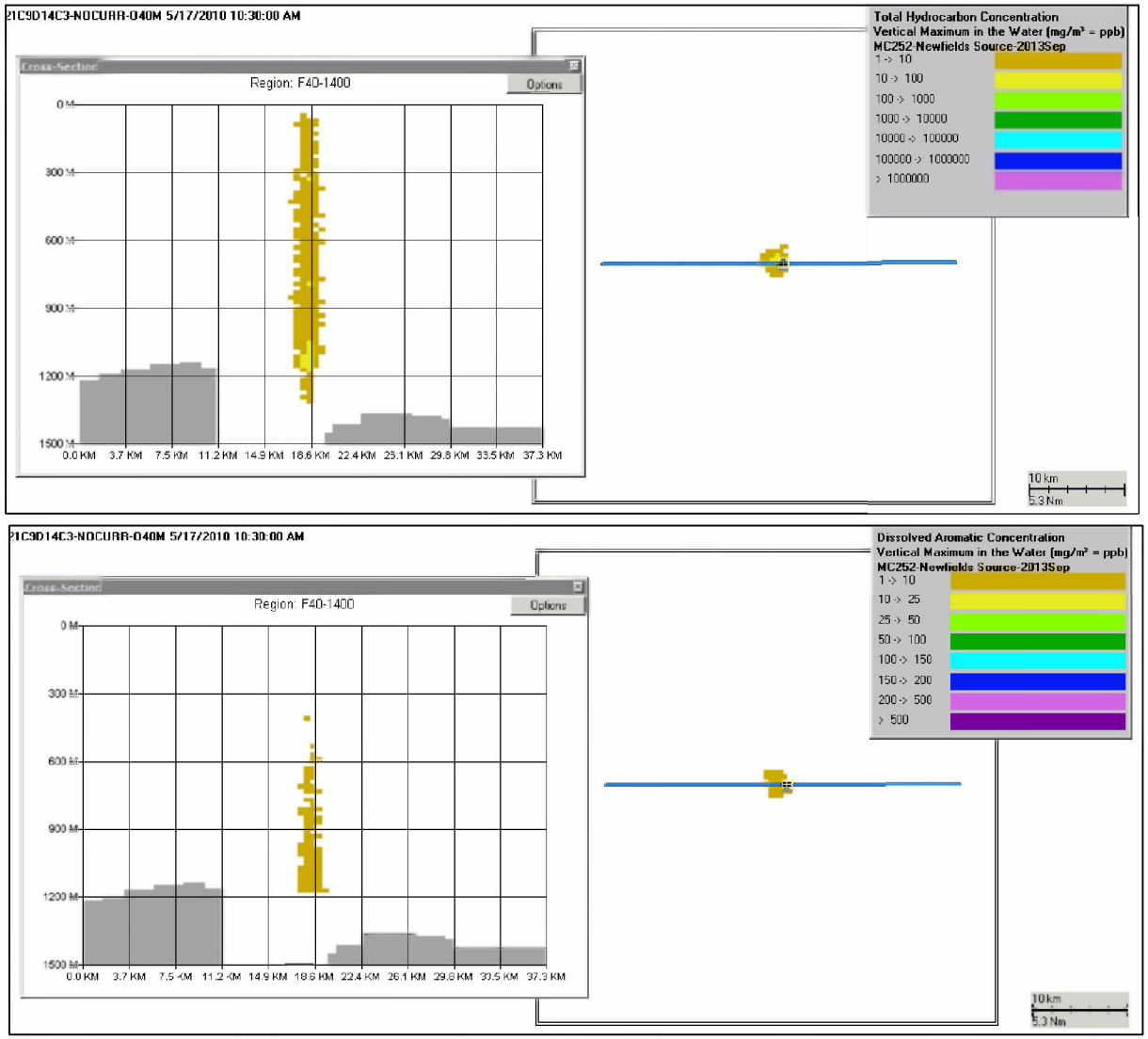

Figure F.2-17. Concentrations produced by the Static Cone simulation on May 17 – AR6 component (C3-C4 naphthalenes, µg/L) in droplets (top) and in the dissolved phase (bottom).

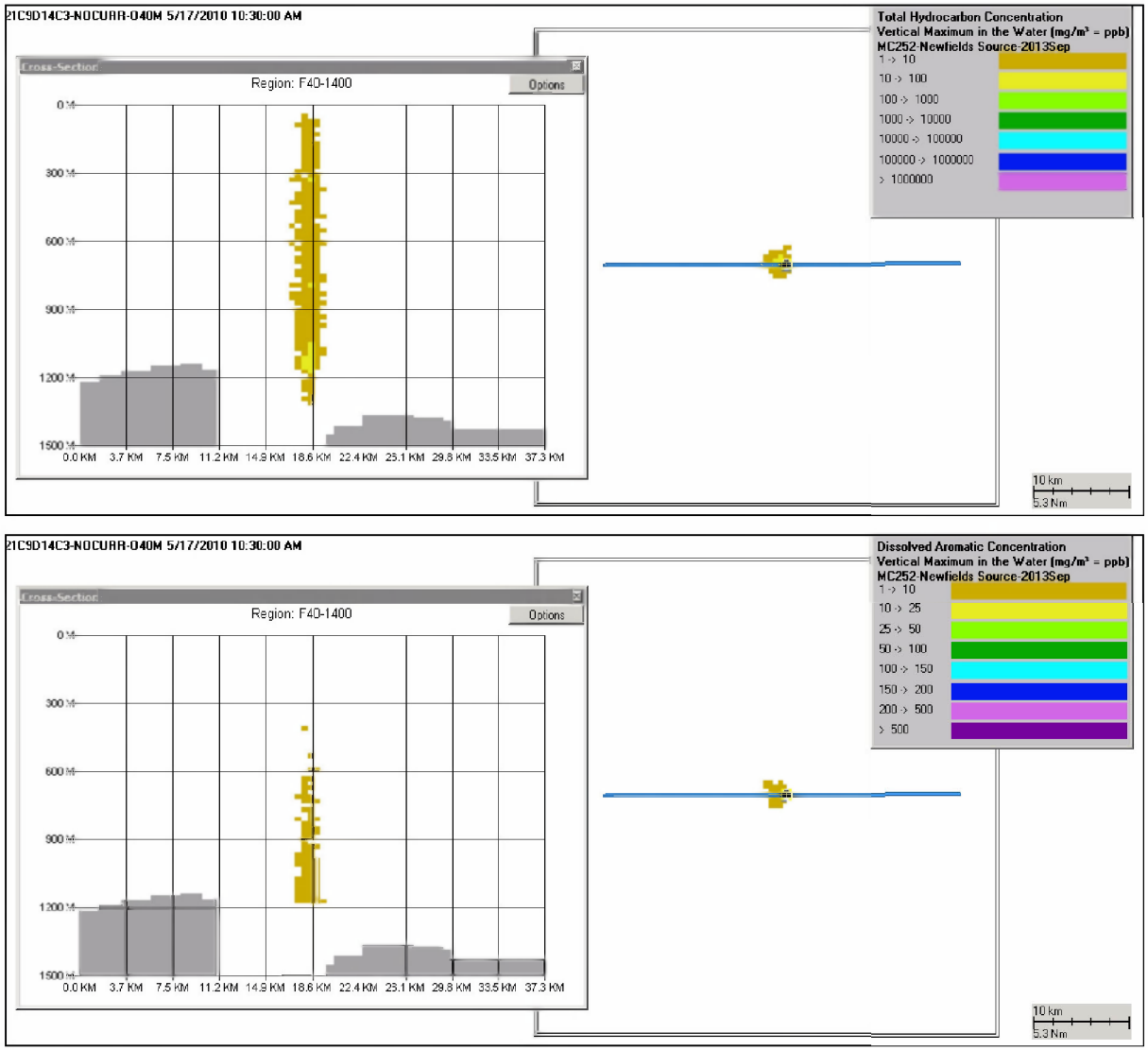

Figure F.2-18. Concentrations produced by the Static Cone simulation on May 17 – AR7 component (fluorenes & C0-C1 3-ring PAHs, µg/L) in droplets (top) and in the dissolved phase (bottom).

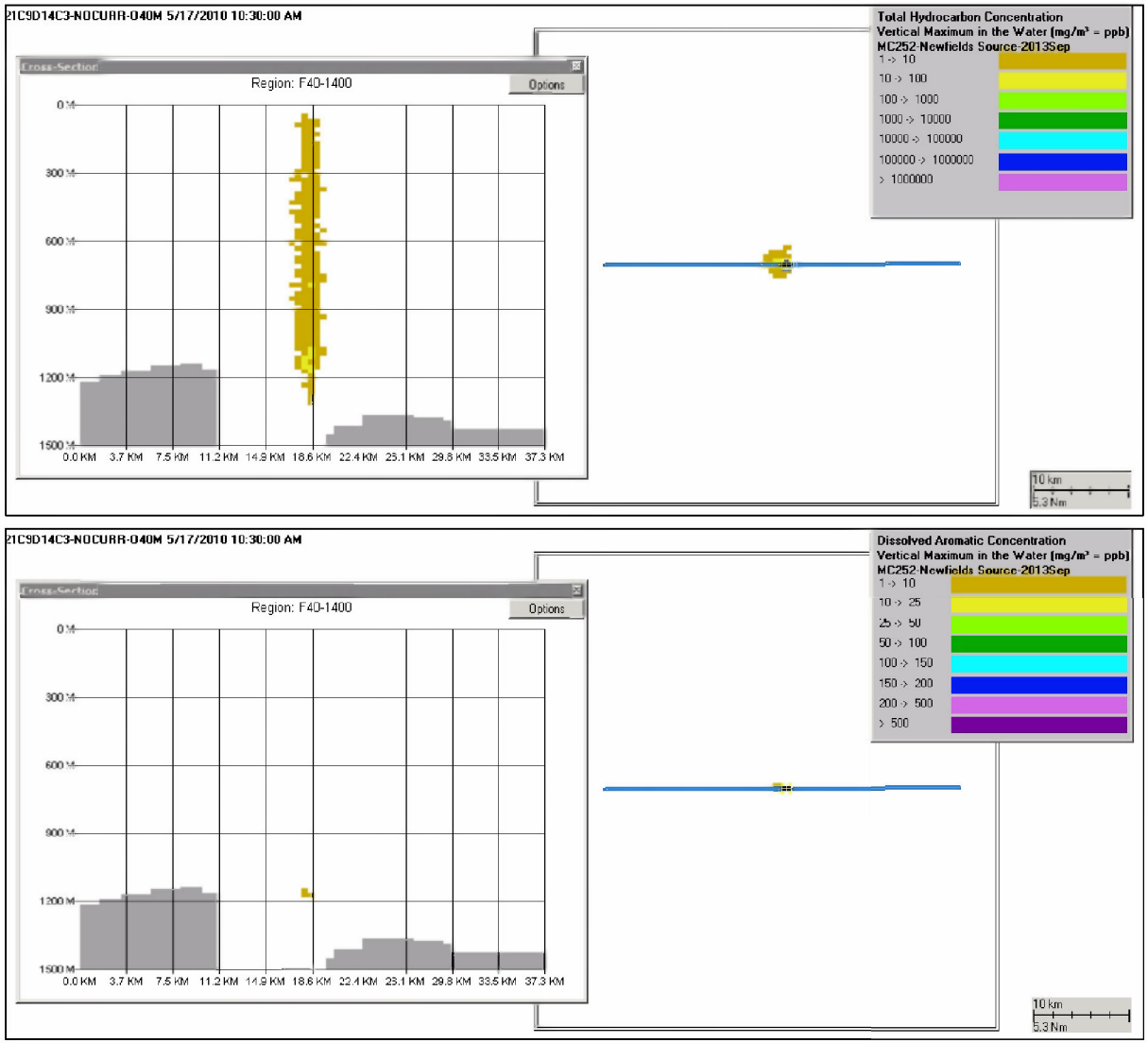

Figure F.2-19. Concentrations produced by the Static Cone simulation on May 17 – AR8 component (4-ring PAHs & C2-C3 3-ring PAHs, μg/L) in droplets (top) and in the dissolved phase (bottom).

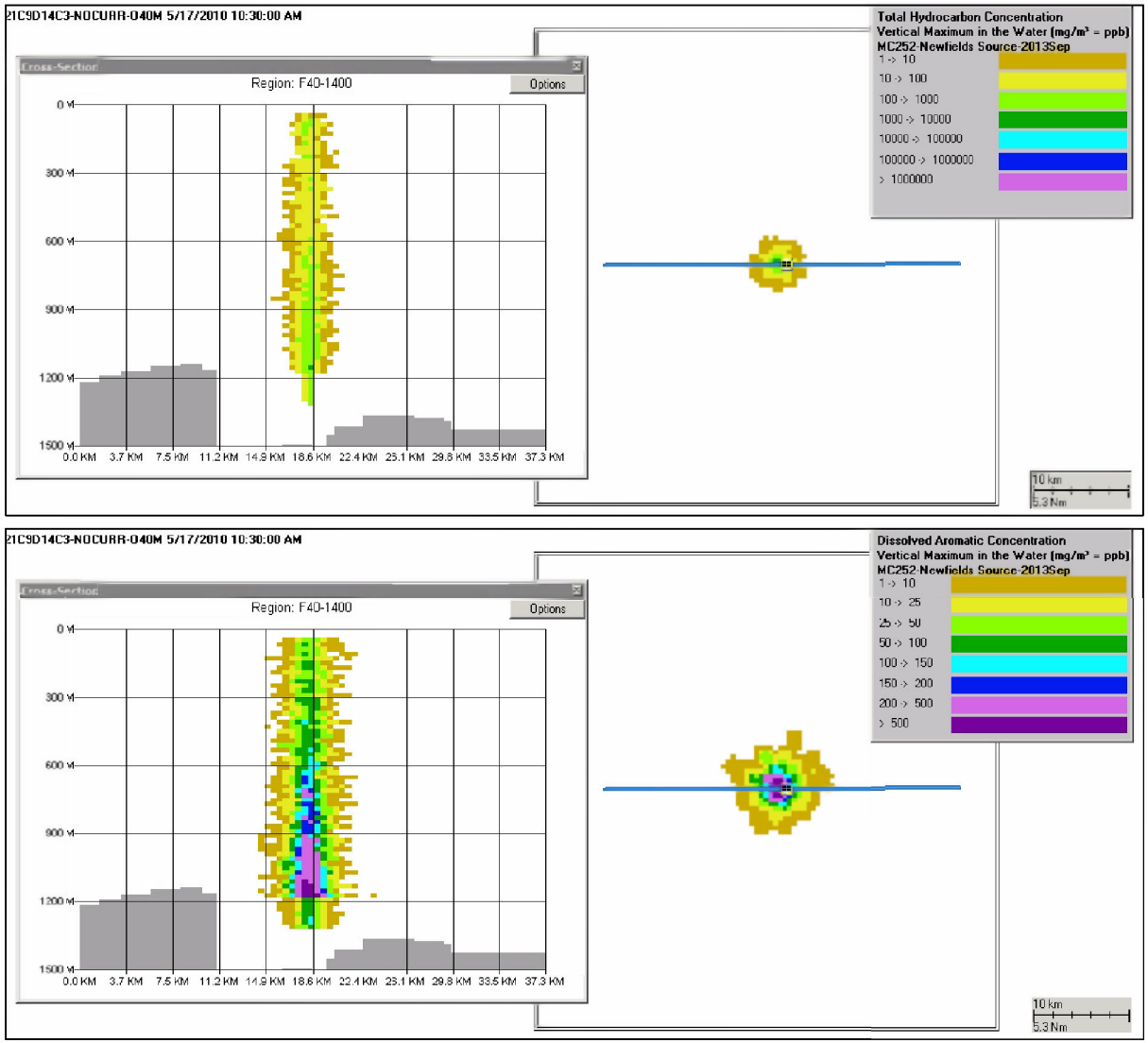

Figure F.2-20. Concentrations produced by the Static Cone simulation on May 17 – AR9 component (low molecular weight alkanes, isoalkanes, cycloalkanes, μg/L) in droplets (top) and in the dissolved phase (bottom).

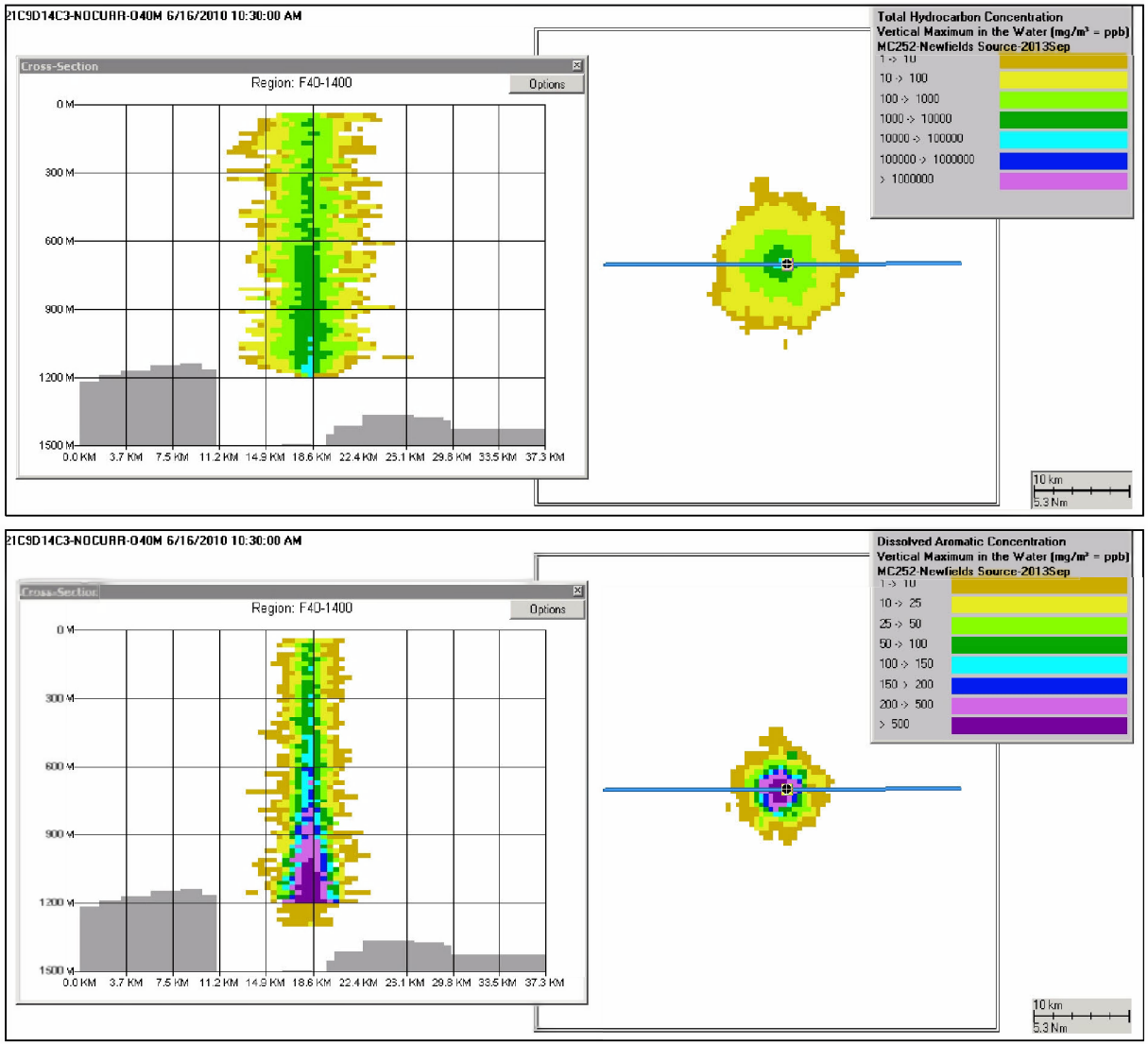

Figure F.2-21. Concentrations produced by the Static Cone simulation on June 16 – total hydrocarbons (μg/L) in droplets (top) and in the dissolved phase (bottom).

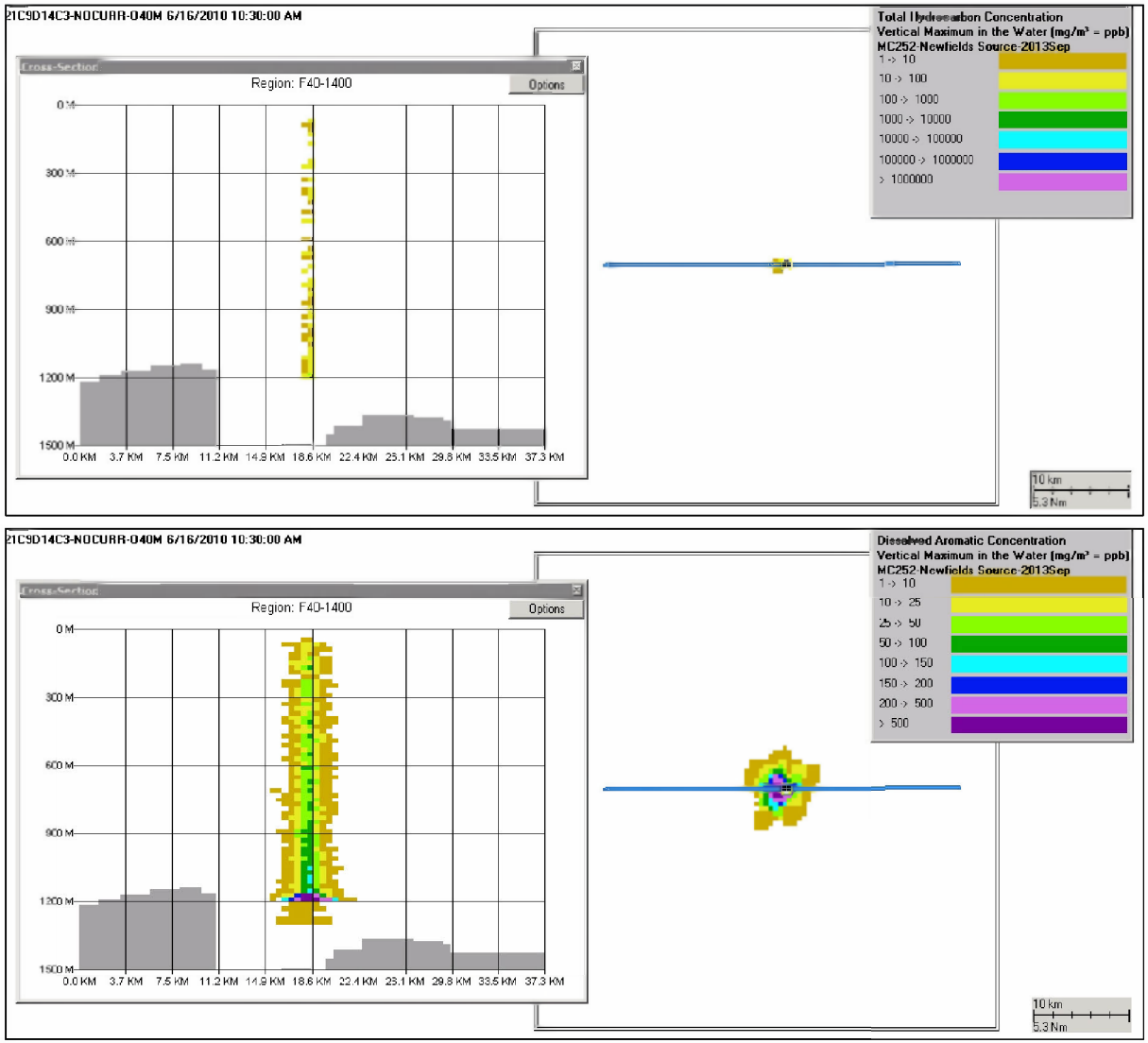

Figure F.2-22. Concentrations produced by the Static Cone simulation on June 16 – AR1 component (BTEX, μg/L) in droplets (top) and in the dissolved phase (bottom).

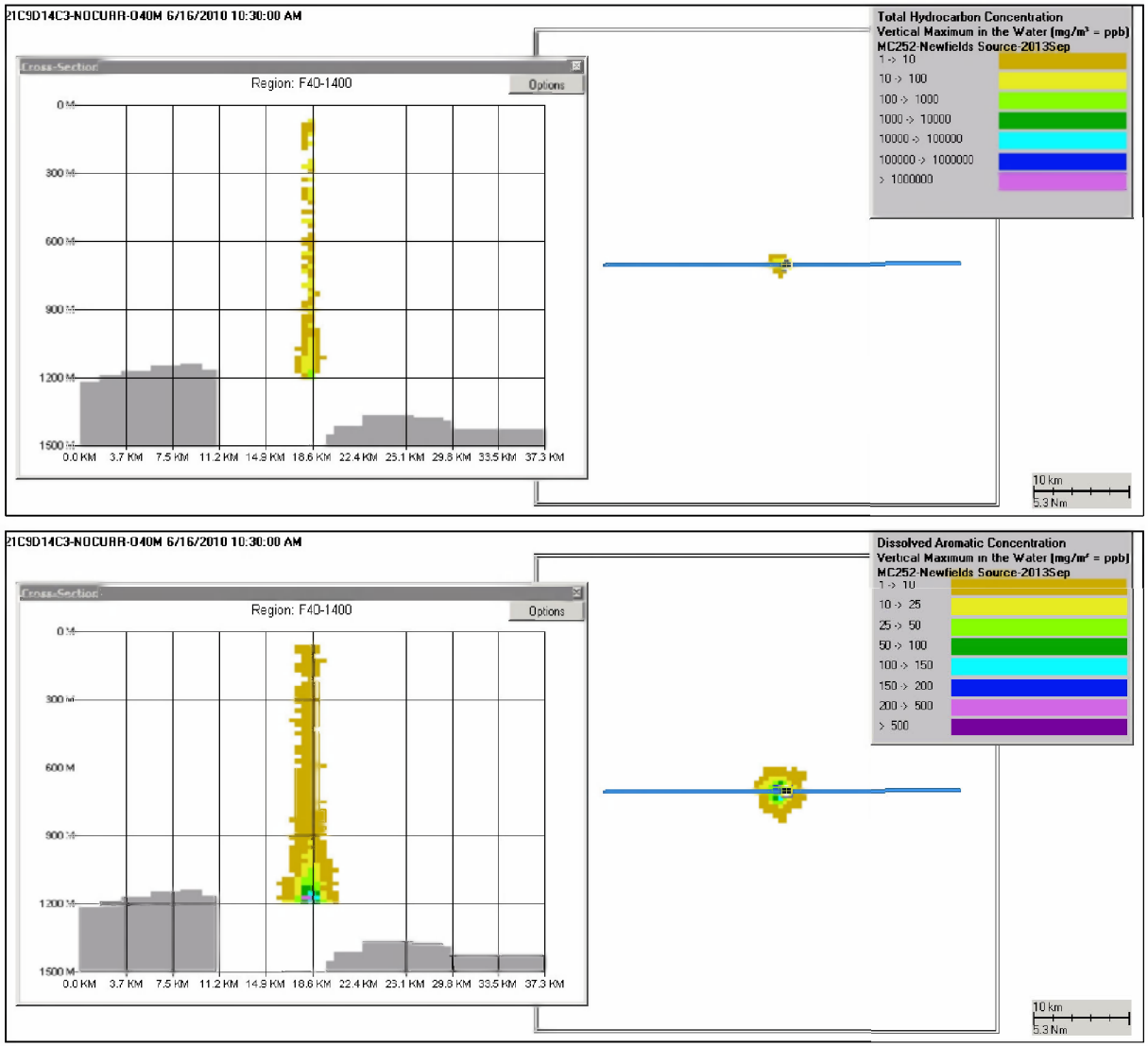

Figure F.2-23. Concentrations produced by the Static Cone simulation on June 16 – AR2 component (C3-benzenes, μg/L) in droplets (top) and in the dissolved phase (bottom).

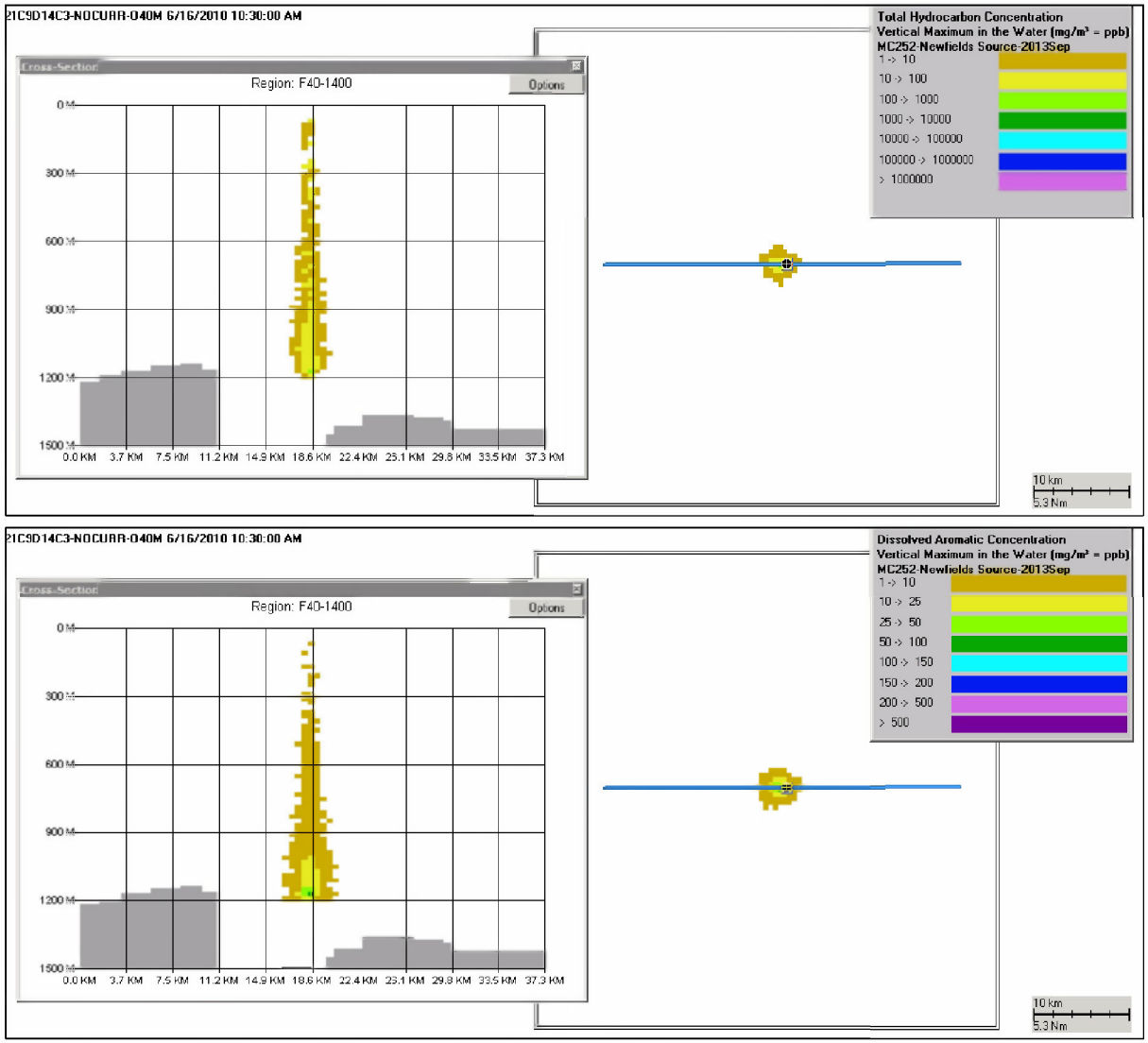

Figure F.2-24. Concentrations produced by the Static Cone simulation on June 16 – AR3 component (C4-benzenes, μg/L) in droplets (top) and in the dissolved phase (bottom).

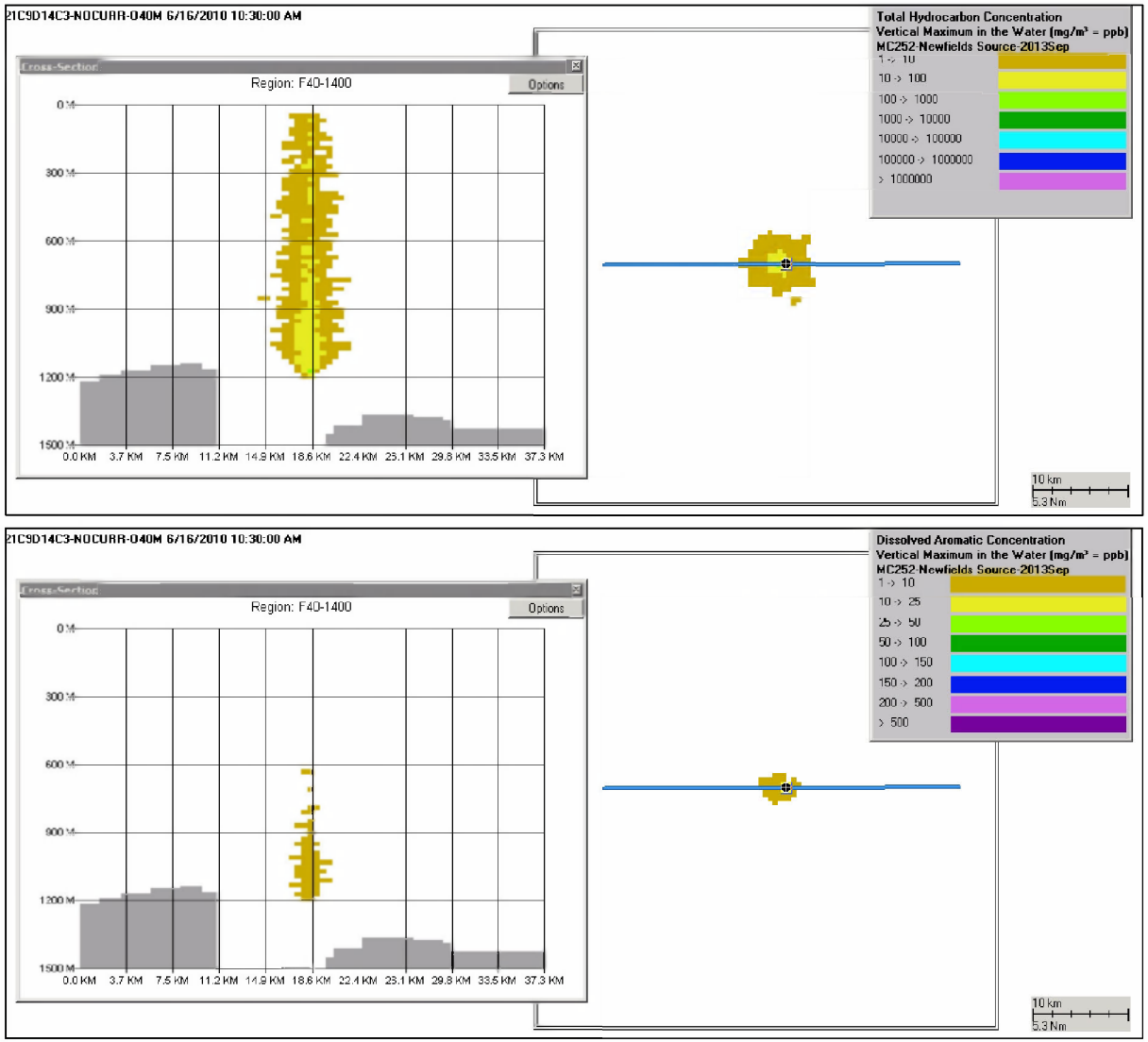

Figure F.2-25. Concentrations produced by the Static Cone simulation on June 16 – AR4 component (decalins, μg/L) in droplets (top) and in the dissolved phase (bottom).

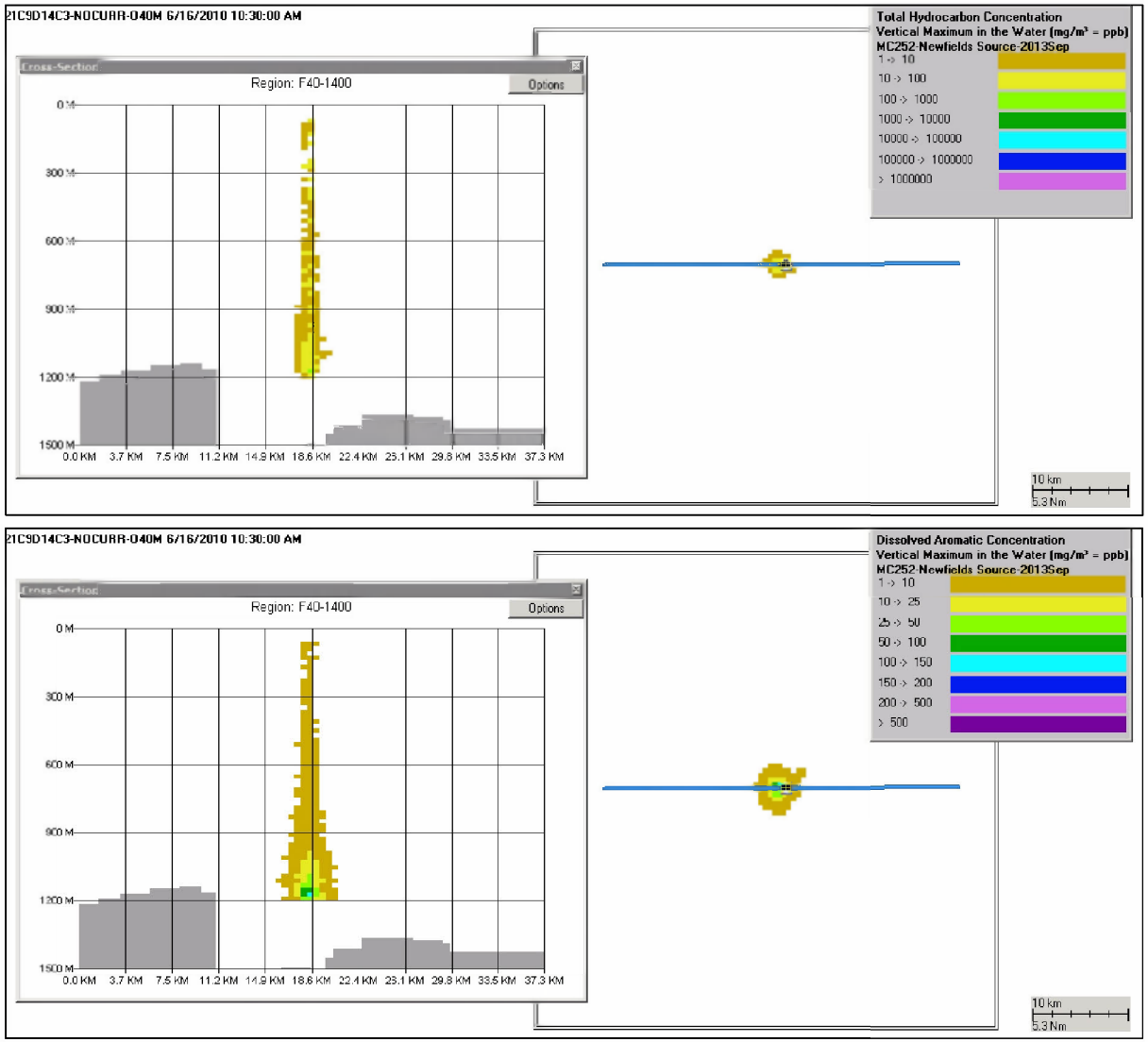

Figure F.2-26. Concentrations produced by the Static Cone simulation on June 16 – AR5 component (C0-C2 naphthalenes, μg/L) in droplets (top) and in the dissolved phase (bottom).

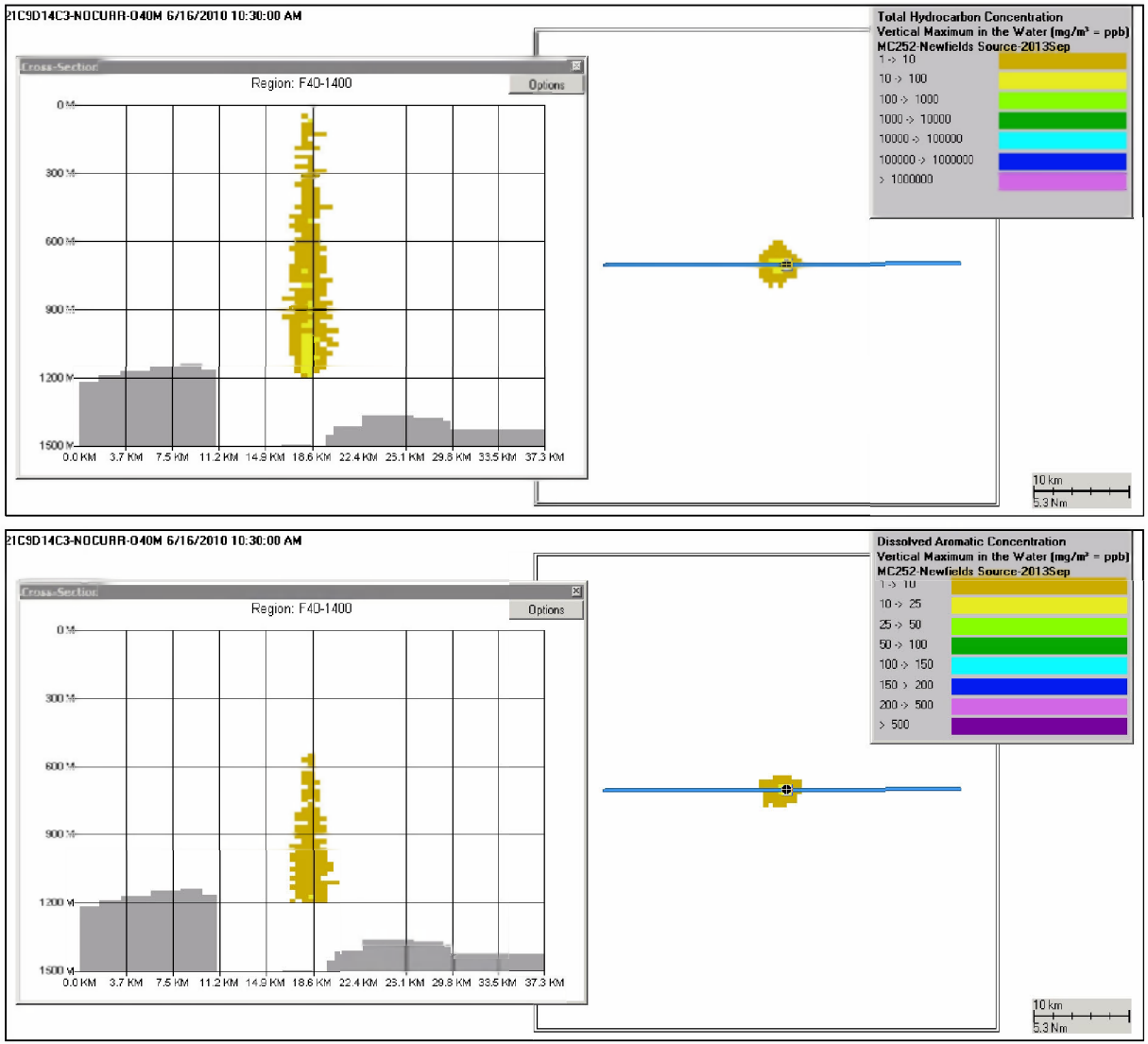

Figure F.2-27. Concentrations produced by the Static Cone simulation on June 16 – AR6 component (C3-C4 naphthalenes, μg/L) in droplets (top) and in the dissolved phase (bottom).

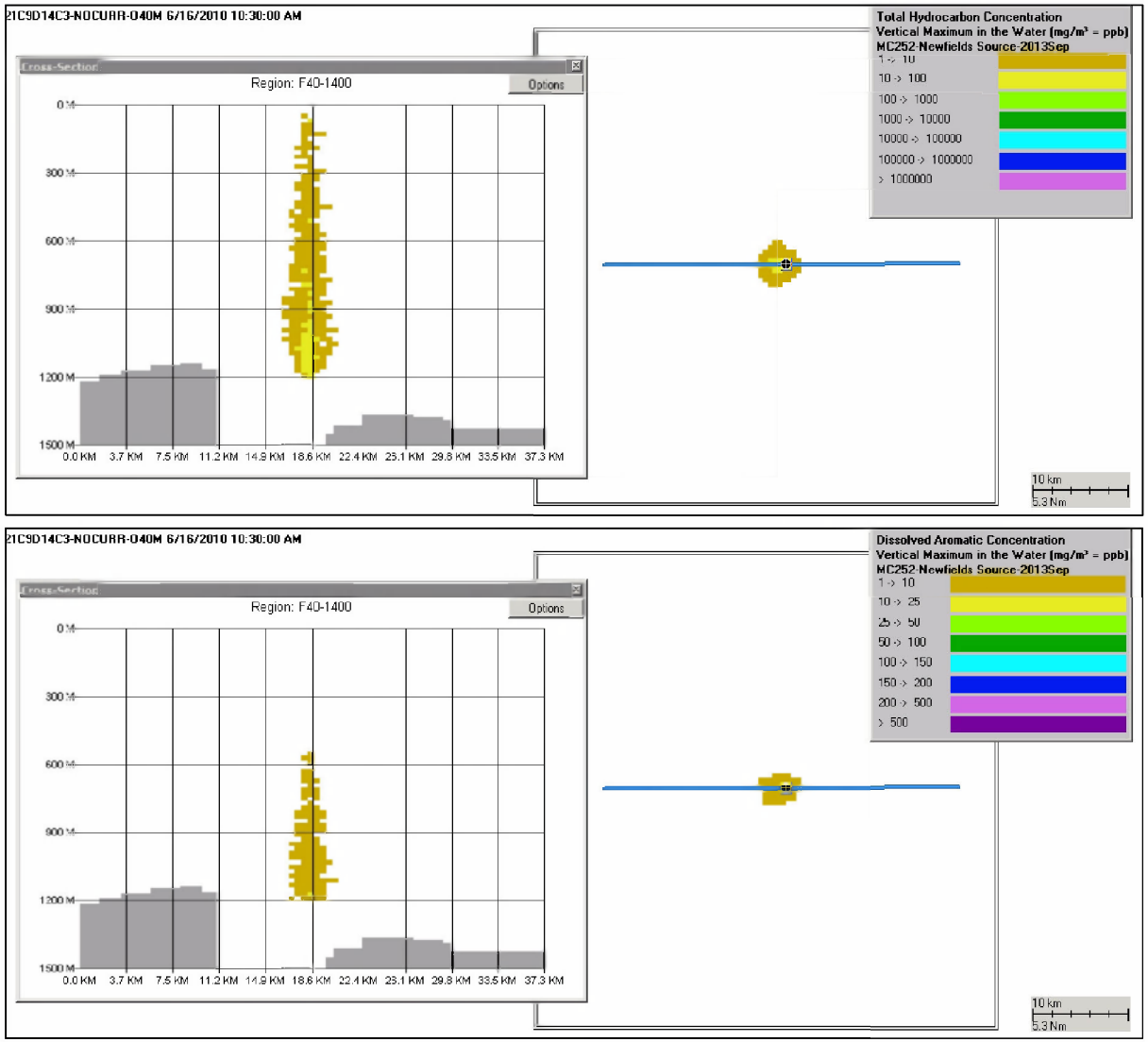

Figure F.2-28. Concentrations produced by the Static Cone simulation on June 16 – AR7 component (fluorenes & C0-C1 3-ring PAHs, μg/L) in droplets (top) and in the dissolved phase (bottom).

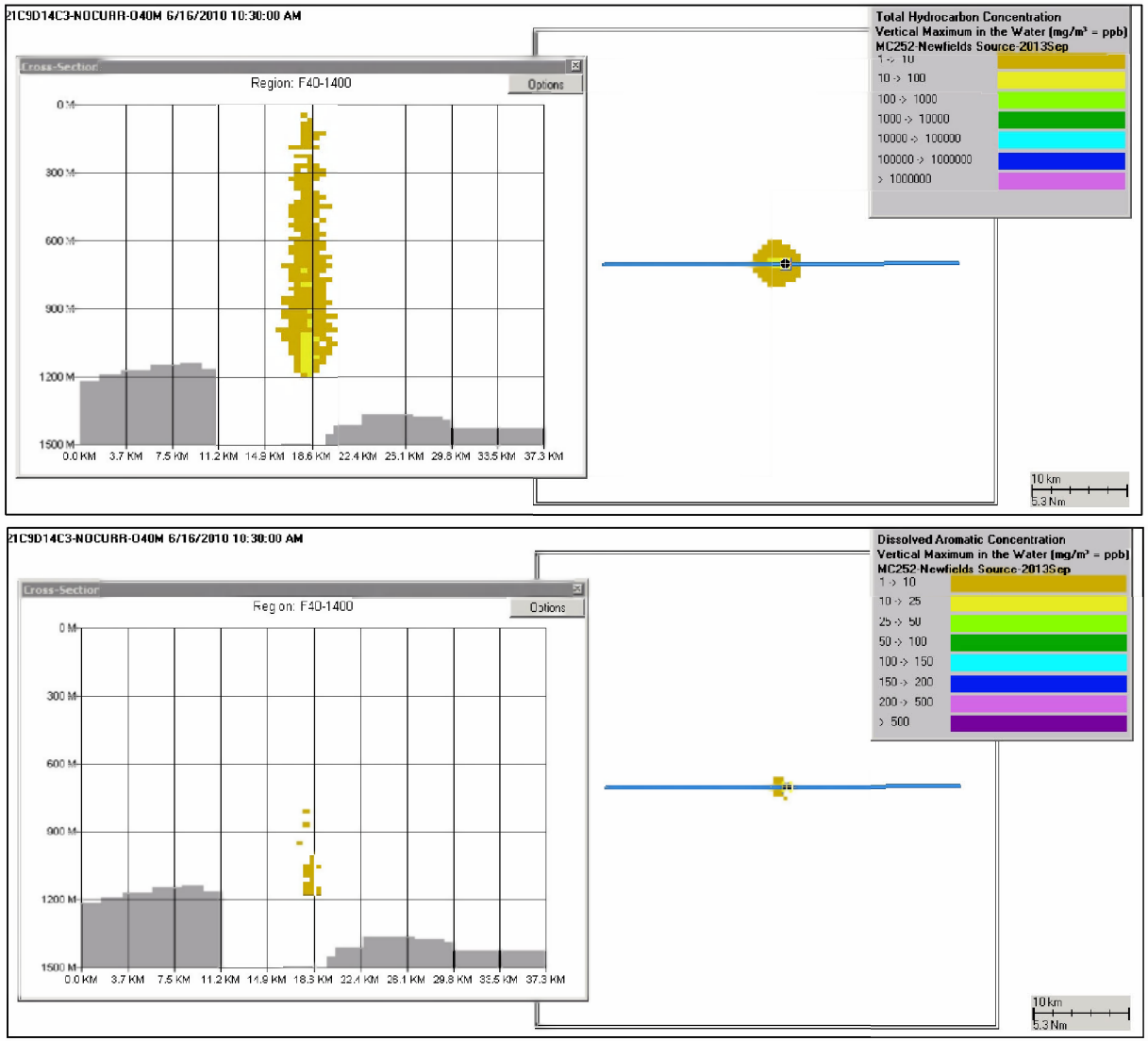

Figure F.2-29. Concentrations produced by the Static Cone simulation on June 16 – AR8 component (4-ring PAHs & C2-C3 3-ring PAHs, μg/L) in droplets (top) and in the dissolved phase (bottom).

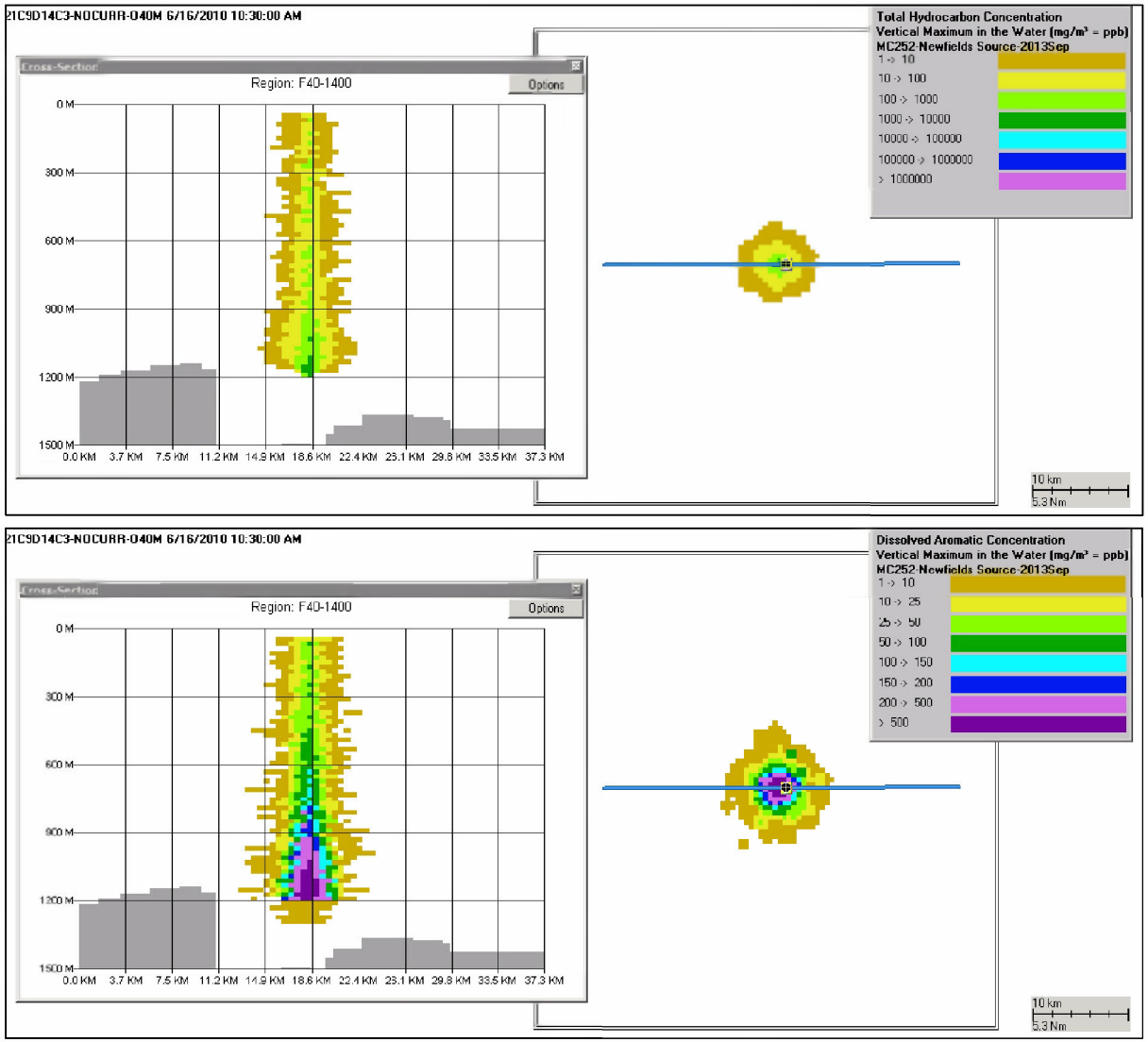

Figure F.2-30. Concentrations produced by the Static Cone simulation on June 16 – AR9 component (low molecular weight alkanes, isoalkanes, cycloalkanes, μg/L) in droplets (top) and in the dissolved phase (bottom).

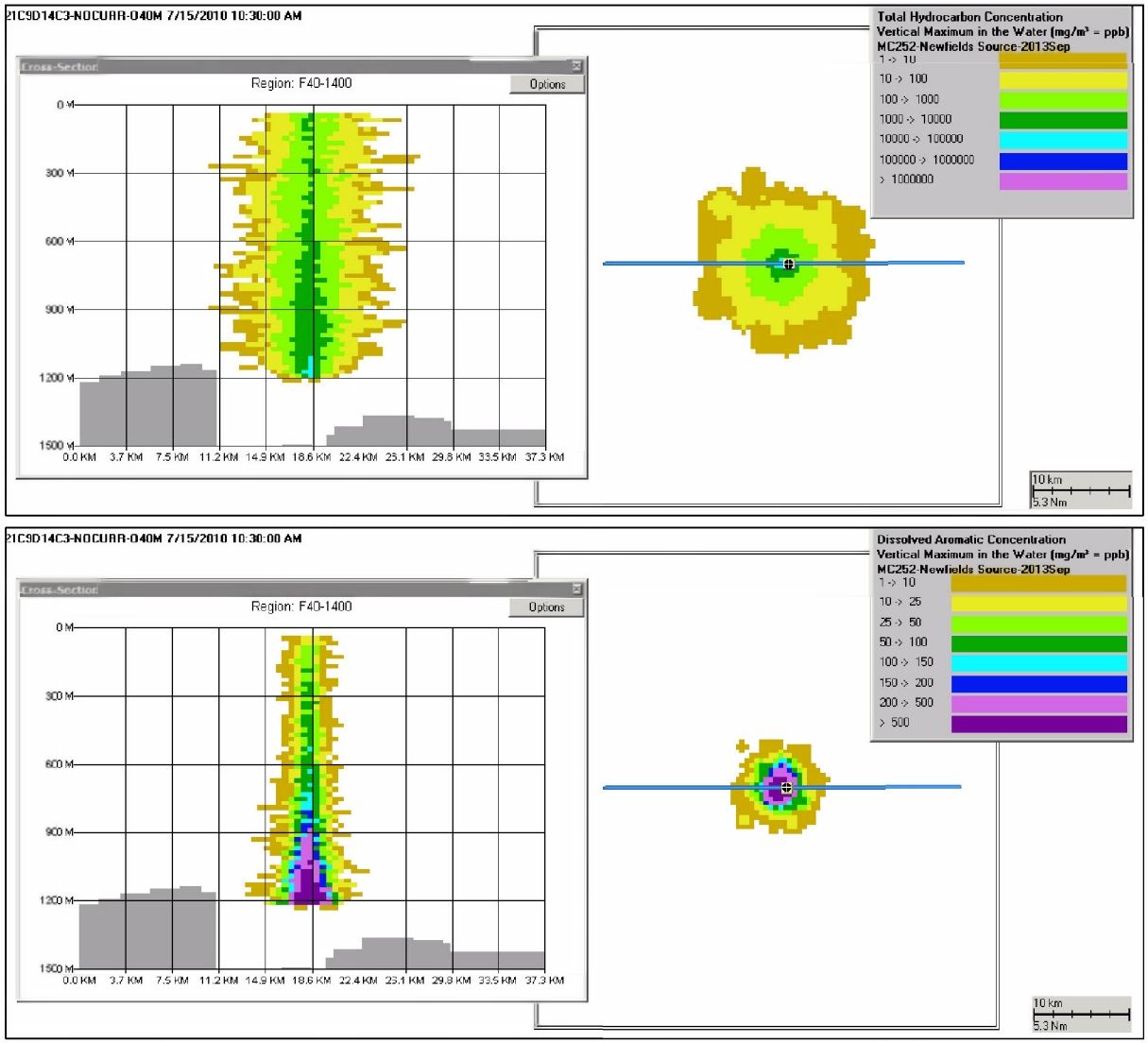

Figure F.2-31. Concentrations produced by the Static Cone simulation on July 15 – total hydrocarbons (μg/L) in droplets (top) and in the dissolved phase (bottom).

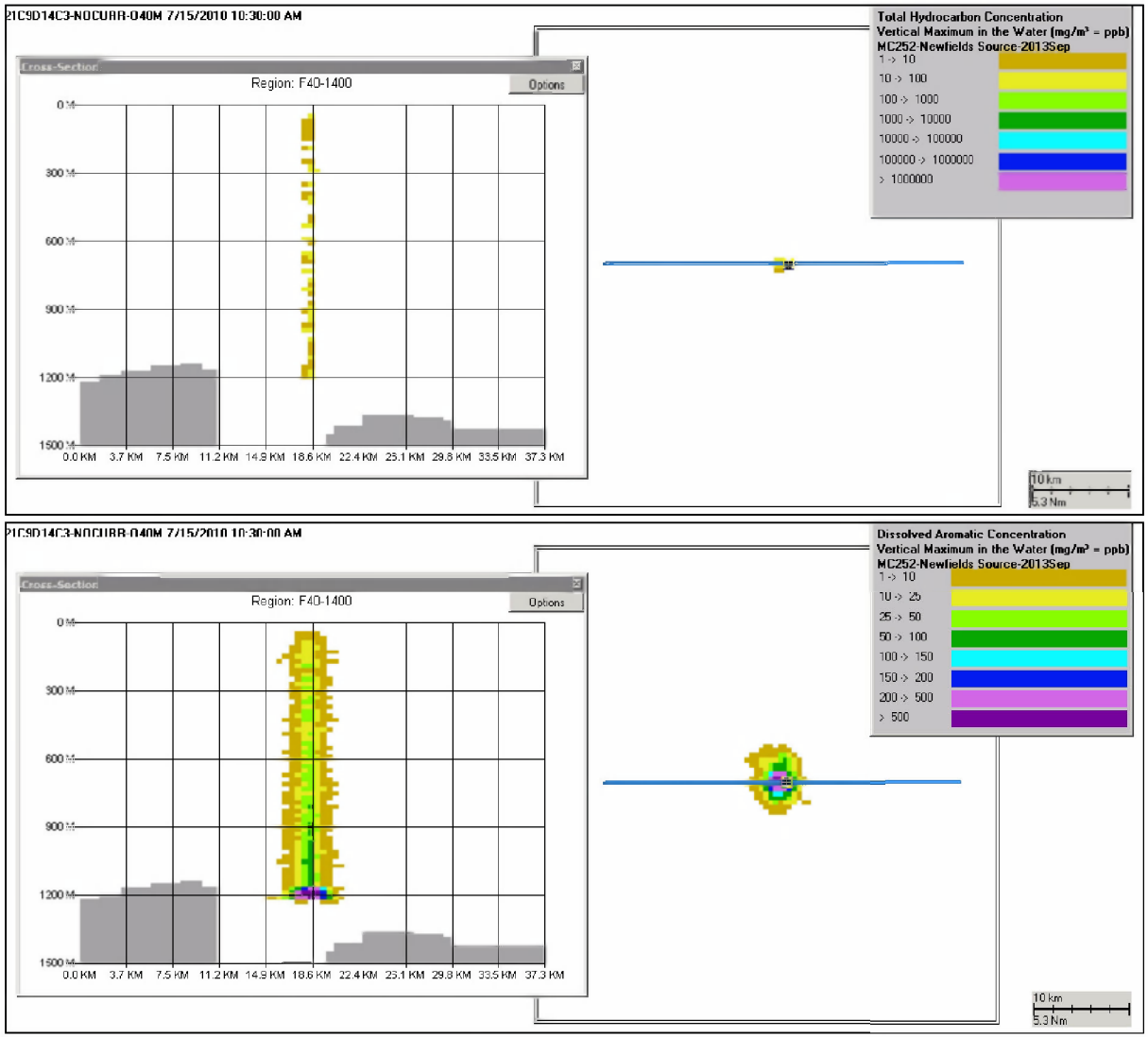

Figure F.2-32. Concentrations produced by the Static Cone simulation on July 15 – AR1 component (BTEX, µg/L) in droplets (top) and in the dissolved phase (bottom).

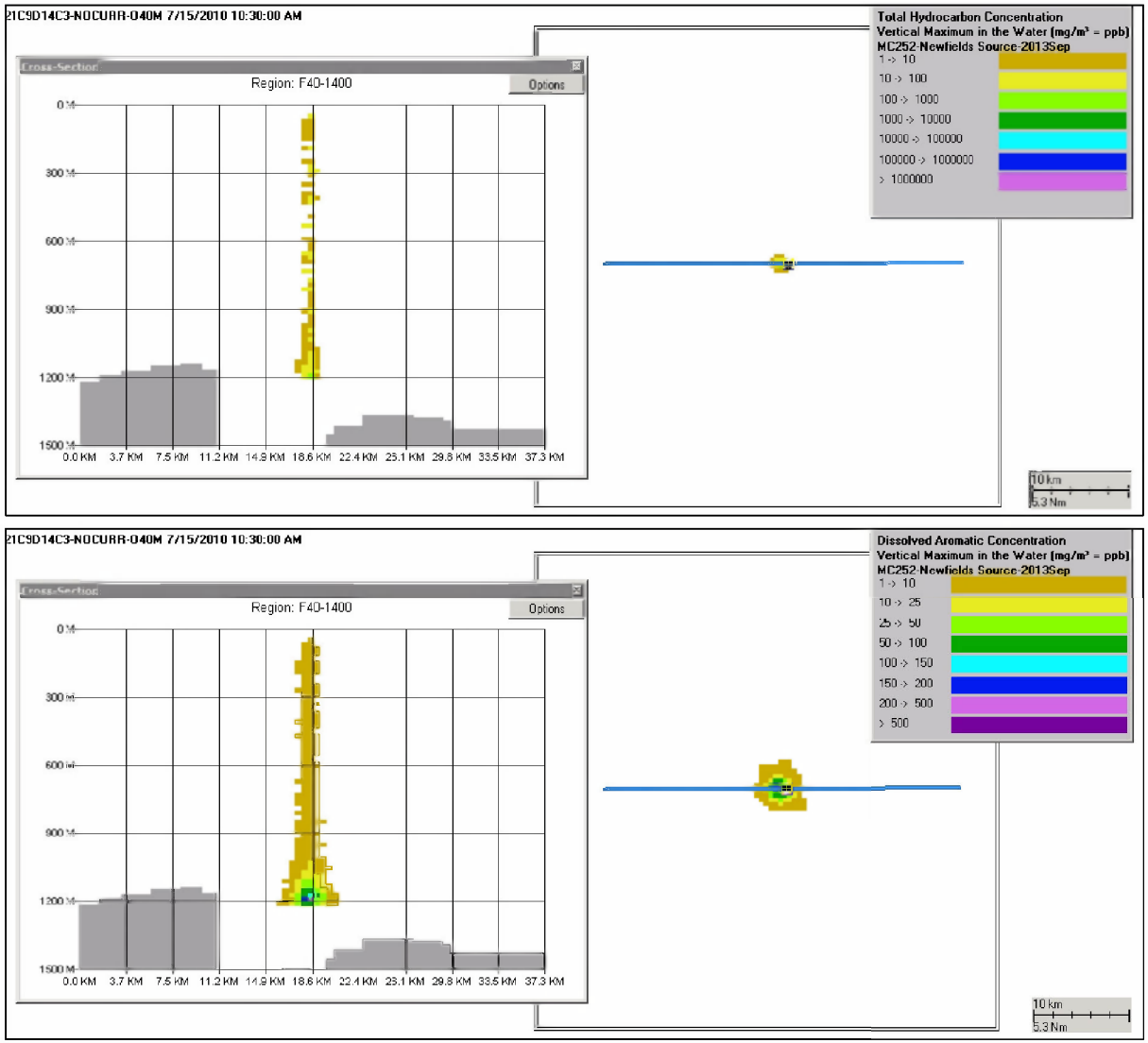

Figure F.2-33. Concentrations produced by the Static Cone simulation on July 15 – AR2 component (C3-benzenes, μg/L) in droplets (top) and in the dissolved phase (bottom).

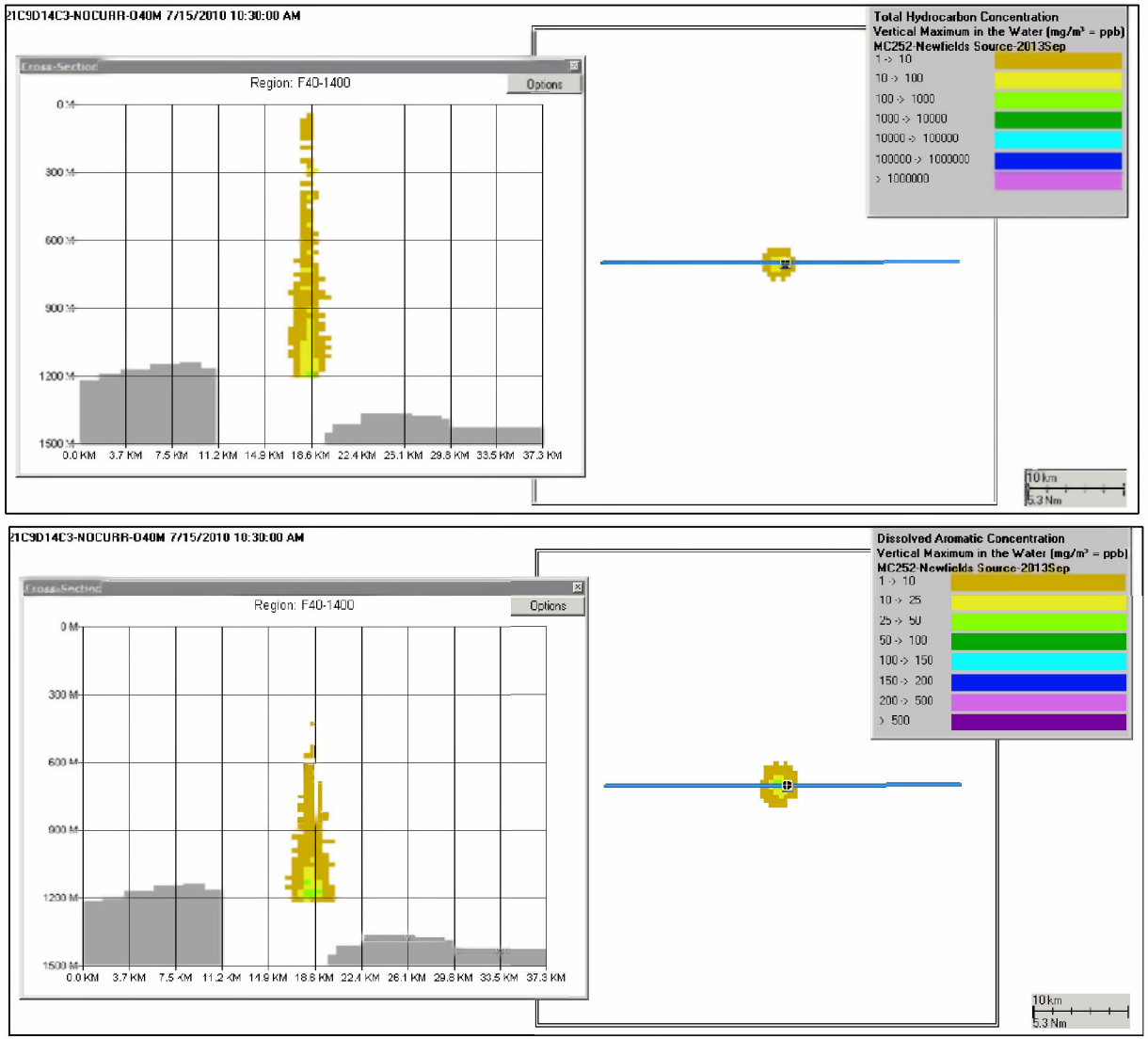

Figure F.2-34. Concentrations produced by the Static Cone simulation on July 15 – AR3 component (C4-benzenes, μg/L) in droplets (top) and in the dissolved phase (bottom).

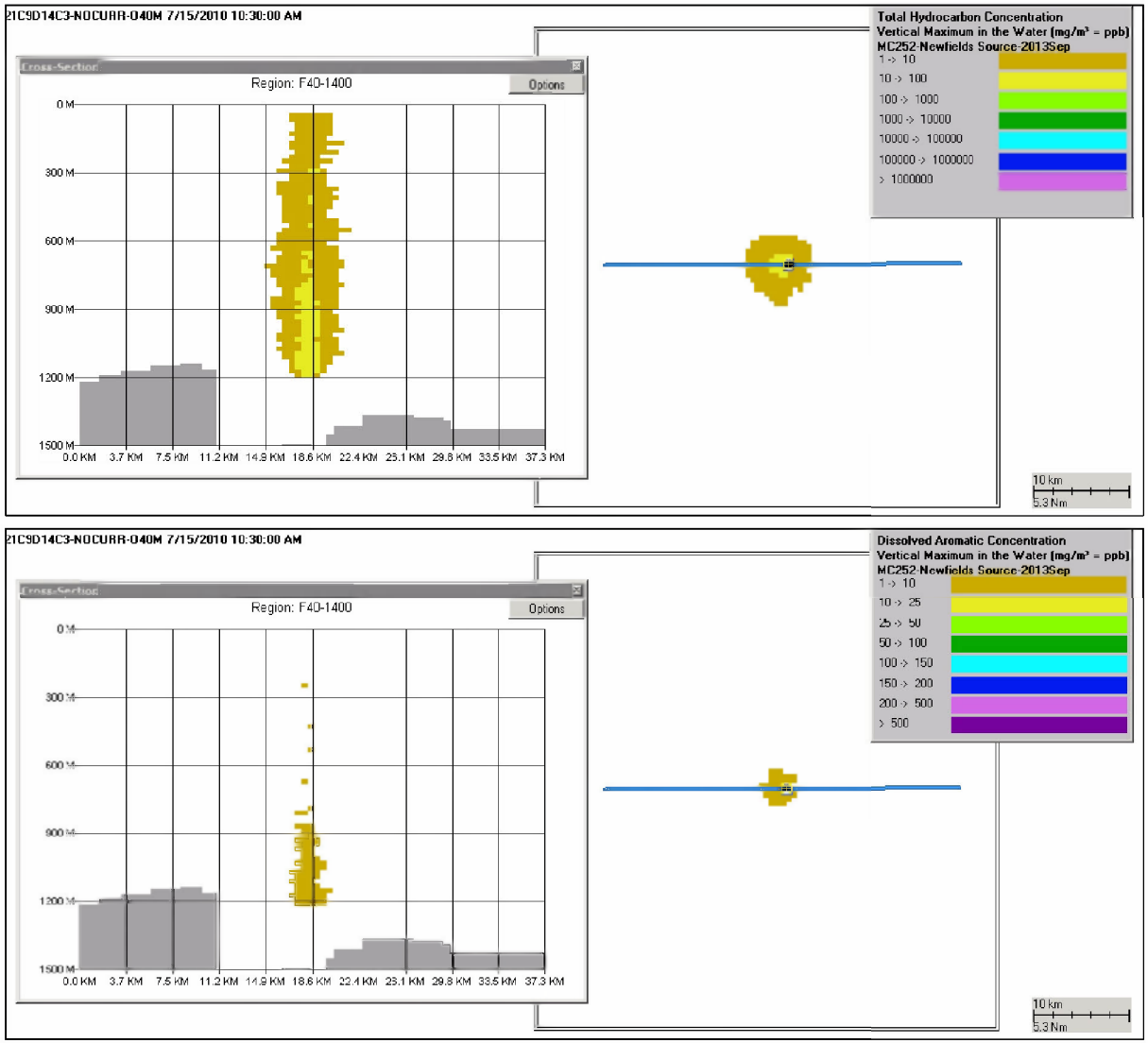

Figure F.2-35. Concentrations produced by the Static Cone simulation on July 15 – AR4 component (decalins, μg/L) in droplets (top) and in the dissolved phase (bottom).

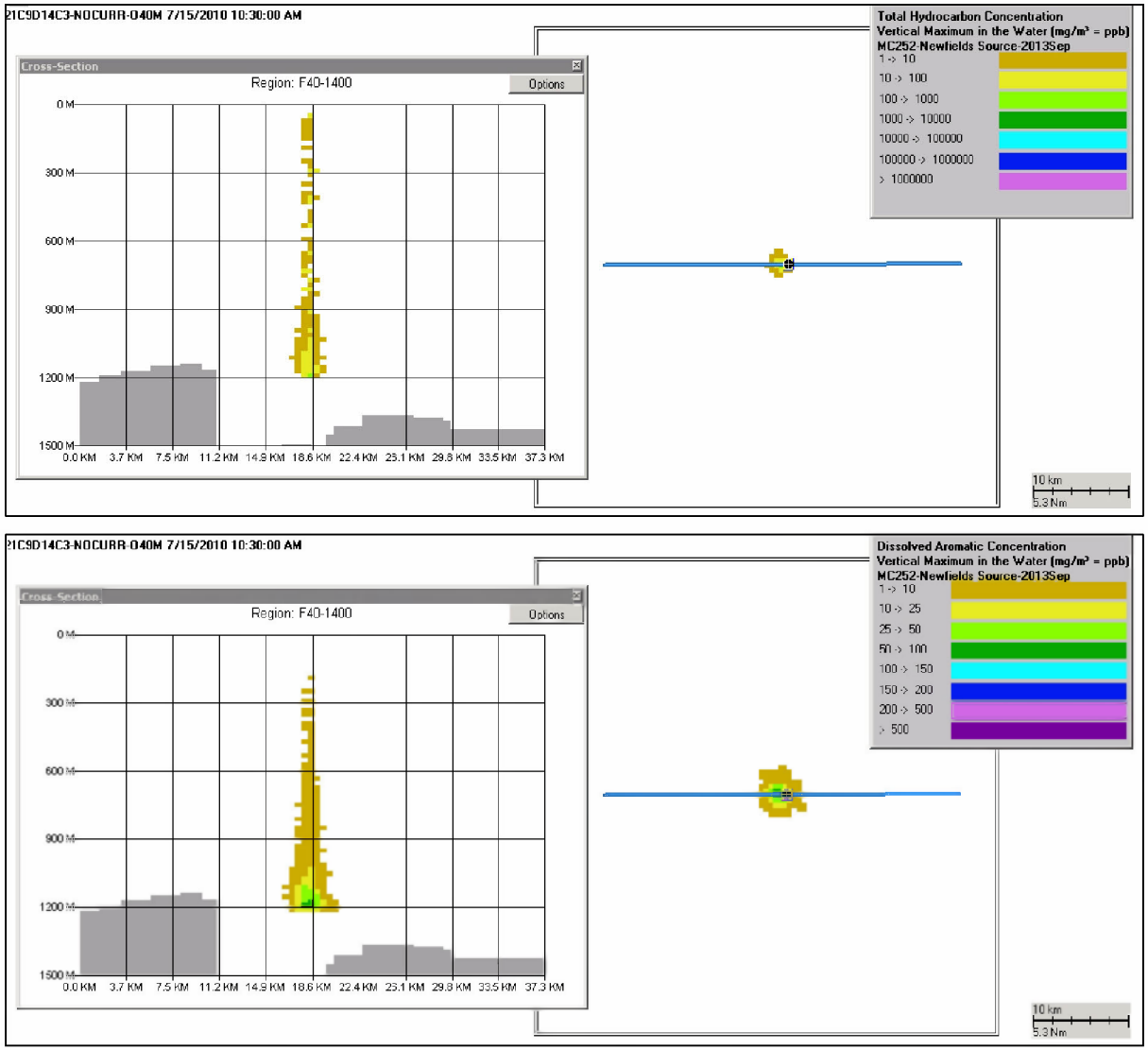

Figure F.2-36. Concentrations produced by the Static Cone simulation on July 15 – AR5 component (C0-C2 naphthalenes, μg/L) in droplets (top) and in the dissolved phase (bottom).

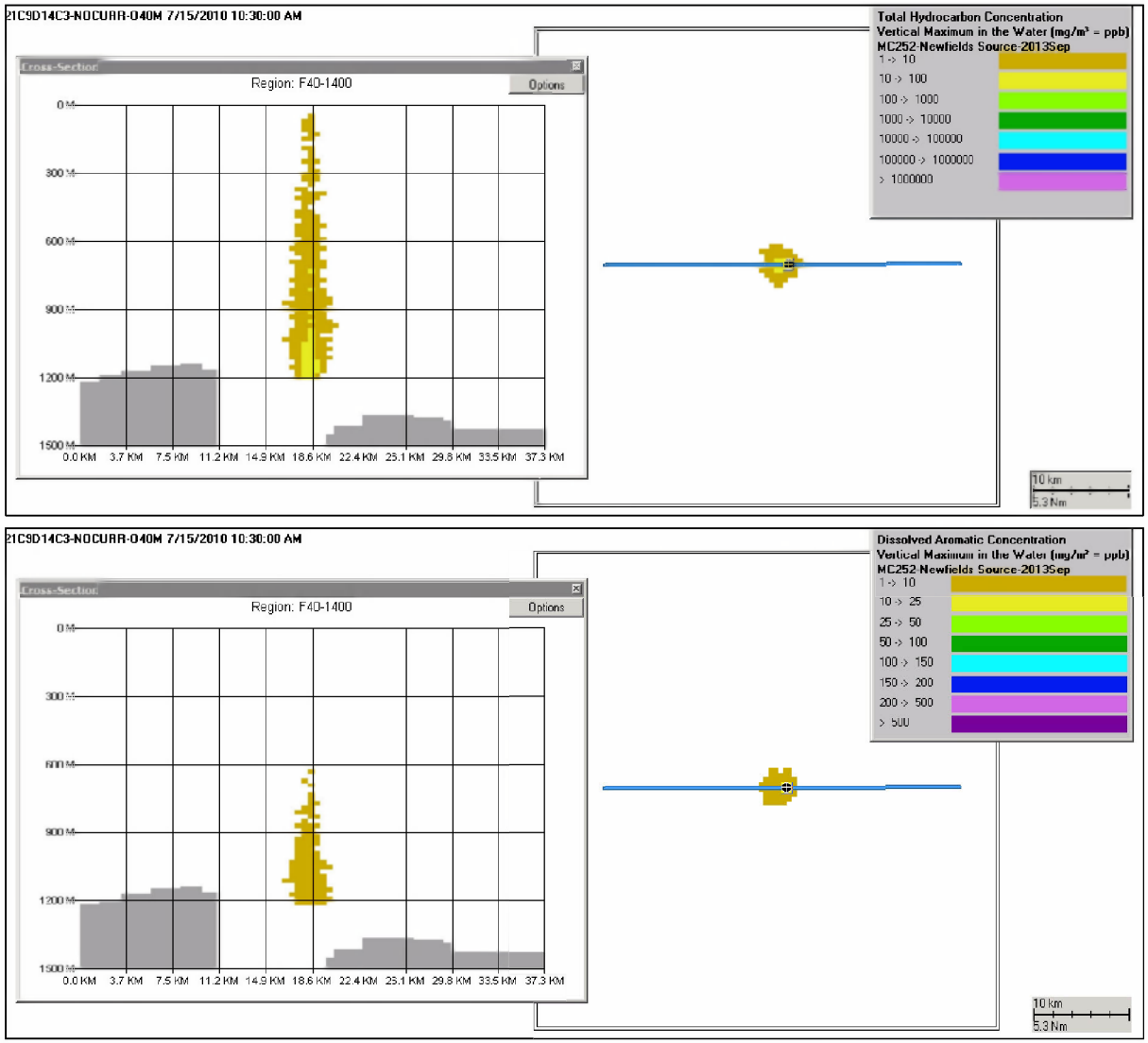

Figure F.2-37. Concentrations produced by the Static Cone simulation on July 15 – AR6 component (C3-C4 naphthalenes, µg/L) in droplets (top) and in the dissolved phase (bottom).

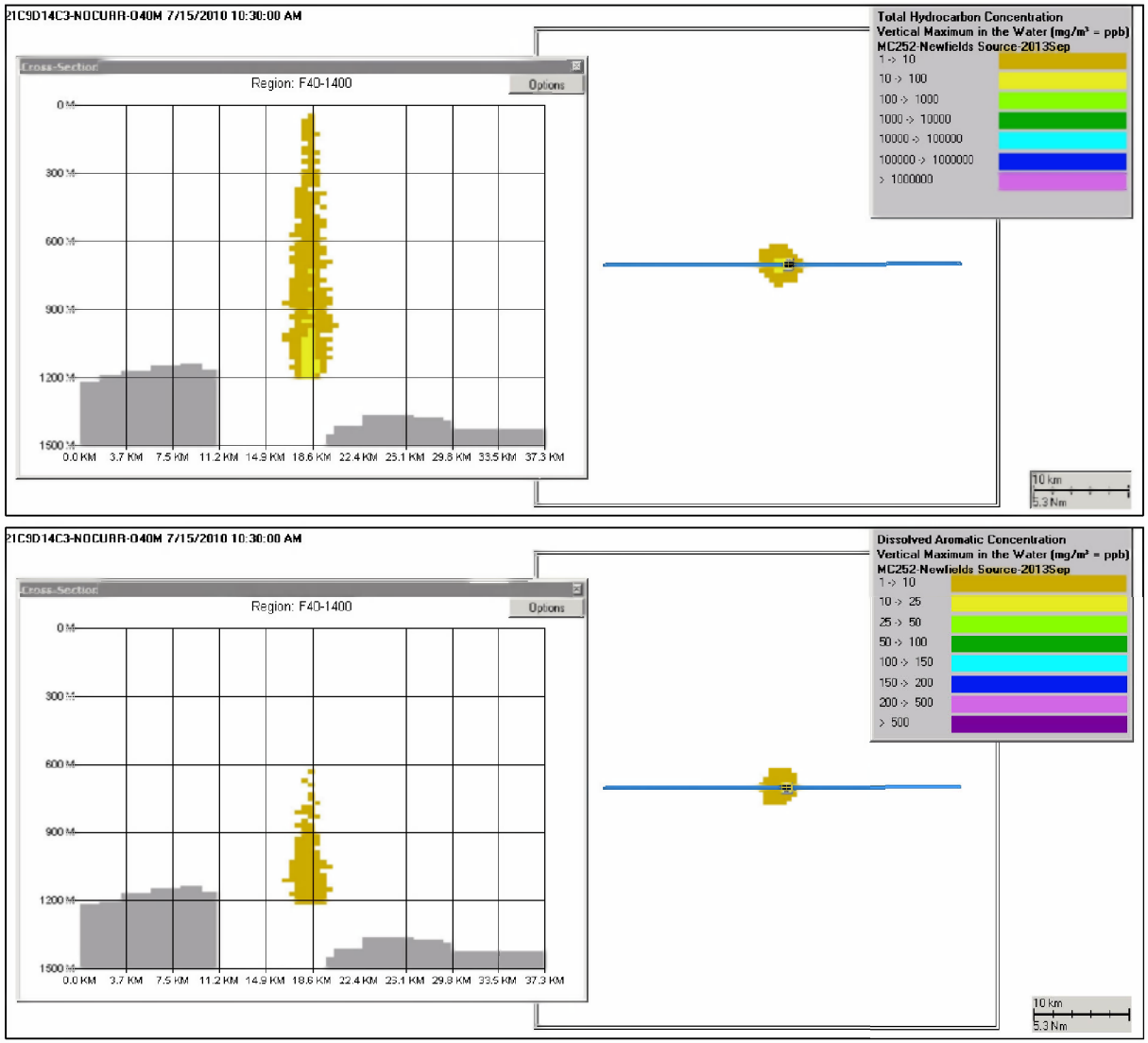

Figure F.2-38. Concentrations produced by the Static Cone simulation on July 15 – AR7 component (fluorenes & C0-C1 3-ring PAHs, µg/L) in droplets (top) and in the dissolved phase (bottom).

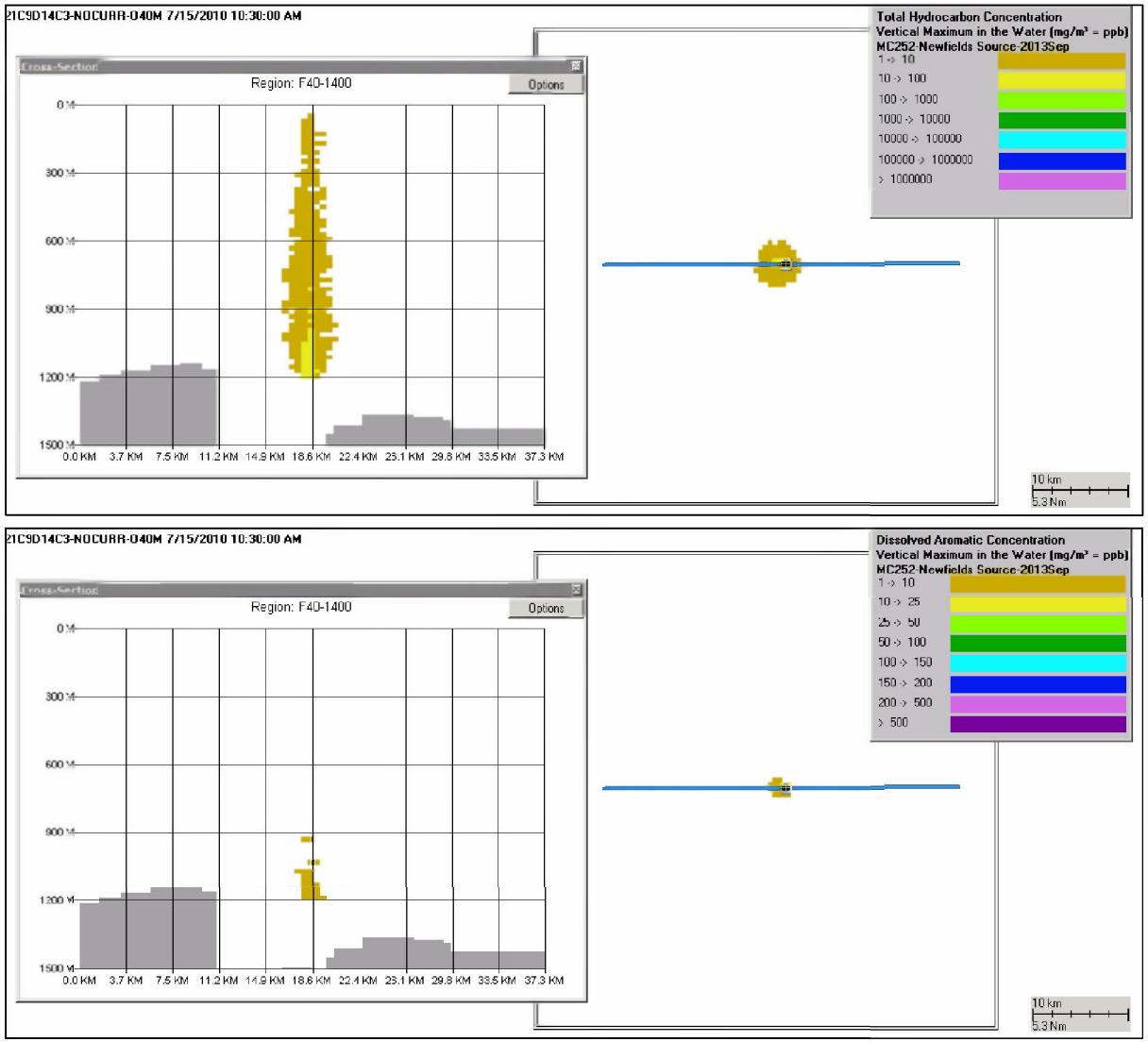

Figure F.2-39. Concentrations produced by the Static Cone simulation on July 15 – AR8 component (4-ring PAHs & C2-C3 3-ring PAHs, μg/L) in droplets (top) and in the dissolved phase (bottom).

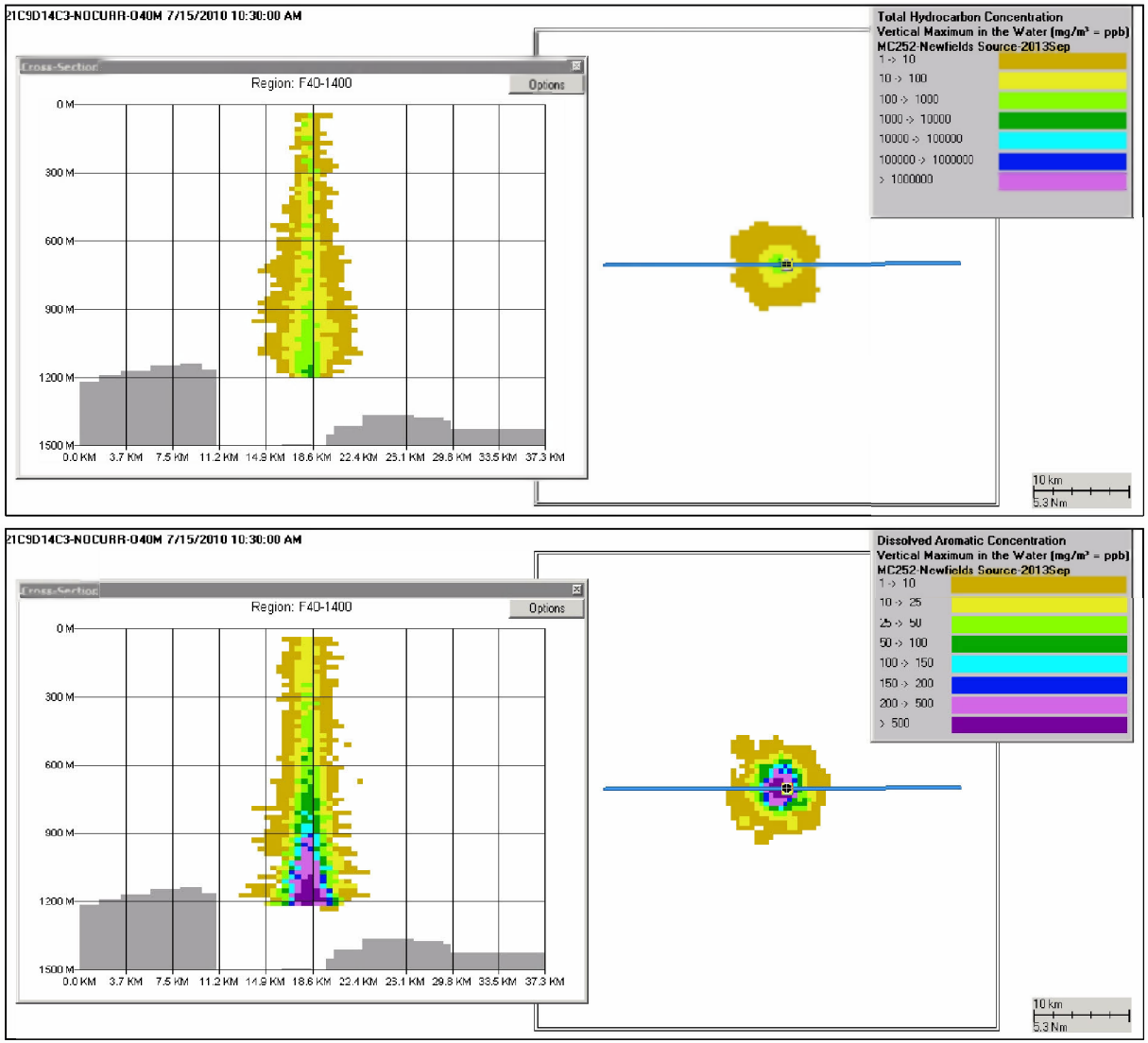

Figure F.2-40. Concentrations produced by the Static Cone simulation on July 15 – AR9 component (low molecular weight alkanes, isoalkanes, cycloalkanes, μg/L) in droplets (top) and in the dissolved phase (bottom).

F.3 Simulation Using Currents from IASROMS

Figures F.3-1 to F.3-14 provide snapshots at 14 dates of the vertical maximum concentrations in the deep plume (1100-1300m) produced by the simulation using currents from IASROMS. Each figure shows top-down views mapping the vertical maximum in-droplet (top) and dissolved (bottom) total hydrocarbon concentrations in the modeled depth range of 1100-1400m. Figures F.3-15 to F.3-27 provide snapshots at 13 dates of the spillet trajectory, with each spillet color-coded by age (i.e., hours since release). As the concentrations move and change rapidly, it is difficult to portray the results in static figures such as these.

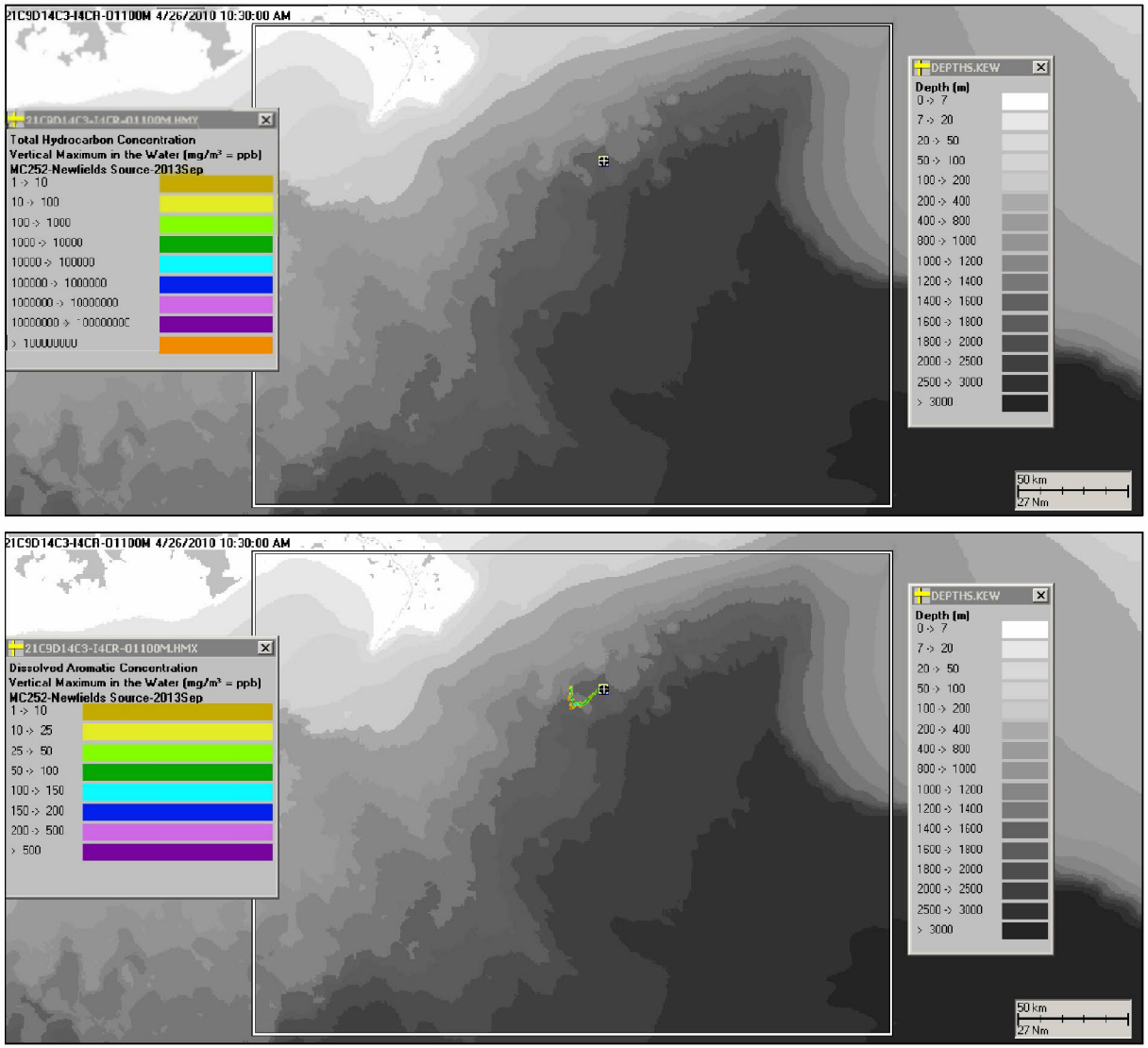

Figure F.3-1. Vertical maximum concentrations produced in the deep plume layer (1100-1300m) by the simulation using IASROMS currents on April 26 – total hydrocarbons in droplets (top) and in the dissolved phase (bottom).

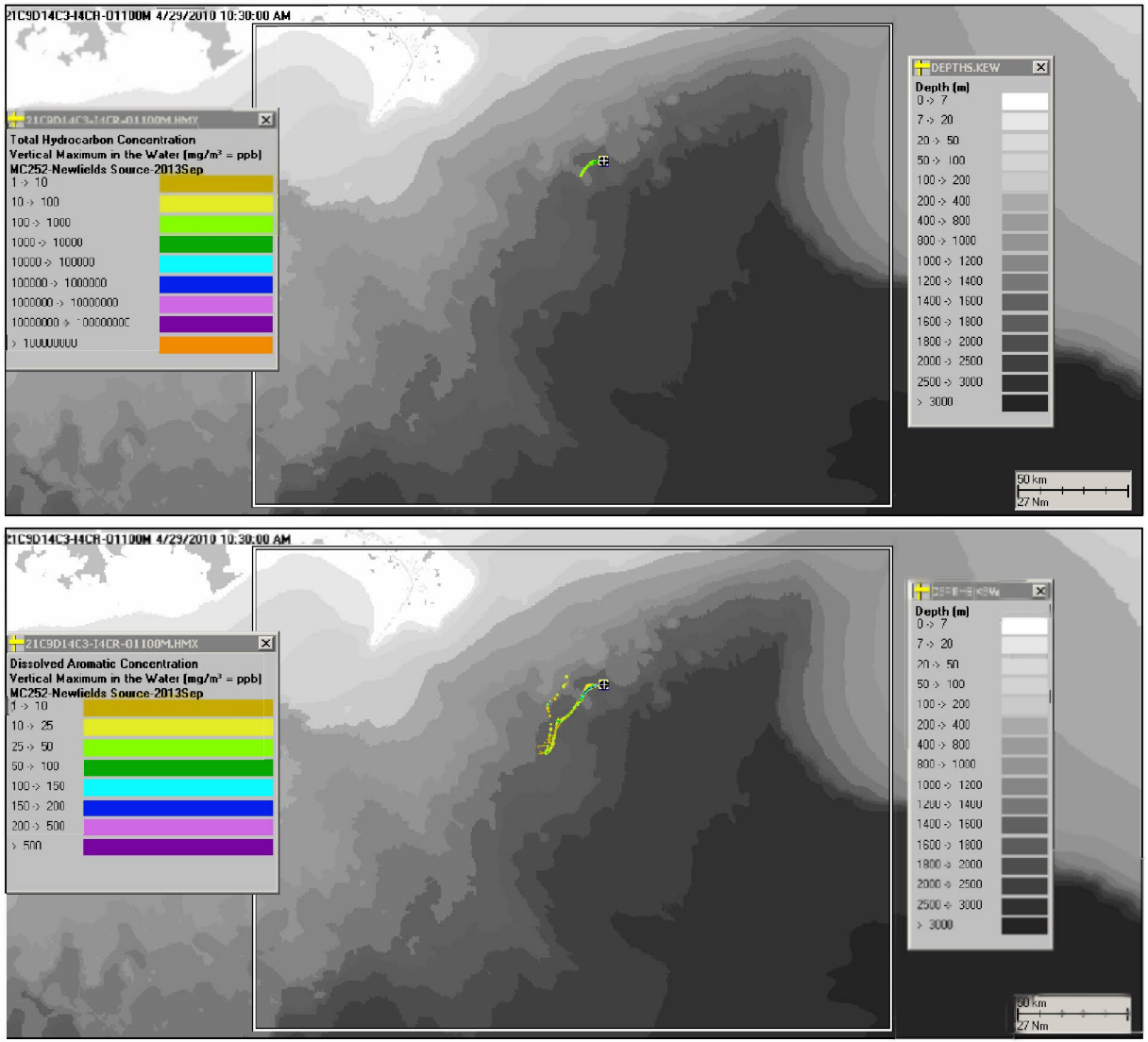

Figure F.3-2. Vertical maximum concentrations produced in the deep plume layer (1100-1300m) by the simulation using IASROMS currents on April 29 – total hydrocarbons in droplets (top) and in the dissolved phase (bottom).

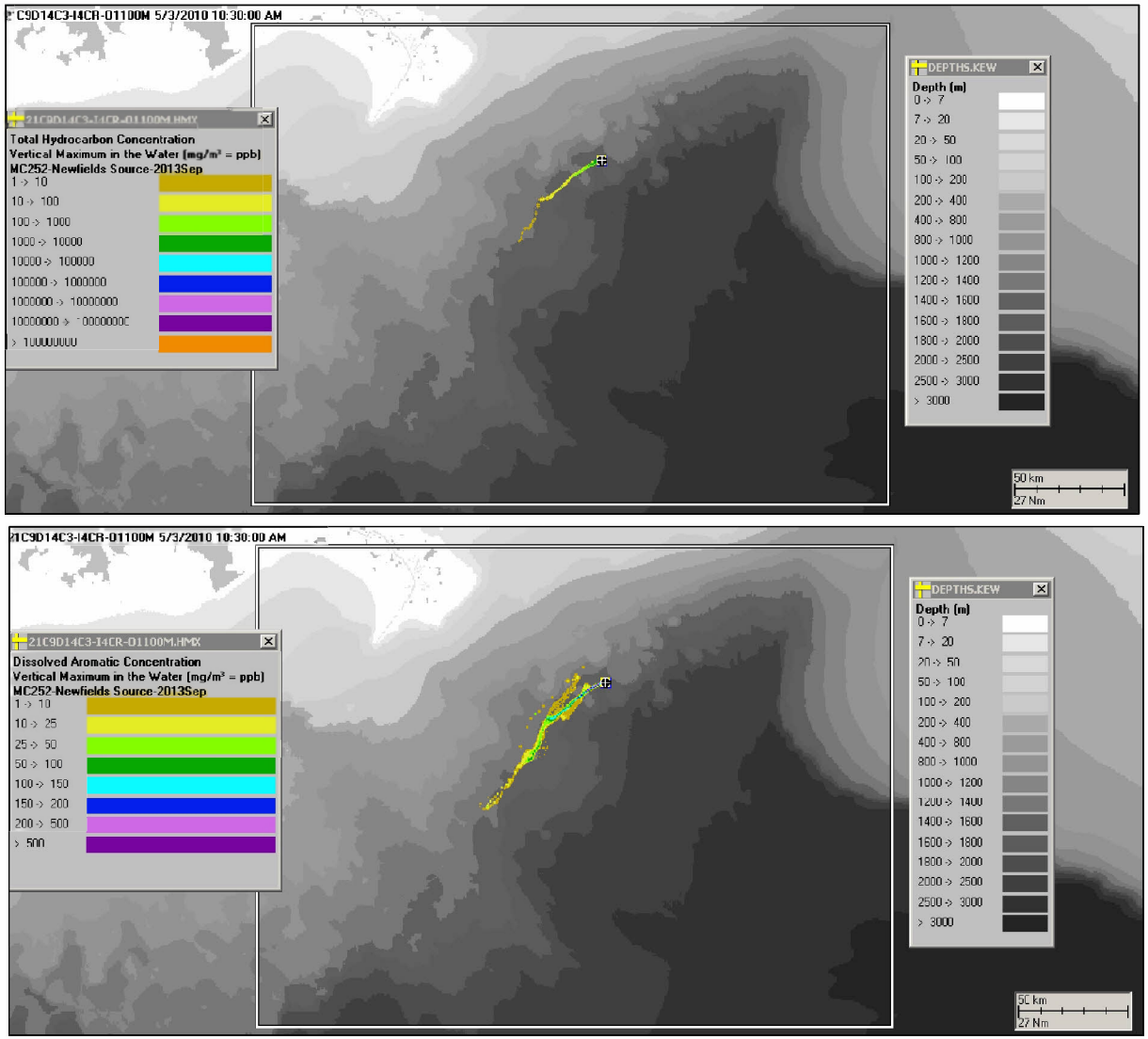

Figure F.3-3. Vertical maximum concentrations produced in the deep plume layer (1100-1300m) by the simulation using IASROMS currents on May 3 – total hydrocarbons in droplets (top) and in the dissolved phase (bottom).

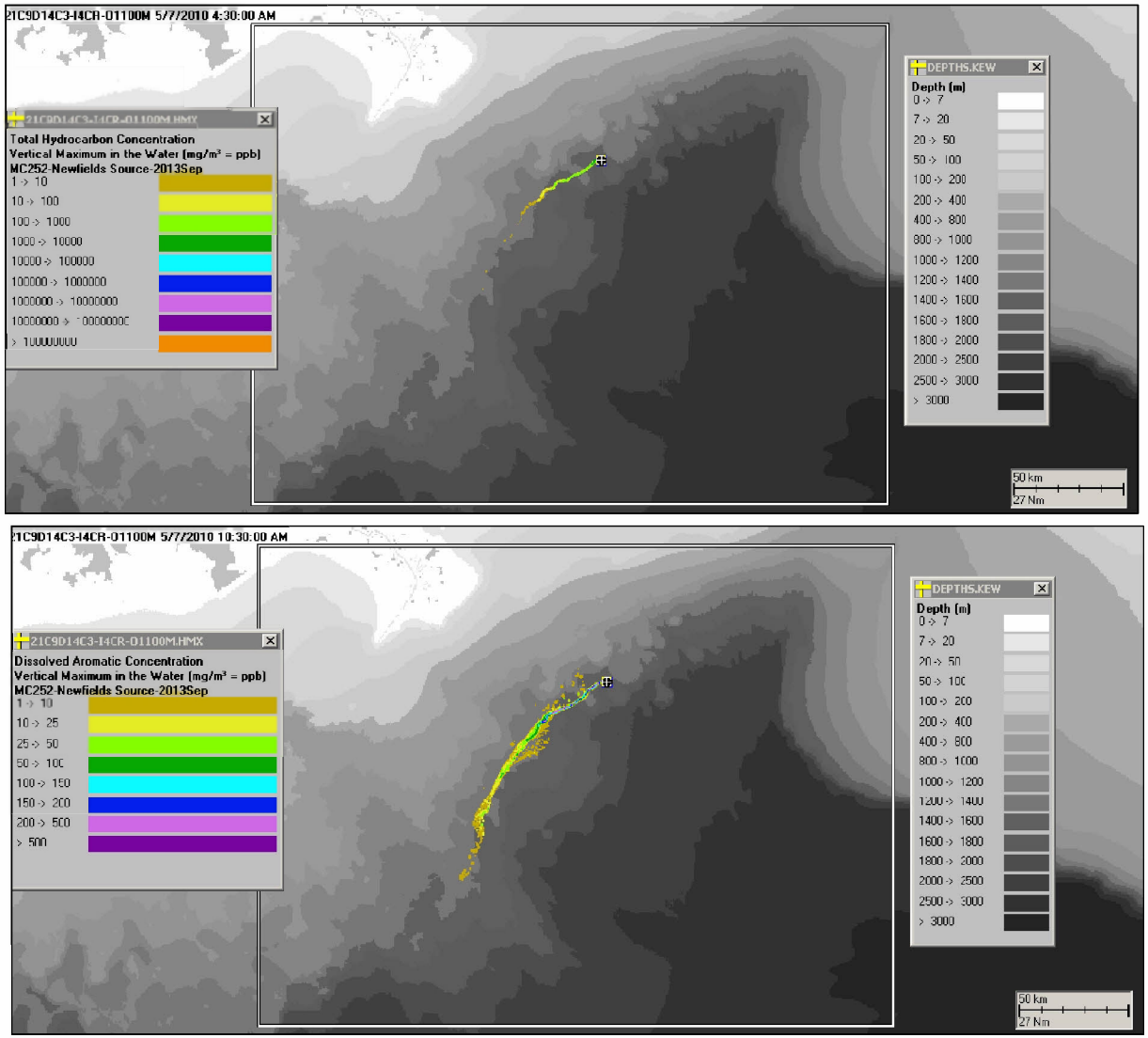

Figure F.3-4. Vertical maximum concentrations produced in the deep plume layer (1100-1300m) by the simulation using IASROMS currents on May 7 – total hydrocarbons in droplets (top) and in the dissolved phase (bottom).

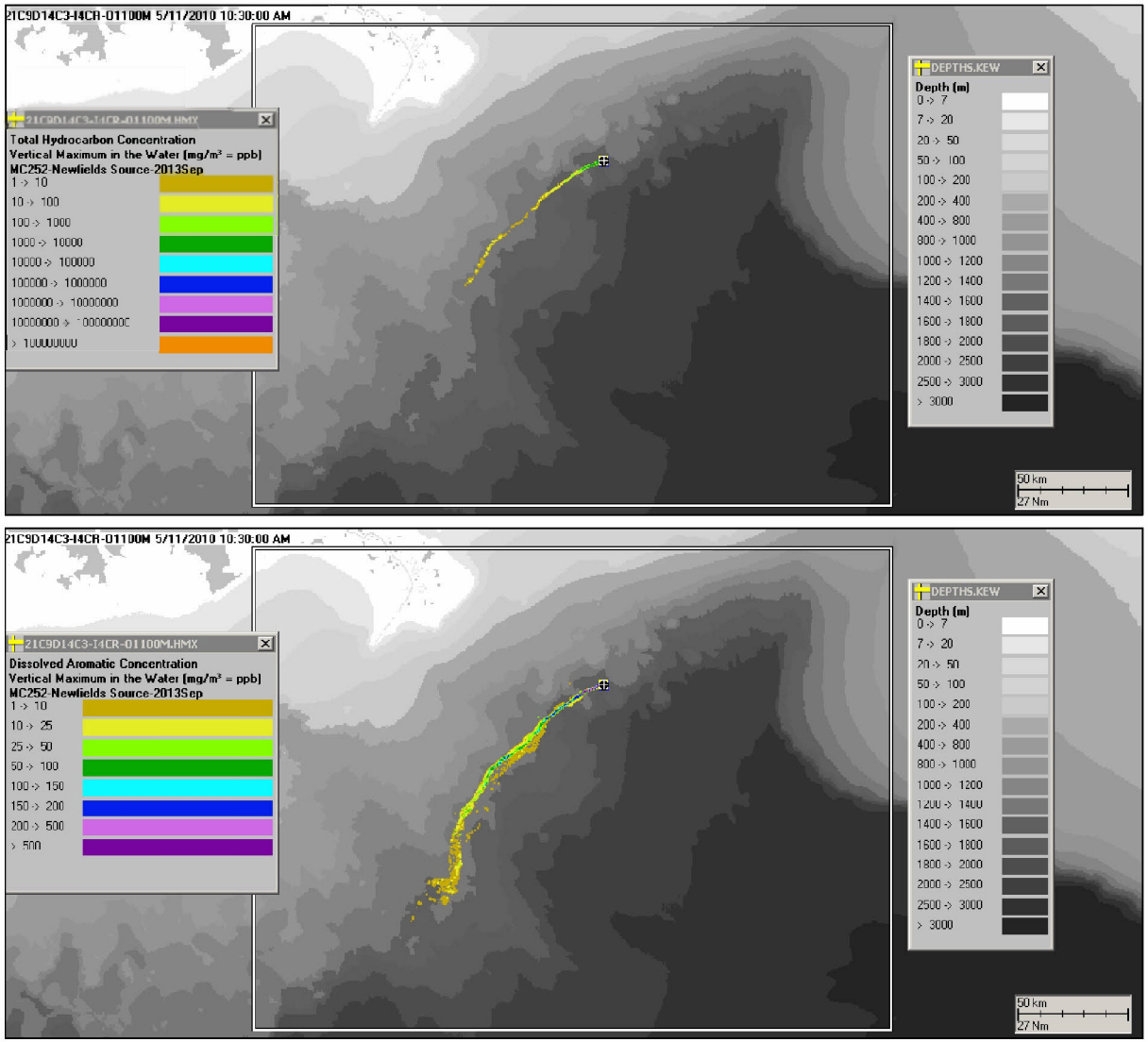

Figure F.3-5. Vertical maximum concentrations produced in the deep plume layer (1100-1300m) by the simulation using IASROMS currents on May 11 – total hydrocarbons in droplets (top) and in the dissolved phase (bottom).

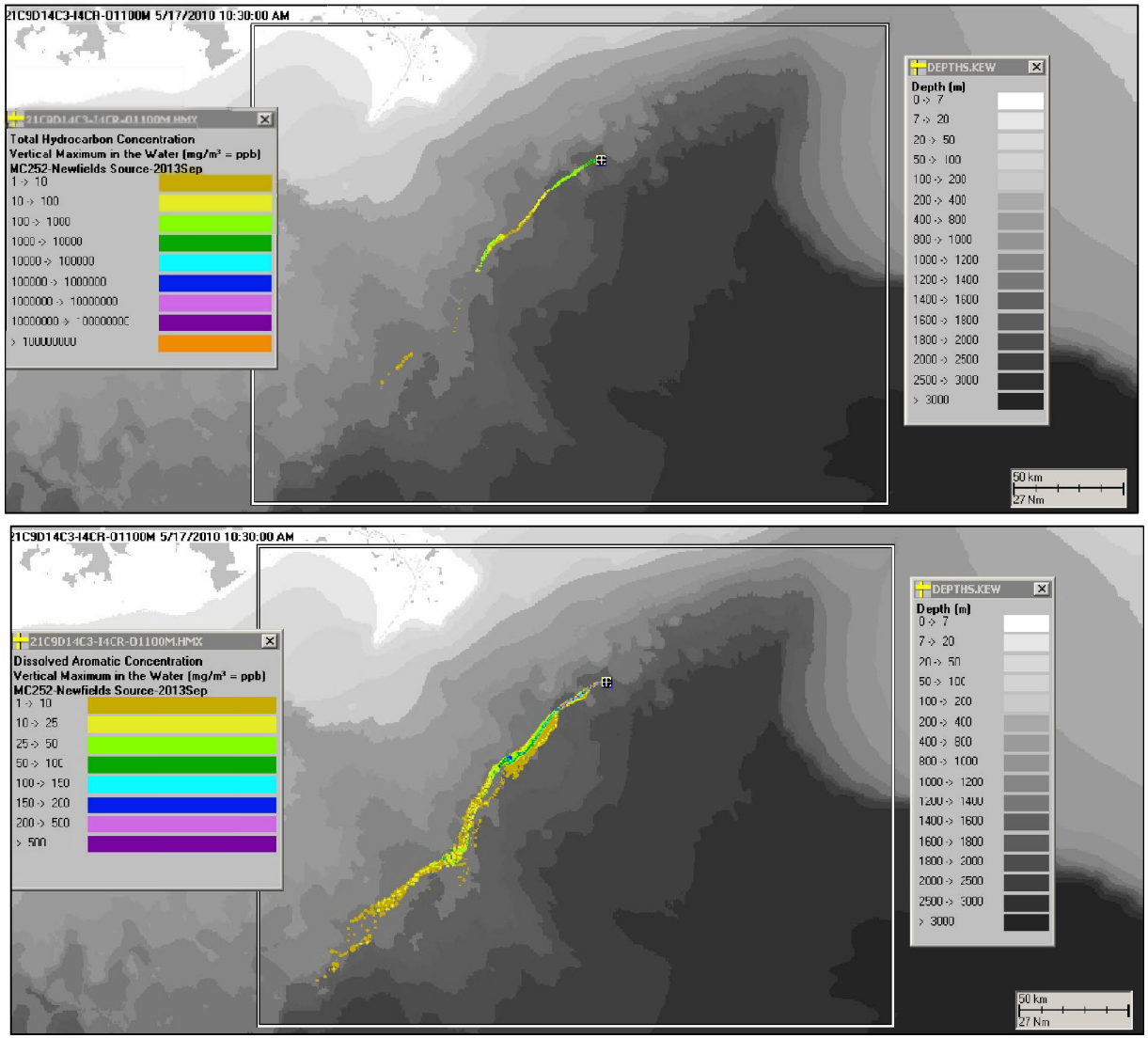

Figure F.3-6. Vertical maximum concentrations produced in the deep plume layer (1100-1300m) by the simulation using IASROMS currents on May 17 – total hydrocarbons in droplets (top) and in the dissolved phase (bottom).

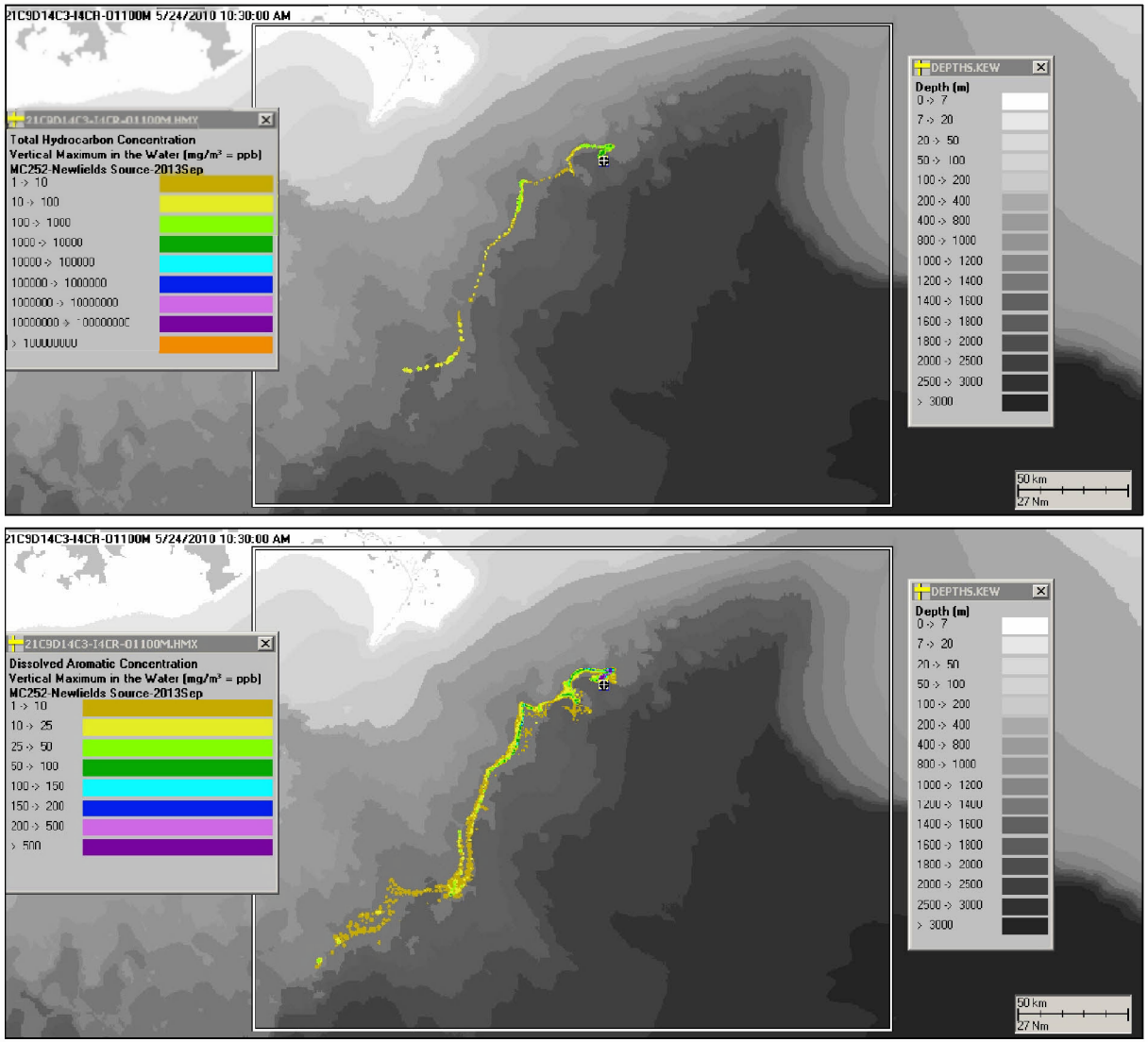

Figure F.3-7. Vertical maximum concentrations produced in the deep plume layer (1100-1300m) by the simulation using IASROMS currents on May 24 – total hydrocarbons in droplets (top) and in the dissolved phase (bottom).

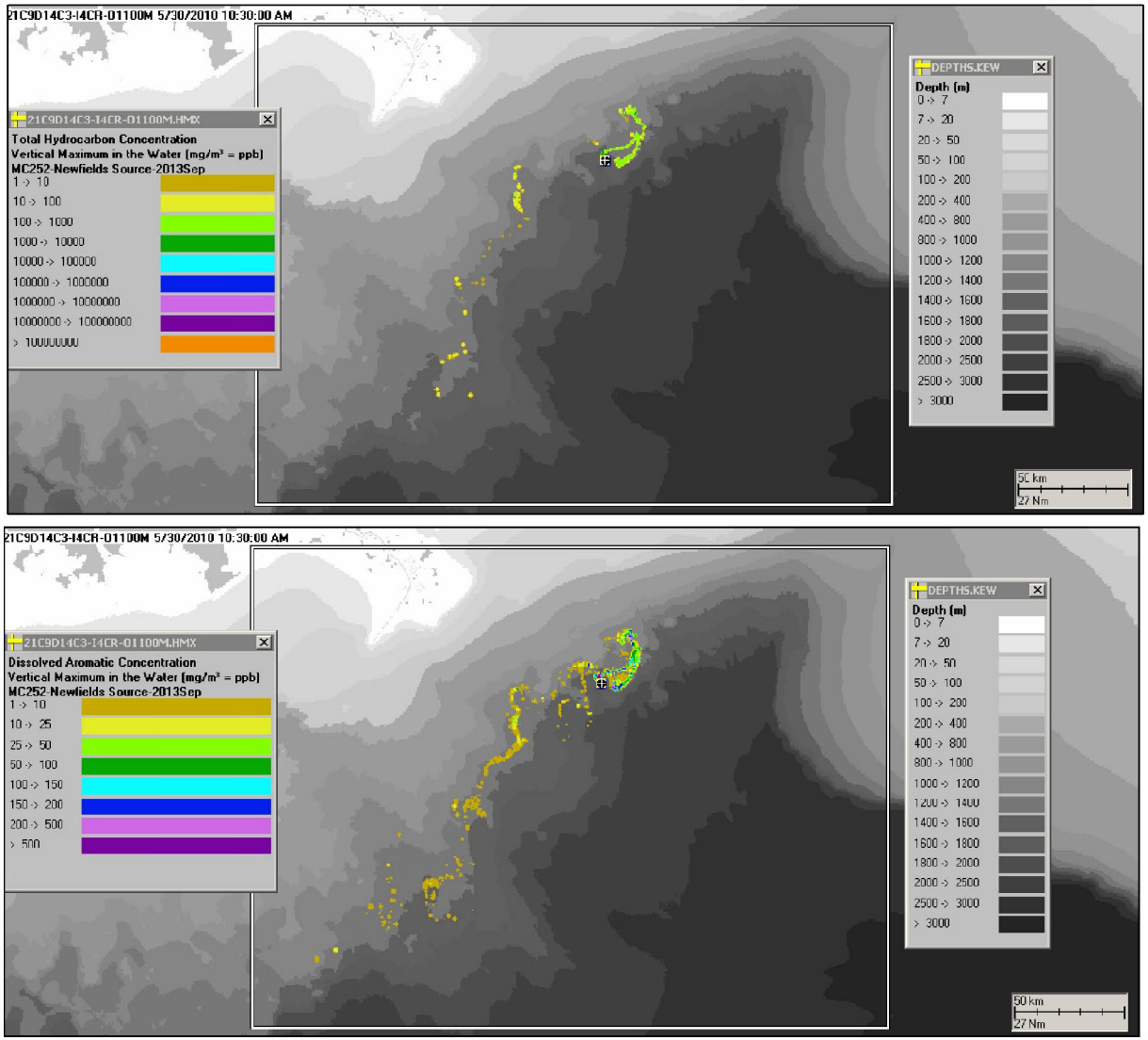

Figure F.3-8. Vertical maximum concentrations produced in the deep plume layer (1100-1300m) by the simulation using IASROMS currents on May 30 – total hydrocarbons in droplets (top) and in the dissolved phase (bottom).

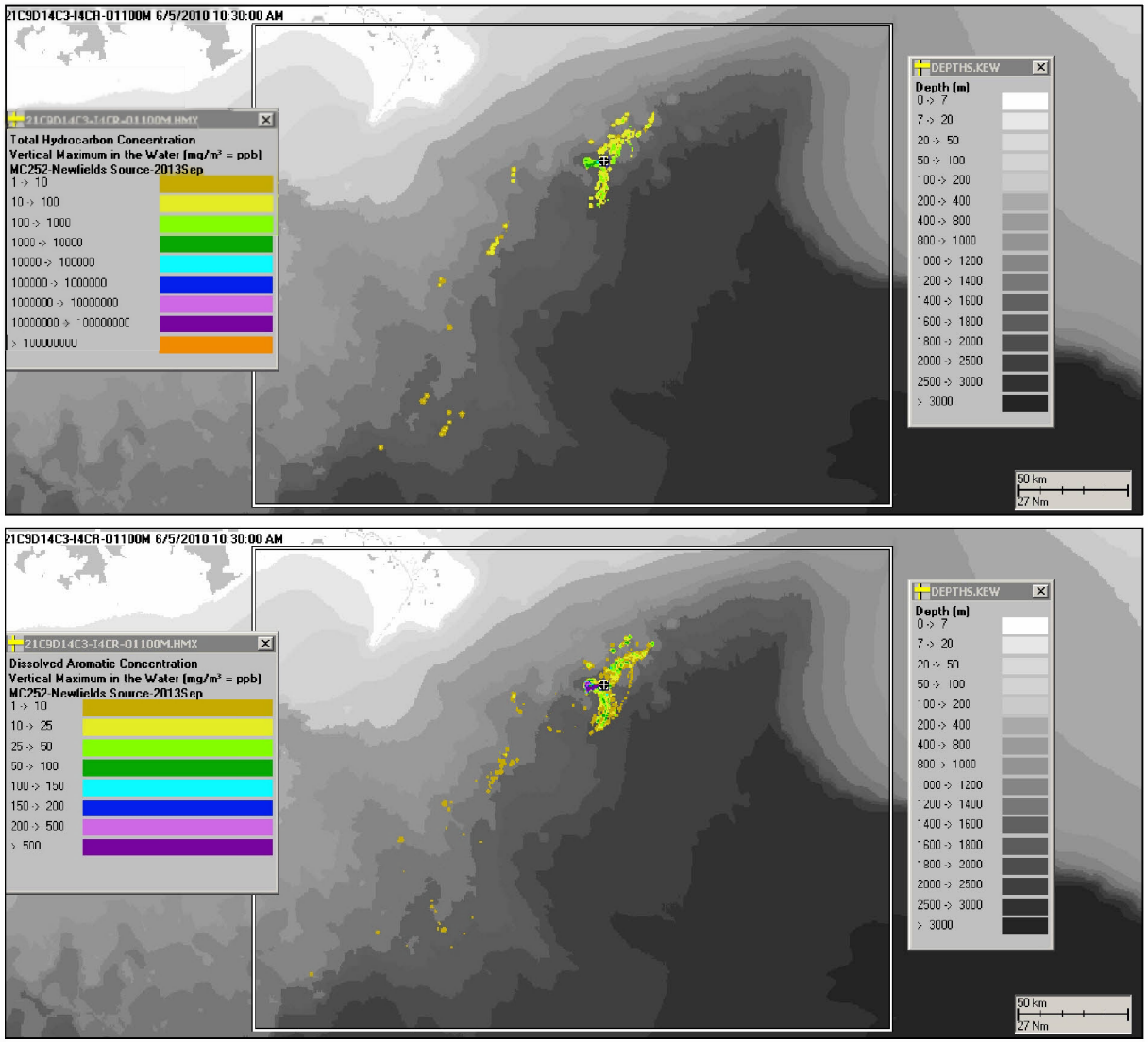

Figure F.3-9. Vertical maximum concentrations produced in the deep plume layer (1100-1300m) by the simulation using IASROMS currents on June 5 – total hydrocarbons in droplets (top) and in the dissolved phase (bottom).

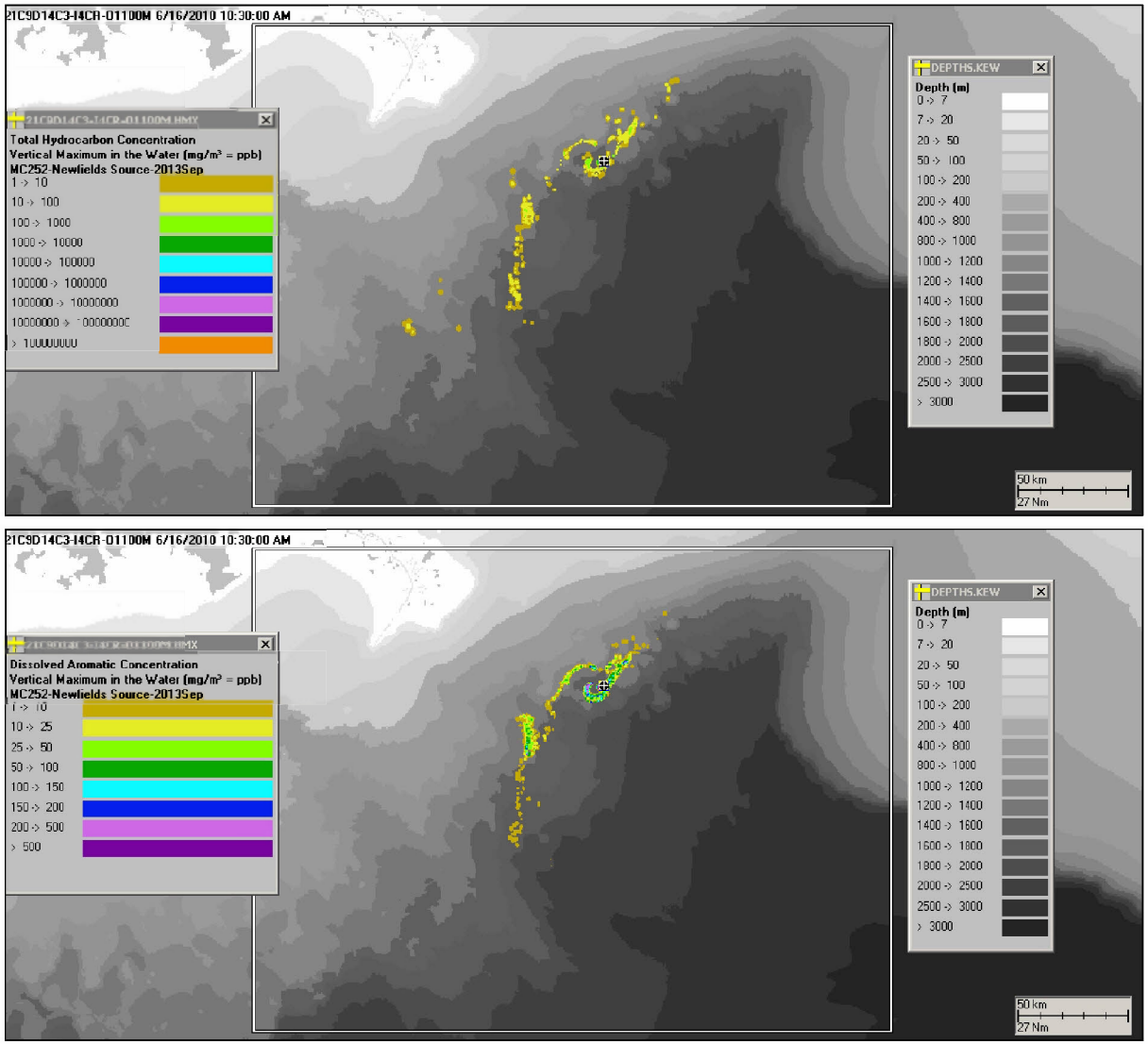

Figure F.3-10. Vertical maximum concentrations produced in the deep plume layer (1100-1300m) by the simulation using IASROMS currents on June 16 – total hydrocarbons in droplets (top) and in the dissolved phase (bottom).

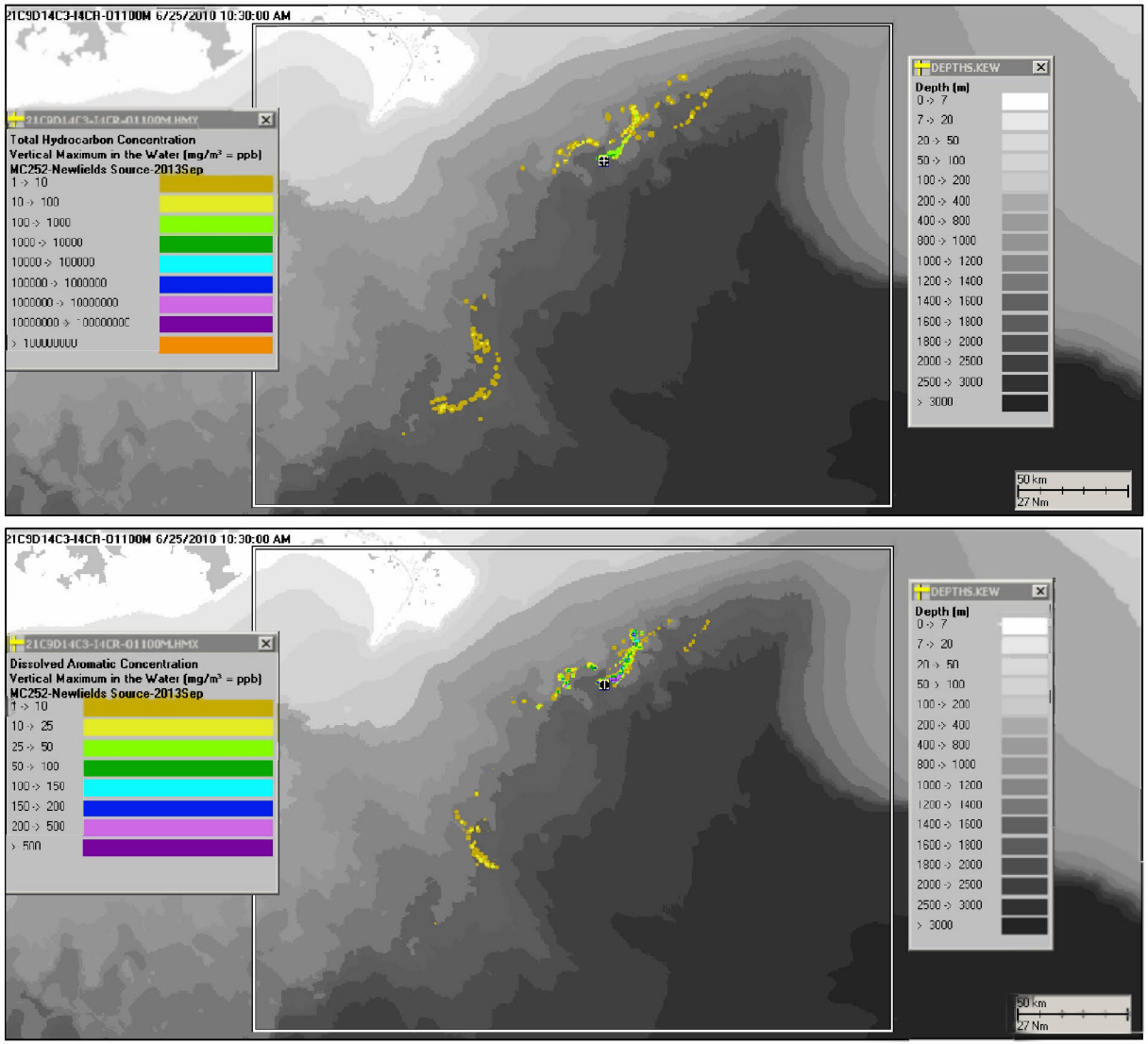

Figure F.3-11. Vertical maximum concentrations produced in the deep plume layer (1100-1300m) by the simulation using IASROMS currents on June 25 – total hydrocarbons in droplets (top) and in the dissolved phase (bottom).

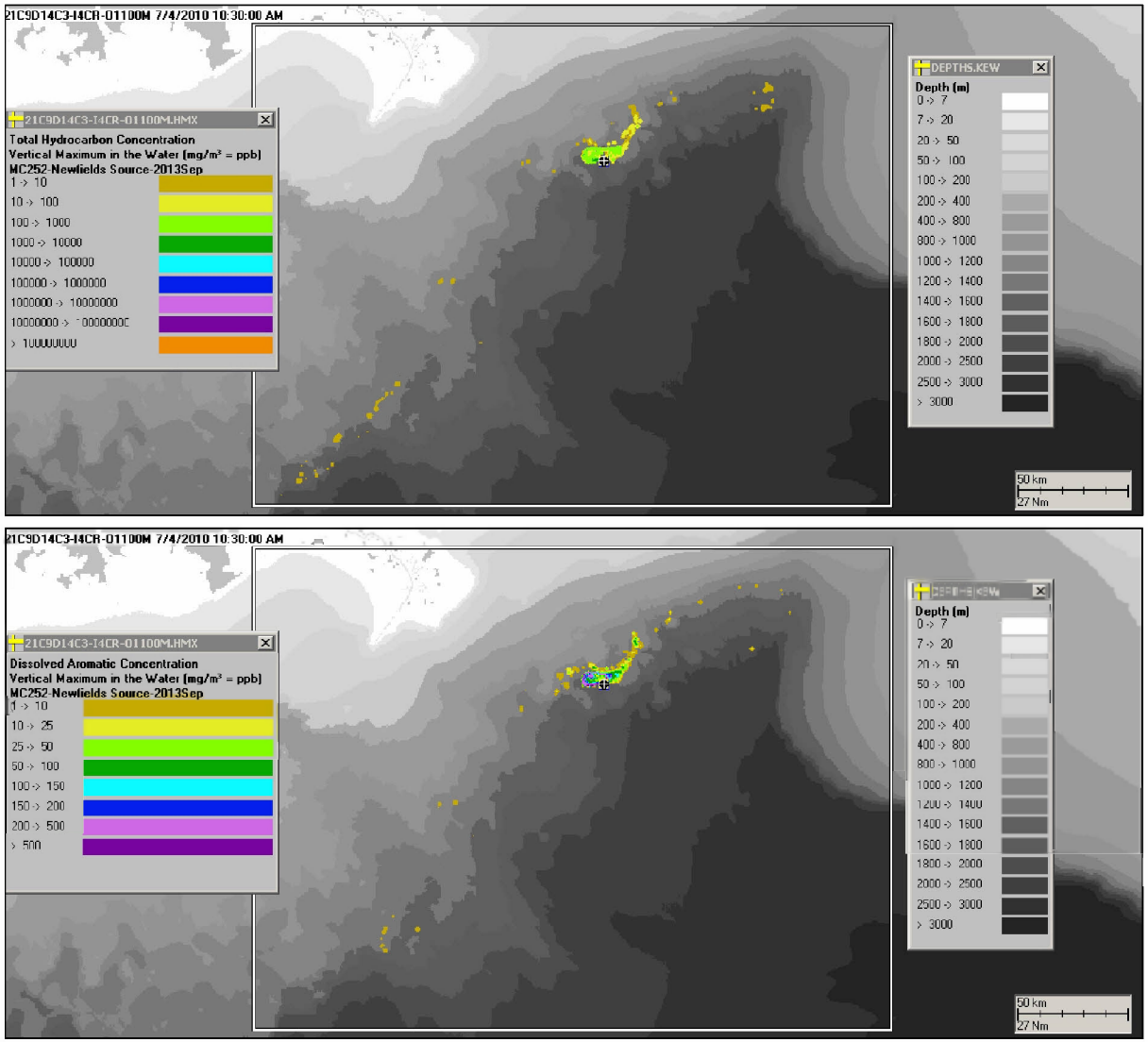

Figure F.3-12. Vertical maximum concentrations produced in the deep plume layer (1100-1300m) by the simulation using IASROMS currents on July 4 – total hydrocarbons in droplets (top) and in the dissolved phase (bottom).

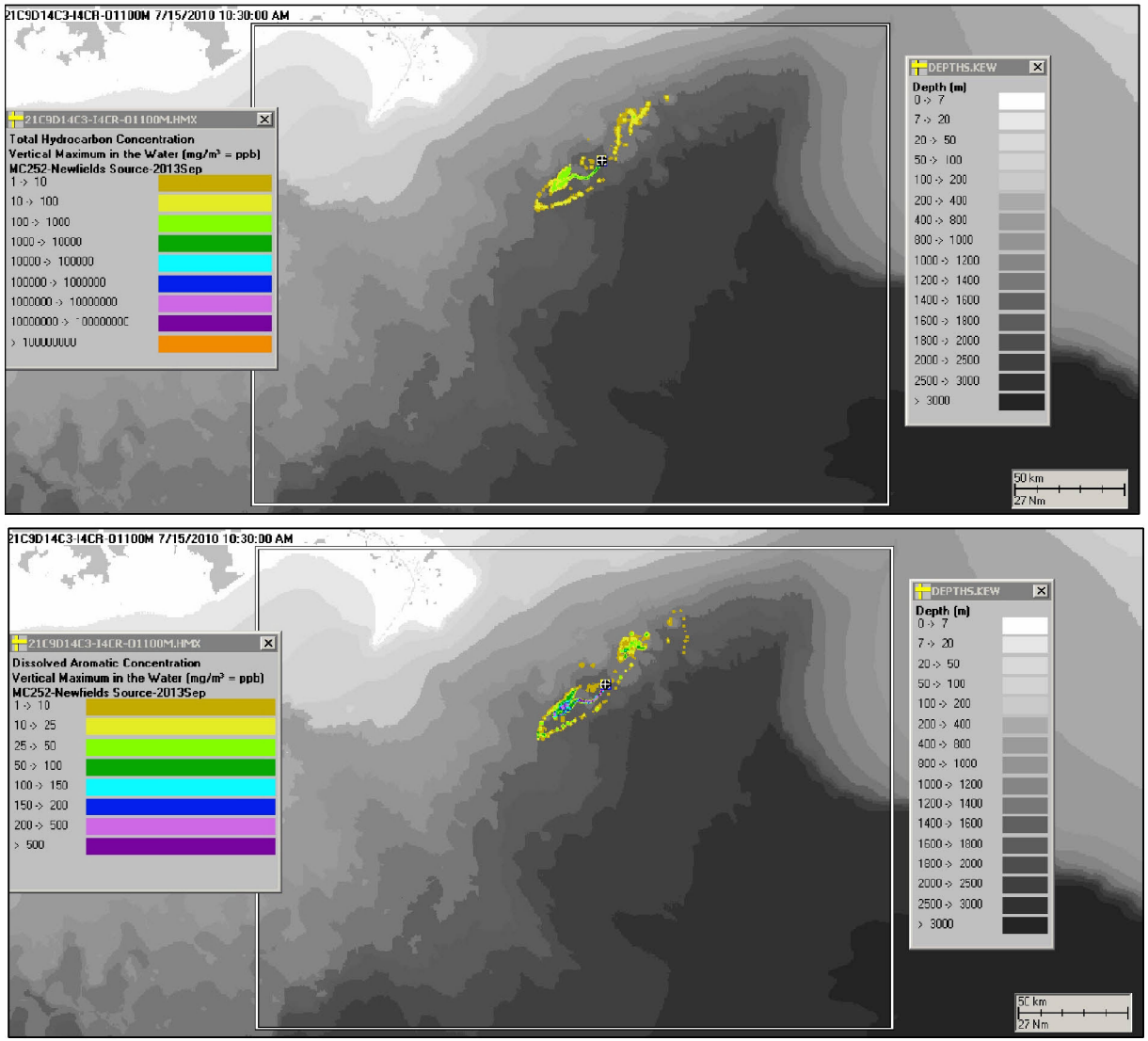

Figure F.3-13. Vertical maximum concentrations produced in the deep plume layer (1100-1300m) by the simulation using IASROMS currents on July 15 – total hydrocarbons in droplets (top) and in the dissolved phase (bottom).

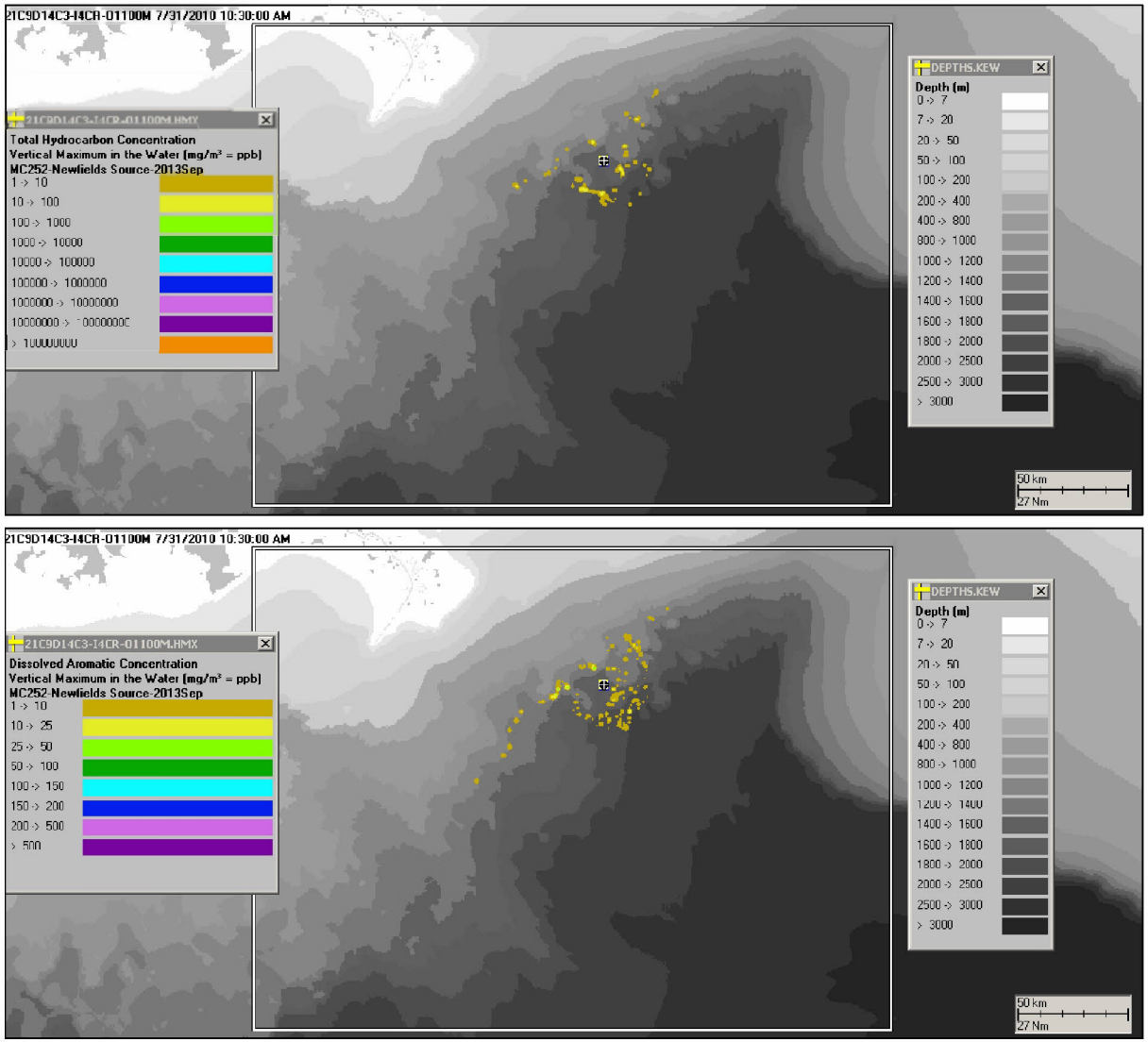

Figure F.3-14. Vertical maximum concentrations produced in the deep plume layer (1100-1300m) by the simulation using IASROMS currents on July 31 – total hydrocarbons in droplets (top) and in the dissolved phase (bottom).

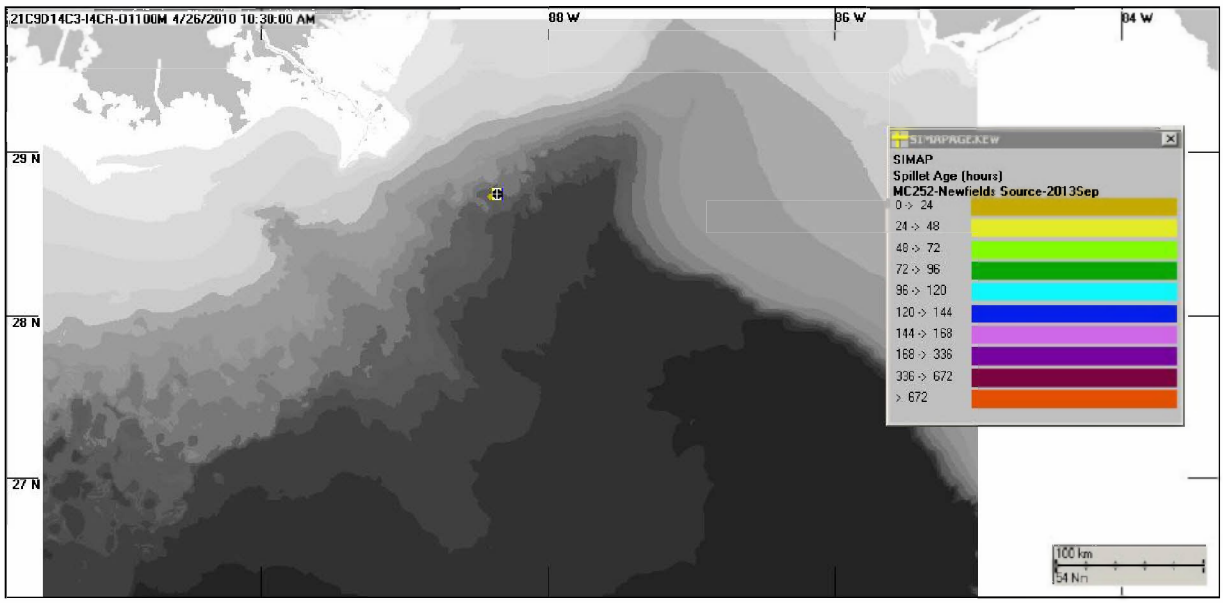

Figure F.3-15. Snapshot of the spillet trajectory, vertically integrated 1,100-1,400 m, with each spillet color-coded by age (i.e., hours since release) – April 26.

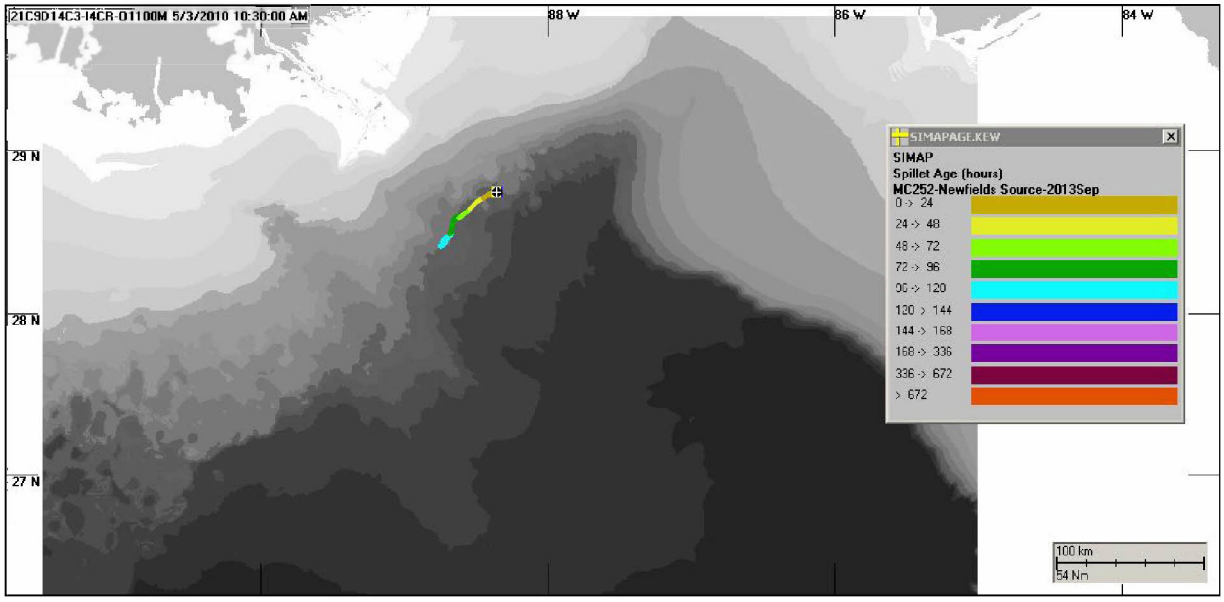

Figure F.3-16. Snapshot of the spillet trajectory, vertically integrated 1,100-1,400 m, with each spillet color-coded by age (i.e., hours since release) – May 3.

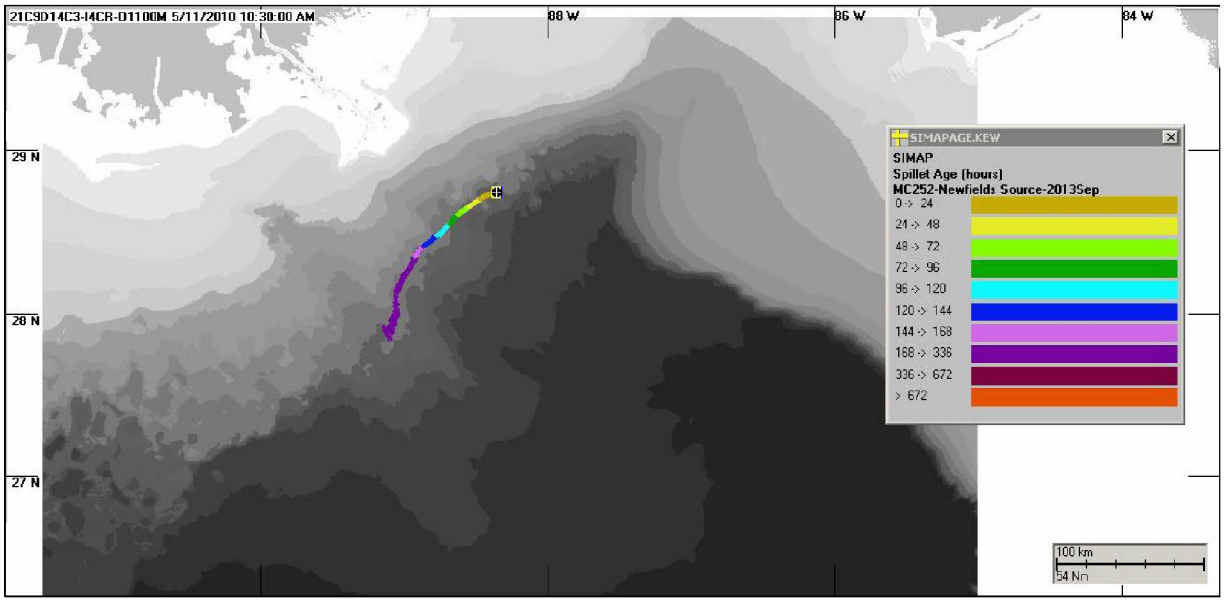

Figure F.3-17. Snapshot of the spillet trajectory, vertically integrated 1,100-1,400 m, with each spillet color-coded by age (i.e., hours since release) – May 11.

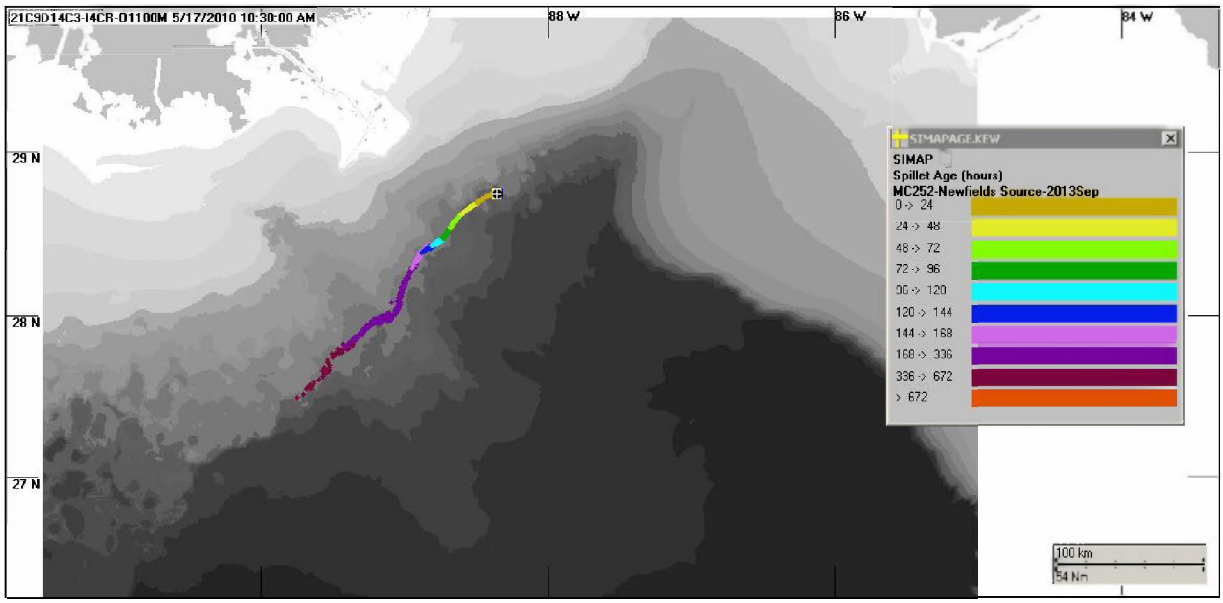

Figure F.3-18. Snapshot of the spillet trajectory, vertically integrated 1,100-1,400 m, with each spillet color-coded by age (i.e., hours since release) – May 17.

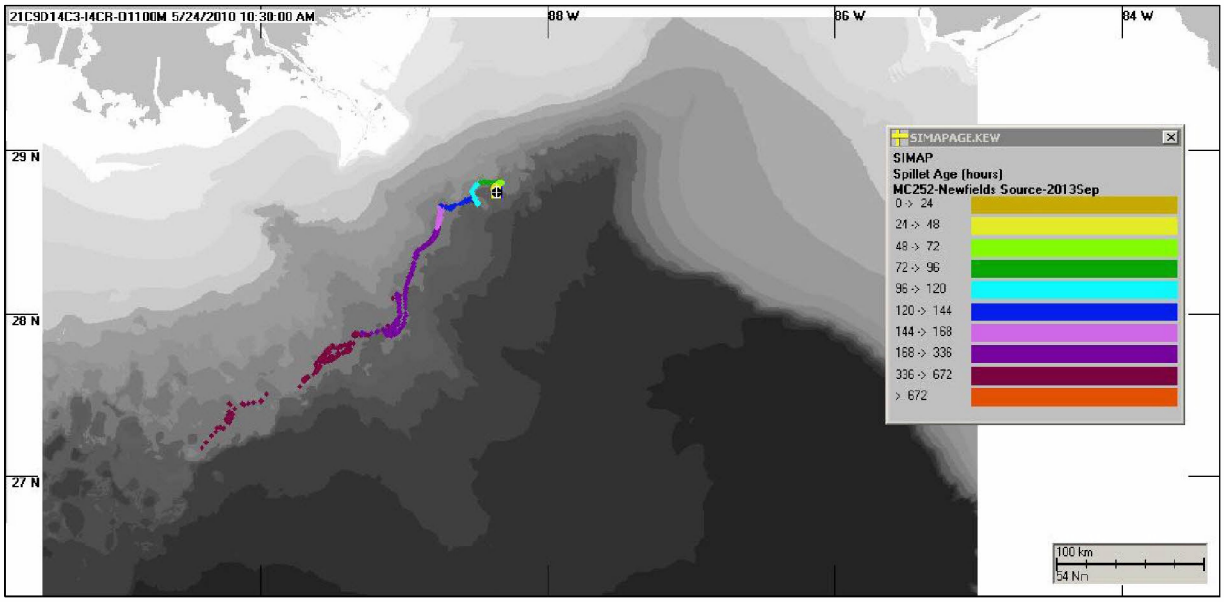

Figure F.3-19. Snapshot of the spillet trajectory, vertically integrated 1,100-1,400 m, with each spillet color-coded by age (i.e., hours since release) – May 24.

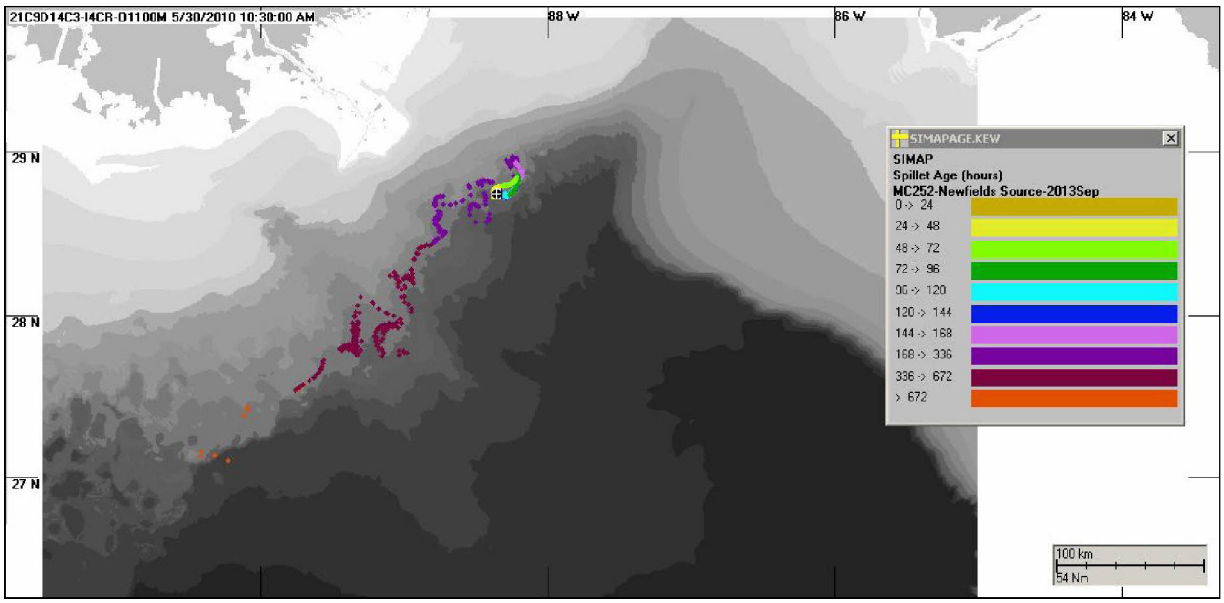

Figure F.3-20. Snapshot of the spillet trajectory, vertically integrated 1,100-1,400 m, with each spillet color-coded by age (i.e., hours since release) – May 30.

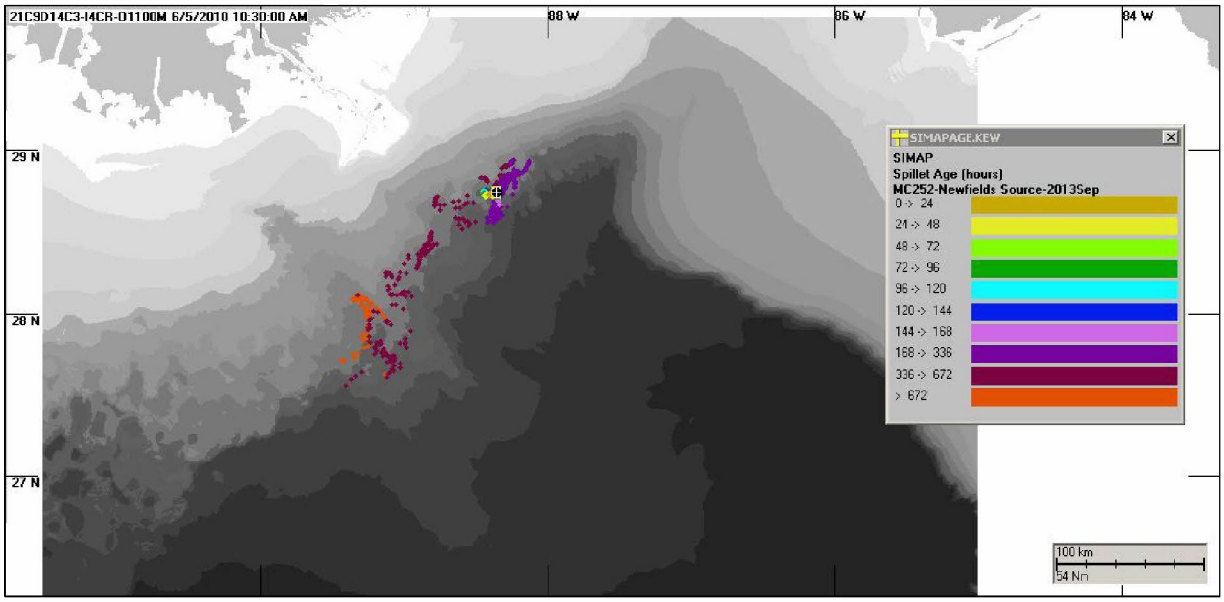

Figure F.3-21. Snapshot of the spillet trajectory, vertically integrated 1,100-1,400 m, with each spillet color-coded by age (i.e., hours since release) – June 5.

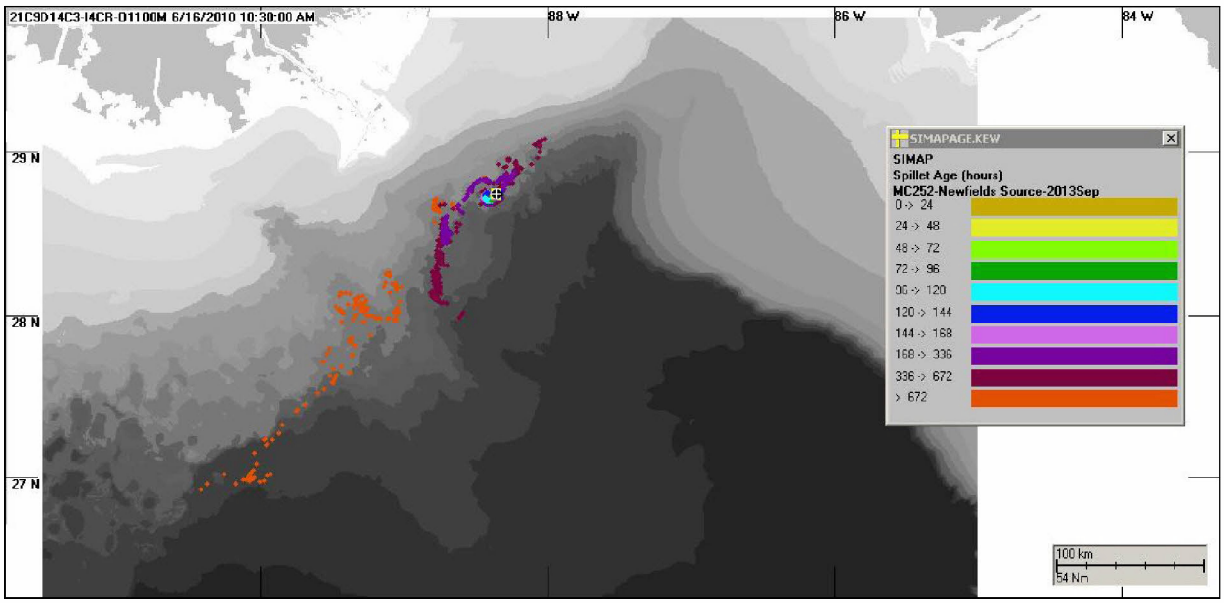

Figure F.3-22. Snapshot of the spillet trajectory, vertically integrated 1,100-1,400 m, with each spillet color-coded by age (i.e., hours since release) – June 16.

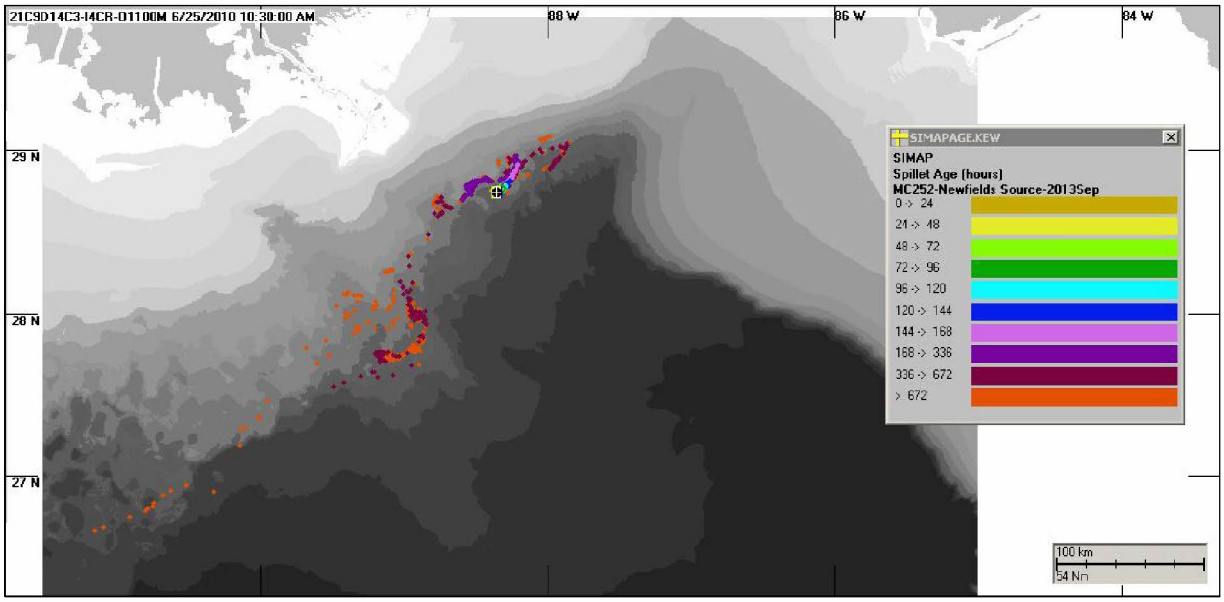

Figure F.3-23. Snapshot of the spillet trajectory, vertically integrated 1,100-1,400 m, with each spillet color-coded by age (i.e., hours since release) – June 25.

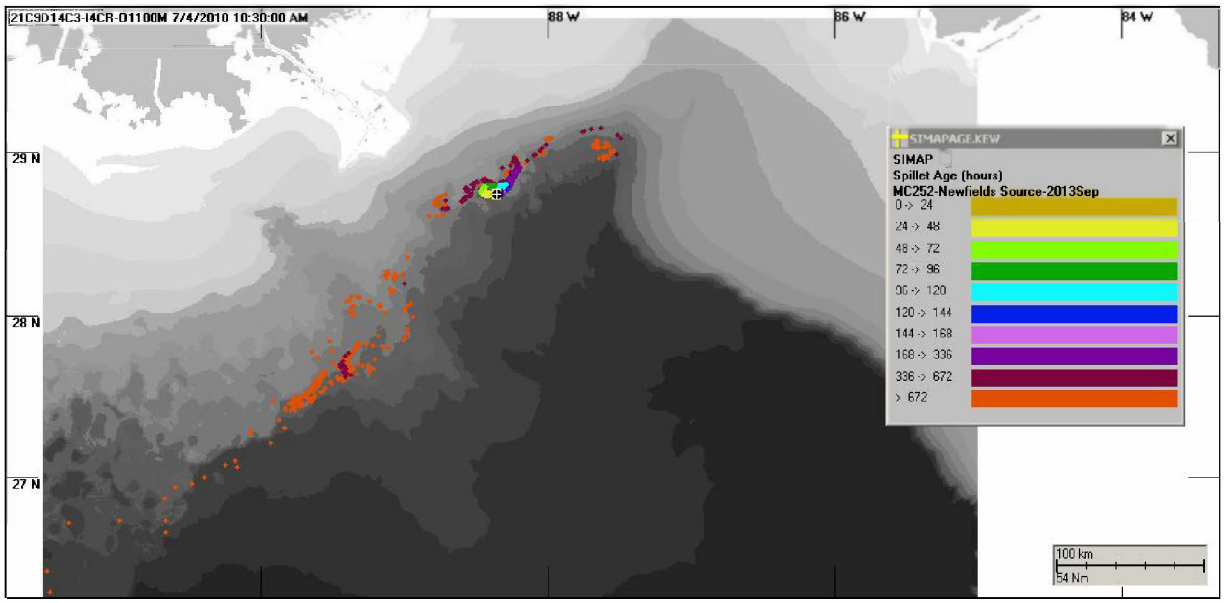

Figure F.3-24. Snapshot of the spillet trajectory, vertically integrated 1,100-1,400 m, with each spillet color-coded by age (i.e., hours since release) – July 4.

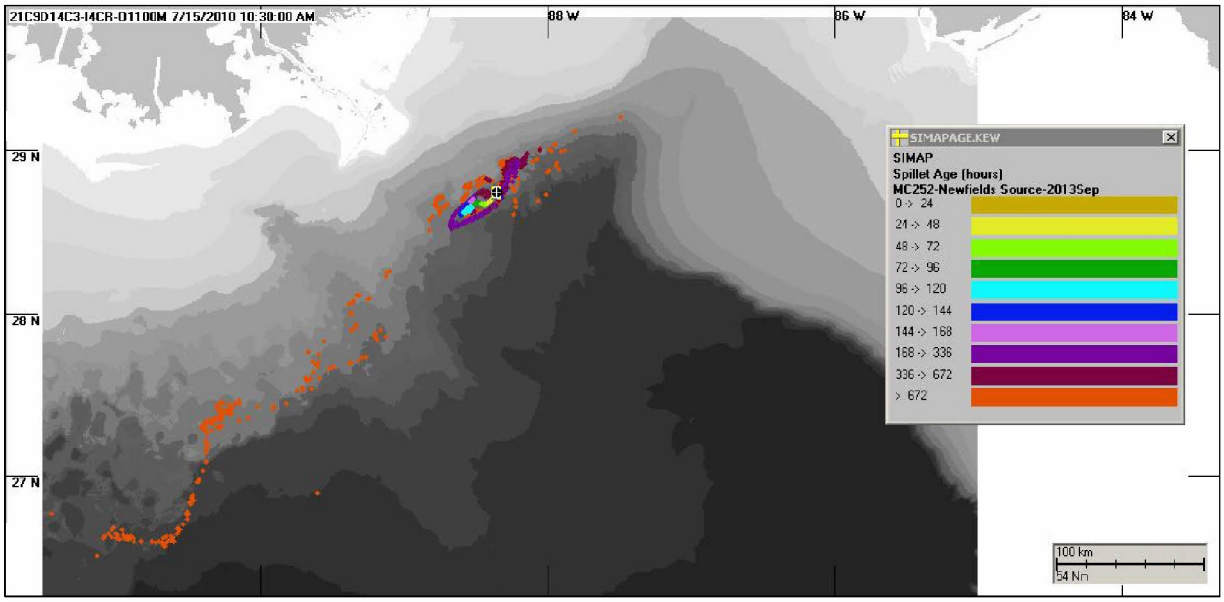

Figure F.3-25. Snapshot of the spillet trajectory, vertically integrated 1,100-1,400 m, with each spillet color-coded by age (i.e., hours since release) – July 15.

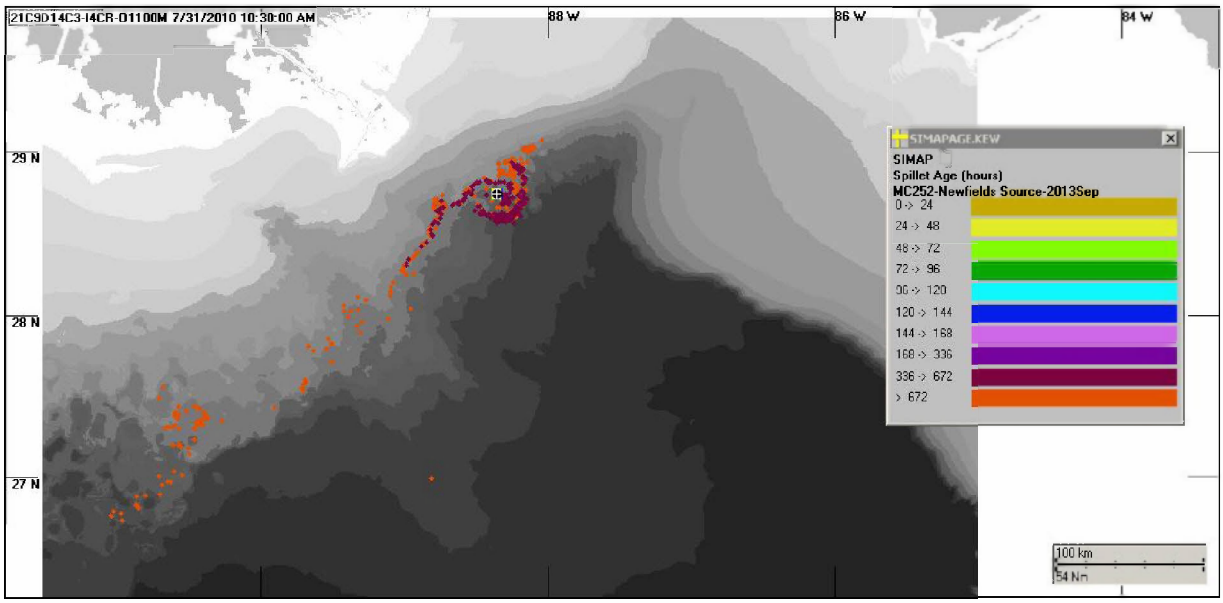

Figure F.3-26. Snapshot of the spillet trajectory, vertically integrated 1,100-1,400 m, with each spillet color-coded by age (i.e., hours since release) – July 31.

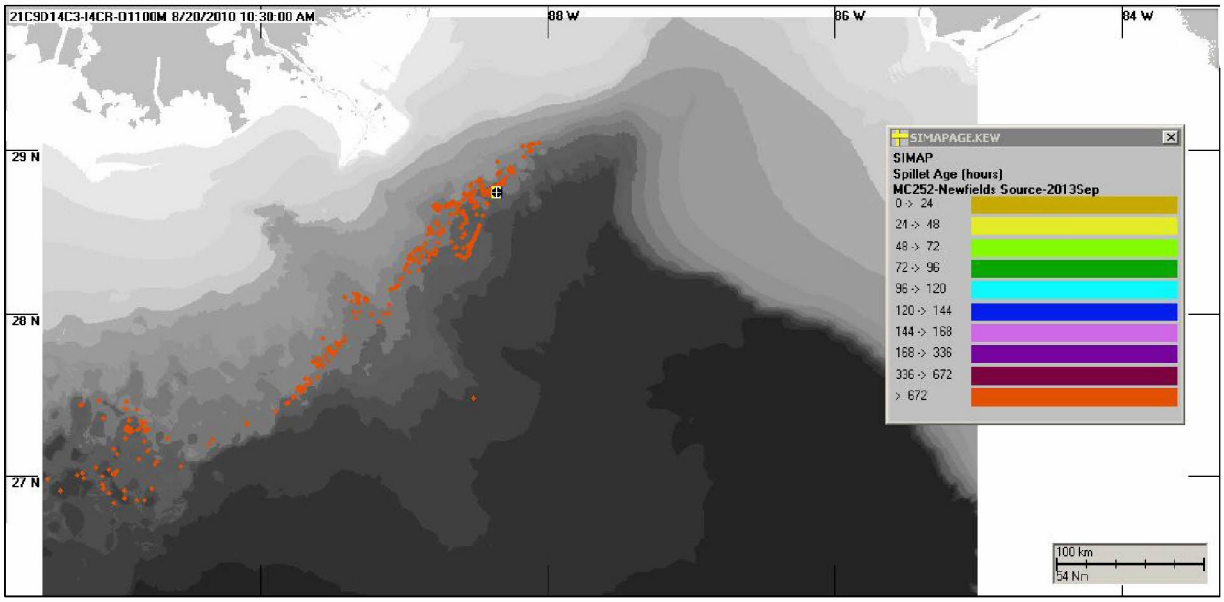

Figure F.3-27. Snapshot of the spillet trajectory, vertically integrated 1,100-1,400 m, with each spillet color-coded by age (i.e., hours since release) – Aug 20.

Technical Reports for Deepwater Horizon Water Column Injury Assessment

WC_TR.14: Modeling Oil Fate and Exposure Concentrations in the Deepwater Plume and Rising Oil Resulting from the Deepwater Horizon Oil Spill

Appendix G. Comparison of the Modeled Concentrations to Field Measurements

Authors: Deborah French McCay, Katherine Jayko, Zhengkai Li, Matthew Horn, Yong Kim, Tatsu Isaji, Deborah Crowley, Malcolm Spaulding, Lauren Decker, Cathleen Turner, Stefanie Zamorski, Jeremy Fontenault, Rachel Shmookler, and Jill Rowe

Revised: September 29, 2015
Project Number: 2011-144
RPS ASA 55 Village Square Drive, South Kingstown, RI 02879

Table of Contents

List of Figures

List of Tables

G.1 Introduction

This appendix provides figures that illustrate the comparison of oil fate model results using SIMAP with chemistry data from 2010 field samples. The discussion of these results is in the main report in Section 6.4.

Table G-1 summarizes the time domains (named as "OCR"#) used for the statistical analysis. The single latitude, longitude, and depth domain is:

Longitude: 88.628° to 88.130° W

Latitude: 28.51° to 28.96° N

Depth range: 40-1400m (divided into 5 depth intervals: 40-200m, 200-500m, 500-800m, 800-1100m, 1100-1400m)

Table G-1. Time domains used for the comparison of modeled to observed component concentrations.

Period	Events	Time	
		Start Time	End Time
OCR1	pre-top-kill	4/22/2010	5/26/2010
OCR2	top-kill, riser-cutting, and initial top-hat	5/26/2010	6/6/2010
OCR3	post-cut and collection	6/6/2010	7/15/2010
OCR4	post-cap	7/15/2010	9/30/2010

Figures in this Appendix graphically show comparisons of results for April 22 - July 15 2010 (OCR1 through OCR3), for both the no-current (Appendix G.2) and the IASROMS currents (Appendix G.3) simulations of the spill. Probability distributions of the modeled and measured concentrations are plotted in the left panel (cumulative frequency distribution) and the upper right panel (as a histogram of percentages of sample and model results in concentration intervals). The maps in the lower center and right panels plot the sample concentrations as circular symbols, colored according to the measured concentration, over top of modeled gridded concentrations. The left map shows the 95th percentile results, whereas the right map shows the maximum concentrations, for both samples and the model.

The oil components for which comparisons are shown herein are:

- AR1 (BTEX)
- AR5 (C0-C2 naphthalenes)
- AR6 (C3-C4 naphthalenes)
- AR7 (fluorenes & C0-C1 3-ring PAHs)
- AR8 (4-ring PAHs & C2-C3 3-ring PAHs)
- AR9 (soluble alkanes: low molecular weight alkanes, isoalkanes, cycloalkanes)

Figures G.2-1 to G.2-90 in Section G.2 show comparisons of modeled concentrations of each of the oil components to measurement data from chemistry samples for the Static Cone simulation. Figures G.3-1 to G.3-18 in Section G.3 show comparisons of modeled concentrations of each of the oil components to measurement data from chemistry samples for

the simulation using IAS ROMS currents as input. Only the 1100-1400m depth range is evaluated for the IAS ROMS simulation.

Explanation of the Content of Figures in Appendix G

The depth range listed in the figure legend specifies the investigated region as a layer of the ocean. Only chemistry samples and SIMAP prediction data within this depth interval and the geographic bounds (a 25 km by 25 km box centered on the wellhead) are presented.

Frequency distribution plots are used to compare overlaid modeled concentrations as calculated for the grid cells to measured samples. This is presented in a cumulative percentile format (left panel) and a histogram of percentage in each concentration bin indicated on the x-axis of the upper-right panel. The maximum modeled chemistry concentration for the time and depth interval is provided at the top of the left panel of each figure. Selected percentiles are plotted as horizontal lines (minty green) for representative values between 50-100%. If for example the observed chemistry, plotted as points in the left panel, falls to the left of the frequency distribution for the SIMAP model it indicates that the observed chemistry values as a whole are higher than the modeled values.

In the top right panel of each figure, a histogram of binned chemistry concentrations (μg/L) for observed samples (blue) and gridded model results (green) is plotted as the percentage of the total number of samples/grid cells. Results have been binned into concentrations ranges. The first bar on the left represents all concentrations between 0.1 and 0.5 μg/L. Note the range increases non-linearly and that the sum of all percentages may not add up to 100%, as a large number of observed samples and modeled grid cells may fall below 0.1 μg/L.

The two spatial maps in in each figure show the 95th percentile and maximum modeled concentrations in each horizontal (500 m x 500 m) cell of the 25 km by 25 km domain, evaluated over the time and depth interval. Overlaid are dots indicating the locations and concentrations measured in the samples. Open symbols indicate chemical concentrations below the analytical detection limit (i.e., they represent the qualitative presence of an analyte presented as the Method Detection Limit (MDL) for that component grouping; however the concentration was not high enough to report a quantified value). The right map shows the maximum model concentrations over the (OCR) time interval and the depth range. The modeled concentration in a horizontal grid cell for each of the 20-m vertical layers and each time step is considered a sample for the model at the location in the map. The left map shows the 95th percentile model results compared to the chemistry measurement. Note that the variation in the spatial distribution of the chemistry sample measurements is typically much higher than that shown by the model results in the maps, particularly when the model result is presented as a maximum (or 95^{th} percentile) over time. However, in the probability distributions (left and upper right panels), where model-predicted concentrations for all grid cells and time steps in the overall depth range are treated as the set of predictions, the variance of the modeled results is completely characterized.

For further detail and discussion, refer to the main report, Section 6.4.

Example Evaluation for Figure G.2-1.

Figure G.2-1 compares modeled BTEX concentrations to measurements from chemistry samples for April 22 – May 26, 2010 in 1100-1400m. The modeled BTEX at low concentrations

within the frequency distribution of all samples in this 500 m x 500 m x 300 m box (comprised of fifteen 20 m layers) were high compared to observed data, while modeled concentrations at the high end under-represented what was measured. From the frequency distribution plot, about 25% of the modeled concentrations were below the MDL (< 10-3 µg/L), whereas in fact about 55% of the measured samples were below the MDL. Above that threshold, all of the measured sample's concentrations were greater than the modeled values.

From the two overhead maps, the left one (at the 95th percentile of the maximum 3138.7 µg/L observed concentration) shows the same overall footprint, but more of it is made up of lower-concentration (darker blue 10-1 µg/L concentrations compared to the right one that has a predominance of 101 and 102 µg/L concentrations. Finally, most of the measured samples (small green circles) were within the modeled footprint over the 300 m water column, but they were generally in the 102 to 103 µg/L range compared to the modeled 101 µg/L concentrations.

G.2 Static Cone Simulation

G.2.1 April 22 – May 26, 2010

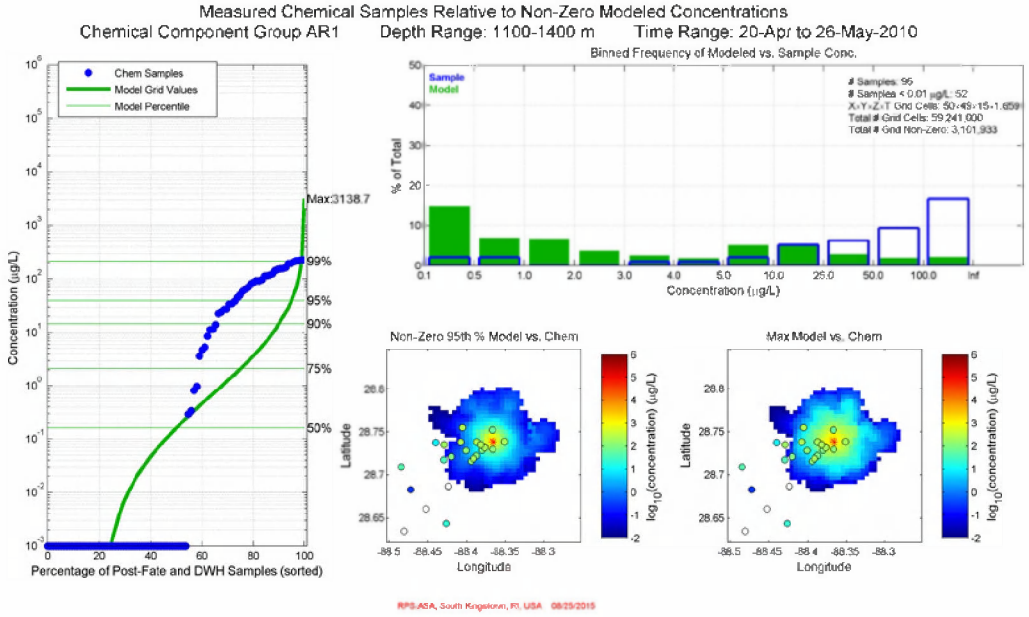

Figure G.2-1. Comparison of total (in-droplet + dissolved) concentrations (µg/L) produced by the Static Cone simulation to measurements from chemistry samples for April 22 – May 26, 2010 in 1100-1400m: AR1 component (BTEX). Left: Cumulative frequency distribution of concentrations for observed chemistry samples and gridded model results. The maximum modeled chemistry concentration is provided at the top of the panel. Top right: Histogram of binned concentrations for observed samples (blue) and gridded model results (green) plotted as the percentage of the total number of samples/grid cells. Center bottom and bottom right: Spatial color maps of the 95th percentile and maximum (respectively) modeled concentration within each grid cell over the time interval, overlaid with dots representing the chemistry sample observations. Open symbols indicate chemical concentrations below the analytical detection limit.

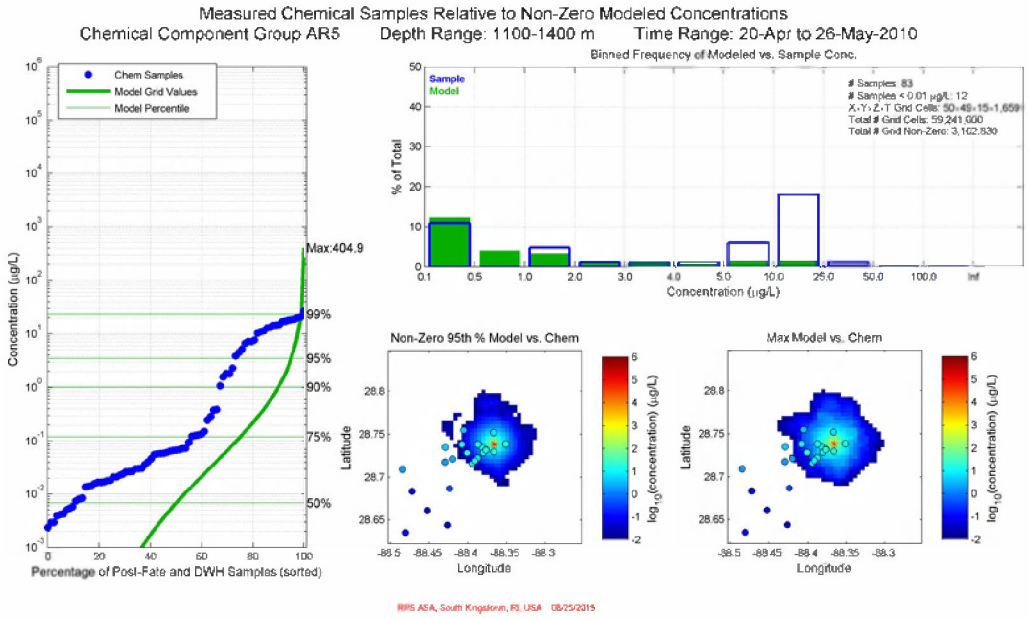

Figure G.2-2. Comparison of total (in-droplet + dissolved) concentrations (µg/L) produced by the Static Cone simulation to measurements from chemistry samples for April 22 – May 26, 2010 in 1100-1400m: AR5 component (C0-C2 naphthalenes). Left: Cumulative frequency distribution of concentrations for observed chemistry samples and gridded model results. The maximum modeled chemistry concentration is provided at the top of the panel. Top right: Histogram of binned concentrations for observed samples (blue) and gridded model results (green) plotted as the percentage of the total number of samples/grid cells. Center bottom and bottom right: Spatial color maps of the 95th percentile and maximum (respectively) modeled concentration within each grid cell over the time interval, overlaid with dots representing the chemistry sample observations. Open symbols indicate chemical concentrations below the analytical detection limit.

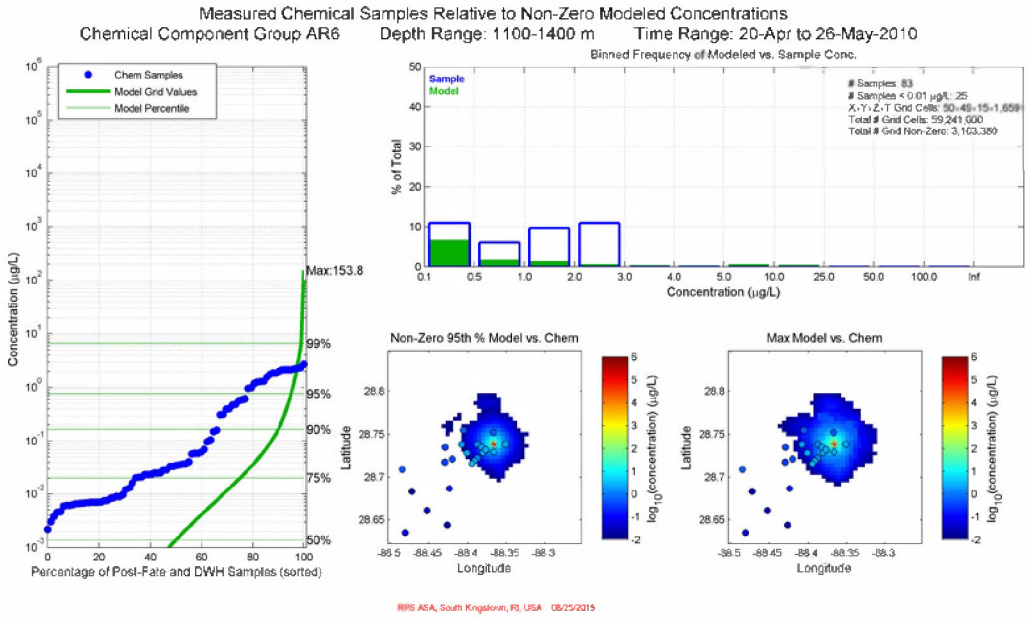

Figure G.2-3. Comparison of total (in-droplet + dissolved) concentrations (µg/L) produced by the Static Cone simulation to measurements from chemistry samples for April 22 – May 26, 2010 in 1100-1400m: AR6 component (C3-C4 naphthalenes). Left: Cumulative frequency distribution of concentrations for observed chemistry samples and gridded model results. The maximum modeled chemistry concentration is provided at the top of the panel. Top right: Histogram of binned concentrations for observed samples (blue) and gridded model results (green) plotted as the percentage of the total number of samples/grid cells. Center bottom and bottom right: Spatial color maps of the 95th percentile and maximum (respectively) modeled concentration within each grid cell over the time interval, overlaid with dots representing the chemistry sample observations. Open symbols indicate chemical concentrations below the analytical detection limit.

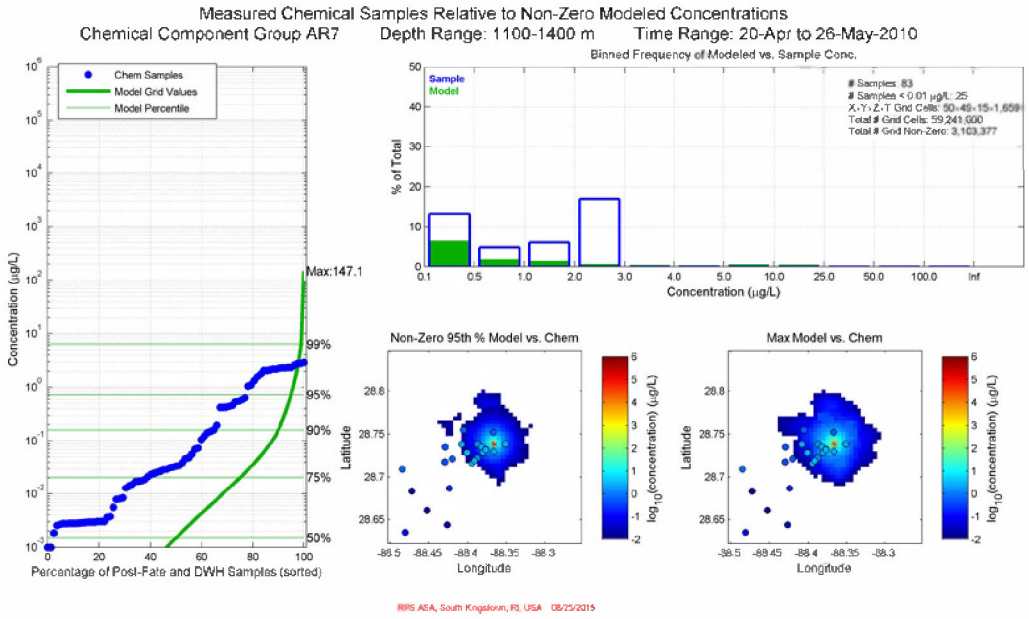

Figure G.2-4. Comparison of total (in-droplet + dissolved) concentrations (µg/L) produced by the Static Cone simulation to measurements from chemistry samples for April 22 – May 26, 2010 in 1100-1400m: AR7 component (fluorenes & C0-C1 3-ring PAHs). Left: Cumulative frequency distribution of concentrations for observed chemistry samples and gridded model results. The maximum modeled chemistry concentration is provided at the top of the panel. Top right: Histogram of binned concentrations for observed samples (blue) and gridded model results (green) plotted as the percentage of the total number of samples/grid cells. Center bottom and bottom right: Spatial color maps of the 95th percentile and maximum (respectively) modeled concentration within each grid cell over the time interval, overlaid with dots representing the chemistry sample observations. Open symbols indicate chemical concentrations below the analytical detection limit.

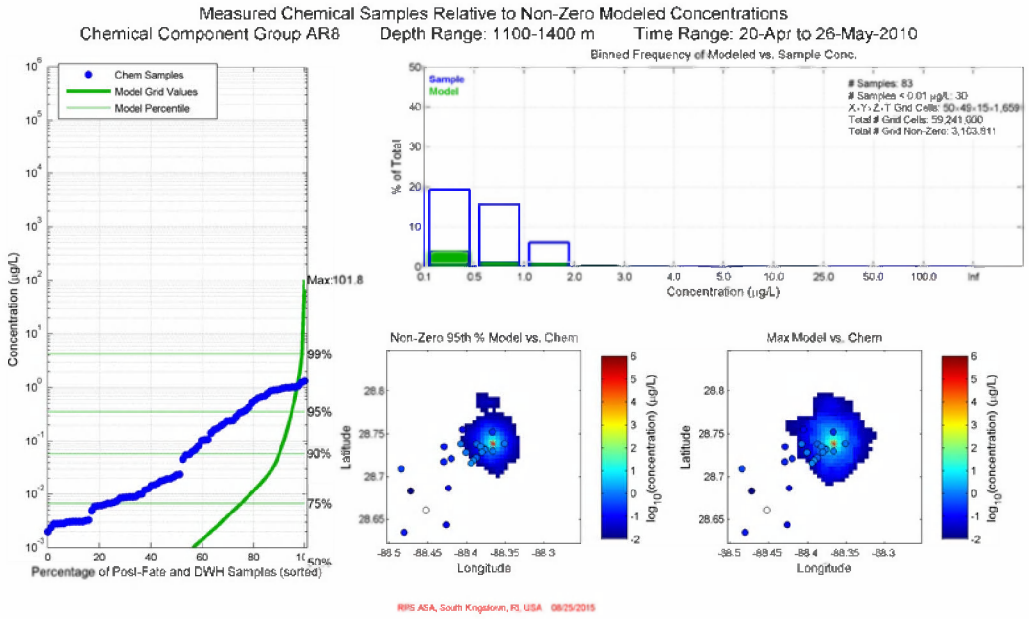

Figure G.2-5. Comparison of total (in-droplet + dissolved) concentrations (µg/L) produced by the Static Cone simulation to measurements from chemistry samples for April 22 – May 26, 2010 in 1100-1400m: AR8 component (4-ring PAHs & C2-C3 3-ring PAHs). Left: Cumulative frequency distribution of concentrations for observed chemistry samples and gridded model results. The maximum modeled chemistry concentration is provided at the top of the panel. Top right: Histogram of binned concentrations for observed samples (blue) and gridded model results (green) plotted as the percentage of the total number of samples/grid cells. Center bottom and bottom right: Spatial color maps of the 95th percentile and maximum (respectively) modeled concentration within each grid cell over the time interval, overlaid with dots representing the chemistry sample observations. Open symbols indicate chemical concentrations below the analytical detection limit.

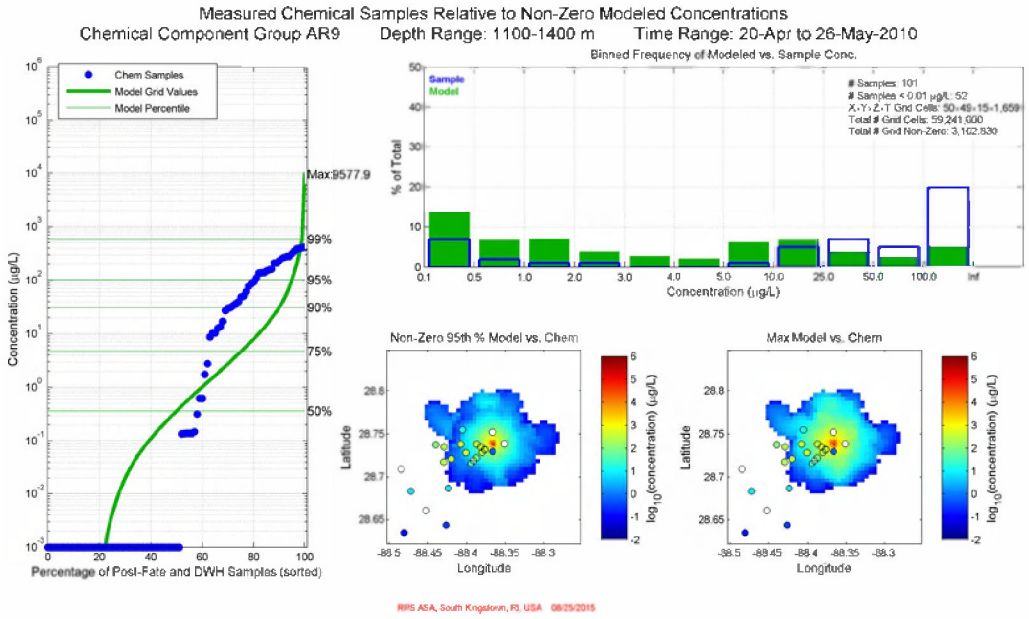

Figure G.2-6. Comparison of total (in-droplet + dissolved) concentrations (µg/L) produced by the Static Cone simulation to measurements from chemistry samples for April 22 – May 26, 2010 in 1100-1400m: AR9 component (soluble alkanes). Left: Cumulative frequency distribution of concentrations for observed chemistry samples and gridded model results. The maximum modeled chemistry concentration is provided at the top of the panel. Top right: Histogram of binned concentrations for observed samples (blue) and gridded model results (green) plotted as the percentage of the total number of samples/grid cells. Center bottom and bottom right: Spatial color maps of the 95th percentile and maximum (respectively) modeled concentration within each grid cell over the time interval, overlaid with dots representing the chemistry sample observations. Open symbols indicate chemical concentrations below the analytical detection limit.

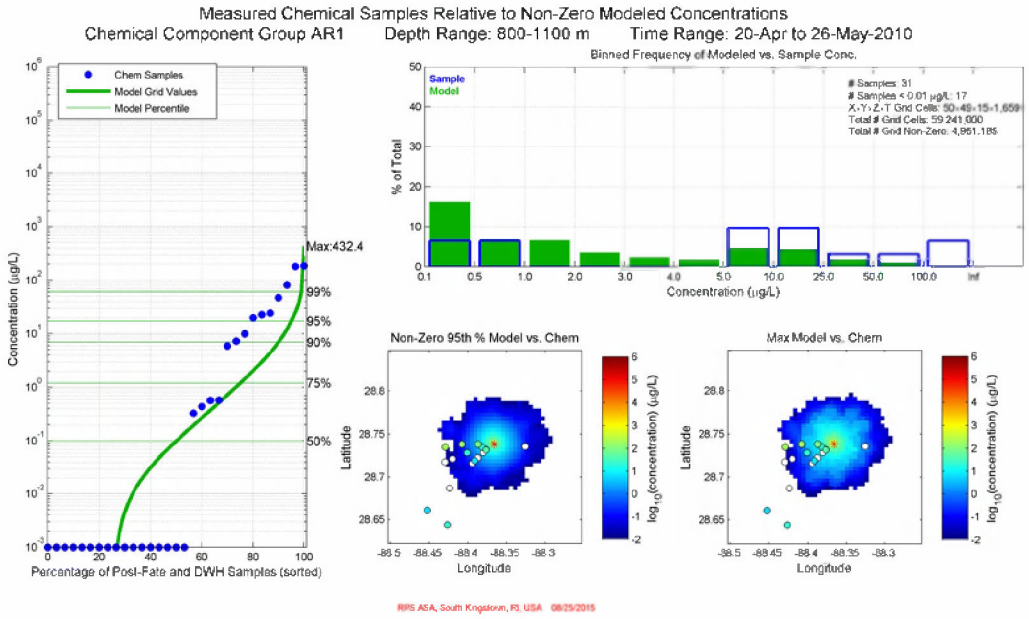

Figure G.2-7. Comparison of total (in-droplet + dissolved) concentrations (µg/L) produced by the Static Cone simulation to measurements from chemistry samples for April 22 – May 26, 2010 in 800-1100m: AR1 component (BTEX). Left: Cumulative frequency distribution of concentrations for observed chemistry samples and gridded model results. The maximum modeled chemistry concentration is provided at the top of the panel. Top right: Histogram of binned concentrations for observed samples (blue) and gridded model results (green) plotted as the percentage of the total number of samples/grid cells. Center bottom and bottom right: Spatial color maps of the 95th percentile and maximum (respectively) modeled concentration within each grid cell over the time interval, overlaid with dots representing the chemistry sample observations. Open symbols indicate chemical concentrations below the analytical detection limit.

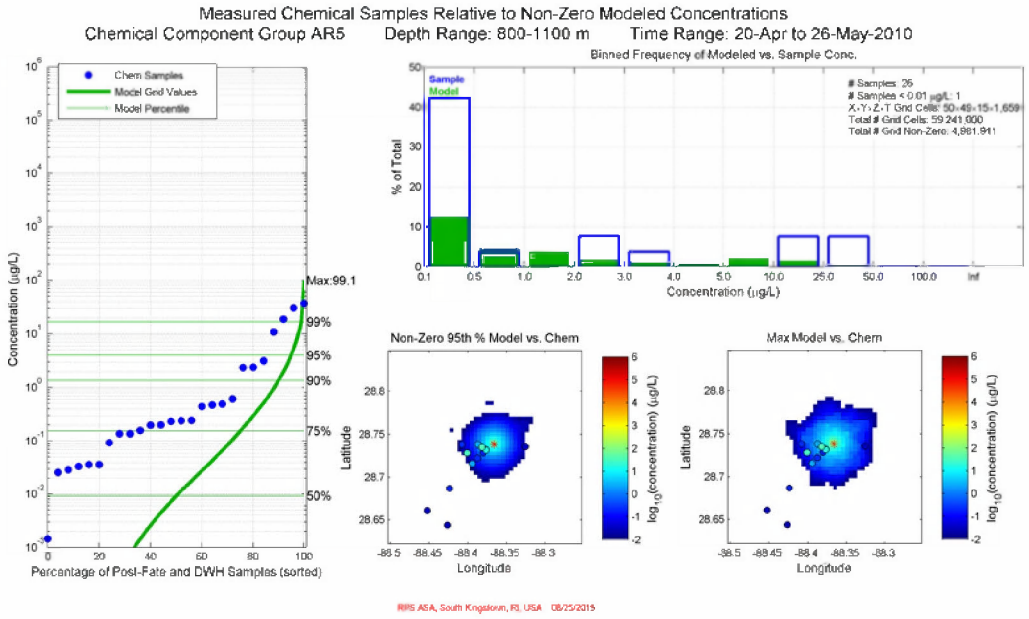

Figure G.2-8. Comparison of total (in-droplet + dissolved) concentrations (µg/L) produced by the Static Cone simulation to measurements from chemistry samples for April 22 – May 26, 2010 in 800-1100m: AR5 component (C0-C2 naphthalenes). Left: Cumulative frequency distribution of concentrations for observed chemistry samples and gridded model results. The maximum modeled chemistry concentration is provided at the top of the panel. Top right: Histogram of binned concentrations for observed samples (blue) and gridded model results (green) plotted as the percentage of the total number of samples/grid cells. Center bottom and bottom right: Spatial color maps of the 95th percentile and maximum (respectively) modeled concentration within each grid cell over the time interval, overlaid with dots representing the chemistry sample observations. Open symbols indicate chemical concentrations below the analytical detection limit.

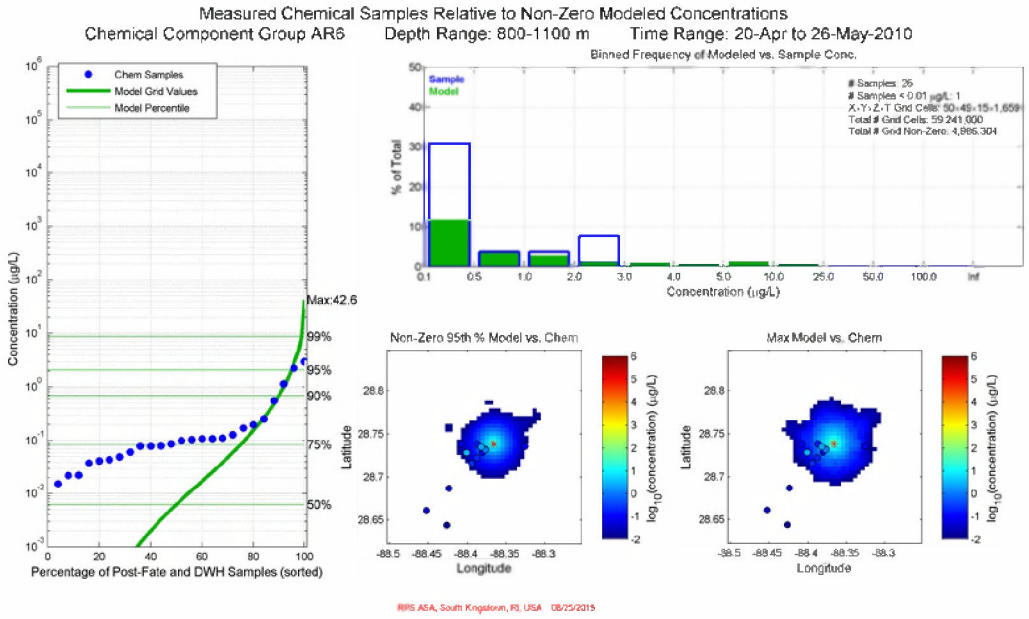

Figure G.2-9. Comparison of total (in-droplet + dissolved) concentrations (µg/L) produced by the Static Cone simulation to measurements from chemistry samples for April 22 – May 26, 2010 in 800-1100m: AR6 component (C3-C4 naphthalenes). Left: Cumulative frequency distribution of concentrations for observed chemistry samples and gridded model results. The maximum modeled chemistry concentration is provided at the top of the panel. Top right: Histogram of binned concentrations for observed samples (blue) and gridded model results (green) plotted as the percentage of the total number of samples/grid cells. Center bottom and bottom right: Spatial color maps of the 95th percentile and maximum (respectively) modeled concentration within each grid cell over the time interval, overlaid with dots representing the chemistry sample observations. Open symbols indicate chemical concentrations below the analytical detection limit.

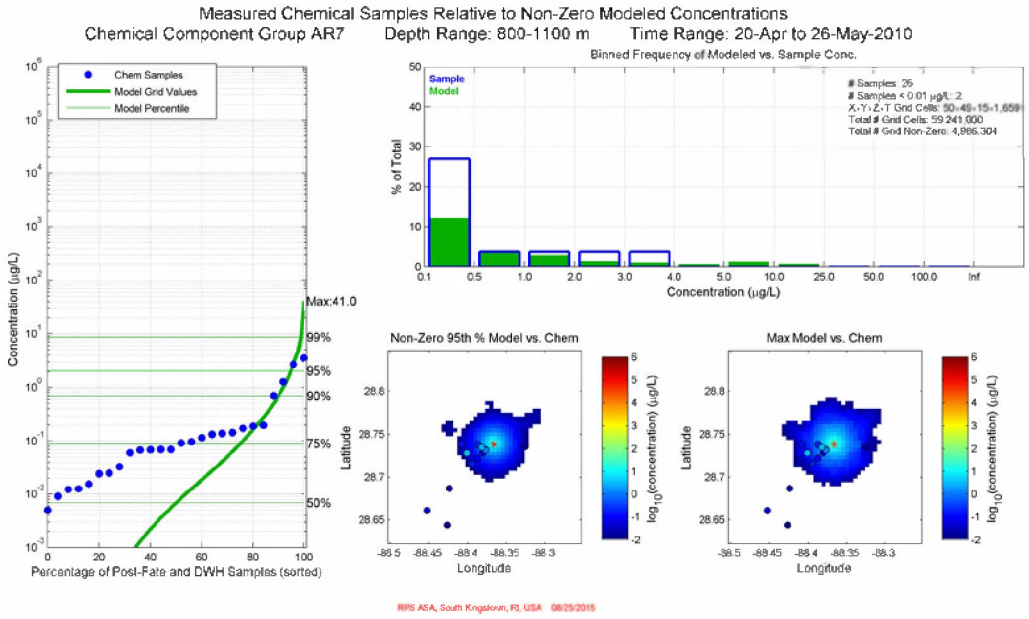

Figure G.2-10. Comparison of total (in-droplet + dissolved) concentrations (µg/L) produced by the Static Cone simulation to measurements from chemistry samples for April 22 – May 26, 2010 in 800-1100m: AR7 component (fluorenes & C0-C1 3-ring PAHs). Left: Cumulative frequency distribution of concentrations for observed chemistry samples and gridded model results. The maximum modeled chemistry concentration is provided at the top of the panel. Top right: Histogram of binned concentrations for observed samples (blue) and gridded model results (green) plotted as the percentage of the total number of samples/grid cells. Center bottom and bottom right: Spatial color maps of the 95th percentile and maximum (respectively) modeled concentration within each grid cell over the time interval, overlaid with dots representing the chemistry sample observations. Open symbols indicate chemical concentrations below the analytical detection limit.

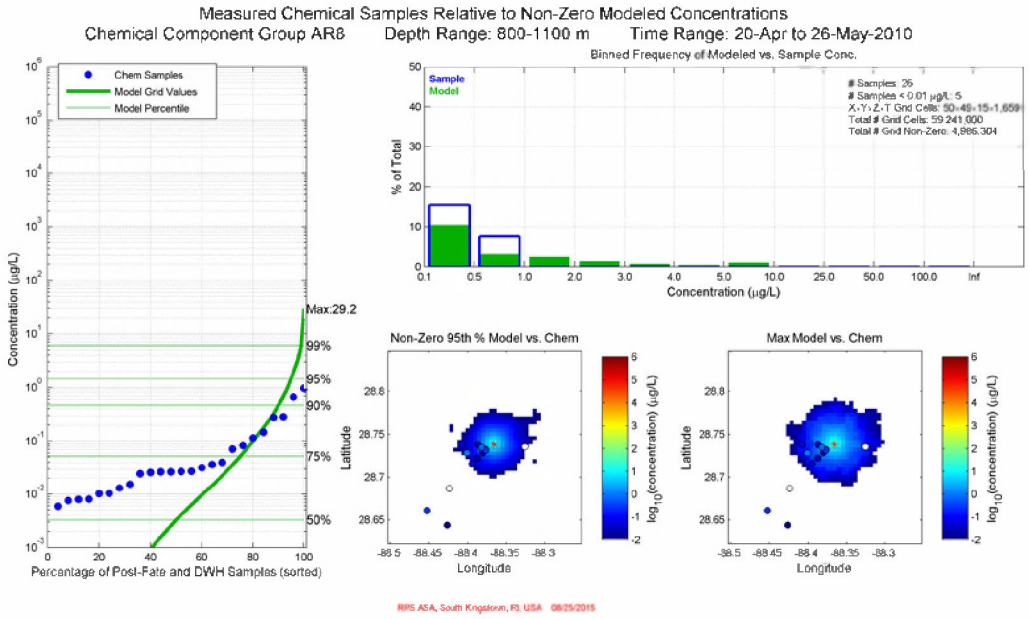

Figure G.2-11. Comparison of total (in-droplet + dissolved) concentrations (µg/L) produced by the Static Cone simulation to measurements from chemistry samples for April 22 – May 26, 2010 in 800-1100m: AR8 component (4-ring PAHs & C2-C3 3-ring PAHs). Left: Cumulative frequency distribution of concentrations for observed chemistry samples and gridded model results. The maximum modeled chemistry concentration is provided at the top of the panel. Top right: Histogram of binned concentrations for observed samples (blue) and gridded model results (green) plotted as the percentage of the total number of samples/grid cells. Center bottom and bottom right: Spatial color maps of the 95th percentile and maximum (respectively) modeled concentration within each grid cell over the time interval, overlaid with dots representing the chemistry sample observations. Open symbols indicate chemical concentrations below the analytical detection limit.

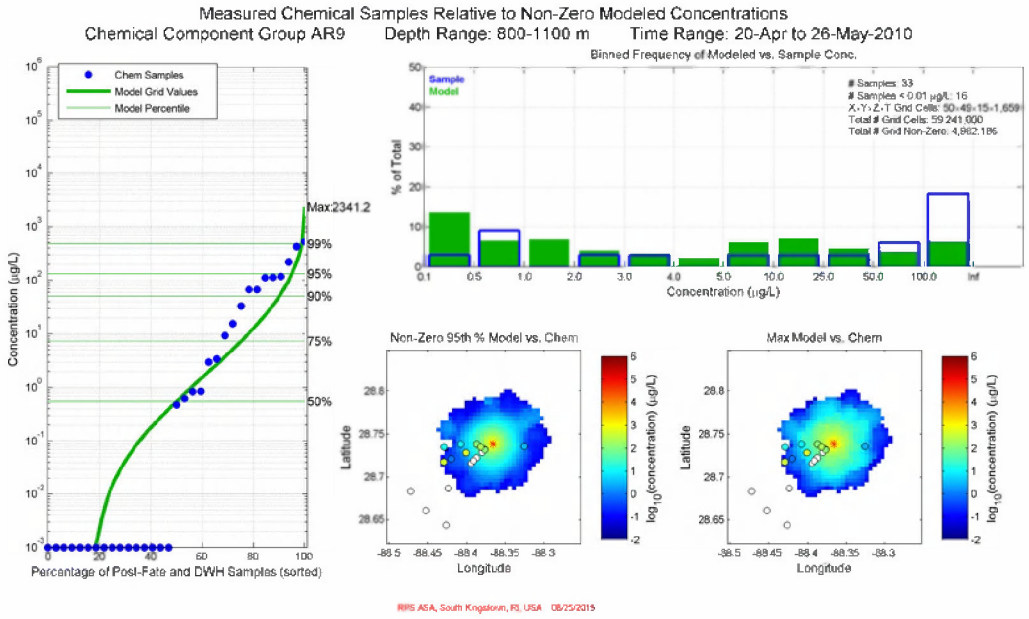

Figure G.2-12. Comparison of total (in-droplet + dissolved) concentrations (µg/L) produced by the Static Cone simulation to measurements from chemistry samples for April 22 – May 26, 2010 in 800-1100m: AR9 component (soluble alkanes). Left: Cumulative frequency distribution of concentrations for observed chemistry samples and gridded model results. The maximum modeled chemistry concentration is provided at the top of the panel. Top right: Histogram of binned concentrations for observed samples (blue) and gridded model results (green) plotted as the percentage of the total number of samples/grid cells. Center bottom and bottom right: Spatial color maps of the 95th percentile and maximum (respectively) modeled concentration within each grid cell over the time interval, overlaid with dots representing the chemistry sample observations. Open symbols indicate chemical concentrations below the analytical detection limit.

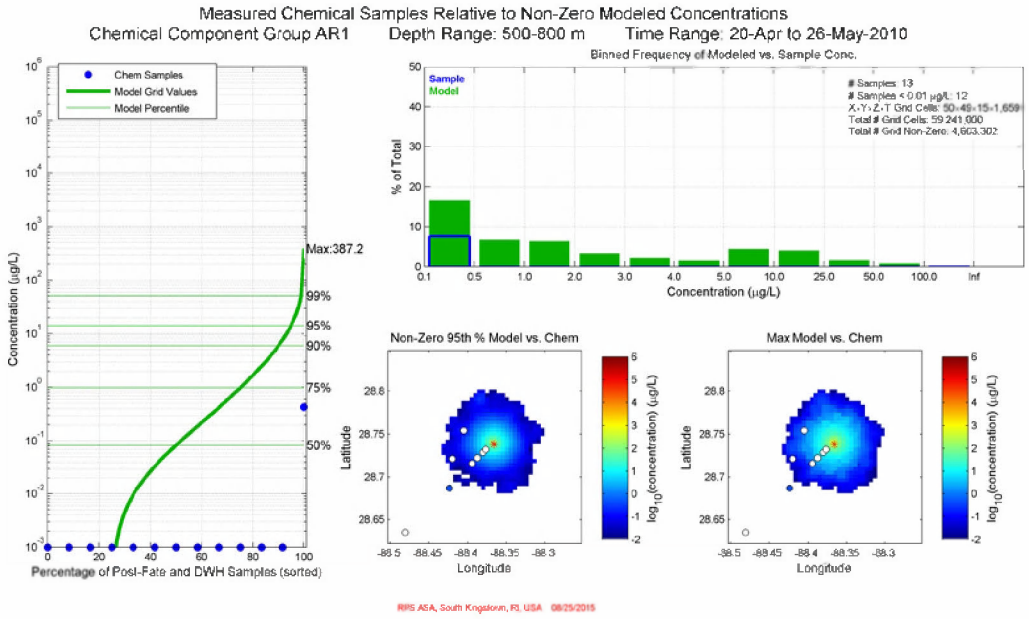

Figure G.2-13. Comparison of total (in-droplet + dissolved) concentrations (µg/L) produced by the Static Cone simulation to measurements from chemistry samples for April 22 – May 26, 2010 in 500-800m: AR1 component (BTEX). Left: Cumulative frequency distribution of concentrations for observed chemistry samples and gridded model results. The maximum modeled chemistry concentration is provided at the top of the panel. Top right: Histogram of binned concentrations for observed samples (blue) and gridded model results (green) plotted as the percentage of the total number of samples/grid cells. Center bottom and bottom right: Spatial color maps of the 95th percentile and maximum (respectively) modeled concentration within each grid cell over the time interval, overlaid with dots representing the chemistry sample observations. Open symbols indicate chemical concentrations below the analytical detection limit.

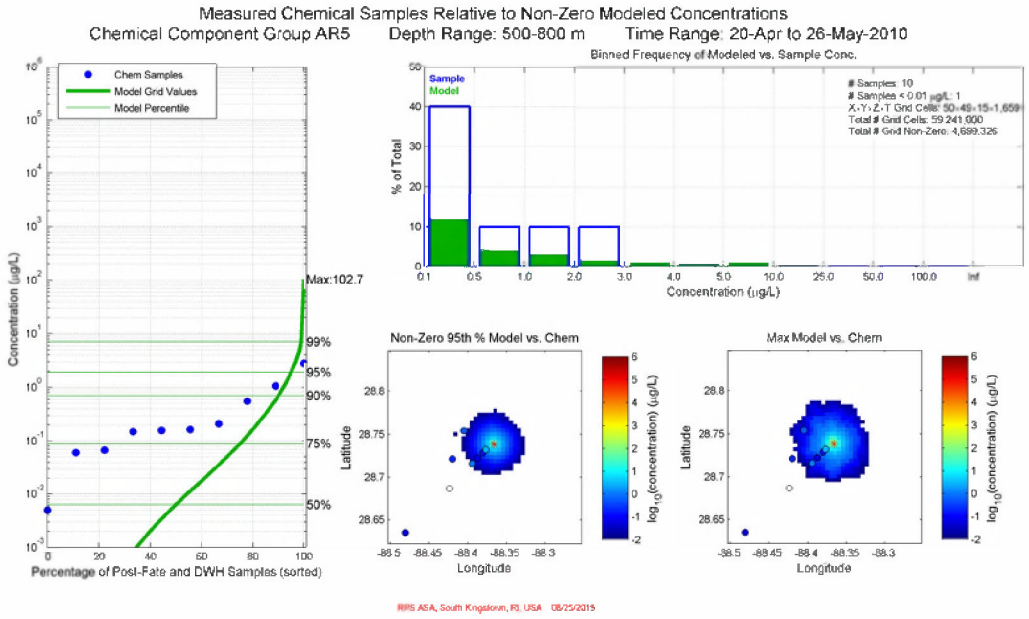

Figure G.2-14. Comparison of total (in-droplet + dissolved) concentrations (µg/L) produced by the Static Cone simulation to measurements from chemistry samples for April 22 – May 26, 2010 in 500-800m: AR5 component (C0-C2 naphthalenes). Left: Cumulative frequency distribution of concentrations for observed chemistry samples and gridded model results. The maximum modeled chemistry concentration is provided at the top of the panel. Top right: Histogram of binned concentrations for observed samples (blue) and gridded model results (green) plotted as the percentage of the total number of samples/grid cells. Center bottom and bottom right: Spatial color maps of the 95th percentile and maximum (respectively) modeled concentration within each grid cell over the time interval, overlaid with dots representing the chemistry sample observations. Open symbols indicate chemical concentrations below the analytical detection limit.

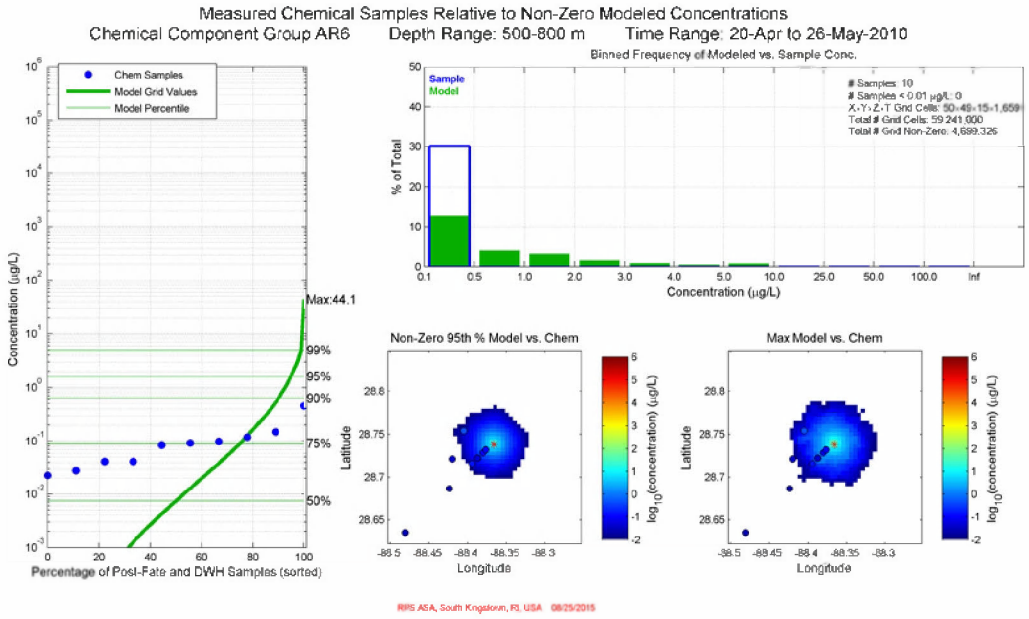

Figure G.2-15. Comparison of total (in-droplet + dissolved) concentrations (µg/L) produced by the Static Cone simulation to measurements from chemistry samples for April 22 – May 26, 2010 in 500-800m: AR6 component (C3-C4 naphthalenes). Left: Cumulative frequency distribution of concentrations for observed chemistry samples and gridded model results. The maximum modeled chemistry concentration is provided at the top of the panel. Top right: Histogram of binned concentrations for observed samples (blue) and gridded model results (green) plotted as the percentage of the total number of samples/grid cells. Center bottom and bottom right: Spatial color maps of the 95th percentile and maximum (respectively) modeled concentration within each grid cell over the time interval, overlaid with dots representing the chemistry sample observations. Open symbols indicate chemical concentrations below the analytical detection limit.

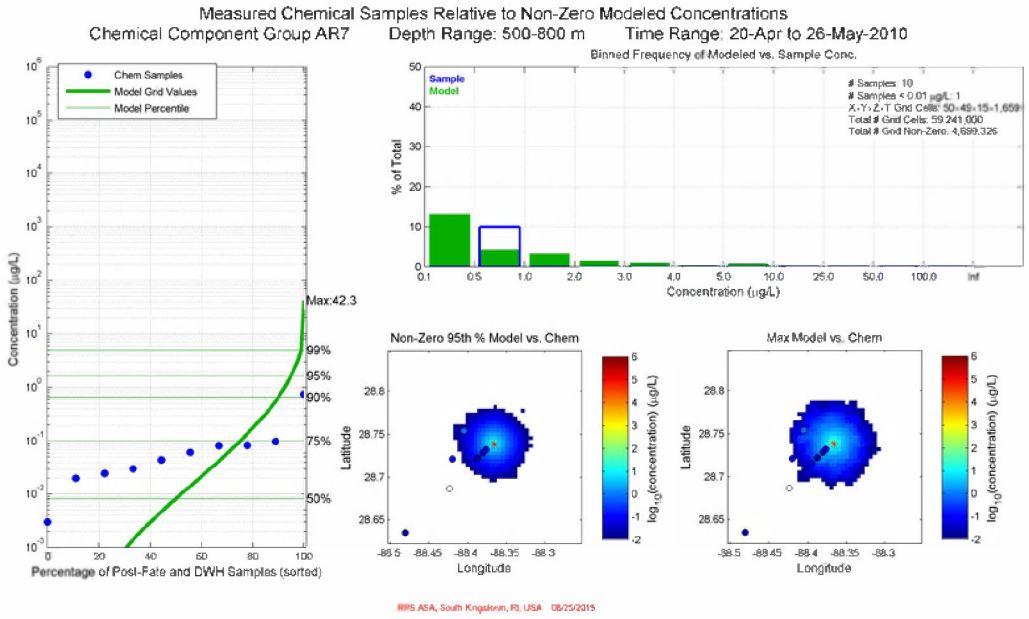

Figure G.2-16. Comparison of total (in-droplet + dissolved) concentrations (µg/L) produced by the Static Cone simulation to measurements from chemistry samples for April 22 – May 26, 2010 in 500-800m: AR7 component (fluorenes & C0-C1 3-ring PAHs). Left: Cumulative frequency distribution of concentrations for observed chemistry samples and gridded model results. The maximum modeled chemistry concentration is provided at the top of the panel. Top right: Histogram of binned concentrations for observed samples (blue) and gridded model results (green) plotted as the percentage of the total number of samples/grid cells. Center bottom and bottom right: Spatial color maps of the 95th percentile and maximum (respectively) modeled concentration within each grid cell over the time interval, overlaid with dots representing the chemistry sample observations. Open symbols indicate chemical concentrations below the analytical detection limit.

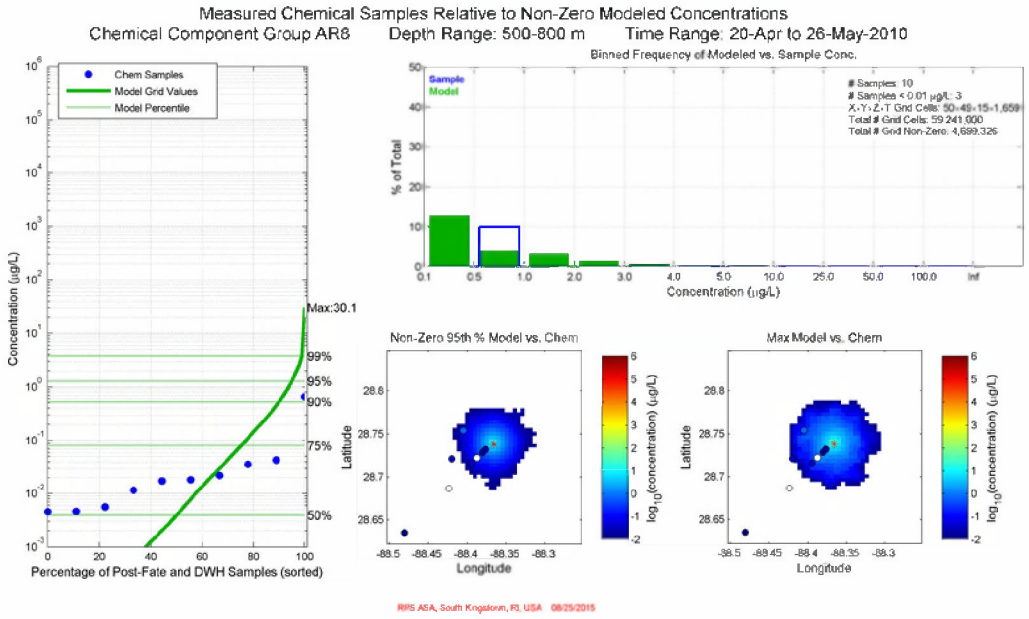

Figure G.2-17. Comparison of total (in-droplet + dissolved) concentrations (µg/L) produced by the Static Cone simulation to measurements from chemistry samples for April 22 – May 26, 2010 in 500-800m: AR8 component (4-ring PAHs & C2-C3 3-ring PAHs). Left: Cumulative frequency distribution of concentrations for observed chemistry samples and gridded model results. The maximum modeled chemistry concentration is provided at the top of the panel. Top right: Histogram of binned concentrations for observed samples (blue) and gridded model results (green) plotted as the percentage of the total number of samples/grid cells. Center bottom and bottom right: Spatial color maps of the 95th percentile and maximum (respectively) modeled concentration within each grid cell over the time interval, overlaid with dots representing the chemistry sample observations. Open symbols indicate chemical concentrations below the analytical detection limit.

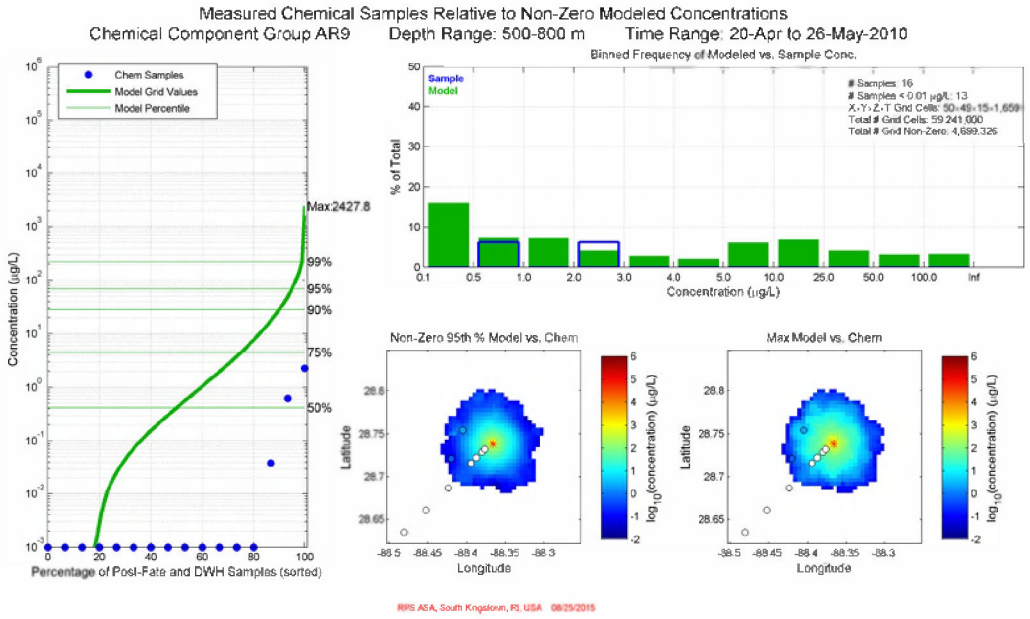

Figure G.2-18. Comparison of total (in-droplet + dissolved) concentrations (µg/L) produced by the Static Cone simulation to measurements from chemistry samples for April 22 – May 26, 2010 in 500-800m: AR9 component (soluble alkanes). Left: Cumulative frequency distribution of concentrations for observed chemistry samples and gridded model results. The maximum modeled chemistry concentration is provided at the top of the panel. Top right: Histogram of binned concentrations for observed samples (blue) and gridded model results (green) plotted as the percentage of the total number of samples/grid cells. Center bottom and bottom right: Spatial color maps of the 95th percentile and maximum (respectively) modeled concentration within each grid cell over the time interval, overlaid with dots representing the chemistry sample observations. Open symbols indicate chemical concentrations below the analytical detection limit.

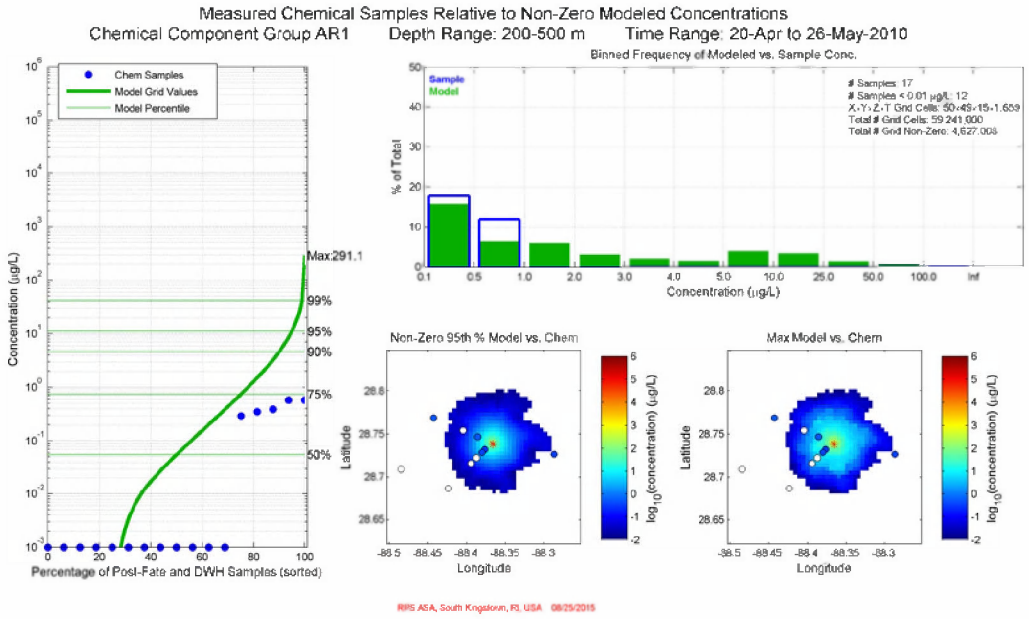

Figure G.2-19. Comparison of total (in-droplet + dissolved) concentrations (µg/L) produced by the Static Cone simulation to measurements from chemistry samples for April 22 – May 26, 2010 in 200-500m: AR1 component (BTEX). Left: Cumulative frequency distribution of concentrations for observed chemistry samples and gridded model results. The maximum modeled chemistry concentration is provided at the top of the panel. Top right: Histogram of binned concentrations for observed samples (blue) and gridded model results (green) plotted as the percentage of the total number of samples/grid cells. Center bottom and bottom right: Spatial color maps of the 95th percentile and maximum (respectively) modeled concentration within each grid cell over the time interval, overlaid with dots representing the chemistry sample observations. Open symbols indicate chemical concentrations below the analytical detection limit.

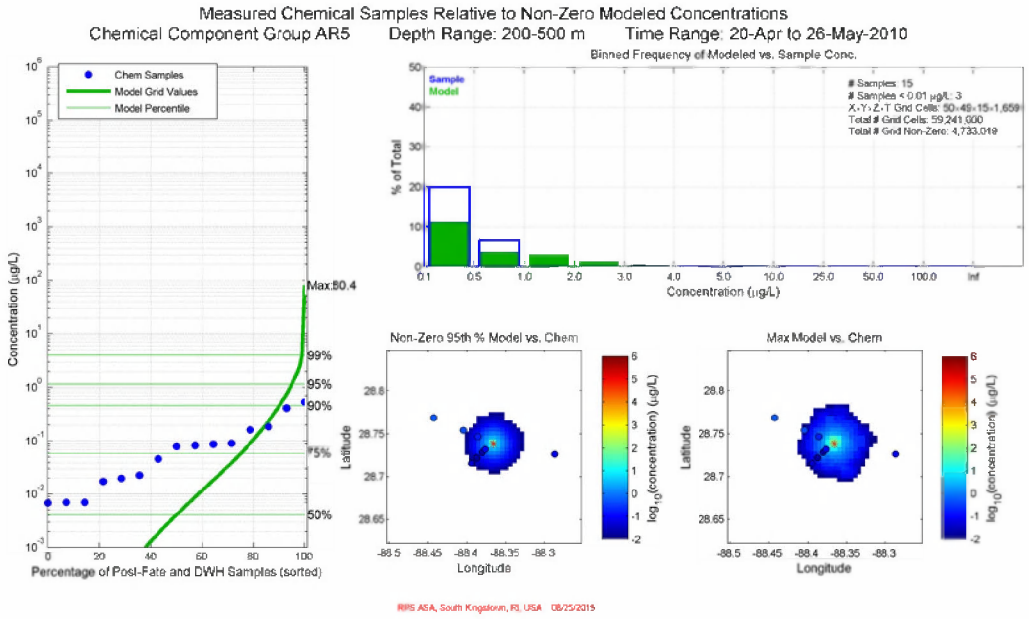

Figure G.2-20. Comparison of total (in-droplet + dissolved) concentrations (µg/L) produced by the Static Cone simulation to measurements from chemistry samples for April 22 – May 26, 2010 in 200-500m: AR5 component (C0-C2 naphthalenes). Left: Cumulative frequency distribution of concentrations for observed chemistry samples and gridded model results. The maximum modeled chemistry concentration is provided at the top of the panel. Top right: Histogram of binned concentrations for observed samples (blue) and gridded model results (green) plotted as the percentage of the total number of samples/grid cells. Center bottom and bottom right: Spatial color maps of the 95th percentile and maximum (respectively) modeled concentration within each grid cell over the time interval, overlaid with dots representing the chemistry sample observations. Open symbols indicate chemical concentrations below the analytical detection limit.

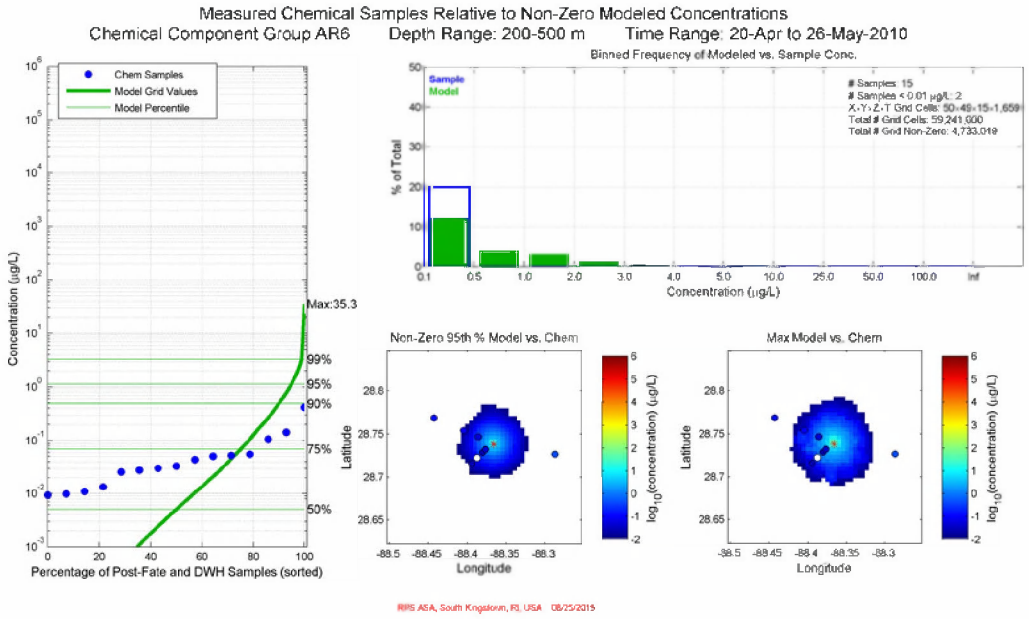

Figure G.2-21. Comparison of total (in-droplet + dissolved) concentrations (µg/L) produced by the Static Cone simulation to measurements from chemistry samples for April 22 – May 26, 2010 in 200-500m: AR6 component (C3-C4 naphthalenes). Left: Cumulative frequency distribution of concentrations for observed chemistry samples and gridded model results. The maximum modeled chemistry concentration is provided at the top of the panel. Top right: Histogram of binned concentrations for observed samples (blue) and gridded model results (green) plotted as the percentage of the total number of samples/grid cells. Center bottom and bottom right: Spatial color maps of the 95th percentile and maximum (respectively) modeled concentration within each grid cell over the time interval, overlaid with dots representing the chemistry sample observations. Open symbols indicate chemical concentrations below the analytical detection limit.

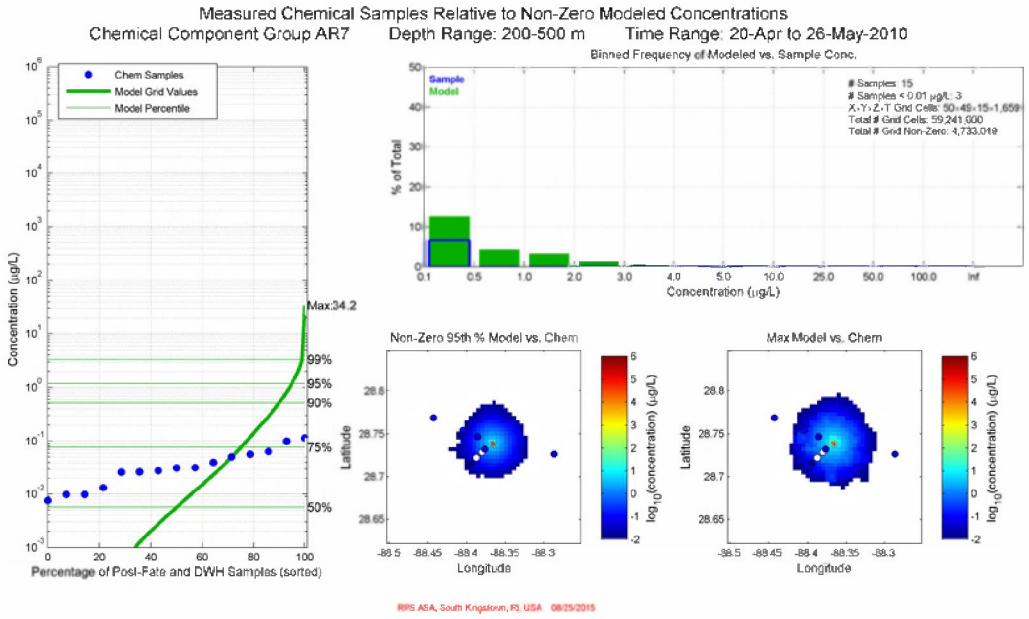

Figure G.2-22. Comparison of total (in-droplet + dissolved) concentrations (µg/L) produced by the Static Cone simulation to measurements from chemistry samples for April 22 – May 26, 2010 in 200-500m: AR7 component (fluorenes & C0-C1 3-ring PAHs). Left: Cumulative frequency distribution of concentrations for observed chemistry samples and gridded model results. The maximum modeled chemistry concentration is provided at the top of the panel. Top right: Histogram of binned concentrations for observed samples (blue) and gridded model results (green) plotted as the percentage of the total number of samples/grid cells. Center bottom and bottom right: Spatial color maps of the 95th percentile and maximum (respectively) modeled concentration within each grid cell over the time interval, overlaid with dots representing the chemistry sample observations. Open symbols indicate chemical concentrations below the analytical detection limit.

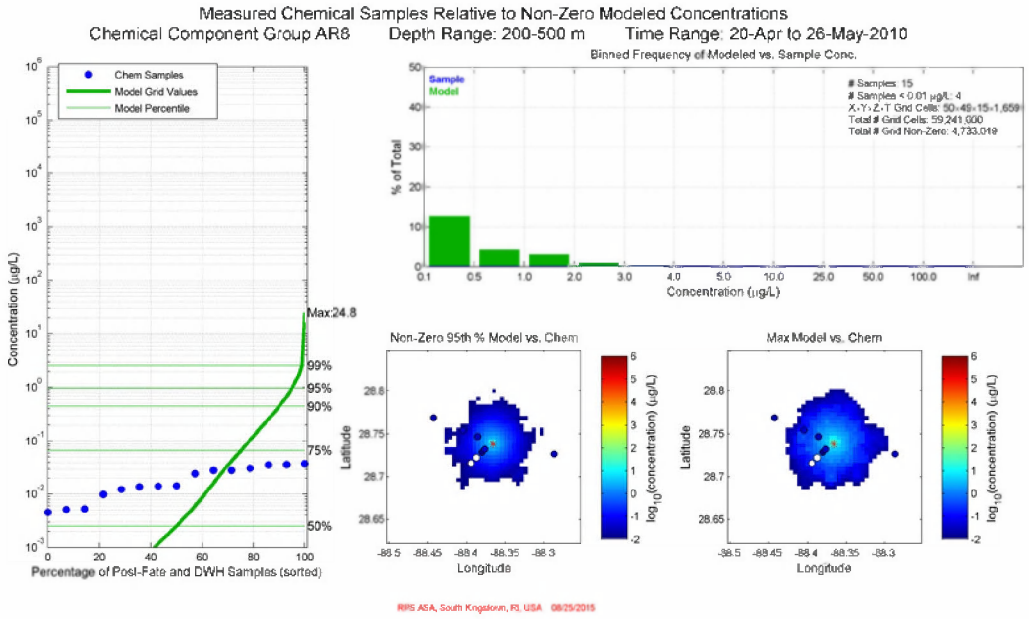

Figure G.2-23. Comparison of total (in-droplet + dissolved) concentrations (µg/L) produced by the Static Cone simulation to measurements from chemistry samples for April 22 – May 26, 2010 in 200-500m: AR8 component (4-ring PAHs & C2-C3 3-ring PAHs). Left: Cumulative frequency distribution of concentrations for observed chemistry samples and gridded model results. The maximum modeled chemistry concentration is provided at the top of the panel. Top right: Histogram of binned concentrations for observed samples (blue) and gridded model results (green) plotted as the percentage of the total number of samples/grid cells. Center bottom and bottom right: Spatial color maps of the 95th percentile and maximum (respectively) modeled concentration within each grid cell over the time interval, overlaid with dots representing the chemistry sample observations. Open symbols indicate chemical concentrations below the analytical detection limit.

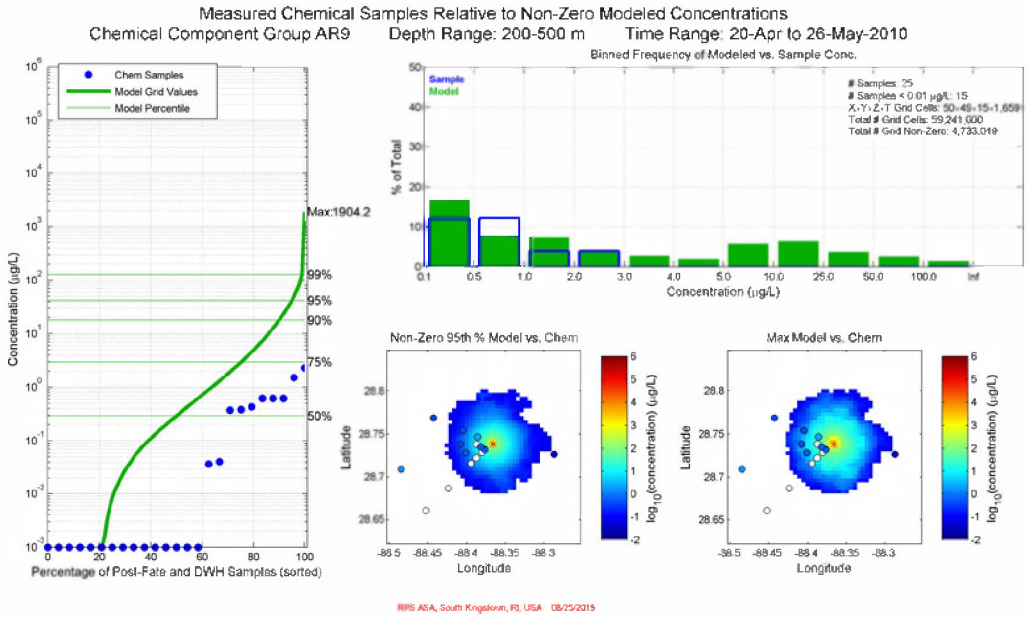

Figure G.2-24. Comparison of total (in-droplet + dissolved) concentrations (µg/L) produced by the Static Cone simulation to measurements from chemistry samples for April 22 – May 26, 2010 in 200-500m: AR9 component (soluble alkanes). Left: Cumulative frequency distribution of concentrations for observed chemistry samples and gridded model results. The maximum modeled chemistry concentration is provided at the top of the panel. Top right: Histogram of binned concentrations for observed samples (blue) and gridded model results (green) plotted as the percentage of the total number of samples/grid cells. Center bottom and bottom right: Spatial color maps of the 95th percentile and maximum (respectively) modeled concentration within each grid cell over the time interval, overlaid with dots representing the chemistry sample observations. Open symbols indicate chemical concentrations below the analytical detection limit.

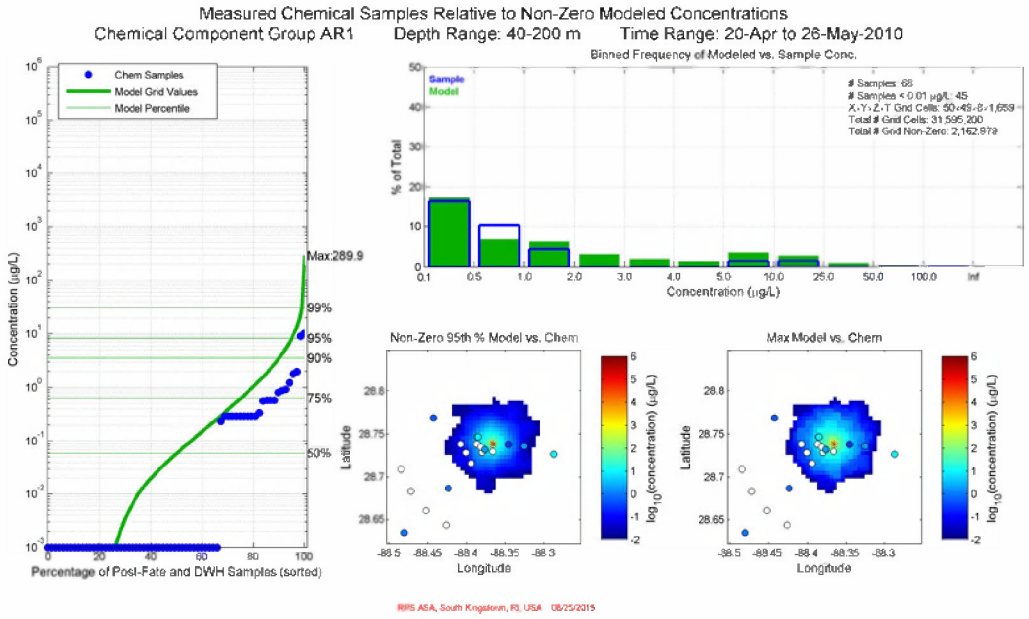

Figure G.2-25. Comparison of total (in-droplet + dissolved) concentrations (µg/L) produced by the Static Cone simulation to measurements from chemistry samples for April 22 – May 26, 2010 in 40-200m: AR1 component (BTEX). Left: Cumulative frequency distribution of concentrations for observed chemistry samples and gridded model results. The maximum modeled chemistry concentration is provided at the top of the panel. Top right: Histogram of binned concentrations for observed samples (blue) and gridded model results (green) plotted as the percentage of the total number of samples/grid cells. Center bottom and bottom right: Spatial color maps of the 95th percentile and maximum (respectively) modeled concentration within each grid cell over the time interval, overlaid with dots representing the chemistry sample observations. Open symbols indicate chemical concentrations below the analytical detection limit.

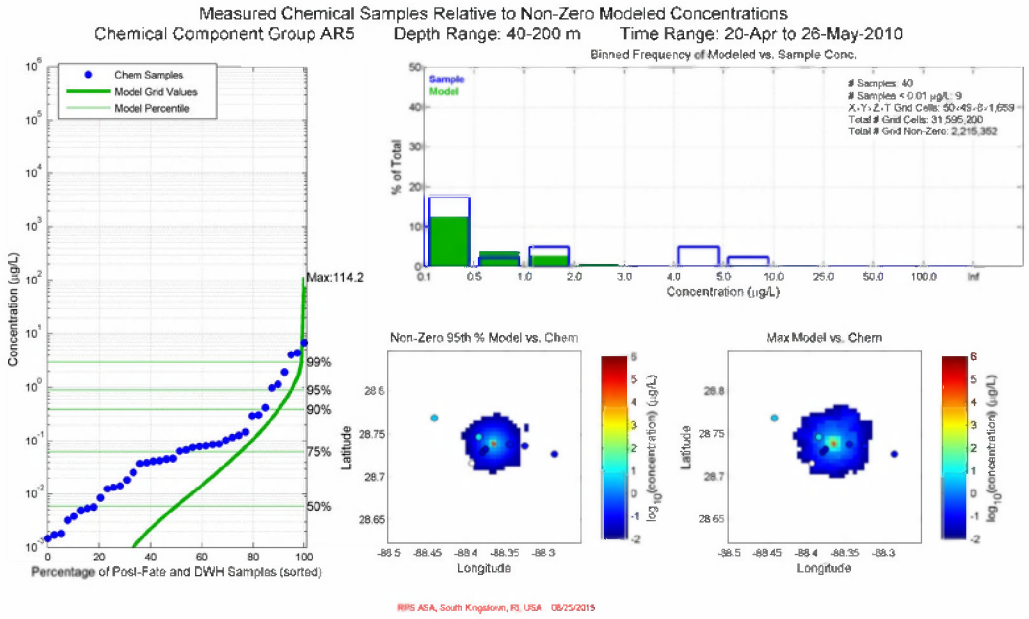

Figure G.2-26. Comparison of total (in-droplet + dissolved) concentrations (µg/L) produced by the Static Cone simulation to measurements from chemistry samples for April 22 – May 26, 2010 in 40-200m: AR5 component (C0-C2 naphthalenes). Left: Cumulative frequency distribution of concentrations for observed chemistry samples and gridded model results. The maximum modeled chemistry concentration is provided at the top of the panel. Top right: Histogram of binned concentrations for observed samples (blue) and gridded model results (green) plotted as the percentage of the total number of samples/grid cells. Center bottom and bottom right: Spatial color maps of the 95th percentile and maximum (respectively) modeled concentration within each grid cell over the time interval, overlaid with dots representing the chemistry sample observations. Open symbols indicate chemical concentrations below the analytical detection limit.

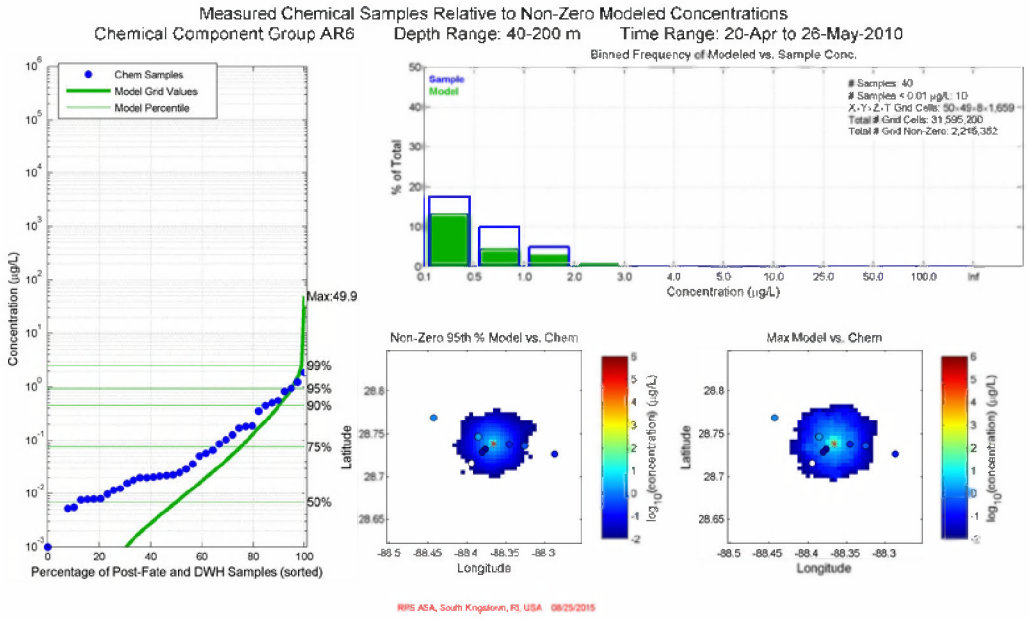

Figure G.2-27. Comparison of total (in-droplet + dissolved) concentrations (µg/L) produced by the Static Cone simulation to measurements from chemistry samples for April 22 – May 26, 2010 in 40-200m: AR6 component (C3-C4 naphthalenes). Left: Cumulative frequency distribution of concentrations for observed chemistry samples and gridded model results. The maximum modeled chemistry concentration is provided at the top of the panel. Top right: Histogram of binned concentrations for observed samples (blue) and gridded model results (green) plotted as the percentage of the total number of samples/grid cells. Center bottom and bottom right: Spatial color maps of the 95th percentile and maximum (respectively) modeled concentration within each grid cell over the time interval, overlaid with dots representing the chemistry sample observations. Open symbols indicate chemical concentrations below the analytical detection limit.

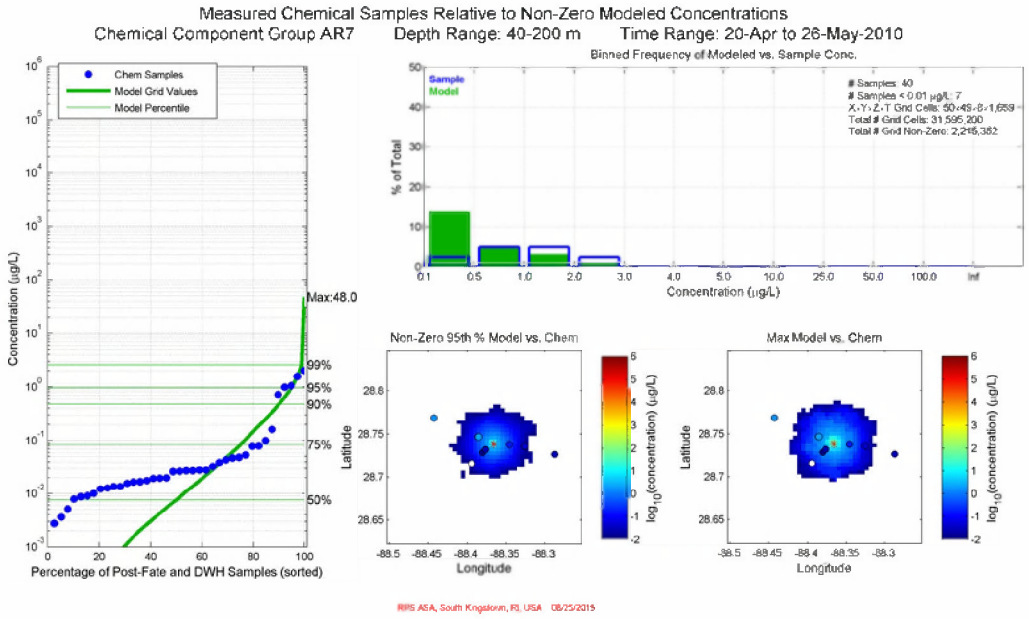

Figure G.2-28. Comparison of total (in-droplet + dissolved) concentrations (µg/L) produced by the Static Cone simulation to measurements from chemistry samples for April 22 – May 26, 2010 in 40-200m: AR7 component (fluorenes & C0-C1 3-ring PAHs). Left: Cumulative frequency distribution of concentrations for observed chemistry samples and gridded model results. The maximum modeled chemistry concentration is provided at the top of the panel. Top right: Histogram of binned concentrations for observed samples (blue) and gridded model results (green) plotted as the percentage of the total number of samples/grid cells. Center bottom and bottom right: Spatial color maps of the 95th percentile and maximum (respectively) modeled concentration within each grid cell over the time interval, overlaid with dots representing the chemistry sample observations. Open symbols indicate chemical concentrations below the analytical detection limit.

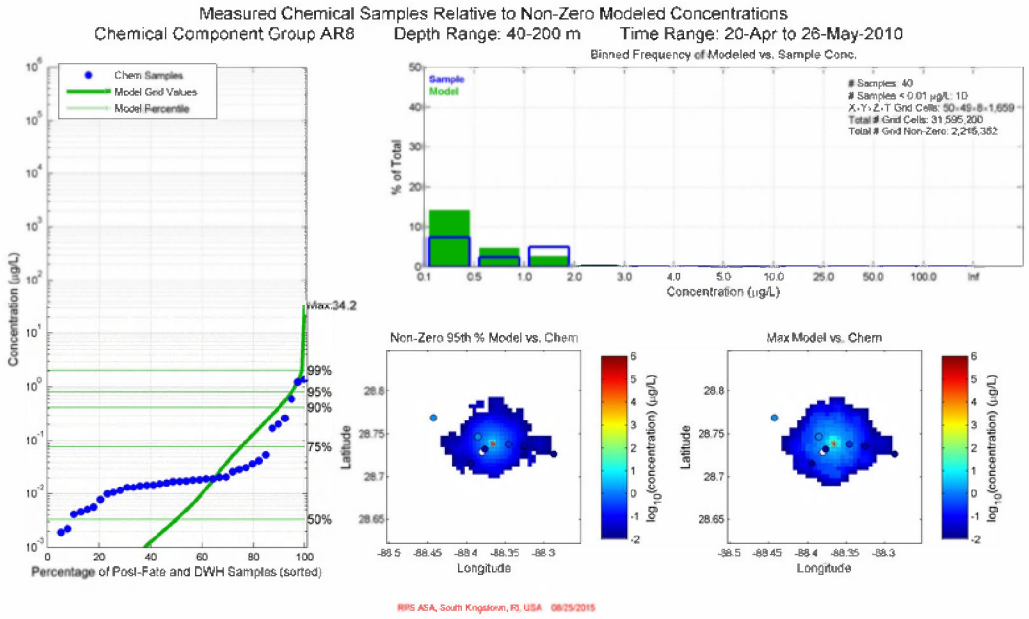

Figure G.2-29. Comparison of total (in-droplet + dissolved) concentrations (µg/L) produced by the Static Cone simulation to measurements from chemistry samples for April 22 – May 26, 2010 in 40-200m: AR8 component (4-ring PAHs & C2-C3 3-ring PAHs). Left: Cumulative frequency distribution of concentrations for observed chemistry samples and gridded model results. The maximum modeled chemistry concentration is provided at the top of the panel. Top right: Histogram of binned concentrations for observed samples (blue) and gridded model results (green) plotted as the percentage of the total number of samples/grid cells. Center bottom and bottom right: Spatial color maps of the 95th percentile and maximum (respectively) modeled concentration within each grid cell over the time interval, overlaid with dots representing the chemistry sample observations. Open symbols indicate chemical concentrations below the analytical detection limit.

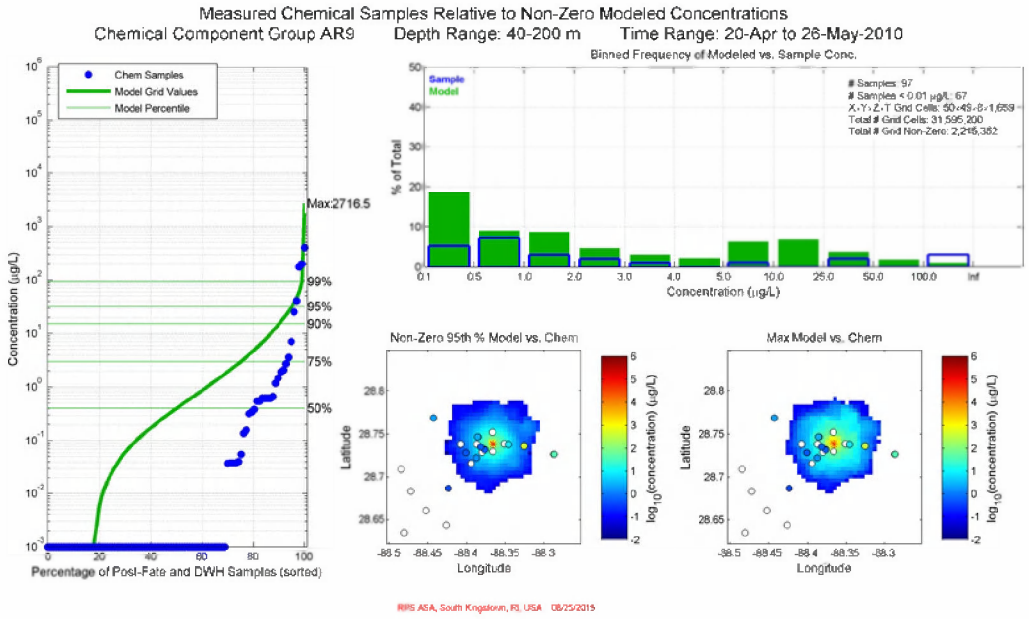

Figure G.2-30. Comparison of total (in-droplet + dissolved) concentrations (µg/L) produced by the Static Cone simulation to measurements from chemistry samples for April 22 – May 26, 2010 in 40-200m: AR9 component (soluble alkanes). Left: Cumulative frequency distribution of concentrations for observed chemistry samples and gridded model results. The maximum modeled chemistry concentration is provided at the top of the panel. Top right: Histogram of binned concentrations for observed samples (blue) and gridded model results (green) plotted as the percentage of the total number of samples/grid cells. Center bottom and bottom right: Spatial color maps of the 95th percentile and maximum (respectively) modeled concentration within each grid cell over the time interval, overlaid with dots representing the chemistry sample observations. Open symbols indicate chemical concentrations below the analytical detection limit.

G.2.2 May 26 – June 6, 2010

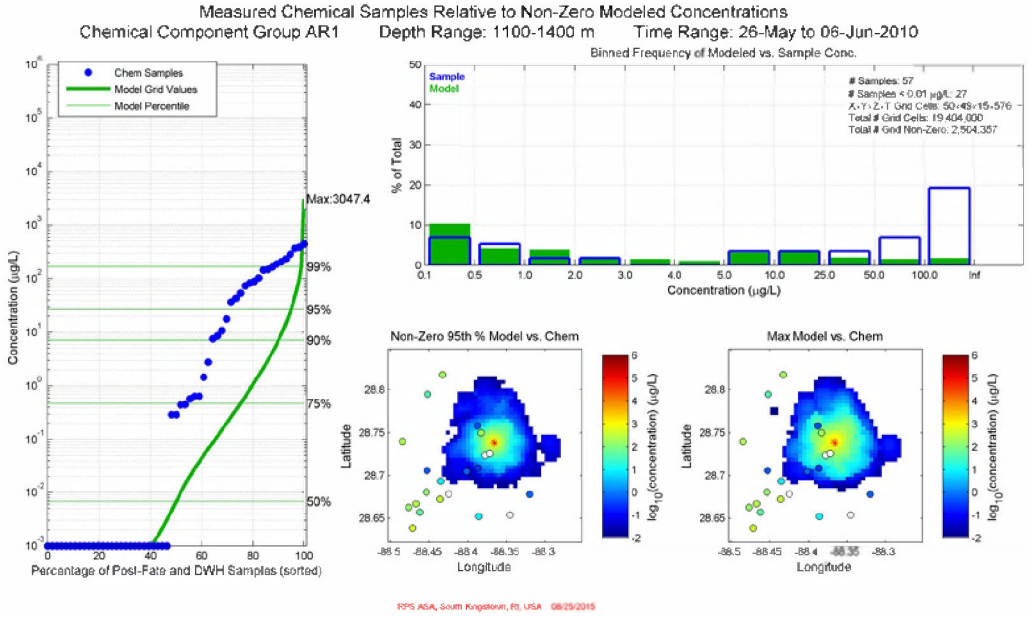

Figure G.2-31. Comparison of total (in-droplet + dissolved) concentrations (µg/L) produced by the Static Cone simulation to measurements from chemistry samples for May 26 – June 6, 2010 in 1100-1400m: AR1 component (BTEX). Left: Cumulative frequency distribution of concentrations for observed chemistry samples and gridded model results. The maximum modeled chemistry concentration is provided at the top of the panel. Top right: Histogram of binned concentrations for observed samples (blue) and gridded model results (green) plotted as the percentage of the total number of samples/grid cells. Center bottom and bottom right: Spatial color maps of the 95th percentile and maximum (respectively) modeled concentration within each grid cell over the time interval, overlaid with dots representing the chemistry sample observations. Open symbols indicate chemical concentrations below the analytical detection limit.

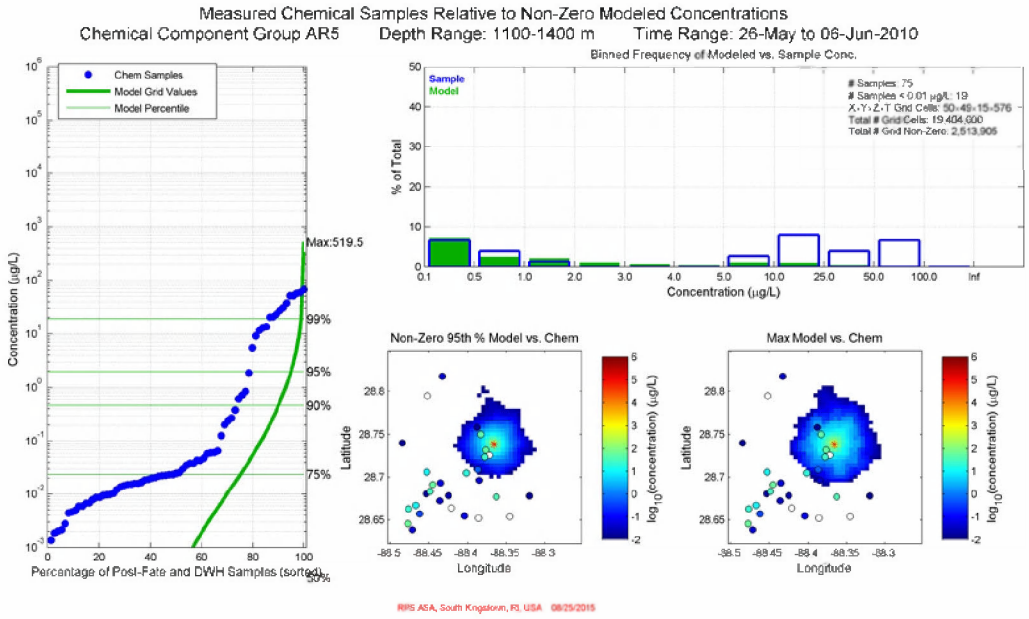

Figure G.2-32. Comparison of total (in-droplet + dissolved) concentrations (µg/L) produced by the Static Cone simulation to measurements from chemistry samples for May 26 – June 6, 2010 in 1100-1400m: AR5 component (C0-C2 naphthalenes). Left: Cumulative frequency distribution of concentrations for observed chemistry samples and gridded model results. The maximum modeled chemistry concentration is provided at the top of the panel. Top right: Histogram of binned concentrations for observed samples (blue) and gridded model results (green) plotted as the percentage of the total number of samples/grid cells. Center bottom and bottom right: Spatial color maps of the 95th percentile and maximum (respectively) modeled concentration within each grid cell over the time interval, overlaid with dots representing the chemistry sample observations. Open symbols indicate chemical concentrations below the analytical detection limit.

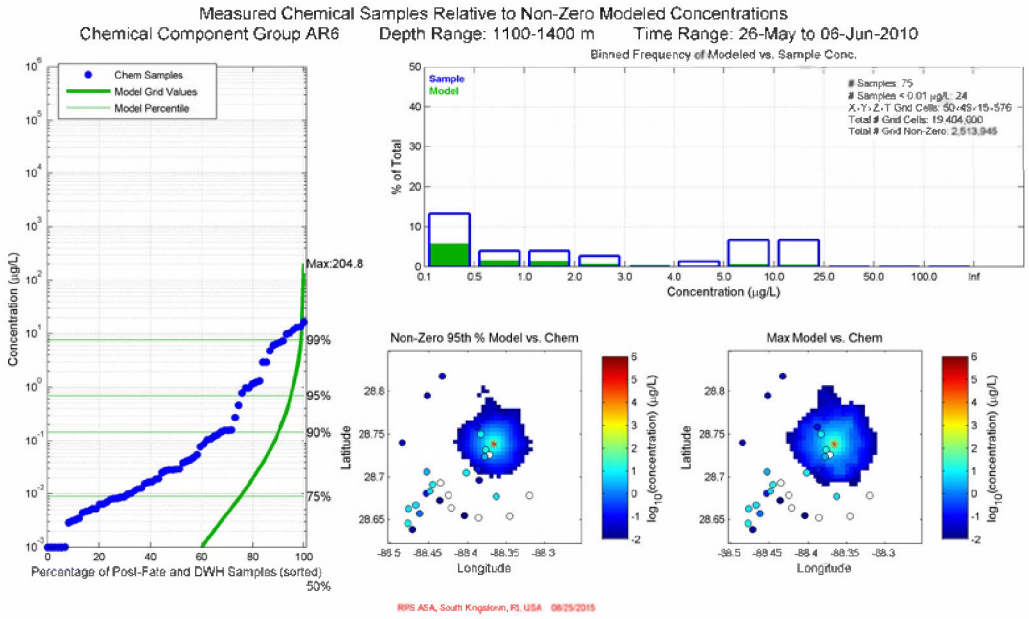

Figure G.2-33. Comparison of total (in-droplet + dissolved) concentrations (µg/L) produced by the Static Cone simulation to measurements from chemistry samples for May 26 – June 6, 2010 in 1100-1400m: AR6 component (C3-C4 naphthalenes). Left: Cumulative frequency distribution of concentrations for observed chemistry samples and gridded model results. The maximum modeled chemistry concentration is provided at the top of the panel. Top right: Histogram of binned concentrations for observed samples (blue) and gridded model results (green) plotted as the percentage of the total number of samples/grid cells. Center bottom and bottom right: Spatial color maps of the 95th percentile and maximum (respectively) modeled concentration within each grid cell over the time interval, overlaid with dots representing the chemistry sample observations. Open symbols indicate chemical concentrations below the analytical detection limit.

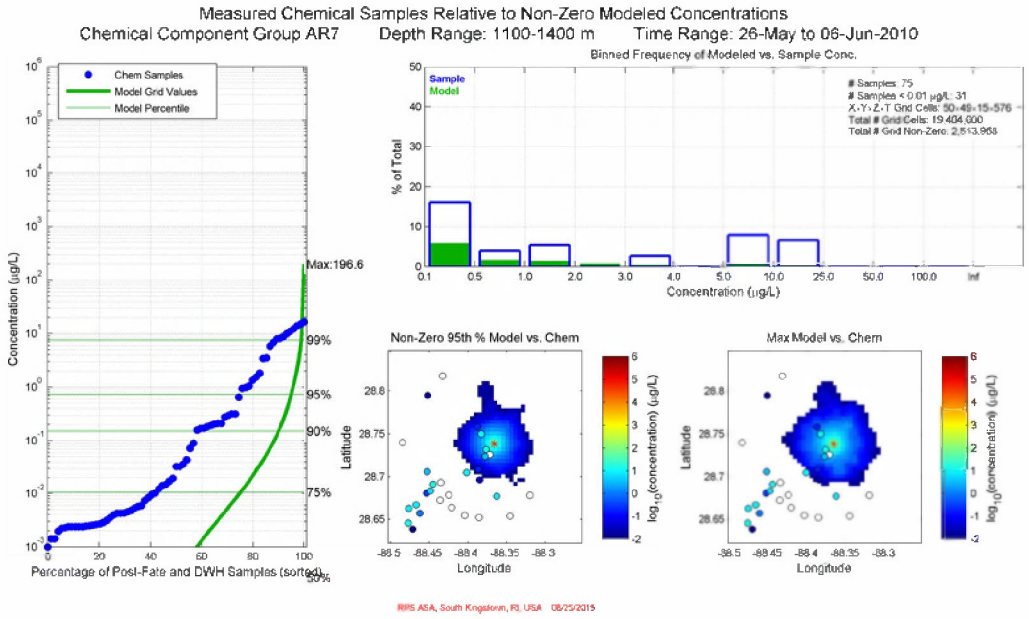

Figure G.2-34. Comparison of total (in-droplet + dissolved) concentrations (µg/L) produced by the Static Cone simulation to measurements from chemistry samples for May 26 – June 6, 2010 in 1100-1400m: AR7 component (fluorenes & C0-C1 3-ring PAHs). Left: Cumulative frequency distribution of concentrations for observed chemistry samples and gridded model results. The maximum modeled chemistry concentration is provided at the top of the panel. Top right: Histogram of binned concentrations for observed samples (blue) and gridded model results (green) plotted as the percentage of the total number of samples/grid cells. Center bottom and bottom right: Spatial color maps of the 95th percentile and maximum (respectively) modeled concentration within each grid cell over the time interval, overlaid with dots representing the chemistry sample observations. Open symbols indicate chemical concentrations below the analytical detection limit.

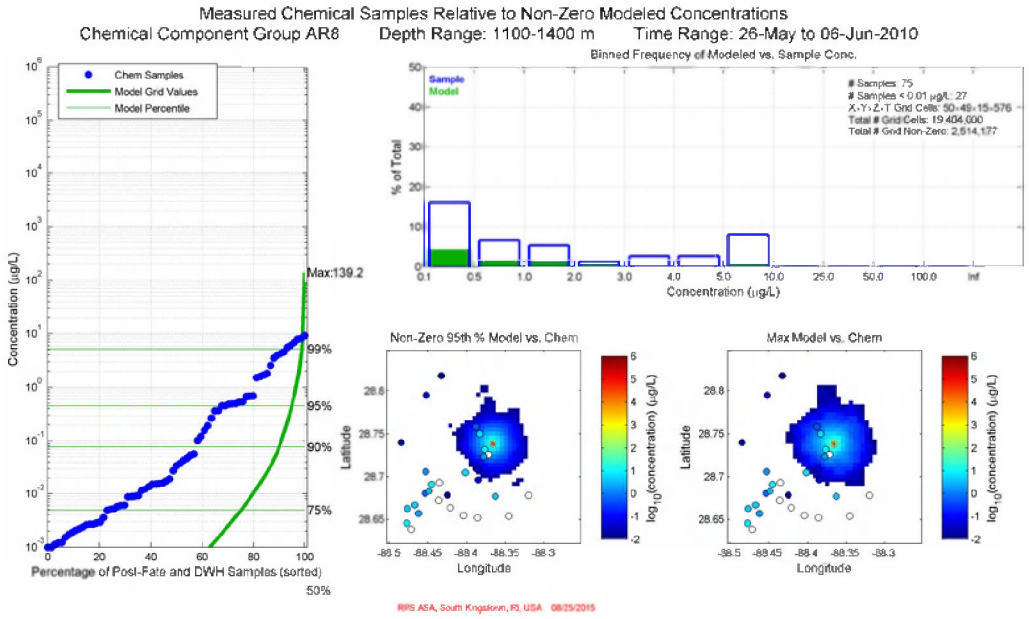

Figure G.2-35. Comparison of total (in-droplet + dissolved) concentrations (µg/L) produced by the Static Cone simulation to measurements from chemistry samples for May 26 – June 6, 2010 in 1100-1400m: AR8 component (4-ring PAHs & C2-C3 3-ring PAHs). Left: Cumulative frequency distribution of concentrations for observed chemistry samples and gridded model results. The maximum modeled chemistry concentration is provided at the top of the panel. Top right: Histogram of binned concentrations for observed samples (blue) and gridded model results (green) plotted as the percentage of the total number of samples/grid cells. Center bottom and bottom right: Spatial color maps of the 95th percentile and maximum (respectively) modeled concentration within each grid cell over the time interval, overlaid with dots representing the chemistry sample observations. Open symbols indicate chemical concentrations below the analytical detection limit.

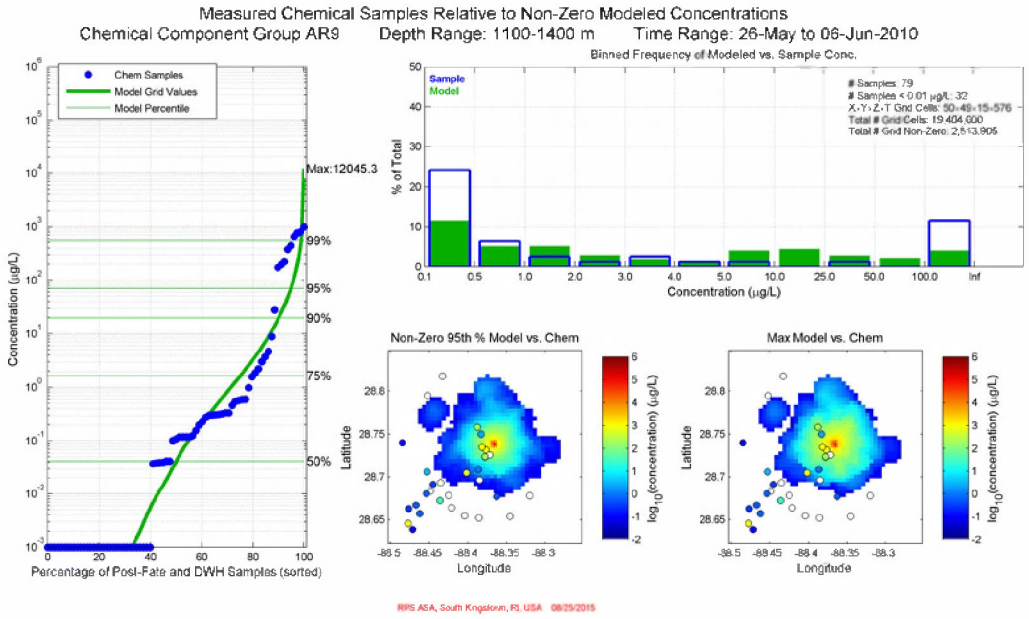

Figure G.2-36. Comparison of total (in-droplet + dissolved) concentrations (µg/L) produced by the Static Cone simulation to measurements from chemistry samples for May 26 – June 6, 2010 in 1100-1400m: AR9 component (soluble alkanes). Left: Cumulative frequency distribution of concentrations for observed chemistry samples and gridded model results. The maximum modeled chemistry concentration is provided at the top of the panel. Top right: Histogram of binned concentrations for observed samples (blue) and gridded model results (green) plotted as the percentage of the total number of samples/grid cells. Center bottom and bottom right: Spatial color maps of the 95th percentile and maximum (respectively) modeled concentration within each grid cell over the time interval, overlaid with dots representing the chemistry sample observations. Open symbols indicate chemical concentrations below the analytical detection limit.

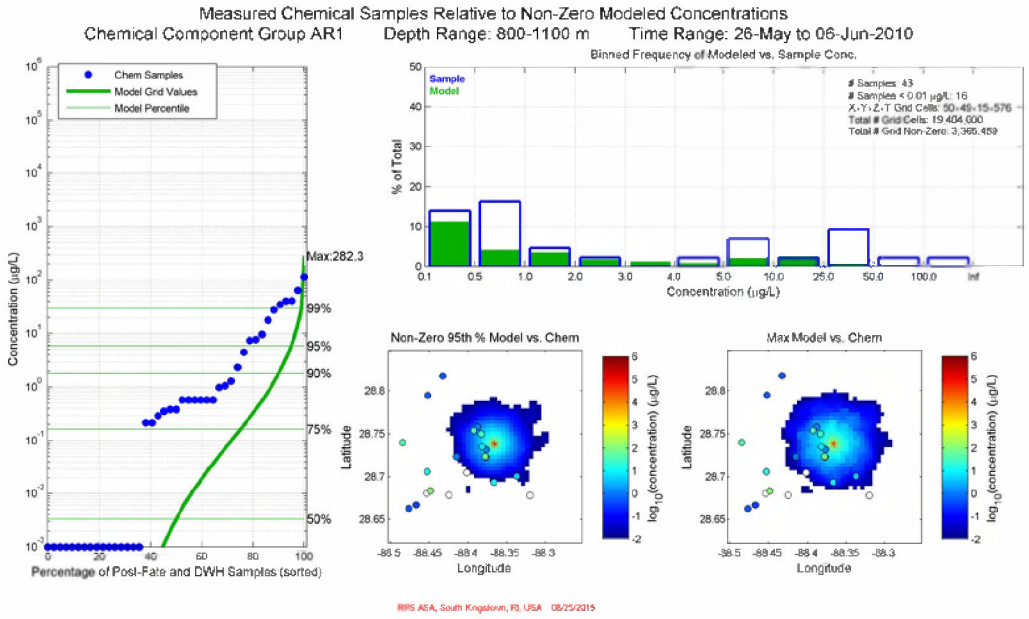

Figure G.2-37. Comparison of total (in-droplet + dissolved) concentrations (µg/L) produced by the Static Cone simulation to measurements from chemistry samples for May 26 – June 6, 2010 in 800-1100m: AR1 component (BTEX). Left: Cumulative frequency distribution of concentrations for observed chemistry samples and gridded model results. The maximum modeled chemistry concentration is provided at the top of the panel. Top right: Histogram of binned concentrations for observed samples (blue) and gridded model results (green) plotted as the percentage of the total number of samples/grid cells. Center bottom and bottom right: Spatial color maps of the 95th percentile and maximum (respectively) modeled concentration within each grid cell over the time interval, overlaid with dots representing the chemistry sample observations. Open symbols indicate chemical concentrations below the analytical detection limit.

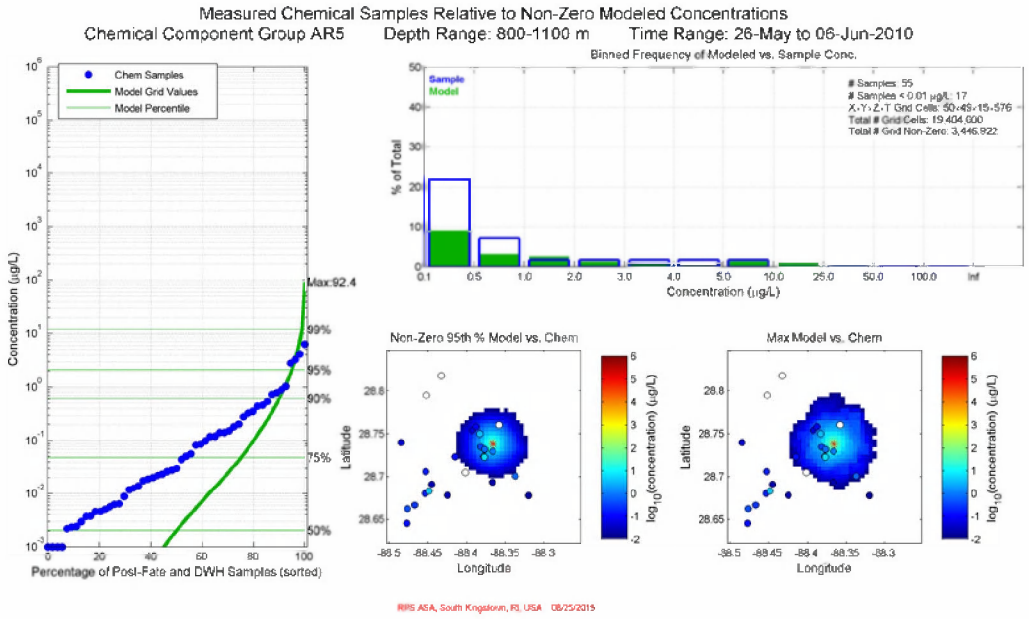

Figure G.2-38. Comparison of total (in-droplet + dissolved) concentrations (µg/L) produced by the Static Cone simulation to measurements from chemistry samples for May 26 – June 6, 2010 in 800-1100m: AR5 component (C0-C2 naphthalenes). Left: Cumulative frequency distribution of concentrations for observed chemistry samples and gridded model results. The maximum modeled chemistry concentration is provided at the top of the panel. Top right: Histogram of binned concentrations for observed samples (blue) and gridded model results (green) plotted as the percentage of the total number of samples/grid cells. Center bottom and bottom right: Spatial color maps of the 95th percentile and maximum (respectively) modeled concentration within each grid cell over the time interval, overlaid with dots representing the chemistry sample observations. Open symbols indicate chemical concentrations below the analytical detection limit.

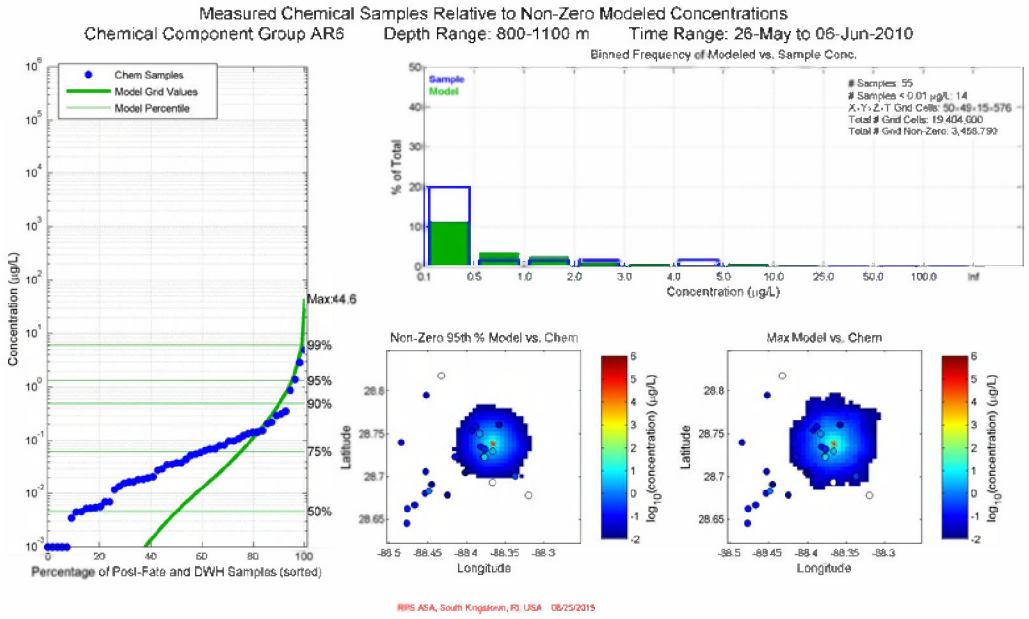

Figure G.2-39. Comparison of total (in-droplet + dissolved) concentrations (µg/L) produced by the Static Cone simulation to measurements from chemistry samples for May 26 – June 6, 2010 in 800-1100m: AR6 component (C3-C4 naphthalenes). Left: Cumulative frequency distribution of concentrations for observed chemistry samples and gridded model results. The maximum modeled chemistry concentration is provided at the top of the panel. Top right: Histogram of binned concentrations for observed samples (blue) and gridded model results (green) plotted as the percentage of the total number of samples/grid cells. Center bottom and bottom right: Spatial color maps of the 95th percentile and maximum (respectively) modeled concentration within each grid cell over the time interval, overlaid with dots representing the chemistry sample observations. Open symbols indicate chemical concentrations below the analytical detection limit.

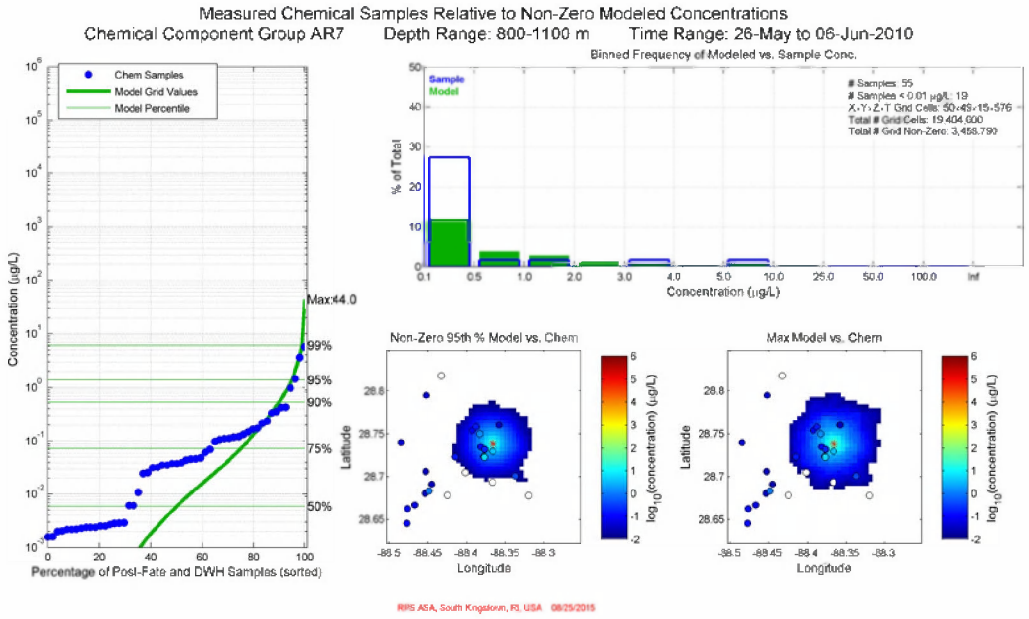

Figure G.2-40. Comparison of total (in-droplet + dissolved) concentrations (µg/L) produced by the Static Cone simulation to measurements from chemistry samples for May 26 – June 6, 2010 in 800-1100m: AR7 component (fluorenes & C0-C1 3-ring PAHs). Left: Cumulative frequency distribution of concentrations for observed chemistry samples and gridded model results. The maximum modeled chemistry concentration is provided at the top of the panel. Top right: Histogram of binned concentrations for observed samples (blue) and gridded model results (green) plotted as the percentage of the total number of samples/grid cells. Center bottom and bottom right: Spatial color maps of the 95th percentile and maximum (respectively) modeled concentration within each grid cell over the time interval, overlaid with dots representing the chemistry sample observations. Open symbols indicate chemical concentrations below the analytical detection limit.

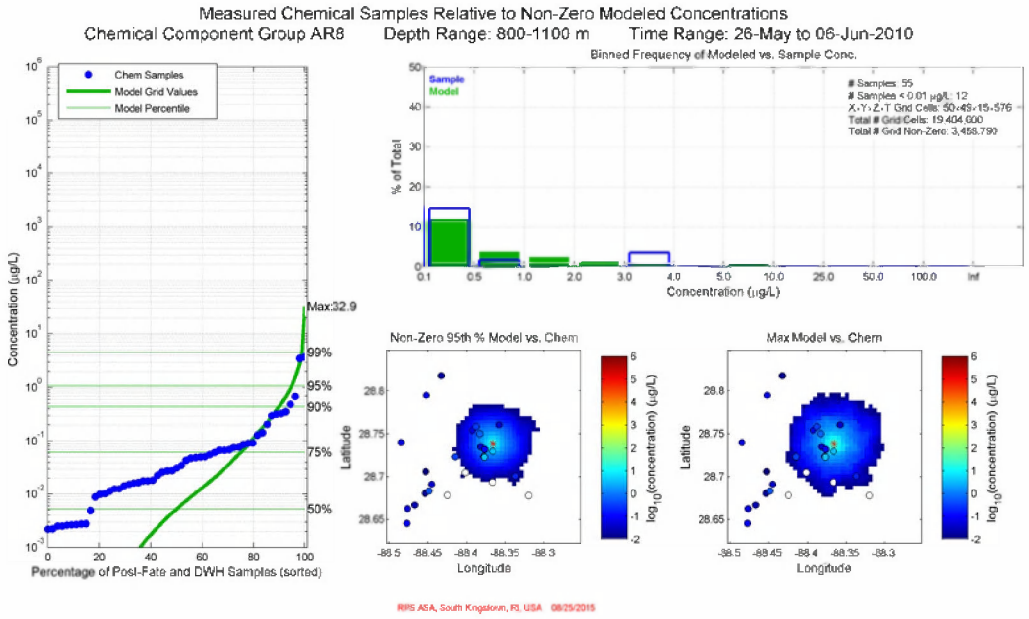

Figure G.2-41. Comparison of total (in-droplet + dissolved) concentrations (µg/L) produced by the Static Cone simulation to measurements from chemistry samples for May 26 – June 6, 2010 in 800-1100m: AR8 component (4-ring PAHs & C2-C3 3-ring PAHs). Left: Cumulative frequency distribution of concentrations for observed chemistry samples and gridded model results. The maximum modeled chemistry concentration is provided at the top of the panel. Top right: Histogram of binned concentrations for observed samples (blue) and gridded model results (green) plotted as the percentage of the total number of samples/grid cells. Center bottom and bottom right: Spatial color maps of the 95th percentile and maximum (respectively) modeled concentration within each grid cell over the time interval, overlaid with dots representing the chemistry sample observations. Open symbols indicate chemical concentrations below the analytical detection limit.

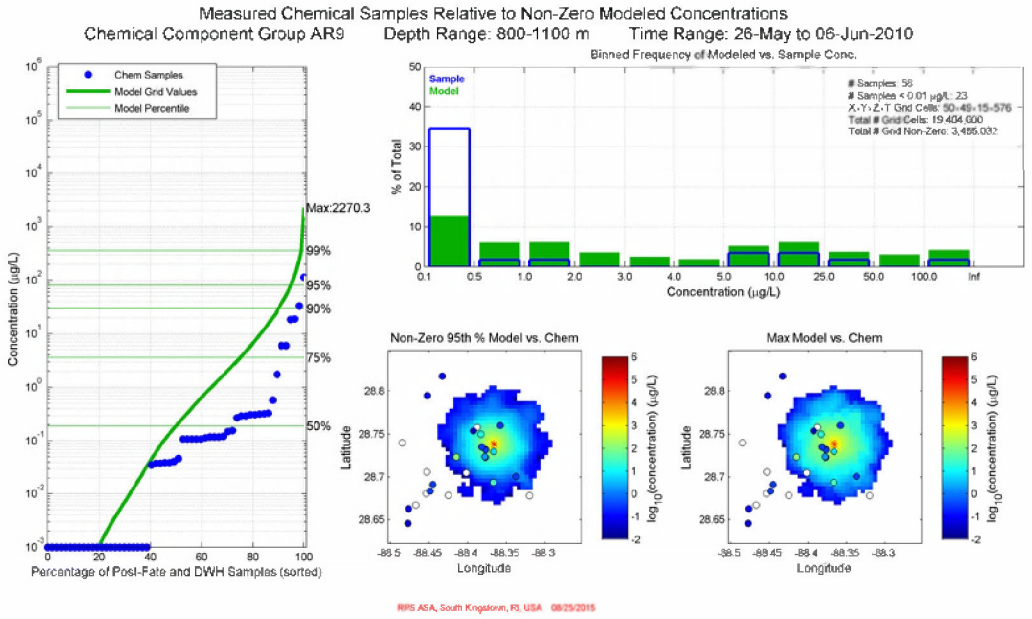

Figure G.2-42. Comparison of total (in-droplet + dissolved) concentrations (µg/L) produced by the Static Cone simulation to measurements from chemistry samples for May 26 – June 6, 2010 in 800-1100m: AR9 component (soluble alkanes). Left: Cumulative frequency distribution of concentrations for observed chemistry samples and gridded model results. The maximum modeled chemistry concentration is provided at the top of the panel. Top right: Histogram of binned concentrations for observed samples (blue) and gridded model results (green) plotted as the percentage of the total number of samples/grid cells. Center bottom and bottom right: Spatial color maps of the 95th percentile and maximum (respectively) modeled concentration within each grid cell over the time interval, overlaid with dots representing the chemistry sample observations. Open symbols indicate chemical concentrations below the analytical detection limit.

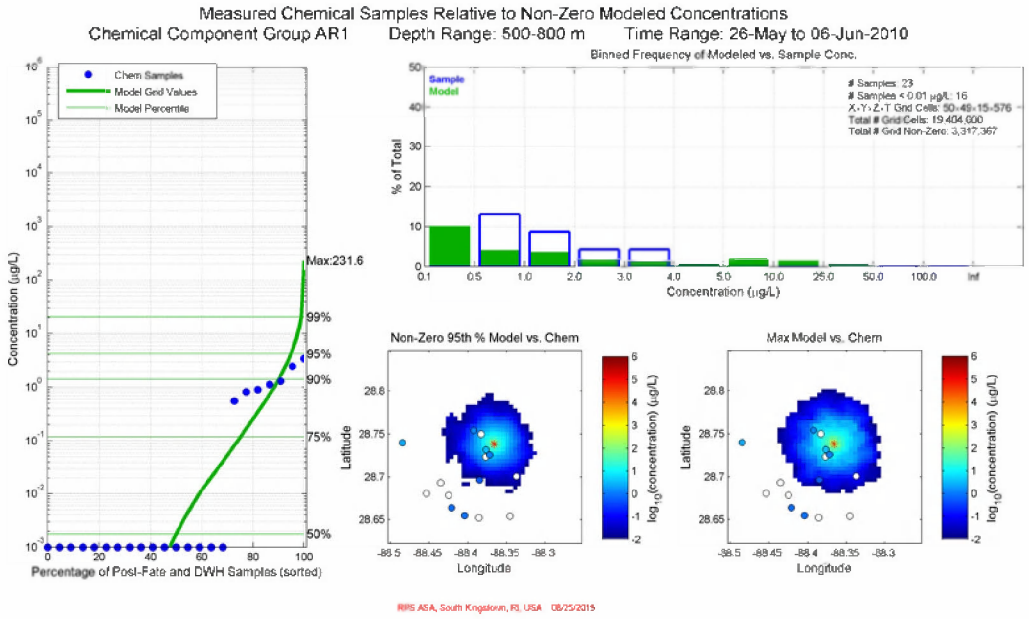

Figure G.2-43. Comparison of total (in-droplet + dissolved) concentrations (µg/L) produced by the Static Cone simulation to measurements from chemistry samples for May 26 – June 6, 2010 in 500-800m: AR1 component (BTEX). Left: Cumulative frequency distribution of concentrations for observed chemistry samples and gridded model results. The maximum modeled chemistry concentration is provided at the top of the panel. Top right: Histogram of binned concentrations for observed samples (blue) and gridded model results (green) plotted as the percentage of the total number of samples/grid cells. Center bottom and bottom right: Spatial color maps of the 95th percentile and maximum (respectively) modeled concentration within each grid cell over the time interval, overlaid with dots representing the chemistry sample observations. Open symbols indicate chemical concentrations below the analytical detection limit.

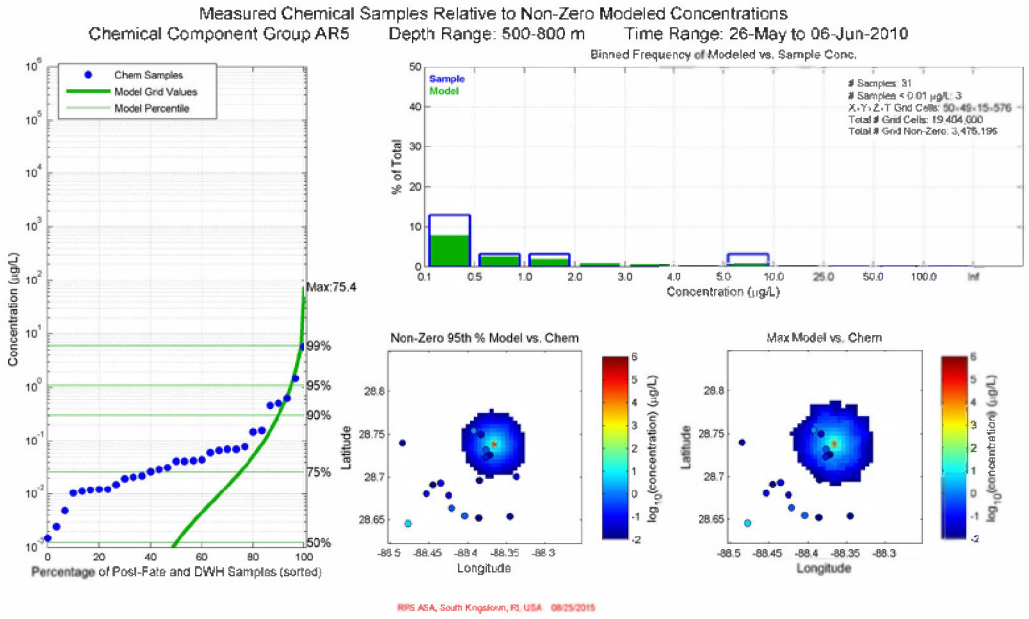

Figure G.2-44. Comparison of total (in-droplet + dissolved) concentrations (µg/L) produced by the Static Cone simulation to measurements from chemistry samples for May 26 – June 6, 2010 in 500-800m: AR5 component (C0-C2 naphthalenes). Left: Cumulative frequency distribution of concentrations for observed chemistry samples and gridded model results. The maximum modeled chemistry concentration is provided at the top of the panel. Top right: Histogram of binned concentrations for observed samples (blue) and gridded model results (green) plotted as the percentage of the total number of samples/grid cells. Center bottom and bottom right: Spatial color maps of the 95th percentile and maximum (respectively) modeled concentration within each grid cell over the time interval, overlaid with dots representing the chemistry sample observations. Open symbols indicate chemical concentrations below the analytical detection limit.

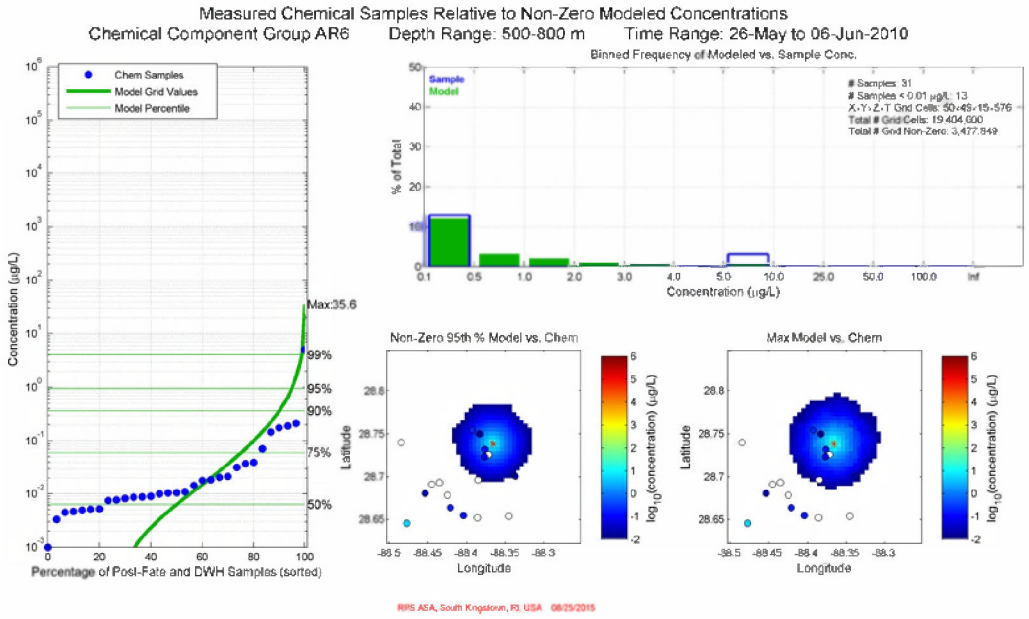

Figure G.2-45. Comparison of total (in-droplet + dissolved) concentrations (µg/L) produced by the Static Cone simulation to measurements from chemistry samples for May 26 – June 6, 2010 in 500-800m: AR6 component (C3-C4 naphthalenes). Left: Cumulative frequency distribution of concentrations for observed chemistry samples and gridded model results. The maximum modeled chemistry concentration is provided at the top of the panel. Top right: Histogram of binned concentrations for observed samples (blue) and gridded model results (green) plotted as the percentage of the total number of samples/grid cells. Center bottom and bottom right: Spatial color maps of the 95th percentile and maximum (respectively) modeled concentration within each grid cell over the time interval, overlaid with dots representing the chemistry sample observations. Open symbols indicate chemical concentrations below the analytical detection limit.

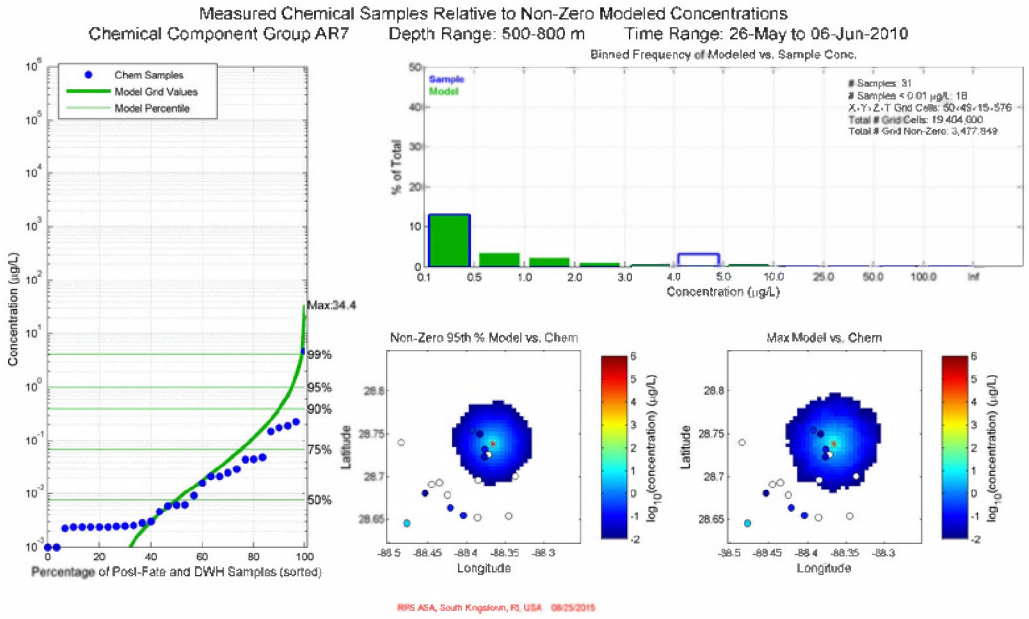

Figure G.2-46. Comparison of total (in-droplet + dissolved) concentrations (µg/L) produced by the Static Cone simulation to measurements from chemistry samples for May 26 – June 6, 2010 in 500-800m: AR7 component (fluorenes & C0-C1 3-ring PAHs). Left: Cumulative frequency distribution of concentrations for observed chemistry samples and gridded model results. The maximum modeled chemistry concentration is provided at the top of the panel. Top right: Histogram of binned concentrations for observed samples (blue) and gridded model results (green) plotted as the percentage of the total number of samples/grid cells. Center bottom and bottom right: Spatial color maps of the 95th percentile and maximum (respectively) modeled concentration within each grid cell over the time interval, overlaid with dots representing the chemistry sample observations. Open symbols indicate chemical concentrations below the analytical detection limit.

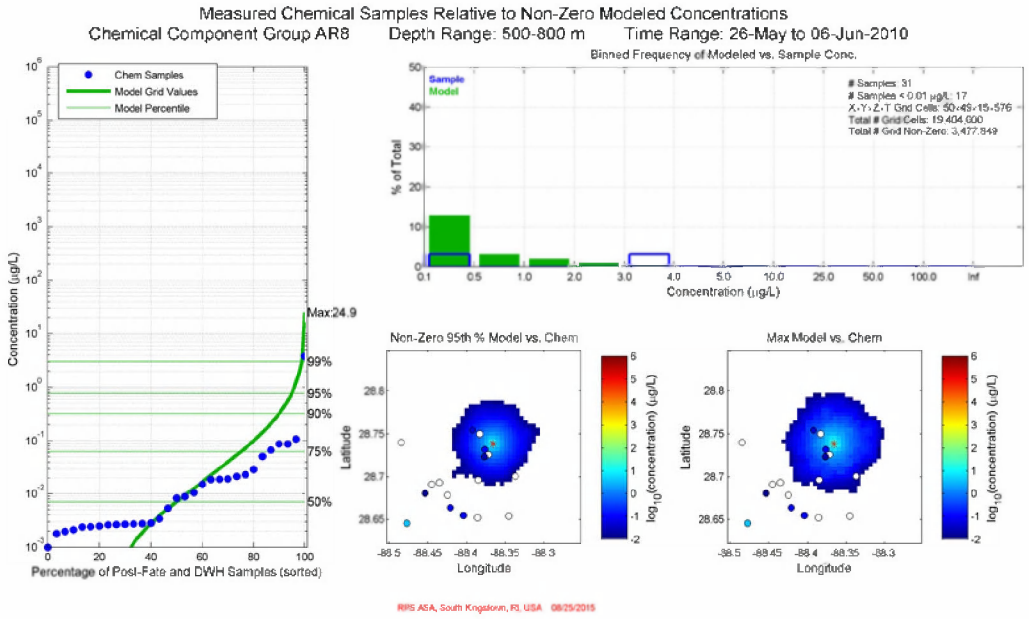

Figure G.2-47. Comparison of total (in-droplet + dissolved) concentrations (µg/L) produced by the Static Cone simulation to measurements from chemistry samples for May 26 – June 6, 2010 in 500-800m: AR8 component (4-ring PAHs & C2-C3 3-ring PAHs). Left: Cumulative frequency distribution of concentrations for observed chemistry samples and gridded model results. The maximum modeled chemistry concentration is provided at the top of the panel. Top right: Histogram of binned concentrations for observed samples (blue) and gridded model results (green) plotted as the percentage of the total number of samples/grid cells. Center bottom and bottom right: Spatial color maps of the 95th percentile and maximum (respectively) modeled concentration within each grid cell over the time interval, overlaid with dots representing the chemistry sample observations. Open symbols indicate chemical concentrations below the analytical detection limit.

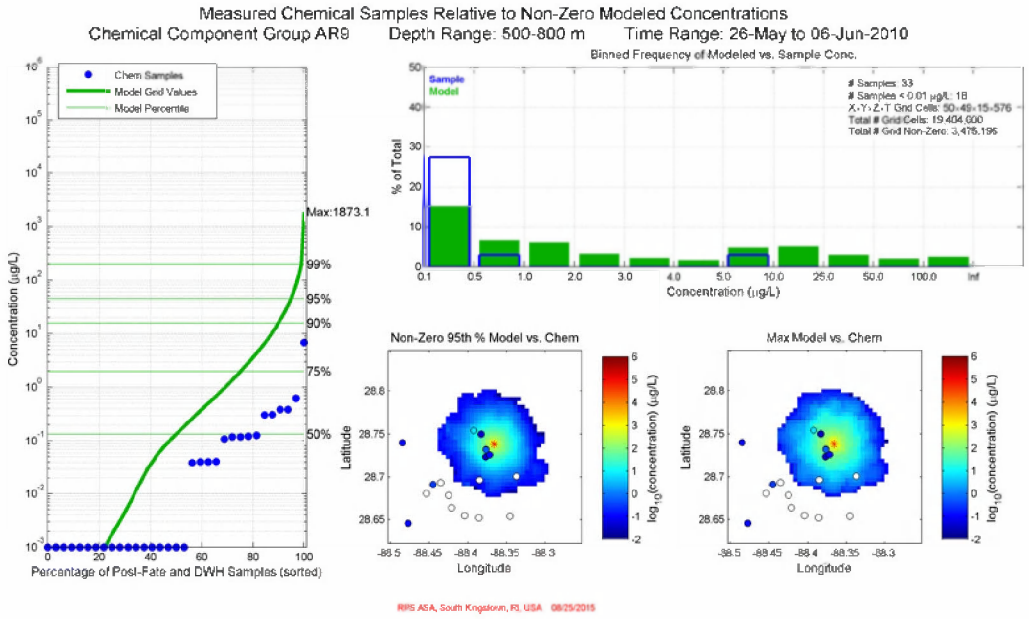

Figure G.2-48. Comparison of total (in-droplet + dissolved) concentrations (µg/L) produced by the Static Cone simulation to measurements from chemistry samples for May 26 – June 6, 2010 in 500-800m: AR9 component (soluble alkanes). Left: Cumulative frequency distribution of concentrations for observed chemistry samples and gridded model results. The maximum modeled chemistry concentration is provided at the top of the panel. Top right: Histogram of binned concentrations for observed samples (blue) and gridded model results (green) plotted as the percentage of the total number of samples/grid cells. Center bottom and bottom right: Spatial color maps of the 95th percentile and maximum (respectively) modeled concentration within each grid cell over the time interval, overlaid with dots representing the chemistry sample observations. Open symbols indicate chemical concentrations below the analytical detection limit.

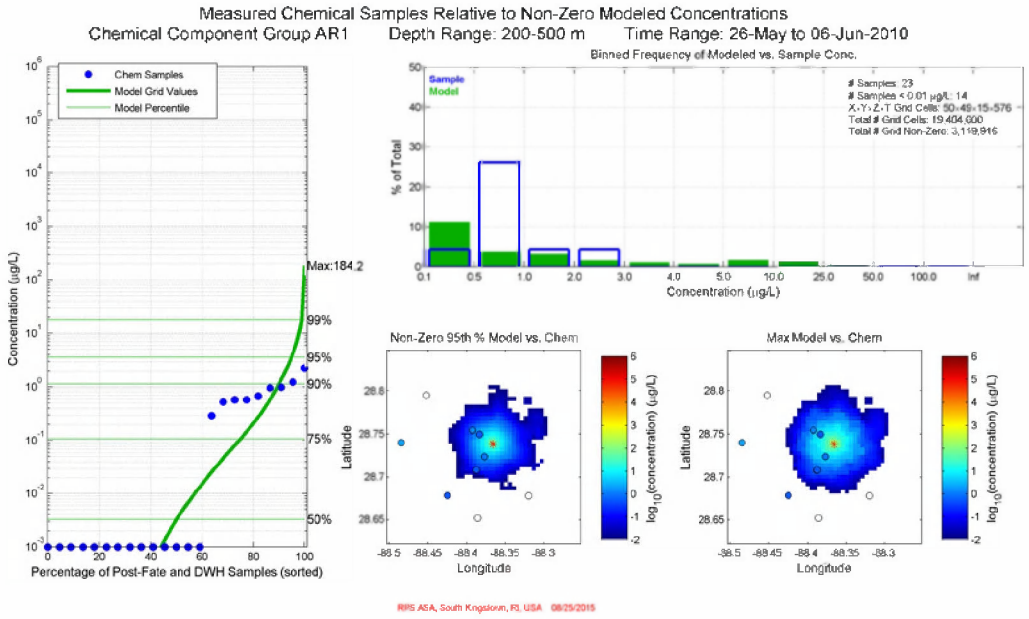

Figure G.2-49. Comparison of total (in-droplet + dissolved) concentrations (µg/L) produced by the Static Cone simulation to measurements from chemistry samples for May 26 – June 6, 2010 in 200-500m: AR1 component (BTEX). Left: Cumulative frequency distribution of concentrations for observed chemistry samples and gridded model results. The maximum modeled chemistry concentration is provided at the top of the panel. Top right: Histogram of binned concentrations for observed samples (blue) and gridded model results (green) plotted as the percentage of the total number of samples/grid cells. Center bottom and bottom right: Spatial color maps of the 95th percentile and maximum (respectively) modeled concentration within each grid cell over the time interval, overlaid with dots representing the chemistry sample observations. Open symbols indicate chemical concentrations below the analytical detection limit.

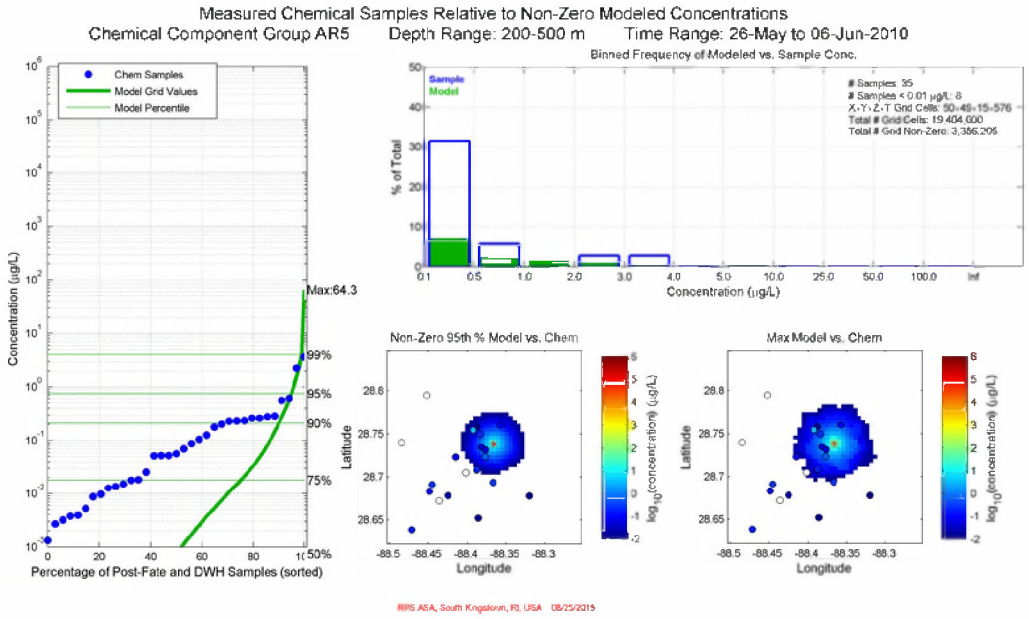

Figure G.2-50. Comparison of total (in-droplet + dissolved) concentrations (µg/L) produced by the Static Cone simulation to measurements from chemistry samples for May 26 – June 6, 2010 in 200-500m: AR5 component (C0-C2 naphthalenes). Left: Cumulative frequency distribution of concentrations for observed chemistry samples and gridded model results. The maximum modeled chemistry concentration is provided at the top of the panel. Top right: Histogram of binned concentrations for observed samples (blue) and gridded model results (green) plotted as the percentage of the total number of samples/grid cells. Center bottom and bottom right: Spatial color maps of the 95th percentile and maximum (respectively) modeled concentration within each grid cell over the time interval, overlaid with dots representing the chemistry sample observations. Open symbols indicate chemical concentrations below the analytical detection limit.

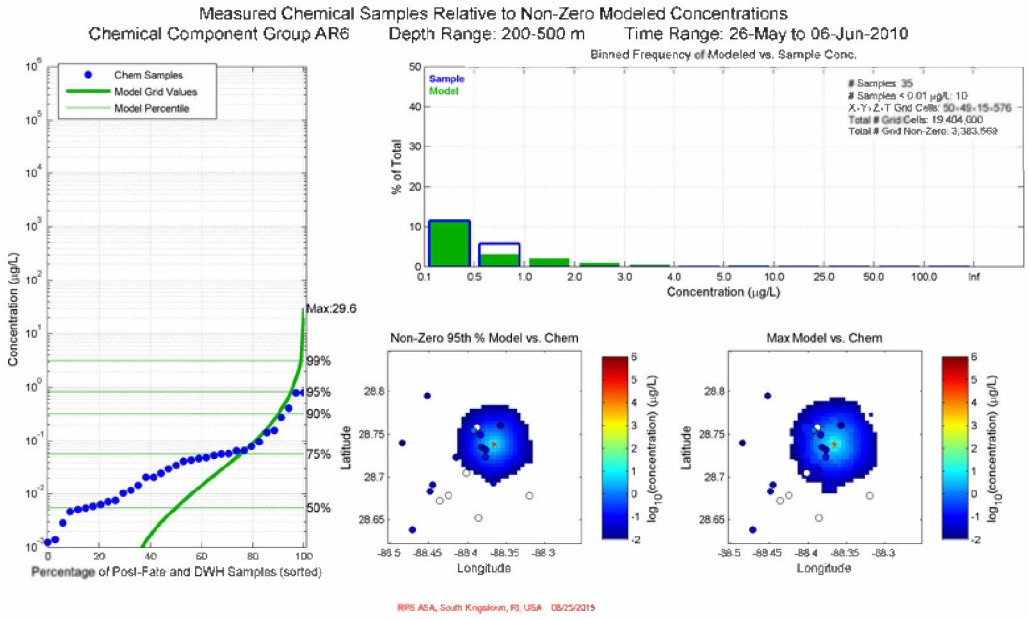

Figure G.2-51. Comparison of total (in-droplet + dissolved) concentrations (µg/L) produced by the Static Cone simulation to measurements from chemistry samples for May 26 – June 6, 2010 in 200-500m: AR6 component (C3-C4 naphthalenes). Left: Cumulative frequency distribution of concentrations for observed chemistry samples and gridded model results. The maximum modeled chemistry concentration is provided at the top of the panel. Top right: Histogram of binned concentrations for observed samples (blue) and gridded model results (green) plotted as the percentage of the total number of samples/grid cells. Center bottom and bottom right: Spatial color maps of the 95th percentile and maximum (respectively) modeled concentration within each grid cell over the time interval, overlaid with dots representing the chemistry sample observations. Open symbols indicate chemical concentrations below the analytical detection limit.

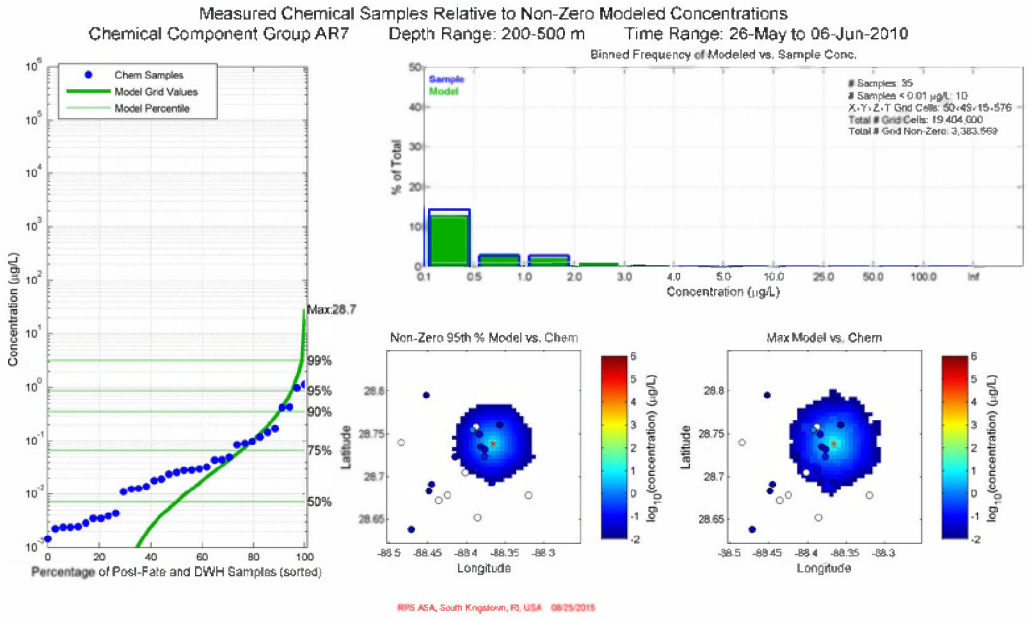

Figure G.2-52. Comparison of total (in-droplet + dissolved) concentrations (µg/L) produced by the Static Cone simulation to measurements from chemistry samples for May 26 – June 6, 2010 in 200-500m: AR7 component (fluorenes & C0-C1 3-ring PAHs). Left: Cumulative frequency distribution of concentrations for observed chemistry samples and gridded model results. The maximum modeled chemistry concentration is provided at the top of the panel. Top right: Histogram of binned concentrations for observed samples (blue) and gridded model results (green) plotted as the percentage of the total number of samples/grid cells. Center bottom and bottom right: Spatial color maps of the 95th percentile and maximum (respectively) modeled concentration within each grid cell over the time interval, overlaid with dots representing the chemistry sample observations. Open symbols indicate chemical concentrations below the analytical detection limit.

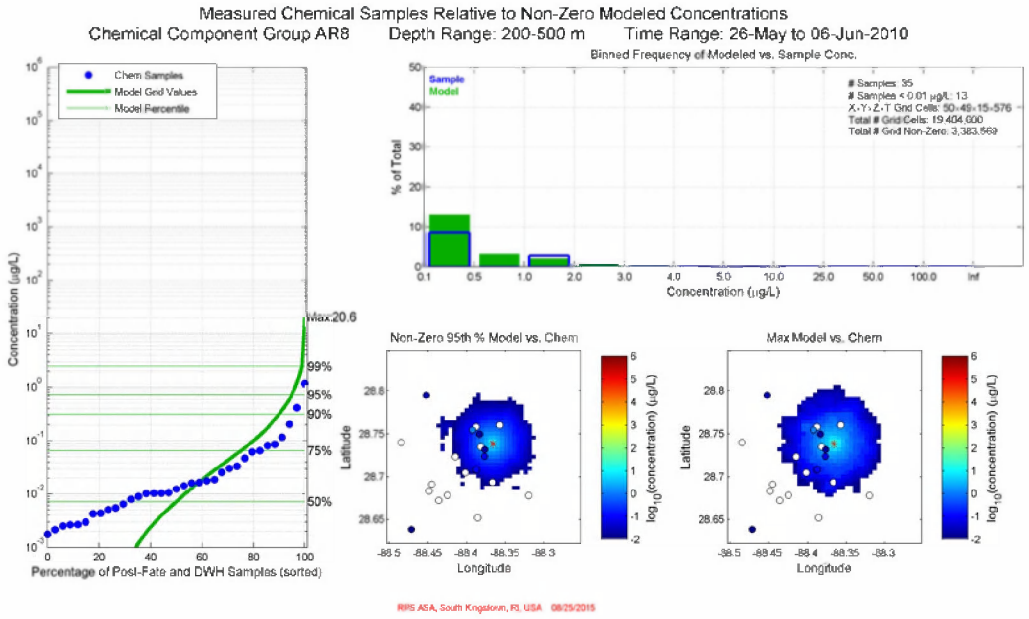

Figure G.2-53. Comparison of total (in-droplet + dissolved) concentrations (µg/L) produced by the Static Cone simulation to measurements from chemistry samples for May 26 – June 6, 2010 in 200-500m: AR8 component (4-ring PAHs & C2-C3 3-ring PAHs). Left: Cumulative frequency distribution of concentrations for observed chemistry samples and gridded model results. The maximum modeled chemistry concentration is provided at the top of the panel. Top right: Histogram of binned concentrations for observed samples (blue) and gridded model results (green) plotted as the percentage of the total number of samples/grid cells. Center bottom and bottom right: Spatial color maps of the 95th percentile and maximum (respectively) modeled concentration within each grid cell over the time interval, overlaid with dots representing the chemistry sample observations. Open symbols indicate chemical concentrations below the analytical detection limit.

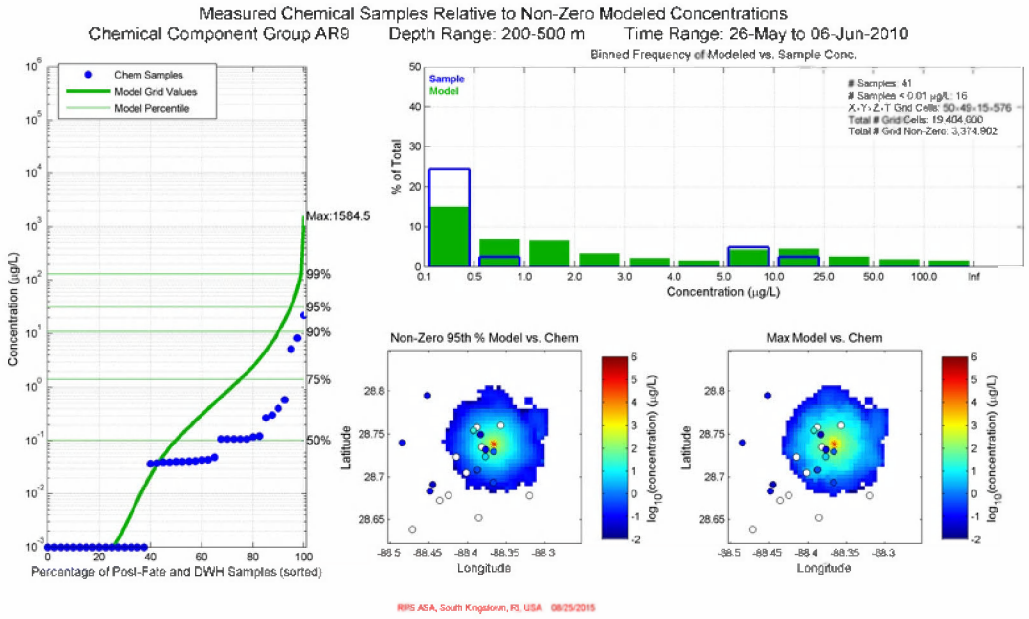

Figure G.2-54. Comparison of total (in-droplet + dissolved) concentrations (µg/L) produced by the Static Cone simulation to measurements from chemistry samples for May 26 – June 6, 2010 in 200-500m: AR9 component (soluble alkanes). Left: Cumulative frequency distribution of concentrations for observed chemistry samples and gridded model results. The maximum modeled chemistry concentration is provided at the top of the panel. Top right: Histogram of binned concentrations for observed samples (blue) and gridded model results (green) plotted as the percentage of the total number of samples/grid cells. Center bottom and bottom right: Spatial color maps of the 95th percentile and maximum (respectively) modeled concentration within each grid cell over the time interval, overlaid with dots representing the chemistry sample observations. Open symbols indicate chemical concentrations below the analytical detection limit.

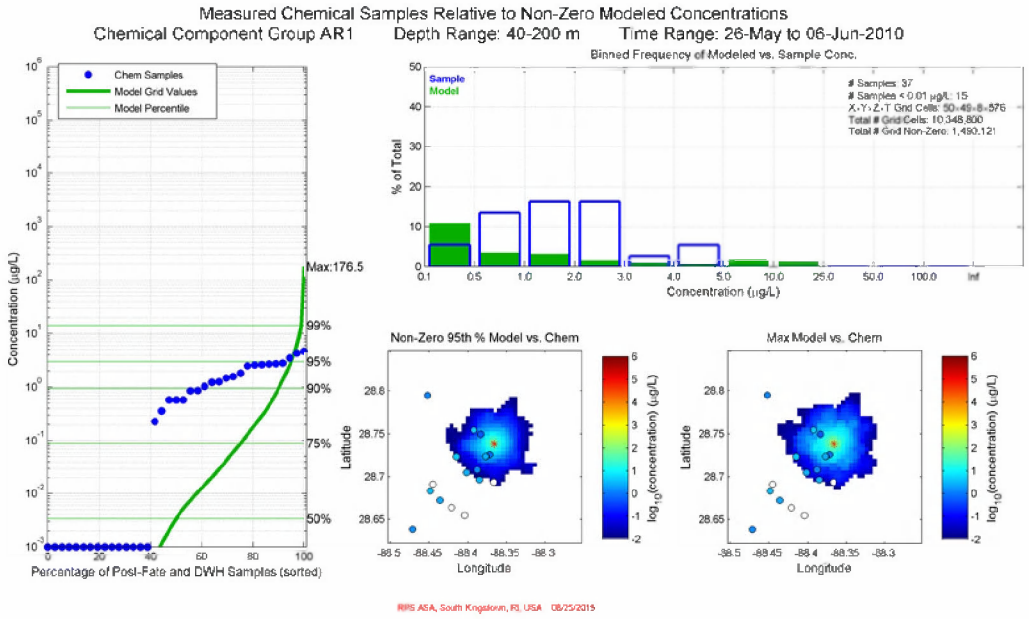

Figure G.2-55. Comparison of total (in-droplet + dissolved) concentrations (µg/L) produced by the Static Cone simulation to measurements from chemistry samples for May 26 – June 6, 2010 in 40-200m: AR1 component (BTEX). Left: Cumulative frequency distribution of concentrations for observed chemistry samples and gridded model results. The maximum modeled chemistry concentration is provided at the top of the panel. Top right: Histogram of binned concentrations for observed samples (blue) and gridded model results (green) plotted as the percentage of the total number of samples/grid cells. Center bottom and bottom right: Spatial color maps of the 95th percentile and maximum (respectively) modeled concentration within each grid cell over the time interval, overlaid with dots representing the chemistry sample observations. Open symbols indicate chemical concentrations below the analytical detection limit.

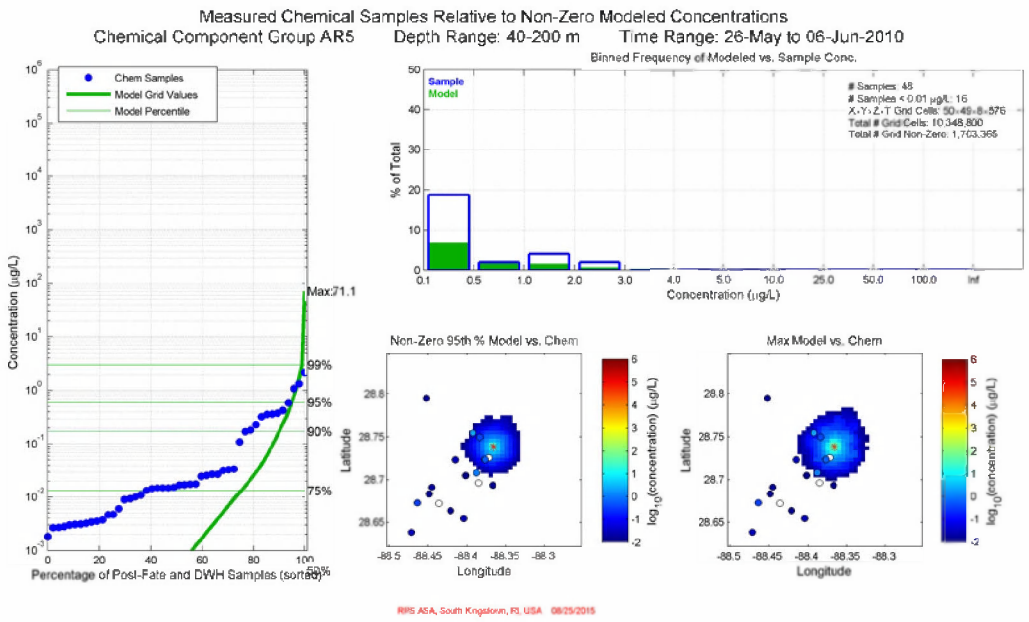

Figure G.2-56. Comparison of total (in-droplet + dissolved) concentrations (µg/L) produced by the Static Cone simulation to measurements from chemistry samples for May 26 – June 6, 2010 in 40-200m: AR5 component (C0-C2 naphthalenes). Left: Cumulative frequency distribution of concentrations for observed chemistry samples and gridded model results. The maximum modeled chemistry concentration is provided at the top of the panel. Top right: Histogram of binned concentrations for observed samples (blue) and gridded model results (green) plotted as the percentage of the total number of samples/grid cells. Center bottom and bottom right: Spatial color maps of the 95th percentile and maximum (respectively) modeled concentration within each grid cell over the time interval, overlaid with dots representing the chemistry sample observations. Open symbols indicate chemical concentrations below the analytical detection limit.

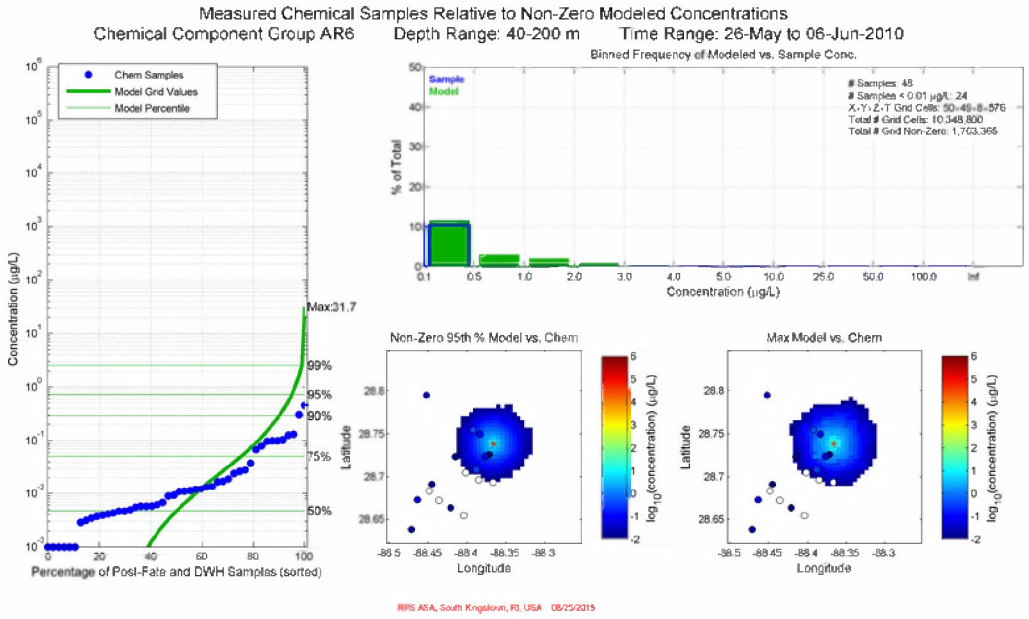

Figure G.2-57. Comparison of total (in-droplet + dissolved) concentrations (µg/L) produced by the Static Cone simulation to measurements from chemistry samples for May 26 – June 6, 2010 in 40-200m: AR6 component (C3-C4 naphthalenes). Left: Cumulative frequency distribution of concentrations for observed chemistry samples and gridded model results. The maximum modeled chemistry concentration is provided at the top of the panel. Top right: Histogram of binned concentrations for observed samples (blue) and gridded model results (green) plotted as the percentage of the total number of samples/grid cells. Center bottom and bottom right: Spatial color maps of the 95th percentile and maximum (respectively) modeled concentration within each grid cell over the time interval, overlaid with dots representing the chemistry sample observations. Open symbols indicate chemical concentrations below the analytical detection limit.

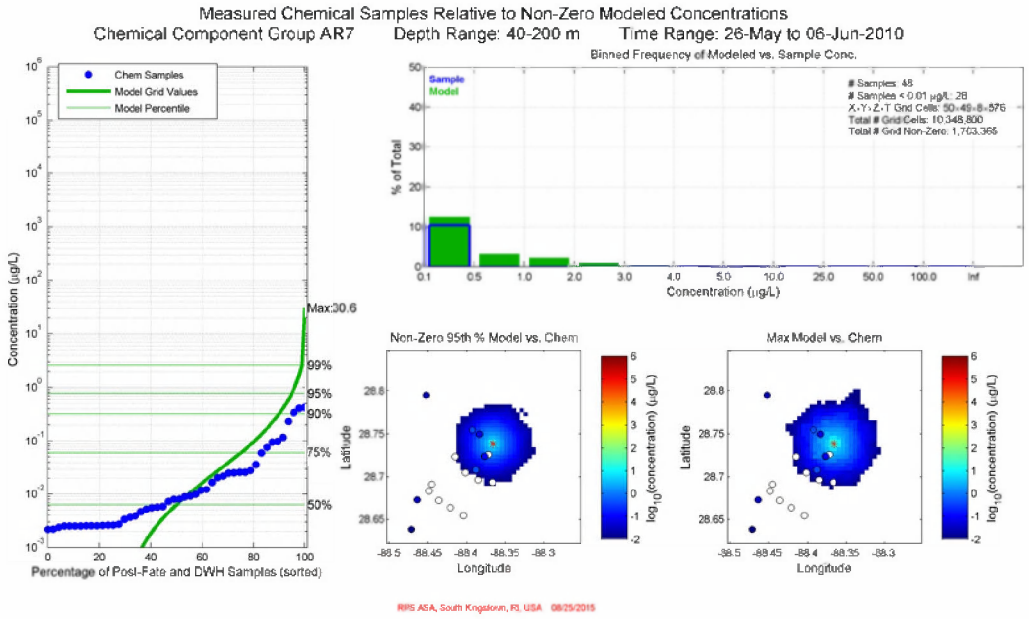

Figure G.2-58. Comparison of total (in-droplet + dissolved) concentrations (µg/L) produced by the Static Cone simulation to measurements from chemistry samples for May 26 – June 6, 2010 in 40-200m: AR7 component (fluorenes & C0-C1 3-ring PAHs). Left: Cumulative frequency distribution of concentrations for observed chemistry samples and gridded model results. The maximum modeled chemistry concentration is provided at the top of the panel. Top right: Histogram of binned concentrations for observed samples (blue) and gridded model results (green) plotted as the percentage of the total number of samples/grid cells. Center bottom and bottom right: Spatial color maps of the 95th percentile and maximum (respectively) modeled concentration within each grid cell over the time interval, overlaid with dots representing the chemistry sample observations. Open symbols indicate chemical concentrations below the analytical detection limit.

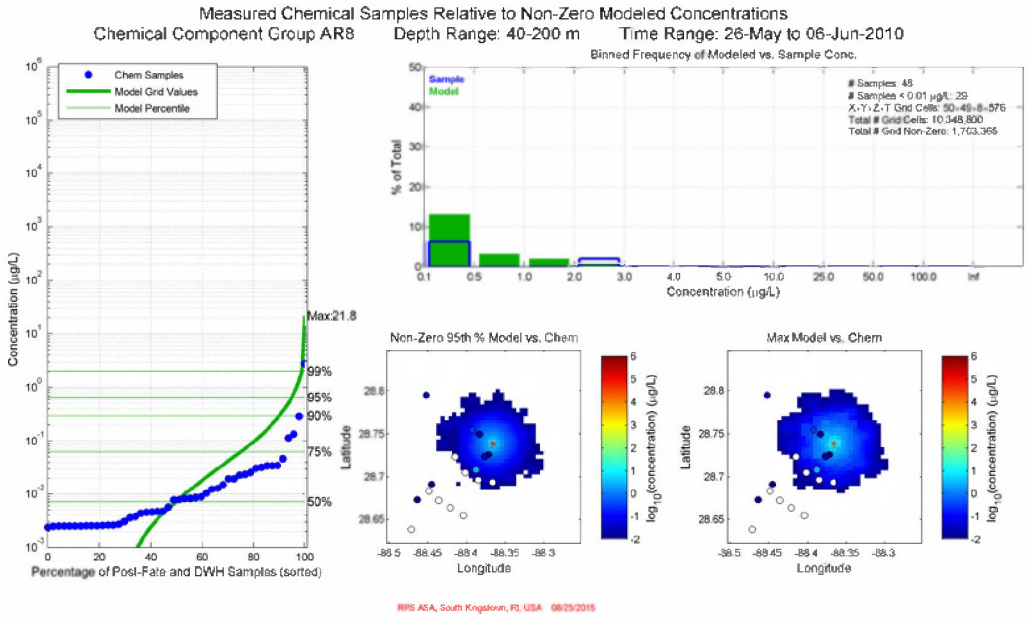

Figure G.2-59. Comparison of total (in-droplet + dissolved) concentrations (µg/L) produced by the Static Cone simulation to measurements from chemistry samples for May 26 – June 6, 2010 in 40-200m: AR8 component (4-ring PAHs & C2-C3 3-ring PAHs). Left: Cumulative frequency distribution of concentrations for observed chemistry samples and gridded model results. The maximum modeled chemistry concentration is provided at the top of the panel. Top right: Histogram of binned concentrations for observed samples (blue) and gridded model results (green) plotted as the percentage of the total number of samples/grid cells. Center bottom and bottom right: Spatial color maps of the 95th percentile and maximum (respectively) modeled concentration within each grid cell over the time interval, overlaid with dots representing the chemistry sample observations. Open symbols indicate chemical concentrations below the analytical detection limit.

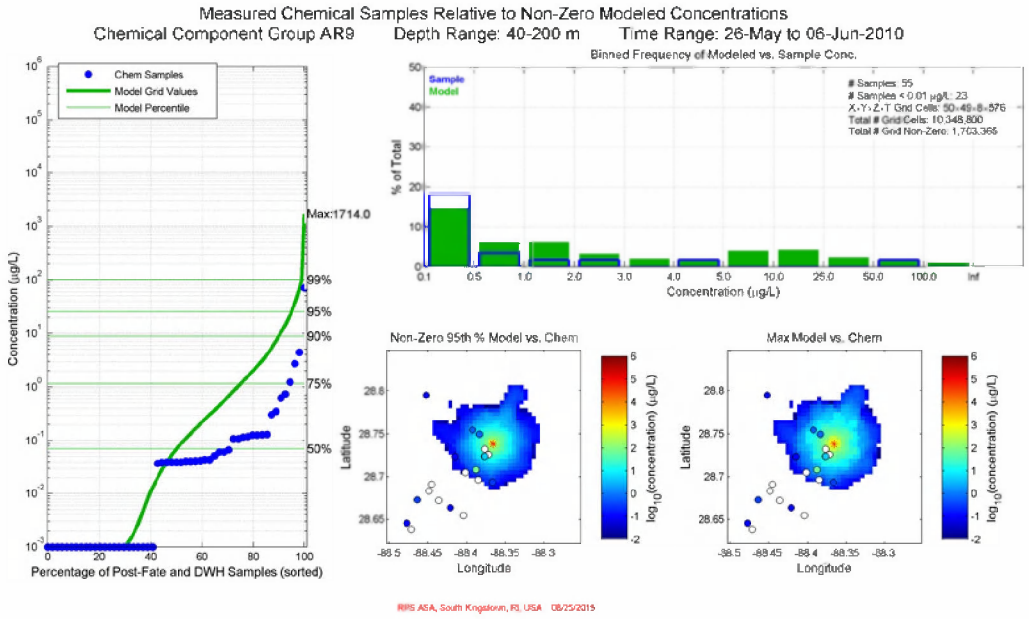

Figure G.2-60. Comparison of total (in-droplet + dissolved) concentrations (µg/L) produced by the Static Cone simulation to measurements from chemistry samples for May 26 – June 6, 2010 in 40-200m: AR9 component (soluble alkanes). Left: Cumulative frequency distribution of concentrations for observed chemistry samples and gridded model results. The maximum modeled chemistry concentration is provided at the top of the panel. Top right: Histogram of binned concentrations for observed samples (blue) and gridded model results (green) plotted as the percentage of the total number of samples/grid cells. Center bottom and bottom right: Spatial color maps of the 95th percentile and maximum (respectively) modeled concentration within each grid cell over the time interval, overlaid with dots representing the chemistry sample observations. Open symbols indicate chemical concentrations below the analytical detection limit.

G.2.3 June 6 – July 15, 2010

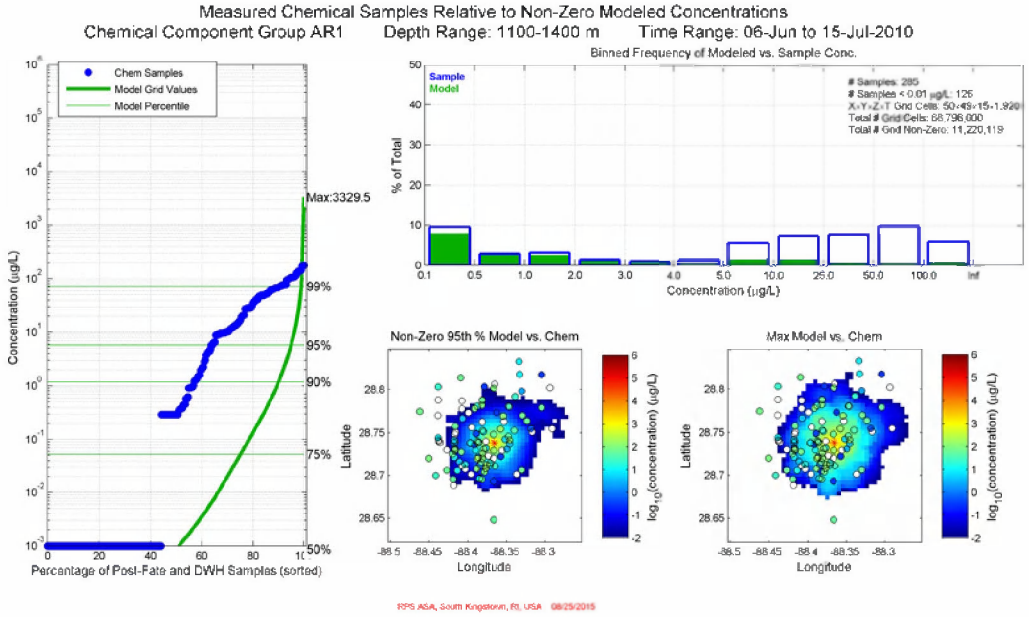

Figure G.2-61. Comparison of total (in-droplet + dissolved) concentrations (μg/L) produced by the Static Cone simulation to measurements from chemistry samples for June 6 – July 15, 2010 in 1100-1400m: AR1 component (BTEX). Left: Cumulative frequency distribution of concentrations for observed chemistry samples and gridded model results. The maximum modeled chemistry concentration is provided at the top of the panel. Top right: Histogram of binned concentrations for observed samples (blue) and gridded model results (green) plotted as the percentage of the total number of samples/grid cells. Center bottom and bottom right: Spatial color maps of the 95th percentile and maximum (respectively) modeled concentration within each grid cell over the time interval, overlaid with dots representing the chemistry sample observations. Open symbols indicate chemical concentrations below the analytical detection limit.

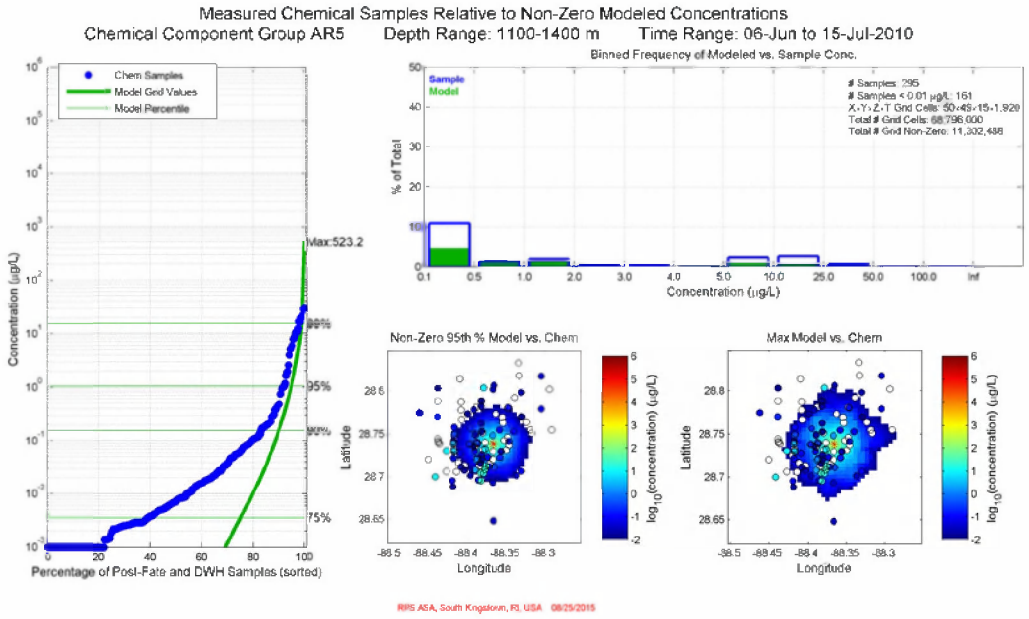

Figure G.2-62. Comparison of total (in-droplet + dissolved) concentrations (µg/L) produced by the Static Cone simulation to measurements from chemistry samples for June 6 – July 15, 2010 in 1100-1400m: AR5 component (C0-C2 naphthalenes). Left: Cumulative frequency distribution of concentrations for observed chemistry samples and gridded model results. The maximum modeled chemistry concentration is provided at the top of the panel. Top right: Histogram of binned concentrations for observed samples (blue) and gridded model results (green) plotted as the percentage of the total number of samples/grid cells. Center bottom and bottom right: Spatial color maps of the 95th percentile and maximum (respectively) modeled concentration within each grid cell over the time interval, overlaid with dots representing the chemistry sample observations. Open symbols indicate chemical concentrations below the analytical detection limit.

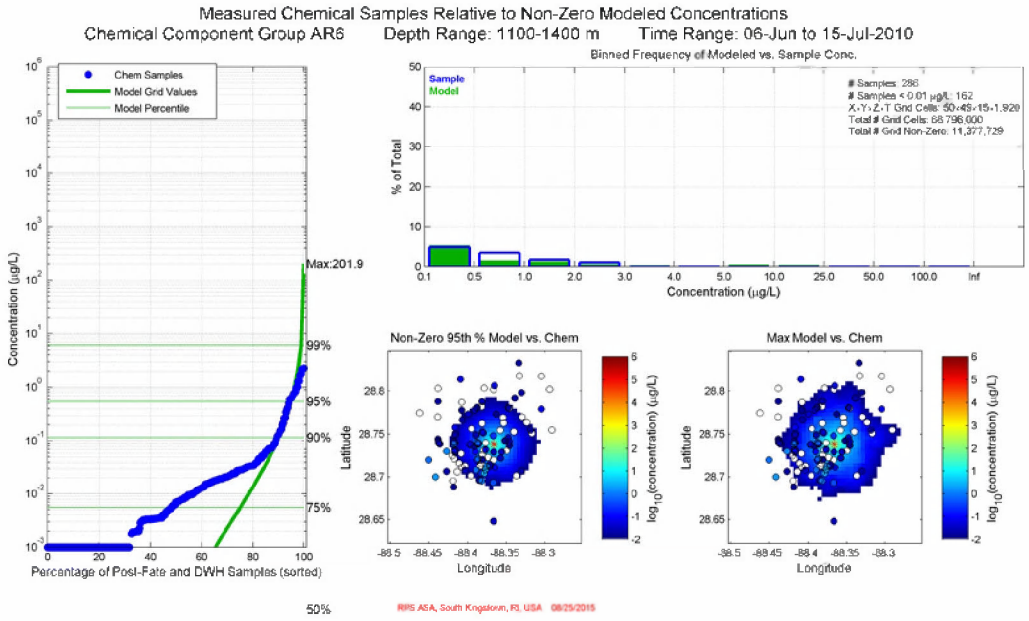

Figure G.2-63. Comparison of total (in-droplet + dissolved) concentrations (µg/L) produced by the Static Cone simulation to measurements from chemistry samples for June 6 – July 15, 2010 in 1100-1400m: AR6 component (C3-C4 naphthalenes). Left: Cumulative frequency distribution of concentrations for observed chemistry samples and gridded model results. The maximum modeled chemistry concentration is provided at the top of the panel. Top right: Histogram of binned concentrations for observed samples (blue) and gridded model results (green) plotted as the percentage of the total number of samples/grid cells. Center bottom and bottom right: Spatial color maps of the 95th percentile and maximum (respectively) modeled concentration within each grid cell over the time interval, overlaid with dots representing the chemistry sample observations. Open symbols indicate chemical concentrations below the analytical detection limit.

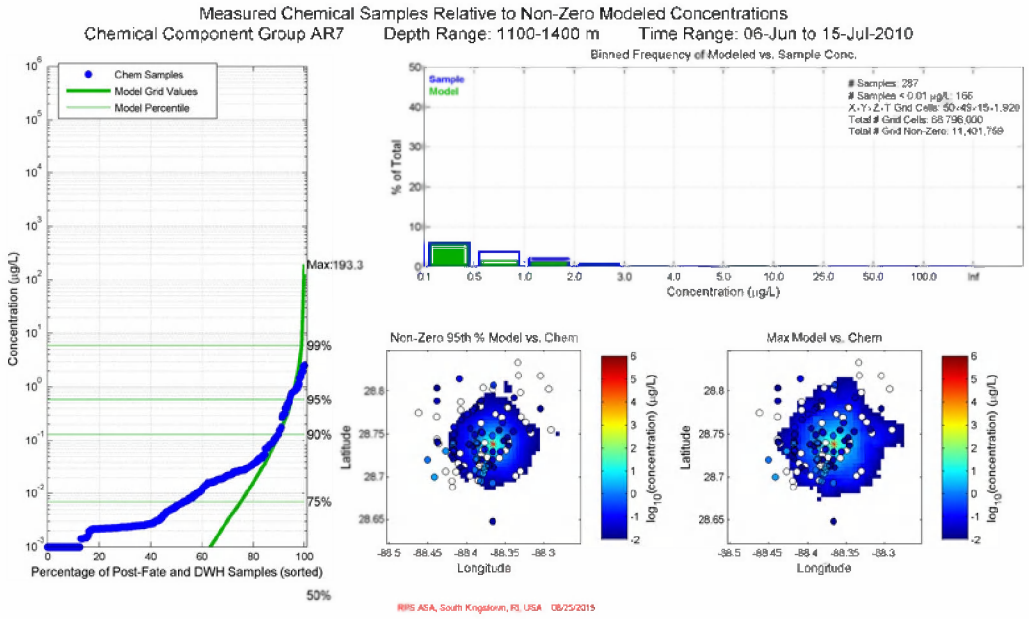

Figure G.2-64. Comparison of total (in-droplet + dissolved) concentrations (µg/L) produced by the Static Cone simulation to measurements from chemistry samples for June 6 – July 15, 2010 in 1100-1400m: AR7 component (fluorenes & C0-C1 3-ring PAHs). Left: Cumulative frequency distribution of concentrations for observed chemistry samples and gridded model results. The maximum modeled chemistry concentration is provided at the top of the panel. Top right: Histogram of binned concentrations for observed samples (blue) and gridded model results (green) plotted as the percentage of the total number of samples/grid cells. Center bottom and bottom right: Spatial color maps of the 95th percentile and maximum (respectively) modeled concentration within each grid cell over the time interval, overlaid with dots representing the chemistry sample observations. Open symbols indicate chemical concentrations below the analytical detection limit.

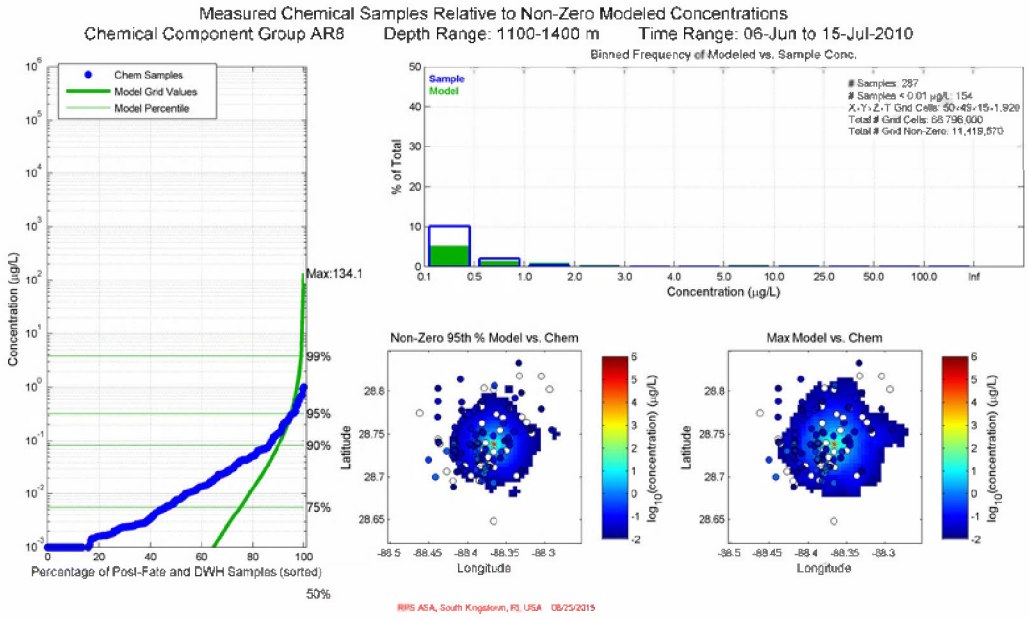

Figure G.2-65. Comparison of total (in-droplet + dissolved) concentrations (µg/L) produced by the Static Cone simulation to measurements from chemistry samples for June 6 – July 15, 2010 in 1100-1400m: AR8 component (4-ring PAHs & C2-C3 3-ring PAHs). Left: Cumulative frequency distribution of concentrations for observed chemistry samples and gridded model results. The maximum modeled chemistry concentration is provided at the top of the panel. Top right: Histogram of binned concentrations for observed samples (blue) and gridded model results (green) plotted as the percentage of the total number of samples/grid cells. Center bottom and bottom right: Spatial color maps of the 95th percentile and maximum (respectively) modeled concentration within each grid cell over the time interval, overlaid with dots representing the chemistry sample observations. Open symbols indicate chemical concentrations below the analytical detection limit.

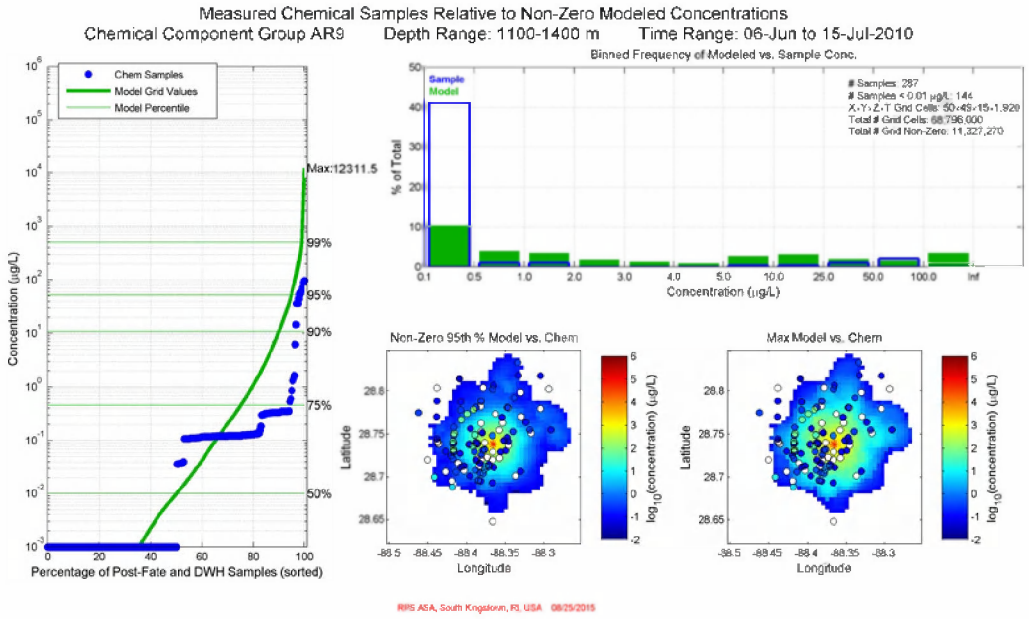

Figure G.2-66. Comparison of total (in-droplet + dissolved) concentrations (µg/L) produced by the Static Cone simulation to measurements from chemistry samples for June 6 – July 15, 2010 in 1100-1400m: AR9 component (soluble alkanes). Left: Cumulative frequency distribution of concentrations for observed chemistry samples and gridded model results. The maximum modeled chemistry concentration is provided at the top of the panel. Top right: Histogram of binned concentrations for observed samples (blue) and gridded model results (green) plotted as the percentage of the total number of samples/grid cells. Center bottom and bottom right: Spatial color maps of the 95th percentile and maximum (respectively) modeled concentration within each grid cell over the time interval, overlaid with dots representing the chemistry sample observations. Open symbols indicate chemical concentrations below the analytical detection limit.

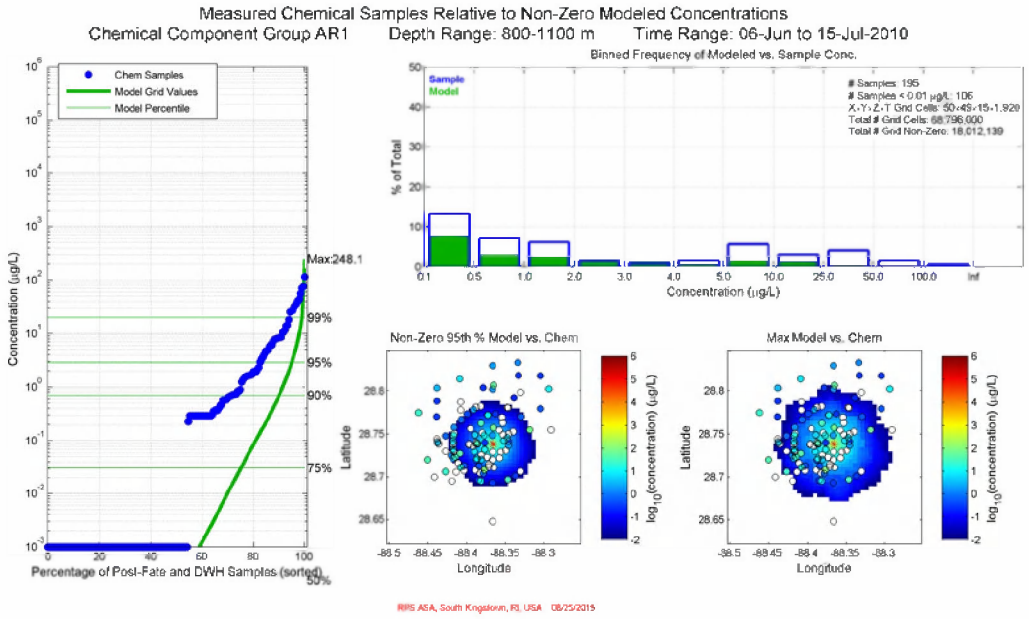

Figure G.2-67. Comparison of total (in-droplet + dissolved) concentrations (µg/L) produced by the Static Cone simulation to measurements from chemistry samples for June 6 – July 15, 2010 in 800-1100m: AR1 component (BTEX). Left: Cumulative frequency distribution of concentrations for observed chemistry samples and gridded model results. The maximum modeled chemistry concentration is provided at the top of the panel. Top right: Histogram of binned concentrations for observed samples (blue) and gridded model results (green) plotted as the percentage of the total number of samples/grid cells. Center bottom and bottom right: Spatial color maps of the 95th percentile and maximum (respectively) modeled concentration within each grid cell over the time interval, overlaid with dots representing the chemistry sample observations. Open symbols indicate chemical concentrations below the analytical detection limit.

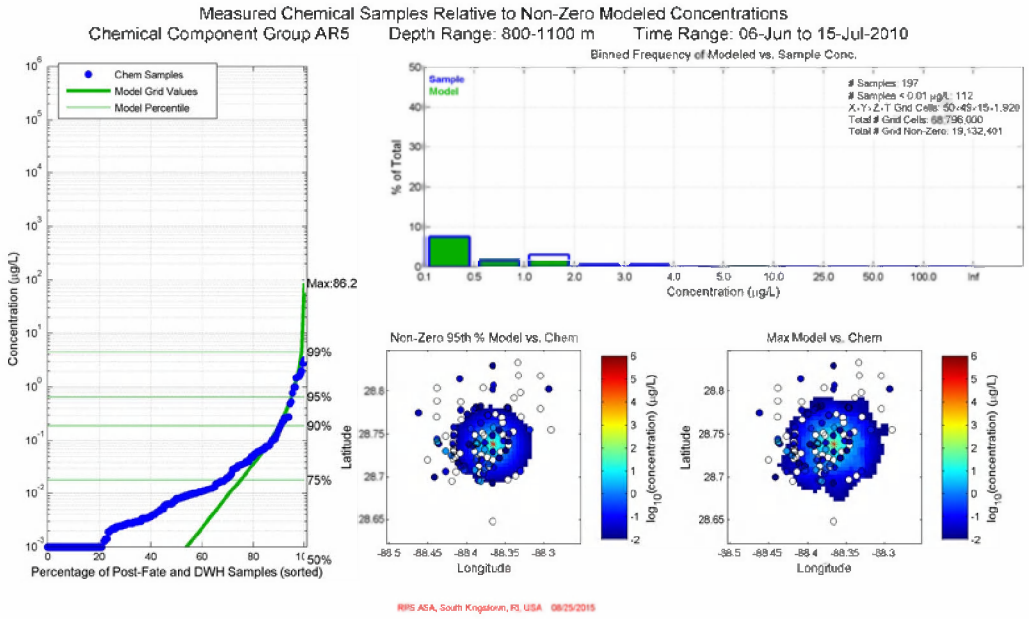

Figure G.2-68. Comparison of total (in-droplet + dissolved) concentrations (µg/L) produced by the Static Cone simulation to measurements from chemistry samples for June 6 – July 15, 2010 in 800-1100m: AR5 component (C0-C2 naphthalenes). Left: Cumulative frequency distribution of concentrations for observed chemistry samples and gridded model results. The maximum modeled chemistry concentration is provided at the top of the panel. Top right: Histogram of binned concentrations for observed samples (blue) and gridded model results (green) plotted as the percentage of the total number of samples/grid cells. Center bottom and bottom right: Spatial color maps of the 95th percentile and maximum (respectively) modeled concentration within each grid cell over the time interval, overlaid with dots representing the chemistry sample observations. Open symbols indicate chemical concentrations below the analytical detection limit.

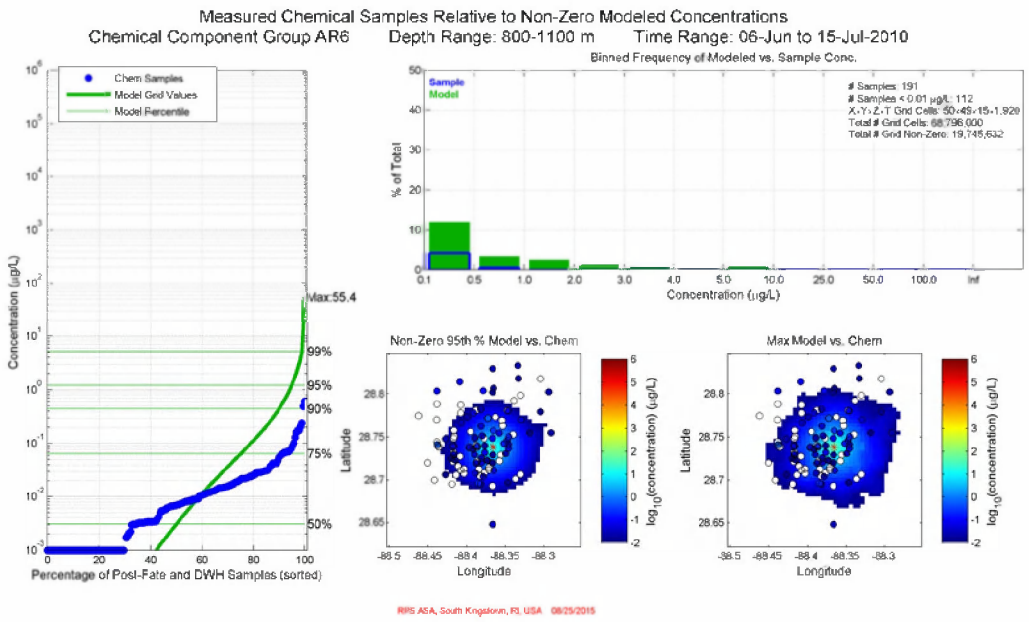

Figure G.2-69. Comparison of total (in-droplet + dissolved) concentrations (µg/L) produced by the Static Cone simulation to measurements from chemistry samples for June 6 – July 15, 2010 in 800-1100m: AR6 component (C3-C4 naphthalenes). Left: Cumulative frequency distribution of concentrations for observed chemistry samples and gridded model results. The maximum modeled chemistry concentration is provided at the top of the panel. Top right: Histogram of binned concentrations for observed samples (blue) and gridded model results (green) plotted as the percentage of the total number of samples/grid cells. Center bottom and bottom right: Spatial color maps of the 95th percentile and maximum (respectively) modeled concentration within each grid cell over the time interval, overlaid with dots representing the chemistry sample observations. Open symbols indicate chemical concentrations below the analytical detection limit.

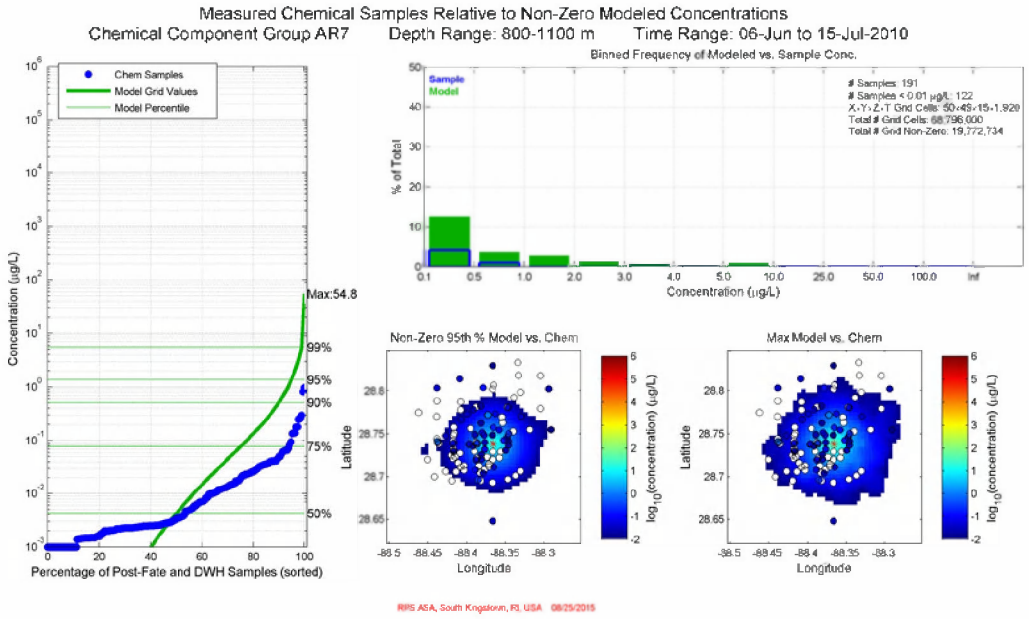

Figure G.2-70. Comparison of total (in-droplet + dissolved) concentrations (µg/L) produced by the Static Cone simulation to measurements from chemistry samples for June 6 – July 15, 2010 in 800-1100m: AR7 component (fluorenes & C0-C1 3-ring PAHs). Left: Cumulative frequency distribution of concentrations for observed chemistry samples and gridded model results. The maximum modeled chemistry concentration is provided at the top of the panel. Top right: Histogram of binned concentrations for observed samples (blue) and gridded model results (green) plotted as the percentage of the total number of samples/grid cells. Center bottom and bottom right: Spatial color maps of the 95th percentile and maximum (respectively) modeled concentration within each grid cell over the time interval, overlaid with dots representing the chemistry sample observations. Open symbols indicate chemical concentrations below the analytical detection limit.

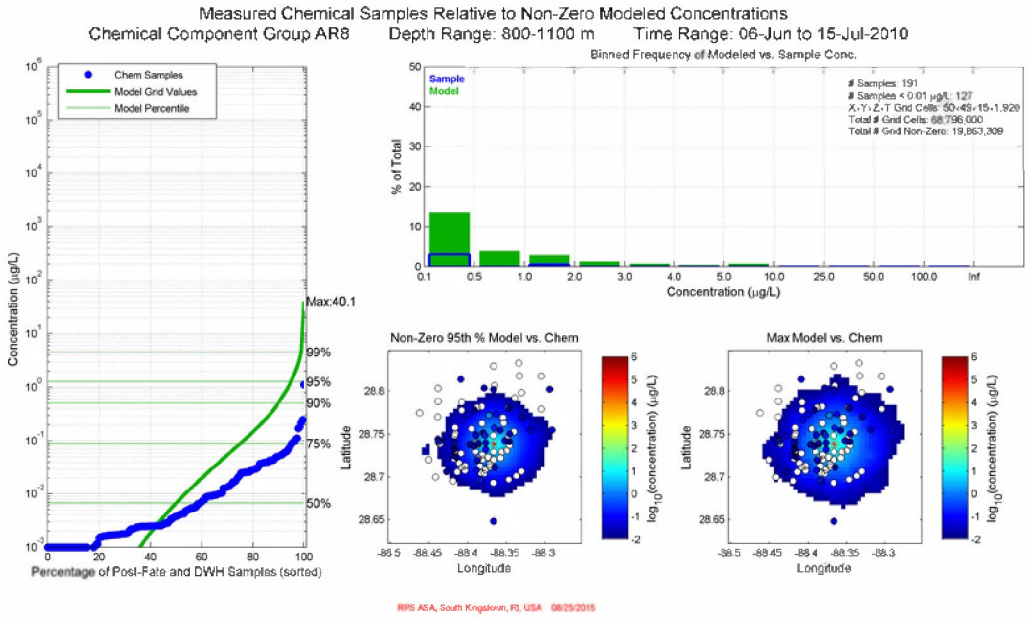

Figure G.2-71. Comparison of total (in-droplet + dissolved) concentrations (µg/L) produced by the Static Cone simulation to measurements from chemistry samples for June 6 – July 15, 2010 in 800-1100m: AR8 component (4-ring PAHs & C2-C3 3-ring PAHs). Left: Cumulative frequency distribution of concentrations for observed chemistry samples and gridded model results. The maximum modeled chemistry concentration is provided at the top of the panel. Top right: Histogram of binned concentrations for observed samples (blue) and gridded model results (green) plotted as the percentage of the total number of samples/grid cells. Center bottom and bottom right: Spatial color maps of the 95th percentile and maximum (respectively) modeled concentration within each grid cell over the time interval, overlaid with dots representing the chemistry sample observations. Open symbols indicate chemical concentrations below the analytical detection limit.

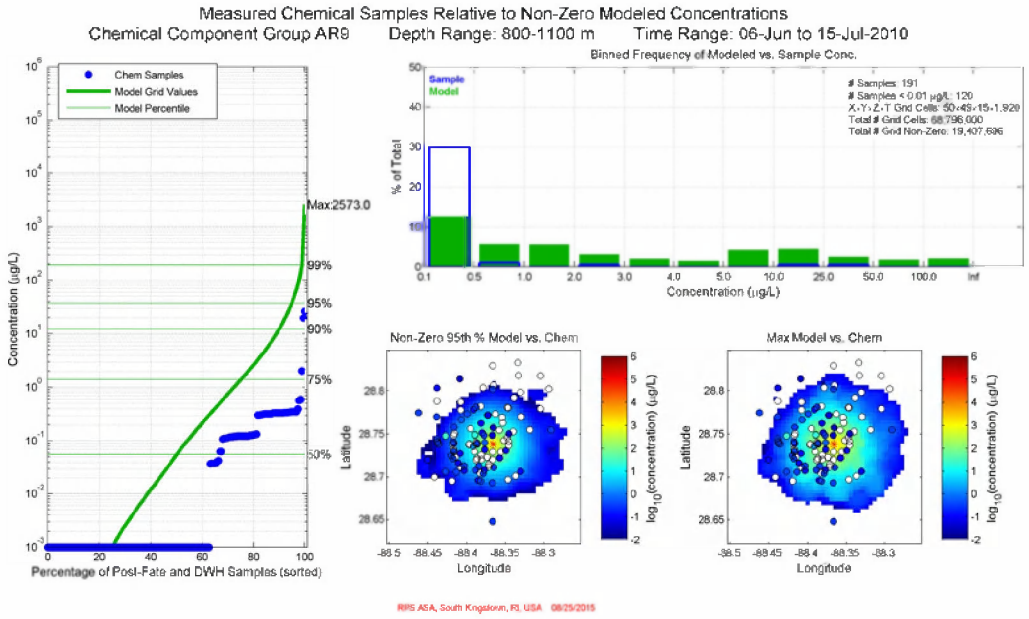

Figure G.2-72. Comparison of total (in-droplet + dissolved) concentrations (µg/L) produced by the Static Cone simulation to measurements from chemistry samples for June 6 – July 15, 2010 in 800-1100m: AR9 component (soluble alkanes). Left: Cumulative frequency distribution of concentrations for observed chemistry samples and gridded model results. The maximum modeled chemistry concentration is provided at the top of the panel. Top right: Histogram of binned concentrations for observed samples (blue) and gridded model results (green) plotted as the percentage of the total number of samples/grid cells. Center bottom and bottom right: Spatial color maps of the 95th percentile and maximum (respectively) modeled concentration within each grid cell over the time interval, overlaid with dots representing the chemistry sample observations. Open symbols indicate chemical concentrations below the analytical detection limit.

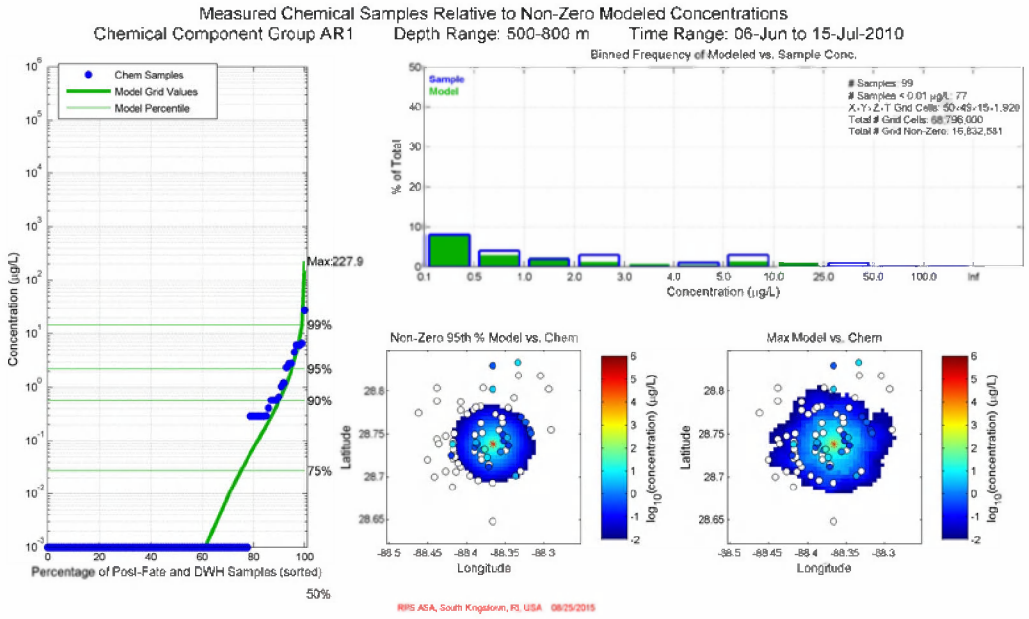

Figure G.2-73. Comparison of total (in-droplet + dissolved) concentrations (µg/L) produced by the Static Cone simulation to measurements from chemistry samples for June 6 – July 15, 2010 in 500-800m: AR1 component (BTEX). Left: Cumulative frequency distribution of concentrations for observed chemistry samples and gridded model results. The maximum modeled chemistry concentration is provided at the top of the panel. Top right: Histogram of binned concentrations for observed samples (blue) and gridded model results (green) plotted as the percentage of the total number of samples/grid cells. Center bottom and bottom right: Spatial color maps of the 95th percentile and maximum (respectively) modeled concentration within each grid cell over the time interval, overlaid with dots representing the chemistry sample observations. Open symbols indicate chemical concentrations below the analytical detection limit.

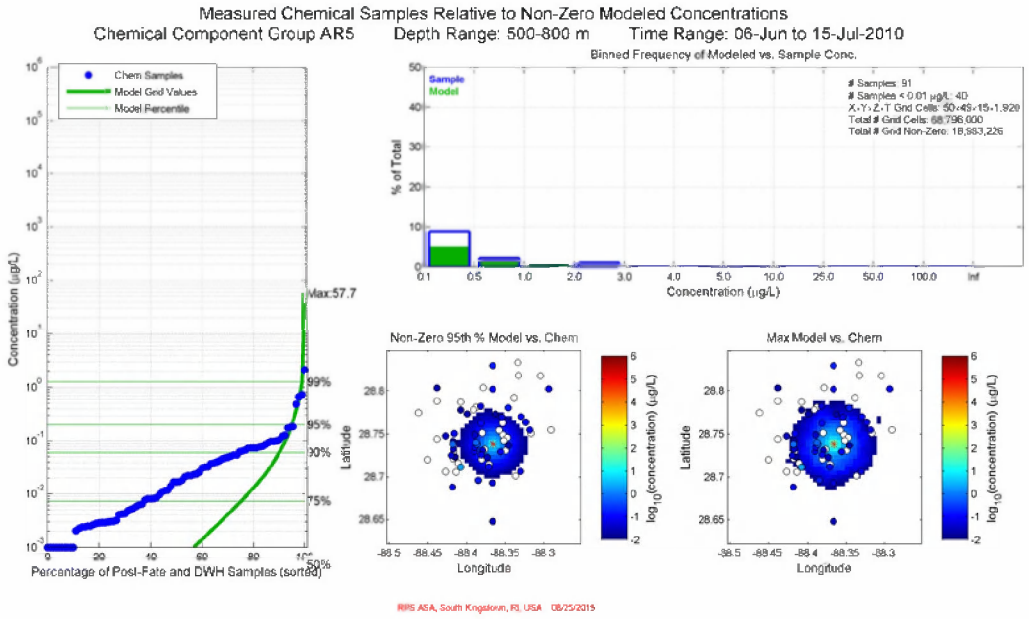

Figure G.2-74. Comparison of total (in-droplet + dissolved) concentrations (μg/L) produced by the Static Cone simulation to measurements from chemistry samples for June 6 – July 15, 2010 in 500-800m: AR5 component (C0-C2 naphthalenes). Left: Cumulative frequency distribution of concentrations for observed chemistry samples and gridded model results. The maximum modeled chemistry concentration is provided at the top of the panel. Top right: Histogram of binned concentrations for observed samples (blue) and gridded model results (green) plotted as the percentage of the total number of samples/grid cells. Center bottom and bottom right: Spatial color maps of the 95th percentile and maximum (respectively) modeled concentration within each grid cell over the time interval, overlaid with dots representing the chemistry sample observations. Open symbols indicate chemical concentrations below the analytical detection limit.

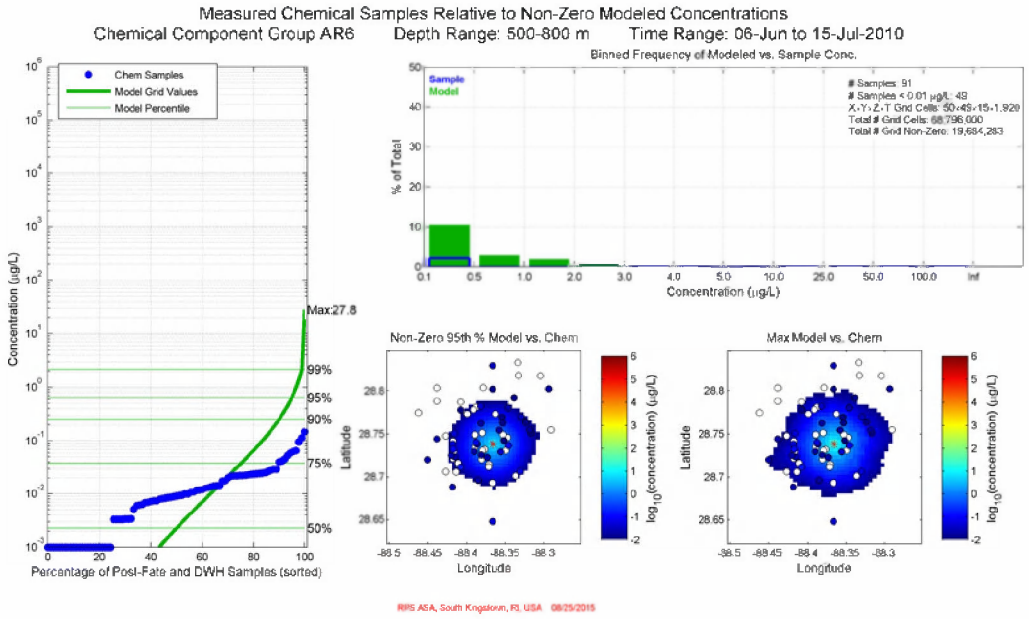

Figure G.2-75. Comparison of total (in-droplet + dissolved) concentrations (µg/L) produced by the Static Cone simulation to measurements from chemistry samples for June 6 – July 15, 2010 in 500-800m: AR6 component (C3-C4 naphthalenes). Left: Cumulative frequency distribution of concentrations for observed chemistry samples and gridded model results. The maximum modeled chemistry concentration is provided at the top of the panel. Top right: Histogram of binned concentrations for observed samples (blue) and gridded model results (green) plotted as the percentage of the total number of samples/grid cells. Center bottom and bottom right: Spatial color maps of the 95th percentile and maximum (respectively) modeled concentration within each grid cell over the time interval, overlaid with dots representing the chemistry sample observations. Open symbols indicate chemical concentrations below the analytical detection limit.

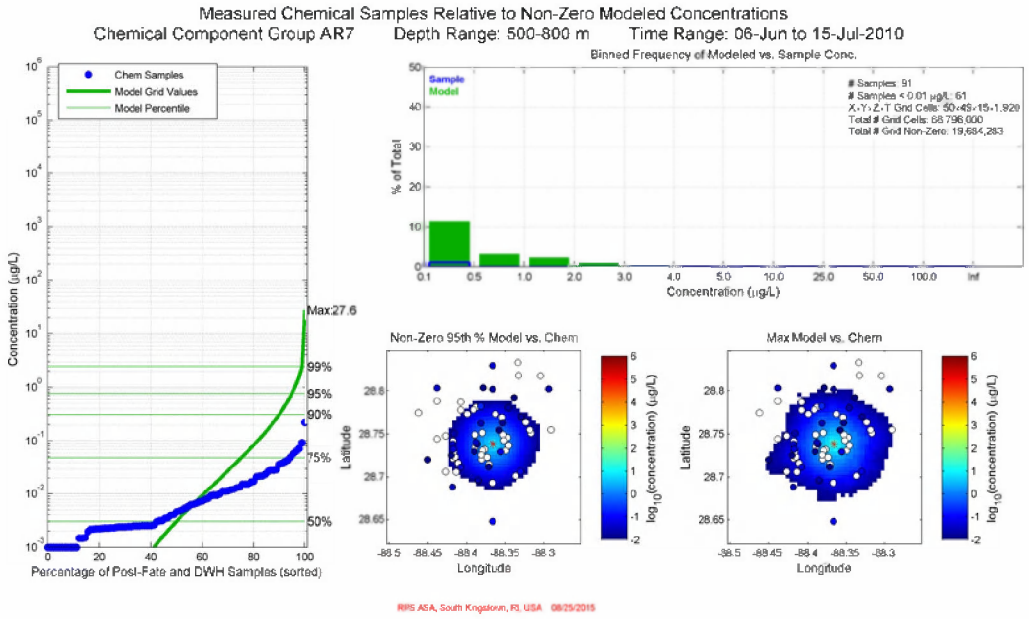

Figure G.2-76. Comparison of total (in-droplet + dissolved) concentrations (µg/L) produced by the Static Cone simulation to measurements from chemistry samples for June 6 – July 15, 2010 in 500-800m: AR7 component (fluorenes & C0-C1 3-ring PAHs). Left: Cumulative frequency distribution of concentrations for observed chemistry samples and gridded model results. The maximum modeled chemistry concentration is provided at the top of the panel. Top right: Histogram of binned concentrations for observed samples (blue) and gridded model results (green) plotted as the percentage of the total number of samples/grid cells. Center bottom and bottom right: Spatial color maps of the 95th percentile and maximum (respectively) modeled concentration within each grid cell over the time interval, overlaid with dots representing the chemistry sample observations. Open symbols indicate chemical concentrations below the analytical detection limit.

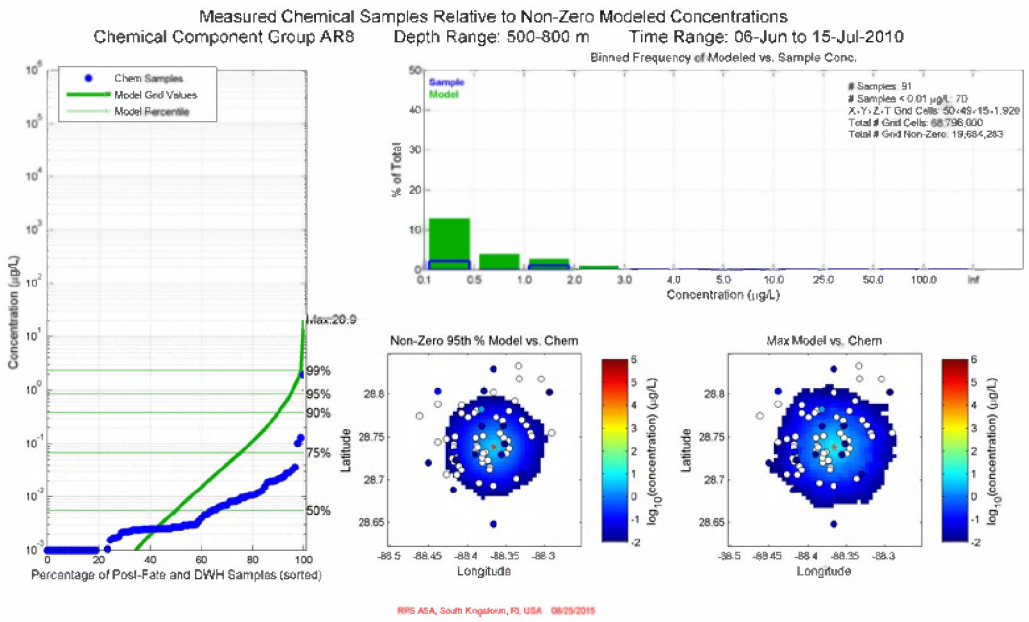

Figure G.2-77. Comparison of total (in-droplet + dissolved) concentrations (µg/L) produced by the Static Cone simulation to measurements from chemistry samples for June 6 – July 15, 2010 in 500-800m: AR8 component (4-ring PAHs & C2-C3 3-ring PAHs). Left: Cumulative frequency distribution of concentrations for observed chemistry samples and gridded model results. The maximum modeled chemistry concentration is provided at the top of the panel. Top right: Histogram of binned concentrations for observed samples (blue) and gridded model results (green) plotted as the percentage of the total number of samples/grid cells. Center bottom and bottom right: Spatial color maps of the 95th percentile and maximum (respectively) modeled concentration within each grid cell over the time interval, overlaid with dots representing the chemistry sample observations. Open symbols indicate chemical concentrations below the analytical detection limit.

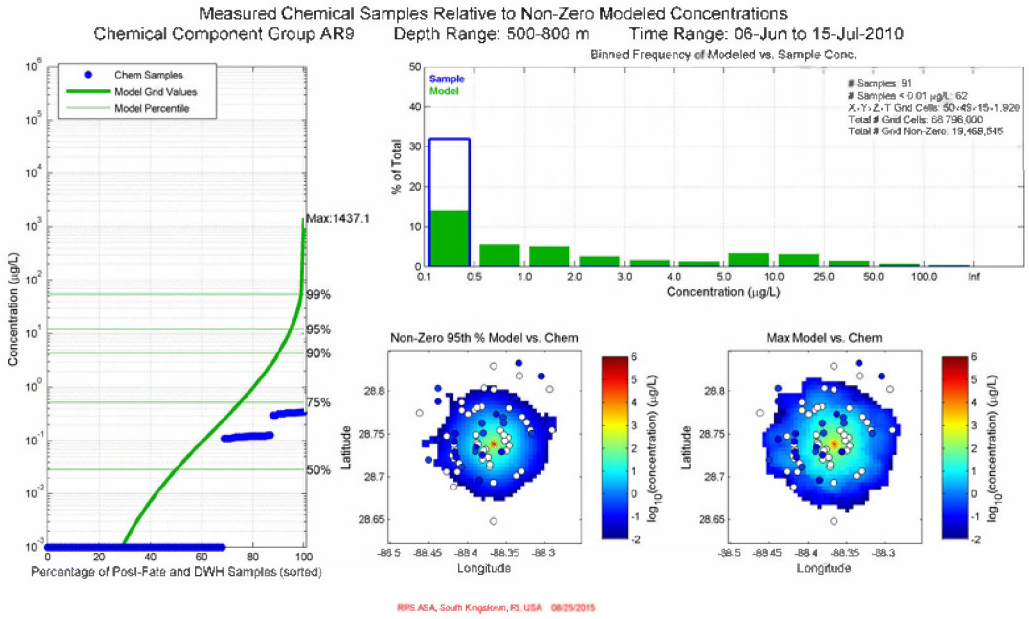

Figure G.2-78. Comparison of total (in-droplet + dissolved) concentrations (µg/L) produced by the Static Cone simulation to measurements from chemistry samples for June 6 – July 15, 2010 in 500-800m: AR9 component (soluble alkanes). Left: Cumulative frequency distribution of concentrations for observed chemistry samples and gridded model results. The maximum modeled chemistry concentration is provided at the top of the panel. Top right: Histogram of binned concentrations for observed samples (blue) and gridded model results (green) plotted as the percentage of the total number of samples/grid cells. Center bottom and bottom right: Spatial color maps of the 95th percentile and maximum (respectively) modeled concentration within each grid cell over the time interval, overlaid with dots representing the chemistry sample observations. Open symbols indicate chemical concentrations below the analytical detection limit.

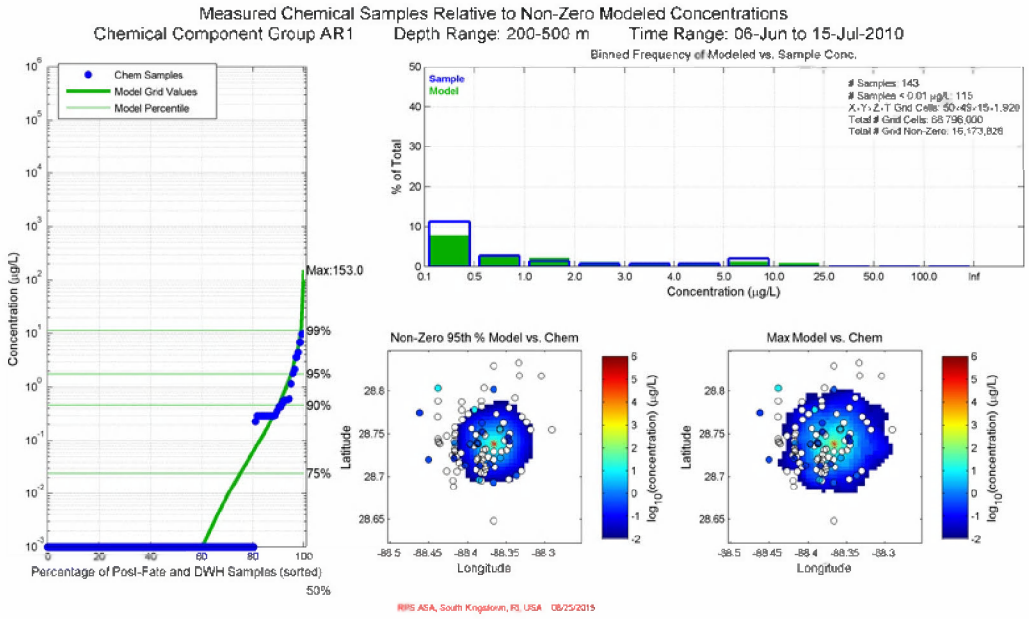

Figure G.2-79. Comparison of total (in-droplet + dissolved) concentrations (µg/L) produced by the Static Cone simulation to measurements from chemistry samples for June 6 – July 15, 2010 in 200-500m: AR1 component (BTEX). Left: Cumulative frequency distribution of concentrations for observed chemistry samples and gridded model results. The maximum modeled chemistry concentration is provided at the top of the panel. Top right: Histogram of binned concentrations for observed samples (blue) and gridded model results (green) plotted as the percentage of the total number of samples/grid cells. Center bottom and bottom right: Spatial color maps of the 95th percentile and maximum (respectively) modeled concentration within each grid cell over the time interval, overlaid with dots representing the chemistry sample observations. Open symbols indicate chemical concentrations below the analytical detection limit.

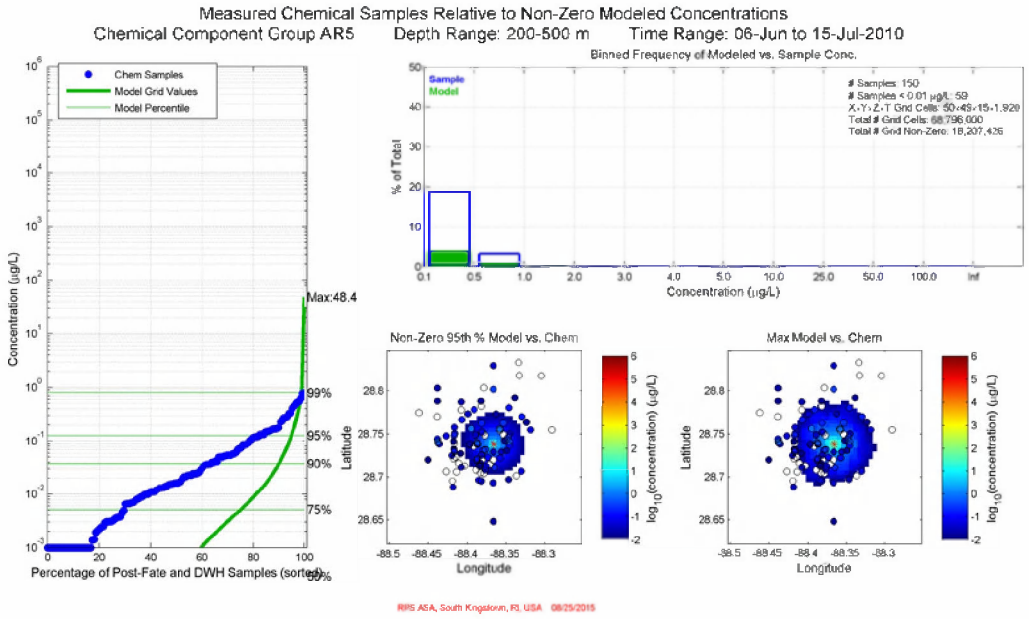

Figure G.2-80. Comparison of total (in-droplet + dissolved) concentrations (µg/L) produced by the Static Cone simulation to measurements from chemistry samples for June 6 – July 15, 2010 in 200-500m: AR5 component (C0-C2 naphthalenes). Left: Cumulative frequency distribution of concentrations for observed chemistry samples and gridded model results. The maximum modeled chemistry concentration is provided at the top of the panel. Top right: Histogram of binned concentrations for observed samples (blue) and gridded model results (green) plotted as the percentage of the total number of samples/grid cells. Center bottom and bottom right: Spatial color maps of the 95th percentile and maximum (respectively) modeled concentration within each grid cell over the time interval, overlaid with dots representing the chemistry sample observations. Open symbols indicate chemical concentrations below the analytical detection limit.

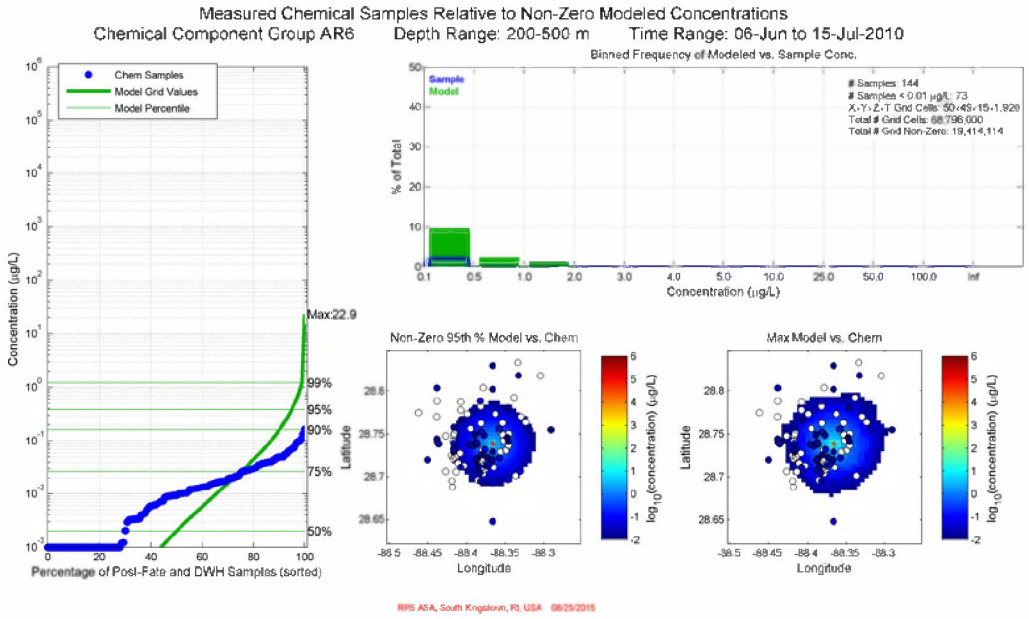

Figure G.2-81. Comparison of total (in-droplet + dissolved) concentrations (µg/L) produced by the Static Cone simulation to measurements from chemistry samples for June 6 – July 15, 2010 in 200-500m: AR6 component (C3-C4 naphthalenes). Left: Cumulative frequency distribution of concentrations for observed chemistry samples and gridded model results. The maximum modeled chemistry concentration is provided at the top of the panel. Top right: Histogram of binned concentrations for observed samples (blue) and gridded model results (green) plotted as the percentage of the total number of samples/grid cells. Center bottom and bottom right: Spatial color maps of the 95th percentile and maximum (respectively) modeled concentration within each grid cell over the time interval, overlaid with dots representing the chemistry sample observations. Open symbols indicate chemical concentrations below the analytical detection limit.

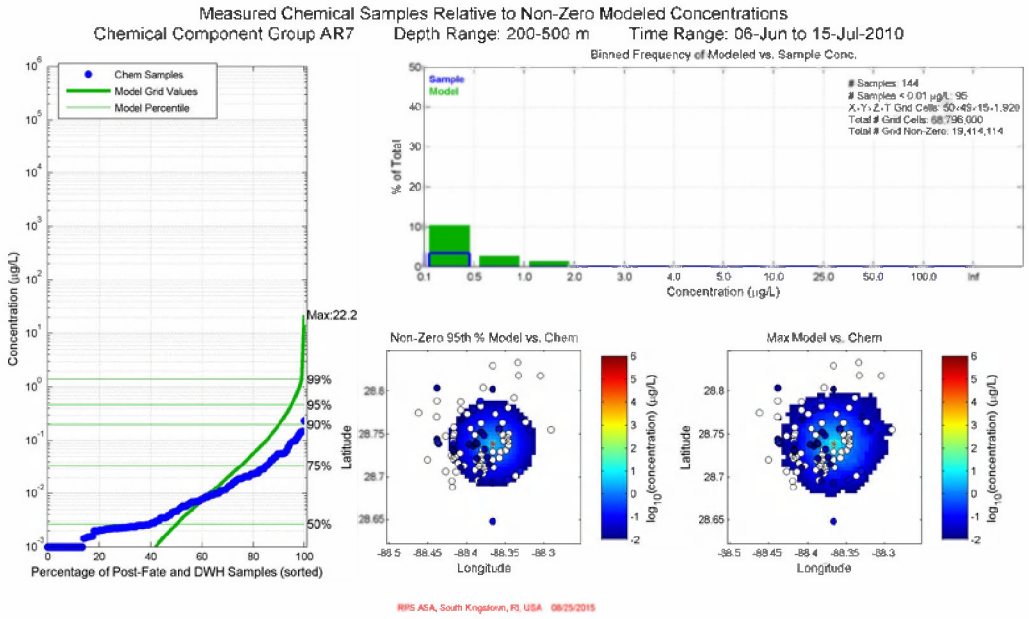

Figure G.2-82. Comparison of total (in-droplet + dissolved) concentrations (µg/L) produced by the Static Cone simulation to measurements from chemistry samples for June 6 – July 15, 2010 in 200-500m: AR7 component (fluorenes & C0-C1 3-ring PAHs). Left: Cumulative frequency distribution of concentrations for observed chemistry samples and gridded model results. The maximum modeled chemistry concentration is provided at the top of the panel. Top right: Histogram of binned concentrations for observed samples (blue) and gridded model results (green) plotted as the percentage of the total number of samples/grid cells. Center bottom and bottom right: Spatial color maps of the 95th percentile and maximum (respectively) modeled concentration within each grid cell over the time interval, overlaid with dots representing the chemistry sample observations. Open symbols indicate chemical concentrations below the analytical detection limit.

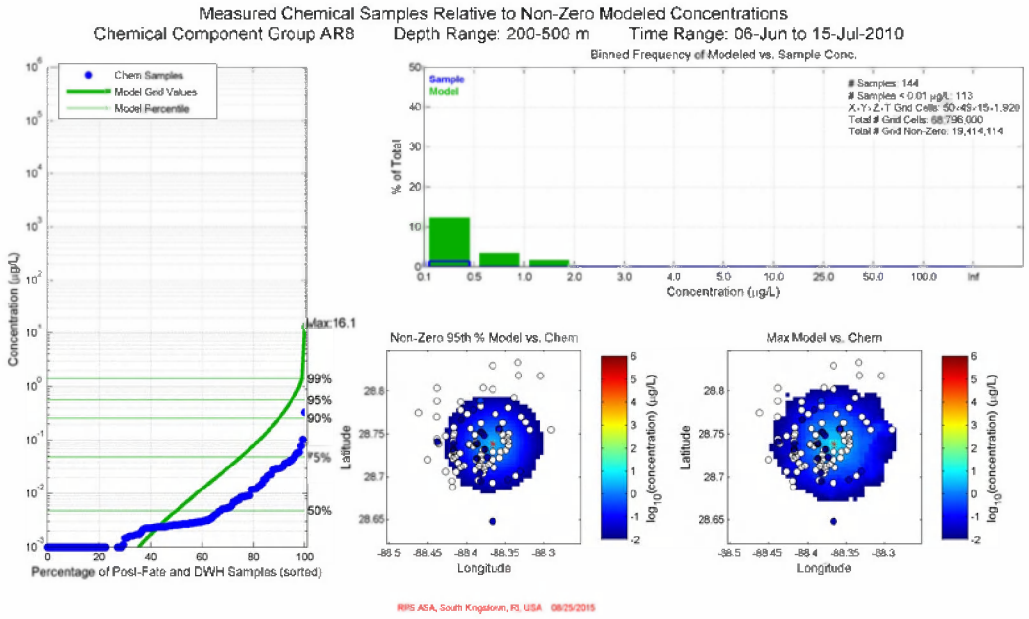

Figure G.2-83. Comparison of total (in-droplet + dissolved) concentrations (µg/L) produced by the Static Cone simulation to measurements from chemistry samples for June 6 – July 15, 2010 in 200-500m: AR8 component (4-ring PAHs & C2-C3 3-ring PAHs). Left: Cumulative frequency distribution of concentrations for observed chemistry samples and gridded model results. The maximum modeled chemistry concentration is provided at the top of the panel. Top right: Histogram of binned concentrations for observed samples (blue) and gridded model results (green) plotted as the percentage of the total number of samples/grid cells. Center bottom and bottom right: Spatial color maps of the 95th percentile and maximum (respectively) modeled concentration within each grid cell over the time interval, overlaid with dots representing the chemistry sample observations. Open symbols indicate chemical concentrations below the analytical detection limit.

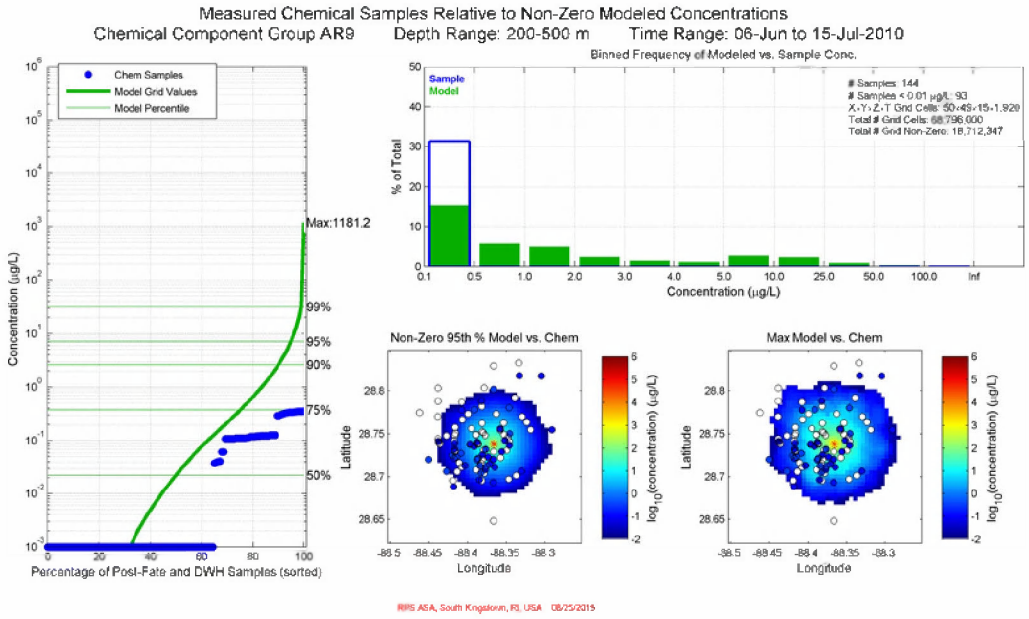

Figure G.2-84. Comparison of total (in-droplet + dissolved) concentrations (µg/L) produced by the Static Cone simulation to measurements from chemistry samples for June 6 – July 15, 2010 in 200-500m: AR9 component (soluble alkanes). Left: Cumulative frequency distribution of concentrations for observed chemistry samples and gridded model results. The maximum modeled chemistry concentration is provided at the top of the panel. Top right: Histogram of binned concentrations for observed samples (blue) and gridded model results (green) plotted as the percentage of the total number of samples/grid cells. Center bottom and bottom right: Spatial color maps of the 95th percentile and maximum (respectively) modeled concentration within each grid cell over the time interval, overlaid with dots representing the chemistry sample observations. Open symbols indicate chemical concentrations below the analytical detection limit.

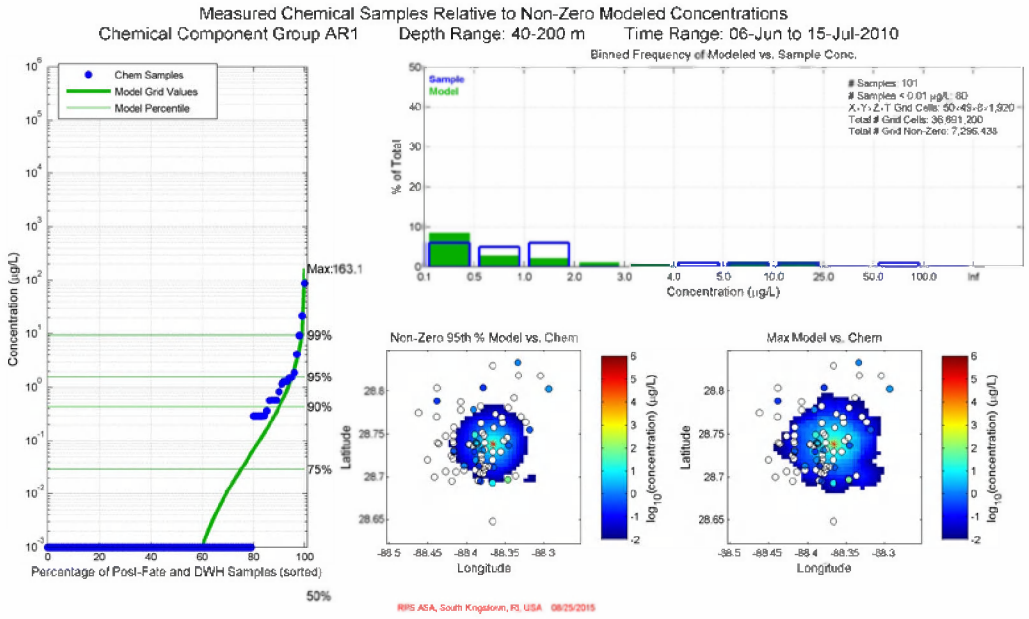

Figure G.2-85. Comparison of total (in-droplet + dissolved) concentrations (µg/L) produced by the Static Cone simulation to measurements from chemistry samples for June 6 – July 15, 2010 in 40-200m: AR1 component (BTEX). Left: Cumulative frequency distribution of concentrations for observed chemistry samples and gridded model results. The maximum modeled chemistry concentration is provided at the top of the panel. Top right: Histogram of binned concentrations for observed samples (blue) and gridded model results (green) plotted as the percentage of the total number of samples/grid cells. Center bottom and bottom right: Spatial color maps of the 95th percentile and maximum (respectively) modeled concentration within each grid cell over the time interval, overlaid with dots representing the chemistry sample observations. Open symbols indicate chemical concentrations below the analytical detection limit.

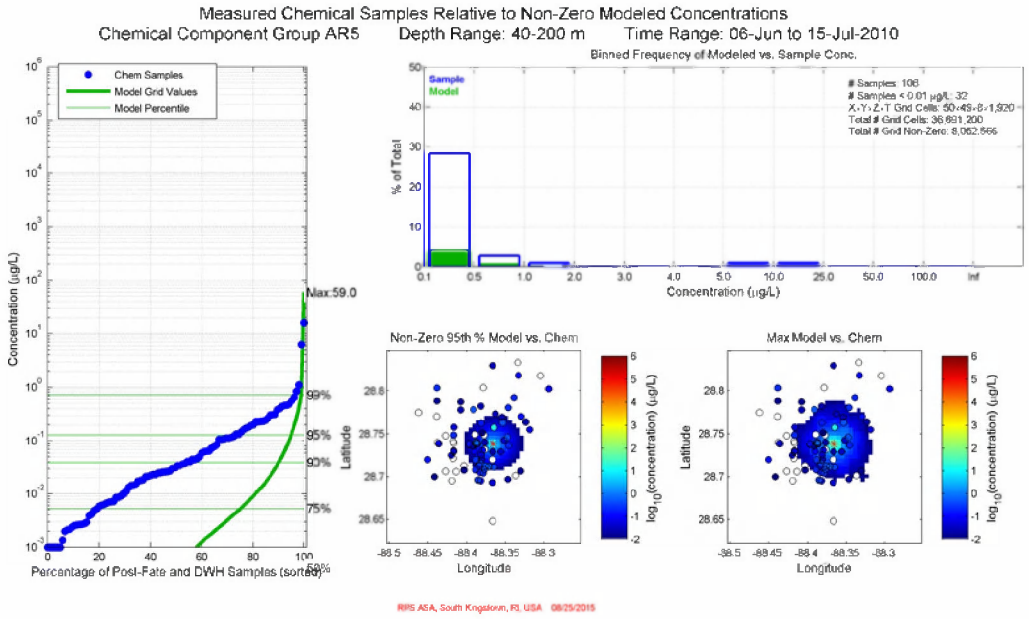

Figure G.2-86. Comparison of total (in-droplet + dissolved) concentrations (µg/L) produced by the Static Cone simulation to measurements from chemistry samples for June 6 – July 15, 2010 in 40-200m: AR5 component (C0-C2 naphthalenes). Left: Cumulative frequency distribution of concentrations for observed chemistry samples and gridded model results. The maximum modeled chemistry concentration is provided at the top of the panel. Top right: Histogram of binned concentrations for observed samples (blue) and gridded model results (green) plotted as the percentage of the total number of samples/grid cells. Center bottom and bottom right: Spatial color maps of the 95th percentile and maximum (respectively) modeled concentration within each grid cell over the time interval, overlaid with dots representing the chemistry sample observations. Open symbols indicate chemical concentrations below the analytical detection limit.

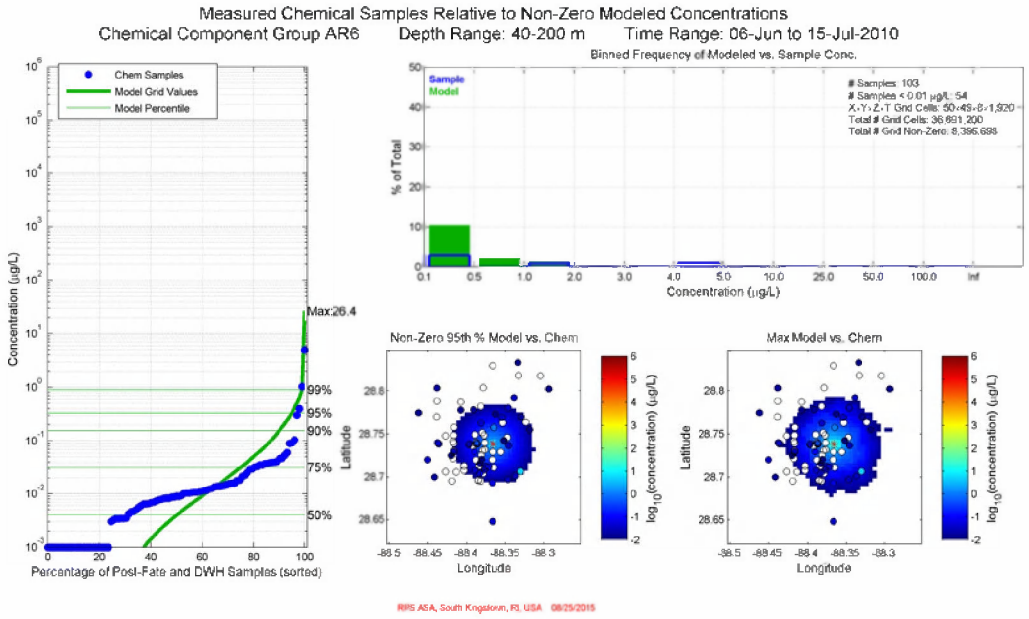

Figure G.2-87. Comparison of total (in-droplet + dissolved) concentrations (µg/L) produced by the Static Cone simulation to measurements from chemistry samples for June 6 – July 15, 2010 in 40-200m: AR6 component (C3-C4 naphthalenes). Left: Cumulative frequency distribution of concentrations for observed chemistry samples and gridded model results. The maximum modeled chemistry concentration is provided at the top of the panel. Top right: Histogram of binned concentrations for observed samples (blue) and gridded model results (green) plotted as the percentage of the total number of samples/grid cells. Center bottom and bottom right: Spatial color maps of the 95th percentile and maximum (respectively) modeled concentration within each grid cell over the time interval, overlaid with dots representing the chemistry sample observations. Open symbols indicate chemical concentrations below the analytical detection limit.

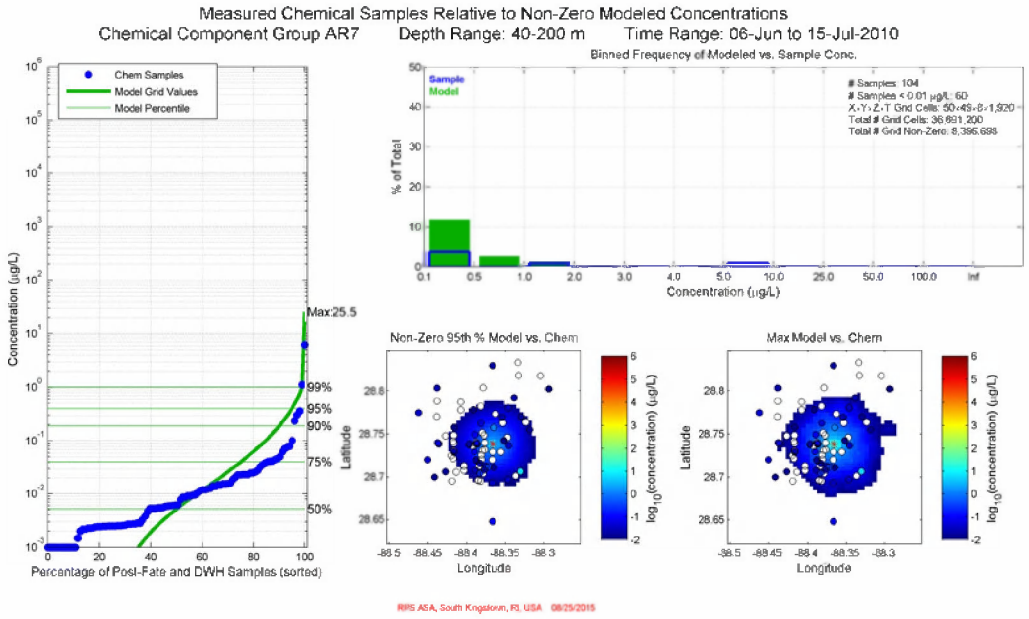

Figure G.2-88. Comparison of total (in-droplet + dissolved) concentrations (µg/L) produced by the Static Cone simulation to measurements from chemistry samples for June 6 – July 15, 2010 in 40-200m: AR7 component (fluorenes & C0-C1 3-ring PAHs). Left: Cumulative frequency distribution of concentrations for observed chemistry samples and gridded model results. The maximum modeled chemistry concentration is provided at the top of the panel. Top right: Histogram of binned concentrations for observed samples (blue) and gridded model results (green) plotted as the percentage of the total number of samples/grid cells. Center bottom and bottom right: Spatial color maps of the 95th percentile and maximum (respectively) modeled concentration within each grid cell over the time interval, overlaid with dots representing the chemistry sample observations. Open symbols indicate chemical concentrations below the analytical detection limit.

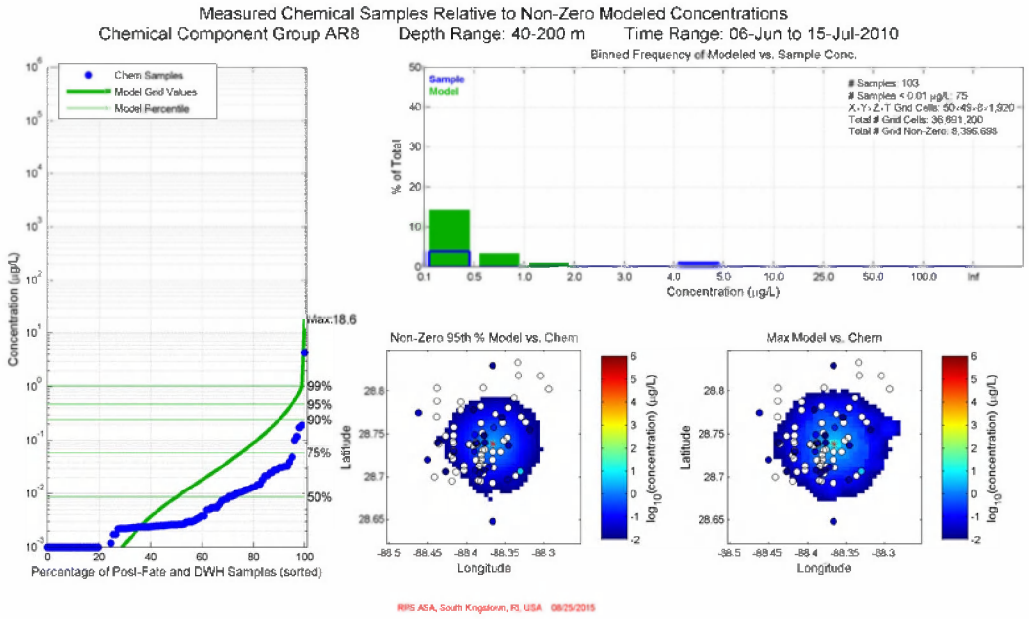

Figure G.2-89. Comparison of total (in-droplet + dissolved) concentrations (µg/L) produced by the Static Cone simulation to measurements from chemistry samples for June 6 – July 15, 2010 in 40-200m: AR8 component (4-ring PAHs & C2-C3 3-ring PAHs). Left: Cumulative frequency distribution of concentrations for observed chemistry samples and gridded model results. The maximum modeled chemistry concentration is provided at the top of the panel. Top right: Histogram of binned concentrations for observed samples (blue) and gridded model results (green) plotted as the percentage of the total number of samples/grid cells. Center bottom and bottom right: Spatial color maps of the 95th percentile and maximum (respectively) modeled concentration within each grid cell over the time interval, overlaid with dots representing the chemistry sample observations. Open symbols indicate chemical concentrations below the analytical detection limit.

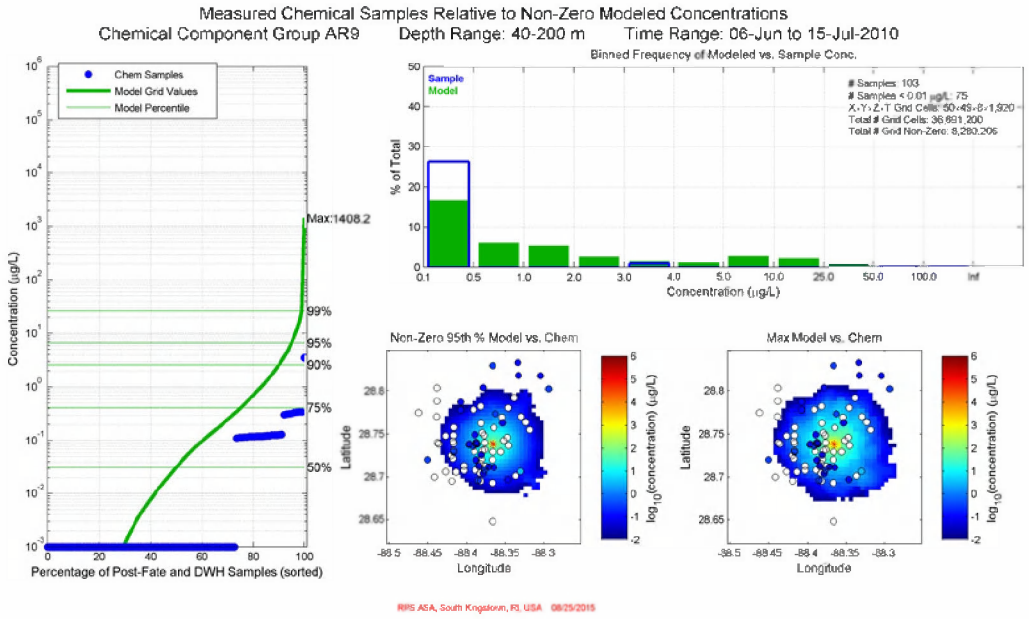

Figure G.2-90. Comparison of total (in-droplet + dissolved) concentrations (µg/L) produced by the Static Cone simulation to measurements from chemistry samples for June 6 – July 15, 2010 in 40-200m: AR9 component (soluble alkanes). Left: Cumulative frequency distribution of concentrations for observed chemistry samples and gridded model results. The maximum modeled chemistry concentration is provided at the top of the panel. Top right: Histogram of binned concentrations for observed samples (blue) and gridded model results (green) plotted as the percentage of the total number of samples/grid cells. Center bottom and bottom right: Spatial color maps of the 95th percentile and maximum (respectively) modeled concentration within each grid cell over the time interval, overlaid with dots representing the chemistry sample observations. Open symbols indicate chemical concentrations below the analytical detection limit.

G.3 Simulation Using Currents from IASROMS

G.3.1 April 22 – May 26, 2010

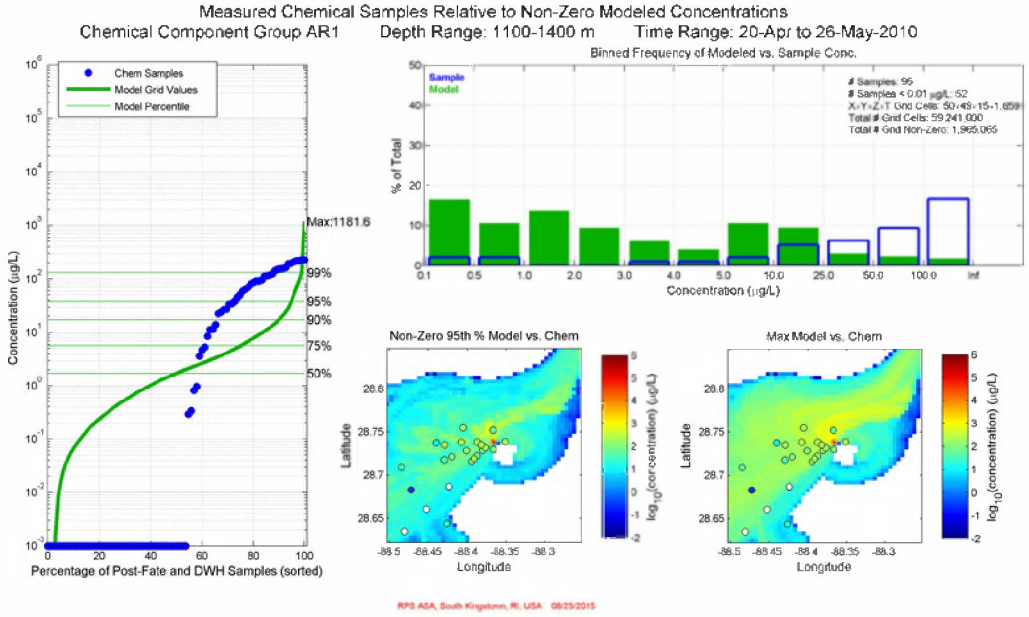

Figure G.3-91. Comparison of total (in-droplet + dissolved) concentrations (µg/L) produced by the simulation with IASROMS currents to measurements from chemistry samples for April 22 – May 26, 2010 in 1100-1400m: AR1 component (BTEX). Left: Cumulative frequency distribution of concentrations for observed chemistry samples and gridded model results. The maximum modeled chemistry concentration is provided at the top of the panel. Top right: Histogram of binned concentrations for observed samples (blue) and gridded model results (green) plotted as the percentage of the total number of samples/grid cells. Center bottom and bottom right: Spatial color maps of the 95th percentile and maximum (respectively) modeled concentration within each grid cell over the time interval, overlaid with dots representing the chemistry sample observations. Open symbols indicate chemical concentrations below the analytical detection limit.

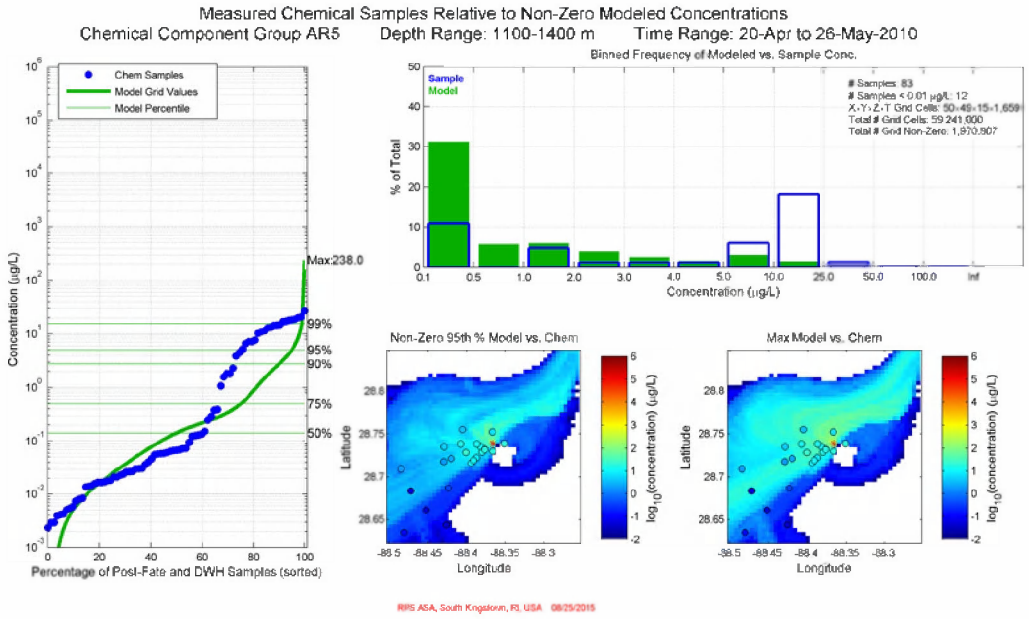

Figure G.3-92. Comparison of total (in-droplet + dissolved) concentrations (µg/L) produced by the simulation with IASROMS currents to measurements from chemistry samples for April 22 – May 26, 2010 in 1100-1400m: AR5 component (C0-C2 naphthalenes). Left: Cumulative frequency distribution of concentrations for observed chemistry samples and gridded model results. The maximum modeled chemistry concentration is provided at the top of the panel. Top right: Histogram of binned concentrations for observed samples (blue) and gridded model results (green) plotted as the percentage of the total number of samples/grid cells. Center bottom and bottom right: Spatial color maps of the 95th percentile and maximum (respectively) modeled concentration within each grid cell over the time interval, overlaid with dots representing the chemistry sample observations. Open symbols indicate chemical concentrations below the analytical detection limit.

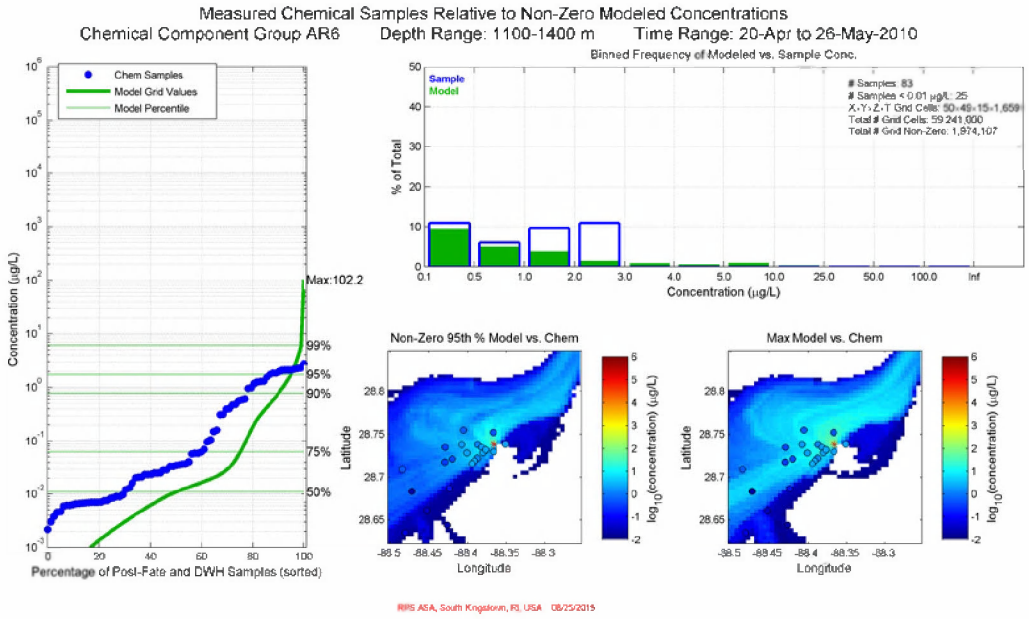

Figure G.3-93. Comparison of total (in-droplet + dissolved) concentrations (µg/L) produced by the simulation with IASROMS currents to measurements from chemistry samples for April 22 – May 26, 2010 in 1100-1400m: AR6 component (C3-C4 naphthalenes). Left: Cumulative frequency distribution of concentrations for observed chemistry samples and gridded model results. The maximum modeled chemistry concentration is provided at the top of the panel. Top right: Histogram of binned concentrations for observed samples (blue) and gridded model results (green) plotted as the percentage of the total number of samples/grid cells. Center bottom and bottom right: Spatial color maps of the 95th percentile and maximum (respectively) modeled concentration within each grid cell over the time interval, overlaid with dots representing the chemistry sample observations. Open symbols indicate chemical concentrations below the analytical detection limit.

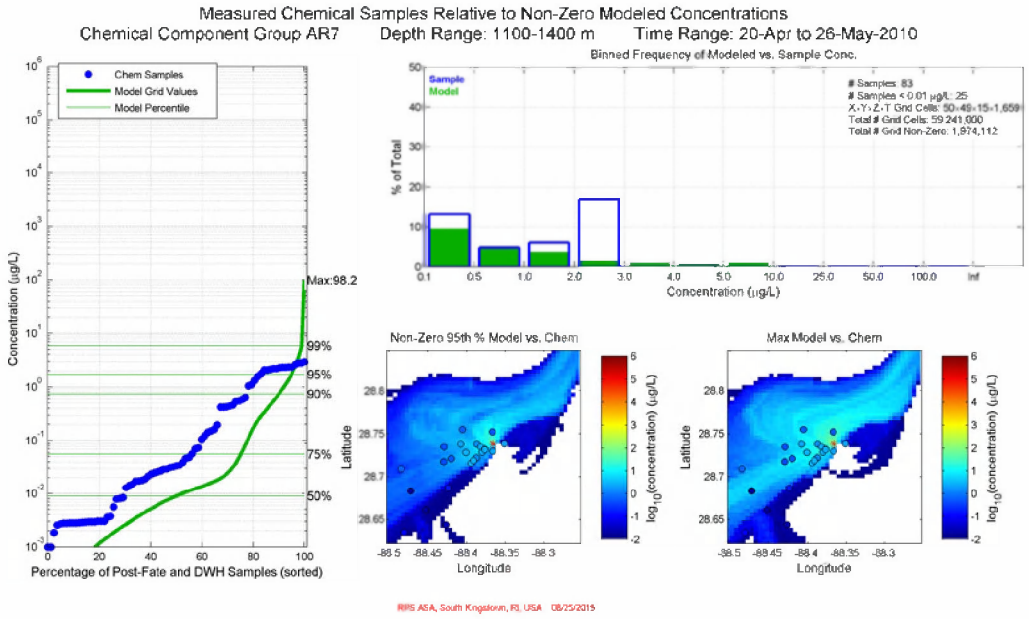

Figure G.3-94. Comparison of total (in-droplet + dissolved) concentrations (µg/L) produced by the simulation with IASROMS currents to measurements from chemistry samples for April 22 – May 26, 2010 in 1100-1400m: AR7 component (fluorenes & C0-C1 3-ring PAHs). Left: Cumulative frequency distribution of concentrations for observed chemistry samples and gridded model results. The maximum modeled chemistry concentration is provided at the top of the panel. Top right: Histogram of binned concentrations for observed samples (blue) and gridded model results (green) plotted as the percentage of the total number of samples/grid cells. Center bottom and bottom right: Spatial color maps of the 95th percentile and maximum (respectively) modeled concentration within each grid cell over the time interval, overlaid with dots representing the chemistry sample observations. Open symbols indicate chemical concentrations below the analytical detection limit.

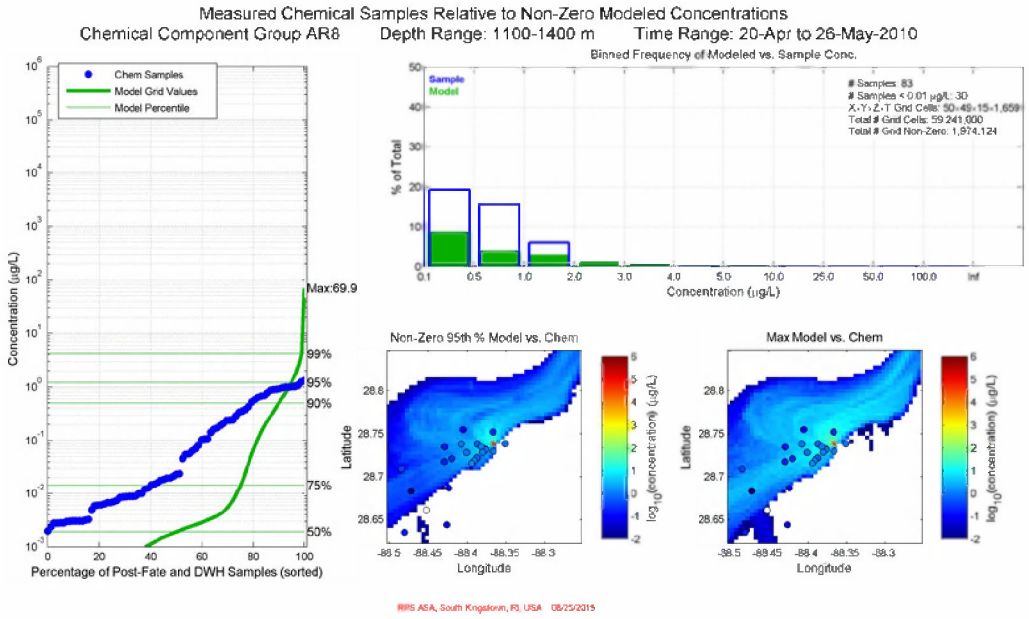

Figure G.3-95. Comparison of total (in-droplet + dissolved) concentrations (µg/L) produced by the simulation with IASROMS currents to measurements from chemistry samples for April 22 – May 26, 2010 in 1100-1400m: AR8 component (4-ring PAHs & C2-C3 3-ring PAHs). Left: Cumulative frequency distribution of concentrations for observed chemistry samples and gridded model results. The maximum modeled chemistry concentration is provided at the top of the panel. Top right: Histogram of binned concentrations for observed samples (blue) and gridded model results (green) plotted as the percentage of the total number of samples/grid cells. Center bottom and bottom right: Spatial color maps of the 95th percentile and maximum (respectively) modeled concentration within each grid cell over the time interval, overlaid with dots representing the chemistry sample observations. Open symbols indicate chemical concentrations below the analytical detection limit.

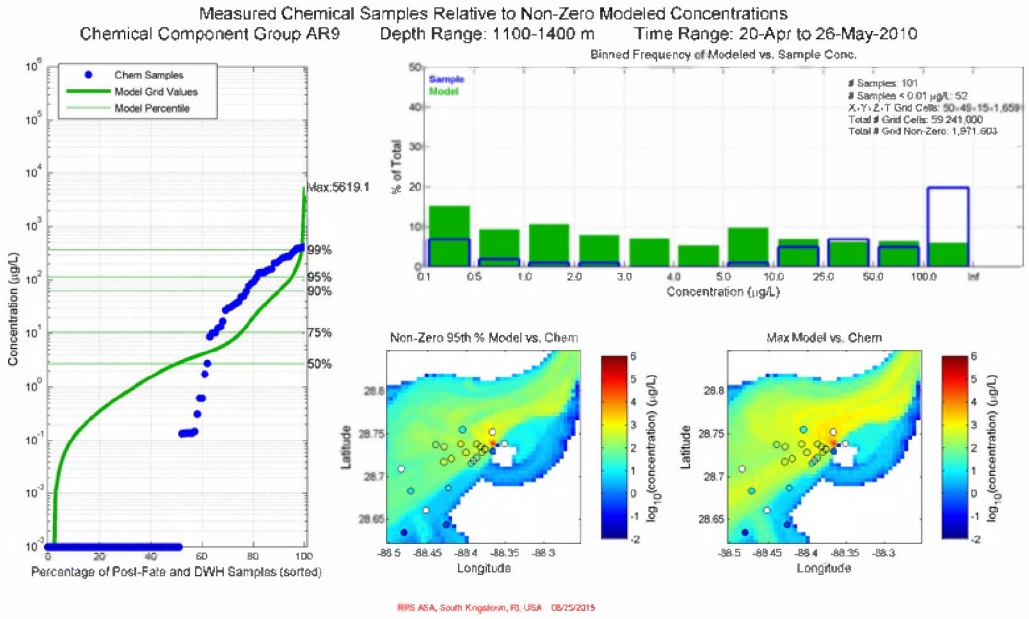

Figure G.3-96. Comparison of total (in-droplet + dissolved) concentrations (µg/L) produced by the simulation with IASROMS currents to measurements from chemistry samples for April 22 – May 26, 2010 in 1100-1400m: AR9 component (soluble alkanes). Left: Cumulative frequency distribution of concentrations for observed chemistry samples and gridded model results. The maximum modeled chemistry concentration is provided at the top of the panel. Top right: Histogram of binned concentrations for observed samples (blue) and gridded model results (green) plotted as the percentage of the total number of samples/grid cells. Center bottom and bottom right: Spatial color maps of the 95th percentile and maximum (respectively) modeled concentration within each grid cell over the time interval, overlaid with dots representing the chemistry sample observations. Open symbols indicate chemical concentrations below the analytical detection limit.

G.3.2 May 26 – June 6, 2010

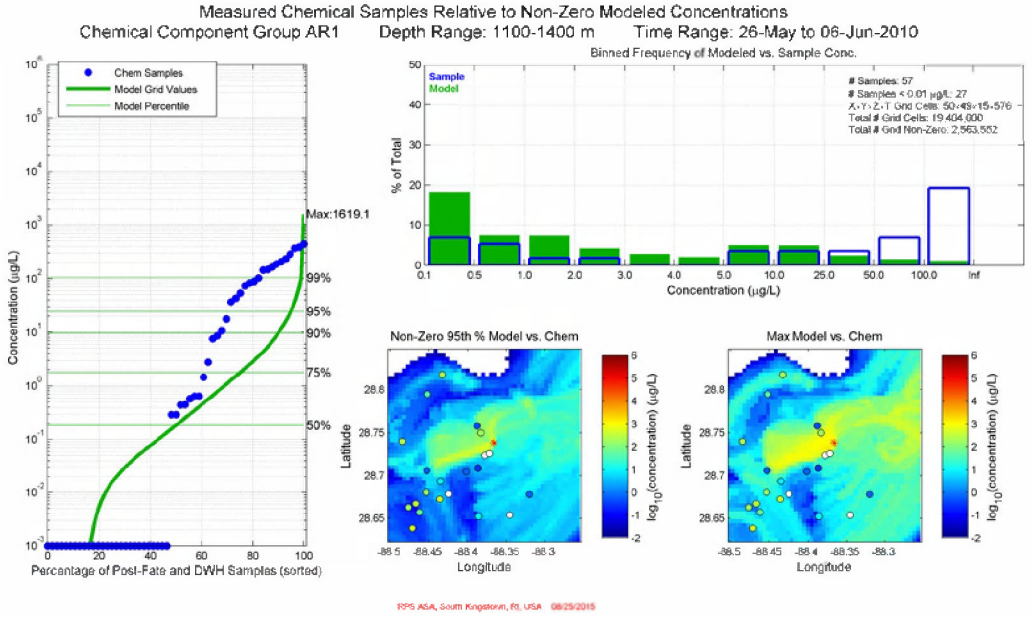

Figure G.3-97. Comparison of total (in-droplet + dissolved) concentrations (µg/L) produced by the simulation with IASROMS currents to measurements from chemistry samples for May 26 – June 6, 2010 in 1100-1400m: AR1 component (BTEX). Left: Cumulative frequency distribution of concentrations for observed chemistry samples and gridded model results. The maximum modeled chemistry concentration is provided at the top of the panel. Top right: Histogram of binned concentrations for observed samples (blue) and gridded model results (green) plotted as the percentage of the total number of samples/grid cells. Center bottom and bottom right: Spatial color maps of the 95th percentile and maximum (respectively) modeled concentration within each grid cell over the time interval, overlaid with dots representing the chemistry sample observations. Open symbols indicate chemical concentrations below the analytical detection limit.

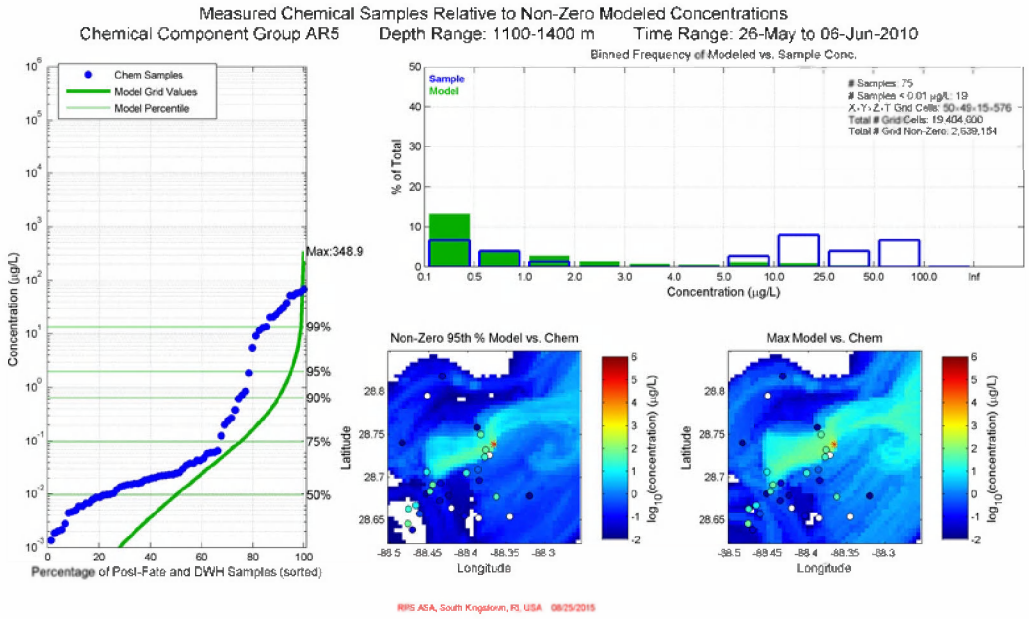

Figure G.3-98. Comparison of total (in-droplet + dissolved) concentrations (µg/L) produced by the simulation with IASROMS currents to measurements from chemistry samples for May 26 – June 6, 2010 in 1100-1400m: AR5 component (C0-C2 naphthalenes). Left: Cumulative frequency distribution of concentrations for observed chemistry samples and gridded model results. The maximum modeled chemistry concentration is provided at the top of the panel. Top right: Histogram of binned concentrations for observed samples (blue) and gridded model results (green) plotted as the percentage of the total number of samples/grid cells. Center bottom and bottom right: Spatial color maps of the 95th percentile and maximum (respectively) modeled concentration within each grid cell over the time interval, overlaid with dots representing the chemistry sample observations. Open symbols indicate chemical concentrations below the analytical detection limit.

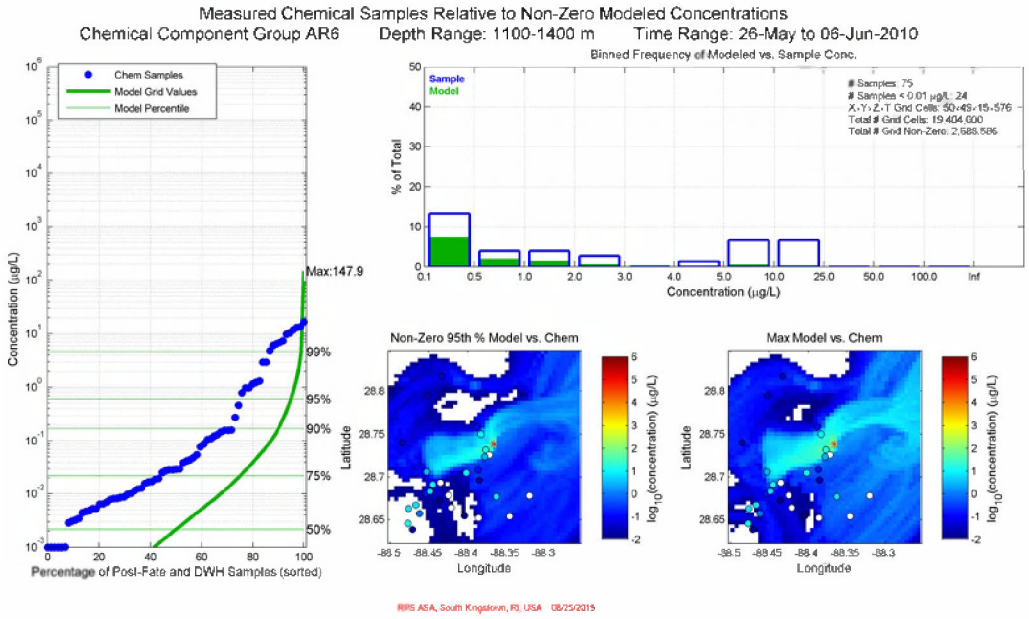

Figure G.3-99. Comparison of total (in-droplet + dissolved) concentrations (µg/L) produced by the simulation with IASROMS currents to measurements from chemistry samples for May 26 – June 6, 2010 in 1100-1400m: AR6 component (C3-C4 naphthalenes). Left: Cumulative frequency distribution of concentrations for observed chemistry samples and gridded model results. The maximum modeled chemistry concentration is provided at the top of the panel. Top right: Histogram of binned concentrations for observed samples (blue) and gridded model results (green) plotted as the percentage of the total number of samples/grid cells. Center bottom and bottom right: Spatial color maps of the 95th percentile and maximum (respectively) modeled concentration within each grid cell over the time interval, overlaid with dots representing the chemistry sample observations. Open symbols indicate chemical concentrations below the analytical detection limit.

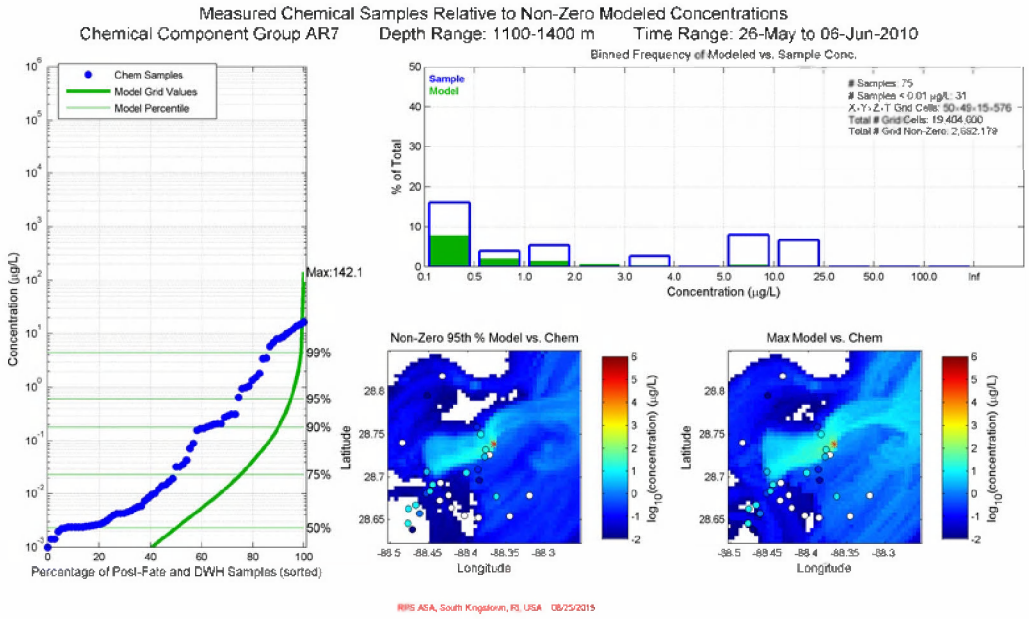

Figure G.3-100. Comparison of total (in-droplet + dissolved) concentrations (µg/L) produced by the simulation with IASROMS currents to measurements from chemistry samples for May 26 – June 6, 2010 in 1100-1400m: AR7 component (fluorenes & C0-C1 3-ring PAHs). Left: Cumulative frequency distribution of concentrations for observed chemistry samples and gridded model results. The maximum modeled chemistry concentration is provided at the top of the panel. Top right: Histogram of binned concentrations for observed samples (blue) and gridded model results (green) plotted as the percentage of the total number of samples/grid cells. Center bottom and bottom right: Spatial color maps of the 95th percentile and maximum (respectively) modeled concentration within each grid cell over the time interval, overlaid with dots representing the chemistry sample observations. Open symbols indicate chemical concentrations below the analytical detection limit.

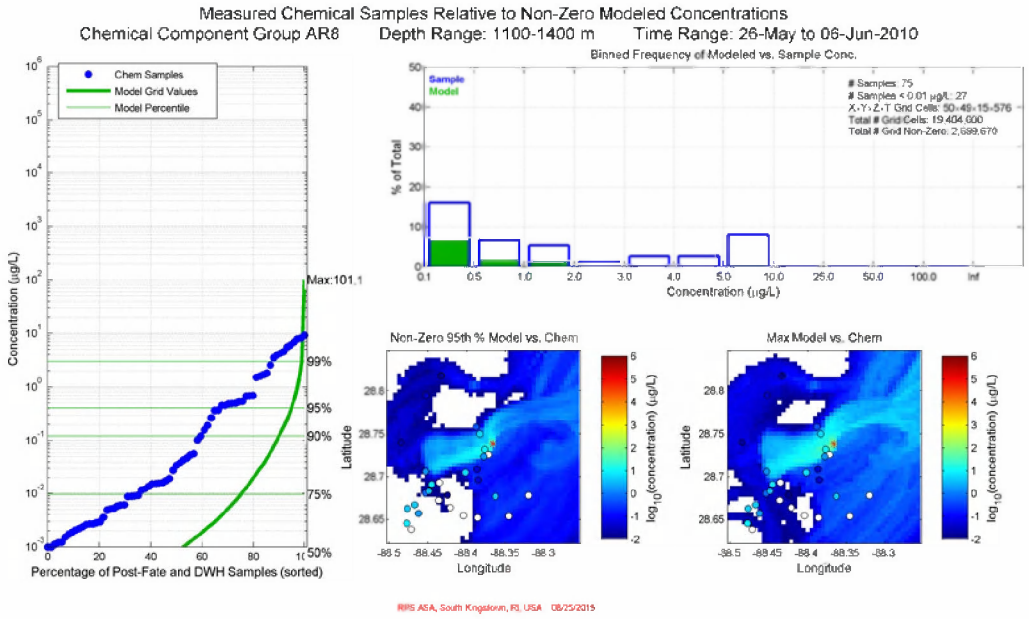

Figure G.3-101. Comparison of total (in-droplet + dissolved) concentrations (µg/L) produced by the simulation with IASROMS currents to measurements from chemistry samples for May 26 – June 6, 2010 in 1100-1400m: AR8 component (4-ring PAHs & C2-C3 3-ring PAHs). Left: Cumulative frequency distribution of concentrations for observed chemistry samples and gridded model results. The maximum modeled chemistry concentration is provided at the top of the panel. Top right: Histogram of binned concentrations for observed samples (blue) and gridded model results (green) plotted as the percentage of the total number of samples/grid cells. Center bottom and bottom right: Spatial color maps of the 95th percentile and maximum (respectively) modeled concentration within each grid cell over the time interval, overlaid with dots representing the chemistry sample observations. Open symbols indicate chemical concentrations below the analytical detection limit.

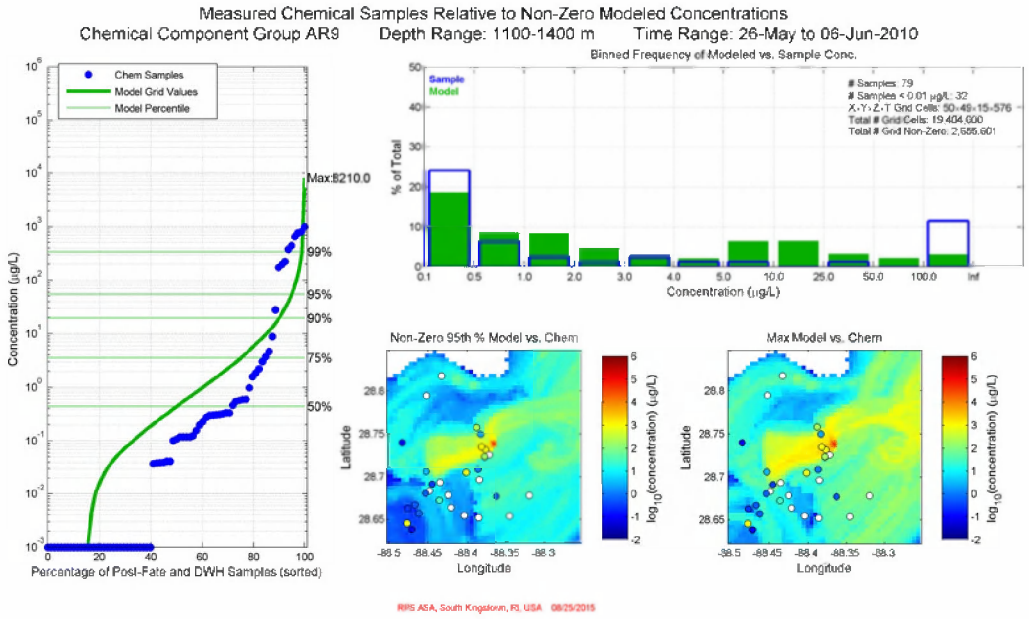

Figure G.3-102. Comparison of total (in-droplet + dissolved) concentrations (µg/L) produced by the simulation with IASROMS currents to measurements from chemistry samples for May 26 – June 6, 2010 in 1100-1400m: AR9 component (soluble alkanes). Left: Cumulative frequency distribution of concentrations for observed chemistry samples and gridded model results. The maximum modeled chemistry concentration is provided at the top of the panel. Top right: Histogram of binned concentrations for observed samples (blue) and gridded model results (green) plotted as the percentage of the total number of samples/grid cells. Center bottom and bottom right: Spatial color maps of the 95th percentile and maximum (respectively) modeled concentration within each grid cell over the time interval, overlaid with dots representing the chemistry sample observations. Open symbols indicate chemical concentrations below the analytical detection limit.

G.3.3 June 6 – July 15, 2010

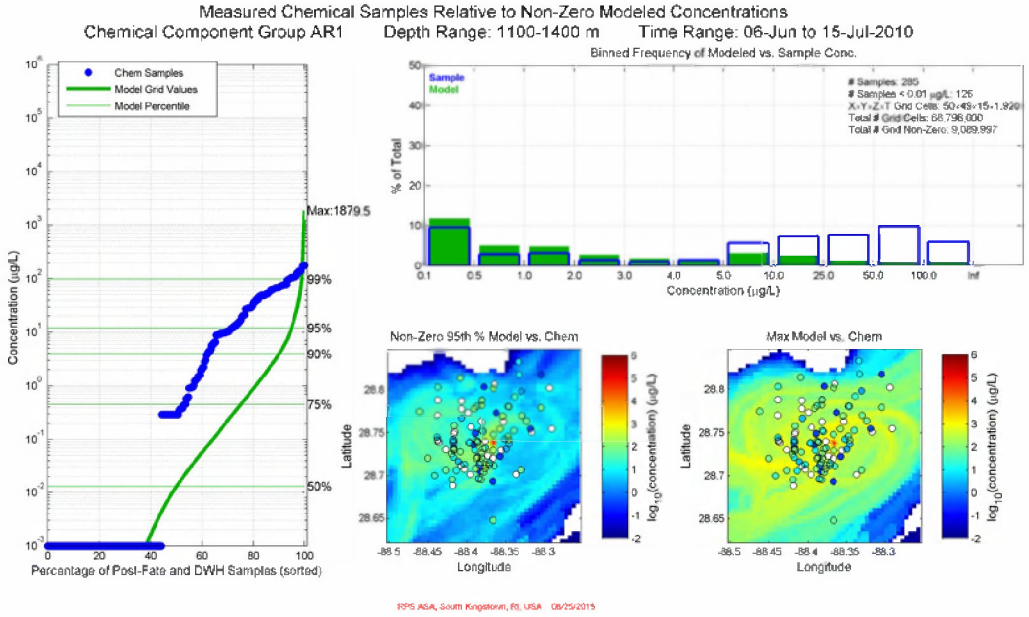

Figure G.3-103. Comparison of total (in-droplet + dissolved) concentrations (µg/L) produced by the simulation with IASROMS currents to measurements from chemistry samples for June 6 – July 15, 2010 in 1100-1400m: AR1 component (BTEX). Left: Cumulative frequency distribution of concentrations for observed chemistry samples and gridded model results. The maximum modeled chemistry concentration is provided at the top of the panel. Top right: Histogram of binned concentrations for observed samples (blue) and gridded model results (green) plotted as the percentage of the total number of samples/grid cells. Center bottom and bottom right: Spatial color maps of the 95th percentile and maximum (respectively) modeled concentration within each grid cell over the time interval, overlaid with dots representing the chemistry sample observations. Open symbols indicate chemical concentrations below the analytical detection limit.

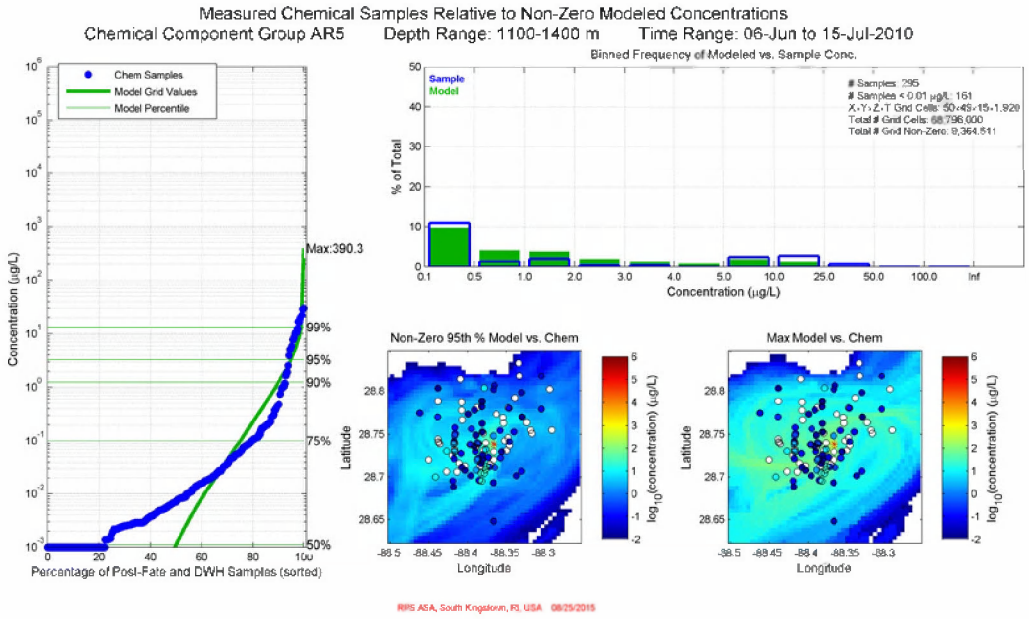

Figure G.3-104. Comparison of total (in-droplet + dissolved) concentrations (µg/L) produced by the simulation with IASROMS currents to measurements from chemistry samples for June 6 – July 15, 2010 in 1100-1400m: AR5 component (C0-C2 naphthalenes). Left: Cumulative frequency distribution of concentrations for observed chemistry samples and gridded model results. The maximum modeled chemistry concentration is provided at the top of the panel. Top right: Histogram of binned concentrations for observed samples (blue) and gridded model results (green) plotted as the percentage of the total number of samples/grid cells. Center bottom and bottom right: Spatial color maps of the 95th percentile and maximum (respectively) modeled concentration within each grid cell over the time interval, overlaid with dots representing the chemistry sample observations. Open symbols indicate chemical concentrations below the analytical detection limit.

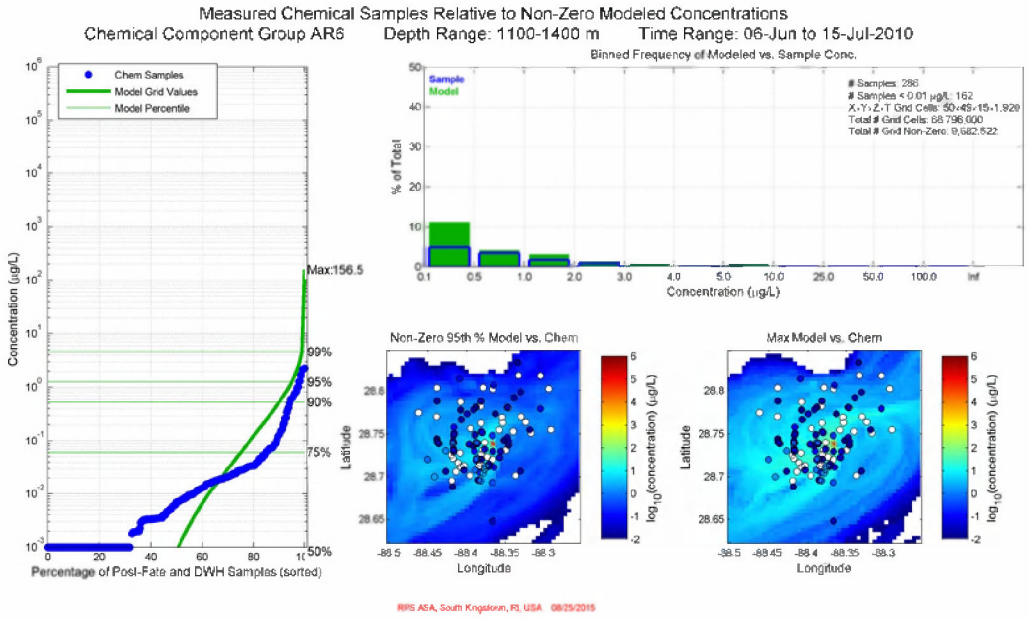

Figure G.3-105. Comparison of total (in-droplet + dissolved) concentrations (µg/L) produced by the simulation with IASROMS currents to measurements from chemistry samples for June 6 – July 15, 2010 in 1100-1400m: AR6 component (C3-C4 naphthalenes). Left: Cumulative frequency distribution of concentrations for observed chemistry samples and gridded model results. The maximum modeled chemistry concentration is provided at the top of the panel. Top right: Histogram of binned concentrations for observed samples (blue) and gridded model results (green) plotted as the percentage of the total number of samples/grid cells. Center bottom and bottom right: Spatial color maps of the 95th percentile and maximum (respectively) modeled concentration within each grid cell over the time interval, overlaid with dots representing the chemistry sample observations. Open symbols indicate chemical concentrations below the analytical detection limit.

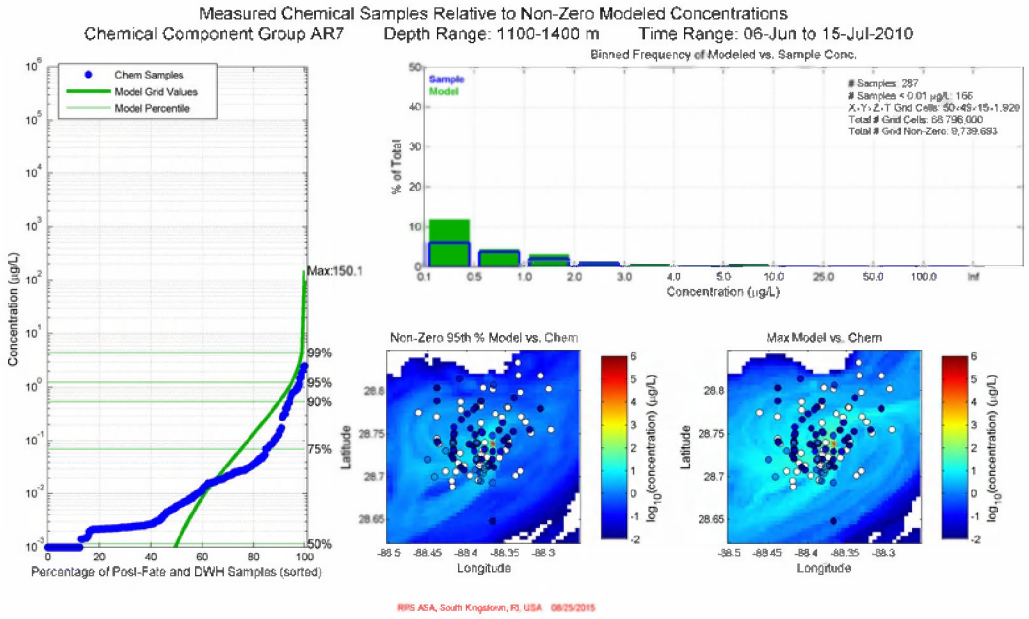

Figure G.3-106. Comparison of total (in-droplet + dissolved) concentrations (µg/L) produced by the simulation with IASROMS currents to measurements from chemistry samples for June 6 – July 15, 2010 in 1100-1400m: AR7 component (fluorenes & C0-C1 3-ring PAHs). Left: Cumulative frequency distribution of concentrations for observed chemistry samples and gridded model results. The maximum modeled chemistry concentration is provided at the top of the panel. Top right: Histogram of binned concentrations for observed samples (blue) and gridded model results (green) plotted as the percentage of the total number of samples/grid cells. Center bottom and bottom right: Spatial color maps of the 95th percentile and maximum (respectively) modeled concentration within each grid cell over the time interval, overlaid with dots representing the chemistry sample observations. Open symbols indicate chemical concentrations below the analytical detection limit.

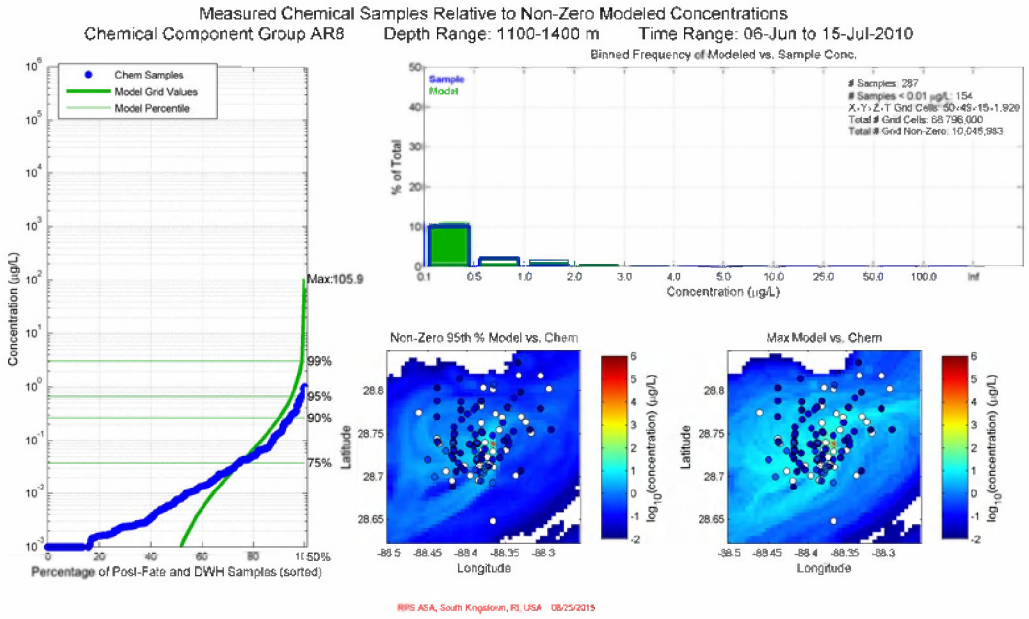

Figure G.3-107. Comparison of total (in-droplet + dissolved) concentrations (µg/L) produced by the simulation with IASROMS currents to measurements from chemistry samples for June 6 – July 15, 2010 in 1100-1400m: AR8 component (4-ring PAHs & C2-C3 3-ring PAHs). Left: Cumulative frequency distribution of concentrations for observed chemistry samples and gridded model results. The maximum modeled chemistry concentration is provided at the top of the panel. Top right: Histogram of binned concentrations for observed samples (blue) and gridded model results (green) plotted as the percentage of the total number of samples/grid cells. Center bottom and bottom right: Spatial color maps of the 95th percentile and maximum (respectively) modeled concentration within each grid cell over the time interval, overlaid with dots representing the chemistry sample observations. Open symbols indicate chemical concentrations below the analytical detection limit.

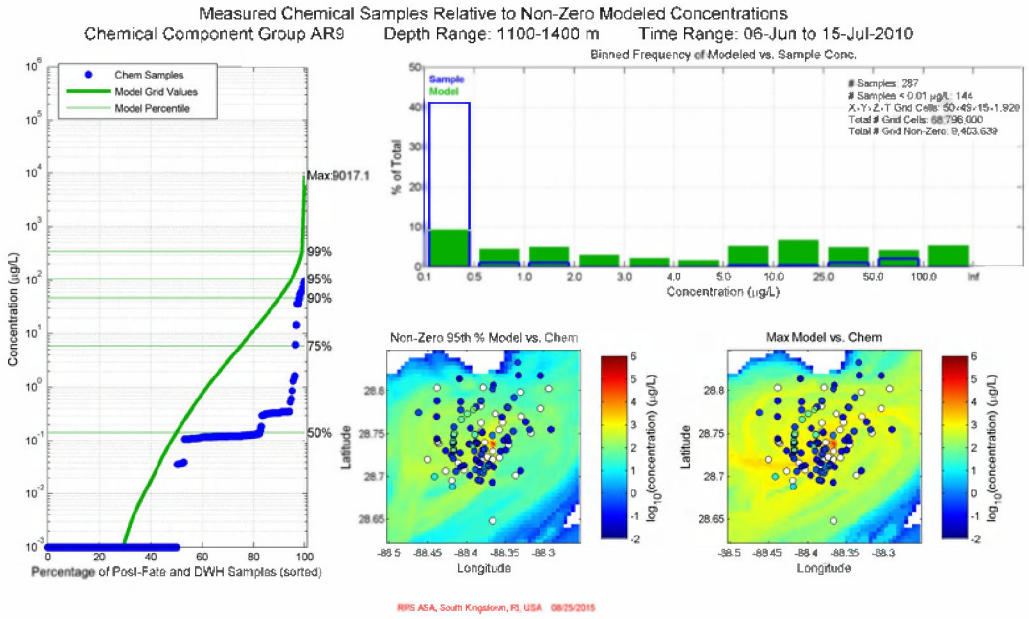

Figure G.3-108. Comparison of total (in-droplet + dissolved) concentrations (µg/L) produced by the simulation with IASROMS currents to measurements from chemistry samples for June 6 – July 15, 2010 in 1100-1400m: AR9 component (soluble alkanes). Left: Cumulative frequency distribution of concentrations for observed chemistry samples and gridded model results. The maximum modeled chemistry concentration is provided at the top of the panel. Top right: Histogram of binned concentrations for observed samples (blue) and gridded model results (green) plotted as the percentage of the total number of samples/grid cells. Center bottom and bottom right: Spatial color maps of the 95th percentile and maximum (respectively) modeled concentration within each grid cell over the time interval, overlaid with dots representing the chemistry sample observations. Open symbols indicate chemical concentrations below the analytical detection limit.